

NASA Conference Publication 3152
Part 2

International Symposium on Magnetic Suspension Technology

(NASA-CP-3152-Pt-2) INTERNATIONAL SYMPOSIUM
ON MAGNETIC SUSPENSION TECHNOLOGY, PART 2
(NASA) 459 p

N92-27788
--THRU--
N92-27816
Unclass

H1/18 0091552

*Proceedings of an international symposium held at
Langley Research Center
Hampton, Virginia
August 19-23, 1991*



*NASA Conference Publication 3152
Part 2*

International Symposium on Magnetic Suspension Technology

Edited by
Nelson J. Groom
*NASA Langley Research Center
Hampton, Virginia*

Colin P. Britcher
*Old Dominion University
Norfolk, Virginia*

Proceedings of an international symposium sponsored by the
National Aeronautics and Space Administration,
Washington, D.C., and held at
Langley Research Center
Hampton, Virginia
August 19–23, 1991



National Aeronautics and
Space Administration
Office of Management
Scientific and Technical
Information Program

1992

INTRODUCTION

An International Symposium on Magnetic Suspension Technology was held at the Langley Research Center in Hampton, Virginia, on August 19–23, 1991. The symposium was sponsored by the Langley Research Center in coordination with the office of Aeronautics, Exploration, and Technology (OAET) in NASA Headquarters and was hosted by the Spacecraft Controls Branch at Langley Research Center. The symposium was chaired by the following people:

Nelson J. Groom, Co-Chairman
NASA
Langley Research Center
Hampton, VA 23665-5225

Dr. Robert A. Kilgore, Co-Chairman
NASA
Langley Research Center
Hampton, VA 23665-5225

Dr. Colin P. Britcher, Technical Program Co-Chairman
Dept. of Mechanical Engineering and Mechanics
Old Dominion University
Norfolk, VA 23529-0247

Dr. James R. Downer, Technical Program Co-Chairman
SatCon Technology Corporation
12 Emily Street
Cambridge, MA 02139-4507

Emily E. Kornegay, Administrative Chairman
NASA
Langley Research Center
Hampton, VA 23665-5225

The goal of the symposium was to examine the state of technology of all areas of magnetic suspension and to review related recent developments in sensors and controls approaches, superconducting magnet technology, and design/implementation practices. The symposium included 17 technical sessions in which 55 papers were presented. The technical sessions covered the areas of bearings, sensors and controls, microgravity and vibration isolation, superconductivity, manufacturing applications, wind tunnel magnetic suspension systems, magnetically levitated trains (MAGLEV), space applications, and large gap magnetic suspension systems. A list of attendees appears at the end of the document.

Certain materials and processes are identified in this publication in order to adequately specify procedures. In no case does such identification imply recommendation or endorsement by the government, nor does it imply that the materials or processes are the only or best ones available for the purpose.

CONTENTS

Introduction	iii
-------------------------------	------------

Part 1*

Session 1 - Introductions and Review Papers

Chairman - Robert A. Kilgore, NASA Langley Research Center

Overview of Magnetic Suspension Research at NASA Langley Research Center	3
Nelson J. Groom	
Professor Jesse W. Beams and the First Practical Magnetic Suspension	25
Paul E. Allaire, Robert R. Humphris, and David W. Lewis	
Large-Gap Magnetic Suspension Systems	33
Colin P. Britcher	

Session 2 - Bearings 1

Chairman - Paul E. Allaire, University of Virginia

Magnetic Bearings: A Key Technology for Advanced Rocket Engines?	53
J. Ph. Girault	
Active Magnetic Bearings—As Applied to Centrifugal Pumps	73
Lev Nelik, Paul Cooper, Graham Jones, Dennis Galecki, Frank Pinckney, and Gordon Kirk	
Precision Magnetic Suspension Linear Bearing	89
David L. Trumper and Michael A. Queen	
Modelling and Design for PM/EM Magnetic Bearings	105
D. Pang, J. A. Kirk, D. K. Anand, R. G. Johnson, and R. B. Zmood	

Session 3 - Sensors and Controls 1

Chairman - Mark Motter, NASA Langley Research Center

Application of Narrow Band Control to Reduce Vibrations in Magnetic Bearing Systems	123
Monique S. Gaffney and Bruce G. Johnson	
Dynamics and Control of High Precision Magnetically Levitated Vibration Isolation Systems	149
K. Youcef-Toumi and T-J Yeh	
Stability and Performance of Notch Filter Controllers for Unbalanced Response	181
Carl R. Knospe	

*Part 1 is presented under separate cover.

Session 4 - Microgravity and Vibration Isolation 1

Chairman - Mike Scott, NASA Langley Research Center

- A Six Degree-of-Freedom Magnetic Bearing for Microgravity Vibration Isolation** 209
A. Peter Allan, Carl R. Knospe
- A Six Degree-of-Freedom Lorentz Force Vibration Isolator with Nonlinear Controls** 219
Ralph C. Fenn, Michael Gerver, and Bruce Johnson

Session 5 - Superconductivity 1

Chairman - Jim Downer, SatCon Technology Corporation

- Recent Progress Towards Developing a High Field, High- T_c Superconducting Magnet for Magnetic Suspension and Balance Systems** 247
L. Pierre de Rochemont, Carlton E. Oakes, Michael R. Squillante, Hong-Min Duan, Allen M. Hermann, Robert J. Andrews, Roger B. Poeppel, Victor A. Maroni, Ingrid A. Carlberg, and Warren C. Kelliher
- Levitation of $YBa_2Cu_3O_{7-x}$ Superconductor in a Variable Magnetic Field** 267
Alexander N. Terentiev and Anatoliy A. Kuznetsov
- Hybrid Superconducting Magnetic Bearing (HSMB) for High Load Devices** 279
C. K. McMichael, K. B. Ma, M. A. Lamb, M. W. Lin, L. Chow, R. L. Meng, P. H. Hor, and W.-K. Chu
- Characterization of Superconducting Magnetic Bearings (Dynamic stiffness and damping coefficients in axial direction)** 289
Ryoichi Takahata, Hirochika Ueyama, and Tsutom Yotsuya

Session 6 - Bearings 2

Chairman - Claude Keckler, NASA Langley Research Center

- Feasibility of Magnetic Bearings for Advanced Gas Turbine Engines** 299
David Hibner and Lewis Rosado
- Low Power Magnetic Bearing Design for High Speed Rotating Machinery** 317
P. E. Allaire, E. H. Maslen, R. R. Humphris, C. K. Sortore, and P. A. Studer
- Progress of Magnetic Suspension Systems and Magnetic Bearings in the USSR** 331
A. V. Kuzin

Session 7 - Sensors and Controls 2

Chairman - Monique Gaffney, SatCon Technology Corporation

- Extended H_2 Synthesis for Multiple Degree-of-Freedom Controllers** 363
R. David Hampton and Carl R. Knospe - University of Virginia

Experimental Results in Nonlinear Compensation of a One Degree-of-Freedom Magnetic Suspension	385
David L. Trumper, James C. Sanders, Tiep H. Nguyen, and Michael A. Queen	
Control Concepts for Active Magnetic Bearings	401
R. Siegwart, D. Vischer, R. Larssonneur, R. Herzog, A. Traxler, H. Bleuler, and G. Schweitzer	
Computer Aided Design of a Digital Controller for Radial Active Magnetic Bearings	423
Zhong Cai, Zupei Shen, Zuming Zhang, and Hongbin Zhao	

Session 8 - Microgravity and Vibration Isolation 2

Chairman - Ralph Fenn, SatCon Technology Corporation

A Microgravity Vibration Isolation Rig	435
Bibhuti B. Banerjee, Carl R. Knospe, and Paul E. Allaire	
Vibration Damping of Elastic Waves in Electrically Conducting Media Subjected to High Magnetic Fields	457
T. G. Horwath	
Coarse-Fine Residual Gravity Cancellation System with Magnetic Levitation	473
S. E. Salcudean, H. Davis, C. T. Chen, D. E. Goertz, and B. V. Tryggvason	
Attendees	493

Part 2

Session 9 - Superconductivity 2

Chairman - Warren C. Kelliher, NASA Langley Research Center

Magnetic Suspension Using High Temperature Superconducting Cores	507
R. G. Scurlock	
Effect of Flux Penetration on the Load Capacity of Passive Superconducting Bearings	519
Dantam K. Rao	
Application of Ceramic Superconductors in High Speed Turbines	535
C. K. McMichael, M. A. Lamb, M. W. Lin, K. B. Ma, and W. K. Chu	
Cryogenic Test Rig with an Aerodynamic Magnetically Levitated Carriage	547
Sergey Yu. Borisov, Anton L. Iskra, and Anatoly P. Philatov	

Session 10 - Bearings 3

Chairman - Jim Downer, SatCon Technology Corporation

The Bearingless Electrical Machine	561
J. Bichsel	

Wide Gap, Permanent Magnet Biased Magnetic Bearing System	575
Karl Boden	
Force Analysis of Magnetic Bearings with Power-Saving Controls	595
Dexter Johnson, Gerald V. Brown, and Daniel J. Inman	

Session 11 - Manufacturing Applications

Chairman - Nelson J. Groom, NASA Langley Research Center

Manipulation and Identification of Objects by Magnetic Forces	617
Benjamin Joffe	
Precise Positioning and Compliance Synthesis for Automatic Assembly Using Lorentz Levitation	639
R. L. Hollis and S. Salcudean	

Session 12 - Bearings 4

Chairman - Timothy Hawkey, SatCon Technology Corporation

Development of a Differentially Balanced Magnetic Bearing and Control System for use with a Flywheel Energy Storage System	657
Mark A. Higgins, David P. Plant, Douglas M. Ries, James A. Kirk, and Davinder K. Anand	
Design of Bearings for Rotor Systems Based on Stability	673
D. Dhar, L. E. Barrett, and C. R. Knospe	
An Evaluation of Some Strategies for Vibration Control of Flexible Rotors	691
C. R. Burrows	

Session 13 - Wind Tunnel Magnetic Suspension Systems

Chairman - Robert A. Kilgore, NASA Langley Research Center

Propulsion Simulator for Magnetically Suspended Wind Tunnel Models	709
P. B. Joshi, M. R. Malonson, G. P. Sacco, C. L. Goldey, K. Garbutt, M. Goodyer, and P. Lawing	
Present Status of the MIT/NASA Langley 6 inch MSBS	741
Timothy Schott, Thomas Jordan, and Taumi Daniels	
Progress of Magnetic Suspension and Balance Systems for Wind Tunnels in the USSR	765
A. V. Kuzin, Y. D. Vyshkov, and G. K. Shapovalov	
Wind Tunnel Magnetic Suspension Systems at the University of Southampton, England	775
Michael J. Goodyer	

Session 14 - Magnetically Levitated Trains (MAGLEV) 1

Chairman - Colin P. Britcher, Old Dominion University

Attractive and Repulsive Magnetic Suspension Systems Overview	791
David B. Cope and Richard R. Fontana	
Change in the Coil Distribution of Electrodynamic Suspension System	813
Hisashi Tanaka	
The Concept of the Mechanically Active Guideway as a Novel Approach to Maglev	827
T. G. Horwath	

Session 15 - Space Applications

Chairman - Nelson J. Groom, NASA Langley Research Center

Space Applications of Diamagnetic Suspensions	847
Ronald E. Pelrine	
Magnetic Bearing Wheels for Very High Pointing Accuracy Satellite Missions	857
J. P. Roland	
An Electrostatically Suspended, Micro-Mechanical Rate Gyroscope	873
Timothy Hawkey and Richard Torti	

Session 16 - Magnetically Levitated Trains (MAGLEV) 2

Chairman - Colin P. Britcher, Old Dominion University

Battery Cars on Superconducting Magnetically Levitated Carriers—One Commuting Solution	895
B. Mike Briggs and Henry Oman	
Knolle Magnettrans, A Magnetically Levitated Train System	907
Ernst G. Knolle	
Computation of Magnetic Suspension of Maglev Systems Using Dynamic Circuit Theory	919
J. L. He, D. M. Rote, and H. T. Coffey	

Session 17 - Large-Gap Magnetic Suspension Systems

Chairman - Nelson J. Groom, NASA Langley Research Center

Large-Gap Magnetic Positioning System Having Advantageous Configuration	941
Paul Chong, Colin Commandeur, Harold Davis, and Lorne Whitehead	
Performance of a Superconducting Large-Angle Magnetic Suspension	955
James R. Downer, Dariusz A. Bushko, Vijay Gondhalekar, and Richard P. Torti	

The Large-Angle Magnetic Suspension Test Fixture	971
Colin P. Britcher, Mehran Ghofrani, Thomas C. Britton, and Nelson J. Groom	
Attendees	987

Part 2

Session 9

SUPERCONDUCTIVITY 2

Chairman - Warren C. Kelliher
NASA Langley Research Center

N92-27789

MAGNETIC SUSPENSION USING HIGH TEMPERATURE SUPERCONDUCTING CORES

R G Scurlock
Institute of Cryogenics, University of Southampton, UK

SUMMARY

The development of YBCO high temperature superconductor, in wire and tape forms, is rapidly approaching the point where the bulk transport current density j vs magnetic field H characteristics with liquid nitrogen cooling will enable its use in model cores. On the other hand, BSCCO high temperature superconductor in wire form has poor j - H characteristics at 77K today, although with liquid helium or hydrogen cooling, it appears to be superior to NbTi superconductor.

Since liquid nitrogen cooling is approximately 100 times cheaper than liquid helium cooling, the use of YBCO is very attractive for use in magnetic suspension.

This paper discusses the design of a model core to accommodate lift and drag loads up to 6000 and 3000 N respectively. A comparison is made between the design performance of a liquid helium cooled NbTi (or BSCCO) superconducting core and a liquid nitrogen cooled YBCO superconducting core.

INTRODUCTION

The concept of using a superconducting core with a persistent mode energising current, contained within a free-flying, liquid helium cooled cryostat was successfully demonstrated with a Mark I model at Southampton, UK in a wind-tunnel magnetic suspension system in 1981⁽¹⁾⁽²⁾. A subsequent design for a Mark 2 free-flying cryostat 800 mm long 126 mm diameter with a liquid helium cooled superconducting core was made in 1984⁽³⁾. This cryostat accommodated lift and drag loads up to 6000N and 3000N respectively and had a sufficiently low liquid helium boil-off to enable polars to be taken over a working period of 3 hours. The solenoid design used a 40A NbTi conductor operating in a central field of 6.5T at a current density of $3 \times 10^4 \text{ A/cm}^2$ yielding a magnetic moment of approximately 30×10^{-3} Weber metre. A further design⁽⁴⁾ for a shortened (450 mm long) version called the Mark 1½ cryostat, was made in 1985 which included all the features of the Mark 2 cryostat; the shorter length enabled the cryostat to be flight tested in the existing magnetic suspension system at Southampton. An additional feature was the introduction of superconducting roll coils in the bore of the main solenoid.

With the discovery and development of high temperature superconductors with critical temperatures above 90K, it is particularly worthwhile to examine the use of these new materials, in the persistent energised mode, for the model cores of a magnetic suspension system.

HIGH TEMPERATURE SUPERCONDUCTORS

Since 1986, a number of materials have been discovered with superconducting transition temperatures significantly higher than those of the liquid helium cooled Type II superconductors of the 1960's and 1970's.

Figure 1 gives a summary of the present position (August 1991) regarding the j - H bulk current density versus magnetic field performance of these new superconductors in comparison with the performance of the widely used liquid helium cooled NbTi and Nb₃Sn superconductors. The data in Figure 1 is for current carrying conductors in wire, tape or thick film form - not thin films ($< 1\mu$ thick) for which much higher current densities j are observed.

The most significant indication from Figure 1 is that current densities in excess of 10^4A/cm^2 at 6.5T can be achieved at a temperature of 77K with YBCO and at 20K with BSCCO. There are, of course, development problems to be overcome at this stage, because these high temperature superconductors are composed of brittle ceramic materials. However, many research laboratories throughout the world are addressing these problems in order to realise the potential of high temperature superconductors in a wide range of applications. For example, current contacts, superconducting joints, persistent current switches, and the construction of composite thermally stabilised and load bearing conductors, are all areas being widely addressed.

THE COOLING OF HIGH TEMPERATURE SUPERCONDUCTORS

While the performance of BSCCO may be realised using liquid hydrogen at 20K, the performance of YBCO requires liquid nitrogen cooling at 77K. No expensive liquid cryogen is required; only low cost liquid nitrogen at perhaps 1-5% of the cost of liquid helium. Unlike liquid helium with its low heat of vaporisation, liquid nitrogen has a latent heat per unit mass some 10 times larger. Taking into account the density difference (a ratio of approximately 6), the volume of liquid nitrogen required to absorb a given heat load is therefore about 60 times smaller. Alternatively, for the same volume of cryogen, one can accept a heat influx 60 times larger and maintain the same operating time.

CRYOSTAT CONTAINMENT AND THERMAL INSULATION

With liquid nitrogen cooling, the limitations of vacuum insulation are no longer necessary for containment. This means that the simplicity of plastic foam insulations is available to provide the necessary thermal insulation. However in the case of the model core, the volume of insulation space needs to be minimised to accommodate the necessary volume of superconducting solenoid to provide the maximum magnetic moment. It would

therefore appear that this is one exception where vacuum insulation can be retained beneficially. The core cylindrical geometry, of course, lends itself to vacuum anyway. Table I provides an indication of the relative performance of different types of insulation across 2.5 cm thickness between 300 and 77K.

Table I shows quite clearly that 4mm of multi-layer insulation MLI in vacuum yields a heat flux approximately 100 times lower than 25mm of polyurethane foam, and 4 times lower than 25mm of evacuated perlite powder.

The conclusion is quite clear; keep to evacuated MLI for minimum heat flux if the thickness of the insulation space is to be minimised.

HIGH LIFT AND DRAG LOADS

The lift and drag loads have to be transferred from the solenoid core to the outer wall of the cryostat through the insulation space, and thence to the model. A number of options are available for transferring these loads. With a high temperature superconducting core, it is tempting to consider the use of plastic foam (Option A) to provide the insulation as well as to transfer the flight loads. The alternative option, Option B, is to use an array of suitable high strength struts in an evacuated enclosure of MLI.

In examining these 2 options, it should be noted that there are 2 operational modes (I) high load flight conditions during polars (II) low load, holding conditions in between polars.

Option A and mode I require a foam capable of transmitting a transverse (radial) load of 6000 N across an area of approximately 50 cm² representing a loading of 1 MPa at 77 K; and a longitudinal load of 3000 N across an area of approximately 25 cm² representing the same loading per unit area. For acceptable nesting of the core, the foam must clearly not suffer any permanent deformation, otherwise the required tight fit of the core will be lost. We therefore need a high density, load-bearing foam which retains its elasticity at 77K up to 1 MPa.

Option A and mode II require the foam to carry zero flight loads only. However, the heat flux is likely to be relatively insensitive to loading, up to the elastic limit of the foam. It follows that Option A will lead to the same high heating loads during both operating modes.

Option B in Mode I requires the use of high strength radial struts to carry the flight loads. To transmit a radial load of 6000 N in compression, the minimum cross section of 304 stainless steel strut would be 6 mm². For epoxy glass fibre laminate in compression, the minimum cross section would be 12 mm². However, the thermal conductance of the epoxy laminate strut would be 5-10 times lower. The drag load of 3000N may be carried by one or more axial rods of epoxy glass fibre in tension.

Option B in mode II requires a much lower strength strut system to yield minimum heat flux during extended periods of holding. The simplest approach is to adopt a dual suspension system, a weak one for B (II) which holds off a strong B(I) system from any thermal contact thereby maintaining a low thermal conductance state in mode II. The system distorts elastically under high flight loads in mode I operation to allow the strong system to take over in a higher thermal conductance state. These dual suspension systems have been used successfully in the past for rocket-launching cryogenic equipment into space. The weak suspension can be achieved via a dished or cone-shaped strut system, while the strong suspension has a co-planar structure such as an 8-pointed star cut from a thick sheet of epoxy resin. (Figures 2, 3, and 4). While such a dual suspension is essential for the liquid helium cooled superconducting core, it may not be necessary for the liquid nitrogen cooled core.

LIQUID HANDLING, FILLING AND LOW BOIL OFF

The model core geometry requires the liquid fill and vapour vent lines to be at one, or both, ends. One end is preferred to enable unimpeded differential thermal contraction to take place. Since the cryostat is required to operate with its axis horizontal and at variable angles to the horizontal, the liquid fill line must contain a cold liquid/vapour separator. The simplest solution is for the liquid fill line to include a single turn 360° helical turn inside the insulated space. This requirement is not required for the vent-line, provided a vapour/liquid separator is included inside the cryostat. However, vapour cooling of the current leads to the solenoid must be provided, and the simplest solution is to enclose the current leads in the vapour vent line. If the cooled length of the leads cannot be met via a re-entrant vacuum insulated end bush, then it may be necessary to include a segment of a helical turn, say 90° in the insulated space.

DESIGN AND PREDICTED PERFORMANCE

The performance of a Mark 2 LHe cooled NbTi superconductor core and cryostat is compared in Table II with that of a Mark 3 LIN cooled YBCO core and cryostat designed to the same overall dimensions of 800 mm length, 126 mm diameter. Figure 2 is a schematic diagram of the 2 cryostats, while Figures 3 and 4 indicate the detailed construction of the ends of the 2 cryostats respectively. The main difference in construction lies with the absence of the intermediate temperature, vapour-cooled shield around the YBCO core, which was a necessity with the NbTi core in order to reduce the liquid helium boil-off to an acceptable performance level. This allows an increase in diameter of the winding space of some 5 mm, and an increase in length of 50 mm. Together, these changes allow an increase in volume of 16% of the winding volume, and a corresponding increase in magnetic moment for the same current density.

CONCLUSIONS

(i) For the liquid helium cooled core, the difference in heat leak between Mode I and Mode II operation is a factor of 5. For the liquid nitrogen cooled core, on the other hand, the estimated difference in heat leak is much smaller at 25%. It is therefore concluded that while the dual suspension system is vital for incorporation in the liquid helium cooled cryostat, it may be unnecessary to introduce this complication with the liquid nitrogen cooled cryostat.

(ii) While the duration of cryogen for the liquid helium cooled system meets the specification for 3 hours operation under Mode I operation, the liquid nitrogen hold times are excessively long. It might therefore be advantageous to increase the winding volume of the solenoid by $1.5 \times 10^6 \text{ mm}^3$ thereby reducing the liquid nitrogen volume by 50%.

(iii) The energisation of a NbTi superconducting solenoid in the persistent current state is standard practise using superconducting switches or shunts across the solenoid windings. The use of YBCO superconductor in a persistent current state is yet to be demonstrated. However the formation of truly superconducting (zero resistance) joints with zero Joule heating between ceramic wires or tapes, which a conventional liquid helium cooled superconducting switch requires, may not be essential bearing in mind that the excess cooling capacity by evaporation of the liquid nitrogen would be capable of absorbing a few watts of Joule heating.

(iv) Associated with (iii), another source of Joule heating with an YBCO solenoid in the persistent current state is the phenomenon of flux creep and decay. As observed at present, the magnetisation decays exponentially to a lower steady-state value. Depending on the time constant and the magnitude of the decay (the order of a few per cent) this might be a problem until the steady state magnetisation state was reached.

(v) Like other applications of high temperature superconductors, the ease with which liquid nitrogen cooling can be used, together with the simplicity of the cryogenic engineering design of the necessary cryostat, makes the future use of these materials in a magnetic suspension system extremely attractive.

REFERENCES

1. Wu, Y.Y.: "Design of a horizontal liquid helium cryostat for refrigerating a flying superconducting magnet in a wind-tunnel". University of Southampton M.Sc thesis (December 1981) NASA-CR-165980, August 1982
2. Britcher, C.P.; Goodyer, M.J.; Scurlock, R.G.; and Wu, Y.Y.: "A flying superconducting magnet and cryostat for magnetic suspension of wind tunnel models". Cryogenics 24, pp 185-189 1989
3. Boom, R.W.; Eyssa, Y.M.; McIntosh, G.E.; Abdelsalem, M.K.; Scurlock, R.G.; Wu, Y.Y.; Goodyer, M.J.; Balcerek, K.; Eskins, J.; Britcher, C.P.: "Superconducting electromagnets for large wind tunnel magnetic suspension and balance systems". Proc. Applied Superconductivity Conference, San Diego, Paper FL-3, 1984
4. Goodyer, M.J.; and Scurlock, R.G.: "Research into superconducting solenoid models for large MSB systems". NASA NSG 7523, 1985

TABLE I. - PERFORMANCE OF INSULATION

Material	Heat flow (W) across 2.5 cm thickness 1 m ² area between 300 and 77 K
Stainless steel	160,000
Epoxy-glass fibre laminate	2,800
Polyurethane foam	200
Perlite powder + vacuum	8
Multi-layer reflectors + vacuum	0.3
Vacuum in glass (across 1-4mm)	500
Vacuum in glass with silvering (across 1-4mm)	8
Vacuum in metal with multi-layer reflectors (across 4mm)	2

TABLE II. - CRYOSTAT DESIGNS

	NbTi core Mark 2 Helium cryostat	YBCO core Mark 3 LIN cryostat
Overall length (mm)	800	800
Overall diameter (mm)	126.2	126.2
Overall volume (mm ³)	9.90 10 ⁶	9.90 10 ⁶
Length of winding space (mm)	650	700
OD of winding space (mm)	107	112
ID of winding space (mm)	75	75
Current density in winding space A/cm ²	3 10 ⁴	3 10 ⁴
Field at centre (Tesla)	6.5	6.5
Magnetic moment (Weber m)	29.5 10 ⁻³	34.8 10 ⁻³
Magnetic moment of Vanadium/Permender occupying cryostat volume	15.7 10 ⁻³	15.7 10 ⁻³
S/C magnet moment/VP moment	1.88	2.22
Length of cryogen container (mm)	690	720
OD of cryogen container (mm)	108	115
Volume of cryogen container (mm ³)	6.3 10 ⁶	7.4 10 ⁶
Volume of cryogen (allowing for core) cm ³	3000	3400
Heat inleak Mode I operation (mW)	700	2300
Boil-off rate Mode I (cm ³ /hr)	1000	60
Duration of cryogen Mode I operation (hours)	3	50
Heat inleak Mode II operation (mW)	140	1800
Boil-off rate Mode II operation (cm ³ /hr)	200	45
Duration of cryogen Mode II operation (hours)	15	66

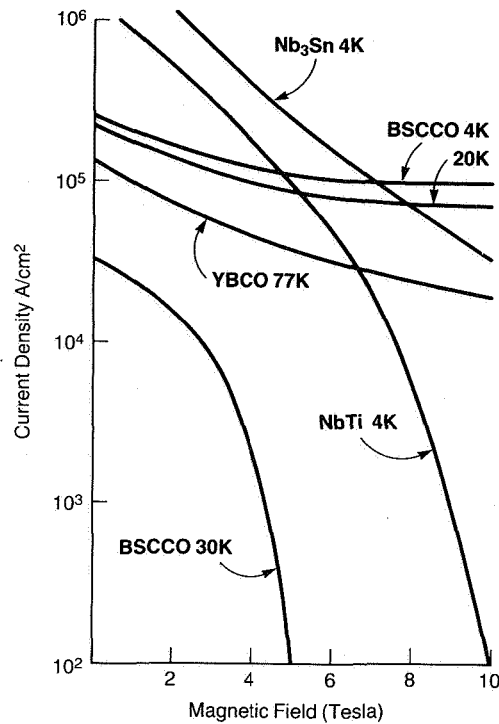
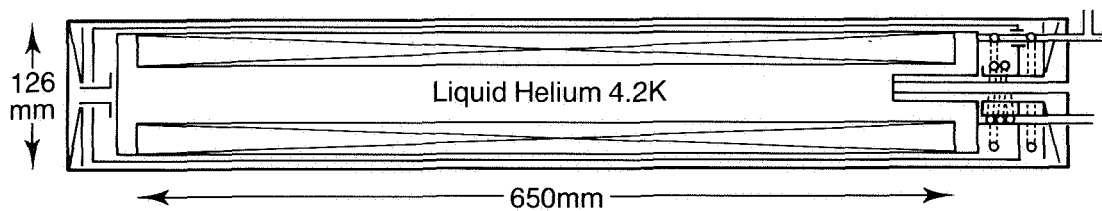


Figure 1. Current density vs magnetic field j-H performance of superconductors August 1991

Flying Cryostat and NbTi Solenoid Mark 2



Flying Cryostat and YBCO Solenoid Mark 3

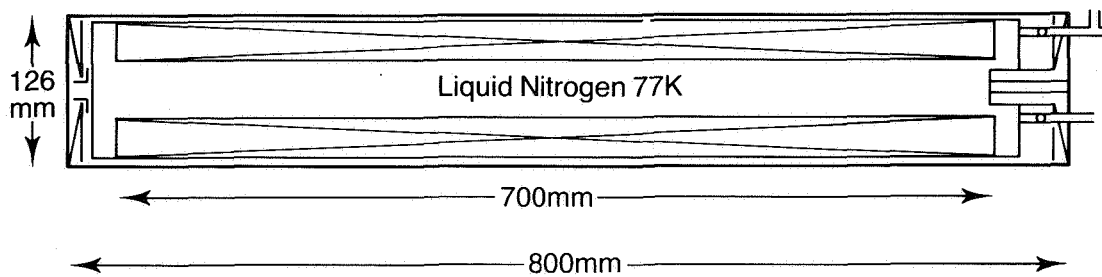


Figure 2. Schematic of flying cryostats using liquid helium cooled NbTi (Mark 2) and liquid nitrogen cooled YBCO (Mark 3) solenoids

Flying Cryostat and Superconducting Solenoid Mark 2. Detail.

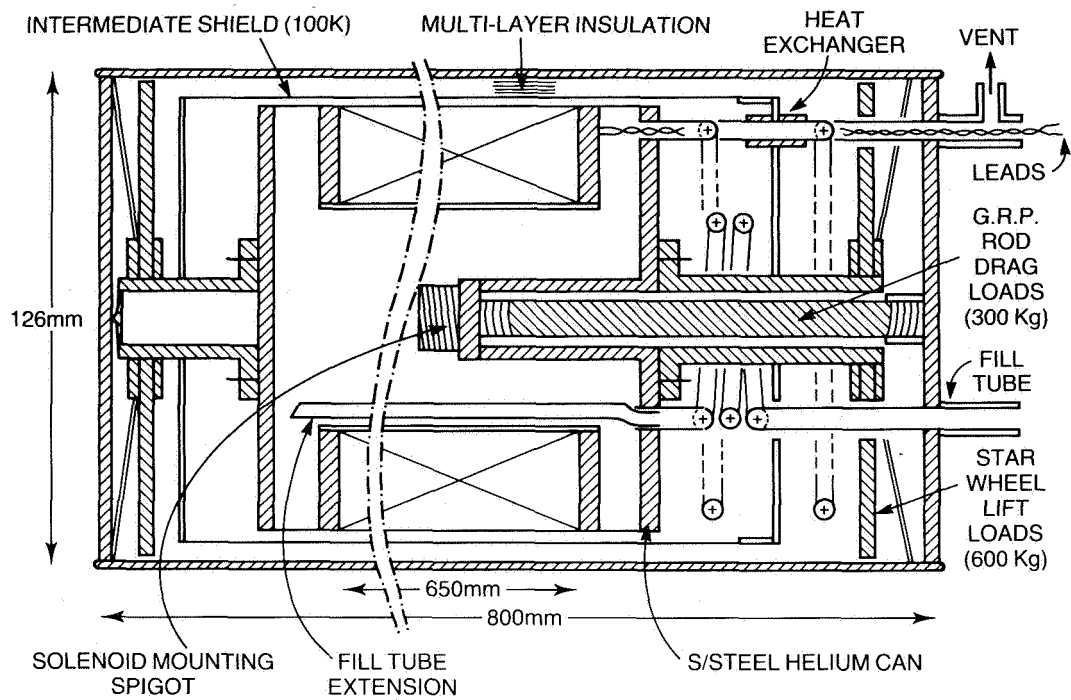


Figure 3. Detail of flying cryostat and liquid helium cooled NbTi solenoid Mark 2

Flying Cryostat and HTS Solenoid Mark 3. Detail.

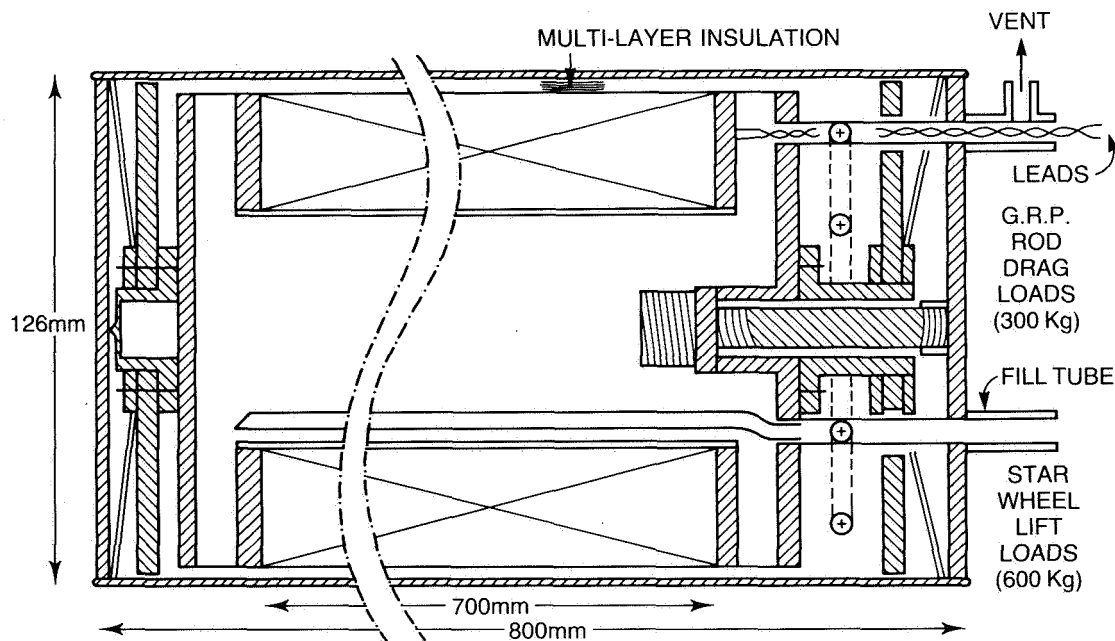


Figure 4. Detail of flying cryostat and liquid nitrogen cooled YBCO solenoid Mark 3

EFFECT OF FLUX PENETRATION ON THE LOAD CAPACITY OF
PASSIVE SUPERCONDUCTING BEARINGS

DANTAM K. RAO
Mechanical Technology Inc.
968 Albany-Shaker Road
Latham, NY, 12110

ABSTRACT

The past year has seen a dramatic improvement in the load capacity of a superconductor-magnet pair. The measured load capacities that stood at 0.1 psi two years back have been improved now to an impressive 40 psi. This improvement is mainly due to better processing techniques developed by the superconducting material processing community. Our analysis indicates that, by using these processing techniques that efficiently prevent flux penetration, we can achieve high load capacities. With these developments, it is possible to insert passive bearings into actual applications within the next few years time frame.

1. INTRODUCTION

Passive Superconducting Bearings (PSB) differ from active magnetic bearings in that they use bulk superconductors to stably levitate a body without using complex control systems and without expenditure of external power (Rao and Dill [1]). A magnet-superconductor pair, consisting of a permanent magnet (PM) and a high temperature superconductor (HTS), separated by a magnetic gap, as shown in Figure 1, forms a typical stable bearing. The static load capacity (commonly called "load capacity") of such a pair is defined as the contact force exerted by the superconductor divided by the load bearing area of the suspended magnet. In the USA, the force is expressed in pounds while the load bearing area is expressed as square inches, so that the units are pounds per square inch or psi.

About two years back, the load capacity of this arrangement, measured at 77K, stood at 0.1 psi. Now, thanks to the immense efforts by the superconducting material development community, improved material processes are available, and the load capacities as high as 40 psi (a 400 -fold increase) can be obtained per Rao [2] and Murakami et al [3]. At lower temperatures of 4 K, recent tests indicate that we can achieve up to 100 psi using these materials per Moon.* It is known that the flux penetrates the superconductor partially, and thus degrades the load capacity. Even though considerable effort has been made in predicting the levitation forces, the force generation mechanism is not fully understood (see Moon [4] for a review of force models) when the gaps are small. An improved understanding of the force generation mechanism at small gaps is currently needed, and this forms the subject matter of this paper.

2. LEVITATION FORCE

2.1 General formula for force

As shown in Figure 2, let (r, θ, z) denote the cylindrical coordinate system erected at the center of the active surface of the superconductor. At a point $P(r, \theta, z)$ inside the superconductor, let $\mathbf{B}_m(P)$ [tesla or N/Am] denote the flux density applied by the magnet alone in free space. As we bring the magnet closer to the superconductor, its moving flux lines cut "rings" of superconductor

*Moon, F., Private Communication, 1991.

material and induce currents of density J_s [A/m²] in them. The net field B at the point P is B_m plus the self field B_i (i.e., the field created by all induced currents) so that $B = B_m + B_i$. The induced currents J_s interact with this net field B to create a net body force $J_s \times B = J_s \times B_m + J_s \times B_i$. But since the force components due to self-field (i.e., $J_s \times B_i$) are internal, they cancel each other, leaving a body force $J_s \times B_m$ external to the superconductor. Thus the force equals the superconductor's current density $J_s(P)$ times magnet's field $B_m(P)$ integrated over the volume V of the superconductor, viz.

$$F = \int_V J \times B_m dv \quad (1)$$

2.2 Superconductor

Macroscopically, we model the superconductor as a collection of closed loop "ring elements", each of which can carry persistent currents of density $J_s(P)$ as discussed above. The general form for the superconductor's magnetization vector is $M_s = M_r r + M_\theta \theta + M_z z$. Because of axisymmetry, however, the tangential component vanishes [$M_\theta = 0$] so that M_s simplifies to $M_s = M_r r + M_z z$, where the components M_r , M_z depend only on r, z coordinates. We substitute this in the Maxwell's law $J_s = \nabla \times M_s$ to compute current density by (2). Note that as a first approximation, we may estimate the magnetization components M_r , M_z from the measured magnetization curve $M(B_m(P))$ and use them to compute J_s from (2). Equation (2) shows that the current density J_s at a point P is the difference between the axial gradient of the radial component of magnetization and the radial gradient of the axial component of magnetization, both evaluated at that point P .

$$J_s = J_\theta \hat{\theta} = \left(\frac{\partial M_r}{\partial z} - \frac{\partial M_z}{\partial r} \right) \hat{\theta} \quad (2)$$

2.3 Magnet

The general form for magnet's field is $\mathbf{B}_m = B_r \mathbf{r} + B_\theta \boldsymbol{\theta} + B_z \mathbf{z}$. We also assume that the magnet's field is axisymmetric. The axisymmetry implies that tangential component vanishes ($B_\theta = 0$) and the radial and axial components B_r and B_z depend only on r and z . This reduces the magnet's field \mathbf{B}_m to

$$\mathbf{B}_m = B_r \hat{\mathbf{r}} + B_z \hat{\mathbf{z}} \quad (3)$$

2.4 Magnet-superconductor Interaction Force

Substituting (2) and (3) in (1) indicates that the interaction force has only the levitation (i.e., axial) component F_z , which is given by

$$\mathbf{F} = F_z \hat{\mathbf{z}} \quad (4)$$

$$F_z = -\int J_\theta B_r \, dv \quad (5a)$$

$$= \int_V \left(\frac{\partial M_z}{\partial r} - \frac{\partial M_r}{\partial z} \right) B_r \, dV \quad (5b)$$

Thus levitation force F_z is the product of the current density J_θ in the superconductor and the magnet's radial field component B_r , integrated over the

entire volume of the superconductor. The radial component of force turns out to be zero, which is consistent with the axisymmetry of the pair.

3. FINITE ELEMENT FIELD CALCULATION RESULTS

In this section, we examine the distribution of the applied field B_r along the radial (and axial) directions. We believe that this spatial nonuniformity of fields greatly affects the estimate of the repulsive force. The levitation force also varies with many other parameters [2], but we have not focussed on these other effects herein. In order to understand the field distribution, we used a finite element code called MAXWELL [5] to plot the flux lines. We used a small magnetic gap of 0.020 in (015 mm) in our calculations.

Figure 3 shows the mesh elements used to model the space occupied by the magnet and superconductor. We found that, in order to achieve a fair degree of accuracy, the regions around the magnetic gap must be represented by meshes that are finer than those in other regions. We used 7676 elements.

Figure 4 shows how the superconductor affects the flux lines from a magnet. For the magnet in free space, the flux lines emanate from it axially but become nearly radial by the time they reach its edge (i.e., they bend by 90 degrees). With the insertion of the superconductor, these flux lines are literally compressed and squeezed inside the narrow magnetic gaps. This flux line compression causes the radial field to be highest around the edge of the magnet and hence increases net force.

Figure 5 compares the experimental and theoretical distribution of flux density applied by the magnet in the axial direction. The experimental and theoretical results are in good agreement, showing that we can simulate the fields with confidence.

In Figure 6 we show how the radial flux density varies with the radial position. It shows that the effect of the superconductor is to nearly double the radial flux density at the periphery of the magnet, from 0.4 tesla to 0.8 tesla (if the

superconductor does not allow any flux penetration). This field increases up to the magnet's diameter and then falls down beyond it.

This general trend in field distribution is confirmed by the calculations done by Argonne National Laboratory recently [6] as shown in Figure 7. The curve (a), plotted by MTI, corresponds to a 20mm diameter magnet while the curve (b) plotted by ANL, corresponds to a 3.2 mm diameter PM [6].

From this plot we conclude that: (1) the radial component of the applied field starts as zero at the center, (2) it increases to a maximum value at the edge of the magnet and then (3) it decreases to a near-zero value at the edge of the superconductor.

4. EXPERIMENTAL AND ANALYTICAL INVESTIGATIONS OF REPULSIVE FORCE

As a first step towards analysis, we measured the force of repulsion between a permanent magnet and a superconductor using a specially designed levitation test rig. We then calculated the force of repulsion using the MAXWELL finite element program to solve the Maxwell equations. Figures 8 through 10 display the results of these experimental and analytical investigations.

Figure 8 shows the measured variation of repulsive force with the magnetic gap. The operational gap range for bearings is usually less than 0.1 in. (2.5 mm). In this range, this plot shows that the force increases in an almost straight line fashion with the magnetic gap. This linearity of force with gap greatly simplifies the analysis and design of passive bearing elements. It is fair to add that this linearity depends on the process of the material.

Figure 9 shows how the computed force of repulsion is influenced by the flux penetration. A magnetic gap of 0.020 in. has been used in these calculations. When the superconductor is diamagnetic (i.e., has a near-zero relative permeability), Figure 9a shows that it does not allow any flux to penetrate, and the force of repulsion is extremely high, of the order of 16 lb. At a relative

permeability of 0.1, the flux begins to penetrate, and we observe degradation of the load capacity to 13 lb. As the relative permeability increases to 0.4, Figure 9d shows a repulsive force of 7.6 lb; this value is quite close to the measured data.

As already indicated, only gaps in the range of up to 0.1 in. is of interest to the bearing designer. Hence we replotted in Figure 10 the experimental and analytical results in this range of interest. This figure shows that there is a good degree of correlation between the experimental and analytical force-gap data. It shows that we can predict (in the small gap range that is of interest to the bearing designer) the repulsion force between the magnet and superconductor with a fair degree of accuracy.

5. SUMMARY

In this paper we have indicated that the superconductor material technology has greatly improved over the past two years to the extent that load capacities of up to 40 psi can be achieved at 77 K temperature with the currently available materials. These load capacities are sufficiently high so that we can construct and test the passive bearings within the next few years. We can also predict and analyze the bearing forces with confidence in the small gap ranges of interest to the bearing designer (i.e., 0 to 0.1 in.).

REFERENCES

- [1] Rao, D.K., and Dill, J.F., "Comparative Assessment of Single Axis Force Generation Mechanism for Superconducting Suspensions", Proc. 25th IECEC, Vol. 5, pp. 149-153, 1990.
- [2] Rao, D.K., "Load Capacity of Passive Superconducting Levitation Systems", presented in the Magnetic Bearings and Dry Gas Seals Conference, Mar. 13-15, 1991, Washington D.C.
- [3] Murakami, H. et al., "Large Levitation Force due to Flux Pinning of MPMG Processed YBCO Superconductors with Ag Doping", Proc. ISS, 1991.
- [4] Moon, F.C., "Magnetic Forces in High-Tc Superconducting Bearings", Applied Electromagnetic in Materials, Vol. 1, 1990, pp. 29-35.
- [5] MAXWELL - User's Manual. 1991.
- [6] Cha, Y.S., Hull, J.R., Mulcahy, T.M., and Rossing, T.D., "Effect of size and Geometry of Levitation Force Measurements between Permanent Magnets and High-Temperature Superconductors", Proc. 5th Joint MMM Intermag. Conference, Pittsburgh, PA, June 18-21, 1991.
- [7] Chang, P.-Z., "Mechanics of Superconducting Magnetic Bearings", Ph.D Thesis, Cornell University, Jan. 1991.

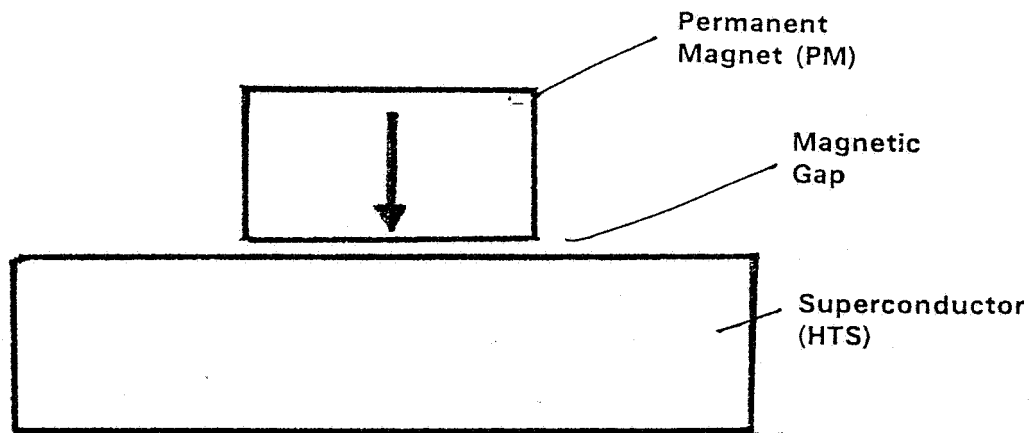


Figure 1. Typical magnet-superconductor pair producing stable levitation.

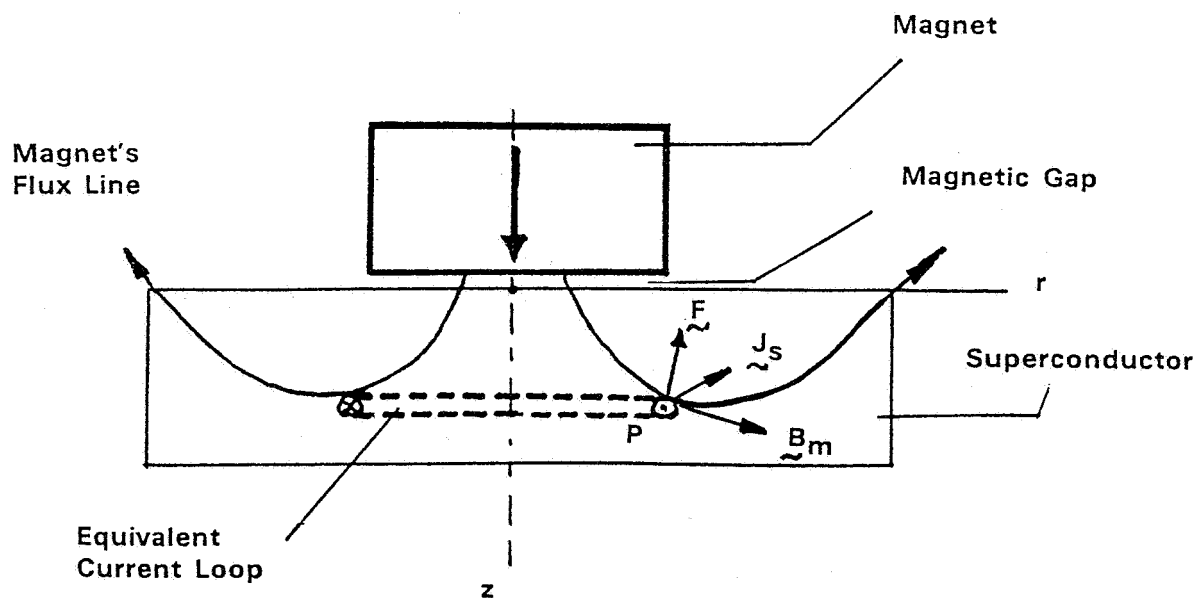


Figure 2. A magnet with flux density B_m interacts with a "ring element" with current density J_s to create a Lorentz force $J_s \times B_m$.

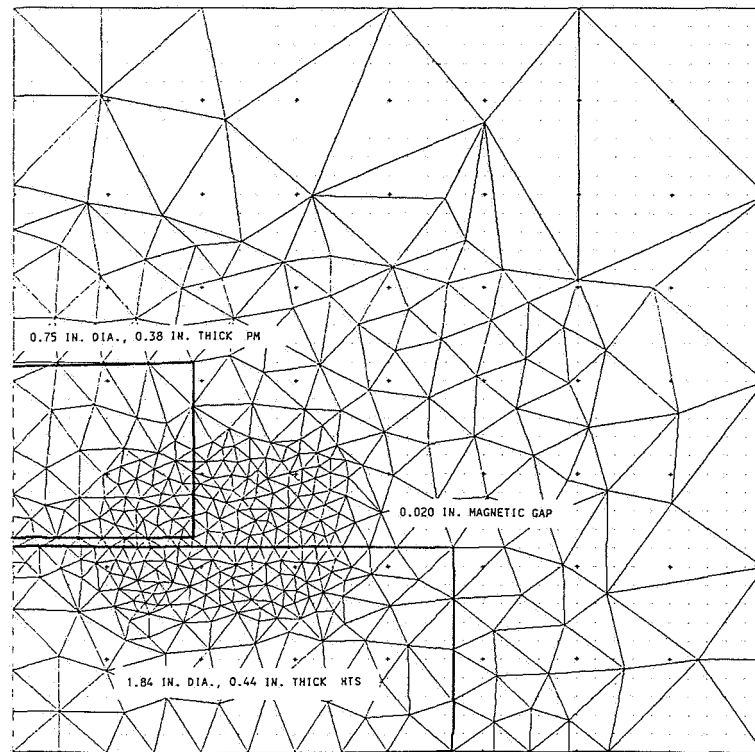


Figure 3. Finite element mesh used to generate flux line plots of magnet-superconductor.

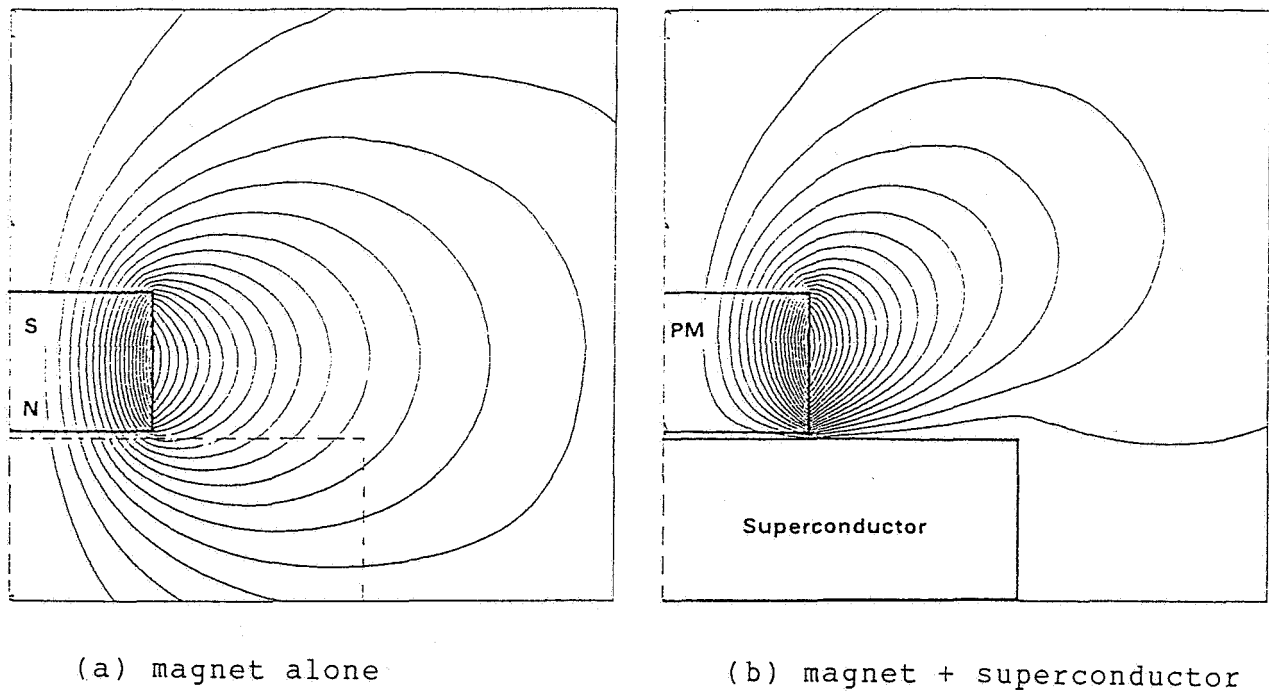


Figure 4. Flux line plots — (a) magnet alone and (b) with the superconductor.

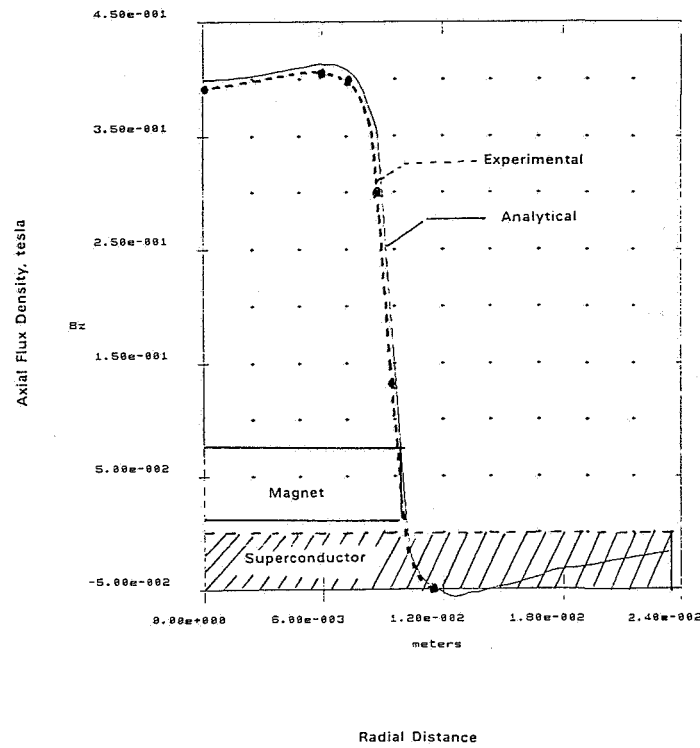


Figure 5. Spatial distribution of flux density along the axial direction. (a) analytical, (b) experimental.

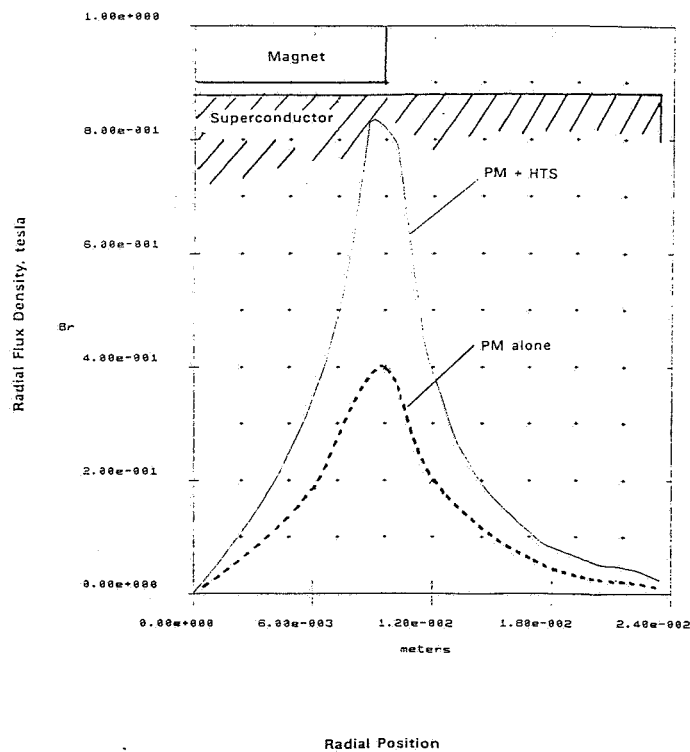


Figure 6. Variation of the field applied a magnet with and without the superconductor.

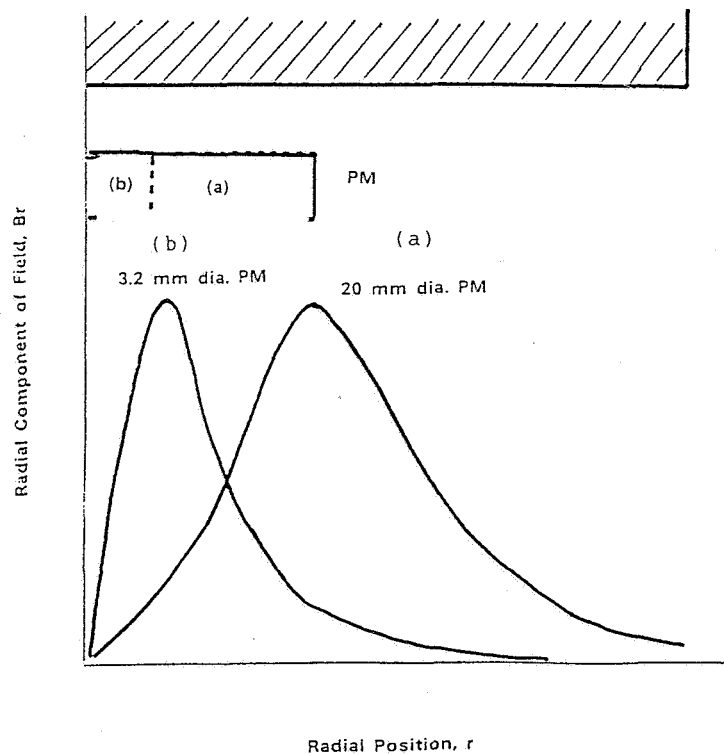


Figure 7. Comparison of fields applied by magnets of different sizes on the superconductor.

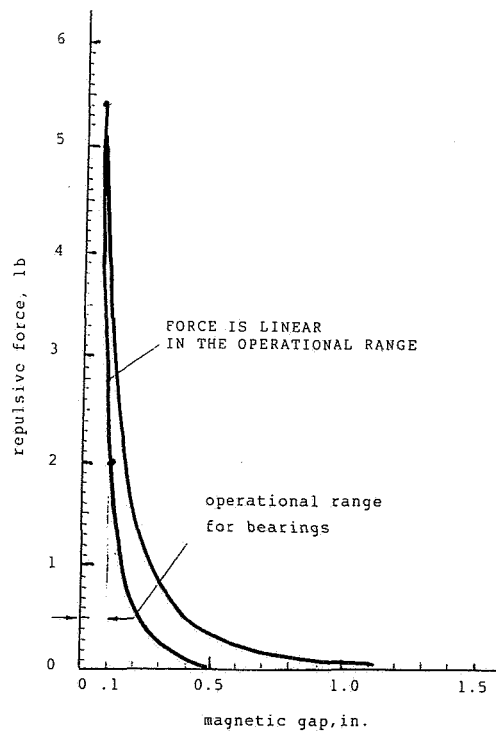
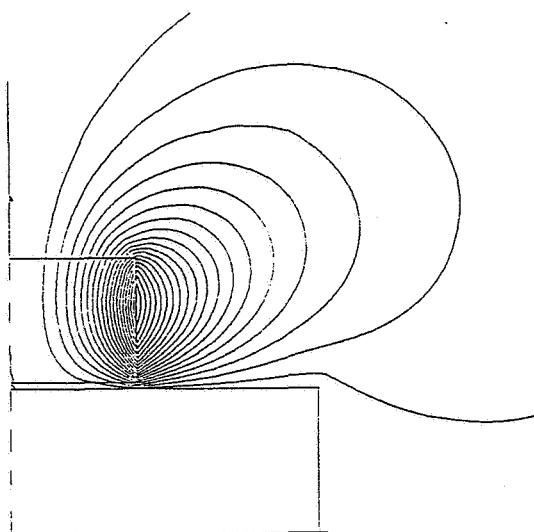


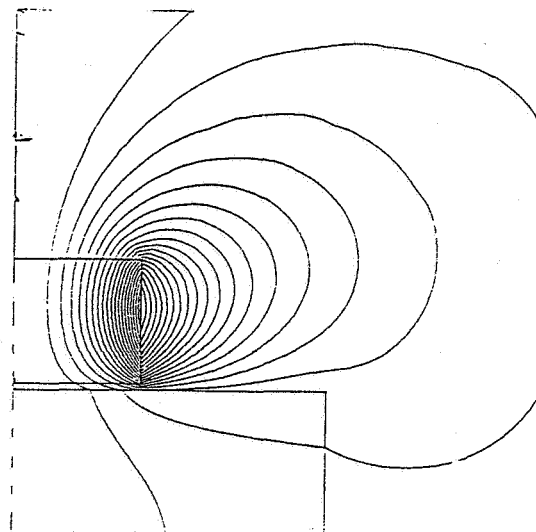
Figure 8. Repulsion force measured between a permanent magnet and a superconductor.



(a)

$$\mu_r = 0.01$$

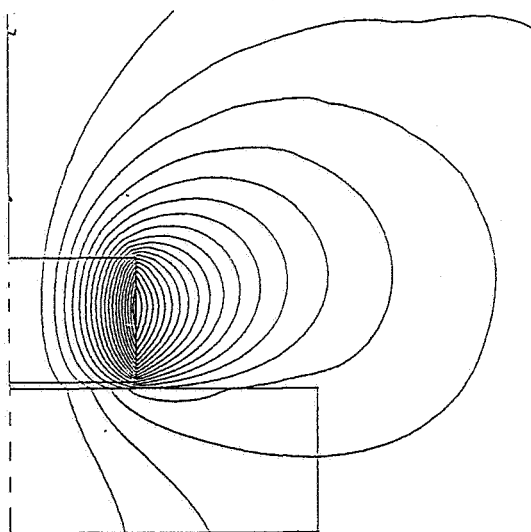
$$F_z = 16.1 \text{ lb (72 N)}$$



(b)

$$\mu_r = 0.1$$

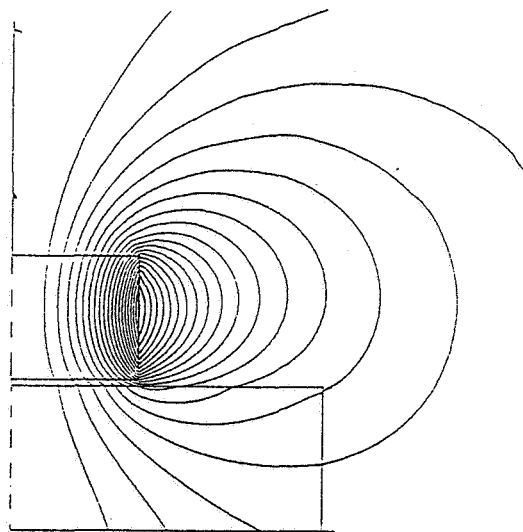
$$F_z = 13.1 \text{ lb}$$



(c)

$$\mu_r = 0.2$$

$$F_z = 11.1 \text{ lb}$$



(d)

$$\mu_r = 0.4$$

$$F_z = 7.6 \text{ lb}$$

Figure 9. Effect of penetration of flux on the load capacity of a magnet-superconductor pair.

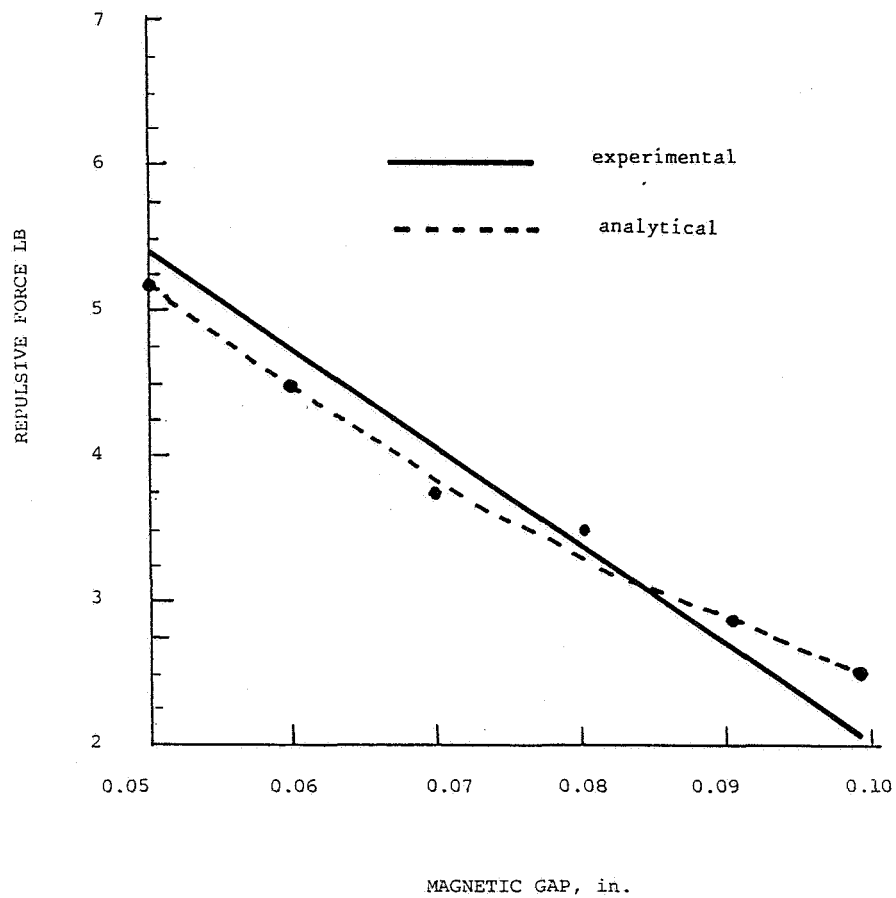


Figure 10. Comparison of analytical and experimental results of repulsive force at small gaps.

N92-27791

Application of Ceramic Superconductors in High Speed Turbines

C. K. McMichael^(a), M. A. Lamb^(b), M. W. Lin^(c), K. B. Ma and W. K. Chu
The Texas Center for Superconductivity at the University of Houston

(a) C. K. McMichael is an undergraduate fellow from the University of Houston.

(b) M. A. Lamb is an undergraduate fellow from the University of Houston.

(c) M. W. Lin is an undergraduate fellow from the California Institute of Technology.

SUMMARY

A turbine system was modified to adapt melt-textured $Y_1Ba_2Cu_3O_{7-\delta}$ (YBCO) with high energy permanent magnets to form a hybrid superconducting magnetic bearing (HSMB). The HSMB/turbine prototype has achieved a static axial thrust capacity exceeding 41 N/cm^2 (60 psi) and a radial magnetic stiffness of 7 N/mm in a field cooled state at 77 K . A comparison was made between different configurations of magnets and superconductor for radial stability, axial instability, and force hystereses. This systematic study led to a greater understanding of the interactions between YBCO and high energy permanent magnets to define design parameters for high rotational devices utilizing the HSMB design.

INTRODUCTION

The advent of high temperature superconductors (HTS) which exhibit type II behavior (pinning effect [1]) has created many possible applications for bulk materials such as $Y_1Ba_2Cu_3O_{7-\delta}$ (YBCO). The ability to levitate passively machinery which rotates at high speeds without active control systems or complex pneumatics with almost zero energy consumption warrants investigation. As low energy consumption is a crucial consideration for operation in a cryogenic environment, it would seem that this requirement makes high temperature superconductors (HTS) ideal for such applications. A simple superconducting magnetic bearing (SMB) utilizing the pinning effect has been demonstrated by the ubiquitous observation of a pair of HTS stators field cooled around a set of permanent magnets [2]. With the onset of higher J_c materials produced by texturing processes [3, 4], and with further increases being very promising with neutron and high energy proton irradiation [5, 6] of bulk YBCO, the corresponding increase in flux pinning could enable oriented samples of YBCO to trap magnetic flux on the same order of magnitude as that of rare earth permanent magnets [7, 8]. Using such high flux trapping samples would raise the levitation and magnetic stiffness effectively. Still, there is a problem with the SMBs in terms of gap stabilization over long periods of time [9].

It is now becoming feasible to use bulk superconductors in the design of

high speed rotational devices requiring multi-axis passive bearing traits. In this paper, we present the hybrid superconducting magnetic bearing (HSMB)/turbine prototype (Fig. 1) which exhibits multi-axis stability in a passive levitated state.

ORIGINAL PAGE
BLACK AND WHITE PHOTOGRAPH

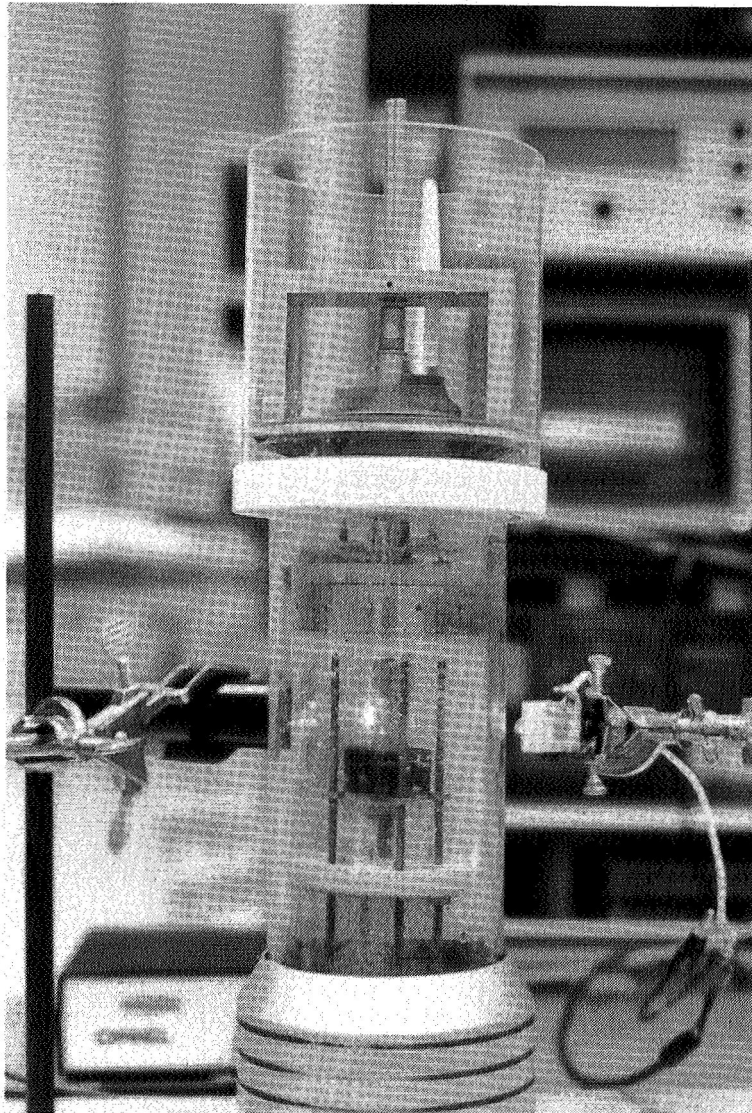


Fig. 1 Photograph of our prototype HSMB.

EXPERIMENTAL

This HSMB/turbine (Fig. 2) is constructed with melt-textured YBCO as the stators and NbFeB as the rotor permanent magnets with a surface field at the center of a pole face of 0.429 T. In the test model, two melt-textured tubes (1.8 cm length, 1.2 cm ID, 2.5 cm OD) were sealed to a 5.7 cm long glass tube to form a journal bearing set. The thrust HTS bearing member was a melt-textured disk (2 cm diameter, 4.75 mm thick) which was sealed to the end of the journal bearing set. The journal and thrust permanent magnet bearing members were aligned to maximize the magnetic field repulsion strength. The rotor shaft (1 cm diameter, 10 cm long) contained three simple dipoles, one at the top for an attractive thrust, one for the journal, and one for repulsive thrust at the bottom. The entire HSMB assembly was immersed in a glass dewar containing liquid nitrogen, while a high pressure gas nozzle was used to drive the turbine.

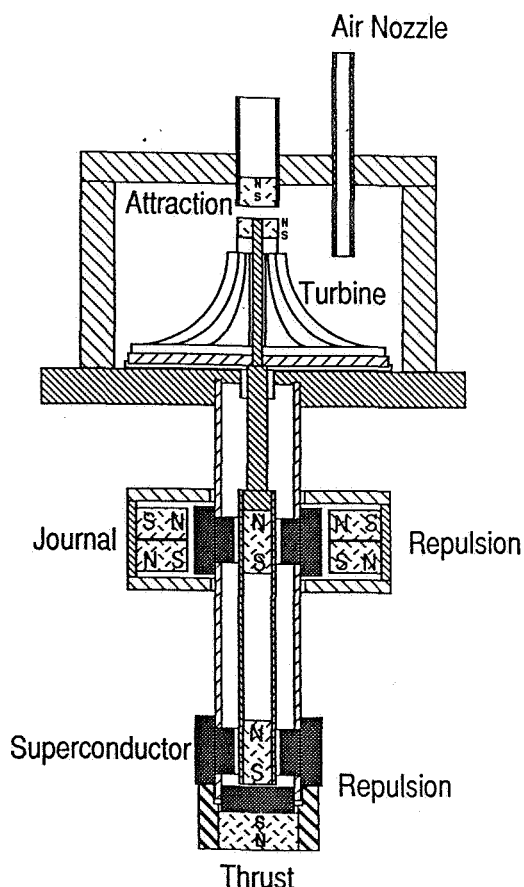


Fig. 2 Drawing of our prototype HSMB.

In a static setup, force measurements were conducted on each bearing element using a cantilever beam-strain gauge apparatus [10]. A stationary cold stage which held the superconductor and magnet assemblies were attached to an optical table. The forces acting within two of the three bearing components were assembled individually and measured. Magnet-magnet attraction and repulsion forces were measured as a function of displacement from the central axis for various gap distances (Fig. 3, 4).

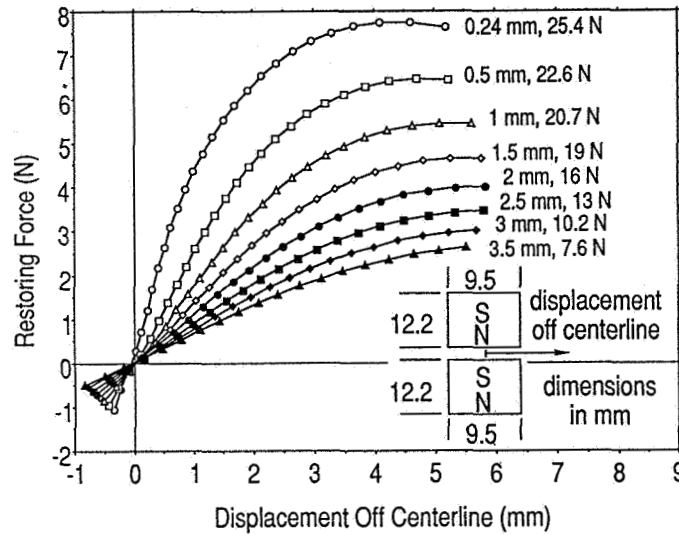


Fig. 3 Radial component of restoring force as a function of radial displacement off central axis for the top bearing component.

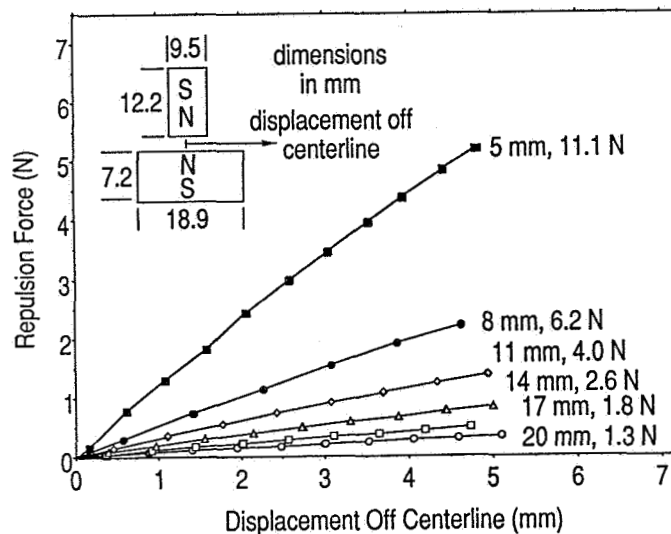


Fig. 4 Radial component of repulsion force as a function of radial displacement off central axis for the bottom bearing component.

Radial and axial hystereses were measured to compare HSMB, field cooled superconductor, and magnet-magnet thrust configurations (Fig. 5, 6).

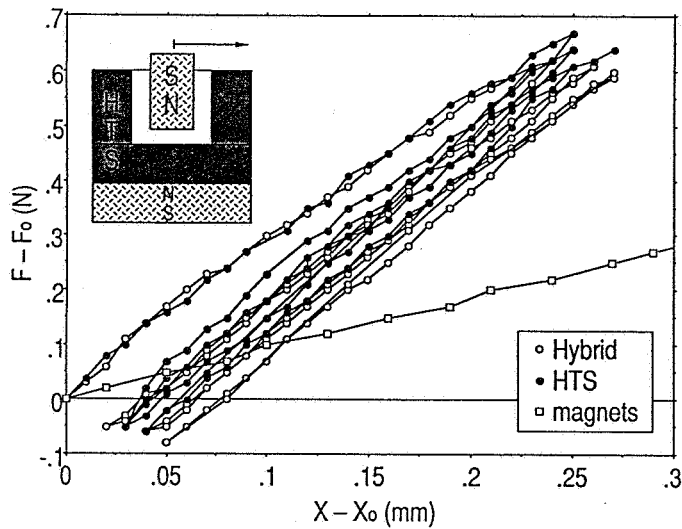


Fig. 5 Radial hysteresis loops - change of force from the initial setup value (different for the three separate cases) as the magnet is displaced across the HTS well, as a function of the displacement from the initial point near the center.

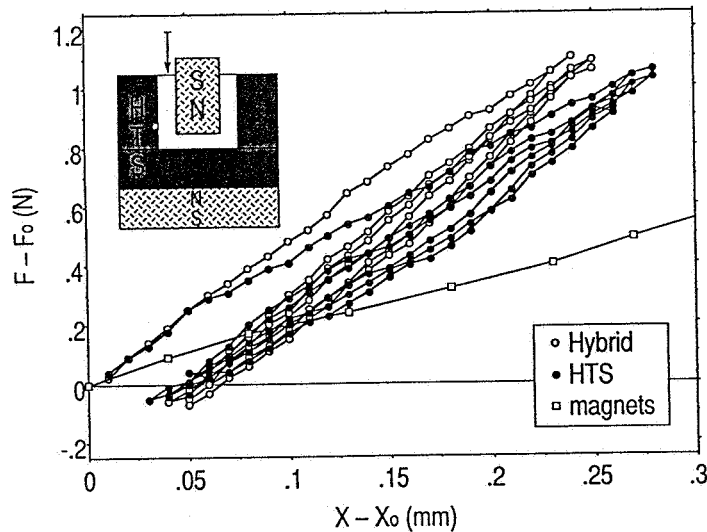


Fig. 6 Axial hysteresis loops - change of force from the initial setup value (different for the three separate cases) as the magnet is lowered into the HTS well, as a function of the displacement from the initial point.

Journal configurations were treated similarly (Figs. 7, 8, 9).

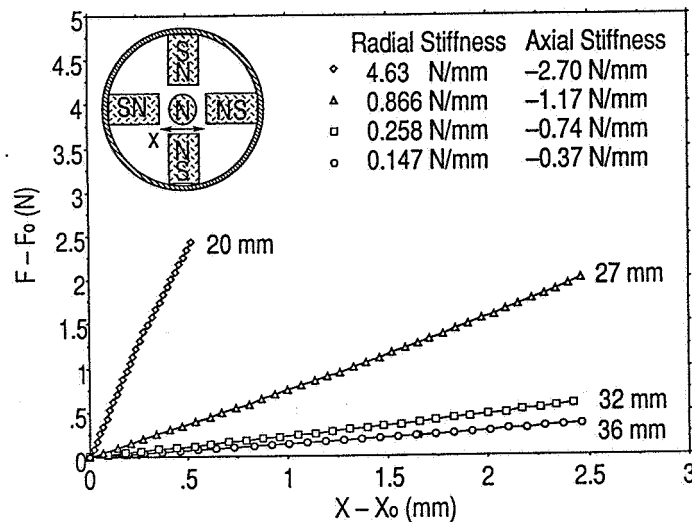


Fig. 7 Restoring forces for the central magnet in the central configuration - change of force from the initial setup value as the central magnet is moved in the plane of the set of four outer magnet pairs, along a line joining two opposite magnet pairs, as a function of the displacement from the initial point near the center.

RESULTS AND DISCUSSION

From the data in Figs. 5 and 6, there is apparently no significant difference between the hybrid and the FC HTS by itself in so far as the stiffness of the configuration is concerned. Even in the axial direction, the effect of the stator magnet is not quite discernible until displacements larger than 0.2 mm. are reached. The net effect of the stator magnet seems to be boosting up the thrust only. Certainly, we do not have to be concerned with the stability provided by the FC HTS being compromised by the presence of an additional magnet in this configuration. It remains to be seen as to how much additional thrust we can get out of the magnet by decreasing the thickness of the intervening HTS layer without compromising excessively on the stability. It is also interesting to ask whether that intervening HTS layer can be eliminated altogether. We believe that there are no inherent principles preventing this from happening.

In contrast, a careful examination of the data in Figs. 8 and 9 shows that the effects from the stator magnet are conspicuous in the journal configurations.

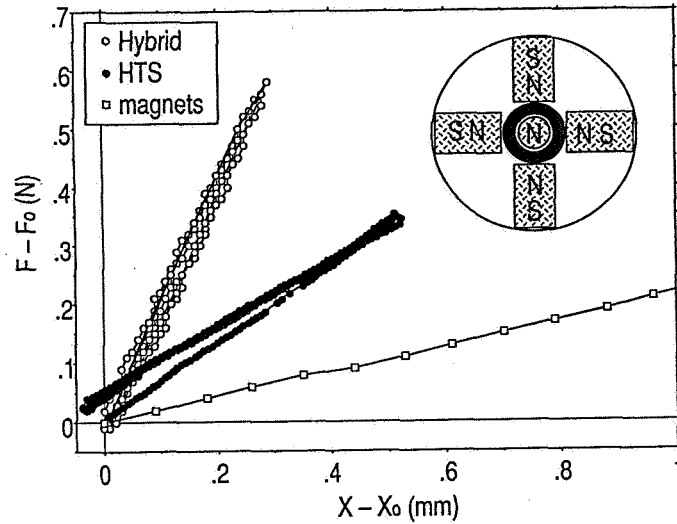


Fig. 8 Radial hysteresis loops - change of force from the initial setup value (different for the three separate cases) as the magnet is displaced across the HTS doughnut, as a function of the displacement from the initial point near the center.

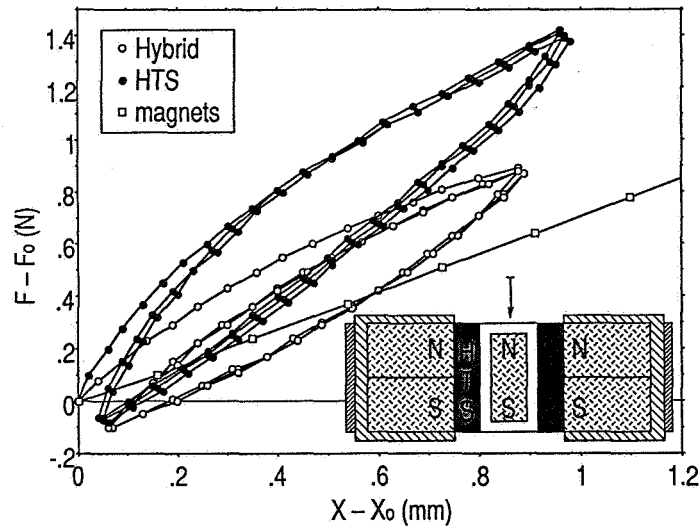


Fig. 9 Axial hysteresis loops - change of force from the initial setup value (different for the three separate cases) as the magnet is poked through the HTS doughnut, as a function of the displacement from the initial point.

The stator magnets are not intended to create an extra thrust, here. They are added to exchange some axial stability for radial stability. Qualitatively, we can see that the radial stiffness of the hybrid is enhanced, while the axial stiffness is suppressed from the FC HTS case, just as the corresponding stiffnesses of the stator magnet configuration would lead us to expect. Also noteworthy are the differences in the characteristics of the hysteresis loops. The axial hysteresis loops are much wider than the radial hysteresis loops for the journal configurations. There is almost no tendency for the loop to drift in the direction of the initial displacement, whereas this was quite pronounced on the thrust configuration. We believe that the former effect is a consequence of the relative geometries of the magnetic field, the superconductor surface and the direction of the displacement, while the latter is a manifestation of force creep.

Overall, this prototype bearing that we have constructed can support a thrust of 41 N/cm² or 60 psi, normalized to the cross-section of the shaft. Of these, about one third comes from the repulsion between the two magnets in the thrust bearing at the bottom, while the remaining two thirds comes from the attraction between two magnets at the top. The bottom thrust bearing has a net radial instability, while the top thrust bearing has a net axial instability. Since these two instabilities stem from forces acting on different ends of the shaft, they would combine to produce a tilt instability even if they appear to cancel each other out. This is just another instance illustrating Earnshaw's theorem [11]. With the HTS pieces, the journal bearing in the middle functions to stabilize against the axial instability of the top bearing, while the HTS well of the thrust bearing at the bottom functions to stabilize against the radial instability from the repelling magnets located in its vicinity. Further refinement of the balance between axial and radial instabilities can be made by adjusting the stator magnets in the journal bearing. When assembled, the overall stiffness of the bearing would be several N/mm, variously distributed amongst the three bearing components.

Finally, we want to add that all our force measurements were performed on a time scale of a fraction of a second. Therefore, we can expect our stiffnesses to apply to vibrational phenomena of a few Hz. Other works [12] have indicated that the stiffnesses are relatively independent of frequency. Thus, our results may still be valid over a wider range of

frequencies. This awaits further investigation.

REFERENCES

1. M. Murakami, T. Oyama, H. Fujimoto, T. Tagughi, S. Gotoh, Y. Shiohara, N. Koshizuka and S. Tanaka, *Jap. J. Appl. Phys.* 26, L1991 (1990).
2. C. K. McMichael, K. B. Ma, M. W. Lin, M. A. Lamb, R. L. Meng, Y. Y. Xue, P. H. Hor and W. K. Chu, to be published in *Appl. Phys. Lett.*
3. R. L. Meng, C. Kinalidis, Y. Y. Sun, L. Gao, Y. K. Tao, P. H. Hor and C. W. Chu, *Nature* 345, 326 (1990).
4. S. Tanaka, *IEEE Trans. MAG* (1991).
5. P. H. Hor, Z. J. Huang, L. Gao, R. L. Meng, Y. Y. Xue Y. C. Jean , J. Farmer and C. W. Chu, *Mod. Phys. Lett. B* 703, 4 (1990).
6. L. Civale, A. D. Marwick, M. W. McElfresh, T. K. Worthington, A. P. Malozemoff, and F. H. Holzberg, J. R. Thompson, M. A. Kirk, *Phys. Rev. Lett.*, 65, 1164 (1990).
7. A. D. Crapo and J. D. Loyd, *IEEE Tran. Mag.*, 27 2244 (1990).
8. R. Weinstein, et al., *Appl. Phys. Lett.* 56, 1475 (1991).
9. F. C. Moon and J. R. Hull, 25th IECEC 3, 425 (1990).
10. F. C. Moon, M. M. Yanoviak, and R. Ware, *Appl. Phys. Lett.* 52, 1534 (1988).
11. S. Earnshaw, "On the Nature of the Molecular Forces which Regulate the Constitution of the Luminiferous Ether," *Trans. Camb. Phil. Soc.* 7, pp. 97-112, (1842).
12. S. A. Basinger, J. R. Hull, and T. M. Mulcahy, *Appl. Phys. Lett.* 57, 2942 (1990).

N 9 2 - 2 7 7 9 2

CRYOGENIC TEST RIG WITH AN AERODYNAMIC MAGNETICALLY LEVITATED CARRIAGE

Sergey Yu. Borisov, Anton L. Iskra, and Anatoly P. Philatov
Central Aero-Hydrodynamic Institute (TsAGI),
Zhukovsky, Moscow region, USSR

ABSTRACT

The results of the investigations carried out by the authors in TsAGI in 1983 - 1984 concerning the use of a magnetically levitated aerodynamic carriage with a model moving in a closed cryogenic channel are presented. The facility dimensions are established, operating ranges are calculated, thermal isolation, cooling and measurement systems are described, comparison of this facility with wind tunnels is given and its advantages are shown.

Figures for this paper were unavailable at time of publication.

SYMBOLS

Names

A	area, m^2
V	speed, m/sec
T	temperature, K
L	linear dimension, m
p	pressure, atm
ρ	density, kg/m^3
m	mass, kg or t
q	dynamic pressure, $kg/m \text{ sec}^2$
g	acceleration due to gravity, m/sec^2
t	time, sec
n	load factor
M	Mach number
Re	Reynolds number
St	Strouhal number
Fr	Froude number
Eu	Euler number
R	thrust, t
A	work, MJ
Q	heat, MJ
C _x	drag aerodynamic coefficient
η	engine efficiency factor
C	specific heat of structural material, kJ/kg K
C _p	specific heat at constant pressure, kJ/kg K
C _v	specific heat at constant volume, kJ/kg K
γ	ratio of specific heats, $\gamma = C_p/C_v$
β	specific cooling capacity of liquid nitrogen, kJ/kg

Subscripts

\bar{c}	reference chord, $0.1 \sqrt{A_{TS}}$
c	carriage
LN ₂	liquid nitrogen
i	initial
f	final
m	model
TS	test section
s	sum value
a	air
1	conditions at acceleration and at T = 82 K
2	conditions at uniform motion and at T = 290 K
3	conditions at deceleration

INTRODUCTION

In the 1970's a conception of increasing wind tunnel Reynolds number for model tests by decreasing gas temperature was developed which underlay the construction of cryogenic wind tunnels [1 - 5]. The idea of the adaptation of the known aerodynamic carriage method to cryogenic temperature of working medium was considered by the authors in 1983 - 1984 [6,7]. The application of a magnetically levitated aerodynamic carriage with a model attached to it was proposed. This principle of motion had been already used in those years in monorail passenger transport facilities in a number of countries, e.g., in Japan. A few other new facility elements were also proposed: flexible screen simulating the ground surface, sluices etc. A paper of P.L. Lawing and W.G. Johnson [8] was published in 1988, which also proposed using the principle of accelerating the model up to hypersonic speeds being held in the center of a special channel using a Magnetic Suspension and Balance Systems (MSBS) [8,9].

The test rig proposed by the authors is intended mainly for model tests in a subsonic speed range so that the tests would be confined to an acceptable channel length. The importance of an accurate simulation in case of testing models with low subsonic flow speeds increases steadily, special requirements of a small working medium turbulence being specified. Essentially atmospheric turbulence is provided in this facility, and acoustic disturbances can also be eliminated almost fully. The facility is featured by a number of other advantages as compared to operating wind tunnels and test rigs with aerodynamic carriages: smaller model dimensions, almost twice the reduction in motion speed as compared to tests at normal temperatures, ground effect simulation at take-off and landing, and investment and energy savings. A very important feature of magnetically levitated transport facilities is their ecological friendliness.

Experimental results for high-temperature superconductivity (at temperatures ≤ 100 K) were obtained in 1985 - 1987. The industrial application of high-temperature superconductivity in the magnetically levitating transport drive systems can contribute to a considerable energy consumption reduction.

In recent years, the interest in the use of heavy gases in wind tunnels to increase the Reynolds number has grown. This concept can be used in the proposed test rig. The value of ratio of specific heats γ for heavy gases that can differ from the value of γ for air is not so significant at small subsonic speeds.

PRINCIPLE OF SIMULATION IN A CRYOGENIC CHANNEL

The theoretical validation of the possibility of using cryogenic flow temperatures in wind tunnels is given in references [2,3]. We shall assume that the flow temperature in conventional low-speed wind tunnels is $T_1 = 300$ K, and the air temperature in the cryogenic test rig channel is equal to the air condensation temperature $T_2 = 82$ K and the pressure is atmospheric. Using the known relations for the speed $V \propto T^{0.5}$ and the Reynolds number $Re \propto T^{1.36}$, we obtain:

$$V_2/V_1 = (T_2/T_1)^{0.5} = 0.523$$

$$Re_2/Re_1 = (T_1/T_2)^{1.36} = 5.84$$

If the full-scale value of the Reynolds number is reproduced, the model size can be reduced in accordance with the relation $L \propto T^{1.36}$. In this case, for the Strouhal number St and Froude number Fr we shall have:

$$St_2/St_1 = (T_1/T_2)^{0.86} = 0.328$$

$$Fr_2/Fr_1 = (T_1/T_2)^{-0.36} = 1.60$$

The Euler number $Eu = p/\rho V^2$ does not depend on temperature. This means that it is possible to reproduce full-scale values of Mach, Reynolds and Euler numbers and the values of Strouhal and Froude numbers that are close to full-scale ones.

DETERMINATION OF FACILITY DIMENSIONS

As a standard operation regime we shall consider tests carried on according to the following program: uniform model acceleration, motion at a constant speed and uniform deceleration. The tunnel length is found as a sum of three lengths of acceleration (L_1), uniform motion (L_2), and deceleration (L_3) sections. The uniform motion time is assumed to be equal to 1 sec. Table 1 gives the motion times for first and third sections and the lengths of all sections L_s in case of uniform model acceleration and deceleration with load factor n for different maximum Mach numbers.

An essential part of the channel is occupied by acceleration and deceleration sections, their lengths being dependent on load factor values. It is difficult to attain supersonic Mach numbers in the tunnel even at considerable load factors $n = 5$ to 10 because of a great channel length (up to 7 km) and increased model strengths required. To obtain high, sub, and transonic Mach numbers at moderate load factors (up to $n = 4$) the required channel length will be approximately 1 km (fig. 1). The most simple solution would be the construction of a channel for take-off and landing speeds. Thus, at $n = 4$ for the Mach number $M = 0.2$, the total channel length amounts to $L_s = 70$ m, and for $M = 0.45$, $L_s = 252$ m. The total channel length should be extended slightly so that safety measures could be provided during model deceleration. Chambers of the diameter of approximately 10 m should be provided at both channel ends for model rotations. These chambers must communicate with sluices for model heating and cooling.

We shall assume such channel cross section area that the Reynolds number

Re_c would have the same value as in the largest operating low-speed wind tunnel at the Ames Research Center, NASA, USA [10]. With the test section of this wind tunnel $A_{TS} = 36 \times 24$ m and maximum speed $V = 50$ m/s, the Reynolds number $Re_c \approx 10$ mil. The same Reynolds number is achieved in the proposed cryogenic test rig at $T = 82$ K with cross section area 6.2×4.1 m. For further calculations we shall assume the following main facility parameters: $M = 0.45$, $n = 4$ (for acceleration and deceleration), $L = 290$ m, $A = 6.2 \times 4.1$ m. Figure 2 presents a sketch of the cryogenic channel.

OPERATING RANGES

An air-nitrogen mixture is used as a working medium. The oxygen-nitrogen ratio in the mixture can be arbitrary, since judging by investigation results, presented in [3], the tests in air and nitrogen are essentially identical. The minimum value of the working gas temperature is equal to the air condensation temperature $T = 82$ K. The maximum gas temperature in the channel is equal to the ambient temperature $T = 290$ K.

Figure 3 shows an operating range of the facility in coordinates of M and Re numbers for a selected channel length $L = 290$ m. This range is confined by lines, that correspond to maximum and minimum temperatures and maximum Mach number. At temperature $T \leq 121$ K, the model can be accelerated up to $M = 0.45$, and at $T = 121$ K the choice should be confined to the values of the Mach number $M < 0.45$. Figures 4 and 5 present uniform motion time t_z and model speed V versus Mach number. The maximum model velocity that can be attained at $n = 4$ is equal to $V = 99$ m/s. At $T = 82$ K and $M = 0.45$, the speed $V = 82$ m/sec

THERMAL ISOLATION, COOLING AND COLD PRESERVATION IN FACILITY

To attain and keep a low temperature of the working medium, the supply of liquid nitrogen is provided which, being evaporated, cools the channel gas. Liquid nitrogen will be supplied to special evaporators distributed uniformly along the channel length. Both the internal and external thermal isolations of the facility can be made of foam plastics. Among various types of the thermal isolation of the cryogenic channel, the application of screen-vacuum or vacuum-powder isolation providing the heat flux about 1 W/m^2 seems to be promising.

We shall evaluate the amount of liquid nitrogen required for initial cooling of the facility. With above chosen dimensions the total facility surface area will be $A = 6550 \text{ m}^2$. The steel casing mass $m \approx 200$ t. The quantity of liquid nitrogen m_{LN_2} is calculated from the heat balance equation (assuming mean values of specific heat of steel C and specific cooling capacity of liquid nitrogen β for the temperature range 82 to 290 K):

$$m_{LN_2} = \frac{mC(T_i - T_f)}{\beta} \approx 50 \text{ t}$$

The total facility volume (channel and chambers) is 8000 m^3 , air mass at room temperature $m_a = 9600$ kg. The following quantity liquid nitrogen is required for its cooling:

$$m_{LN_2} = \frac{m_a C_p (T_i - T_r)}{\beta} \approx 10 \text{ t}$$

The total quantity of the liquid nitrogen for initial cooling of the channel casing and air inside it is equal approximately to 60 t. The mass of the aerodynamic carriage with a model is evaluated to be about 5 t. After an initial model installation or its reinstallation approximately 2 tons of liquid nitrogen are required for cooling. Heat losses due to thermal isolation in case of screen-vacuum isolation cannot be taken into account.

CHOICE OF TRANSPORT DEVICE

One of the main problems in the development of the facility under discussion is the choice and designing of the aerodynamic carriage. In a cryogenic temperature channel it is reasonable to apply a monorail levitating carriage with a linear electric engine. According to information of the late 1970's a high-speed test route with such a transport system had been designed in West Germany for the operation in the open atmosphere, so that to simplify the carriage maneuvers in chambers and sluices it is mounted on an ordinary rail track (fig.2).

The thrust acting on the carriage is equal to:

in the acceleration

$$R_1 = mng + (C_{x,m} A_m + C_{x,c} A_c)q$$

in the uniform motion

$$R_2 = (C_{x,m} A_m + C_{x,c} A_c)q$$

in the deceleration

$$R_3 = -(mng - (C_{x,m} A_m + C_{x,c} A_c)q)$$

where A_m , A_c - the characteristic aerodynamic model and carriage areas.

We think that the carriage is decelerated by means of an electric brake giving up the energy to the network. Assume the following values: $C_{x,m} = 0.5$; $C_{x,c} = 0.1$; $A_m = 2.5 \text{ m}^2$; $A_c = 3.0 \text{ m}^2$. A maximum thrust is required by the end of the model acceleration, e.g., at $M = 0.45$ we obtain $P = 21.8 \text{ t}$.

Figure 6 shows the dependence of the driver power $N = RV/\eta$ (where $\eta = 0.95$) on time for three characteristic ranges: 1) $M = 0.45$, $T = 121 \text{ K}$ (maximum power); 2) $M = 0.45$, $T = 82 \text{ K}$; 3) $M = 0.2$, $T = 82 \text{ K}$. The maximum required power is 23 MW.

We shall find the heat transferred to the channel. The work done in one model run is equal to:

$$A = \int_0^{t_s} (R_1 + R_2 + R_3) dt = (C_{x,m} S_m + C_{x,c} S_c) \int_0^{t_s} \frac{\rho V^3}{2} dt$$

where $t_s = t_1 + t_2 + t_3$, $V_1 = \text{ngt}$, $V_3 = (V_2 - \text{ngt})$. Accounting for the relations $t_1 = t_3$ and $V_2 = \text{ngt}$ we obtain:

$$A = (C_{x,m} S_m + C_{x,c} S_c) \frac{\rho V_2^3}{2} \left(\frac{t_1}{2} + t_2 \right)$$

We also consider that $(1 - \eta)100\% = 5\%$ of current work in the network independent of its direction converts to heat. This heat is equal to:

$$Q = (1 - \eta) \int_0^{t_s} (R_1 + R_2 + R_3) dt = (1 - \eta) \left[m V_2^2 + (C_{x,m} S_m + C_{x,c} S_c) \frac{\rho V_2^3}{2} t_2 \right]$$

For the conditions $M = 0.45$ and $T = 82 \text{ K}$ we have: $A = 3.7 \text{ MJ}$, $Q = 1.8 \text{ MJ}$. To compensate this heat, the following liquid nitrogen is required:

$$m_{\text{LN}_2} = \frac{(A + Q)}{\beta} = 27 \text{ Kg}$$

For the regime $M = 0.2$ and $T = 82 \text{ K}$ we have $m_{\text{LN}_2} = 7 \text{ kg}$. The consumption amount of liquid nitrogen will be less or, at least, commensurable with specific consumption per second of a run in a cryogenic compressor tunnel with test section $6.2 \times 4.1 \text{ m}$ and the same Mach and Reynolds number.

MEASUREMENT SYSTEM

The following important specific requirements are applied to the data measurement, recording and processing system in case of aerodynamic and strength model tests:

1. All instrumentation devices must be mounted on the aerodynamic carriage.
2. The serviceability of all devices must be provided at temperatures $82 - 300 \text{ K}$ and load factor $n = 4$.
3. The speed of data measuring, recording and processing systems must correspond to the experiment time.
4. The measurement accuracy must be no less than that of existing low-speed wind tunnels.

The measuring devices applied in cryogenic and shock wind tunnels can be used for the most part in this facility, too.

FACILITY FEATURES

The absence of working medium disturbances in front of the model makes it

possible to make the facility low-turbulent. Of importance is the absence of a complex labor-consuming tunnel element of the facility, namely: a compressor. At the same time the manufacturing of special supports and models capable of withstanding the load factor of $n = 4$ at the temperature $T = 82$ K will be required.

Note a number of new kinds of unique tests that can be conducted in this facility:

1. The model acceleration and deceleration according to a specified time program simulating aircraft take-off and landing $V = V(t, H)$ by changing the shape of a special flexible screen simultaneously with varying model angle of attack.
2. The determination of the Reynolds number influence on aerodynamic model characteristics by varying the medium temperature.
3. The formation, in a certain tunnel section, of jet gas flows simulating side gusts.

OPERATION ORGANIZATION. COMPARISON WITH WIND TUNNELS

The following operation mode of the facility is assumed. Cooling is undertaken one time a month with its subsequent continuous operation. In order to speed up to model reinstallation it is possible to apply two carriages and to mount one model and test the other one simultaneously. When heating it is possible to carry on tests in the temperature range of $T = 82$ K to 290 K. Model and carriage heating and cooling can be carried on in two special small-volume sluices: in a warm one for heating up and in a cold one for cooling down. The excessive gaseous nitrogen is ejected into the atmosphere through a 50 m-high exhaust tube.

Table 2 presents the main characteristics of the cryogenic channel in comparison with the TsAGI T-101 wind tunnel and the wind tunnel with the test section area 36×24 m (Ames RC, NASA, USA).

CONCLUSIONS

1. The aerodynamic test rig with channel cross section 6.2×4.1 m and with the length of 290 m provides the possibility of model testing at the Reynolds number $Re = 31 \cdot 10^6$ in the Mach number range $M = 0.45$. The steady-state model motion time is 1 sec.
2. The required maximum power of the aerodynamic carriage engine is $N = 23$ MW. The consumption of liquid nitrogen for test rig cooling is about 60 t. For one model run at $M = 0.45$, 27 kg of liquid nitrogen is required, the consumption amount at $M = 0.2$ is 7 kg.
3. The advantages of this facility are
the possibility of attaining those Re , M , Eu , Fr and St numbers at small subsonic speeds ($M < 0.45$) which are close to full-scale ones;

model size reduction as compared to those tested in existing conventional wind tunnels while simulating the same Reynolds numbers;

low medium turbulence;

increasing experimental possibilities as compared to wind tunnels;

the possibility of performing new types of tests: acceleration and deceleration, imitation of the runway effect;

reduction in required power and liquid nitrogen consumption as compared to a cryogenic wind tunnel having the same dimensions and parameters;

ecological friendliness of the facility.

REFERENCES

1. Goodyer, M. J.; and Kilgore, R. A.: The High Reynolds Number Cryogenic Wind Tunnel. AIAA paper 72 - 995, 7th Aerodynamic Testing Conference, Palo Alto, Calif., September 13 - 15, 1972. Also, AIAA Journal, vol. 11, no. 5, May 1973, pp. 613-619.
2. Kilgore, R. A.: The Cryogenic Wind Tunnel for High Reynolds Number Testing. NASA TM - 70207, 1974.
3. Iskra, A. L.; and Machekhina, G. N.: Cryogenic Wind Tunnels. TsAGI Technical Review No 535, 1978 (in Russian).
4. Kilgore, R. A.: Other Cryogenic Wind Projects. Presented at the AGARD - FDR/VKI Special Course, Advances in Cryogenic Wind Tunnel Technology, held at the von Karman Institute for Fluid Dynamics, Rhode-Saint-Genese, Belgium, June 5 - 9, 1989, AGARD-R-774.
5. Tuttle, M. H.; Kilgore, R. A.; and Moore, D. L.: Cryogenic Wind Tunnels, A Comprehensive Annotated Bibliography, NASA TM - 4273, April 1991.
6. Borisov, S. Yu.; Iskra, A. L.; and Philatov, A. P.: Cryogenic Test Rig with Aerodynamic Carriage. Scientific - Research Report TsAGI, June 1983 (in Russian).
7. Borisov, S. Yu.; Iskra, A. L.; and Philatov, A. P.: Aerodynamic Test Rig. Inventor's Certificate No 1230930 with Priority from 20.07.84 (in Russian).
8. Lawing, P. L.; and Johnson, W. G., Jr.: A Forecast of New Test Capability Using Magnetic Suspension and Balance Systems. AIAA 15th Aerodynamic Testing Conference, San Diego, California AIAA Paper No 88 - 2013, May 18 - 20, 1988.
9. Tuttle, M. H.; Kilgore, R. A.; and Boyden, R. P.: Magnetic Suspension and Balance Systems - A Selected, Annotated Bibliography. NASA TM - 84661, 1983.
10. Zemchenkov, J. V.: Test Facilities of USA, NASA, Research Centers. TsAGI Technical Review No 618, 1983 (in Russian).

ACKNOWLEDGEMENT

The authors wish to thank Robert A. Kilgore and the Organizing Committee for the invitation to attend the conference.

TABLE 1. LENGTH OF THE CHANNEL SECTION AND TIME OF THE CARRIAGE
ACCELERATION AND DECELERATION

Mach number	Time t, sec; length L, m	Load factor n					
		1	2	3	4	5	10
0.2	t1 = t3	3.7	1.9	1.2	0.93	0.74	0.37
	L1 = L3	67	34	22	17	13	6.7
	L2	36	36	36	36	36	36
	Ls	170	104	80	70	63	49
0.3	t1 = t3	5.6	2.8	1.9	1.4	1.1	0.56
	L1 = L3	151	76	50	38	30	15
	L2	54	54	54	54	54	54
	Ls	356	206	154	130	114	84
0.45	t1 = t3	8.3	4.2	2.8	2.1	1.7	0.8
	L1 = L3	340	170	113	85	68	34
	L2	82	82	82	82	82	82
	Ls	762	422	308	252	218	150
1.0	t1 = t3	18.6	9.3	6.2	4.6	3.7	1.9
	L1 = L3	1690	845	563	423	338	169
	L2	182	182	182	182	182	182
	Ls	3560	1870	1310	1030	860	520
3.0	t1 = t3	56	28	19	14	11	5.6
	L1 = L3	15120	7560	5070	3780	3030	1510
	L2	544	544	544	544	544	544
	Ls	30790	15680	10630	8110	6530	3570

TABLE 2. COMPARISON OF MAIN CHARACTERISTICS OF THE FACILITIES

Facility parameters	Cryogenic channel	Tunnel T - 101 TsAGI	USA wind tunnel A = 36 x 24 m
Test section area, m	6.2 x 4.1	14 x 24	36 x 24
Facility dimensions, m	310 x 22	175 x 92	420 x 130
Pressure, atm	1	1	1
Temperature, K	82 - 300	300	300
Mach number; speed, m/sec	0.45	up to 60	up to 50
Re numbers, mil	up to 30	6	10
Drive power, MW	23	27	100

Session 10

BEARINGS 3

Chairman - Jim Downer
SatCon Technology Corporation

The Bearingless Electrical Machine

J. Bichsel
Institute of Electrotechnical Developments and Constructions
Swiss Federal Institute of Technology
Zurich, Switzerland

Abstract

Electromagnetic bearings allow the suspension of solids. For rotary applications the most important physical effect is the force of a magnetic circuit to a high-permeable armature, called the MAXWELL-force. Contrary to the commonly used so called MAXWELL-bearings, the bearingless electrical machine will take advantage of the reaction force of a conductor carrying a current in a magnetic field. This kind of force, called LORENTZ-force, generates the torque in direct current, asynchronous and synchronous machines. The magnetic field, which already exists in electrical machines and helps to build up the torque, can also be utilized for the suspension of the rotor. Besides the normal winding of the stator, we have to add a special winding, which generates forces for levitation. So a radial bearing, which is integrated directly in the active part of the machine, and the motor use the laminated core simultaneously. The cost for special punching dies can be dropped. Moreover the actual length of the machine is drastically reduced by omitting the space for the conventional MAXWELL-bearing and by the fact that the coil winding heads for LORENTZ-bearings are smaller than those for MAXWELL-bearings. Furthermore we are able to construct the winding for the levitating forces in a special way so that commercially available standard ac inverters for drives can be used.

Besides wholly magnetic suspended machines, there is a wide range of applications for normal drives with ball bearings. The slots of the laminated core will be filled with a winding for the torque and a special winding for the levitating forces, so it is possible to produce forces which suppress mechanical oscillations. Resonances of the rotor, especially critical speeds, can be dampened actively.

1. Introduction

The goal of the following paper is the derivation and the description of the properties which are necessary to build up a bearingless electrical machine. In chapter two the used symbols are listed and in the third the expressions "the bearingless electrical machine", the "LORENTZ-" and the "MAXWELL-force" are explained. In chapter four each force is illustrated by an example. Afterwards the basic requirements for radial LORENTZ-bearings are shown in passage five. The properties of the power converter are discussed in the next passage. The seventh section describes a prototype machine with a magnetic-bearing on the basis of the LORENTZ-force which is successfully integrated in the active part of an electrical machine, so we have the proof that the bearingless electrical machine is not just an idea but a fact. In the last chapter we make a brief summary and give an outlook for the future.

2. Symbols

B	flux density
\vec{B}	vector of the flux density
B_a	flux density in the air gap
F_M	MAXWELL-force
\vec{F}_L	force-vector of the LORENTZ-force
F_1, \dots, F_8	forces of a segment of the stator
I	current
\vec{l}	vector of the length of the machine
L_1, \dots, L_4	inductivities
q_a	area of a magnetic pole
μ_0	permittivity of the vacuum
μ_r	relative permittivity

3. Definitions

In the following chapter we will explain the expressions of "the bearingless electrical machine", the "LORENTZ-" and the "MAXWELL-force". These two forces are introduced for a good description of the effects of magnetism.

3.1. The Bearingless Electrical Machine

The conception of the bearingless electrical machine can easily be explained by figure 1. On the left side we find a profile of an electrical machine where the shaft is beared by ball-bearings. If we consider the rotor as a rigid body it has six degrees of freedom. Five of them are stabilized by the ball-bearings, the sixth is the rotation of the shaft. On the right side we find a picture of a bearingless electrical machine. The space, formerly used by the ball-bearings is not used any more, because now the stabilization of the five degrees of freedom takes place in the active part of the motor. So the place, where normally only the torque is built up, is also used now for generating the suspension-forces of the rotor. This leads to the next important point: Which kind of physical effects allows the generation of the torque and the suspension-forces at the same place? For electrical machines the most interesting forces are magnetically ones, especially the LORENTZ- and MAXWELL-force. They will be explained in the following section.

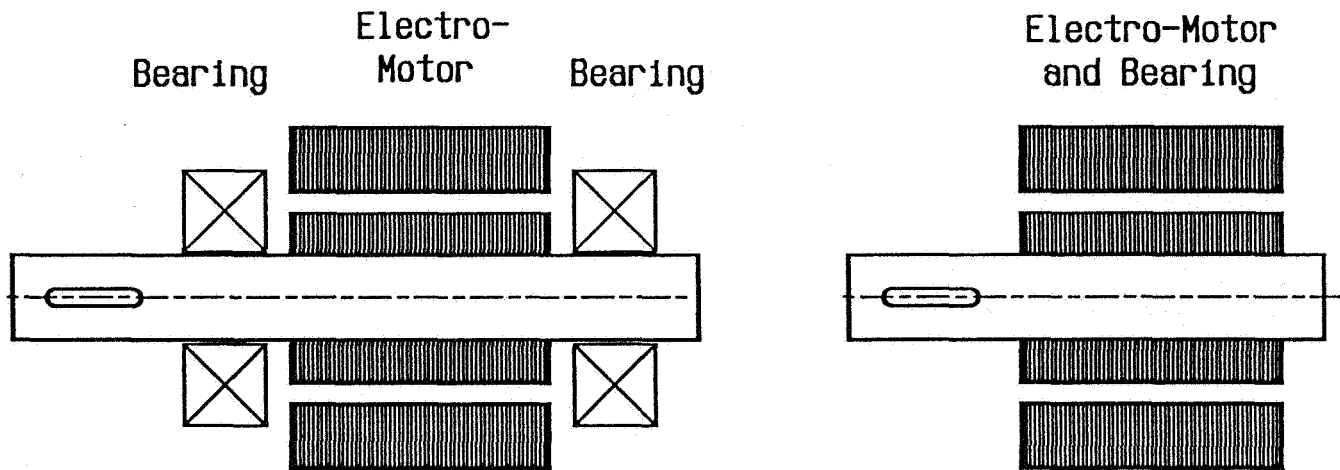


Figure 1: On the left side: electrical machine with ball-bearings.
On the right side: The "bearingless electrical machine".

3.2. Magnetic Forces

Now we will consider two important magnetic forces. To produce a rotation - or better a torque - in electrical machines, like DC, asynchronous or synchronous motors, we use the LORENTZ-force. This force is caused by a conductor carrying a current in a magnetic field. The basic formula is

$$F_L = I (l \times B)$$

with B the vector of the flux density, I the current in the conductor in the magnetic field and l the vector of the length of the machine. Normally in the magnetic suspension technique we take advantage of the force which is caused by a magnetic circuit to a high permeable armature, also called the MAXWELL-force. The most important application is the attracting force of a magnetic field to a core assembly in the vacuum. Here the formula for high values of relative permittivity ($\mu_r \gg 1$) is

$$F_M = \frac{B_a^2 q_a}{2 \mu_0}$$

where B_a is the flux density in the air-gap, q_a is the active area and μ_0 the permittivity in the vacuum.

Some points are interesting: The LORENTZ-force grows linearly with the B-field and can therefore either be attractive or repulsive. Contrary to this, the MAXWELL-force, whose force grows in square-law to the B-field, can only be attractive, independent of the direction of the B-field.

4. Typical Applications for Different Kinds of Magnetic Forces

The LORENTZ-force is typically used to produce the torque in electrical machines. The force at the rotor can be calculated by the LORENTZ-force formula or more visual by the right-hand rule where the thumb goes in the direction of the B-field, the forefinger in the direction of the current and the middle finger points in the direction of the force vector. Looking at figure 2 we will get, by dividing the rotor and stator in six sectors, F_1 through F_6 ; graphically by the right-hand rule or more mathematically by the LORENTZ-law. With the length l of the machine, the current I and the B-field the force-vectors F_1 to F_6 are determined. Together they form the torque M . With a constant flux density B , the amplitude of the torque can directly be controlled by the amplitude of the current.

The MAXWELL-force is best known by the magnetic suspension-technique. As an example we will take a radial bearing with two degrees of freedom as in figure 3. As we can see from the MAXWELL-force formula only attractive forces are possible. Considering only one axis, which corresponds to one degree of freedom, we have to add a second magnetic circuit to get a symmetrical solution.

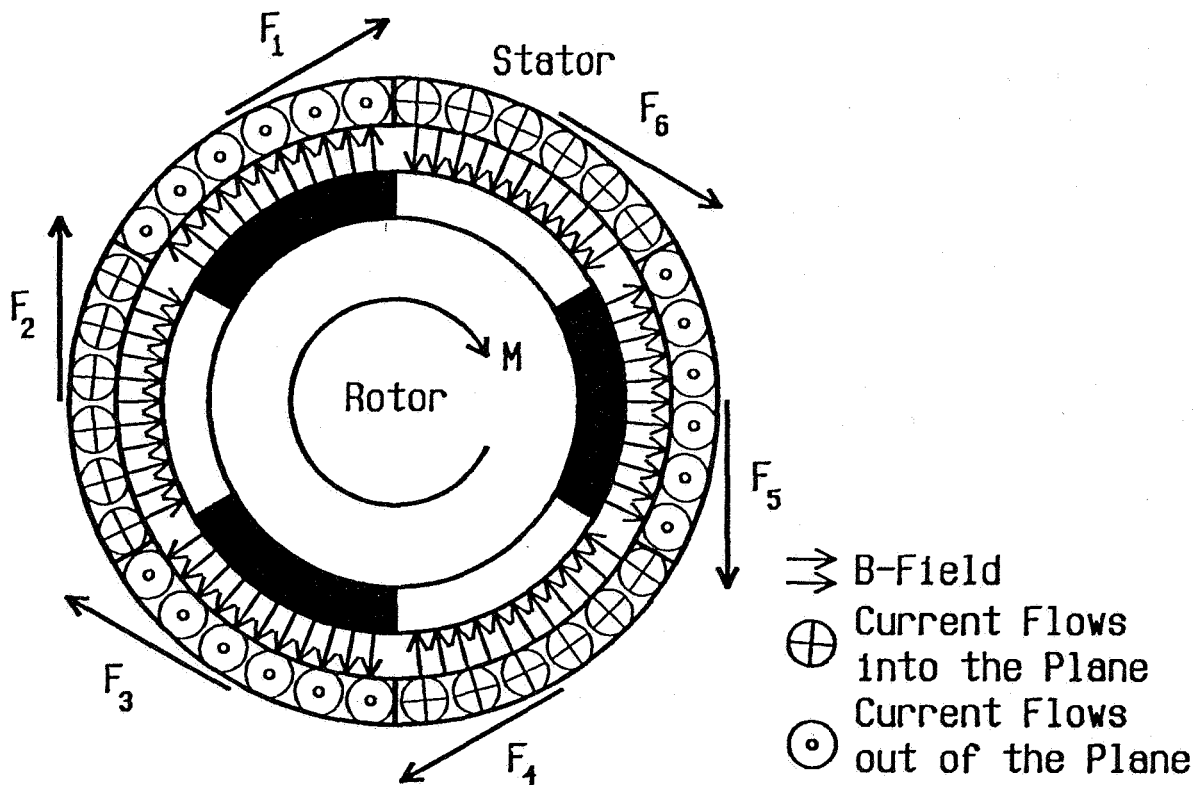


Figure 2: Generation of torque in an electrical machine.

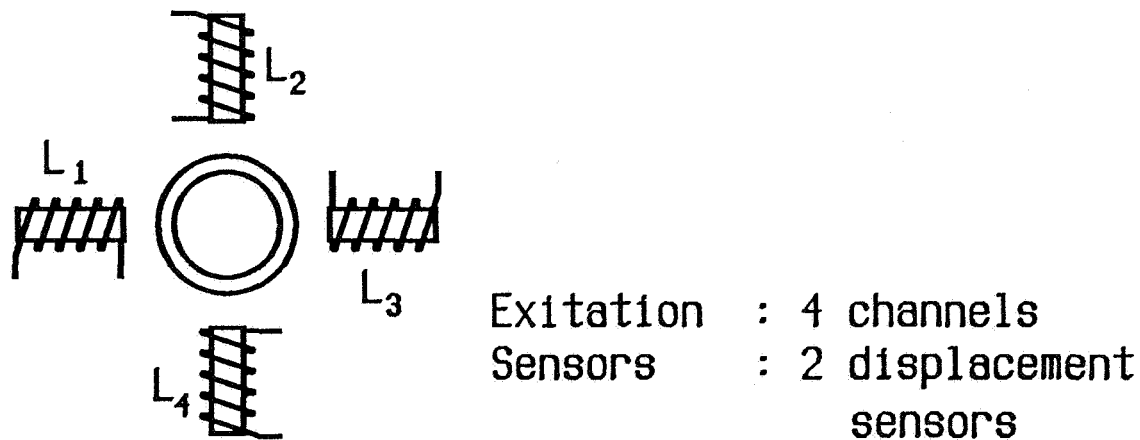


Figure 3: Symbolic inductors for a radial magnetic bearing with two degrees of freedom using the MAXWELL-force.

5. Using the LORENTZ-Force for a Magnetic Bearing

We may now raise the question, if it is possible to use the LORENTZ-force in an electrical machine not only to build up the torque but to produce a suspension force as well. In the years 1973 to 1975 Professor Hermann from Berlin made three patents[1,2,3] which give the theoretical basis for the LORENTZ-bearings. The basic idea is to integrate a LORENTZ-bearing in an electrical machine. In an electrical machine having n poles a new winding with $n + 1$ or (and) $n - 1$ poles must be added to generate a suspension force. This will be possible by controlling the current in a special way together with the corresponding air-gap-sensors and shaft-encoder. We can control the direction of force by adjusting the angle of the current in the stator. The amplitude of the force is regulated by the amperage. Analog to figure 2, we can split the stator and rotor of figure 4 in eight separate sections. So we will get, using the LORENTZ-force formula, the forces F_1 to F_8 . The sum of the sector-forces will give the resulting force F .

The most important problem is the control technique. Today we are able to control the LORENTZ-bearing with digital signal-processors, which works with high speed and precision. In our opinion it is the only way to find a satisfactory and practicable solution of this control problem. The continued considerations which were made at the Swiss Federal Institute of Technology, especially at the Institute of Electrotechnical Developments and Constructions, led to four new requests for patents[4,5,6,7].

The suspension-force in LORENTZ-bearings can be controlled by measuring the spatial orientation of the flux density. The theoretical basis for the determination of the flux-orientation can be found in the vector controlled management of the asynchronous and synchronous machine. Corresponding to this control we have to transform the machine-coordinates to the decoupled model-coordinates in order to get a more elementary description of the LORENTZ-bearing.

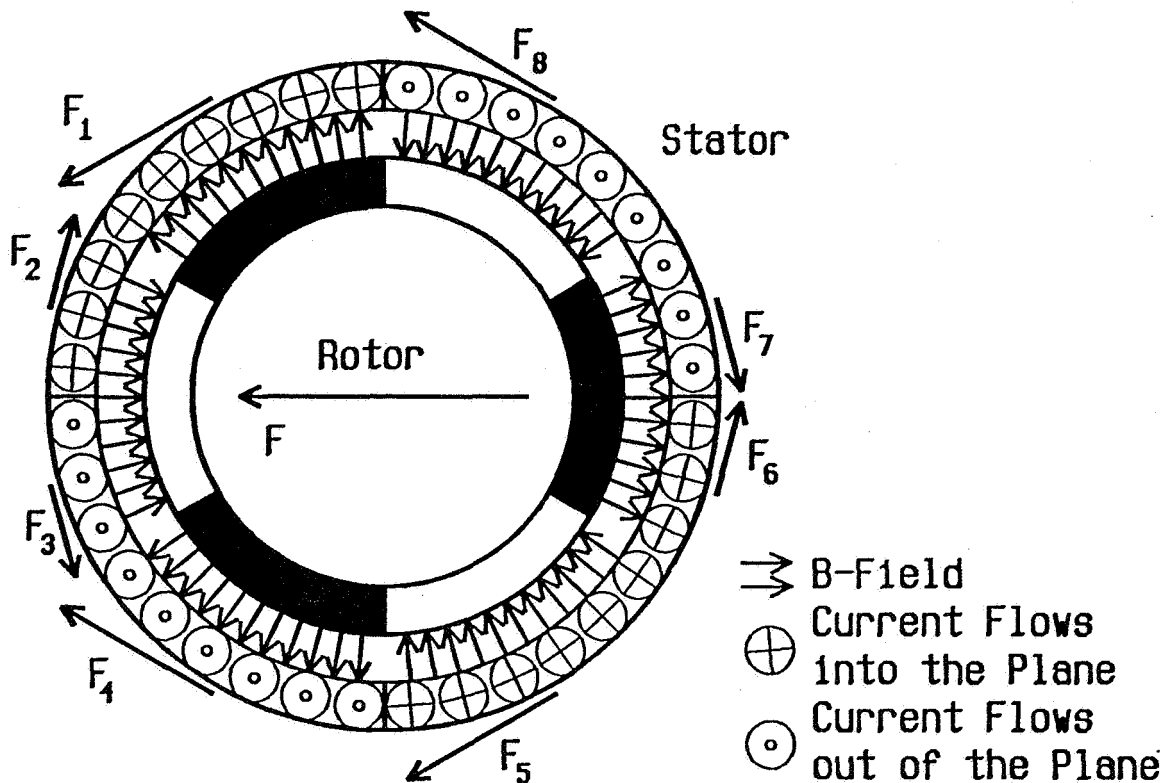


Figure 4: Force vectors for a LORENTZ-bearing.

6. The Power Converters

In magnetically beared machines we have to distinguish between power converters for the torque and for the suspension-forces. Power converters for torque are nowadays produced in quantity, but converters for magnetic bearings are more or less special solutions.

Moreover we have to consider that for MAXWELL-bearings the force is unilateral and therefore we need another type of power converter. It is called a half-bridge converter.

The situation is totally different for LORENTZ-bearings. Here we can, by inverting the direction of the current, change the direction of the force. So the electronic power converter must be a circuit with a full bridge. By using sophisticated core-windings it is possible to use normal AC-drive converters. Cost for special developments can be omitted. We only have to take care that the used power converters have a dynamic range large enough to control disturbances.

7. The Prototype Machine

In the preceding parts of this paper we have described possible solutions which allow us to build up a magnetic bearing with the LORENTZ-force. To verify the theoretical results we have constructed a prototype machine with which we could proof the theory[8].

As an example take a rigid body. It has six degrees of freedom: These are three rotations around the main axis and three translations along the main axis. To build up a more practical model corresponding to the prototype machine we have two degrees of freedom for translation in radial direction on both sides of the machine and a transversal degree of freedom. The sixth degree of freedom is the rotation of the shaft.

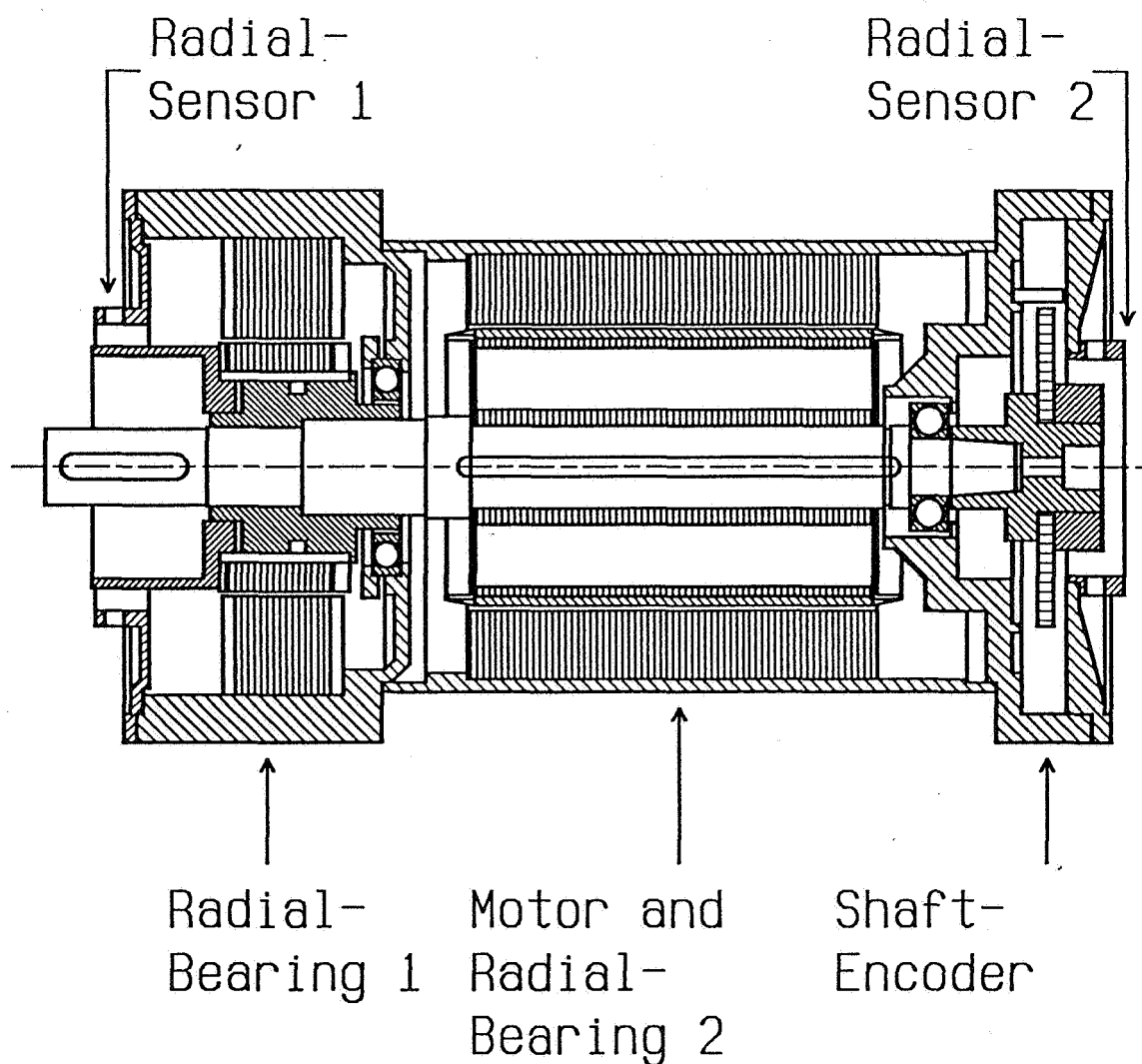


Figure 5: Cross section of the prototype machine.

In the prototype machine we have to control five degrees of freedom by magnetic bearings. Two degrees of freedom are controlled by LORENTZ-bearings and two by MAXWELL-bearings. The fifth is passively held in the center by magnetic forces, but could easily be controlled actively. The sixth degree of freedom, the rotation of the shaft, is controlled by a conventional electrical machine, here it is a synchronous machine with permanent magnet rotor. The torque of the machine is generated at the same place as the suspensions-forces for the LORENTZ-bearing. The power-rating of the machine is 1kW at 2000 rpm. In figure 5 we can see a cross section and in figure 6 a photograph of the machine.

ORIGINAL PAGE
BLACK AND WHITE PHOTOGRAPH

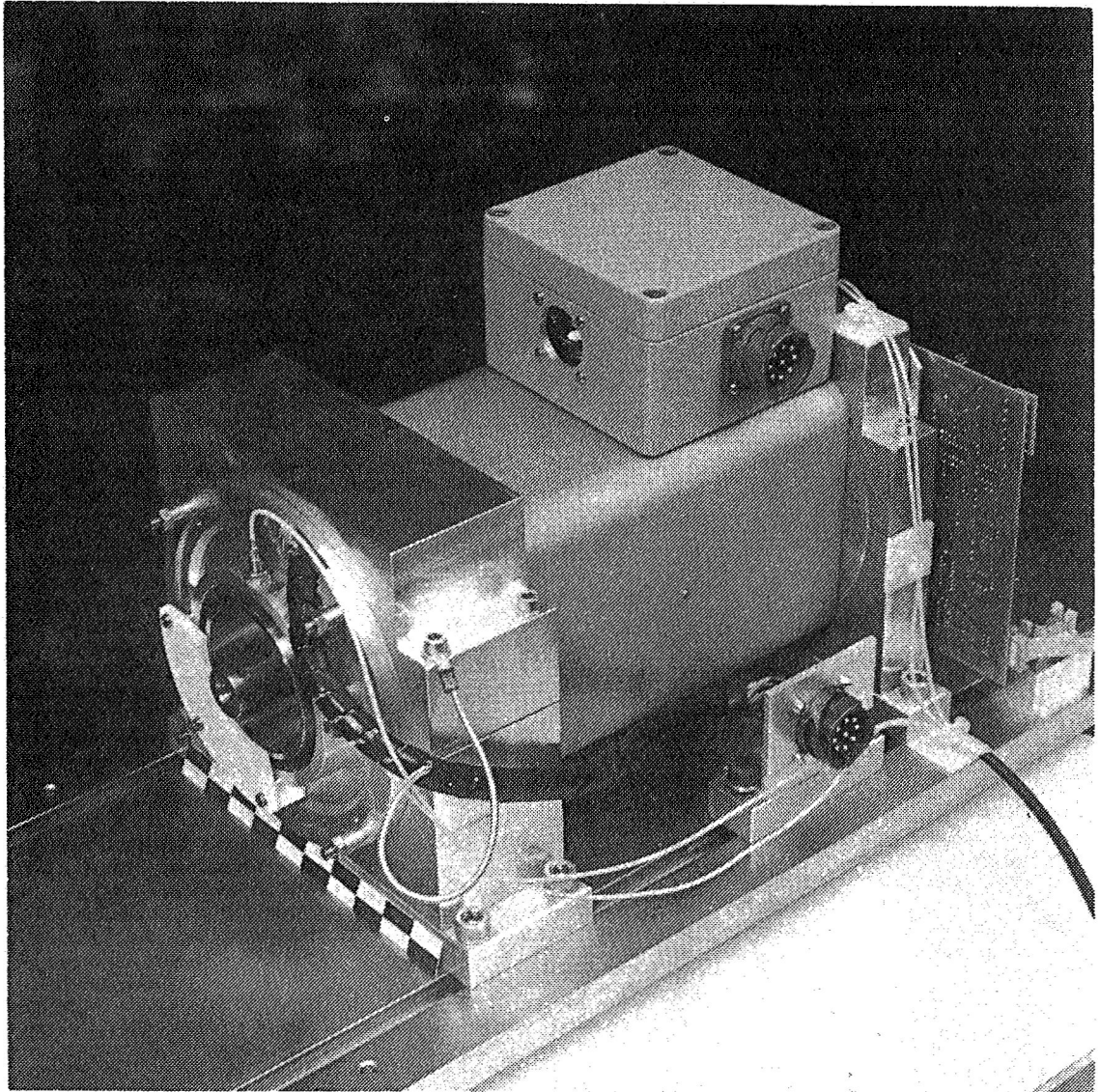


Figure 6: Photograph of the prototype machine.

Figure 7 shows the principle control mechanism of the prototype machine. The user can communicate over a PC with the magnetic bearing system. Signal-processors will analyze the incoming signals from the air-gap-sensors, the shaft-encoder and parameters from the user. The new values for the control-circuit are calculated and sent to the power converters.

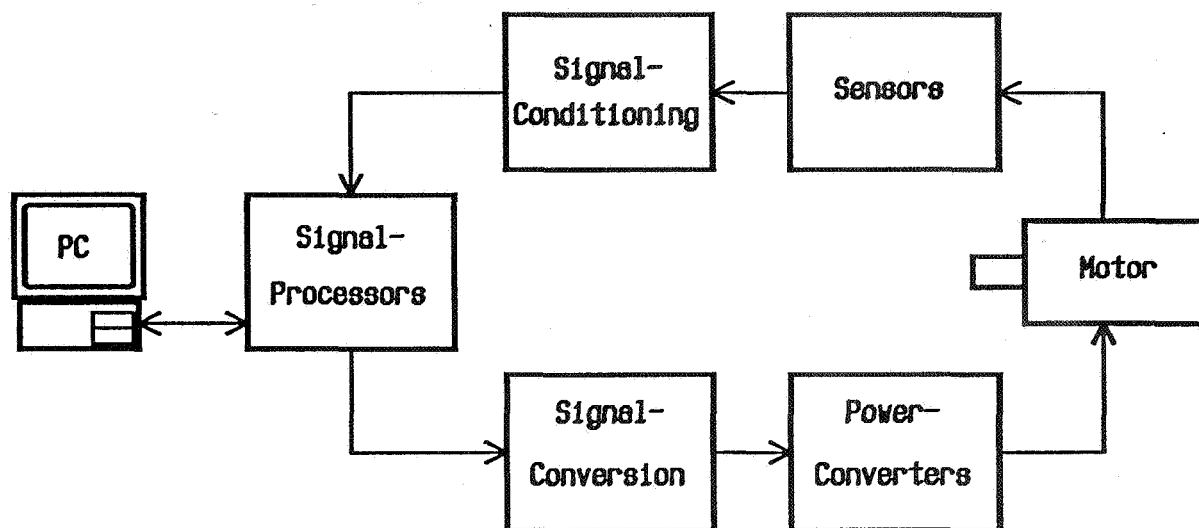


Figure 7: Block diagram of the whole system.

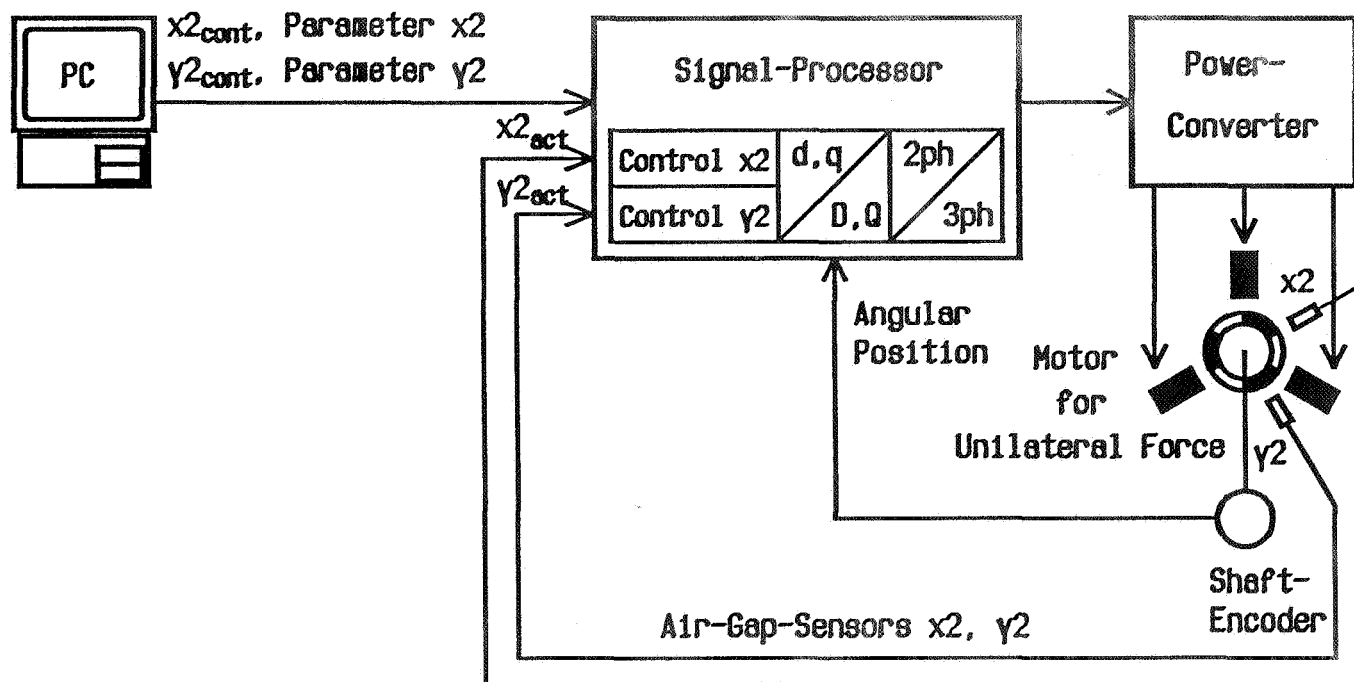


Figure 8: Control scheme for the LORENTZ-bearing.

Figure 8 shows a more detailed picture of the control-mechanism of the LORENTZ-bearing. As a basis we need the signals of the air-gap-sensors and the information of the shaft-encoder. With these data the signal-processor calculates the new values for the power converter in less than $20\mu\text{s}$, including the decoupling and transformation of the coordinates.

8. Conclusions

With this paper we have added some new aspects to the magnetic suspension technique. In conventional magnetic bearings the attracting force of a magnetic field to a core assembly is used. The newly described LORENTZ-force for a magnetic-levitated-system takes advantage of a conductor carrying a current in a magnetic field. Therefore it is possible to construct new types of machines with bearings integrated in the active part of a motor. On a prototype machine with integrated LORENTZ-radial-bearing and a second active MAXWELL-bearing we could prove that this kind of bearing is not only a theoretical game but can be realized with an adequate expenditure.

For the future we have to investigate some important aspects, which are listed below:

- The mechanical and electrical behaviours of fully integrated machines have to be analyzed.
- The characteristics of LORENTZ-bearings in high speed applications have to be investigated.
- A detailed model of the machine, considering effects of saturation, must be gained.
- A better control technique with observer and state space representation will improve the properties of the LORENTZ-bearing.
- LORENTZ-bearings which are designed for industrial applications must prove their qualities.

References

- [1] Hermann, P.
Deutsche Patent-Auslegeschrift P 23 58 527.5-32, 1973
- [2] Hermann, P.
Deutsche Patent-Offenlegungsschrift P 24 57 0841-32, 1974
- [3] Hermann, P.
Deutsche Patent-Offenlegungsschrift P 24 06 790.1-32, 1975
- [4] Bichsel, J.
Schweizerisches Patentgesuch Nr. 04 049/90-2, 1990
- [5] Bichsel, J.
Schweizerisches Patentgesuch Nr. 04 050/90-2, 1990
- [6] Bichsel, J.
Schweizerisches Patentgesuch Nr. 04 052/90-2, 1990
- [7] Bichsel, J.
Schweizerisches Patentgesuch Nr 04 051/90-0, 1990
- [8] Bichsel, J.
Beiträge zum lagerlosen Elektromotor, Dissertation ETH Zürich, 1990

N92-27794

WIDE GAP, PERMANENT MAGNET BIASED MAGNETIC BEARING SYSTEM

Karl Boden
Institut für Grenzflächenforschung und Vakuumphysik
Forschungszentrum Jülich, Postfach 1913
D-5170 Jülich
Germany

ABSTRACT

The unique features and applications of the presented electro-permanent magnetic bearing system essentially result from three facts: (1) The only bearing rotor components are non-laminated ferromagnetic steel collars or cylinders; (2) all radial and axial forces are transmitted via radial gaps; (3) large radial bearing gaps can be provided with minimum electric power consumption. The large gaps allow for effective encapsulation and shielding of the rotors at elevated or low temperatures, corrosive or ultra clean atmosphere or vacuum or high pressure environment. Two significant applications are described: (1) A magnetically suspended X-ray rotary anode was operated under high-vacuum conditions at 100 KV anode potential, 600°C temperature at the rotor collars and speed 18000 r.p.m. with 13 mm radial bearing gap. (2) An improved Czochralski-type crystal growth apparatus using the hot-wall-method for pulling GaAs-single-crystals of low dislocation density. Both, crystal and crucible are carried and transported by magnetically suspended shafts inside a hermetically sealed housing at 800°C shaft and wall temperature. The radial magnetic bearing gap measures 24 mm.

1. INTRODUCTION

Drive shafts are commonly used in mechanical applications, where linear and/or rotating motion of the shaft is necessary to perform a task. A variety of guide and drive means are developed for effecting the desired relative longitudinal and/or rotary movements of workpieces along a predetermined axis. But there are a lot of problems which are not satisfactorily solvable by the conventionally used bearing and sliding techniques.

Often it is not practical to include such guide- and drive-means within the work chamber, where the drive shaft or the workpiece is expected to operate in extreme conditions - for example contaminant-free or evacuated environment, elevated working temperatures or corrosive atmosphere. Under such conditions the means are, themselves, a source of contaminants and corrosive products or they are not able to work sufficiently. In such cases the drive shaft has to extend from without into the chamber and the means for controlling the movements of the workpiece are arranged outside the chamber. Usually it has

been the practice heretofore to employ dynamic sliding seals cooperable between the enclosure and the drive shaft.

Sealing a sliding shaft is a difficult task. One conventional method is to surround the shaft with a close-fitting sleeve and then fill the annular space between the shaft and the sleeve with a high density lubricant (Fig. 1).

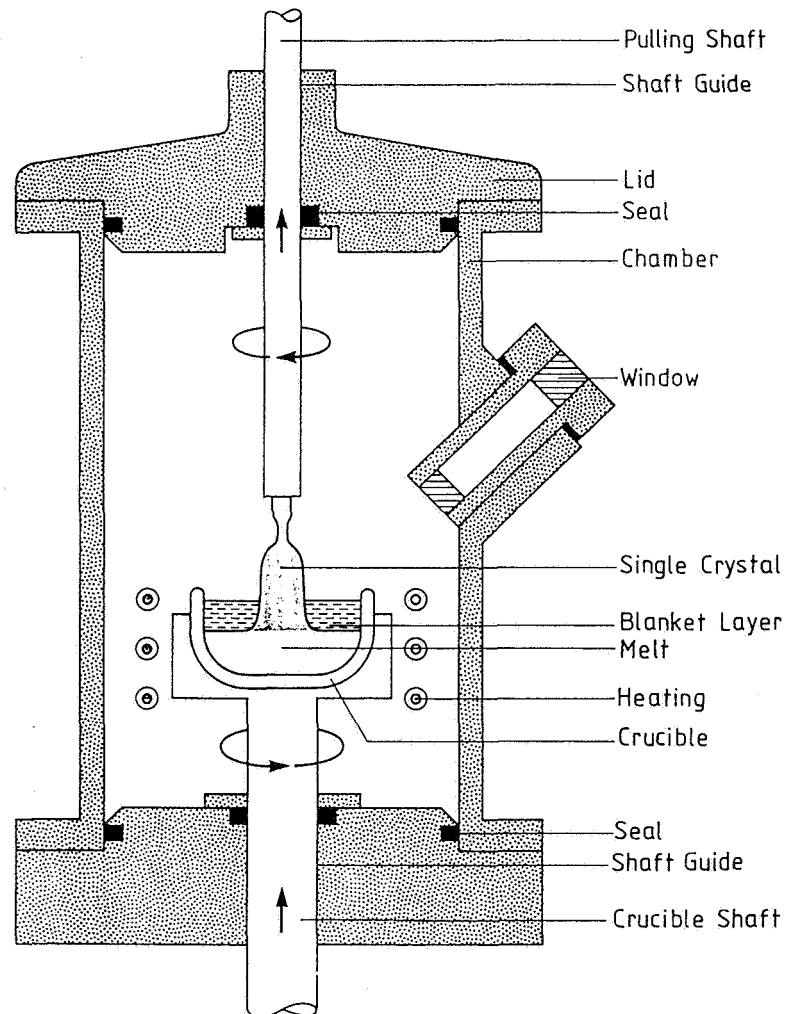


Fig. 1: Czochralski crystal growth apparatus

A modern improvement in sealing technology calls for the use of a magnetic fluid as lubricant working in conjunction with a magnetic shaft piece and a magnetically permeable sleeve or vice versa. This concept suffers from the problems of migration of the lubricant out of the annular space, limited working temperature and poor corrosion

resistance. Furthermore seals are vulnerable to destructive action of deposits generated by the process, which find their way to the moving parts of the seals and have an abrasive or deteriorating effect thereon.

Vice versa, abrasion products generated by the residual friction effects in the seals may pollute and destroy the working process taking place inside the chamber.

The reliability of such seals is influenced adversely according to the degree to which atmospheric gas leaks past the seals into the enclosure or volatile process gas leaks out. These leakage effects depend on the problems summarized above. So the reliability of this mechanical solution is often less than satisfactory in the mentioned situations or applications.

Moreover, friction generated vibrations or scattering resulting from the mentioned frictional contact between shaft and sleeves may result and give rise to spontaneous defects of sensitive processes.

Because of the relatively stiff contact of the housing with the shaft, external influences on the apparatus in the form of vibrations or shocks also can not be prevented from detrimentally affecting processes.

Thus, also from the standpoint of vibration and shock isolation this solution is impractical in many situations as is described, by way of example, later on.

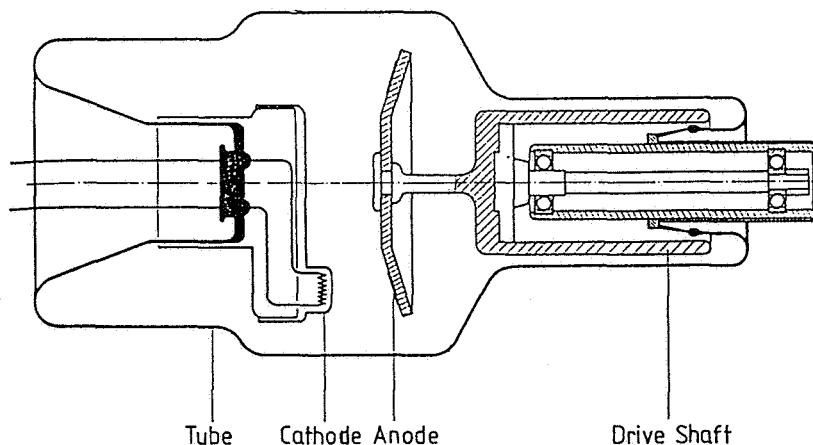


Fig. 2: Rotary anode X-ray tube

A more or less sufficient conventional method provides only the driving means, like electric motor stators or magnetic coupling cages, outside the chamber and arranges the shaft including the bearing unit within this enclosure. Thus, the chamber may be hermetically closed. In vacuum applications, as shown in Fig. 2, special non-lubricated

ball bearings have to be used. Appropriate bearings for heated and/or corrosive environments are not commonly available.

The bearing wear increases with the square of rotary speed. It is not possible to avoid bearing noises, which increase with rotary speed. At high rotational speed applications these effects are a main disadvantage, particularly in medical work, as demonstrated later on.

For this area, classical systems using conventional ball bearings are not well fitted. To overcome the mentioned problems, modern magnetic bearing technology may be used. This paper presents a wide gap permanent magnet biased magnetic bearing system. Its performance is demonstrated by example of two significant applications.

2. PERMANENT MAGNET BIASED MAGNETIC BEARING

The basic configuration of the magnetic bearing system used in the applications mentioned above was designed in the late 60's. It is described in more detail in previous papers [1,2].

Figure 3 shows the basic system using a non-laminated rotor collar made of ferromagnetic mild steel and an annular stator magnet made e.g. of bariumferrite-material. The axially magnetized permanent magnet surrounds the collar, thus forming an annular ring-shaped gap between the collar and the magnet.

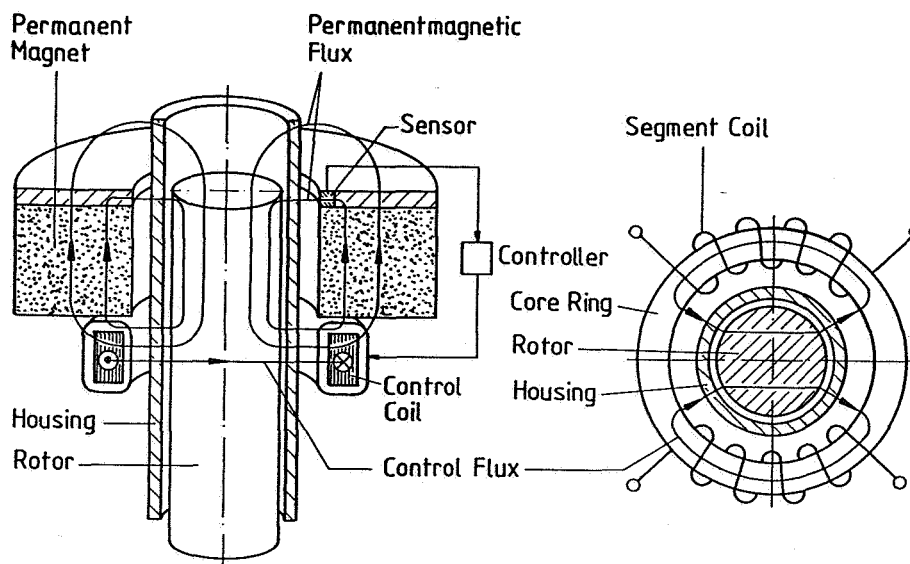


Fig. 3: Wide gap, permanent magnet biased magnetic bearing system

Along the axial direction, the rotor shaft is stably suspended within the region of maximum field energy density of the permanent magnet. The stiffness of this magnetic spring may be influenced by an addi-

tional active stabilization (not shown). This means can also be used to enhance the low structural damping. But in many applications the passive stabilization of the axial collar position results in sufficient conditions.

In the radial directions an equilibrium position exists for the collar at the symmetry axis of the ring magnet. But this equilibrium is unstable and therefore a conversion of the unstable equilibrium in a stable one is required. It means that active stabilization of the collar position in two orthogonal radial axes is necessary.

The active stabilizing device comprises contactless position sensors, electronic control means and electromagnetic actuators.

In this bearing system magnetoresistive field plates can be used for pick-up of the radial collar or shaft position. This allows for the accommodation of a metallic tube between rotor shaft and the stator package, which would not be possible by using optical or high-frequency actuated pick-up means. The biasing field required for proper operation of these sensors is supplied by the permanent magnet. The thermal sensitivity of the magnetoresistive pick-up system does not introduce any drift problems of the shaft position, due to an automatic zero power control circuit incorporated in the stabilization electronics. So the radial collar position is merely determined by the permanent configuration and the static radial load exerted to the shaft.

Two pairs of actuator coils wound on a common laminated ferromagnetic ring shaped core are arranged immediately next to the permanent magnet. The permanent magnetic flux passes through the lower gap in parallel to the control flux. Thus the control flux modulates the normally symmetric permanent biasing flux in an antisymmetric manner, hence producing controllable radial forces. The radial magnetic forces exerted to the shaft are proportional to the product of B_0 and ΔB , where B_0 represents the biasing induction and ΔB the differential amplitude of the control induction generated by the control coils in radial direction.

Besides the conversion of the radial instability into a stable one, the biasing effect provides the desirable benefits of

- linearizing the force versus current relationship
- multiplying the effectiveness of the control ampereturns
- zero force at zero current in the passive equilibrium position, which consequently may represent the reference axis for the position control circuit
- minimizing of electric power consumption
- feasibility of large radial gaps between rotor and stator

Therefore, the electronic control device may have a relatively simple structure because it is freed from linearization networks for either sensor and force signals and needs only small power consumption. So it can be flexible adapted to the application requirements.

The mentioned applications mainly derive benefit from the following

facts:

- All radial as well as axial forces exerted to the shaft are transmitted from the stator to the shaft via radial gaps
- Relatively large radial gaps can be provided between the rotor and stator elements which are magnetically excited by no electric power consuming permanent magnets - the volume and material of these stator magnets can be easily adapted to the required magnetic energy in the gaps.
- The bearing concept allows for the accommodation of compact tubes in the gap, as a hermetic seal between the working environment of the shaft and the outer atmosphere - neither windows nor feed-throughs are necessary
- The arrangement of thick-walled tubes of non-magnetic stainless steel and/or heating, insulating and cooling elements in the annular gap is possible.
- The only bearing components attached to the shaft are non laminated ferromagnetic steel collars or cylinders - a variety of materials ranging from mild steel to ferromagnetic stainless steel has been realized and used.
- The use of iron-cobalt alloys gives the chance to set out the shaft to elevated working temperatures - materials with a Curie-temperature up to 950°C are available
- Linear motion of the shaft along the tube axis without geometrical limitation by bearing or drive components is accomplished
- Very low transmissibility of shocks and vibrations from the environment is achieved - the magnetic bearing acts as a vibration isolator

Thus the mentioned magnetic bearing concept covers a lot of the complex requirements imposed by modern technical applications.

3. APPLICATIONS OF THE MAGNETIC BEARING SYSTEMS

3.1 Rotary anode X-ray tube

3.1.1 State of the art

Rotary anode X-ray tubes for medical diagnostics are designed such that its anode is rotated at high speed in a highly evacuated seal glass envelope (Fig. 2). The anode emits X-rays as it is bombarded by high speed electrons emitted from a cathode. Unfortunately, the electron beam energy is mostly converted into heat. Thus, the anode is heated up to elevated temperatures depending on the electron energy and the exposure time. In order to keep the anode temperature in a limited range the energy is spread over the circumference of the rotating anode. That means the exposure time has to be in correlation with the revolution time of the anode.

This type of X-ray tube is cooled only by giving off heat radiation to the surrounding environment. The application range of these tubes extends besides operation for fluoroscopy, for which the rotary anode

tube must possess a high permanent load-carrying capacity, to operation at high power flash and spot density with exposure times in the range of a few milliseconds. Such short time exposures are applied in medical diagnosis, for example in taking x-ray pictures of an organ in a living body. In such cases the rotary anode has to run at full rotation speed only during the short flash for taking the picture.

As the rotational revolution time is matching the exposure time the flash energy is uniformly distributed at the anode rim. For example, at a desired exposure time of 3 milliseconds the suitable rotational anode frequency should be in the range of 300 RPS.

In the case of conventional tubes this frequency is limited to typically 150 RPS in view of life time, temperature, noise and power restrictions caused by the up to now used ball bearings. Due to the wear of these bearings, which causes the most serious lifetime limit of the tube, it is not possible to let the anode continuously turn longer than is necessary. Therefore, the tube is not ready for photographing at any time: It has to be accelerated from still stand to the working frequency before and broken to stillstand after each flash. Powerful drive units with a power of several Kilowatts have to be installed to keep the acceleration and breaking time as short as possible in order, on the one hand, to keep the waiting time of the operator as short as possible, and, on the other hand, to diminish the bearing wear, which increases, as mentioned above, with the square of the bearing speed. A further disadvantage is that this drive and bearing means are the source of unwanted noises which increase with the rotating frequency and with the drive power. This sound emission is bound to be disturbing, particularly in the field of human medicine.

3.1.2 Advanced design

To overcome the above mentioned problems an improved rotary X-ray tube of the type generally described above has been developed in our laboratory in collaboration with Siemens AG, Erlangen [3]. In this machine a contactless and therefore wearing free support of the drive shaft of the anode is provided and the anode current is supplied via a touching contact which is designed as a magnetic switch.

Figure 4 shows a longitudinal section of this embodiment. The disc shaped anode is located inside the glass housing opposite to the cathode. It is fixed on the closed end of the drive shaft which has the form of a hollow cylinder. The shaft consists of a series of collars fixed to each other coaxially to the shaft axis. The bearing collars in the area of the magnetic bearings are made of ferromagnetic mild steel while the connecting collar consists of non magnetic steel. At the open end of the shaft a drive collar made of copper is affixed to the shaft. The shaft parts are connected by welding or soldering methods in order to prevent slits and holes which may be the source of outgassing effects and resulting vacuum contamination. The bearing and drive package is arranged outside of the envelope. Two magnetic bearing stators of the type described and the drive stator are coaxially fixed in this stator package.

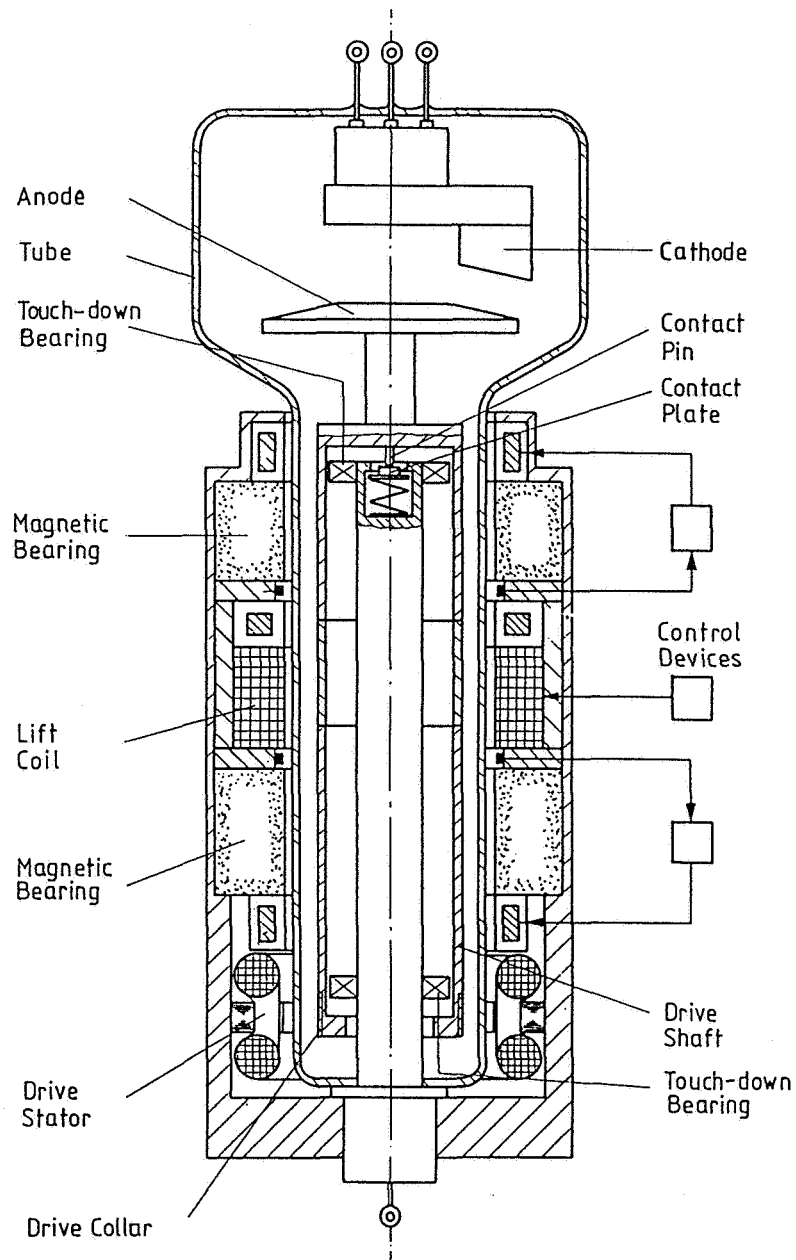


Fig. 4: Rotary anode X-ray tube with magnetically supported anode

An additional electromagnetic coil is provided in the space between the bearing stators. The wire of this coil is wound in the circumferential direction. Thus the current generated magnetic field of this coil causes an axial force exerted to the shaft which causes an axial motion of the shaft. The resulting shift direction corresponds to the current direction, the shift amplitude to the current amplitude. Hence also with this rotary anode design it is possible to set or adjust the rotary anode at different working positions by external control of the coil current. The procedure can be used to open

and close the axial touching contact for current supply to the anode.

This contact, for example, consists of a pin coaxially affixed to the drive shaft and a spring mounted contact plate at the stationary axis. The axis is surrounded by the hollow shaft and carries the anode voltage. Thus the anode current is fed from outside the tube via the axle to the anode. The construction allows opening and closing of the slip contact in the anode voltage circuit by moving the anode to open and close position while the drive shaft is kept in continuous rotation. In the consequence this X-ray tube is in practice ready for operation without loss of time under condition of minimum wear, because wear happens only at very short slip contact time.

Two lubricant-free touch-down bearings are fixed to the axle. Due to a given radial and axial clearance they only come into action in the event of bearing breakdown or switch off. Thus, such a construction provides reliable operation because by accident the shaft is caught approximately in position by the axle.

A wide radial gap is provided between the drive shaft and the stator elements in order to insulate the shaft electrically from the housing tube. Also the stationary axle is connected to the stator unit via electrically insulating materials. A gap width of 13 mm enables the anode to operate at voltages up to 100 KV positive with respect to ground. Therefore a significant increase of the electron voltage by the factor 2 up to 200 KV may be achieved only by using conventional 100 KV voltage supply equipment.

The concept described has been realized and tested in 1979. (Fig. 4,5)

The significant test results are the following:

- Working speed: 300 RPS
- Drive power: A few watts at working speed
- Anode-cathode-voltage: 150 KV, symmetric to ground
- Shaft-temperature: 600°C
- Stator-temperature: 120°C

This machine was the first known rotary anode x-ray tube provided with contactless magnetic bearings. The unique features of this concept are confirmed by test:

- Continuous anode rotation resulting in steady state operation
- Increase of efficiency due to the realisation of
 - increased speed rotation of the anode
 - increased electron voltage
 - low drive power consumption
- Easy installation
- Quiet operation due to low power motor and the absence of noise generating rolling bearings and friction effects

By using the described contactless magnetic bearing concept the effectiveness, the handling procedure, the load capacity and the compa-

tibility with the environment of rotary anode X-ray tubes are significantly improved.

ORIGINAL PAGE
BLACK AND WHITE PHOTOGRAPH

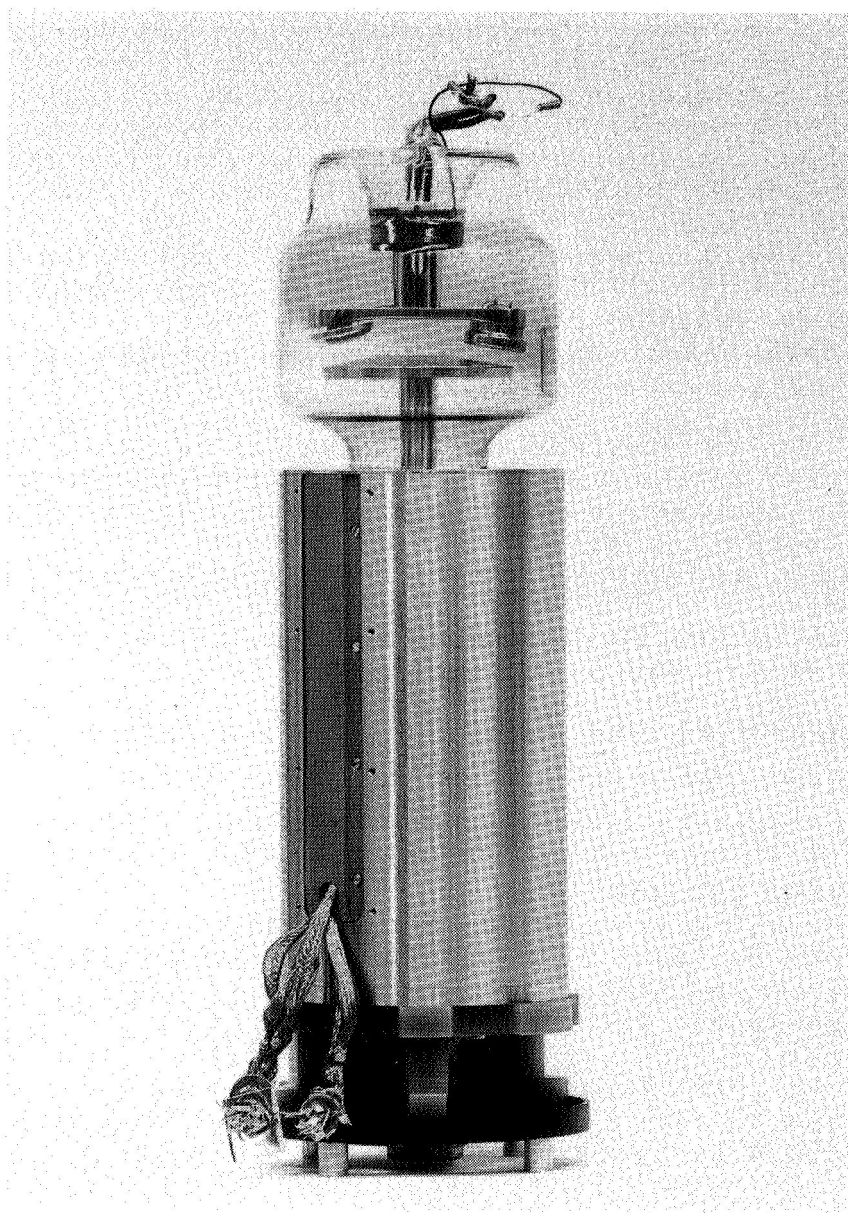


Fig. 5: Rotary anode X-ray tube with magnetically supported anode

3.2 Apparatus for growing semiconductor crystals from the melt

3.2.1 State of the art

3.2.1.1 Czochralski-Method

Similar complex bearing and sealing condition are required in the fabrication area of high quality semiconducting crystals.

Such crystals are typically formed using the Czochralski crucible melt method (Fig. 1) [4] in which single crystals are pulled from a melt which is contained in a crucible. The necessary pull motion is usually achieved by axially moving and rotating of both the melt and the growing crystal by supporting shafts.

In order to ensure continuous growth of the crystal of utmost perfection, i.e. orderly crystal lattice structure, certain process and apparatus requirements have to be fulfilled. In growing such crystals, it is an essential demand that the crystal-growing operation is conducted in a contaminant-free environment so that the crystals formed are of utmost purity. Therefore, the growing process has to be performed in a closed chamber to enable any desired atmosphere to be maintained in the working area. The number of seals, windows and feedthroughs has to be reduced as far as possible in order to minimize the risk of breakage, air leakage or toxical gas leaking out.

Dynamic seals of drive shafts are vulnerable to destructive action of deposits of the heated material or by chemically reactive process gas; so they may foul the drive shaft and its seal at the point of entry into the chamber.

Furthermore it is very important that both the crystal and the melt are moved extremely smoothly and in a very controlled manner to ensure continuous growth of the crystal with an orderly lattice structure. Slightest discontinuities of the shaft velocity as caused by vibrations, shocks and unbalances may introduce unstable, disturbing effects into the solidification front, which result in dislocations in the final crystal structure.

As mentioned above, either the commonly used seals themselves, as well as the driving and supporting means of the shaft are a source of the undesired effects. These elements need essential refinements in order to achieve a sufficiently controlled motion of the shaft.

Furthermore, it is necessary to control the size of the growing crystal body in order to keep the cylindrical part used for electronic device production within tight limits. Usually direct video measurement of the crystal diameter via an observation window supports closed-loop automatic diameter control. Another diameter monitoring method currently used is based on controlling the rate of the crystal weight gain. The control is realized by means of closed-loop adjustment of the shaft lift rate and/or melt temperature.

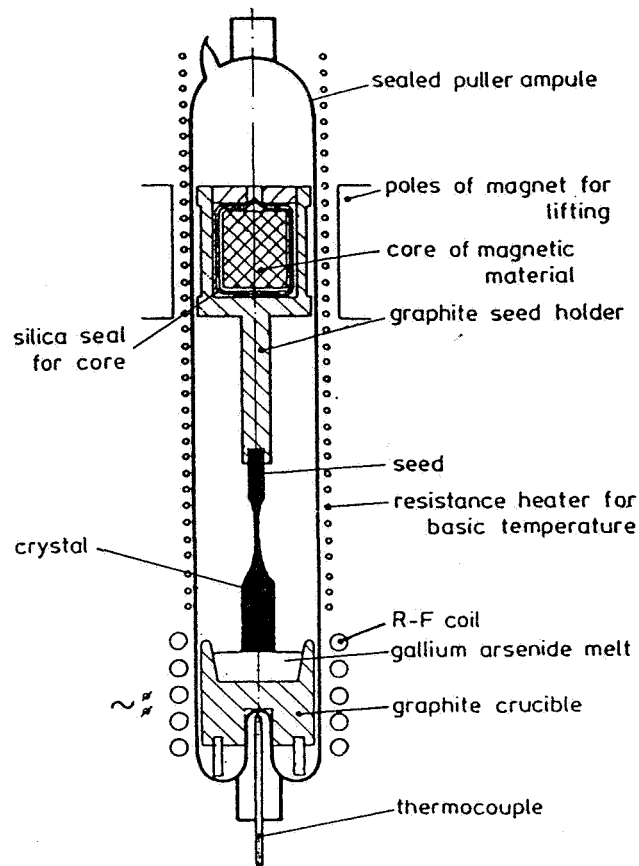


Fig. 6: Gremmelmaier crystal growth apparatus

The growth of compound semiconductor crystals as for example gallium-marsenide creates many more processing problems than single element crystals like silicon. It is the main demand that the ratio of the compound elements gallium and arsenic has to be kept precisely stable during the growing process. Unfortunately, arsenic is very volatile at the melting point of GaAs, so that it tends to evaporate from the melt. Consequently, the stoichiometry of the melt and the growing crystal is disturbed.

Up to now two methods are used to avoid these disturbances:

3.2.1.2 Liquid-Encapsulated Czochralski-Method

In the so called LEC (Liquid-Encapsulated-Czochralski)-process a blanket layer of molten boron oxide is floated on top of the melt as to prevent the mentioned evaporation.

Unfortunately this LEC-layer is responsible for a relatively high dislocation density. Plastic crystal deformation is caused by the high temperature gradient on the crystal surface when pushed through the layer surface. Currently no LEC-apparatus is known which maintains the temperature gradient in a sufficiently narrow range.

3.2.1.3 Gremmelmaier-Method

The so called HWC (Hot-Wall Czochralski)-process [5] as shown in Figure 6 provides heating of the process chamber to a temperature above the sublimation and condensation point of arsenic ($\sim 600^{\circ}\text{C}$). So an arsenic ambient is created inside the chamber. The transport of arsenic out of the melt is prevented and the stoichiometry is not lost. The chamber is completely sealed by a puller ampule. The crystal support shaft is magnetically coupled to drive means, which are arranged outside the chamber and are moved while radially sliding at the chamber inner wall surface. Due to the friction induced problems of vibration and wear the operation control is very difficult and the load capability is limited to several hundred grams, so this method has not succeeded for application at an industrial scale.

Also the diameter control of the described growth methods for GaAs is much more difficult than with silicon. Either the blanket encapsulation layer or the sliding coupling means prevent a sufficiently precise control of the diameter of the growing crystal.

3.2.2 Advanced design

An embodiment of an improved apparatus suitable for the growth of crystal according to the mentioned aspects will now be described with reference to Figure 7. This drawing is a vertical sectional view of an Hot-Wall-Czochralski-apparatus for the growth of GaAs crystals from the melt utilizing the magnetic bearing technique presented above [6,7].

Both crystal and crucible are carried and transported by shafts which are magnetically suspended by the surrounding stator means. These stator means and the annular drive stator are assembled to a compact stator package similar to the X-ray tube embodiment described.

The stators are mechanically connected to linear drive means which effect the axial motion of crystal and crucible. The rotary motion is accomplished by rotary drive stators.

The bearing means are designed to provide a load capability of more than 20 kg at a gap width of 26 mm. This gap allows for the accommodation of hermetically sealed tubes made of Quartz and additional heating, insulating and cooling means. The inner surface of the tube can be heated up to 800°C while the outer surface of the tube unit can be maintained near room temperature. Thus overheating of the stator unit is prevented.

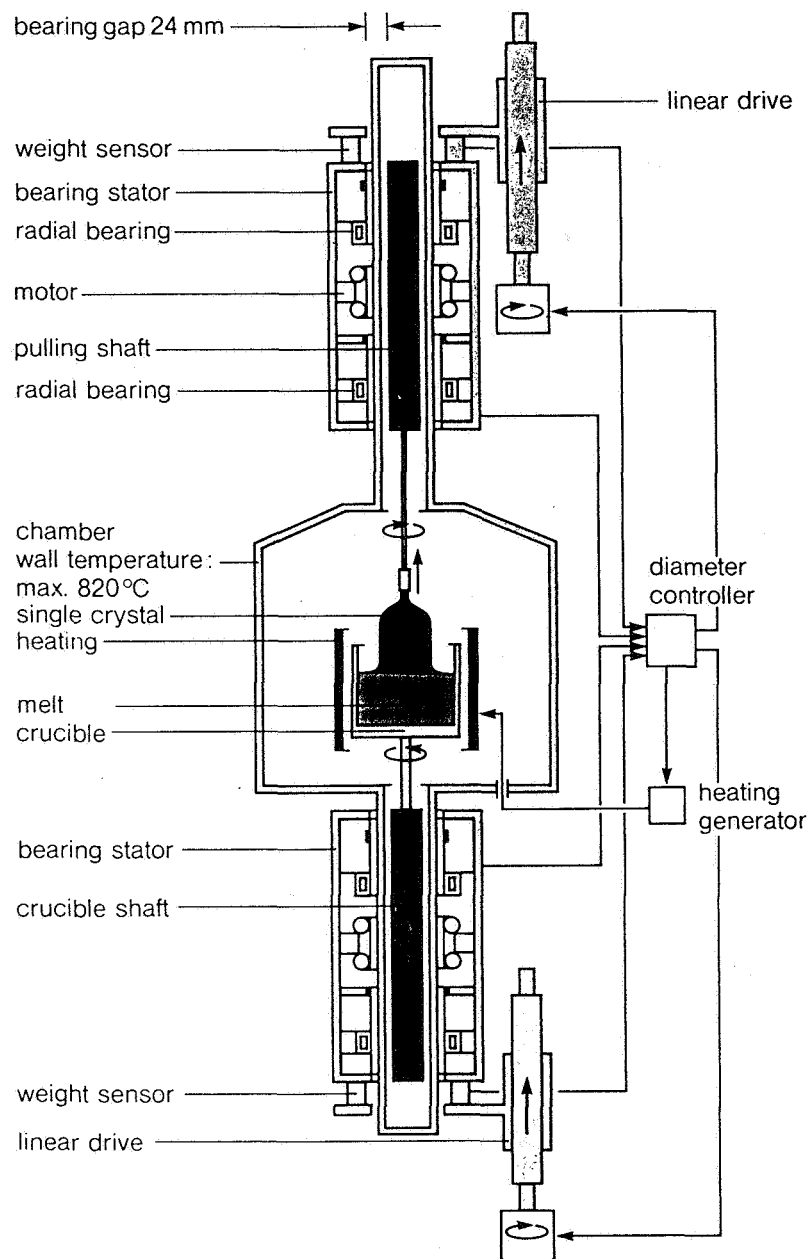


Fig. 7: Hot-wall Czochralski crystal growth apparatus with magnetically suspended pulling and crucible shaft

The bearing collars, which are fixed to the shaft in a similar manner as shown with the X-ray tube, are made of an iron-cobalt alloy with a Curie-temperature of 950°C. The entire shaft including the motor means is hermetically cladded by a corrosion-resistant quartz tube.

Consequently, this machine fulfills the basic requirements of the HWC-method for the growth of GaAs monocrystals at an industrial scale.

Beyond it this concept further provides two different simultaneously usable methods for monitoring the diameter of the growing crystal[8]:

- (1) Force transducers are provided between the stator unit and the linear drive means measuring the weight of the entire moving parts. The rate of crystal and melt weight gain derived from the force signal enables the method for a diameter control. The complete measuring unit is arranged outside the growth chamber. Consequently, this detection procedure is effected in a completely frictionless manner, and is also free from signal disturbing effects such as corrosion, pressure or temperature.
- (2) In the second method, the drive energy consumed by the viscous friction between crystal and melt is detected. This depends mainly on the radius of the growing crystal and on the rotational frequency. The preferred application comprises
 - the rotary drive unit, in this case, designed as an asynchronous motor
 - sensor means for detecting the rotational frequency of the shafts and
 - a control device for keeping the crystal or crucible in constant rotation.

Under such conditions, the drive currents or voltages only depend on the crystal diameter and consequently can be used as actuating signals in a closed-loop diameter control unit as mentioned above. Also in this embodiment no window or feedthrough is necessary.

In summary, the machine provides a contactless and wearless suspension of the crucible and the crystal carrying shafts in a hermetically sealed process chamber. The concept reduces to a minimum the number of static and dynamic seals, feedthroughs and windows, eliminates any source of friction and wear inside the growing chamber, provides high-precision monitoring systems for process automation, permits corrosive process atmosphere at elevated process temperatures, performs effective vibration and shock isolation.

Consequently, this machine permits us to make use of the Hot-Wall-Crzychalski-method for the growth of GaAs crystals of excellent purity and perfection at an industrial scale.

In cooperation with the competent German company Leybold AG, Alzenau, this concept has been successfully tested (Figure 8). Several crystals with weights up to several kg have been grown under hot-wall conditions, i.e. the shaft had been heated up to 820°C. A prototype of the machine for industrial fabrication of crystals has been built up and is just going under final test.

ORIGINAL PAGE
BLACK AND WHITE PHOTOGRAPH

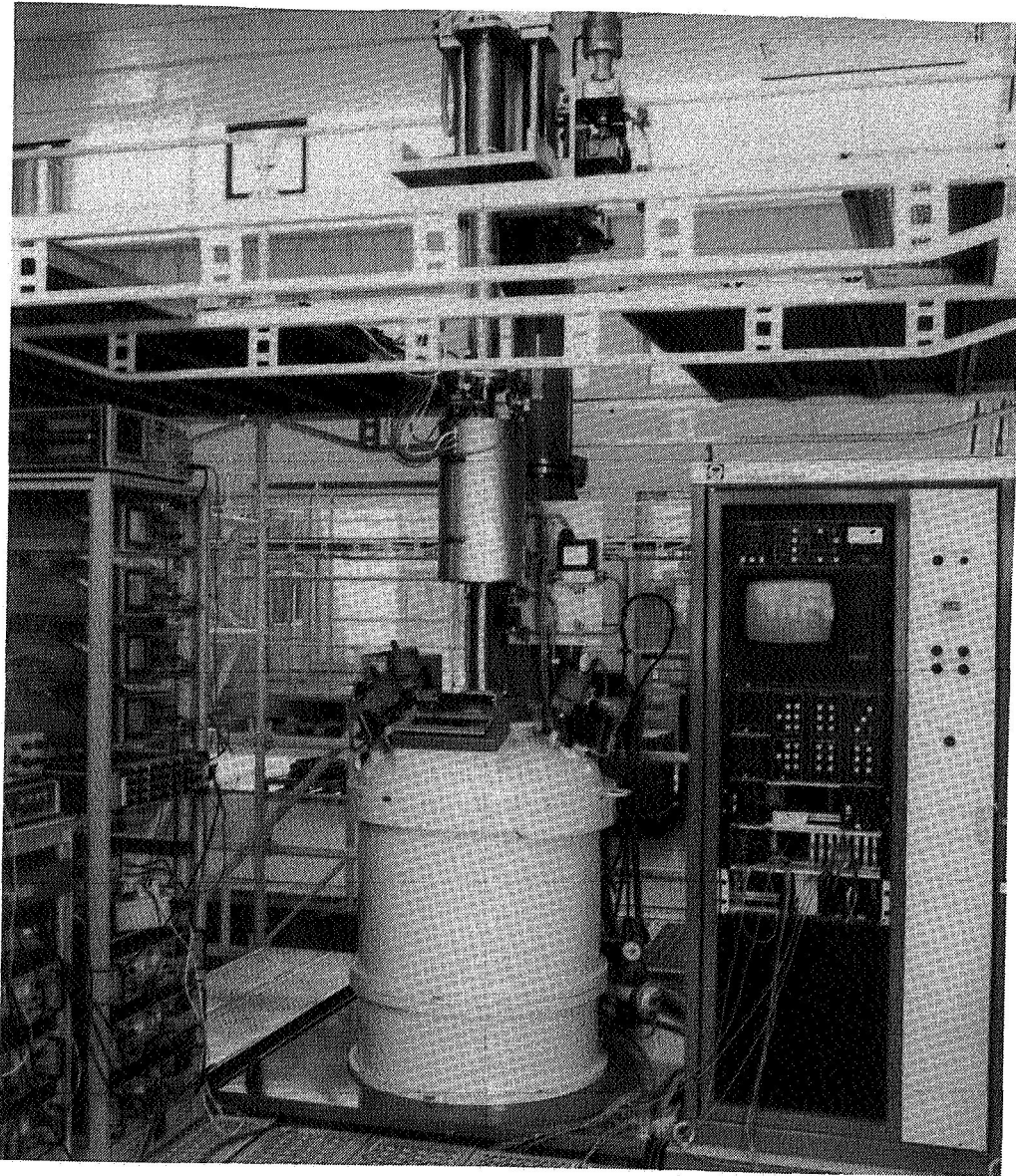


Fig. 8: Test set-up at Leybold AG, Alzenau

4. CONCLUSION

A practical permanent magnet biased magnetic bearing system is presented which permits relatively large gaps between stator and shaft (Fig. 9).

ORIGINAL PAGE
BLACK AND WHITE PHOTOGRAPH



Fig. 9: View into the bearing gap (24 mm)

It works very effectively, yet the bearing parts are very simple and inexpensive. For example, flat annular radio loudspeaker magnets, made of cheap Bariumferrite-material, simple coils and sensor systems and mild steel collars make up the entire parts of stator and shaft.

This bearing covers a lot of particular application requirements, as for example

- simplicity of rotor design
- low power consumption
- high and low rotor speed
- elevated process temperatures
- corrosive or ultra-clean process environment
- convenient assembling

Due to these advantageous particularities the concept may solve restricting problems of many modern technical systems affected to conventional guide technique thus enhancing their capacity to perform a task. As demonstrated by way of example two pretenting applications meet their technical liability free from the drawbacks of classical bearing, sealing and supporting means: A magnetically suspended rotary anode for medical X-ray tubes has been developed, which has been satisfactorily tested. An apparatus for growing GaAs-crystals from the melt using the Hot-Wall-Czochralski-techniques has been provided with magnetically suspended drive shafts and improved automatic process control devices. This machine allows for the production of GaAs monocrystals of improved quality and purity.

The applications exemplified derive their benefit essentially from the fact that large gaps can be realized between stator and rotor elements by using the magnetic bearing system described. As a consequence, this bearing concept enables us to overcome the restricting features of the conventionally used guiding and sealing technique for drive shafts and renders possible new advantageous design for a growing number of complex applications.

REFERENCES

- [1] Fremerey, J.K. and Boden, K.: J. Phys. E; Sci. Instrum., Vol. 11, (1978), 108-113
- [2] Boden, K.: Magnetic bearings: proceedings of the first international symposium. ETH Zürich, Switzerland, (1988) 41-52
- [3] Boden, K.; Fremerey, J.K.; Comsa, G.; Gudden, F.; Appelt, G.; Friedel, R.; Geldner, E.: German patent 2716079 (1977)
- [4] Czochralski, J.: Z. Phys. Chem. 92, (1971), 219
- [5] Gremmelmaier, R.: Z. f. Naturforschung 11a (1956) 511
- [6] Boden, K.; Ibach, H.; Linke, U.: German patent 3432467 (1984)
- [7] Boden, K.; Ibach, H.; Linke, U.: German patent 3530417 (1985)
- [8] Boden, K.; Janssen, F.: Deutsche Offenlegungsschrift DE 3718260 (1987)

FORCE ANALYSIS OF MAGNETIC BEARINGS
WITH POWER-SAVING CONTROLS

Dexter Johnson and Gerald V. Brown
NASA Lewis Research Center

Daniel J. Inman
State University of New York at Buffalo

ABSTRACT

Most magnetic bearing control schemes use a bias current with a superimposed control current to linearize the relationship between the control current and the force it delivers. For most operating conditions the existence of the bias current requires more power than alternative methods that do not use conventional bias. This paper examines two such methods which diminish or eliminate bias current.

In the typical bias control scheme it is found that for a harmonic control force command into a voltage-limited transconductance amplifier, the desired force output is obtained only up to certain combinations of force amplitude and frequency. Above these values the force amplitude is reduced and a phase lag occurs. The power-saving alternative control schemes typically exhibit such deficiencies at even lower command frequencies and amplitudes. To assess the severity of these effects, a time history analysis of the force output is performed for the bias method and the alternative methods. The frequency content of the actual force is compared to that of the commanded force. A Fourier series representation is used with a concentration on the fundamental frequency component, which is necessary to evaluate the stability of the resulting closed loop system. Results of the above analysis show that the alternative approaches may be viable.

The various control methods examined here were mathematically modeled using nondimensionalized variables to facilitate comparison of the various methods. For example, values of critical frequency, which is the lowest frequency at which a force deficiency occurs, can be compared.

INTRODUCTION

The present operation of magnetic bearings involves the standard usage of bias current in addition to a superimposed control current. This linearizes the relationship between the control current input and the force output of the magnetic bearing. With the existence of the bias current, even in no load conditions, there is always some power consumption. In earthbound applications of magnetic bearings this constant power loss may not be of critical importance but in aerospace applications it becomes an important concern.

In this paper two alternative control methods will be examined and compared with the bias method. Primarily, we will be looking at the nonlinear aspects of the magnetic bearing and its controls (see [1-2]). The controls that are proposed are designed to reduce the power loss effect of bias while continuing to provide satisfactory control performance. Research into the limitations of the performance of conventional magnetic bearings, due to their nonlinear nature, has been reported in [3]. Peak force capacity and force slew rate limitation are examples of the phenomena that are encountered when the performance of magnetic bearings is pushed to extreme conditions. Peak force capacity is primarily due to the limitation of the current of the magnetic bearing power supply and the force slew rate limitation is mostly due to the limiting rate at which current to the magnetic bearing can be changed because of power supply voltage limits.

The nonlinear nature of the magnetic bearing due to operational limitations such as a saturated voltage supply, as opposed to the inherent nonlinear relationship between force output and current, can be observed by examining the force response or output for a given amplitude and frequency of control current input. Specifically, for a given frequency, if the output amplitude is not proportional to the input amplitude then the system has some type of nonlinearity present. Here we examine the frequency content of the force output obtained (as opposed to desired force output) for a current command input with varying frequency and amplitude. By doing so we obtain the degree of force output distortion, if any, and its implications on stability. We also show that in comparison to the conventional bias method the alternative methods perform satisfactorily with a saving in power consumption.

Conventional Bias Operation

In Fig. 1 there is shown a general diagram of a magnetic bearing. It involves two electromagnets situated on opposite sides of the levitated or attracted object (usually a rotor). Each electromagnet has a magnetic core which is wound with electrically conducting wire. When current flows through the coils a magnetic force of attraction is produced. Two opposing magnets constitute a force actuator for that axis (in the figure it is shown as the x axis) and allow one dimensional positioning of the attracted object.

The magnetic bearing system is an inherently unstable one. This is because the attractive force generated by the magnetic bearing increases as the distance between it and the attracted object decreases; thus the system behaves like a nonlinear spring-mass system with negative spring constants. Therefore, an electronic control system must be used with the bearing to provide stability. Typically, proportional-derivative control is used.

The basic force relation for a single coil is given by

$$F = K(I/g)^2 \quad (1)$$

where F is the attractive force, K is a constant (for nominal operational conditions) that depends on the magnetic flux, number of coil turns, magnetic reluctance, and other parameters related to magnetic properties (see [3]), I is the current in the coils, and g is the air gap distance between the magnet poles and the attracted object.

For the bearing shown in Fig. 1 with two electromagnets, the net force on the attracted object is

$$F_{net} = K[(I_1/g_1)^2 - (I_2/g_2)^2] \quad (2)$$

where the subscripts denote a particular magnet and its variables. It should be noted that typically there is another set of electromagnets situated along the vertical axis allowing two-dimensional positioning of the object. Our focus here is on the one-dimensional operation; the analysis applies to both axes if examined independently.

The relationship between the current in the coils and the resulting force by the bearing is clearly nonlinear. It is preferred, when implementing control systems, to have a linear system such that classical linear control methods may be used. This is desired due to the difficulty in controlling nonlinear systems. To convert the net force-current relationship into a linear one it is very common to introduce a bias current control mode of operation. This mode of operation involves having the current that flows in the coils of the opposing magnets consist of two parts. This is accomplished by the following method.

$$I_1 = I_b + I_c \quad (3)$$

and

$$I_2 = I_b - I_c \quad (4)$$

where I_b is the bias current, which has a constant value, and I_c is the control current which can be fluctuated as desired. The result is a net force from the two opposing magnets which is directly proportional to the control current, i.e.

$$F_{net} = K_1 I_c \quad (5)$$

where K_1 is a constant which is dependent on K and I_b .

This mode of operation is acceptable for earthbound application but for space applications the concern for power savings becomes increasingly important. The ever present bias current produces a constant power loss. It is one of the objectives of this research to investigate other possible operational modes which will minimize or eliminate excessive power loss due to the bias effect. Presented here will be an analysis of the effect on the force output of the magnetic bearing for some proposed power-saving controls.

NONDIMENSIONAL VARIABLES

The operation of magnetic bearings involves additional hardware which affects its performance, such as power supplies, transconductance amplifiers, sensors, and the rotor (i.e. the plant). Here we consider only the magnetic bearing with a transconductance amplifier and a voltage limited power supply. The following simple circuit relationship is obtained:

$$L \frac{dI}{dt} + IR = V \quad (6)$$

where L is the coil inductance of the magnetic bearing, R is the lumped resistance of the circuit, dI/dt is the time derivative of I, which is the current, and V is the voltage applied to the circuit by the transconductance amplifier. If the output voltage does not reach its limits, this equation can be used to find the voltage required to produce a commanded current. On the other hand the commanded current and its derivative may require more voltage than is available. The equation can then be integrated with respect to time to find the actual current, which will differ from the commanded current as long as the voltage is at its limit. This equation was nondimensionalized by using the parameters L, R, a nominal bias current equal to half the maximum allowable current, I_b , and the limiting voltage value of the power supply, V_{max} . Specifically, we define the nondimensional variables, $v \equiv V/V_{max}$, $i \equiv I/I_b$, $\beta \equiv R/(V_{max}/I_b)$, and $\tau \equiv [V_{max}/I_b L]t$. The final result is

$$\frac{di}{d\tau} + \beta i = v \quad (7)$$

which is the nondimensional equation used for simulation.

SIMULATION

In a typical biased operation for a given v, Eqn. (7) can be solved to yield the current, i. If the current is known the force output can be determined from Eqn. (2). We have used a computer

solution method in which v is a feedback function related to the difference between the desired force and the actual force. The method of solution is analogous to a control loop that uses force feedback. A computer simulation was performed where the desired force is a cosine function with an amplitude of I_{\max}^2 (the maximum allowable current in the coils, squared) equal to four and zero phase. Throughout this paper we consider only commanded force of a single frequency. The actual force is determined by the currents produced via Eqn. (7). The voltage demanded is proportional to the difference of these two forces. The result of this simulation is shown in Fig. 2 for a frequency ratio (as will be defined below) of 0.6 which does not cause the voltage to reach its limits (the time variable has been normalized by using the cycle period of the commanded force for the abscissa in all force, current and voltage simulations). It shows the time history of the currents in each opposing magnet along with the net force and the voltage supplied (demanded). Current in magnet 2 is plotted as negative as a convenience in all similar figures. If the voltage demanded is greater than that which the power supply can deliver then the desired force output will not be achieved. The occurrence of this phenomenon appears at a particular value of desired cosine force frequency for a fixed amplitude. This frequency will be defined as the critical frequency and it must be specified with an accompanying force or current amplitude level. Additionally, the frequency ratio will be defined as the ratio between the force command frequency and the critical frequency. A simulation for a frequency ratio of 1.2 and which causes voltage limited operation, is shown in Fig. 3.

ALTERNATIVE CONTROL SCHEMES

As discussed previously, the level of current used in the operation of the magnetic bearing gives an indication of the power loss that would be observed. With current flowing in the two opposing magnets at all times there will always be a power loss. If we can operate one magnet at a time or decrease the period of time that they operate together, a power saving can be realized, the coils will run cooler and rotor heating from eddy currents and hysteresis will be reduced.

In method A below we simulate a strategy in which (for a cosine commanded force) magnet 1 is requested to produce all the force f for f greater than zero and magnet 2 for f less than zero. Lagging response will be seen to occur near f equal to zero because of voltage railing (saturation). The lag is reduced in method B, which anticipates the zero crossing of force, by initiating current in the opposing magnet when the voltage applied to the operating magnet reaches its limit.

Method A

In this method, for one cycle of desired (commanded) force, we command enough current (according to Eqn. (1)) in magnet 1 to produce the desired force when that force is positive and current in magnet 2 when that force is negative. Thus magnets 1 and 2 are not intended to operate concurrently. Unfortunately due to the inductive effects in

the coils, there will be some current flowing in both magnet coils for a small duration of time. The simulation of this mode of operation, for a frequency ratio of 0.5, is shown in Fig. 4. The current in magnet 1 produces the commanded force until the amplifier voltage reaches its negative limit. Thereafter the force does not decrease as rapidly as desired. Furthermore the buildup of negative force (i.e. force directed towards magnet 2) is not as rapid as requested because the voltage for magnet 2 rails immediately upon start-up.

This method has actually been used to suspend a very flexible rotor through two critical speeds.

Method B

In this method, for one cycle of current demanded, the current in the coils of magnet 2 begins to flow when the voltage required by magnet 1 reaches its maximum negative value equal to the voltage limit of the power supply. The operation of magnet 1 ceases when the current through its coils becomes zero. When magnet 2 demands the maximum positive voltage the current in magnet 1 again begins to flow. The simulation of this method, with a frequency ratio of 0.5, is shown in Fig. 5.

FORCE ANALYSIS

It is desired of the magnetic bearing to produce a force in accordance with a given control criterion. When there is a voltage limitation due to frequency and amplitude modulation the desired force output may not be obtainable and some distorted response is obtained instead. Therefore, our main focus here is to examine the effects of the resulting force deficiency.

The method of examination involves looking at the describing function (see [4,5]) representation of the force output. This method is an extended version of the frequency response method for linear systems and is designed to approximately analyze and predict nonlinear behavior. The concept which underlies this method is that a steady-state sinusoidal input into a nonlinear element will produce an output that has components of the same frequency as well as its harmonics. Describing function analysis focuses on only the fundamental component. It relates the amplitude and phase of the fundamental component of the nonlinear element's output to the amplitude and phase of the sinusoidal input. Using this method involves acquiring the Fourier series representation of the nonlinear element output response. The Fourier series analysis assumes for an input of

$$x(t) = A \sin(\omega t) \quad (8)$$

that the output $y(t)$ can be expressed as follows

$$y(t) = A_0 + \sum_{n=1}^{\infty} A_n \cos(n\omega t) + B_n \sin(n\omega t) \quad (9)$$

which can be written as

$$y(t) = A_0 + \sum_{n=1}^{\infty} Y_n \sin(n\omega t + \phi_n) \quad (10)$$

where

$$A_n = \frac{1}{\pi} \int_0^{2\pi} y(t) \cos(n\omega t) d(n\omega t) \quad (11)$$

$$B_n = \frac{1}{\pi} \int_0^{2\pi} y(t) \sin(n\omega t) d(n\omega t) \quad (12)$$

$$Y_n = \sqrt{A_n^2 + B_n^2} \quad (13)$$

$$\phi_n = \arctan \frac{A_n}{B_n} \quad (14)$$

For the describing function analysis only the first terms are of interest. Consequently, this results in revealing output magnitude and phase versus command input frequency. There is an interest as to whether higher harmonics due to the deficiency in force can affect the control properties of the magnetic bearing as a force actuator, but for now we investigate only the fundamental effects. This analysis helps in comparing the different methods and thus yields information as to whether the power saving methods are viable in comparison to the bias case.

In Fig. 6 the magnitudes and phases of the describing functions are shown. For the bias method there is no decrease in output magnitude for low frequency ratio. As the frequency ratio increases and

surpasses the critical frequency, a decrease in output magnitude is observed. As the frequency ratio approaches the high end of the frequency spectrum the slope of the response appears to become constant. There is no phase lag below the critical frequency ratio (numerical inaccuracy causes the small value shown in the figure). As the frequency ratio increases beyond the critical frequency ratio the phase lag increases. As the frequency ratio progresses even further the slope of the phase lag tends to level off at some constant value.

For method A the magnitude is approximately constant at the low end of the frequency spectrum as in the bias method but there is an earlier initiation of magnitude fall-off which is prior to the bias critical frequency. (For comparison sake, all references to the critical frequency in the analysis to follow will be to the bias critical frequency, which is defined for the maximum allowable current amplitude. It is shown below that the other two methods always have force distortion; thus a critical frequency of zero.) As the frequency increases the magnitude continues to decrease until it begins to level off for high frequency ratios. The phase increases in a smooth and continuous fashion for low frequency ratios.

The magnitude and phase for Method B behave like those of Method A but the magnitude fall-off and phase lag are less than those for method A for all frequencies.

COMPARISON OF RESULTS

The operation of the magnetic bearings under the various methods examined here is similar. The differences are primarily the magnitudes of the effects and not the qualitative characteristics. All of the methods introduce phase lag and magnitude fall-off. The range of their occurrence is for all operation frequencies for Methods A and B and beyond the critical frequency for the bias method. Deviations from ideal behavior of the bias method phase and magnitude begin abruptly at the critical frequency ratio while for the other methods, the magnitudes and phases vary in a smooth and continuous manner. The bias method shows no variation of magnitude or phase below the critical frequency. This indicates that no force deficiency is present in this operation range. The other methods always distort the force output but for low frequencies this effect is small. The bias method yields the lowest distortion throughout the spectrum whereas Method A shows the most.

More specifically, on the low end of the frequency ratio spectrum (less than 0.4) the magnitudes of all the methods vary very little from each other, but there is a slight separation in value of phase lag between Method A and the other methods with all methods having less than 5 degrees of phase lag introduced. For the region of critical frequency between 0.4 and 1.0 the differences between the methods become very pronounced. The magnitude ranges from a value of 4.0 for bias down to 2.7 with Method A obtaining the lowest value. The introduction of phase lag for this range varies from 0 to 26 degrees. After the critical frequency the rates at which the magnitude fall-off and

phase lag occur appear to be similar for all methods although the values are different due to the differences which occur at lower frequency ratios.

Command Amplitude Variation

The describing functions obtained from reducing the amplitude of the current flowing in the magnets coils to half the maximum allowable amplitude is shown in Fig. 7 for the various methods. It shows that there is no force distortion for the bias method for the given range of frequency ratios. This is because the voltage supplied is never above its limiting value. Therefore, the bandwidth of the bias method is increased and force distortion is delayed to a higher frequency ratio (not shown in the figure).

For method A and B the describing functions show much less magnitude fall-off and phase lag than for the higher command force amplitude. As for the effect in the bias case, it results in increasing the bandwidth of operation, and broadens the range where no force distortion occurs. Once again, method A has the greatest force distortion over the given frequency ratio range of all the methods and bias, the least.

The magnitudes at the critical frequency ratio range from about 1.0 to 0.95 and for a frequency ratio of 2.0 from about 1.0 to 0.7. For phase lag the range is 0 to 5 degrees at the critical frequency ratio and 0 to 27 degrees for a frequency ratio of 2.0.

DISCUSSION OF RESULTS

The results show that the methods proposed as power-saving controls operate using less current than the commonly used bias method but have qualitatively similar effects on force output. The bias has the definite advantage over the other methods from a linear controls viewpoint in that it has a particular operating range where the force output is not distorted. The force distortion produced in methods A and B possibly can be tolerated and may be of little consequence for some range of operation frequencies.

The most viable method of the two proposed methods is clearly method B. At frequency ratios below 1.0 for the maximum current amplitude case the magnitude decreases no more than seven percent and even more importantly the phase lag is no more than 10 degrees. These deficiencies are not of great magnitude. Method A is not as viable as method B but for smaller ranges of operation frequencies it too can be used without appreciable decline in performance while still saving power.

The power saving that is realized is qualitatively evident by examining the amount of current flowing in the coils of the magnets. In the bias case, control current is flowing in both magnets almost all the time, in addition to the ever-present bias current. In method A

current is commanded in only one magnet at time, but inductive effects cause some overlap. In method B simultaneous currents are actually commanded during a portion of a cycle. Since power loss is related to current, method A would have the least power loss, method B would be next and the bias method would have the greatest.

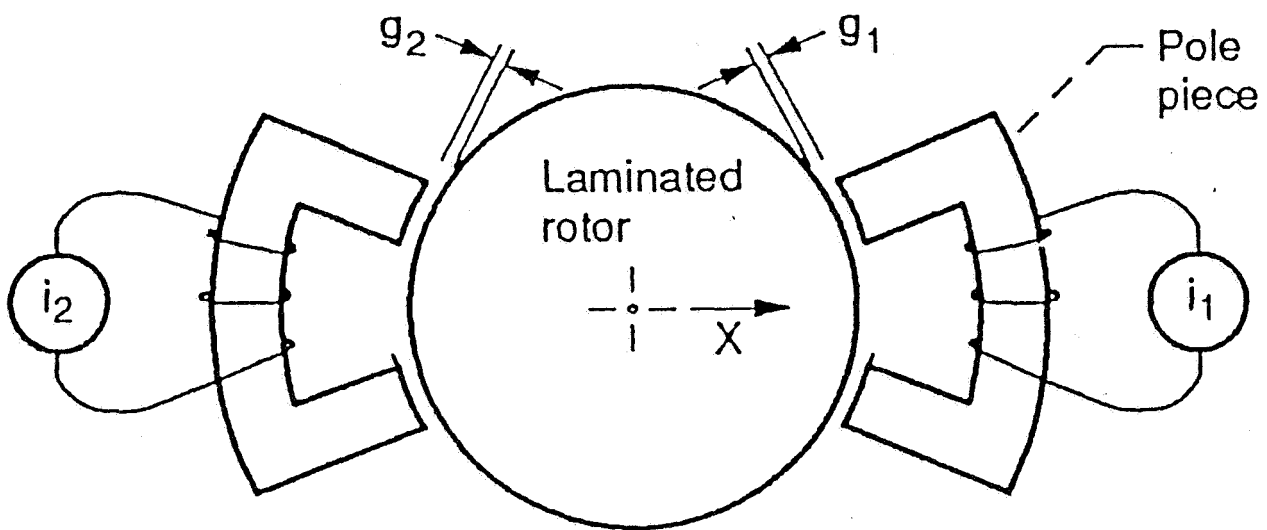
Implications as to the effects on stability primarily lie within the amount of phase lag produced. With increased phase lag, stability may deteriorate. The extent of its effect can only be determined from the analysis of the closed loop system with the magnetic bearing and the proposed controls considered here as elements of the system. The relative comparison of the amount of phase lag for each method has been shown.

In conclusion, the specified methods show some ability to provide alternative power-saving modes of operation in comparison to the widely used bias method. Other limitations not considered here, such as harmonic production, may need to be included in future analysis. Future work will involve proposing and evaluating other alternative methods with more quantitative analysis, e.g. calculated power loss, effect of force harmonics, and response to nonsinusoidal force commands.

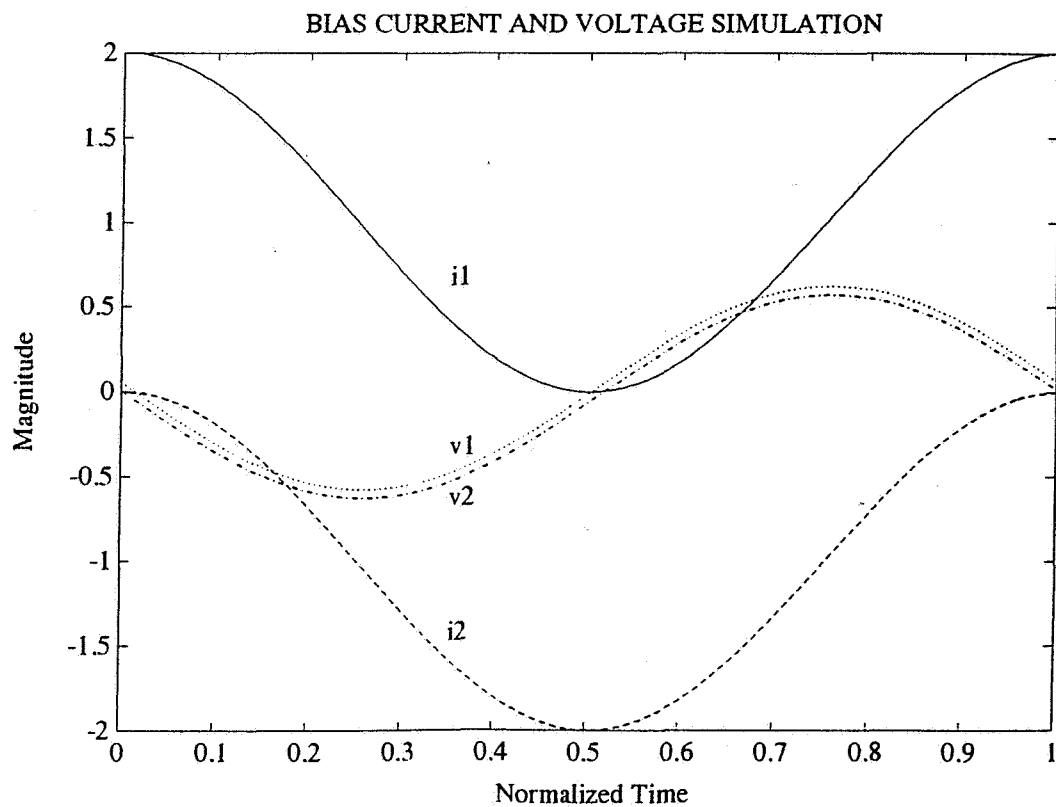
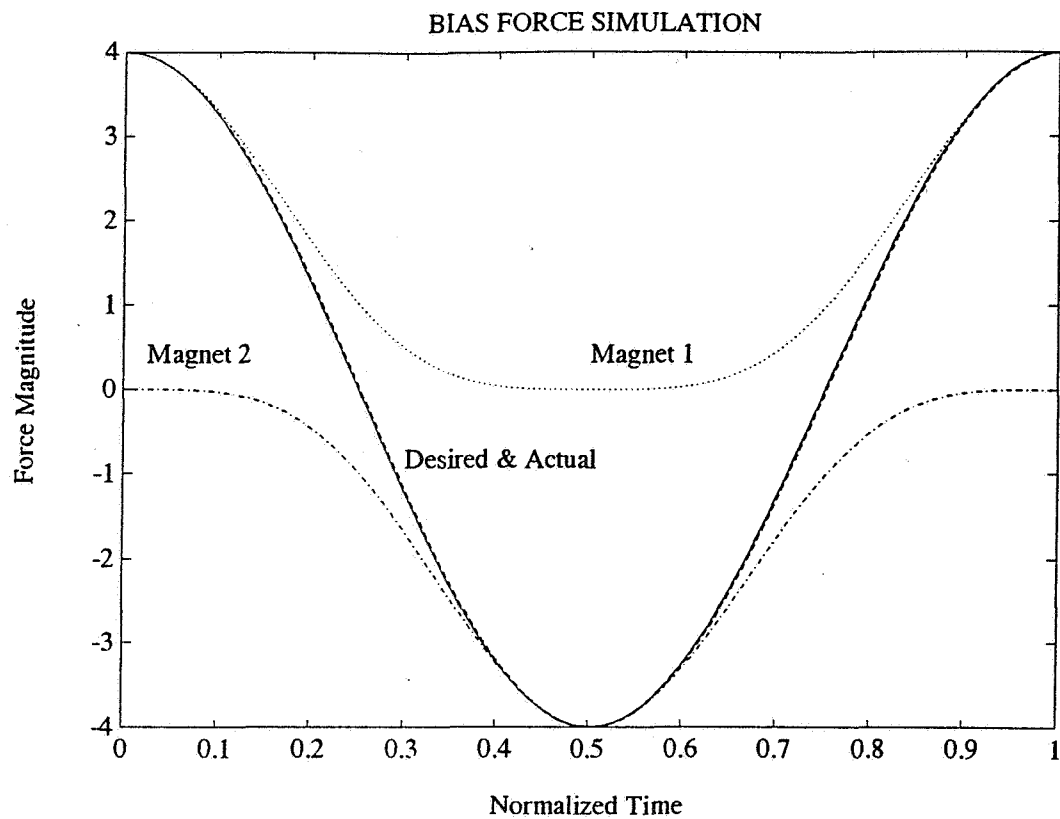
REFERENCES

1. Brown, G. V.; Grodsinsky, C. M.: Magnetic Bearings with Zero Bias. NASA Publication 10066, part 1., Aerospace Applications of Magnetic Suspension Technology, NASA Langley Research Center, March 1991, pp 165-182.
2. Ishida, S.: Linear Compensation for Magnetic Bearings. Proceedings of the 2nd International Symposium on Magnetic Bearings, Tokyo, Japan, July 12-14, 1990.
3. Maslen, E.; Hermann, P.; Scott, M.; Humphris, R.: Practical Limits to the Performance of Magnetic Bearings: Peak Force, Slew Rate, and Displacement Sensitivity. Journal of Tribology, vol 111, April 1989, pp. 331-336.
4. Franklin, G. F.; Powell, D. J.; Workman, M. L.: Digital Control of Dynamic Systems. Addison-Wesley Publishing Company, Inc., 1990.
5. Slotine, J.-J. E.; Li, W.: Applied Nonlinear Control. Prentice Hall, Inc., 1991.

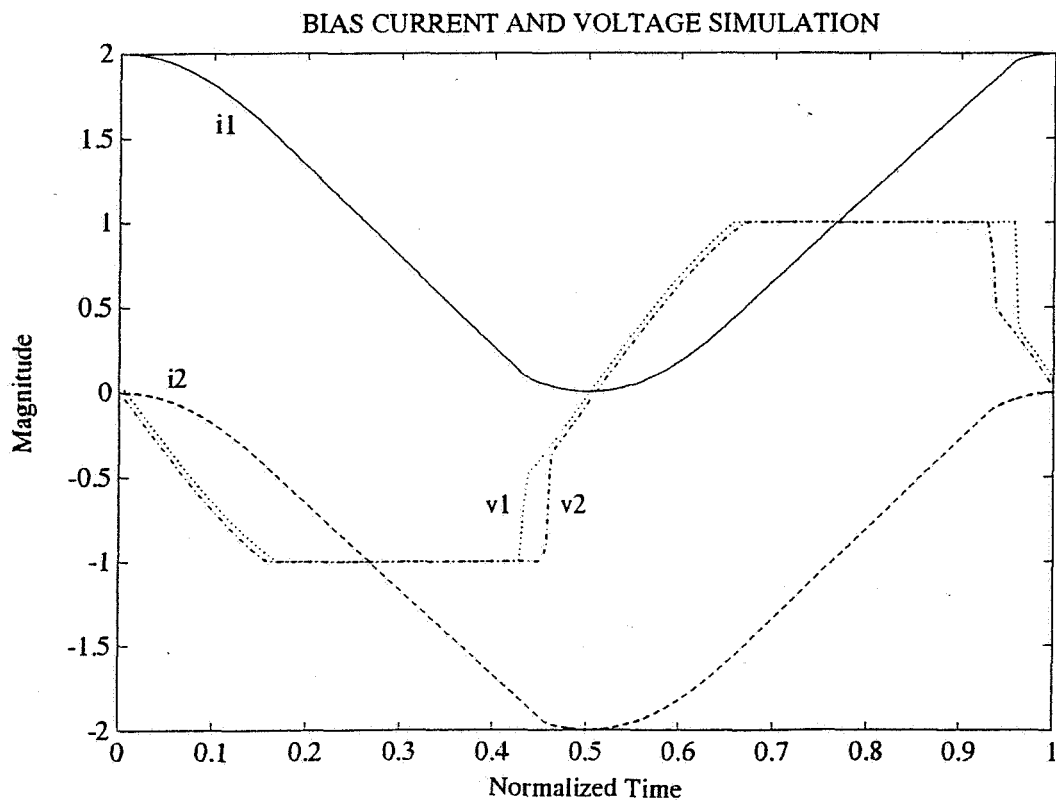
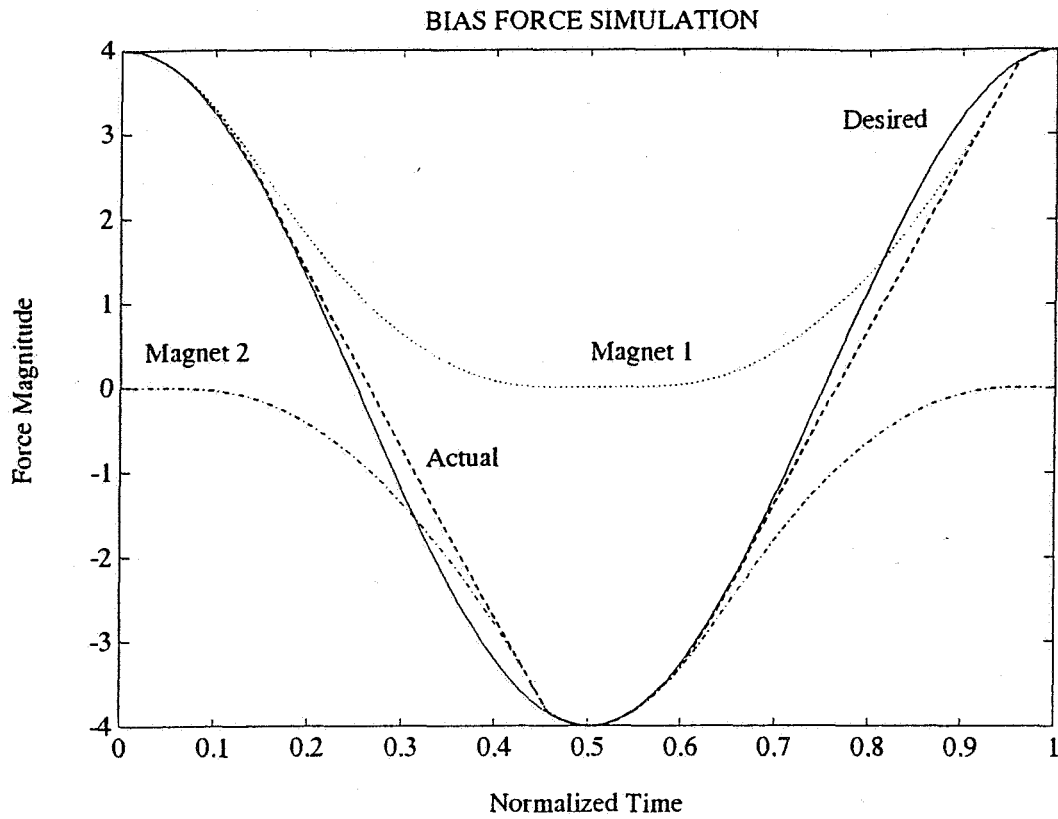
MAGNETIC BEARING



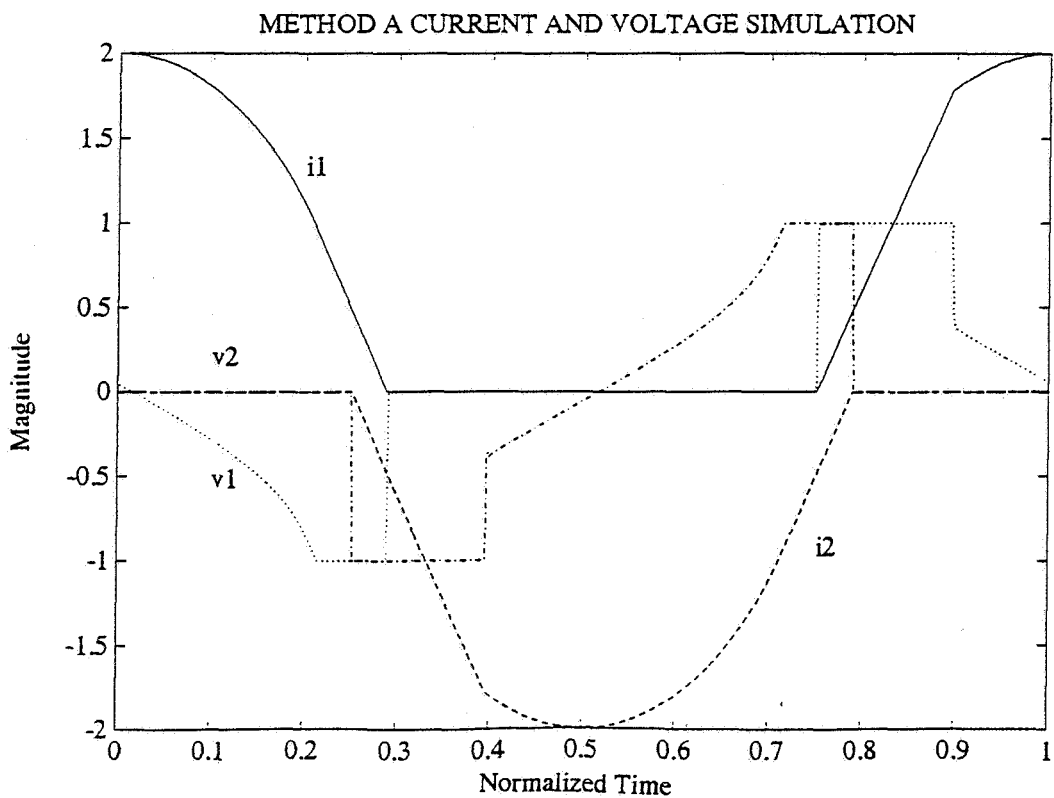
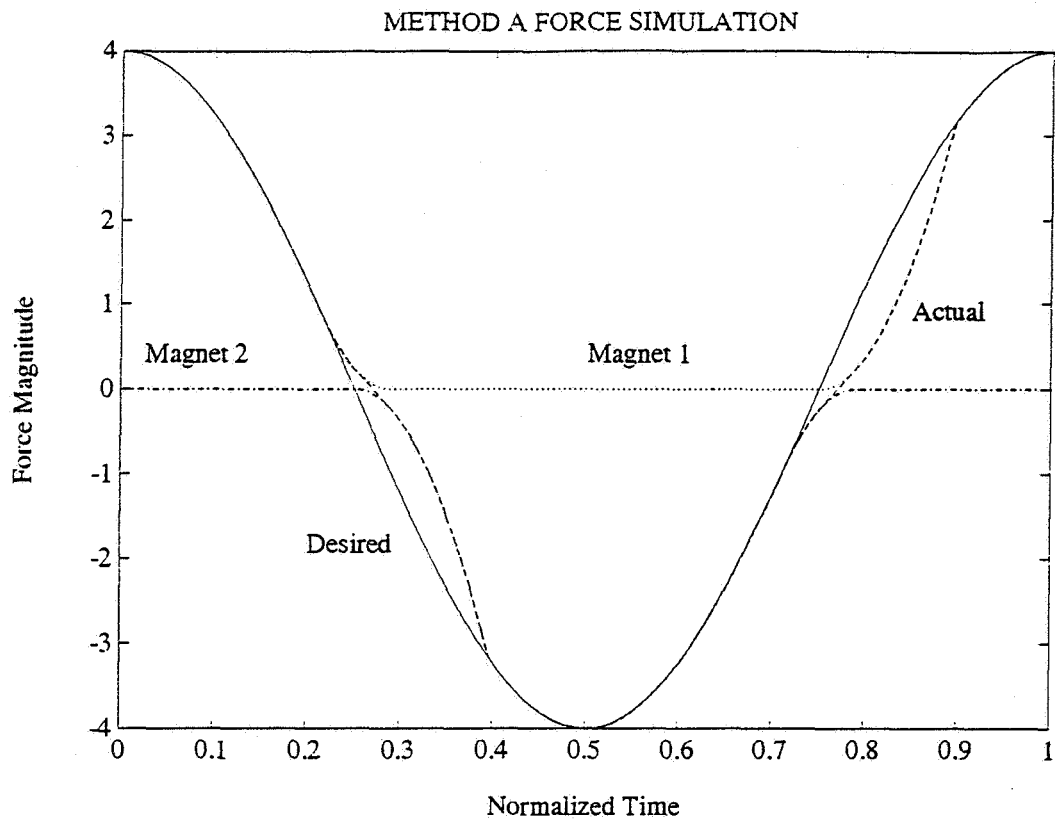
1. Diagram of magnetic bearing components operating along a single axis.



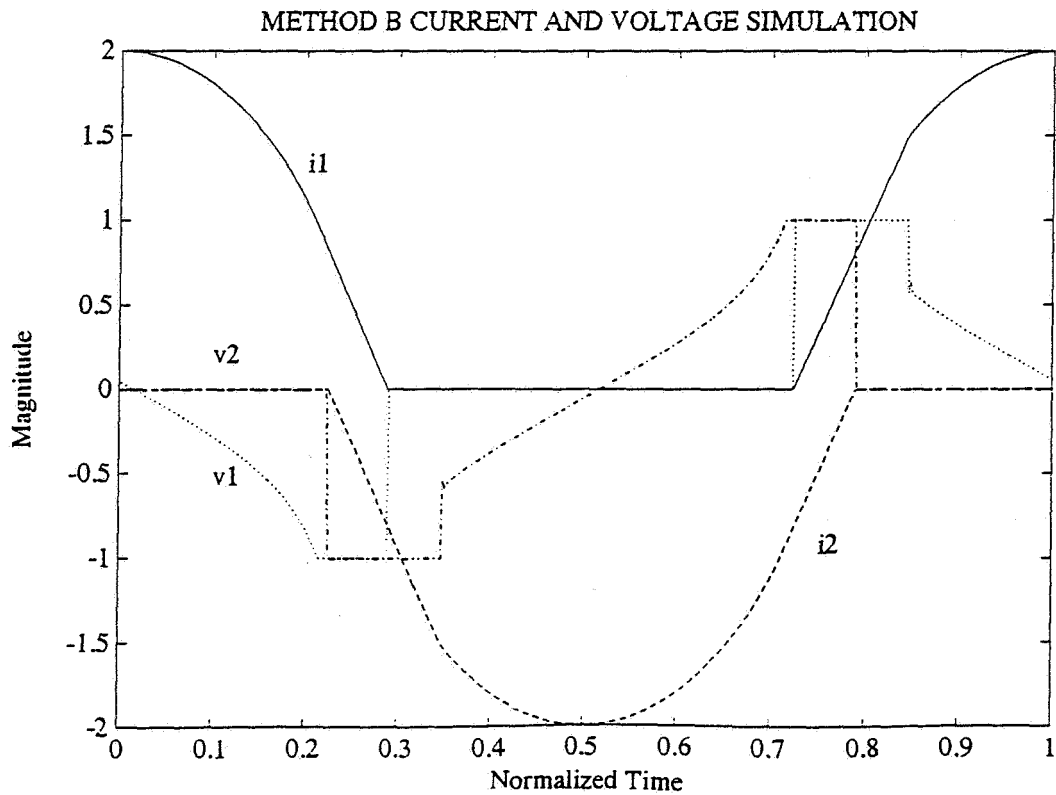
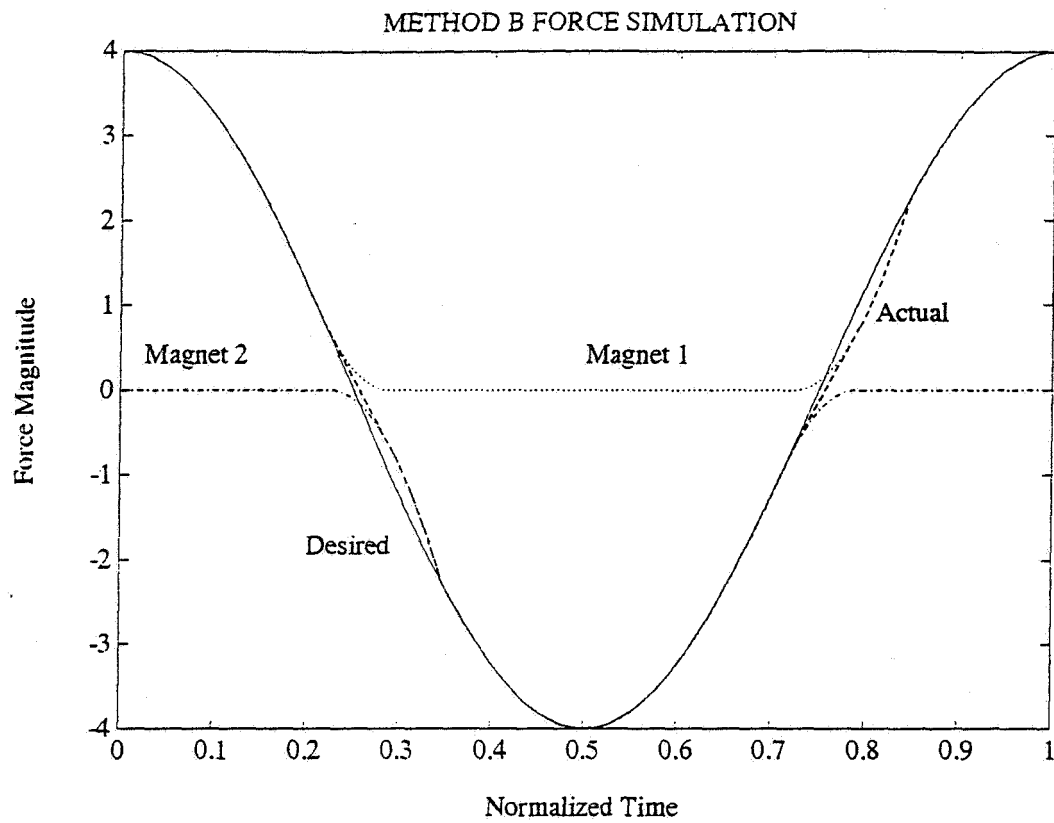
2. Simulation of Bias method for a frequency ratio of 0.6 showing a.) force magnitude and b.) current and voltage magnitude.



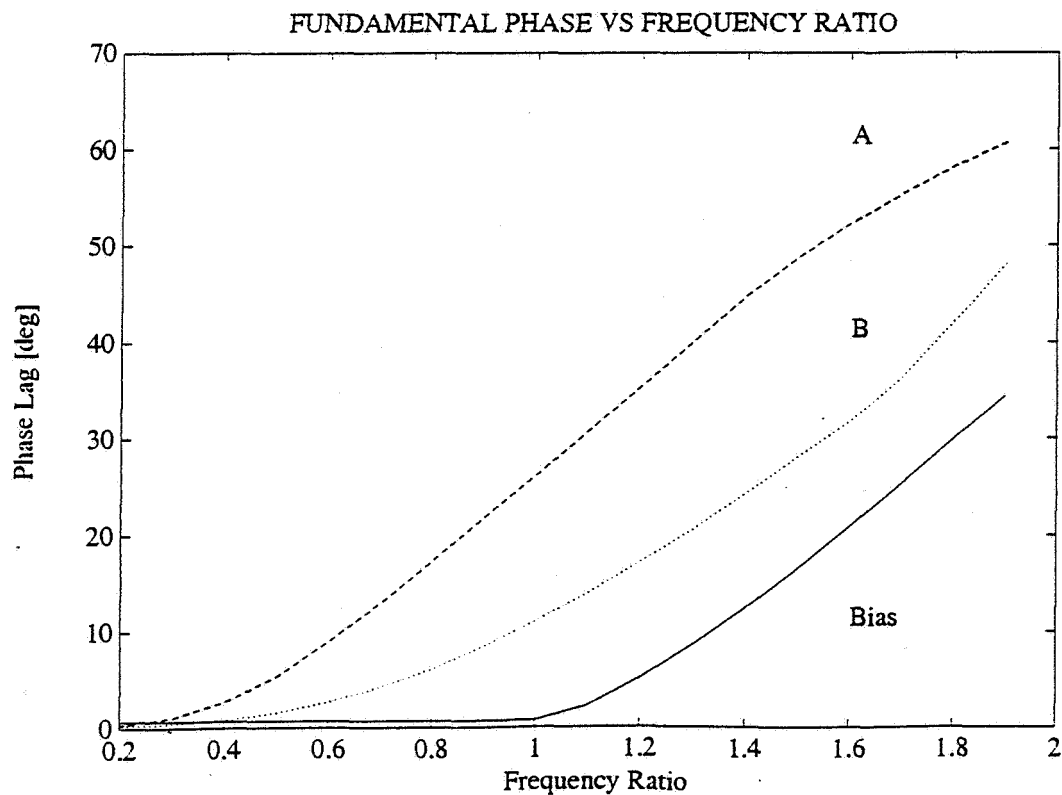
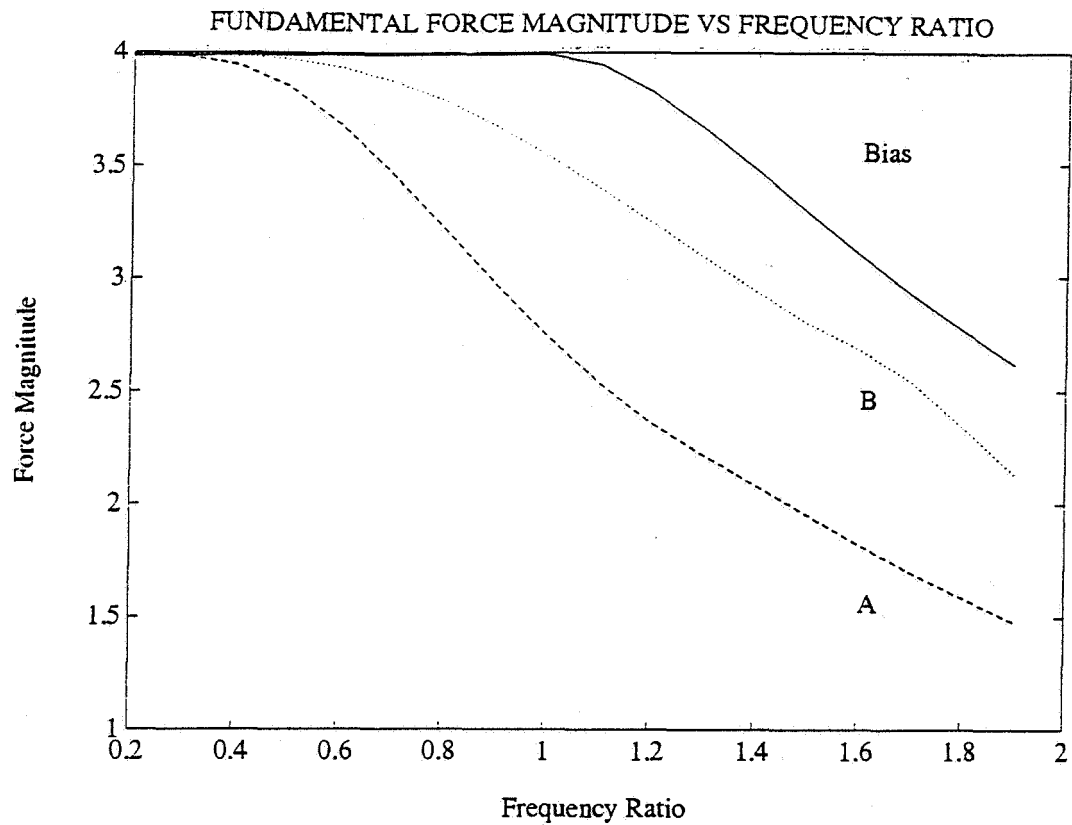
3. Simulation of Bias method for a frequency ratio of 1.2 showing a.) force magnitude and b.) current and voltage magnitude.



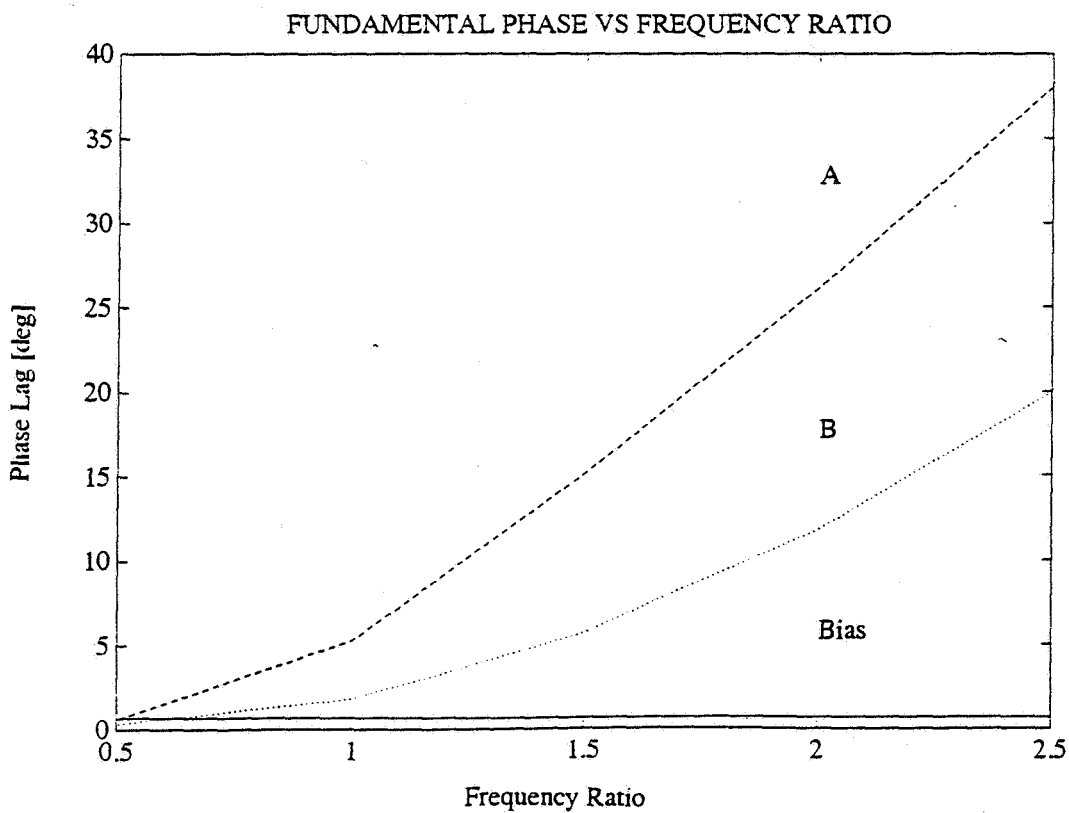
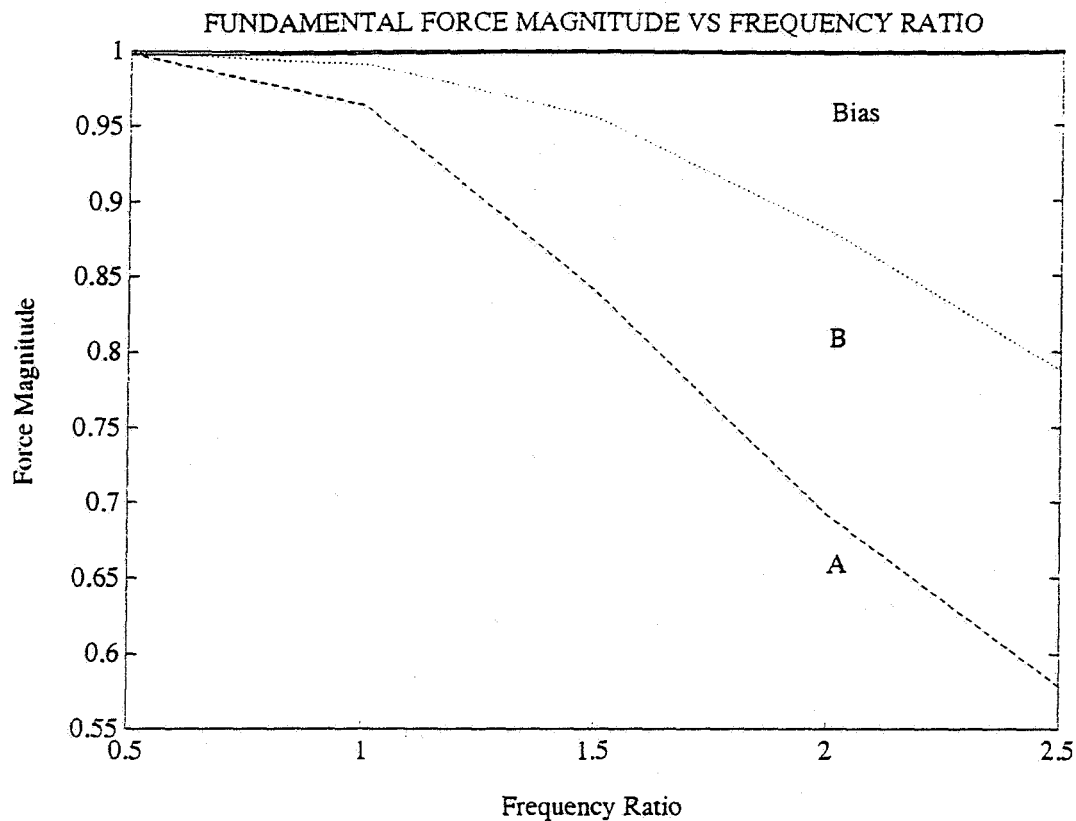
4. Simulation of method A for a frequency ratio of 0.5 showing a.) force magnitude and b.) current and voltage magnitude.



5. Simulation of method B for a frequency ratio of 0.5 showing a.) force magnitude and b.) current and voltage magnitude.



6. Describing function for method A, B, and the Bias method for a maximum desired force amplitude of 4., showing a.) the fundamental Fourier series component magnitude and b.) the fundamental Fourier series component phase.



7. Describing function for method A, B, and the Bias method for a desired force amplitude of 1., showing a.) the fundamental Fourier series component magnitude and b.) the fundamental Fourier series component phase.

Session 11

MANUFACTURING APPLICATIONS

Chairman - Nelson J. Groom
NASA Langley Research Center

N92-27796

MANIPULATION AND IDENTIFICATION OF OBJECTS BY MAGNETIC FORCES

Benjamin Joffe

Guidance and Control Section, Jet Propulsion Laboratory
California Institute of Technology, Pasadena, California

SUMMARY

This paper presents an overview of the results of research and engineering design activities over the past twenty years in the area of identification and manipulation of objects by magnetic forces. It discusses the relationship between the properties of objects and the parameters of magnetic fields, with the view toward being able to create forces for efficient manipulation and identification of different kinds of parts. Some of this information, particularly regarding nonferromagnetic materials, is relatively new and can be used to solve a variety of engineering problems by creating new types of automation systems. Topics covered include identification and orientation of bodies by magnetostatic and electrodynamic forces, electromagnetic recognition and orientation of nonsymmetric parts, and assembly and position control of parts by electrodynamic forces.

INTRODUCTION

At this symposium, broad exposition is given to the scientific and technical aspects of contactless manipulation of objects relative to a given coordinate system, via contactless application of forces induced by external magnetic fields. Presented here are a number of technical approaches applied to solve such problems as:

- contactless suspension and motion of objects relating to high-speed trains and other forms of transportation
- contactless containment and holding of parts of mechanisms and machines in given positions by use of magnetic bearings.

In previous publications several other problems connected with the manipulation and movement of objects have been examined. These include:

- contactless containment of molten metal used in metallurgy to obtain alloys of high purity
- contactless orientation and identification of machine parts.

Common to the solutions of the above-mentioned and other technical problems is the characteristic of a contactless application of force to the object. This force is generated as the result of the interaction of primary (external) and induced secondary magnetic/electromagnetic fields.

At this symposium, sufficient attention is already given to problems and technical approaches related to magnetic levitation and magnetic bearings. Therefore, these types of magnetic manipulation are not touched upon in this overview. We will consider the problems connected with

- manipulation, orientation, and assembly of a group of bodies based on their spacial relations
- recognition of objects by their external as well as hidden characteristics.

IDENTIFICATION AND ORIENTATION OF BODIES BY MAGNETOSTATIC FORCES

From electrostatic field theory it is known that with the appropriate choice of field characteristics and intensity it is possible to induce forces capable of contactless action on bodies made of various materials.

As known [1], a moment of force (moment of couple) M capable of orienting a body is created by the interaction of an induced magnetic moment P_M in the body with an external magnetic field having magnetic induction B .

For the body in the form of an ellipsoid, the moment of force is dependent on the following parameters of the field and the body:

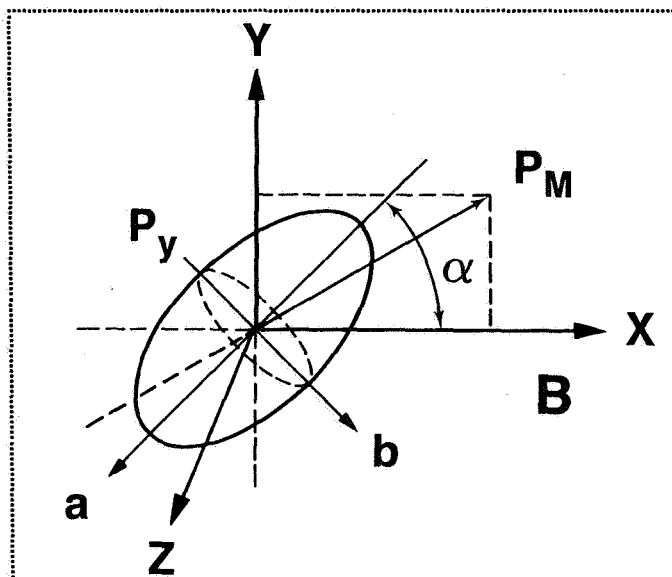
$$M = -\frac{1}{2} V k_M^2 B^2 \sin 2\alpha \frac{N_b - N_a}{(1 + N_a k_M)(1 + N_b k_M)} \quad (1)$$

where:

- | | | |
|----------|---|--|
| V | = | volume of the body |
| k_M | = | magnetic permeability of the body |
| μ | = | magnetic permeability of the material |
| α | = | angle between major axis of the ellipsoid and induction vector of magnetic field |
| N | = | demagnetization factor |

Figure 1

Ellipsoid in a magnetostatic field. Direction of magnetic field induction coincides with X axis.



For an ellipsoid, the demagnetization factor N relative to the axis of the body is $N_a + N_b + N_c = 1$, where c is an axis normal to the a and b axes of an ellipsoid (Figure 1).

On the basis of the above expression, when $N_a = N_b = N_c = 1/3$ (for a sphere), then $M = 0$. Therefore, for a body of spherical form the moment of force does not exist. For an ellipsoid ($N_a \neq N_b$), moment of force exists and is oriented collinear to the field. The maximum value of the moment of force, with all other variables being equal, corresponds to the position of the ellipsoid with $\alpha = 45^\circ$. $M = 0$ when $\alpha = 0^\circ$ or $\alpha = 90^\circ$.

We will examine the relationship between this moment of force and the material properties of the body. Since the magnetic permeability of the body is $k_M = \mu - 1$, bodies made of material possessing magnetic permeability close to one have a moment of force of zero.

Therefore, in the magnetostatic field it is possible to orient bodies that have nonsymmetric form or structure, provided the magnetic permeability of the body differs from the magnetic permeability of the ambient surrounding. For those bodies made of conductive, nonmagnetic materials (aluminum, copper, brass, bronze, steel parts heated beyond the Curie point, etc.) whose magnetic permeability is close to one, it is not practically possible to orient them via a magnetostatic field. Naturally, a magnetic field is incapable of orienting bodies made of dielectric materials, since the magnetic permeability of a dielectric is close to the magnetic permeability of ambient air. Hence, manipulation by forces created in magnetostatic fields is effective only for bodies with ferromagnetic qualities [3-5].

Specific parts can be represented in the form of an oblate spheroid (washer, plate), as a cylinder with spherical ends (rod-shaped parts), and so on. Given data regarding the demagnetization factor with respect to geometrical configuration of the bodies, the moment of forces can be computed.

In a case in which it is desired to move a part in a particular direction, it is well known that the force can be established using a gradient of field. Here, the force acting on the body is directed along the gradient of the field and is equal in the first approximation to:

$$F = \frac{1}{2} k_M V \nabla B^2 \quad (2)$$

where ∇ is the field gradient.

In the study of manipulation of ferromagnetic parts by interaction with magnetic fields, considerable contributions were made by a number of organizations and individuals throughout the world. These include General Motors Corp., Western Electric, and Eriez Magnetics Co. in the United States; Siemens-Schuckert A.G. and Telefunken in Germany; Phillipe Francois van Eeck and Vallourec in France; and the Institute of Physics of the Latvian Academy of Science [2-9].

The concept of using the gradient of the magnetic field for the manipulation of ferromagnetic parts will be illustrated by various methods and devices. However, due to the limited length of this article, only a short description of the main design ideas for one such device is presented here.

An example of the application of a force induced by a magnetic field acting on a ferromagnetic body is a device for arranging ferromagnetic components at a set distance from one another, described in a patent [10]. Such a device permits noncontact arrangement and transportation of components with a fixed interval between them. It is suitable for manipulating both rods and flat components of complex shape.

The device in Figure 2 is composed of a permanent electromagnet 1 with a magnetizing winding 2. Stationary pole pieces 3 of the electromagnet profile and define a narrowing pole gap with a profile made so as to form a desired field gradient. Near the exit port of the guide 4, made from nonmagnetic material, the pole pieces are provided with movable magnetic poles 6. These poles are arranged so that the planes in which they lie are normal to the axis of symmetry of the pole gap, and they are adapted to move in these planes relative to the exit port of the guide 4 in a direction along their length. The "teeth" of the poles 6 are spaced apart by intervals h selected according to the desired specifications.

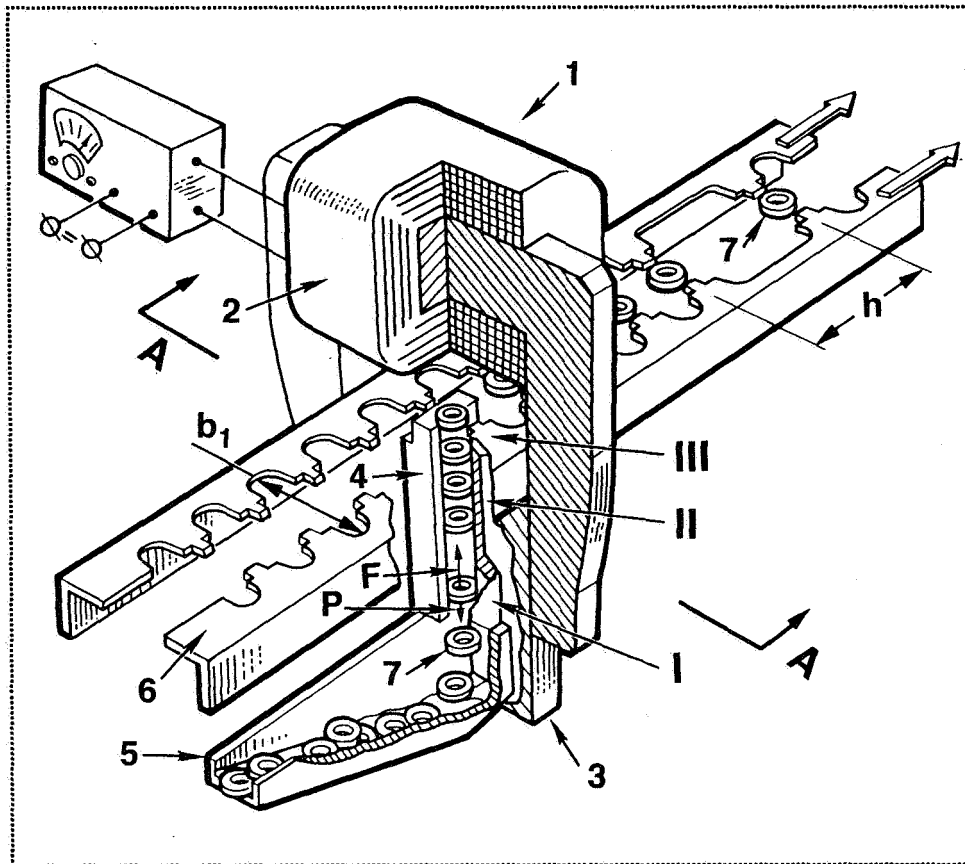


Figure 2. View of a magnetic device for arranging ferromagnetic components at a preset distance from one another.

Figure 3 is a section view taken along line A-A of Figure 2. The distribution of intensity B of the magnetic field of the electro-magnet in the pole gap along axis OX of symmetry is shown in Figure 4.

To move parts 7 from their lower position I to the next position II, it is necessary to generate a force F exceeding the force of gravity P acting on the part, which can be done by generating a field with a specific gradient. To achieve this, the pole gap of the magnetic system in Figure 2 is made according to Figure 3, which assures an increase in the magnitude of the induction of the magnetic field along axis OX in correspondence with curve 8-9 (Figure 4).

The magnitude of the magnetic induction in the pole gap of the movable magnetic poles 6 is shown by curve 11-12. Between its "teeth", the magnitude of magnetic induction must be greater, as shown by curve 13-14.

As parts are introduced into the pole gap, they acquire unidirectional magnetization, which provides for their mutual

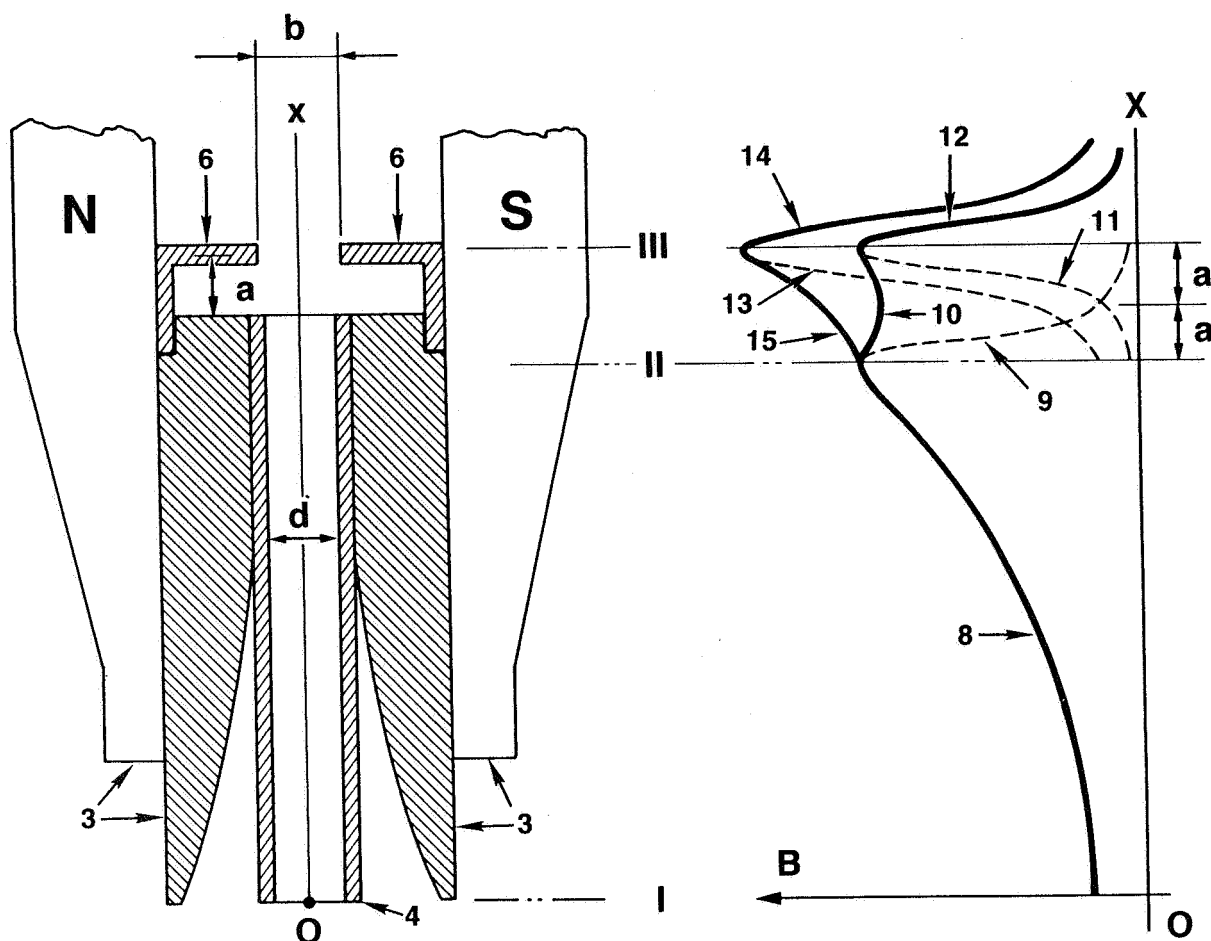


Figure 3. Section view A-A of the magnetic device in Figure 2.

Figure 4. Distribution of the magnetic field intensity along the OX axis of symmetry of the pole gap in Figure 3.

force of repulsion. This, in turn, forms an ordered flow of parts (Figure 2).

The distance between the movable magnetic poles 6 and the parallel plane of stationary magnetic poles 3 is related to dimension d of the work-parts and the dimension of the pole gap b , specifically $a = (0.5 \text{ to } 0.8)d$ and $b = 1.1d$. Distance b_1 between the movable magnetic poles 6 is chosen with the constraint that the magnitude of induction at level III in the pole gap must be approximately equal to the maximal magnitude of induction of the stationary pole pieces. Therefore, the resultant profile of the magnitude of induction is represented by curve 8-10-12; moreover, due to the dip in the portion of the

curve 10, the possibility of movement of the parts is excluded between positions II and III. As the movable magnetic pole 6 brings its "teeth" over the guide 4 containing work-pieces 7, an increase in the magnitude of magnetic induction is observed, as shown in the curve 8-14-15. Under the action of the field with such a gradient, a force is induced capable of translating the part from position II to position III, and due to the unidirectional magnetization only one part can occupy this position in the pole gap. Only when the next set of "teeth" of the movable pole gap 6 is brought over the channel 4 will the next part in the channel move from position II to position III, and so on.

From the above example, it can be seen that with the appropriate choice of field distribution it is possible to sharply define the effects on the arrangement of ferromagnetic parts.

The effect of magnetic field gradient manipulation can also be achieved by shunting sections of the pole gap, therefore providing for an effective control of the positioning of ferromagnetic objects [11].

IDENTIFICATION AND ORIENTATION OF BODIES BY ELECTRODYNAMIC FORCES

The mechanism for the creation of forces acting on nonmagnetic and ferromagnetic conducting bodies in alternating magnetic fields is based on the interaction of external and induced (by the body itself) secondary fields.

With the goal of determining parameters influencing the magnitude and direction of the moment of force, we will examine a nonmagnetic conducting body, such as an ellipsoid. An ellipsoid at first approximation can be replaced by some electrodynamic equivalents: one, two, or several ring-coils closed on some impedance

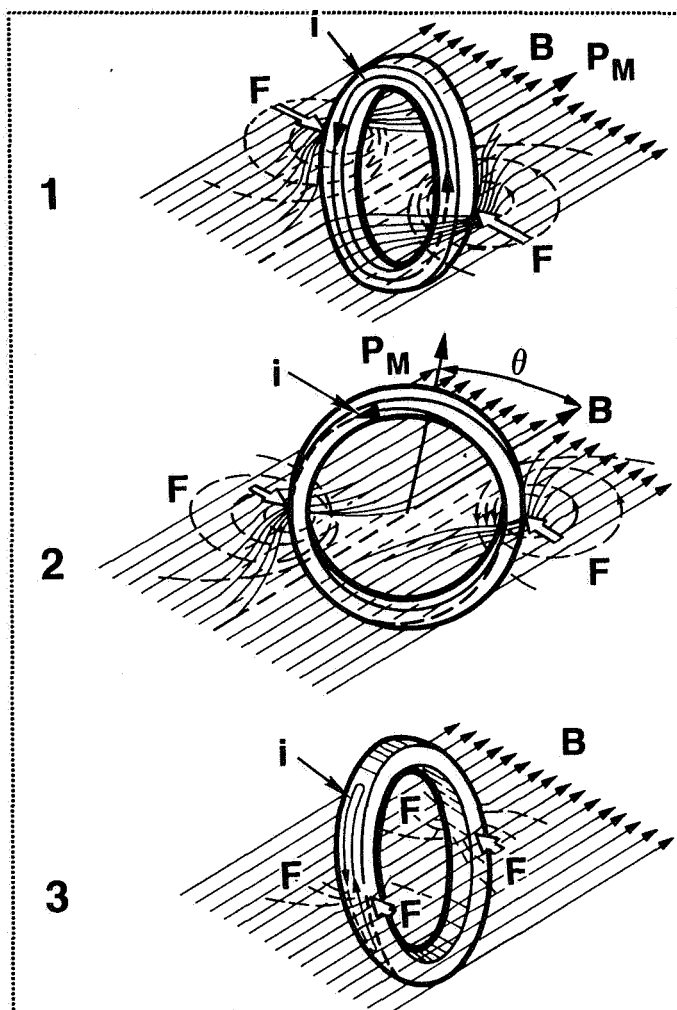
$$Z = R + j\left(\omega L - \frac{1}{\omega C}\right) \quad (3)$$

In the case of a nonmagnetic conducting ring, radius $r = a$ with impedance Z , we will consider total impedance of the ring. Due to the small capacitive effect we may omit the $j/\omega C$ term in (3) and write

$$Z = R + j\omega L = R(1 + j\tan\varphi_0) \quad (4)$$

Figure 5.

Conducting ring in an alternating magnetic field, shown for clarity in only one plane. 1 - ring placed perpendicular to the field with an arbitrary alignment; 2 - transient unstable alignment; 3 - oriented ring in a stable alignment.



If an external magnetic field is not significantly deformed by an induced current in the ring, the result is that the ring is penetrated by

$$\Phi = B_0 e^{j\omega t} S \cos \theta \quad (5)$$

Therefore we have an induced EMF of

$$\epsilon = -\frac{\partial \Phi}{\partial t} = -i \omega B_0 S \cos \theta e^{j\omega t} \quad (6)$$

The current in the ring contour is

$$i = \frac{\varepsilon}{Z} = \frac{i \omega B_o \cos \theta e^{j\omega t}}{R(1 + j \tan \varphi_o)} \quad (7)$$

where:

$\omega = 2\pi f$ = circular frequency of an alternating magnetic field

φ_o = angle of phase difference between the induction of an external magnetic field and the induced loop current

S = ring contour area

$\tan \varphi = \omega L / R$ = loop inductive impedance/active impedance.

Magnitudes L and R are computed in the first approximation, taking into account the skin effect on the circular contour carrying a current. Skin effect in a loop of circular section was studied even back in 1930 on the basis of solution for skin layer in case of infinite half plane [2,8].

Electric current in the ring can be represented as an alternating magnetic dipole with a moment

$$P_M = -iS = \frac{\omega B_o S^2 \cos \theta}{R} \cdot \frac{(-j) e^{j\omega t}}{1 + j \tan \varphi_o} \quad (8)$$

after some simplification:

$$P_M = \frac{\omega B_o S^2 \cos \Phi_o \cos \theta}{R} e^{i(\omega t - \frac{\pi}{2} - \varphi)} \quad (9)$$

For the instantaneous value of the moment of force for the interaction of the ring with the magnetic field $M = B \sin \theta$, and for the average value,

$$M_{eff} = \frac{P_M B^* + P_M^* B}{4} \sin \theta \quad (10)$$

or

$$P_M = |P_M| e^{j(\omega t - \frac{\pi}{2} - \varphi_o)} \quad (11)$$

where

$$|P_M| = \frac{\omega B_o S^2 \cos \varphi_o \cos \theta}{R} \quad (12)$$

The absolute moment of electrodynamic force according to (10) is

$$M_{eff} = \frac{|P_M| e^{j(\omega t - \frac{\pi}{2} - \varphi_o)} B_o e^{-j\omega t} + |P_M| e^{-(\omega t - \frac{\pi}{2} - \varphi_o)} B_o e^{j\omega t}}{4} \sin \theta \quad (13)$$

or

$$M_{eff} = \frac{|P_M| B_o \sin \varphi_o \sin \theta}{2} \quad (14)$$

Substituting the value of $|P_M|$ yields

$$M_{eff} = \frac{\omega B_o S^2 \cos \varphi_o \cos \theta}{R} \cdot \frac{B_o \sin \varphi_o \sin \theta}{2} \quad (15)$$

The final result, after some simplification, is

$$M_{eff} = -\frac{\omega B_o^2 S^2 \sin 2\varphi_o}{8R} \sin 2\theta \quad (16)$$

The phase angle φ_o between the induction of the external (primary) field and the magnetic moment P_M , formed by the induced ring current i , has a significant effect on the magnitude of forces and the moment of force.

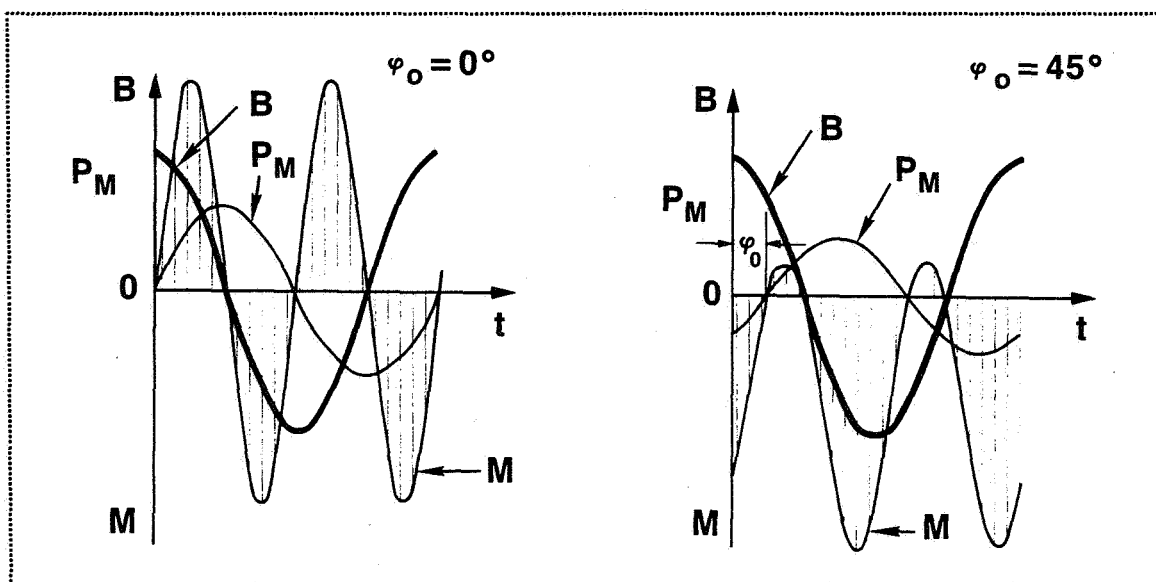


Figure 6. Relation between the magnitude of the moment of electrodynamic force M acting on a conductive ring and the angle of phase shift φ_0 of the magnetic moment P_M relative to induction B of the magnetic field.

Comparing the magnitudes of the sum of the moments of electrodynamic forces dependent on the angle of phase shift, it becomes clear that M is zero at $\varphi_0 = 0^\circ$ and that M is maximal at $\varphi_0 = 45^\circ$.

This means that, with all the other parameters of the body and the primary magnetic field, selection of the frequency of the magnetic field has the deciding effect on the magnitude of induced forces and therefore on the possibilities of manipulation of an object by the interaction of forces.

Investigations carried out at the Institute of Physics of the Latvian Academy of Science allowed determination of a number of interesting effects [2,7,12]. For example, it was established that at the lower frequencies the greater the relative outer diameter of the ring $\bar{d}^* = d/D$, the smaller the moment of force (d = inner diameter, D = outer diameter). This was to be expected. However, as the frequencies are increased the value of the moment of force corresponds to that of a solid disk (Figure 7). With further increase in frequency of the field an increase in the moment of force was observed. For rings with \bar{d}^* between 0.80 and 0.95 the increase in the moment of force was 50 percent greater than the moment of force in a solid disk. With a fixed value of the field frequency for each diameter of a disk there is a corresponding value of the moment of force. Therefore, the value of the moment of force determines the dimension of the opening in the part. This allows the use of this effect, for example, to sort parts based on geometric considerations.

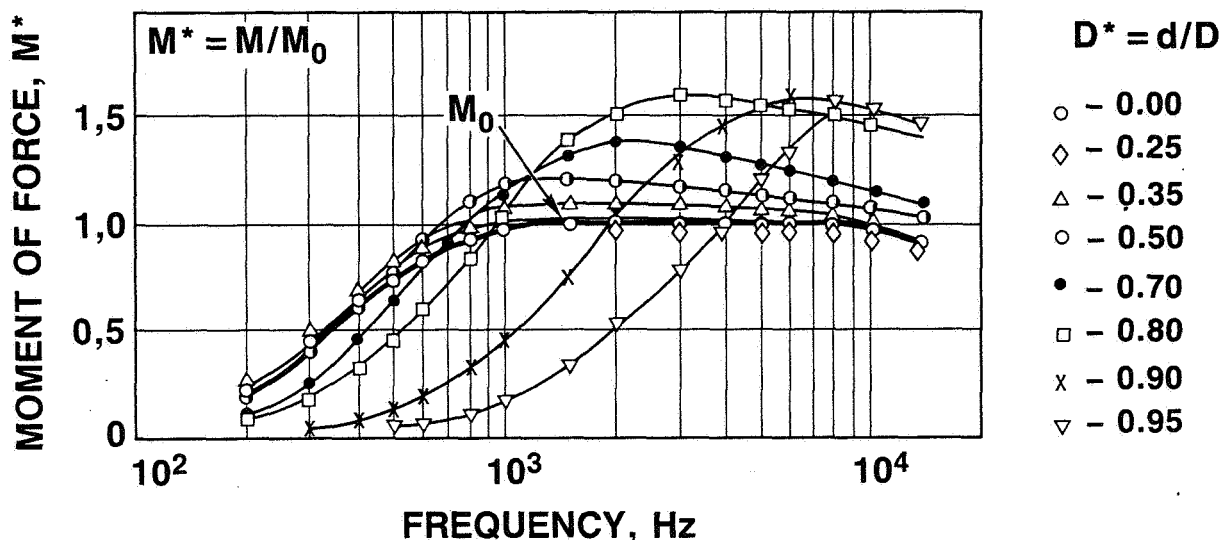


Figure 7. Dependency of the moment of electrodynamic force on the frequency of magnetic field for different values of the central hole in an aluminum washer, constrained to $B = \text{constant}$.

Cylindrical parts with a central opening show interesting relationships. Specifically, if the moment of force acting on a solid cylinder achieves a maximum at $\theta = 45^\circ$, then for the hollow cylinder the value of this angle may be different. This angle depends on the frequency of the field. It was established that the final orienting position of such tube-like bodies can be manipulated by varying the field frequency [7].

The question of how the moment of electromagnetic forces depends on hidden characteristics was investigated by placing a non-magnetic conducting cover on a bushing with a cut in its side. Based on the theory of skin effect, one could expect that in the presence of a nonmagnetic conducting cover acting as an electromagnetic screen, a decrease of the interaction force would be observed. To determine the effect of the cover on the moment of electrodynamic force acting on a bushing with a cut, both a bushing without a cover (thickness of cover $\delta = 0$) and bushings with covers of various thicknesses made of the same material were placed in fields of specific characteristics and frequency. As a result, it was discovered that if the induction in the zone of electromagnetic effect was constant, then with the frequency of the magnetic field sufficient for penetration of the field through the entire assembly the moment of force with the increase of thickness of cover δ does not decrease but actually increases (Figure 8). Only at frequencies of pronounced skin effect does the moment of force decrease with the increase of thickness of

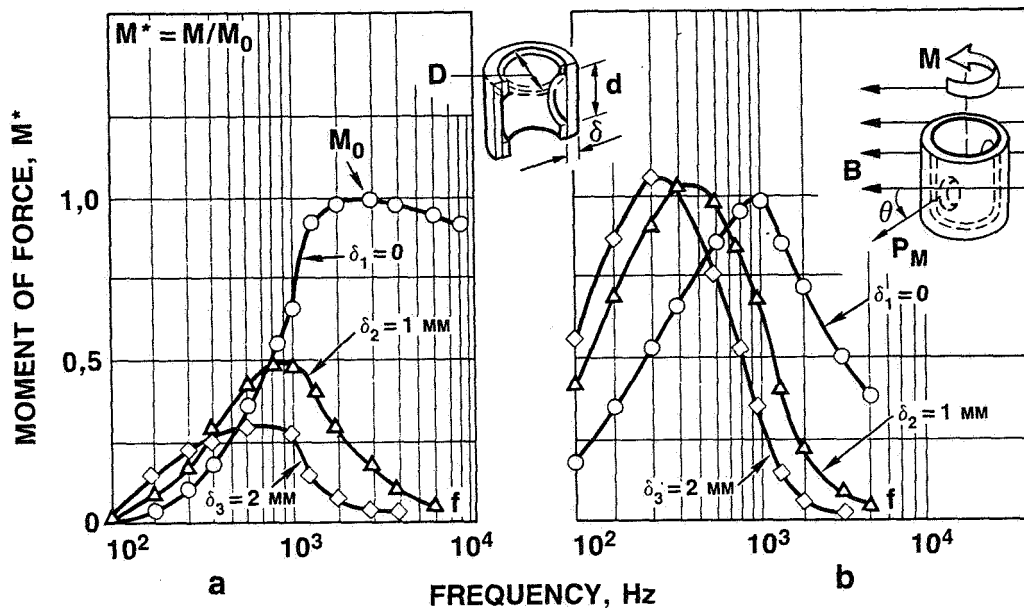


Figure 8. Dependence of M on f for a bushing with a cut in it, screened with a cylindrical cover of thickness δ . (a) - $B = \text{const}$; (b) - $fB^2 = \text{const}$.

cover. Even more evident is the force interaction with a constant power used in the formation of the magnetic field. Variation of the value of induction with respect to the frequency of the magnetic field is possible under the restriction $fB^2 = \text{constant}$ [2,7].

As shown in Figure 8, the moment of force acting on a screened part at a corresponding frequency can be more than twice the magnitude of the moment acting on the part without a cover at frequencies less than 1.0 kHz. This demonstrates the possibility of effective methods of manipulation by internal hidden characteristics of a wide variety of parts. The condition that for the frequencies above 1 kHz a marked decrease of the moment of force is observed in the case of the presence of a cover gives testimony that it is possible not only to manipulate an assembly by its internal hidden characteristics but also to carry out the identification of an assembly, for example, by the thickness of the cover.

The application of the above effects can also be used in the development of new types of mechanisms.

Research in this area has shown other equally interesting results [2], but because of space limitations I will have to restrict myself to these few examples.

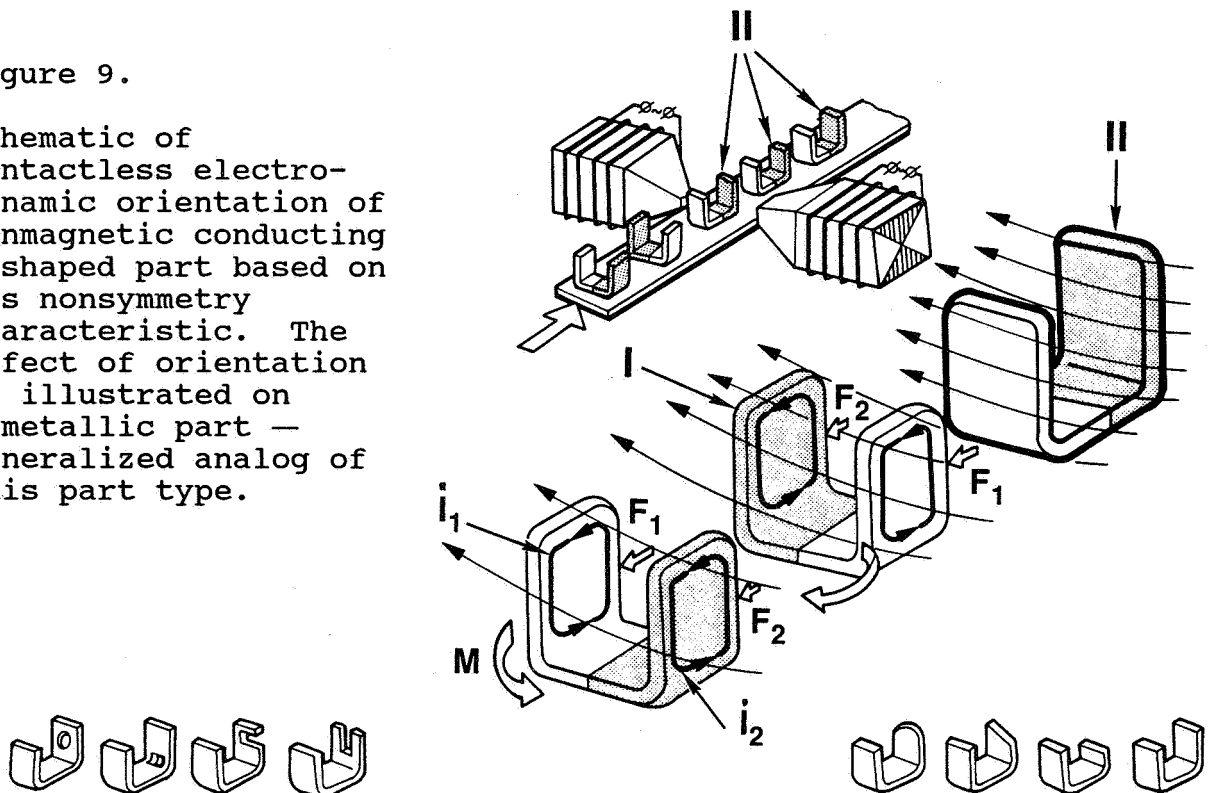
ELECTROMAGNETIC RECOGNITION AND ORIENTATION OF NONSYMMETRIC PARTS

In engineering practice, difficulties most commonly arise in orientation of parts by one or more of the characteristics of nonsymmetry. An example of recognition and orientation of parts with a common type of nonsymmetry by means of electrodynamic forces is shown in Figure 9.

Various asymmetric U-shaped clamps with holes, slots, and notches may be assumed as a clamp-analog, symmetric in shape, but asymmetric with respect to the electric conductivity of its component parts (Figure 9). When such a part is transferred from position I in the direction of the axis of symmetry of the alternating magnetic field, currents i_1 and i_2 are induced in separate vertical sections of the clamp. The interaction of these currents with the non-uniform magnetic field gives rise to a resultant component of electrodynamic forces. Assume the center of gravity of the clamp-analog to be on the geometric axis (a more complicated case, with respect to orientation by standard methods), while the section of the part marked by dots has greater electric resistance. Therefore, $i_1 > i_2$, and, because the parts are placed in the non-uniform alternating magnetic field, the separate vertical sections of the clamp are acted upon by forces F_1 and F_2 , where $F_1 > F_2$. These forces create a moment that rotates the clamp-analog to position II. Hence, given two indeterminate positions, the asymmetric clamp occupies a single, unique position corresponding to a stable orientation.

Figure 9.

Schematic of contactless electrodynamic orientation of nonmagnetic conducting U-shaped part based on its nonsymmetry characteristic. The effect of orientation is illustrated on bimetallic part — generalized analog of this part type.



According to results of investigations of the electrodynamic action upon bimetal U-shaped clamps differing in magnitudes of nonsymmetry, even a relatively small nonsymmetry in electric conductivity in different sections of the part gives rise to a sufficient moment of electrodynamic forces. This adequately solves the problem of active contactless orientation [13-20].

As the electromagnetic method is suitable for the analog, it also is applicable to all variations in a group defined by this analog. This indicates a great versatility of the methods and means for contactless identification and manipulation of components [2,7,12], even though only one example has been shown here.

A multifunctional capacity is characteristic to all the electromagnetic devices. Given an adequate choice of parameters of a magnetic field and the geometry of the electromagnet working zone, it is possible to perform the functions of identification, orientation, locking, and piece-by-piece feeding of parts.

The functionality of devices based on electromagnetic principles is applicable to parts falling into the following categories:

- size of part: 1 to 100 mm.
- mass of part: 0.01 to 2,000 gram
- conductivity of material: $1 \cdot 10^6$ to $60 \cdot 10^6$ 1/Ohm·m.

The effect of active identification and manipulation of the position of such parts is ensured by an electromagnetic field with the following parameters:

- induction: 0.1 to 1.0 T
- frequency: 50 to $50 \cdot 10^3$ Hz
- power: 0.1 to 1.5 W.

These parameters have predetermined magnitudes for specific parts. The time required to manipulate parts typical of the instrument manufacturing industry is on the order of 0.1 to 0.2 seconds, while that of the larger bodies is 0.6 to 1.2 seconds [7].

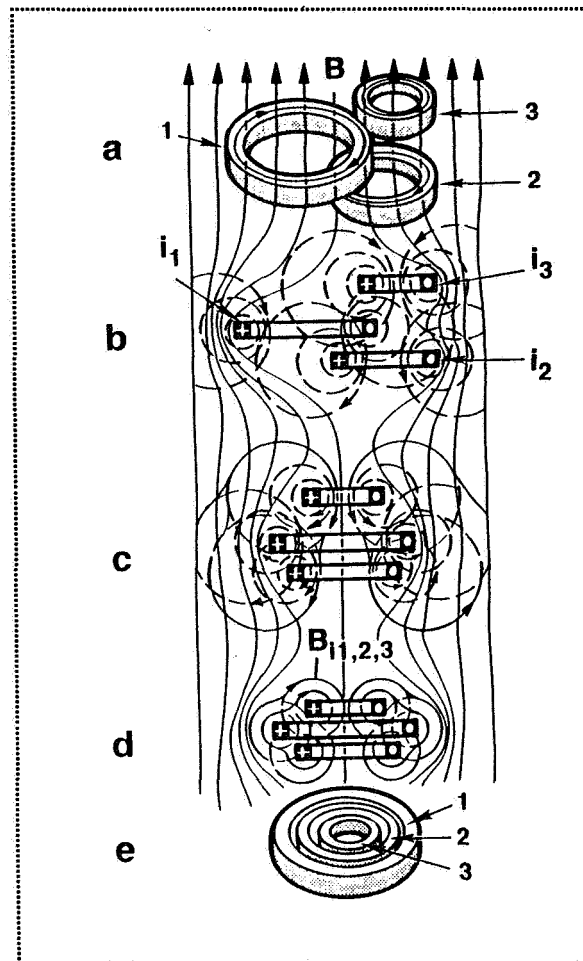
ASSEMBLY AND POSITION CONTROL OF PARTS BY ELECTRODYNAMIC FORCES

The underlying idea for assembly by electrodynamic forces is based on placing individual components in an alternating magnetic field with the vector of induction directed along the axis of assembly [20].

When parts 1, 2, and 3 (rings, for example) are placed in such a field (Figure 10), attractive forces are generated which collect rings on a single axis.

Figure 10.

Process of ring assembly under the influence of electrodynamic forces. **a,b** - initial placement of rings; **c,d** - placement of rings at intermediate positions; **e** - final assembly.



Assembly is accomplished not by the method of directed physical alignment as is the case in ordinary mechanical assembly, but by force interaction between secondary magnetic fields generated by induced currents i_1 through i_3 in the rings. Furthermore, the parts move into a final assembly position via the shortest trajectories.

Figure 10(b) shows the dynamics of interaction of the primary magnetic field with the magnetic fields of the induced currents in parts 1 through 3. The induced fields in the rings create resistance to the primary field, with the result that the primary field is bowed out from the ring area. On the ring periphery, zones of increased field induction are generated and form electrodynamic forces that move parts onto the axis of assembly (Figure 10(c)). As a result of the interaction of magnetic fields generated by currents i_1 through i_3 , the effect of field coupling takes place and forms a magnetic loop (Figure 10(c,d)), encompassing all the rings. The resulting electrodynamic forces cause further contactless convergence and centering of the rings, as shown in Figure 10(e).

As the primary magnetic field B reverses direction, the induced currents i_1 through i_3 and subsequently their magnetic fields reverse direction as well, in a manner similar to that shown in Figure 6. However, the resulting force action formed in the process of primary and secondary field interaction remains the same for each case examined (Figure 10(b-e)).

The process of the assembly of such elements can be carried out even if the offset error of the initial positioning is 80 percent of the linear dimension between their respective axes. For this type of assembly it is necessary that the contours of currents in the initial positioning of the parts overlap at least partially.

Although only one new kind of magnetic assembly has been shown here, other methods are presented in [9,21,22].

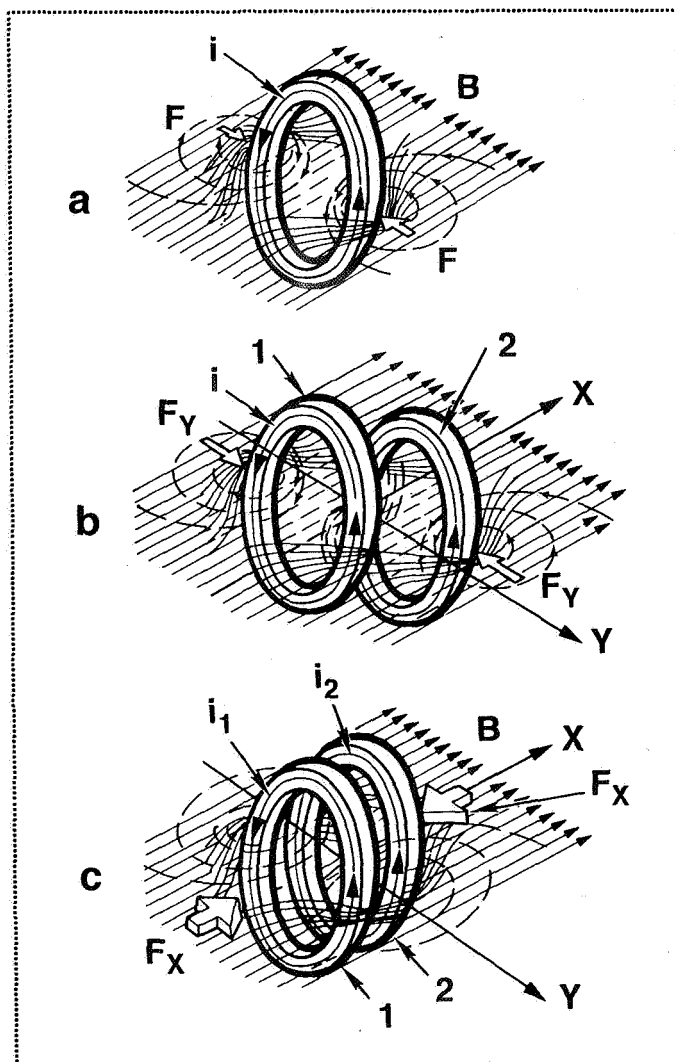
Investigating the effect of force interaction of nonmagnetic conducting parts in a primary alternating magnetic field with the

Figure 11.

Shown is an example of a closed conducting loop 1 used in generating a specific field gradient used to control the position of ring 2. For clarity the magnetic field is shown in only one plane.

(a) - Distribution of the external magnetic field as the result of interaction with the secondary field induced by loop current i .

(b), (c) - Distribution of the external magnetic field and characteristics of resulting electrodynamic forces acting on ring 2 in proximity with loop 1.



presence of nearby additional conductive contour shows the effect to be equivalent in some ways to the presence of a pronounced local field gradient. This condition is illustrated in Figure 11(a). When a nonmagnetic conductive loop 1 is introduced into an alternating external magnetic field, the interaction between the primary and the induced (by loop current i) secondary magnetic fields forms zones of depleted and saturated field in the periphery of loop 1. This generates a pronounced local field gradient. Clearly, as the position, dimension, or geometry of loop 1 are changed, the distribution of the resulting magnetic field will change. Figure 11(b) shows one such field redistribution, as a second body 2, which for clarity of demonstration is in the form of a ring, is placed in the proximity of loop 1. When the diameters of rings 1 and 2 are equal, the resulting stable configuration of the rings is shown in Figure 11(c). The resulting force acting on ring 2 also depends on the interaction of fields induced by loop currents in rings 1 and 2. The dynamics of the movement of ring 2 relative to ring 1 correspond to the case illustrated in Figure 10.

By introducing a number of nonmagnetic conductive contours, each equipped by an externally controllable closing/opening switch, it is possible to create complex field gradients. These, in turn, allow new types of electromagnetic devices to be created [23,24].

A literature search to determine the level of scientific and technological advancements in this field showed that some of the information presented here, developed at the Institute of Physics, Latvian Academy of Science, is still innovative.

CONCLUDING REMARKS

By using force interactions of magnetic fields, recognition and manipulation effects can be achieved for parts that vary in both form and materials. Such methods continue to be useful for a wide variety of earth-bound automation applications. At the same time, because they can be applied remotely, involve contactless interactions, and are universal in the sense that one system can be used for parts of different configurations, they may also have potential applications for automated manipulation and identification of objects in space activities.

These processes are relatively simple, are extremely reliable, and can perform in a wide variety of environmental conditions. Because of this, the knowledge gained through the study of these techniques can open the way to the development of new types of mechanisms for spacecraft.

I wish to thank the members of the Actuators and Inertial Sensors Group, Guidance and Control Section, Jet Propulsion Laboratory, for their assistance and encouragement, and for their perceptive criticism of this paper.

REFERENCES

1. Kirko I.M.; Preis V.F.; Joffe B.A.: "Contactless Methods of Orientation of Discrete Bodies-Parts in Magnetic and Electric Fields," in Theory of Machines of Automatic Action. Moscow: "NAUKA" Science Publishing House, 1970, pp.129-142
2. Joffe B.A.; Kalnin R.K.: Orientation of Parts by Electromagnetic Field. Riga, "Zinatne," Latvian Academy of Sciences Publishing House, 1972.
3. Moskowitz L.R.: Permanent Magnet Design and Application Handbook. Boston, Massachusetts. Gahners Books International, Inc. 1976.
4. Baltvilks A.T.; Joffe B.A.; Kalnin P.K.: "Force Interaction of Ferromagnetic Cylinders and Disks in Completing by Magnetic Field," in Automation of Assembly Processes, Installment 6. Riga, Polytechnic Institute, 1977, pp. 7-22.
5. Baltvilks A.T.; Joffe B.A.; Kulberg A.Y.: "Investigation of Magnetostatic Interaction of Ferromagnetic Parts in the Zone of Magnetic Saturation Applicable to Solution of Problems of Assembly," in Automation of Assembly Processes, ISSN 0320-6963. Riga, Polytechnic Institute, 1978, pp. 47-59.
6. Edminster J.A.: Theory and Problems of Electromagnetics. New York. McGraw-Hill Book Co., 1979.
7. Davydenko E.P.; Kanaev A.S.: Mechanization of the Production by Means of EMAGO Devices. Riga, "Zinatne," Latvian Academy of Sciences Publishing House, 1984.
8. Burke H.E.: Handbook of Magnetic Phenomena. New York. Van Nostrand Reinhold Co., 1986.
9. Sandler B.Z.: Robotics. Designing the Mechanisms for Automated Machinery. Englewood Cliffs, N.J. Prentice-Hall International, Inc., 1991.
10. Kulberg A.Y.; Joffe B.A.; et. al.: "Device for arranging ferromagnetic components at preset distance from one another," US Patent No. 4,153,151 class 198/456.
11. Ryzhov V.D.; Joffe B.A.; et al.: "Device for Contactless Separation of Individual Ferromagnetic Components from a Flow of Components," US Patent No. 4,113,142 class 271/171.
12. Sommer U.A.: Orientation of Plane Asymmetric Parts by Means of EMAGO. Riga, LatInti, 1975.

13. Joffe B.A.; et al.: "Method for Orientation of Current-Conducting Nonmagnetic Bodies in a Magnetic Field and a Device for Carrying same into Effect."
US Patent No. 3,636,486 class 335/219.
14. US Patent No. 3,645,377 class 193/33.
15. US Patent No. 3,651,439 class 335/219.
16. US Patent No. 3,656,075 class 335/219.
17. US Patent No. 3,661,241 class 198/33.
18. US Patent No. 3,924,211 class 335/284.
19. US Patent No. 3,930,212 class 335/284.
20. Kalnin R.K.; Joffe B.A.; et al.: "Method of Assembly of Nonmagnetic Current-Conducting Components," US Patent No. 4,238,658.
21. Sermons G.Y.: Dynamics of Rigid Bodies in Electromagnetic Field. Riga, "Zinatne," Latvian Academy of Sciences Publishing House, 1974.
22. Zhuk V.V.: Electrodynamic Method for Clustered Assembly of Parts. Riga, LatInti, 1979.
23. Joffe B.A.; et al.: "Method of Oriented Feeding of Nonmagnetic Current-Conducting Components and Devices for Effecting the Same," US Patent No. 4,077,027 class 335/219.
24. Joffe B.A.; et al.: "Device for Making Sets of Nonmagnetic Current-Conducting Components," US Patent No. 4,144,637 class 29/739.

**Precise Positioning and Compliance Synthesis
for Automatic Assembly Using Lorentz Levitation**

R. L. Hollis* and S. Salcudean*

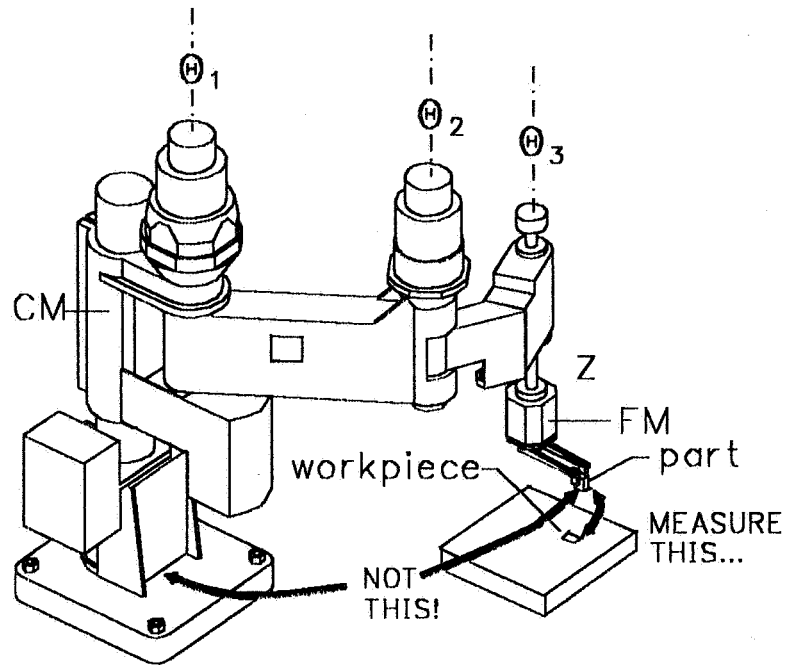
***IBM Research Division
Thomas J. Watson Research Center
Yorktown Heights, NY 10598 USA**

**+Department of Electrical Engineering
University of British Columbia
Vancouver, B.C., Canada**

Abstract

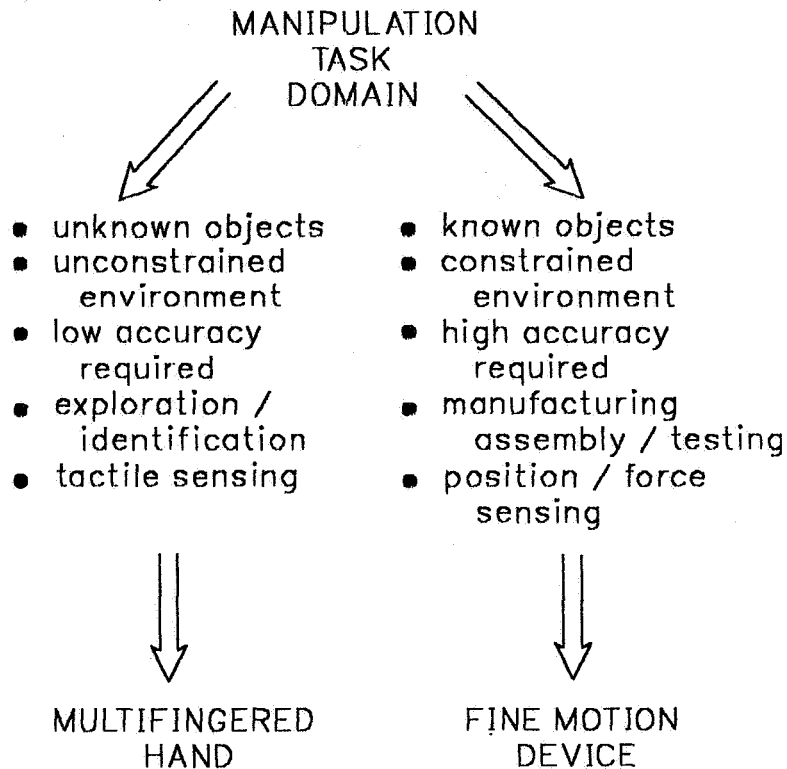
Many manufacturing assembly tasks require fine compliant motion and fast, accurate positioning. Conventional robots perform poorly in these tasks because of their large mass, friction and backlash in gears, cogging in drive motors and other deleterious effects. Even robots equipped with special control systems enabling compliant operation offer only partial solutions. It is therefore difficult or impossible to automate many product assemblies requiring fine, compliant motion. This problem can be greatly alleviated by dividing the manipulation system into coarse and fine domains. In this scenario, a standard industrial robot can serve as a coarse positioner which in turn carries a six-degree-of-freedom fine motion wrist. Thus the robot can access a workspace measured in meters at low bandwidth and low resolution while the wrist can move over millimeters at high bandwidth and high resolution during the final phases of the assembly operation. Our work indicates that fine motion wrists using Lorentz levitation can greatly augment the accuracy and dexterity of robots because they are frictionless, have high bandwidths and have a single back-drivable moving part. Additionally, since there is no contact between the moving and stationary parts, wear and contamination can be eliminated. The use of six Lorentz force actuators in combination with realtime position and orientation sensing offers several important advantages over magnetic bearing approaches.

Coarse-Fine Manipulation



A standard industrial robot can be used as a coarse manipulator (CM) operating in tandem with a specially designed fine manipulator (FM) to obtain a system with large motion range, very high motion resolution, and high bandwidth. The FM carries out manipulation tasks under the guidance of endpoint sensors based on vision, optics, capacitance, inductance, etc. to carry out closed-loop assembly.

Two Manipulation Scenarios



In coarse-fine manipulation, choices can be made between using multi-fingered hands or fine motion devices. The manufacturing environment favors the use of fine motion devices. Fine motion devices must be designed to overcome the problems inherent in the coarse robot: poor resolution, large inertias, static friction in the joints, link bending, etc.

Design Principles for Fine Motion Devices

- **P1 MASS:** lowest total mass → minimal effect on coarse manipulator performance
- **P2 ACCELERATION:** highest force to moving mass ratio → high bandwidth, high throughput and vibration rejection capability
- **P3 STRUCTURE:** single moving element which approaches a rigid body → elimination of structural modes and complex dynamic effects
- **P4 COLOCATION:** closest proximity of endpoint, actuation means, and sensing means → elimination of phase lags and actuator-sensor dynamics
- **P5 STICTION:** frictionless suspension or bearing systems → elimination of stick-slip limit cycles, wear, and contamination
- **P6 SENSING:** noncontact internal position sensing → good closed loop control even in the absence of endpoint sensing information

Lorentz Levitation

- **Magnetic Bearings**

Suspension by controlled DC electromagnets and the force of attraction between magnetized bodies

Principal advantage:

- $\simeq 10 \times$ more efficient than Lorentz levitation

- **Lorentz Levitation**

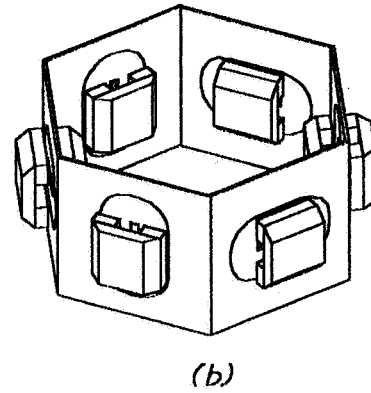
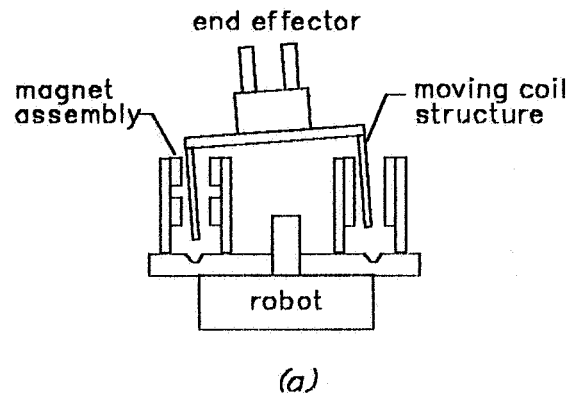
Levitation by forces due to controlled currents in conductors in magnetic fields

Principal advantages:

- greatly reduced suspended mass — no floating iron
- single coil provides bi-directional forces
- no need for "bias" currents★
- essentially linear current vs. force property★
- essentially constant force vs. position property
- greatly reduced coil inductance — fast response
- force generated is approximately in plane of coil
- reduced hysteresis and iron loss
- very high momentary forces possible

★also true of new hybrid-type magnetic bearings

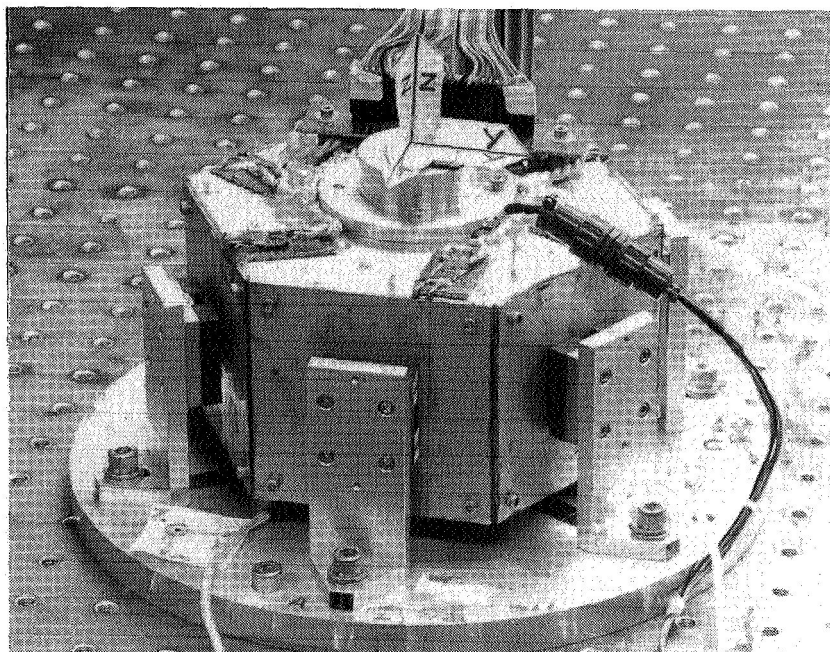
Wrist Geometry



(a) Cross-sectional view, (b) general view.

Magic Wrist Prototype

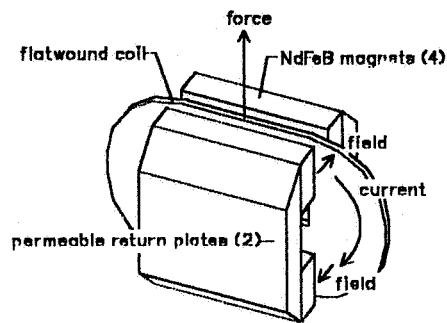
ORIGINAL PAGE
BLACK AND WHITE PHOTOGRAPH



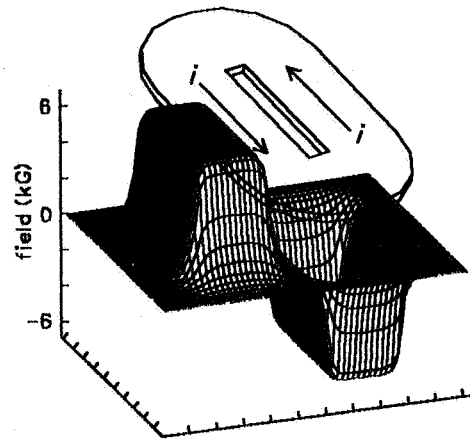
The prototype magic wrist operates on a benchtop. It can position in six degrees of freedom with a resolution of about $1\text{ }\mu\text{m}$ in translation, and 0.00001° in rotation over a workspace of $\pm 5\text{ mm}$ in translation and $\pm 4^\circ$ in rotation. A steady-state load of 32.5 N (7.3 lb.) can be supported with a power expenditure of 60 W .

A robot-mountable version of the wrist is nearing completion.

Lorentz Actuators



(a)

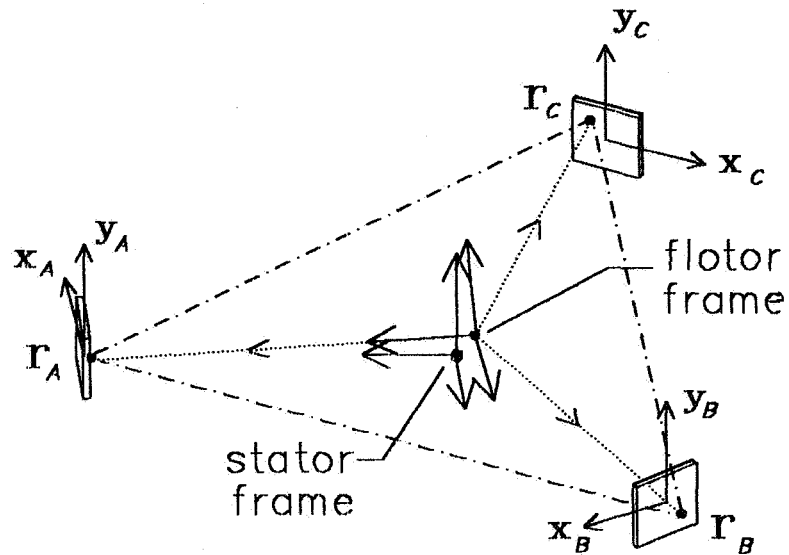


(b)

(a) Flat coil large-gap Lorentz actuator, (b) calculated normal component of the magnetic field.

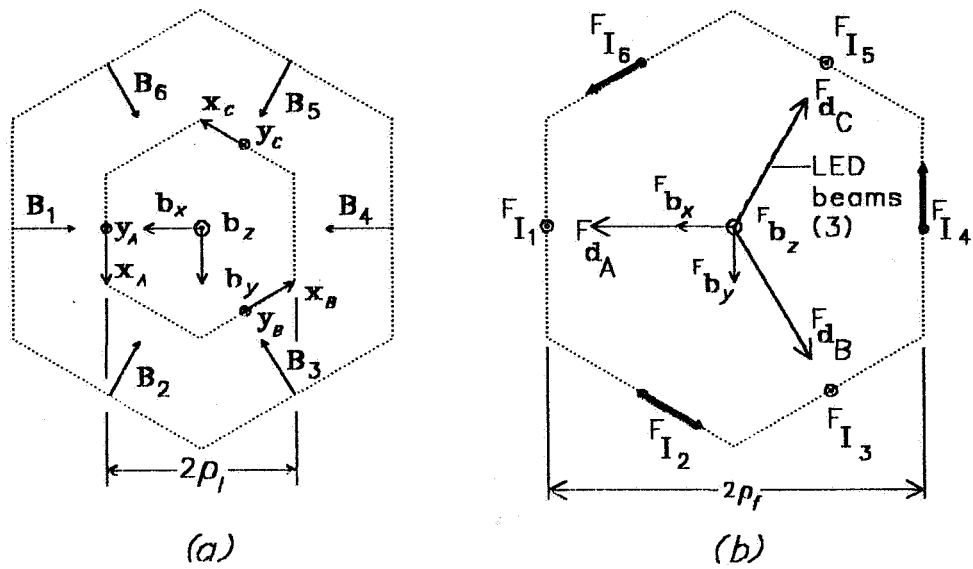
The wrist uses six actuators of this type to produce an arbitrary force/torque vector on the flotor. In the magic wrist, there is a trade-off between high magnetic efficiency with a narrow gap *vs.* the necessity of allowing substantial free motion in all six degrees of freedom, *i.e.*, achievable force *vs.* workspace size.

Six-DOF Optical Sensing Scheme



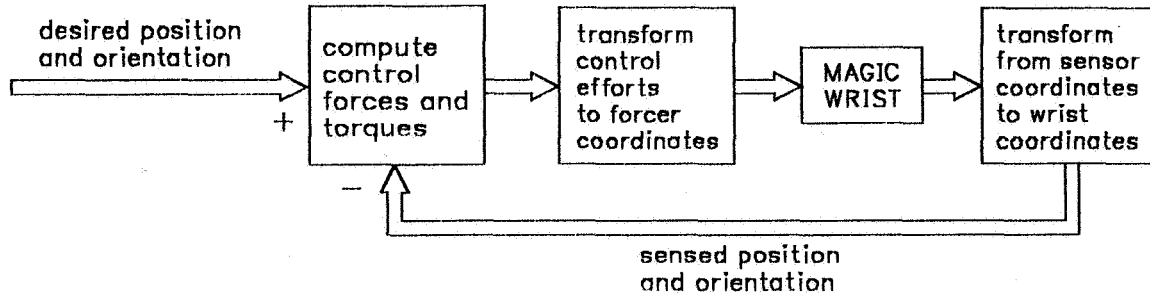
Internal position sensors. Three radial light beams fall on a set of three two-dimensional PSDs to give complete position and orientation sensing.

Stator and Flotor Coordinate Frames



(a) Stator frame vectors. The magnetic field vectors and the PSD coordinate systems are fixed in the wrist stator. (b) Wrist frame vectors. The coil currents and LED beams are fixed in the wrist flotor.

Dynamics and Control



Euler parameter vector

$$\mathbf{p} \triangleq [\beta_0 \ \beta^T]^T = [\cos(\phi/2) \ \sin(\phi/2) \ \mathbf{s}^T]^T,$$

where \mathbf{s} is the axis of rotation ($\|\mathbf{s}\| = 1$) and ϕ is the angle of rotation.

Task space linear dynamics

$$\ddot{\beta} = \frac{1}{2} {}^F\dot{\omega} = \frac{1}{2} {}^FJ^{-1} {}^F\tau \triangleq \mathbf{u}_1$$

$$\ddot{\mathbf{r}}_T = \frac{1}{m} \mathbf{f} + \mathbf{g} - {}^F\mathbf{r}_T \times {}^FJ^{-1} {}^F\tau \triangleq \mathbf{u}_2.$$

PD control law

$$\mathbf{u}_1 = K_p (\beta_d - \beta) - K_v \dot{\beta}$$

$$\mathbf{u}_2 = \tilde{K}_p (\mathbf{r}_d - \mathbf{r}_T) - \tilde{K}_v \dot{\mathbf{r}}_T$$

Gain matrices

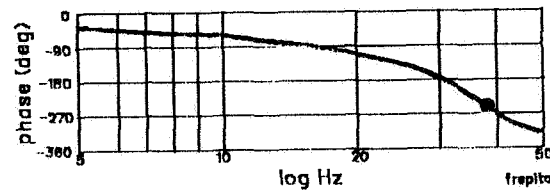
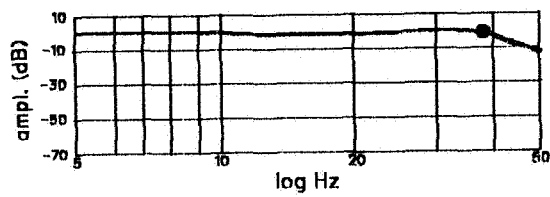
$$K_p \triangleq R^T \text{diag}(k_{p1}, k_{p2}, k_{p3}) R$$

$$K_v \triangleq R^T \text{diag}(k_{v1}, k_{v2}, k_{v3}) R$$

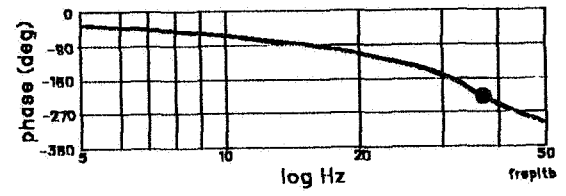
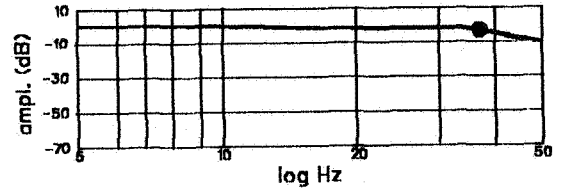
$$\tilde{K}_p \triangleq \tilde{R}^T \text{diag}(\tilde{k}_{p1}, \tilde{k}_{p2}, \tilde{k}_{p3}) \tilde{R}$$

$$\tilde{K}_v \triangleq \tilde{R}^T \text{diag}(\tilde{k}_{v1}, \tilde{k}_{v2}, \tilde{k}_{v3}) \tilde{R}.$$

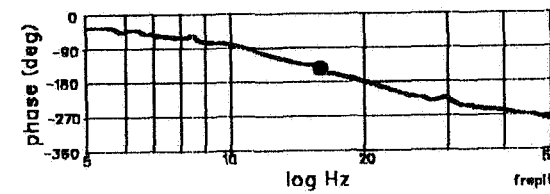
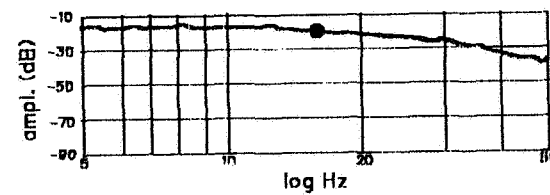
Typical Frequency Responses



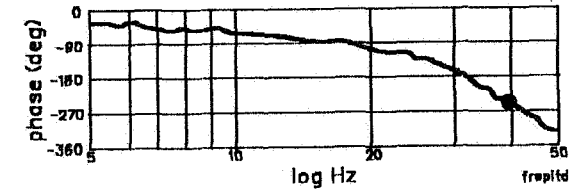
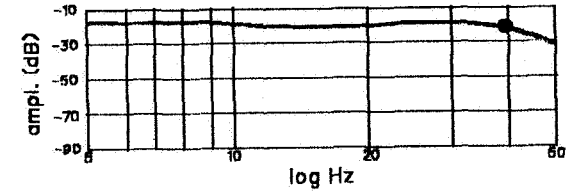
(a)



(b)



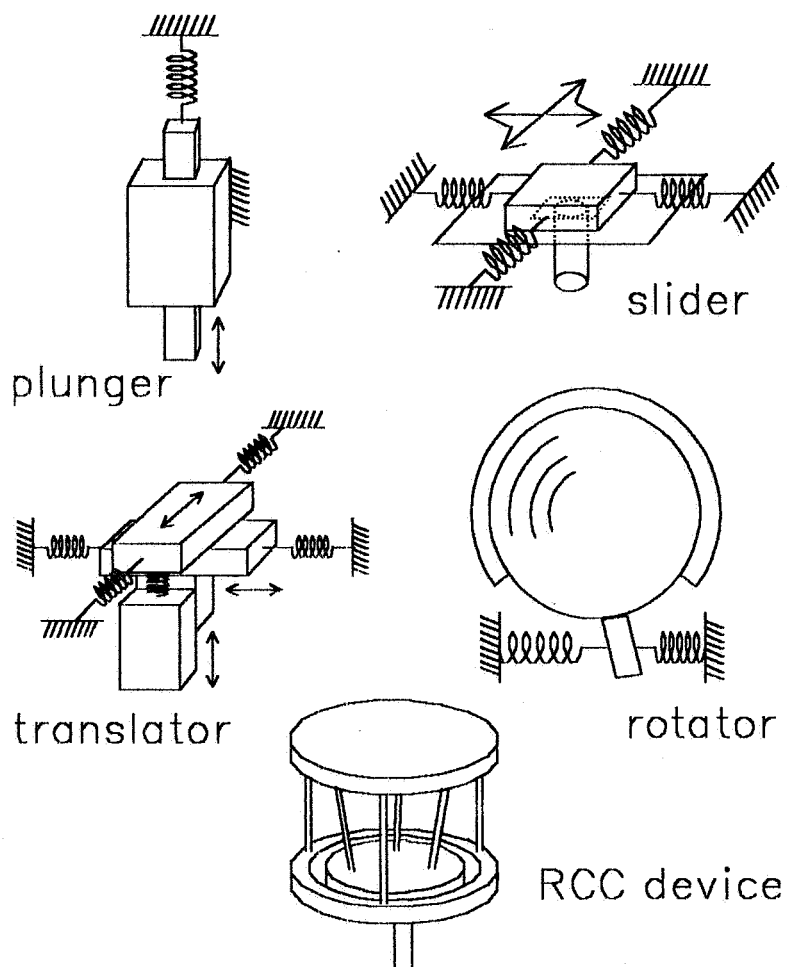
(c)



(d)

Frequency responses. (a) translation along the x axis, (b) translation along the z axis, (c) rotation about the x axis, (d) rotation about the z axis.

Mechanism Emulation



By varying the control gains, the magic wrist can emulate various mechanisms.

Published Material

- "A Six Degree-of-Freedom Magnetically Levitated Variable Compliance Fine Motion Wrist: Design, Modelling and Control," R. L. Hollis, S. Salcudean, and A. P. Allan, *IEEE Transactions on Robotics and Automation* 7[3], June 1991, pp. 320-332.
 - "On the Design and Control of Magnetically Levitated Robot Wrists," R. L. Hollis and S. Salcudean, *Proc. 3rd Int'l Symposium on Robotics and Manufacturing*, Vancouver, B.C., July 18-20, 1990.
 - "Toward a Tele-nanorobotic Manipulation System with Atomic Scale Force Feedback and Motion Resolution," R. L. Hollis, S. Salcudean, and D. W. Abraham, *Proc. Third IEEE Workshop on Micro Electro Mechanical Systems*, Napa Valley, CA, Feb. 12-14, 1990, pp. 115-119.
 - "A Magnetically Levitated Fine Motion Wrist: Design and Feasibility Experiments," R. L. Hollis and A. P. Allan, *ASME Winter Annual Meeting*, Chicago, Illinois, Nov. 27 - Dec. 2, 1988, published in **Symposium on Robotics**, DSC Vol. 11, ed. by K. Youcef-Toumi and H. Kazerooni, ASME, pp. 343 - 352.
 - "A Magnetically Levitated Fine Motion Wrist: Kinematics, Dynamics, and Control," S. Salcudean and R. L. Hollis, *Proceedings of the IEEE International Conference on Robotics and Automation*, pp. 261-266, Philadelphia, PA, April 24-29, 1988.
 - "A Six Degree-of-Freedom Magnetically Levitated Variable Compliance Fine Motion Wrist," R. L. Hollis, A. P. Allan, and S. Salcudean, *4th International Symposium on Robotics Research*, Santa Cruz, Ca., August 9-14, 1987, published in **Robotics Research** vol. 4, pp. 65-73, ed. by R. Bolles and B. Roth, MIT Press.
-

Session 12

BEARINGS 4

Chairman - Timothy Hawkey
SatCon Technology Corporation

N 9 2 - 2 7 7 9 8

**Development of a Differentially Balanced Magnetic Bearing and Control
System for Use with a Flywheel Energy Storage System**

**Mark A. Higgins, David P. Plant and Douglas M. Ries
FARE, Inc., 4716 Pontiac Street, Suite 304, College Park, Maryland 20740**

**James A. Kirk and Davinder K. Anand
Dept. of Mechanical Engineering, University of Maryland, College Park, Maryland 20740**

PRECEDING PAGE BLANK NOT FILMED

657

ABSTRACT

The purpose of a magnetically suspended flywheel energy storage system for electric utility load leveling is to provide a means to store energy during times when energy is inexpensive to produce and then return it to the customer during times of peak power demand when generated energy is most expensive. The design of a 20 kWh flywheel energy storage system for electric utility load leveling applications involves the successful integration of a number of advanced technologies so as to minimize the size and cost of the system without affecting its efficiency and reliability. The flywheel energy storage system uses a carbon-epoxy flywheel, two specially designed low loss magnetic bearings, a high efficiency motor/generator, and a 60 cycle AC power converter all integrated through a microprocessor controller. This paper will discuss in detail the basic design of each of the components that is utilized in the energy storage design.

THE ENERGY STORAGE SYSTEM

At present, electric power utilities face a shortage in meeting their current consumer peak demands in addition to under-utilizing their baseline generating capacity at off peak times. The purpose of the energy storage system is to provide a means to save energy during times when energy is cheap to purchase and inexpensive to produce and then return the energy at times when energy is expensive to purchase and costly to generate. Typically, an energy storage device operates cyclically. For electric utility load levelling applications, a typical daily cycle is 8 hours of charge time, followed by an 8 hour float period, a 4 hour discharge time, and then a second 4 hour float period. It is expected that these systems will have a lifetime in excess of 10 years. Thus the system must be capable of withstanding at least 4000 cycles. Regardless of the application, the principle of operation of the flywheel energy storage system is the same:

- ◆ Take energy in and convert it to an easily stored form.
- ◆ Store the energy with minimal losses until it is needed.
- ◆ Convert the energy back to a suitable output form and return it to the system for use.

To illustrate the advantages of the flywheel energy storage (FES) system, a comparison is made between the flywheel energy storage system and an energy storage system that is currently available

commercially, namely thermal energy storage. The FES system delivers energy to the residence in the form of 220/110 volt alternating current. Thermal energy storage delivers a less useful form of energy, viz: heat. Additionally, the FES system may be used year round, whereas thermal energy storage is primarily effective during the months of the year when heating of the residence is required. In addition, interfacing the FES with existing residences can be a straightforward process by simply working through the existing residential electrical panel. The final benefit of the flywheel energy storage system that will be discussed is that it can be located external to the residence, eliminating the need for useable space within the home.

Electric utilities in the greater Washington D.C. area were surveyed in order to size the energy storage capacity of the flywheel energy storage system. Of primary concern to these utilities was the top 10-20% of the residential power users. This group of utility consumers used a peak power of 7.5-8.5 kW, on average, over a 4-6 hour time period. As a result of our survey of these electric utilities, a system size of approximately 20 kWh was found to satisfy the energy requirements of these high end electricity users.

The flywheel energy storage system is composed of five components and is shown in block form in Figure 1. These components are

1. Flywheel and Enclosure
2. Differentially Balanced Magnetic Bearing
3. Differentially Balanced Magnetic Bearing Control System
4. Motor/Generator
5. Smart Microprocessor Power Conditioner

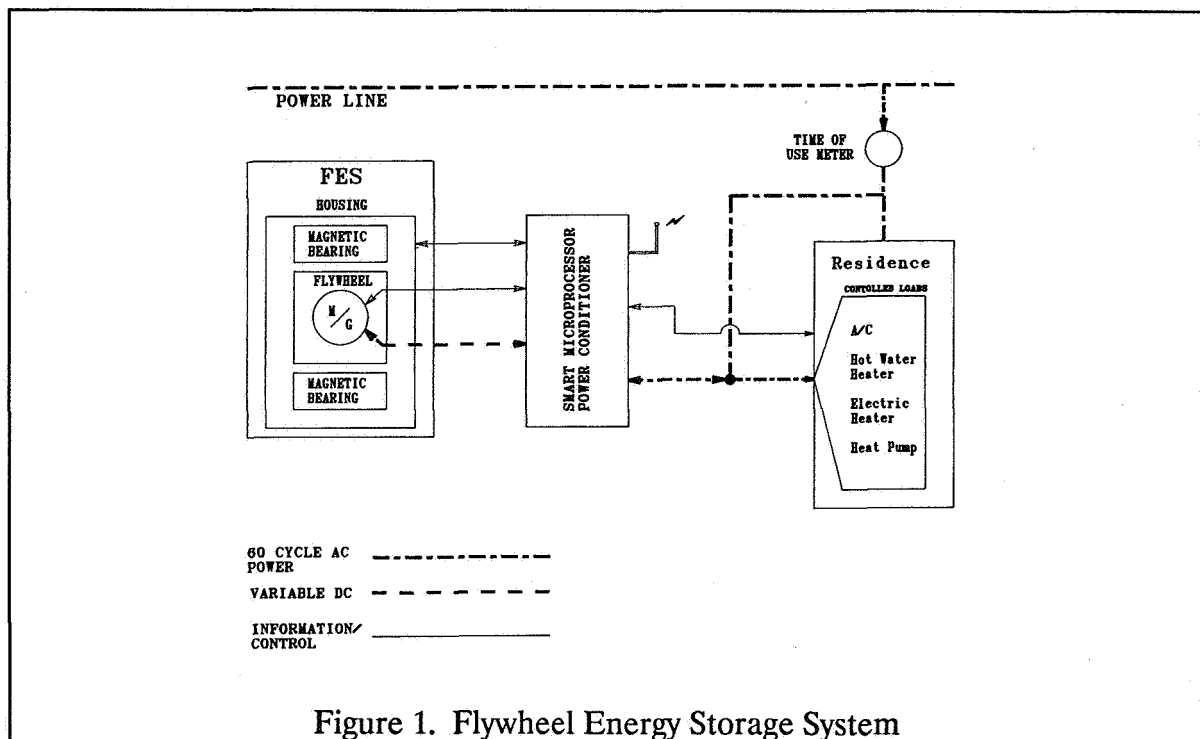


Figure 1. Flywheel Energy Storage System

In the FES system, shown in Figure 2, the flywheel (rotor) is composed of a number of composite material rings which are filament wound and interference assembled to form a multi-ring pierced disk. The rotor is filament wound and interference assembled to improve performance. Two differential balanced magnetic bearings (a new innovative feature) are present in the system, one at each end of the rotor. Two back up bearings are located immediately outboard of the two differential balanced magnetic bearings. Sandwiched between the two magnetic bearings, in the center section of the stator, is a high efficiency brushless motor/generator. The rotor and stator are housed within a vacuum enclosure. The smart microprocessor power conditioner is located external to the flywheel enclosure and provides the necessary power conditioning functions to deliver useful electricity to the customer. The design of the smart microprocessor power conditioner is based upon the state of the art resonant converter technology.

In the following sections of the paper the proposed design methodology of the FES system will be presented as it pertains to each of the individual components listed above.

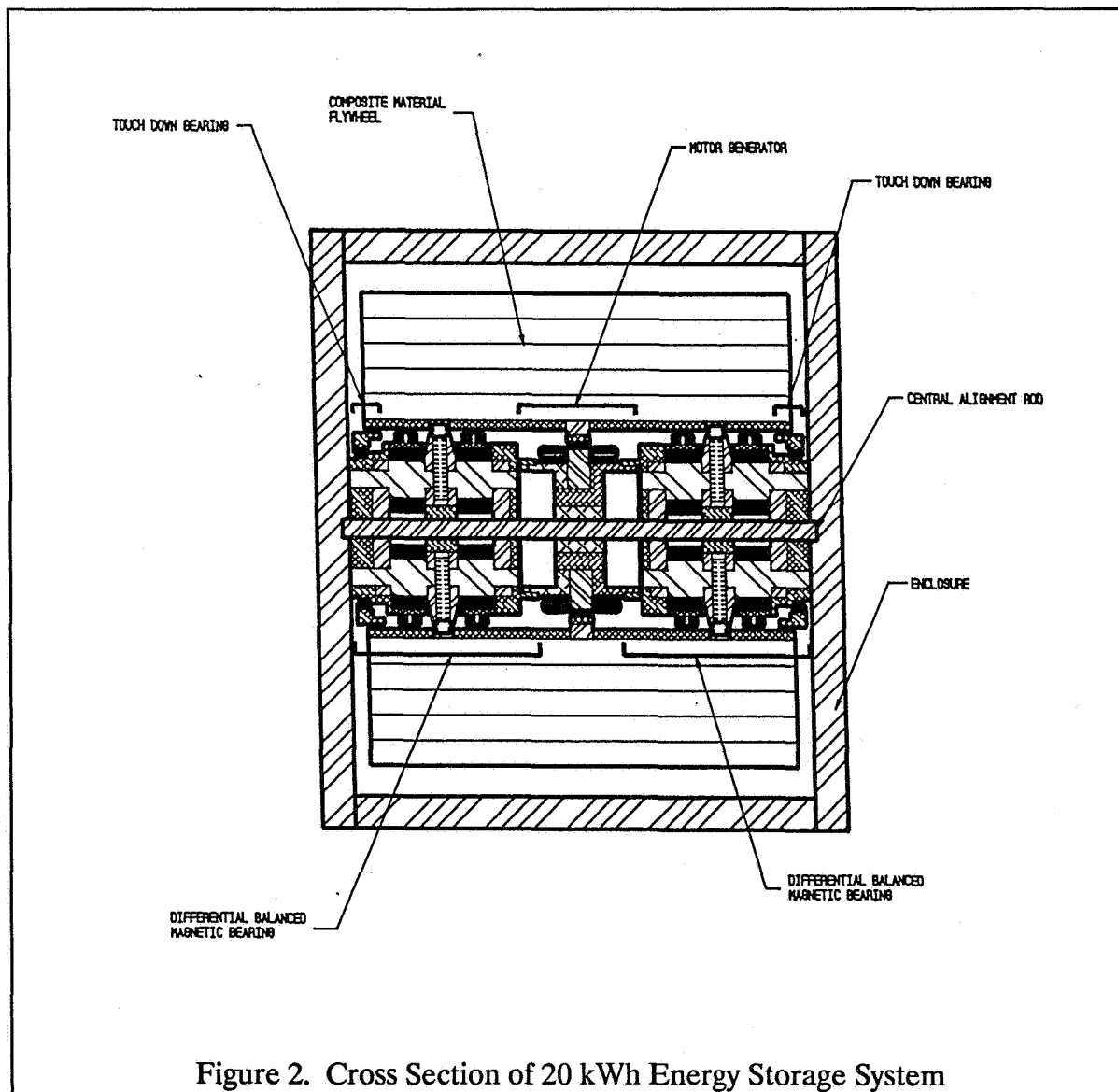


Figure 2. Cross Section of 20 kWh Energy Storage System

SYSTEM DESIGN

The Flywheel and Enclosure

One of the main components of the energy storage system is the flywheel (rotor). A typical figure of merit of a rotor is the amount of stored kinetic energy per unit of rotor weight [1,2]. This parameter is termed the specific energy density and is reducible to the following equation:

$$SED = K_s (\sigma/\gamma)$$

It is desirable to make the SED of the flywheel as high as possible [to minimize the weight and volume of the flywheel] thereby reducing the loads on the differentially balanced magnetic bearings.

It has been shown that composite materials, such as carbon/epoxy, are far superior to steel when used for high SED energy storage applications. The goal of maximizing SED, when using composite materials, is to achieve a uniform state of stress throughout the flywheel. This means that each point in the flywheel simultaneously reaches its working strength, in both the radial and tangential directions [3]. Because composite materials are either anisotropic or orthotropic, their strength can vary from 3,400 MPa [500,000 psi] or more in the tangential direction to 69 MPa [10,000 psi] or less in the radial direction. From a practical point of view, it is desirable to fabricate the flywheel using wet filament winding procedures, with the resultant flywheel having its highest strength in the tangential direction [stresses acting along the fibers] and its lowest strength in the radial direction [stresses acting transverse to the fibers]. A detailed comparison of rotors has been presented by Kirk et al. [4].

The rotor used in this application possesses the following characteristics:

- ◆ The geometry is that of a constant thickness disk, with a hole in the center.
- ◆ The disk is magnetically levitated so that no spokes or shafts are required; thus, there are no stress concentrations.
- ◆ The disk is itself the rotor of a motor/generator set.
- ◆ Energy input is electrical and results in the acceleration of the flywheel with the flywheel running as a motor.
- ◆ Energy output is electrical and results in the deceleration of the flywheel with the flywheel running as a generator.

In this system, the rotor is composed of nine composite material rings which are filament wound and interference assembled to form a multi-ring pierced disk. In addition, a tenth, iron material ring, is attached to the inside of the composite rotor. This iron ring carries the necessary differential balanced magnetic bearing and motor/generator parts.

The FLYANS [FLYwheel ANalysis] and FLYSIZE [FLYwheel SIZE] computer programs, developed at the University of Maryland [3] were used to perform a preliminary sizing for the composite rotor configuration. For flywheel applications, optimizing a rotor consists of maximizing the specific energy density. To maximize the specific energy density of the rotor entails obtaining the optimum ID/OD ratio of the rotor, determining the optimum percent interference allowed

between rotor rings, determining the operating speeds of the rotor, and minimizing the flywheel weight [1,2]. The optimal ID/OD ratio was found to be 0.45. The flywheel will be prestressed using interference assembly techniques. This interference results in favorable stresses in the rings of the flywheel. The optimal amount of interference that should be developed between the rings during assembly was determined to be 0.6%. This amount of interference greatly increases the useable stored energy density, thereby reducing the flywheel weight. It was determined that this amount of interference could be achieved using conventional presses, without damaging the ring during assembly. The operating speed range of the flywheel was designed to cycle between 95% of its maximum speed to 23.8% of its maximum speed [a 4:1 speed range]. Since the rotor stresses are proportional to the square of the speed, the stresses will be cycling between 90% of their maximum to 6% of their maximum. Table 1 summarizes the flywheel specifications.

Inner Diameter	0.254 m (10 in)
Outer Diameter	0.564 m (22.2 in)
Thickness	0.553 m (22 in)
Flywheel Weight	172.8 kg (380 lbs)
Burst Speed	46,345 rpm
Min. Operational Speed	11,610 rpm
Max. Air Gap Growth	0.134 cm (0.053 in)

TABLE 1: Flywheel Specifications

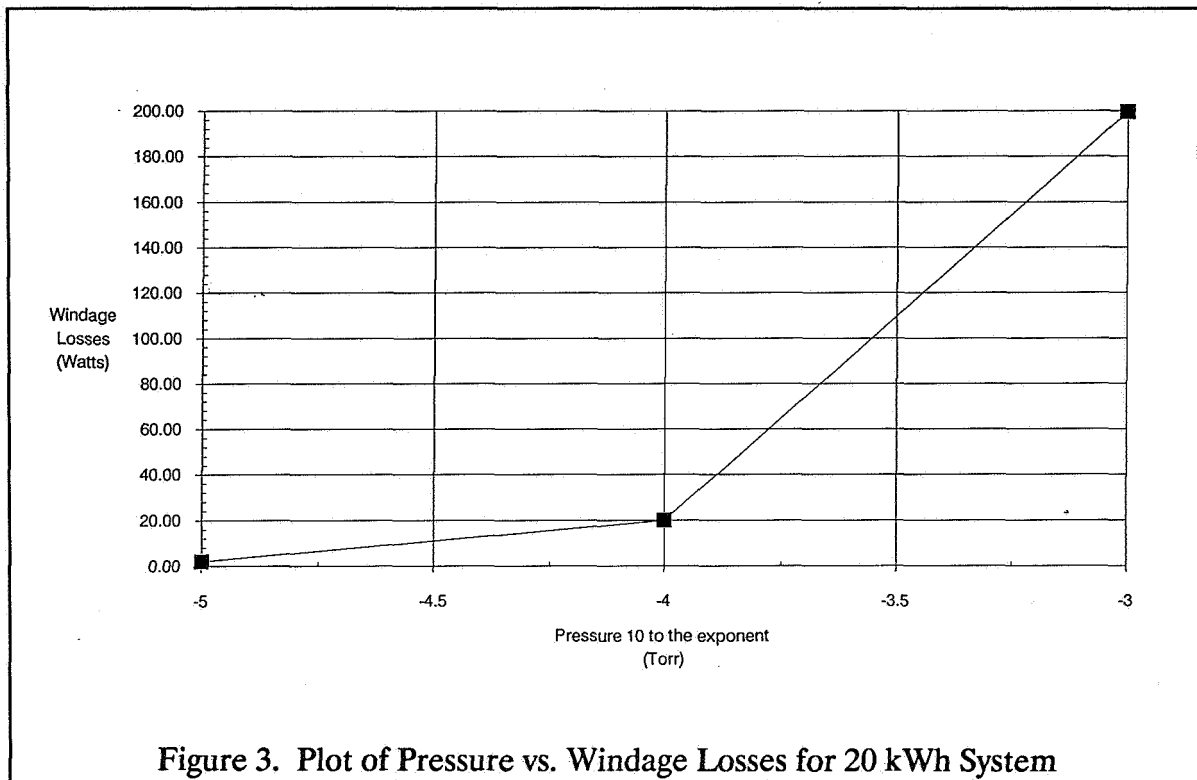
As stated previously, both the stator and rotor portions of the FES will be housed in a vacuum chamber to minimize the windage losses associated with rotation. Three methods of calculating the power loss due to aerodynamic drag loss on the spinning rotor were analyzed. The first method was based on the premise that the the thickness of the rotor was negligible when compared to the outer diameter. The second method was similar to the first in that it modeled the rotating wheel as a disk with negligible thickness. The third and final method modeled the drag on the ring as a result of skin friction which occurs on both the inside and outside diametral surfaces (a disk with a hole in the center), as well as on the top and bottom ring faces [5]. Since the third method of computation most closely resembled the flywheel rotor in this application, it was used as the basis to estimate the drag losses. A plot of the various losses for different operational pressures is given in Figure 3.

During the design analysis it was determined that an operational pressure of 10^{-4} Torr will be sufficient to keep the rotational losses of the flywheel negligible. Furthermore, this pressure can be achieved cheaply and efficiently using conventional vacuum pumps, thus eliminating the need for more costly diffusion pumps.

The Differentially Balanced Magnetic Bearing

Magnetic bearings are used to suspend the composite flywheel because of the high rotational speeds and the need to eliminate contact friction and maximize the operational life of the system. The magnetic bearings used are called differentially balanced magnetic bearings, and incorporate both permanent magnets (PMs), and electromagnets (EMs), that are sandwiched between ferromagnetic plates. The permanent magnets provide a biasing flux in the air gap between the

stator and the return ring while the electromagnets provide a control flux to stabilize the flywheel radially. Both the PM's and the EM's are located on the stator portion of the bearing. A high permeability return ring is attached to the inside diameter of the flywheel and is positioned concentrically around the stator. Sensors located in an orthogonal orientation to the flywheel sense the position of the rotor relative to the stator and provide a feedback signal to the magnetic bearing control system [6].



A possible orientation for the bearing stack is to align the axis of the bearing with the earth's gravitational field. In this orientation, with the flywheel weight in the axial direction, the suspension control of the pancake bearing is passive, meaning that the permanent magnets alone must be able to provide enough axial support to maintain the flywheel in suspension. Since the flywheel used in this application weighs approximately 172.8 kg (380 lbs.), a new and unique method of suspending the wheel was developed.

The 20 kWh flywheel is suspended by orienting the axial axis of the flywheel, and that of the bearing, parallel to the earth's surface (and thus perpendicular to its gravitational field). The weight of the wheel will then be suspended by the magnetic forces generated in the radial direction. As a result of using both EMs and PMs in the differential magnetic bearing design, a linear restoring force is generated in the radial air gap that acts to restore the rotor to its center position. In order to accomplish this task differential size permanent magnets are used. The permanent magnet located in the southern quadrant is larger than the permanent magnet in the northern quadrant so that the attractive forces due to the lower PM are larger than the magnetic attractive

forces generated in the upper PM. Thus, a net restoring suspension force is achieved which suspends the flywheel as a result of the magnetic forces generated by the permanent magnets alone.

If the flywheel is horizontal, then the flux from the permanent magnets passively supports the assembled flywheel weight. Figure 4 shows in detail the flux paths of one of the axes. Path A, the solid line, is created by each PM. Flux flows from each PM and travels up into the top magnet plate across the air gap into the return ring then into the bottom plate and completes the loop by returning to the PM. Path B, the dashed line, is created by the EM coils. As noted above, a transducer is positioned interior to the rotor and senses all radial gap displacements. When the position transducer detects movement of the flywheel relative to the stator, a control flux is introduced as shown in Figure 4. This control flux adds to the PM generated flux on the side of the increasing gap and subtracts from the PM generated flux on the side of the decreasing air gap, thus furnishing a net force to restore the flywheel to its central position.

The magnetic bearing has active control in the radial direction of the flywheel and passive control in the axial direction. The stack is resistant to axial movements because of the passive stiffness of both magnetic bearings in the axial direction. If you consider the flywheel to have six degrees of freedom, three for translation and three for rotation, then the stack controls four of these degrees of freedom with two magnetic bearings. The two radial translation motions are controlled actively by both magnetic bearings. The two rotation motions (commonly called pitch and yaw) are also controlled by the two magnetic bearings. Axial translation is controlled by the static passive stiffness of the bearing and finally the motor/generator controls rotation about the spin axis of the flywheel.

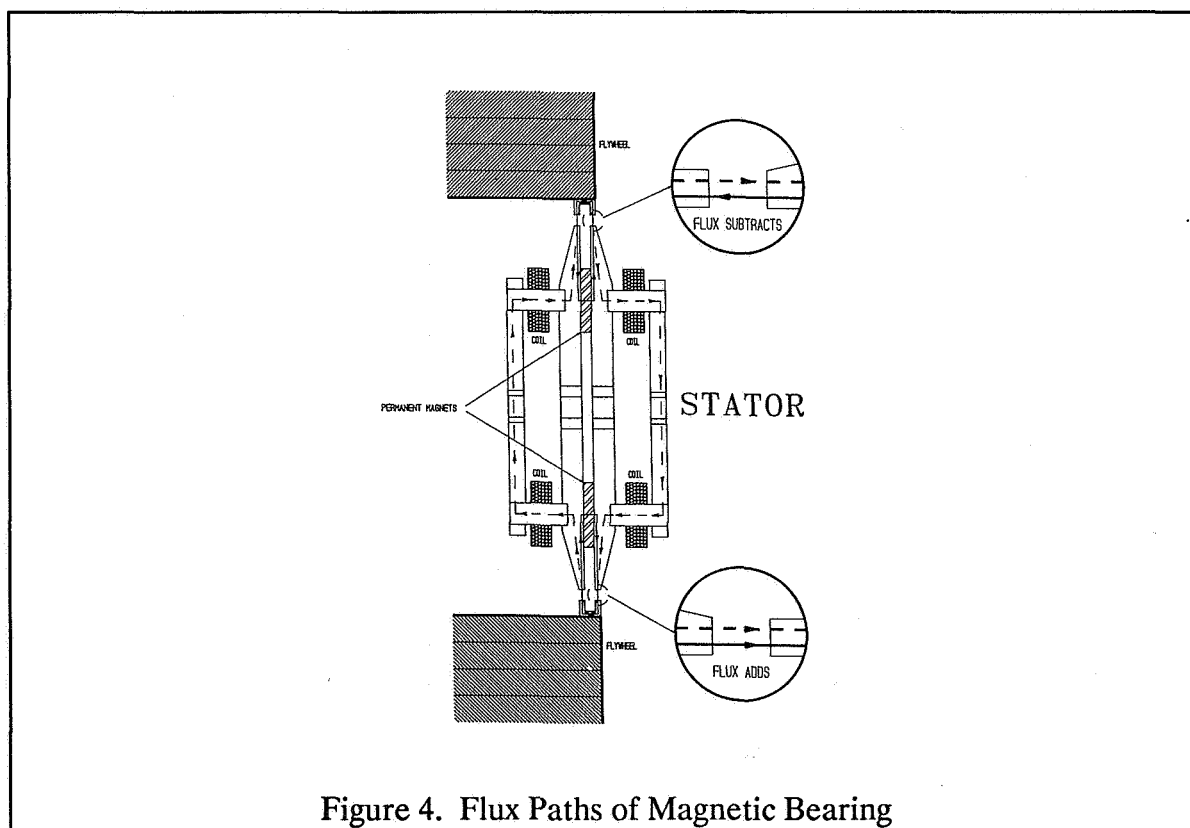


Figure 4. Flux Paths of Magnetic Bearing

Radial Stiffness	1143 kN/m (6527 lbf/in)
Axial Stiffness	146 kN/m (831 lbf/in)
Turns/Electromagnetic Coil	750 turns
Max. Operating Current	2.69 amperes
Gap Operating Range	± 0.097 cm (± 0.038 in.)
Nominal Gap Distance	0.254 cm (0.100 in.)
Stator Radius	1.27 cm (5 in.)
Pole Face Thickness	8.79 cm (3.46 in.)

TABLE 2: Magnetic Bearing Specifications

The important parameters that need to be determined for a specified bearing are the radial stiffness (K_x) of the permanent magnets across the air gap, and the current force sensitivity (K_I) of the coils [7]. These parameters must be determined prior to an in-depth design to determine whether or not the pancake bearing stack will support the flywheel assembly. They are also necessary to the design of the magnetic bearing control system. Table 2 summarizes the preliminary design specifications for the differential balanced magnetic bearings.

The Differential Balanced Magnetic Bearing Control System

The generic control system shown in Figure 5 is composed of a number of blocks which are used to control the physical plant, in this case the flywheel itself. The control system is driven by transducer sensors which determine the instantaneous position of the flywheel. The control system is a simple linear system with lead/lag compensation and a low-pass filter. The corrective force to the plant is provided by the electromagnetic coils whose gain is K_I . The coil is driven by the current amplifier whose maximum calculated output was determined to be approximately 2.7 amps. As long as the plant excursions are small (i.e. in the linear range) the current amplifier operates in the linear mode. If, however, the excursions become large, the amplifier saturates and acts as a limiter. This, and the fact that the electromagnetic coil has inductance, and a small non-linearity, provides the principal reason for non-linear behavior. The control system, therefore, has been carefully designed to operate in the linear region while the inductance of the coil is minimized.

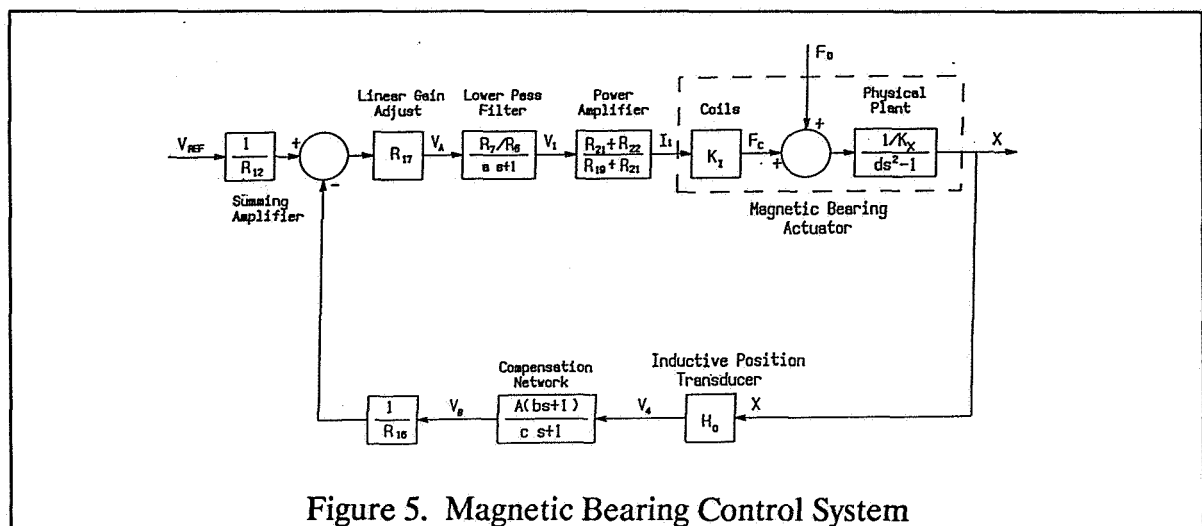


Figure 5. Magnetic Bearing Control System

Two design tools are used in the design and simulation of the stack bearing control system. JEYCAD [8], a computer program for the IBM PC, allows the user to input the component data of the control system and computes the transfer functions and active stiffness of the design. Classical Control, CC, is then utilized to analyze the proposed control system. The CC program plots the frequency and time responses of the control system. These plots can then be analyzed and compared to the specifications in the original parameter design.

The design goals of the differential balanced magnetic bearing control system were defined to be:

1. A maximum excursion of the flywheel should be less than the mechanical touchdown bearing gap.
2. Linear operation with maximum relative stability.

The first requirement is the displacement limit of the flywheel, because the mechanical bearings are built to prevent any damage due to the failure of the magnetic bearing components. The maximum transient overshoot of the control system is designed to be less than the touchdown gap of the mechanical bearing. Mechanical back up ball bearings are located outboard of the differentially balanced magnetic bearings should touchdown occur in the unlikely event of magnetic bearing failure. It also defines a minimum active radial stiffness for a step input of the external disturbing force. The second requirement is met with a gain margin of at least 6 dB and a phase margin of about 45 degrees.

The Motor/Generator

Figure 6 shows a cross-section of a motor/generator system that has been shown to be a viable design for flywheel applications [9,10]. This motor/generator is a brushless permanent magnet device that incorporates optical infra-red sensors for electronic commutation. The absence of brushes on the motor/generator, coupled with magnetic bearings for suspension, eliminates mechanical friction thus making a more efficient energy storage device.

The motor/generator contains an outer ring assembly that is attached to the flywheel and rotates with it as shown in Figure 6. This assembly is composed of several permanent magnets that are attached and evenly spaced around the perimeter of the soft iron backing ring. The north and south poles of the magnets face the coils of the stationary ironless armature (attached to the stator) and create a magnetic field through the control coils. When current from a power supply is pumped through the control coils a torque is generated that causes the flywheel to accelerate. The power supply is shut off, when the flywheel attains its maximum operational speed, and the flywheel spins down to its lowest operational speed, generating a current through the armature coils. The power conditioning electronics yield a voltage that is directly proportional to the flywheel speed. This is the generator mode or discharge cycle of the device. During the motor mode of the device, the coil current is monitored and varied by the electronic commutation mentioned previously. The optical sensors are used to determine the position of the flywheel (as well as the position of the permanent magnets with respect to the coils) by sensing the position of the commutation markings located on the outside of the flywheel. The commutation logic found in the electronics of the device causes the

coil current to be varied in order to accelerate the flywheel or keep it spinning at a constant speed [9].

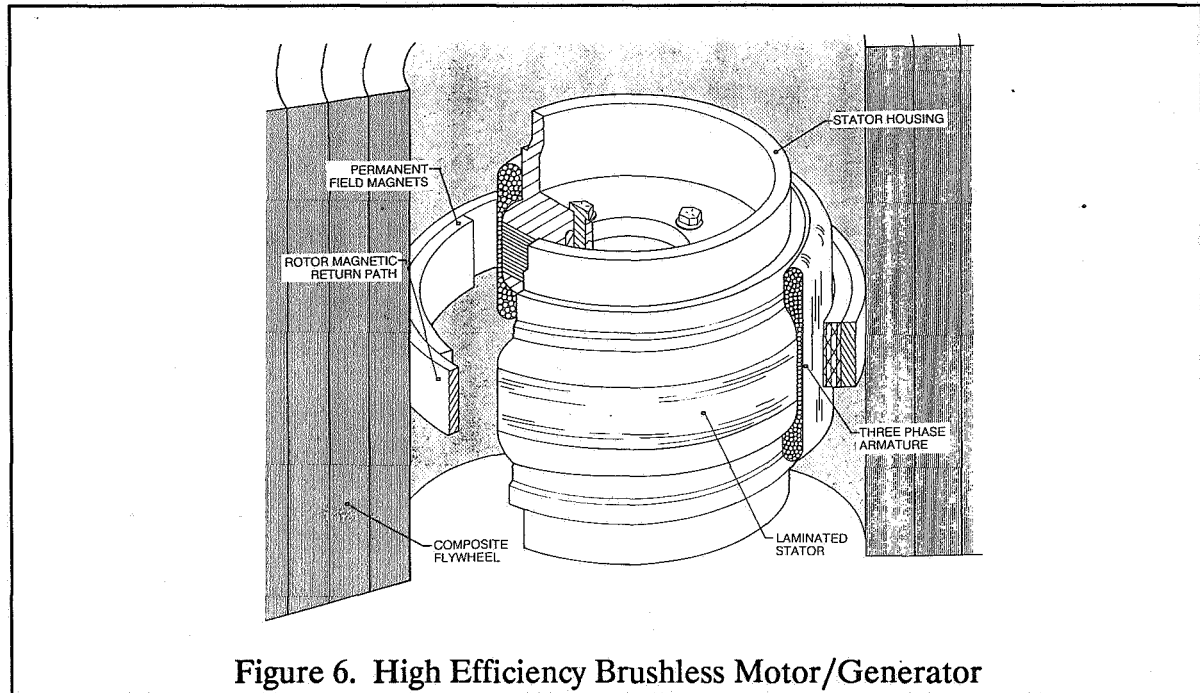


Figure 6. High Efficiency Brushless Motor/Generator

The motor/generator was designed using detailed calculations based on design goal data, flywheel specifications, and magnetic bearing specifications. The first step in the design process was to determine the power, voltage, and armature current variation during the charge cycle of the motor and the discharge cycle of the generator. It was assumed that the bus of the motor receives a constant power of 2.5 kW from the utility grid at 240/110 V $\pm 2\%$ AC. This happens during the charge cycle time of eight hours. Since motor voltage is proportional to flywheel speed and flywheel speed was determined to vary over a four to one ratio using FLYSIZE, a motor voltage profile varying from 680V to 170V was used in the design. Armature current variation (per phase) was determined by dividing the time equation of power by the time equation of voltage. At the beginning of the charge cycle, the armature current/phase was computed to be 29.3 amps and at the end it was computed to be 7.33 amps. A proportional discharge cycle was assumed based upon previous work that has been conducted in this area at the University of Maryland [11]. Over the eight hour peak period the generator discharges a power, on average, of 2.5 kW. Altogether the generator delivers 2.5 kW over eight hours, or 20 kWh of useable stored energy. The voltage variation of the generator is linear from 680V to 170V, with the discharge rate varying as power is delivered to the residence.

Of importance is the maximum current in the armature per phase which is given by $I = P/3V$ or 4.90 amps/phase. This maximum current is used to design the coils in the armature. Table 3 summarizes the preliminary design parameters of the motor/generator. Of final interest was the determination of energy losses within the armature and the power electronics of the device. Armature losses were computed to be 22 watts while the loss due to the ferrite ring was determined to be negligible. Heat generation within the motor/generator was also investigated. The losses

seen in the motor/generator would be generated in the form of core heating. Since the system is contained in a vacuum environment, convection within the system is not possible. To eliminate this problem the central aligning rod is used as a heat sink to conduct the heat generated in the motor/generator to the outside environment (external to the vacuum enclosure).

No. of Poles	8
No. of Conductors/Phase	16
No. of Turns/Phase	2
No. of Armature Coils	16
No. of Coils/Phase	2 (each parallel)
No. of Conductors/Slot	16
Slot Area	36 mm ² (0.056 in ²)
Av. Length of Turn	0.018 m (0.71 in)
Operational Freq. Range	193.5 - 772.4 Hz

TABLE 3: Motor/Generator Specifications

The Smart Microprocessor Power Conditioner

The distribution of electric power in the FES system is accompanied by conversion of that power from one voltage form to another. In the case of the flywheel energy storage system, AC power from the utility is converted to DC power pulses and provided to the motor/generator (which is operating in a motor mode) during the charge cycle of the system. The motor during this charge cycle operates as a permanent magnet brushless DC motor. Power input to the motor is in the form of voltage pulses which are properly sequenced with respect to rotating magnets by a commutation sensor system. During the discharge cycle, the motor/generator is in a generator mode producing variable frequency, variable amplitude, alternating current. This current is produced from the generator as three phase power. The generator output must be converted back to AC power for use in the residence.

A generally accepted utility standard for AC power is that it must be delivered to the residence at a constant voltage of 240/110 volts rms $\pm 2\%$, at 60 Hz. This standard was used in the design so that the generated power (from the FES) is compatible with that delivered from the utility grid. To condition the output power from the FES a power converter or power conditioner is required. Electronic power conditioners contain no moving parts; they are comprised of solid state switches, filters, control circuits and diodes.

The power conditioning element of the flywheel energy storage system is a resonant converter. A block diagram of the converter is shown in Figure 7. This resonant circuit is in the direct path of power flow into and out of the system. Natural commutation is employed to control the flow of power into and out of the "resonant tank". This occurs when either the voltage or current passes naturally through zero. When this occurs the current or voltage is then switched on or off (in order to properly shape the output power to the residence) by a microprocessor that resides within the unit; thus the name smart microprocessor power conditioner. There is little dynamic power loss associated with natural commutation since either the voltage or current at the time of switching is

equal to zero (power equals zero); therefore, the frequency of the resonance can be increased dramatically.

In the motor mode, the smart microprocessor power conditioner functions as a motor controller. Three commutation sensors are positioned 120 electrical degrees apart (on the inside of the flywheel and on the motor/generator) and sense the instantaneous position of the permanent magnets on the rotor. The signals from the commutation sensors are control signals to the resonant converter. The commutation signals determine the sequence of the DC pulses delivered to each phase of the three phase motor/generator. As the frequency of the motor increases the magnitude of the DC voltage pulse is increased to correspondingly increase the speed of the rotor. Scheduling of the required timing of the voltage pulses will be performed by a master controller which will govern both the control of the smart microprocessor power conditioner and the other components of the system.

In the generator mode, the smart microprocessor power conditioner will perform the function of an AC inverter. The three phase AC output (variable frequency and variable amplitude) from the generator will be captured in the resonant tank. This power is then processed in the resonant tank to shape the single phase, 60 Hz, 240/110 volt, alternating current power for use in the residence.

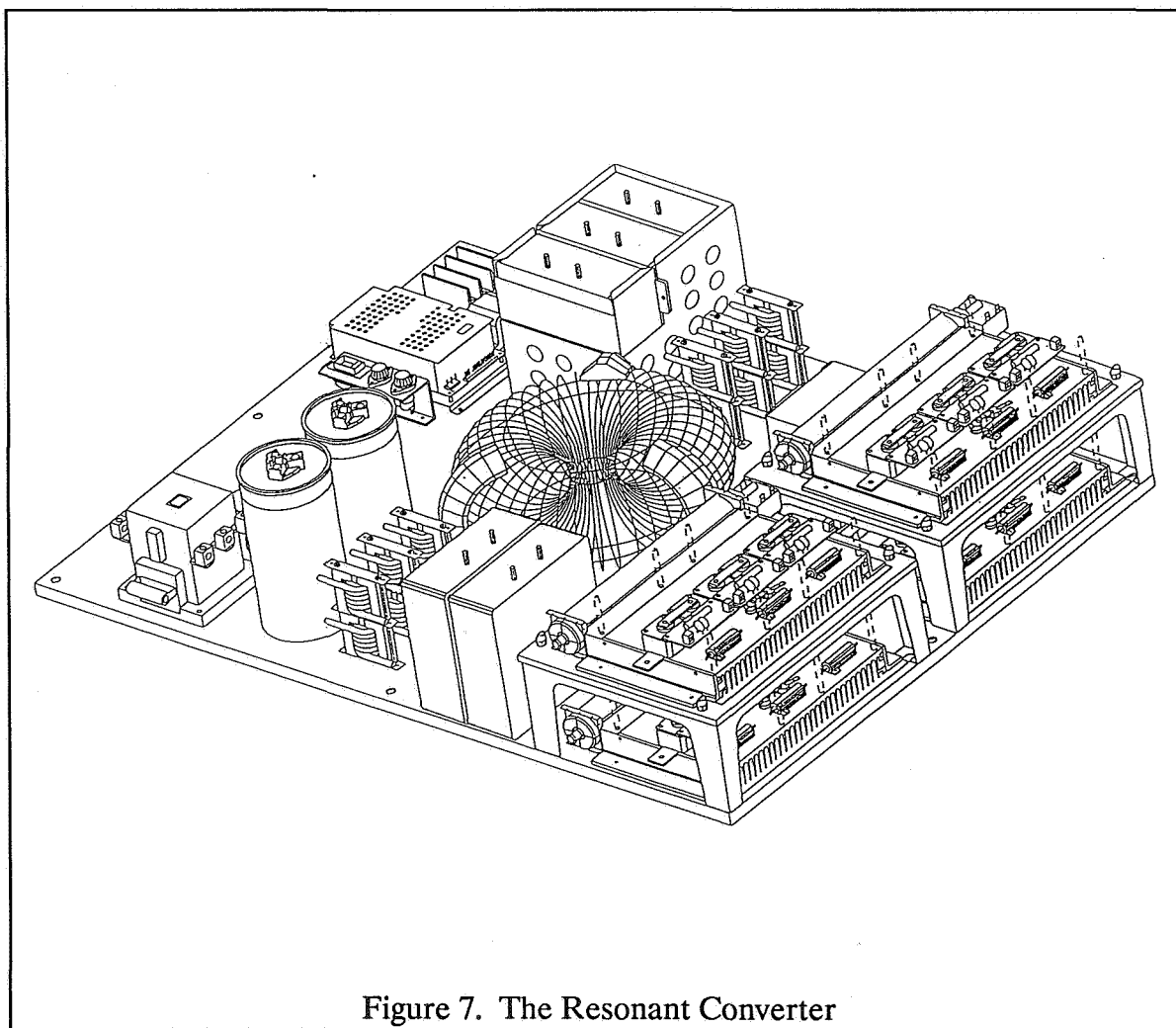


Figure 7. The Resonant Converter

SYSTEM CONSIDERATIONS

System Efficiency

In determining the overall system efficiency of FARE's 20 kWh flywheel energy storage system a typical charge and discharge cycle was assumed as shown in Figure 8. A power budget was prepared that estimated the losses present in the system over the typical 24 hour operational cycle. In order to return 20 kWh of useable energy to the residence, it was estimated that the system would have to store approximately 24.8 kWh of energy.

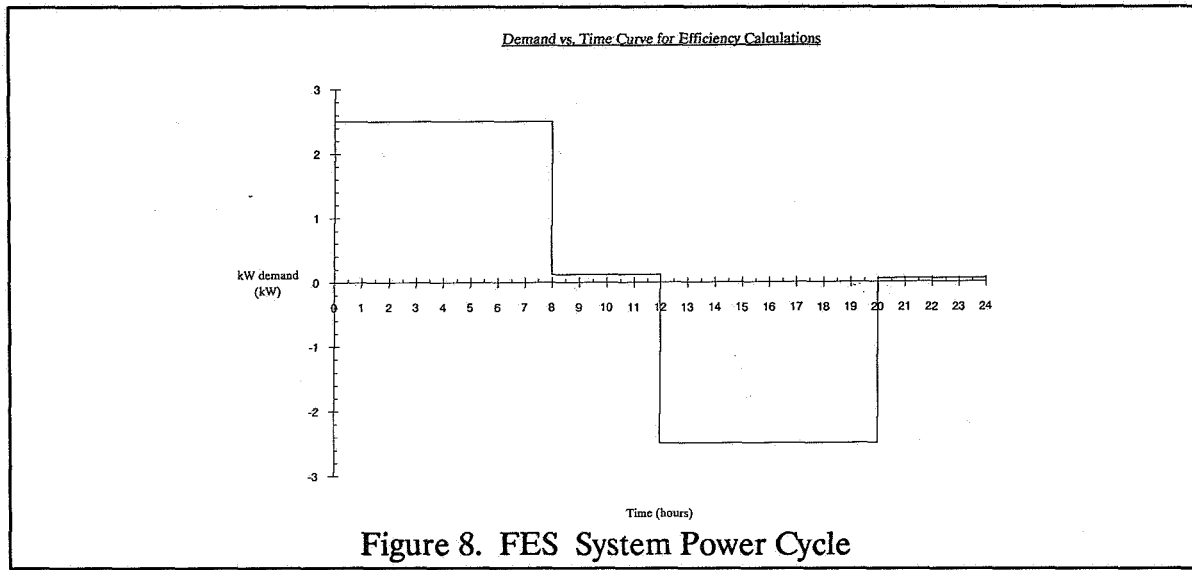


Figure 8. FES System Power Cycle

The round trip efficiency of the system is defined as the amount of useable energy delivered to the residence divided by the amount of energy stored by the system during the charge cycle. Thus system efficiency is:

$$\text{round trip efficiency} = \frac{20 \text{ kWh}}{24.81 \text{ kWh}} = 0.81$$

System Economics

In conducting an economic analysis of FARE's flywheel energy storage system, the up front cost of the system was determined to be \$7500. In addition, the cost of generating power was associated with two different rates, one for off peak generation and the other for peak generation. The approximate savings per year was estimated to be \$2000/year based upon the above rate differential. Knowing the estimated cost savings per year from utilizing the proposed system, and assuming an up-front utility rebate of \$2000 to the consumer, the payback period of the system is calculated to be 3 years.

CONCLUSION

Magnetically suspended flywheel energy storage systems are a unique and superior alternative to other forms of energy storage for electric utility load leveling applications. By utilizing flywheel energy storage systems, utilities possess the capability to save energy and conserve vital fossil fuel resources. In addition, flywheel energy storage systems negate the need for utilities to construct

new generating facilities to satisfy their current, as well as future, peak demands. The magnetically suspended flywheel energy storage system can be designed in modules of 24 kWh that deliver 20 kWh of energy to the residence at a constant voltage of 110/240 volts, alternating current. By using state of the art devices, a round trip efficiency of 81% is achieved. Finally, the economic feasibility of the flywheel energy storage system has been demonstrated to be competitive with other currently available commercial systems, with a payback period of 3 years.

ACKNOWLEDGEMENTS

This work was supported, in part, by a research grant from the Department of Energy.

REFERENCES

1. Kirk, J.A., "Flywheel Energy Storage Part I - Basic Concepts", Int. J. of Mech. Science, Vol. 19, No. 4, 1977, pgs. 223-231.
2. Kirk, J.A. and Studer, P.A., "Flywheel Energy Storage Part II - Magnetically Suspended Superflywheel", Int. J. of Mech. Science, Vol. 19, No. 4, 1977, pgs. 233-245.
3. Kirk, J.A., Anand, D.K., and Khan, A.A., "Rotor Stresses in a Magnetically Suspended Flywheel System", Proc. 20th Intersoc. Energy Conv. Engrg. Conf., Miami, FL, pgs. 2.454-2.462.
4. Kirk, J.A. and Anand, D.K., "Overview of a Flywheel Stack Energy Storage System", Proc. 23rd Intersoc. Energy Conv. Engrg. Conf., Denver, CO, pgs. 2.37-2.42.
5. Kirk, J.A. and Studer, P.A. and Evans, E.E., "Mechanical Capacitor", NASA, Report TN D-8185, March 1976, pgs 45-48.
6. Zmood, R.B., Anand, D.K., and Kirk, J.A., "Analysis Design and Testing of a Magnetic Bearing for a Centrifuge", ASME Pub. DE, Vol. 18-1, Sep. 1989, pgs. 345-350.
7. Jeyasaleen, M., Anand, D.K., and Kirk, J.A., "A CAD Approach to Magnetic Bearing Design", Proc. 23rd Intersoc. Energy Conv. Engrg. Conf., Denver, CO, pgs. 2.87-2.91.
8. Plant, D.P., Anand, D.K., Kirk, J.A., Calomeris, A.J., and Romero, R.L., "Improvements in Magnetic Bearing Performance for Flywheel Energy Storage", Proc. 23rd Intersoc. Energy Conv. Engrg. Conf., Denver, CO, pgs. 2.111-2.116.
9. Niemeyer, W.L., Studer, P.A., Kirk, J.A., Anand, D.K., and Zmood, R.B., "A High Efficiency Motor/Generator for a Magnetically Suspended Flywheel Energy Storage System", Proc. 24th Intersoc. Energy Conv. Engrg. Conf., Wash., DC, pgs. 1511-1616.
10. Neimeyer, L.H., "A High Efficiency Motor for the Magnetically Suspended Flywheel Stack", M.S. Thesis, Univ. of MD, 1989.
11. Kirk, J.A., and Anand, D.K., "Overview of a Flywheel Stack Energy Storage System", Proc. 23rd Intersoc. Energy Conv. Engrg. Conf., Denver, CO, pgs. 2.37-2.42.

N 9 2 - 2 7 7 9 9

**DESIGN OF BEARINGS FOR ROTOR SYSTEMS
BASED ON STABILITY**

D. Dhar, L.E. Barrett, and C.R. Knospe
Center for Magnetic Bearings
University of Virginia

ABSTRACT

Design of rotor systems incorporating stable behavior is of great importance to manufacturers of high speed centrifugal machinery since destabilizing mechanisms (from bearings, seals, aerodynamic cross-coupling, noncolocation effects from magnetic bearings, etc.) increase with machine efficiency and power density. A new method of designing bearing parameters (stiffness and damping coefficients or coefficients of the controller transfer function) is proposed, based on a numerical search in the parameter space. The feedback control law is based on a decentralized low-order controller structure, and the various design requirements are specified as constraints in the specification and parameter spaces. An algorithm is proposed for solving the problem as a sequence of constrained 'minimax' problems, with more and more constraints becoming active in each subsequent stage. This helps in moving the closed-loop eigenvalues into an acceptable region in the complex plane. The algorithm utilizes the method of feasible directions to solve the nonlinear constrained minimization problem at each stage. This methodology emphasizes the designer's interaction with the algorithm to generate acceptable designs by relaxing various constraints and changing initial guesses interactively. A design-oriented user interface is proposed to facilitate the interaction.

INTRODUCTION

Many rotor systems currently in use tend to operate at supercritical speeds, where multiple bending modes are likely to be excited during operation. Under these circumstances, safe and reliable operation under external excitations and internal loadings caused by sudden changes in machine dynamics such as blade loss is warranted, along with reduction of rotor amplitude due to mass imbalance and prevention of rotor instability [ref. 1]. Destabilizing mechanisms such as aerodynamic cross-couplings in turbomachinery, oil-film forces in journal bearings, seal forces, unsymmetric shafts, internal friction, and noncolocation effects in magnetic bearings are the known causes of instability in rotating machinery.

Design of rotating machinery incorporating stable behavior is one of the primary goals of the designer, and has been the subject of ongoing research. Sudden loss of stability may lead to large and uncontrollable rotor amplitude relative to the casing, causing rubs and severe damage leading to machine failure. As such, a designer would like to know during the design process whether a rotor will run stable during its operation, and the size of the stability threshold for the endangered modes of vibration. Moreover, a knowledge of the effect of known parameter variations on the stability characteristics is deemed useful. Using the available design tools, it is the task of the designer to achieve an acceptable steady-state rotor response and also maintain a specified minimum level of stability.

In recent years the development of magnetic bearings has enabled active control of rotor-bearing systems by suppressing the lateral vibration through feedback control. These bearings can be used either to replace oil-film bearings or in addition to them to provide enhanced vibration control and stability characteristics. Several studies have been made on the

control of synchronous vibration and stability of rotating machinery employing these bearings. However, unlike conventional oil-film bearings where there is relatively less flexibility in choice of the bearing parameters (due to their inherent interdependence) and the nature of the feedback control law (which is implicit in the dynamics of the structure-oil film interaction), magnetic bearings offer the designer enormous flexibility to choose the nature of the feedback control and the parameters that govern the law. However, this flexibility cannot be put to effective use due to the limited availability of practical and implementable feedback design methods to exploit the range of available bearing parameters.

The goal of this paper is to bridge this gap and develop a practical and simple feedback control law for design of bearings for rotating machinery. A methodology has been developed based on a simple proportional derivative (PD) controller structure where the feedback control force is essentially a linear function of the "stiffness" and "damping" coefficients (related to the displacement and velocity of the shaft at the bearing location) and the objective is to find acceptable values of these coefficients that satisfy given design specifications and constraints. The formulation is then expanded to design low-order dynamic controllers and find the controller parameters that satisfy the required design criteria.

Research into control system design and optimization has been performed by numerous researchers, and has followed a number of separate paths depending on the final objective and methodology. Eigenvalue placement and eigenstructure assignment has been a particular area of interest, with many differing perspectives and techniques. However, a number of problems beset this method, namely

- i) the choice of a desirable eigenstructure is not obvious,
- ii) the inability to achieve such a structure by output feedback schemes,
- iii) possible poor robustness, and
- iv) a lack of a control magnitude penalty.

Controller design based on dynamic response optimization using a quadratic cost index to obtain an optimal control law is another alternative approach. Such optimization is classified under the title of linear quadratic regulator problem or LQR problem. A fair amount of research has been directed at this problem as applied to the control of mechanical structures, and simultaneous structural and control optimization. Recently, this method has been used to design controllers for rotor bearings systems [ref. 2,3]. A controller designed to minimize a weighted sum of the mean square output (system response) and mean square input (control forces), i.e., to minimize the performance index remedies many of the problems faced by eigenstructure assignment. Moreover, the availability of a closed-loop unique solution of the LQR problem via solution of the Ricatti equation is an attractive feature. The main problems of this method are

- i) the resulting controller requires access to the full set of plant states, or to a state observer,
- ii) the controller is of the same order as the model of the plant, which becomes difficult to design and implement for a structural system (e.g. a multi-level rotor-bearing system),
- iii) actual design specifications must be translated into a choice of weighting matrices,
- iv) a state-observer based controller may have poor stability margins and be very sensitive to modeling errors and parameter variations, and
- v) the scalar quadratic cost function is often inadequate for the representation of certain design objectives.

One approach to overcome some of the above mentioned problems has been the development of suboptimal low-order compensators (static or dynamic fixed-order) by

prespecifying the feedback controller structure but retaining the quadratic cost function adopted in LQR design. The design of such compensators, often called output feedback compensators since they attempt to find a control based on the system output directly involves a numerical parameter optimization of the controller structure [ref. 4–7]. A general solution to the output feedback stabilization problem is not available, and consequently several numerical schemes have been developed. However, the main problems involved with low-order output feedback controller design has been

- i) existence of multiple local optimal encountered during minimization,
- ii) inability to characterize the stability margin properties directly into the problem, and
- iii) inadequacy of the scalar quadratic index to represent the different system performance objectives.

DESIGN VIA PARAMETER OPTIMIZATION

The objective of this paper is to develop a design procedure for a decentralized low-order controller for rotor-bearing systems to achieve certain specifications regarding the stability of the closed loop system. A low-order decentralized controller for rotor systems would consist of a bearing with simple dynamics, that is a simple relationship between the shaft displacement and the bearing force. Decentralized or local control is defined as a control mechanism where only local state information is available, and can be regarded as a particular form of constrained output feedback where certain elements of the feedback transfer matrix are constrained to be zero [ref. 8–12]. In the context of a rotor system, the essential features of such a concept are

- i) the force at the bearing is dependent only on the measurements at the sensor location
- ii) the relationship between the bearing force and the local measurements is a low-order transfer function.

One of the simplest examples of such a scheme is selecting the "stiffness" and "damping" coefficients for a PD controller in order to control rotor response and stability.

The rotor system or the plant is represented as a second-order matrix differential equation, which is a fair approximation of the continuous system for modeling purposes if the number of degrees of freedom chosen to represent the plant is large enough. This can be readily converted to a first-order or state-space form as

$$\begin{aligned}\dot{x} &= A x + B u \\ y &= C x\end{aligned}\tag{1}$$

For plants with high system order, a model reduction may be deemed necessary to improve the computational efficiency in subsequent numerical optimization, and also since the finite-element model is unable to represent the high frequency dynamic behavior and the bandwidth of the controller is limited by practical considerations. A reduced order model can be constructed by using the modal truncation method, dynamic condensation method, the singular perturbation method and the internal balancing method. The modal truncation method has been effectively used to produce reduced order plant models using both the undamped (free-free) modes and damped modes as basis vectors and is adopted for our research.

The magnetic bearings are represented as a low-order static or dynamic controller, the state-space description of which is given as

$$\begin{aligned}\dot{\mathbf{x}}_c &= \mathbf{A}_c \mathbf{x}_c + \mathbf{B}_c y \\ u &= \mathbf{C}_c \mathbf{x}_c + \mathbf{D}_c y\end{aligned}\quad (2)$$

In general, the order of the controller is chosen a priori to the design process. A lower bound on the controller order required to satisfy the design objectives is presently unavailable and needs further theoretical considerations.

The state-space description of the closed loop system including the plant and the controller states is

$$\begin{aligned}\begin{bmatrix} \dot{\mathbf{x}} \\ \dot{\mathbf{x}}_c \end{bmatrix} &= \begin{bmatrix} \mathbf{A} + \mathbf{B}\mathbf{D}_c\mathbf{C} & \mathbf{B}\mathbf{C}_c \\ \mathbf{B}_c\mathbf{C} & \mathbf{A}_c \end{bmatrix} \begin{bmatrix} \mathbf{x} \\ \mathbf{x}_c \end{bmatrix} \\ &= \left\{ \begin{bmatrix} \mathbf{A} & 0 \\ 0 & 0 \end{bmatrix} + \begin{bmatrix} \mathbf{B} & 0 \\ 0 & \mathbf{I} \end{bmatrix} \begin{bmatrix} \mathbf{D}_c & \mathbf{C}_c \\ \mathbf{B}_c & \mathbf{A}_c \end{bmatrix} \begin{bmatrix} \mathbf{C} & 0 \\ 0 & \mathbf{I} \end{bmatrix} \right\} \begin{bmatrix} \mathbf{x} \\ \mathbf{x}_c \end{bmatrix}\end{aligned}\quad (3)$$

or,

$$\dot{\tilde{\mathbf{x}}} = [\mathbf{A}_0 + \tilde{\mathbf{B}} \mathbf{K} \tilde{\mathbf{C}}] \tilde{\mathbf{x}} = \mathbf{A}_{CL} \tilde{\mathbf{x}}$$

The problem has been converted to a static output feedback form, and the goal is to find the controller \mathbf{K} to satisfy the specified design requirements. For the purpose of optimization, it is prudent to convert $(\mathbf{A}_c, \mathbf{B}_c, \mathbf{C}_c, \mathbf{D}_c)$ to a canonical form that minimizes the number of free parameters. In this paper, we have adopted the controller canonical form, where each controller is represented as

$$\begin{aligned}\mathbf{A}_c &= \begin{bmatrix} 0 & 1 & 0 & \dots & 0 \\ 0 & 0 & 1 & \dots & 0 \\ \vdots & \vdots & \vdots & & \vdots \\ 0 & 0 & 0 & \dots & 1 \\ -\beta_0 & -\beta_1 & -\beta_2 & \dots & -\beta_{n-1} \end{bmatrix} & \mathbf{B}_c &= \begin{bmatrix} 0 \\ 0 \\ \vdots \\ 0 \\ 1 \end{bmatrix} \\ \mathbf{C}_c &= [\alpha_0 \ \alpha_1 \ \alpha_2 \ \dots \ \alpha_{n-1}] & \mathbf{D}_c &= \delta_0\end{aligned}\quad (4)$$

and the corresponding transfer function is

$$\begin{aligned}G(s) &= \mathbf{C}_c (s\mathbf{I} - \mathbf{A}_c)^{-1} \mathbf{B}_c + \mathbf{D}_c \\ &= \frac{\alpha_{n-1} s^{n-1} + \alpha_{n-2} s^{n-2} + \dots + \alpha_1 s + \alpha_0}{s^n + \beta_{n-1} s^{n-1} + \beta_{n-2} s^{n-2} + \dots + \beta_1 s + \beta_0} + \delta_0\end{aligned}\quad (5)$$

The problem of finding the controller matrix K is now translated into finding the vector of design parameters

$$z = [\alpha_{n-1} \dots \alpha_1 \alpha_0 \beta_{n-1} \dots \beta_1 \beta_0 \delta_0]$$

for each controller, which satisfies the the closed-loop design criteria.

The controller canonical form may not be the best suited for representing the transfer function, since it leads to numerical ill-conditioning of the augmented system matrix (A_{CL}). A diagonal or Jordan canonical form with real 2×2 block representations of the complex eigenvalue pairs may be a more suitable alternative.

One of the main issues of controller design is the specification of the objective function for minimization. Selection of an appropriate objective function based on stability of the closed-loop system is a primary aspect of this paper. General trend in control system design has been a minimization of the quadratic performance measure (LQR problem) based on weighted state and control cost. However, such an objective function does not give a direct handle on the closed-loop eigenvalue locations and the stability of the system.

To overcome this limitation, we present performance measures and constraints defined in terms of the eigensolution of the closed-loop system. The performance index should ideally measure a weighted sum of the stability margins of the individual eigenvalues. This leads to the formulation of a nonlinear optimization problem and the feedback parameters will be obtained by numerical search over the parameter space.

For rotor systems, stability is often measured in terms of the logarithmic decrement of the damped eigenvalues defined as $\delta_i = -\frac{2\pi p_i}{\omega_i}$ where p_i , ω_i are the real and imaginary parts of the i th damped mode. For most designs of rotor systems, it may suffice to have a minimum log decrement δ_L for modes below a certain lower cut-off frequency ω_L , and another value of log decrement δ_U for modes above another upper cut-off frequency ω_U , and a minimum $\delta_B(\omega_i)$ for modes in between. Also, it may be prescribed that no damped eigenvalue may be within a specified envelope around the operating speed of the machine (typically 10% above and below the running speed). These requirements translate into moving the closed-loop eigenvalues into an *acceptable region* of the complex plane. Attention is focused upon the eigenvalues that are the farthest outside the acceptable region and control effort is spent trying to bring them into the acceptable region [ref. 13]. Mathematically, the objective can be formulated as the minimization of an Acceptability Function A , which is only required to be continuous and differentiable (almost everywhere) and have a value zero in the acceptable region and positive everywhere else.

$$\min A(z)$$

subject to the constraints

$$g_j(z) \leq 0 \quad (6)$$

where z = vector of design parameters

The Acceptability Function is *not* a performance index. It merely indicates if a solution is acceptable or not, and can be chosen at will by the designer to facilitate the minimization. Controller design will proceed based on a numerical search in the design parameter space, and a reduction in the value of A will occur at every iteration unless a local minimum of A is reached. Thus, unless this occurs first, A will be eventually reduced to zero, yielding an acceptable

solution to the problem. Convergence to a local (non-zero) minimum of A would call for restarting the search from a new initial guess, or relax the constraints, or even a change of the acceptability function to get out of the local minimum. Repeated failure to reduce A to zero will indicate the absence of an acceptable solution for the designer specified values.

The design problem requires the satisfaction of a set of specifications. Often, finding an acceptable solution considering all the specifications simultaneously as constraints may become too costly from a computational point of view. This led to the idea of solving the design problem as a sequence of constrained minimization phases [ref. 14]. The order in which these phases occur in the sequence depend on the designer, though the 'harder' or more important constraints are put in as the initial phases. For our case, the optimization proceeds in four phases, with each phase consisting of a constrained (or unconstrained) minimization problem.

Phase I – Satisfaction of stability requirements

$$p_i(z) = \text{Re}\lambda_i(z) \leq 0 \quad \text{where } \lambda_i = \text{ith eigenvalue}$$

The optimization problem is

$$\min \left\{ \sum_{i=1}^m \max [0, p_i(z)] \right\} \quad (7)$$

subject to no constraints

Phase II – Satisfaction of lower and upper bounds on the design parameters

$$z_{j\text{low}} \leq z_j \leq z_{j\text{up}}$$

The optimization problem is

$$\min \left\{ \sum_{j=1}^1 \max [0, (z_{j\text{low}} - z_j), (z_j - z_{j\text{up}})] \right\} \quad (8)$$

subject to $p_i \leq 0$

Stability constraints

Phase III – Satisfaction of acceptability region requirements

$$\delta_i(z) \geq \delta_{i\text{spec}}$$

The optimization problem is

$$\min \left\{ \sum_{i=1}^m \max [0, \delta_{i\text{spec}} - \delta_i] \right\} \quad (9)$$

subject to $p_i \leq 0$

Stability constraints

$$z_{j\text{low}} \leq z_j \leq z_{j\text{up}}$$

Design parameter constraints

Phase IV – Satisfaction of operating speed requirements

$$\begin{aligned} \omega_i &\geq \alpha_U \Omega & \text{where } \omega_i &= i^{\text{th}} \text{ damped frequency} \\ \omega_i &\geq \alpha_L \Omega & \Omega &= \text{operating speed} \\ & & \alpha_U, \alpha_L &= \text{ratios defining} \\ & & & \text{the operating speed envelope.} \end{aligned}$$

The optimization problem is

$$\min \left\{ \sum_{i=1}^m \min [(\alpha_U \Omega - \omega_i), (\omega_i - \alpha_L \Omega)] \right\} \quad (10)$$

subject to $p_i \leq 0$

Stability constraints

$$z_{j\text{low}} \leq z_j \leq z_{\text{up}}$$

Design parameter constraints

$$\delta_i(z) \geq \delta_{i\text{spec}}$$

Acceptability region constraints

Constrained numerical search schemes can be used to minimize the objective/acceptability function within each stage. Sequential unconstrained minimization techniques (SUMT) using penalty function, the method of feasible directions, or the generalized reduced gradient method may be used [ref. 15, 16]. We have adopted the method of feasible directions as our numerical search strategy, which starts from a feasible point and proceeds by iteratively searching along feasible directions. If no constraints are violated, different methods like conjugate gradient (Fletcher–Reeves), variable metric (Davidson Fletcher Powell, Broyden Fletcher Goldfarb Shanno) or nongradient (Powell) may be employed within the feasible directions method. The objective and the constraint functions are evaluated at each iteration and within the unidimensional line search for finding a new estimate of the controller parameters, while the gradient information for the objective function and the 'active' or violated constraints is calculated at the end of each iteration.

APPLICATION EXAMPLE

The rotor system chosen to illustrate the design methodology is a uniform symmetric beam 50 inches in length, and 4 inches in diameter. The rotor has been modeled by 11 mass stations, and the order of the system is 44 (each mass station or node is associated with four degrees of freedom, two translational and two rotational). The rotor is supported at two ends by magnetic bearings represented as two low-order decentralized controllers Fig. (1). For this example, the controllers are implemented as second-order strictly proper transfer functions, with the displacement and velocity at the two ends as the outputs and the control forces at the bearing locations as the input. The initial guess for the transfer functions are

$$\begin{aligned} G_1(s) &= \frac{10^{12}s + 10^{14}}{s^2 + 10^6 + 10^{12}} = \frac{10^{12}(s + 100)}{\{s + 10^5(5 + i 8.6603)\}\{s + 10^5(5 - i 8.6603)\}} \\ G_2(s) &= G_1(s) \end{aligned} \quad (11)$$

The initial design parameter vector consists of the numerator and denominator coefficients of the transfer functions.

$$z^0 = [10^{12} \ 10^{14} \ 10^6 \ 10^{12} \ ; \ 10^{12} \ 10^{14} \ 10^6 \ 10^{12}]^T$$

The pole-zero locations and the bode plot of the transfer function for this initial guess of the design parameters is shown in Fig. (2). The corresponding closed loop eigenvalues are listed in Table 1.

The specifications for the design are laid out as follows

- I. Stability of the system must be insured. This implies

$$\operatorname{Re} \lambda_i(z) \leq 0 \quad \text{or,} \quad p_i \leq 0$$

- II. Upper and lower bounds on the coefficients of the transfer function have been fixed. For this case, the requirements are

$$1 \leq z_j \leq 1 \times 10^{30}$$

- III. The acceptability region for the logarithmic decrement δ has been established

A minimum log dec $\delta_L = 1.5$ for modes below a lower cut-off frequency

$$\omega_L = 800 \text{ rad/sec.}$$

A minimum log dec $\delta_U = 0.01$ for modes above an upper cut-off frequency

$$\omega_U = 30,000 \text{ rad/sec.}$$

A minimum $\delta_B(\omega_i)$ given by a straight line interpolation between δ_L and δ_U for modes with frequency $\omega_L \leq \omega_i \leq \omega_U$.

- IV. No avoidance of operating speed envelope has been requested.

The vector of design parameters is subjected to the optimization procedure as described in the previous section. A variable metric method (BFGS) is adopted, and the optimization terminated after 11 iterations, yielding the final design vector.

$$z^* = [1.266 \times 10^{13} \ 1.76877 \times 10^{13} \ 2.3968 \times 10^6 \ 4.9862 \times 10^{10} \ ; \ 1.266 \times 10^{13} \ 1.76877 \times 10^{13} \ 2.3968 \times 10^6 \ 4.9862 \times 10^{10}]^T$$

Translated into the transfer function form, the resultant controllers are

$$G_1(s) = \frac{1.266 \times 10^{13} s + 1.76877 \times 10^{13}}{s^2 + 2.3968 \times 10^6 s + 4.9862 \times 10^{10}} = \frac{1.266 \times 10^{13} (s+1.3971)}{(s+2.3758 \times 10^6)(s+0.0210 \times 10^6)}$$

$$G_2(s) = G_1(s) \tag{12}$$

It is to be noted that the symmetry is retained though it was not imposed explicitly during the optimization. The pole-zero locations and the bode plot of the transfer function for the resultant decentralized controller are shown in Fig. (3). Even though the structure of the bode

TABLE 1

PHASE III Minimization of Acceptability Region Violation With Stability and Box Constraints

EIGEN- VALUE NO.	REAL PART (1/SEC)	IMAG PART (RAD/S)	LOG DECREMENT	ACCEPTABILITY REQUIREMENT	DIFFERENCE
1	-2.1705	20.6084	.6617	2.0000	1.3383
2	-6.3899	35.4201	1.1335	2.0000	.8665
3	-8.1298	1757.6281	.0291	1.9347	1.9057
4	-7.3796	4747.3243	.0098	1.7310	1.7212
5	-6.3471	9132.3508	.0044	1.4321	1.4278
6	-5.0613	14826.8471	.0021	1.0441	1.0419
7	-3.6631	21760.9279	.0011	.5715	.5704
8	-2.3489	29791.4218	.0005	.0242	.0237
9	-1.2859	38526.9425	.0002	.0100	.0098
10	-.5496	47027.6262	.0001	.0100	.0099
11	-.1330	5 571.5344	.0000	.0100	.0100
12	-499978.2707	866012.8513	3.6275	.0100	.0000
13	-499978.2707	866012.8513	3.6275	.0100	.0000

ACCEPTABILITY MINIMIZATION FN. = 8.92519436

TABLE 2

PHASE III Minimization of Acceptability Region Violation with Stability and Box Constraints

EIGEN- VALUE NO.	REAL PART (1/SEC)	IMAG PART (RAD/S)	LOG DECREMENT	ACCEPTABILITY REQUIREMENT	DIFFERENCE
1	-1.3946	.0000			
2	-1.4032	.0000			
3	-244.3605	789.4629	1.9448	2.0000	.0552
4	-986.1444	3383.5133	1.8313	1.8239	.0000
5	-1991.3497	8470.3625	1.4772	1.4773	.0001
6	-7441.7080	7350.6089	6.3611	1.5536	.0000
7	-7789.6355	7302.0838	6.7027	1.5569	.0000
8	-1370.6901	15194.6896	.5668	1.0190	.4522
9	-667.8307	22222.5295	.1888	.5400	.3512
10	-270.1718	30097.9415	.0564	.0100	.0000
11	-93.3636	38678.1632	.0152	.0100	.0000
12	-26.8946	47084.2560	.0036	.0100	.0064
13	-4.9641	53583.9048	.0006	.0100	.0094
14	-2375944.7970	.0000			
15	-2375986.9465	.0000			

ACCEPTABILITY MINIMIZATION FN. = .87453036

plots remains similar (essentially a PD type structure for the dynamic range of the plant), some loop shaping has occurred leading to an improved design. The corresponding closed-loop eigenvalues are listed in Table 2. The results indicate an appreciable improvement in meeting the specifications over the initial guess, though all the specifications have not been met fully.

A design oriented user interface is extremely important for engineering design optimizations like these, and is currently under development. Ideally, the information at the end of each iteration process should be available graphically to the user, and control must be transferred to the user to enable him/her to change various program variables. Fig. (4) shows the graphical display at the beginning of the design process, for the initial guess of the design vector. The bottom half of the screen shows the acceptability regions for the closed-loop eigenvalues in terms of logarithmic decrement and the real and imaginary parts of the eigenvalues. The top half displays the upper and lower bounds on the design parameters and their values at the initial guess. The corresponding display at the end of the optimization process is shown in Fig. (5), clearly displaying the results of the particular optimization run.

CONCLUSIONS

A method has been presented for the design of low-order decentralized controllers for rotor systems by parameter optimization. The controller has been represented in terms of a control canonical form, to reduce the number of free parameters or design variables. Instead of minimizing a performance index, the method emphasizes satisfying a set of specifications laid down by the designer through a sequence of constrained minimization problems. The proposed methodology has been illustrated by means of an example, and a graphical user interface is currently being developed. Although the method shares the problems of other parameter optimization techniques such as providing a good initial guess and not guaranteeing a solution if one exists, the reduced complexity and flexibility of the controller structure and the ability to handle different design constraints directly make it a very viable alternative to other design methods.

ACKNOWLEDGEMENT

This work was supported in part by the Center for Magnetic Bearings and the Rotating Machinery and Control Laboratory, University of Virginia.

REFERENCES

1. Kirk, R.G. and Hibner, D.H., "A Note on the Blade Loss Dynamics of Rotor-Bearing Systems," *Journal of Engineering for Industry*, Trans. ASME, Vol. 98, 1975, pp. 497-504.
2. Maslen, E.H., "Magnetic Bearing Synthesis for Rotating Machinery," Ph.D. Dissertation, University of Virginia, January 1991.
3. Palazzolo, A.B., et al., "Active Control of Transient Rotordynamic Vibration by Optimal Control Methods," *Journal of Engr. for Gas Turbines and Power*, Trans. ASME, Vol. 111, 1989, pp. 264-270.
4. Kramer, F.S. and Calise, A.J., "Fixed-Order Dynamic Compensation for Multivariable Linear Systems," *J. of Guidance and Control*, Vol. 11, No. 1, 1988, pp. 80-85.
5. Tanaka, N. and Kikushima, Y., "Optimal Design of Active Vibration Isolation Systems," *J. of Vibration, Acoustics, Stress, and Reliability in Design*, Trans. ASME, Vol. 110, 1988, pp. 42-48.
6. Larssonneur, R., "Design and Control of Active Magnetic Bearing Systems for High Speed Rotation," Thesis ETH, Swiss Federal Institute of Technology, Zurich, 1990.
7. Keel, L.H. and Bhattacharya, S.P., "State-Space Design of Low-Order Stabilizers," *IEEE Trans. on Automatic Control*, Vol. 35, No. 2, February 1990.
8. Bleuler, H. and Schweitzer, G., "Dynamics of a Magnetically Suspended Rotor with Decentralized Control," presented at the First IASTED International Symposium on Applied Control and Identification, Copenhagen, Denmark, June 1983.
9. Davison, E.J., "The Robust Decentralized Control of a General Servomechanism Problem," *IEEE Trans. on Automatic Control*, Vol. AC-21, 1976, pp. 14-24.
10. Davison, E.J. and Ferguson, I.J., "The Design of Controllers for the Multivariable Robust Servomechanism Problem Using Parameter Optimization Methods," *IEEE Trans. on Automatic Control*, Vol. AC-26, No. 1, 1981, pp. 93-110.
11. Wenk, C.J. and Knapp, C.H., "Parameter Optimization in Linear Systems with Arbitrarily Constrained Controller Structure," *IEEE Trans. on Automatic Control*, Vol. AC-25, No. 3, 1980, pp. 496-500.
12. Geromel, J.C. and Bernussou, J., "Optimal Decentralized Control of Dynamic Systems," *Automatica*, Vol. 18, No. 5, 1982, pp. 545-557.
13. Sirisena, H.R. and Choi, S.S., "Pole placement in Prescribed Regions of the Complex Plane Using Output Feedback," *IEEE Transactions on Automatic Control*, Vol. 20, 1975, pp. 810-812.
14. Nye, W.T. and Tits, A.L., "An Application-Oriented, Optimization-Based Methodology for Interactive Design of Engineering Systems," *Int. J. Control*, 1986, Vol. 43, No. 6, pp. 1693-1721.

15. Vanderplaats, G.N., Numerical Optimization Techniques for Engineering Design, McGraw Hill, 1984.
16. Tits, A.L., Nye, W.T. and Sangiovanni-Vincentelli, A.L., "Enhanced Methods of Feasible Directions for Engineering Design Problems," J. Optimiz. Theory Applic., Vol. 5, No. 3, December 1986, pp. 475-501.

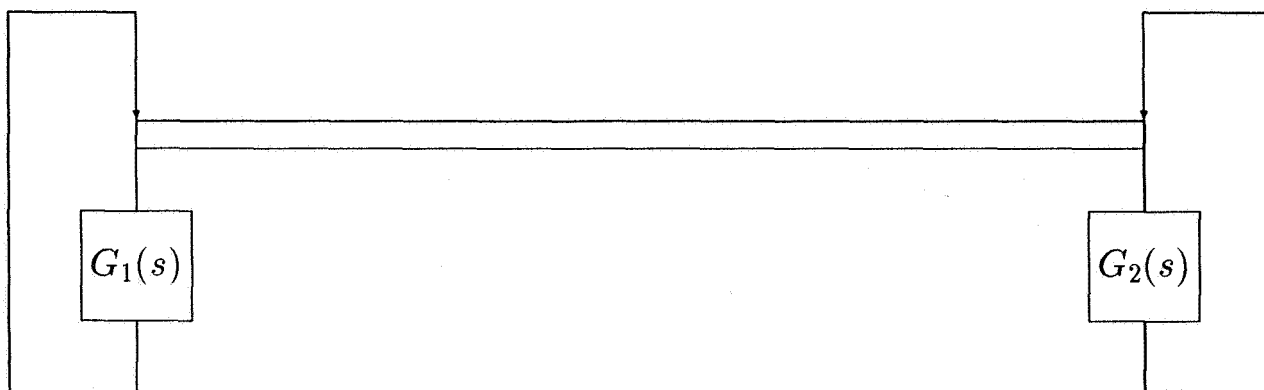


Fig. 1. Rotor supported on two magnetic bearings (low-order decentralized controllers)

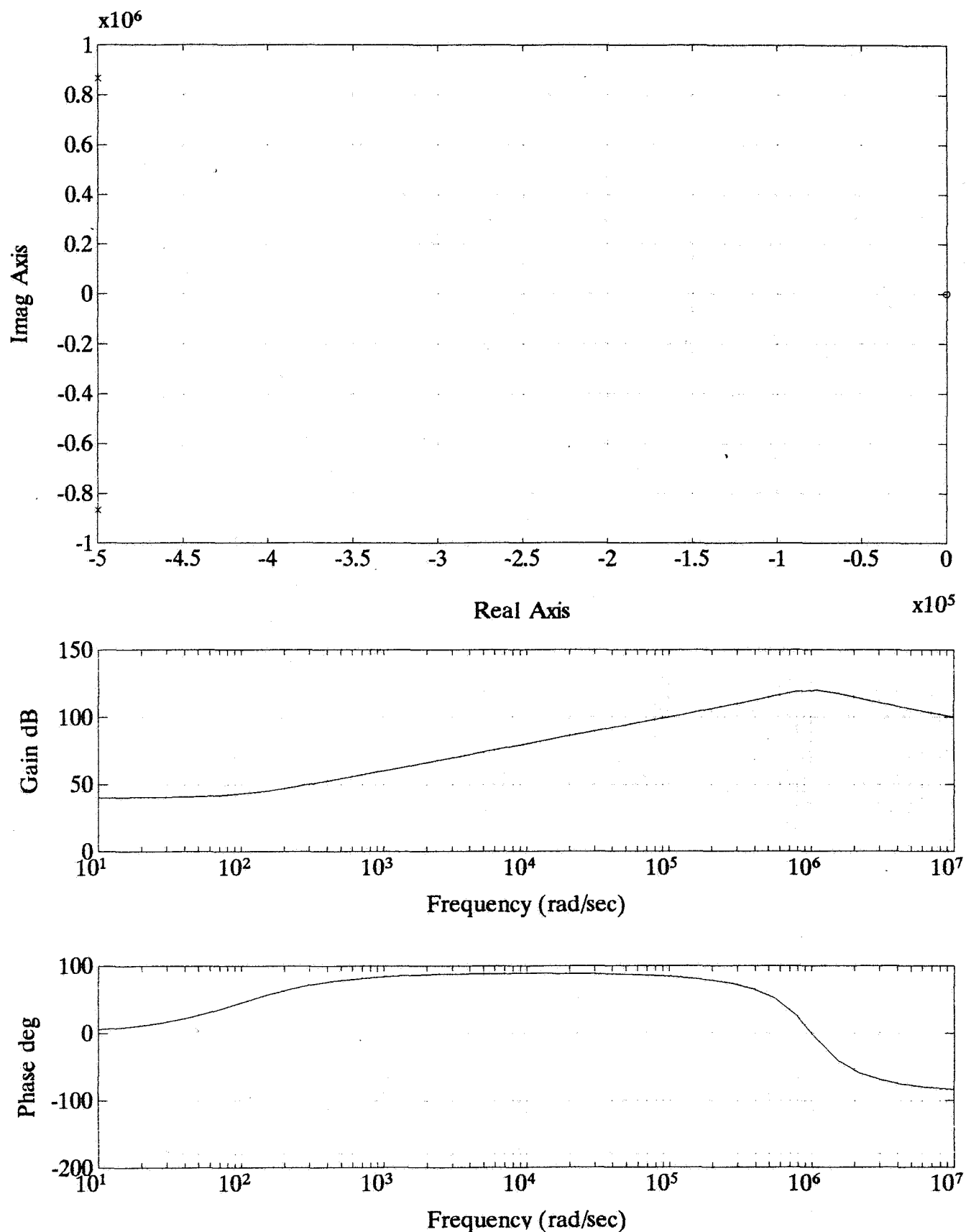


Fig. 2. Pole-zero locations and bode plot of the controller transfer function for initial guess design.

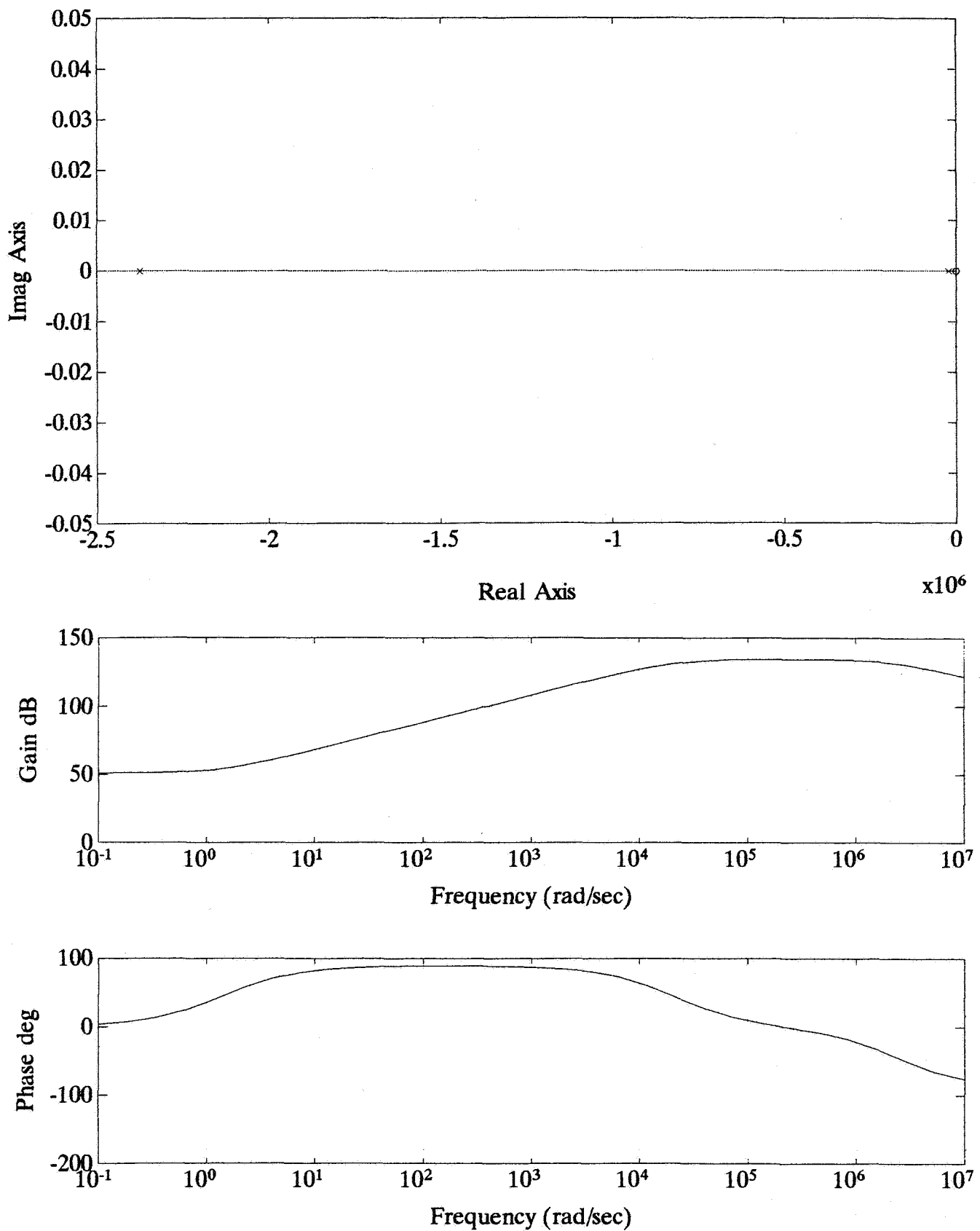


Fig. 3. Pole-zero locations and bode plot of the controller transfer function for optimized design.

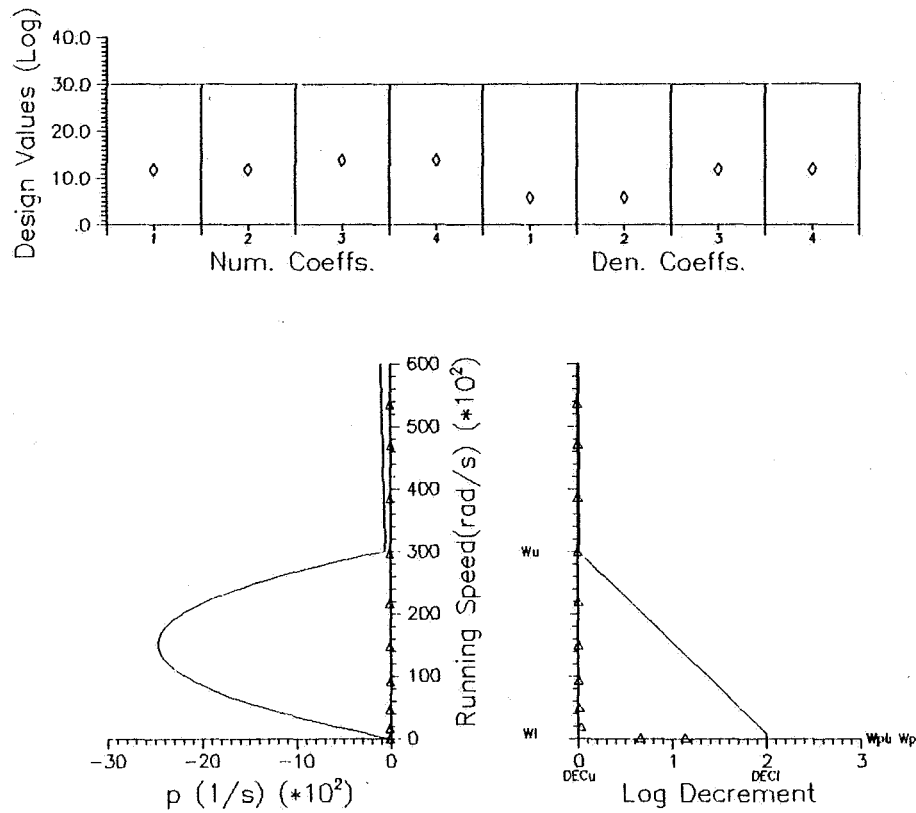


Fig. 4.

Graphical display of design specifications, closed-loop eigenvalues and design parameters for initial guess design.

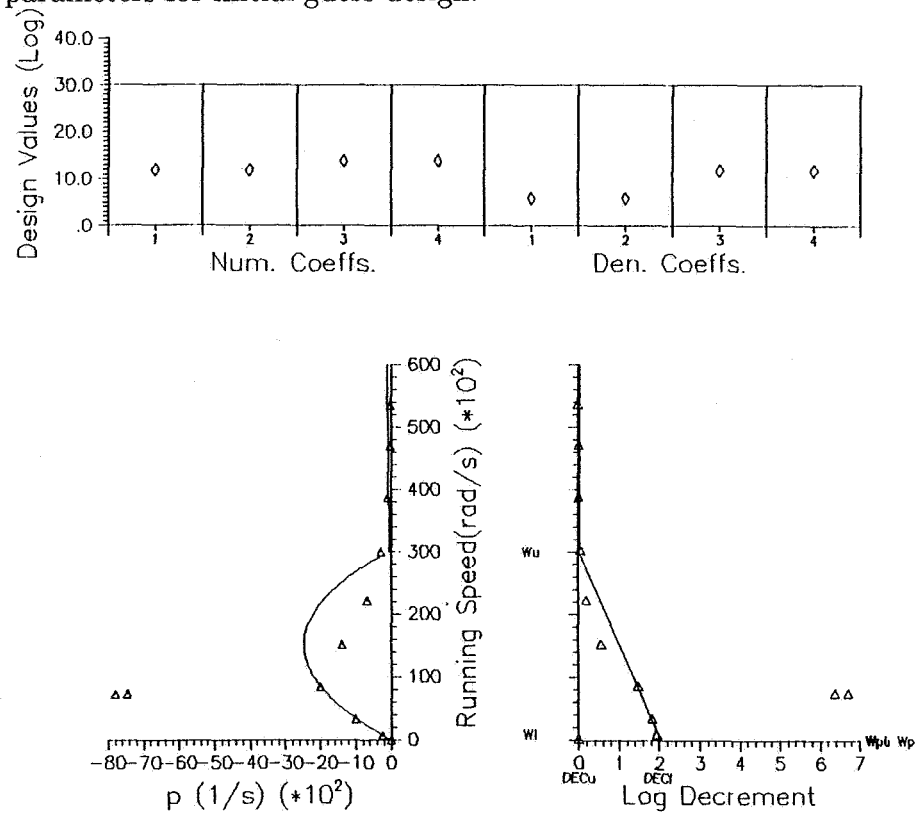


Fig. 5.

Graphical display of design specifications, closed-loop eigenvalues and design parameters for optimized design.

AN EVALUATION OF SOME STRATEGIES FOR VIBRATION CONTROL
OF FLEXIBLE ROTORS

C R Burrows

Professor of Systems Engineering
Head of School of Mechanical Engineering
and
Director of the Fluid Power Centre

University of Bath
United Kingdom

INTRODUCTION

The arguments against using magnetic bearings have remained fairly constant in the last 15 to 20 years, meanwhile a fledgling industry has emerged to confound the critics. The design, development and manufacture of magnetic bearings have reached a stage where their suitability as machine elements has been demonstrated (ref. 1 and ref. 2). In spite of this progress, their use is frequently challenged on the basis of cost or reliability.

The potentially catastrophic effect of bearing failure in a high speed machine due to power failure or electronic component failure is cited as a reason for retaining rolling-element or oil-film bearings. If that argument is successfully countered, excessive cost is the next hurdle which is raised. There is a circular element in this argument. The initial price will not fall until magnetic bearings are in more widespread use; when they are, the spectre of reliability may disappear or be reduced, thereby encouraging more applications and helping to reduce cost. There is already evidence that the reliability of magnetic bearings has achieved an acceptable level in applications when high cost can be tolerated (ref. 3).

This movement towards acceptability would be enhanced if the inherent capability of magnetic bearings as **active** control elements were fully utilised. The capability to 'shape' machine dynamics is not fully exploited when a magnetic bearing or actuator is controlled using only local feedback as is frequently the case.

The central argument in this paper is that the full technological and commercial promise of magnetic bearings will be fulfilled only if attention is focussed on the control problems associated with their use. This fact has stimulated the activity of several groups of academic researchers. Schweitzer has played a leading part in this activity (ref. 4, ref. 5, and ref. 6). The problems of using closed loop control led Burrows and his co-workers to develop an open-loop adaptive strategy (ref. 7, ref. 8 and ref. 9). Other workers have now begun to explore open-loop control strategies (ref. 10 and ref. 11).

Although this paper focuses upon magnetic bearing control as the key issue, it does not deny the importance of striving to improve their force density, safety, and reliability at lower cost. All of these factors are crucial, but secondary to the control issue.

NOMENCLATURE

C, K, M	damping, stiffness and mass matrices respectively
$F(j\omega), F_d(j\omega)$	force vectors (frequency domain)
i	mass station
j	$\sqrt{-1}$
k	integer
p	number of control forces
$\left. \begin{array}{l} \mathbf{g}, \mathbf{g}_d, \mathbf{g}_m, \\ \mathbf{g}_x, \mathbf{g}_y \end{array} \right\}$	displacement vectors (frequency domain)
R, Δ	receptance matrices (frequency domain)
R_x, R_y	receptance vectors
\bar{R}	conjugate of R
U	control vector
U_x, U_y	trial force (frequency domain)
u_x, u_y	forces applied by magnetic actuator
$\delta()$	change in value
ω	frequency
$()^{-1}, ()^T$	matrix inverse and transpose respectively
(\wedge)	estimated value

BEARING OR ACTUATOR

In rotating machines various types of bearings can be used to support a rotor. Oil-film bearings provide some measure of vibration control as well as supporting the rotor. Magnetic bearings have the potential for providing more flexible vibration control, but their load carrying capacity is not as effective as conventional oil-film journal bearings. (For comparison, a typical bearing load for a magnetic bearing is 100kN/m^2 compared with 4000kN/m^2 for an oil-film bearing). There is clearly a benefit in separating the load carrying capacity from the control function. That was the approach studied by Burrows and Sahinkaya (ref. 7) and by Chan Hew Wai and Morel (ref. 2). Another benefit of this configuration is that the passive bearings provide a degree of vibration isolation or control if the magnetic actuator develops a fault.

This paper will focus on the control of transverse vibration of rotors. However, the open-loop adaptive strategy described later can be applied to reduce the effect of longitudinal vibrations (ref. 12) and the same strategy can be adapted to control active equipment mounts.

BACKGROUND

The degree of vibration control that can be exercised by a bearing is dependent upon its stiffness and damping characteristics, as well as the location of the bearings. A bearing located at a node can exercise no control. In a magnetic bearing the stiffness and damping coefficients can be varied by the use of position and velocity signals fed to the control amplifier. The bearing or actuator can be used in an open-loop or closed-loop configuration.

The characteristics of a magnetic bearing for the active control of rotor vibrations were examined by Schweitzer and Lange (ref.13) who derived a multivariable representation for these elements relating the output control force vector to the input vector which can be regarded as current or voltage. The objective is to control the force to counteract the disturbing forces acting on the rotor, for example, fluid forces, internal shaft friction or rotor out of balance. Some force terms cause instability, thus the control strategy must be capable of stabilising the rotor.

The simplest case dynamically is that of a rigid rotor. Bleuler and Schweitzer (ref. 6) described the use of two magnetic bearings to support a rigid rotor. Their scheme required the measurement, or estimation, of eight state variables and hardware to provide 32 feedback coefficients. That approach, if applied to a flexible rotor in which each mass station would be represented by eight state variables (four if only synchronous response is considered) is clearly prohibitive, thus Salm and Schweitzer (ref.5) examined the use of reduced-order models in the design of closed-loop algorithms for vibration control. They showed that unmodelled modes may lead to rotor instability, which can be avoided if the sensors and bearings are located at the same rotor station. This has a simple physical interpretation. The use of local negative feedback of position and velocity to control a magnetic bearing is **ideally** equivalent to replacing the device with **controllable passive** springs and dampers. This approach has been used in a number of commercial applications due to its simplicity and reliability, but it is conceptually unsatisfactory because the full capability of the magnetic device as an active control element is thereby sacrificed.

CONTROL-INDUCED INSTABILITY

The use of local feedback, though conceptually simple and in the **ideal** case inherently stable, may in practice lead to instability owing to the phase lag associated with sensors, signal processing and magnetic circuits. Bradfield et al (ref.14) described experiments on a supercritical shaft carried in rolling element bearings with a magnetic actuator sited in mid-span. They showed that the system could become unstable even when the electro-magnetic actuator was used to apply **nominally** pure damping forces.

The early work of Nyquist in studying closed-loop control systems highlighted the destabilising effect of phase-lag in a feedback loop. Thus the use of notch filters which have featured in some proposals to reduce synchronous vibrations (ref. 15) may cause instability due to phase lag. In a study of active mounts to isolate rotor induced vibration from a helicopter fuselage. Passalidis (ref.16) showed the inherent limitations of using a notch filter.

FEEDBACK CONTROL

Lim (ref.17) studied a rotor-bearing configuration similar to that used by Bradfield et al. Unlike them he did not incorporate a microprocessor in the feedback loop thereby reducing the phase lag in the feedback path. Lim used analogue feedback measurements of the rotor's transverse position and velocity. He employed a microprocessor outside these loops to vary the position and velocity gains to minimise a performance index at each rotor speed.

Lim did not report any cases of rotor instability. However, care must be taken even when adopting this approach because of the noise amplification caused by differentiation. In another project one of the author's students successfully (but inadvertently) measured shaft roughness. The signal, when differentiated, led to unexpected vibration of the rotor and swift operation of the panic button.

Details of Lim's rig are shown in Figure 1. The effectiveness of his approach is demonstrated in Figure 2. Although the rig was a small bench-top unit, Lim's experiments were used to explore the relative merits of closed-loop vibration control with adaptive open-loop control using the algorithm developed by Burrows and Sahinkaya (ref. 7 and ref. 9).

A typical result from station 10 is shown in Figure 2. The excellent fit between the simulated and experimental closed-loop responses was made possible by implementing a frequency-domain algorithm (ref. 18) to estimate system parameter values. The reduction in vibration amplitude using the open-loop algorithm is noticeable. Even more encouraging results were obtained in a parallel investigation involving a 100 mm diameter mild steel shaft of nominal length 2358 mm supporting two 90 mm thick, 406 mm diameter overhung steel discs carried in oil-film journal bearings. The rig has been described elsewhere (ref. 8). The rotor is shown in Figure 3 which also defines the mass stations used. In the experiments, a mid-span electromagnetic actuator was used to control vibration using full active control as outlined later. Chan Hew Wai and Morel (ref. 2) studied a similar arrangement but used only local velocity feedback to damp out shaft vibrations.

OPEN-LOOP ADAPTIVE CONTROL

In their original paper Burrows and Sahinkaya (ref. 7) developed a computationally fast and efficient least-squares algorithm to minimise the vibration of any general rotor-bearing system by the **application of external control forces**. This open-loop adaptive strategy avoids the possibility of instability associated with closed-loop structures for vibration control. However, the use of oil-film bearings introduces the possibility of bearing-induced instability associated with oil-whirl. Sahinkaya and Burrows (ref. 19) have shown that the dual task of controlling the stability threshold and the synchronous response can be achieved by a single magnetic actuator.

In the original formulation, estimation of the control force was dependent upon knowledge of the system parameters and measurement of the unbalance response. These restrictions were removed in a later paper (ref. 9) which allows the control force vector to be determined on-line without any prior knowledge of system parameters. The **algorithm is self-adaptive** to account for changes in system parameters, for example, the oil-film bearing coefficients or rotor unbalance. The latter feature has led some commentators to describe the algorithm as providing automatic balancing, but it is more versatile than that, hence the preferred title 'open-loop adaptive control of rotor vibration'.

A detailed derivation of the algorithm is given elsewhere (ref. 7 and ref. 9). It can be summarised as follows.

Open-loop adaptive control algorithm

A rotor-bearing system can be modelled as a multimass linear system. The k mass stations used in the cases considered in this paper are shown in Figures 1 and 3. If $\mathbf{Q}(j\omega)$ represents the complex displacement vector at these stations, then the synchronous response is given by

$$\mathbf{Q}(j\omega) = \Delta(j\omega) \mathbf{F}(j\omega) \quad (1)$$

where $\Delta(j\omega)$ is the receptance matrix of order $2k \times 2k$, given by

$$\Delta(j\omega) = (-\mathbf{M}\omega^2 + \mathbf{K} + \mathbf{C}(j\omega))^{-1} \quad (2)$$

where $\mathbf{C}, \mathbf{K}, \mathbf{M}$ are damping, stiffness and mass matrices, and the force vector is of order $2k$.

The force vector consists of components due to the distributed out-of-balance force, fluid flow-force etc denoted by \mathbf{F}_d , and the external force $\mathbf{U}(j\omega)$ applied by the electromagnetic actuator, that is

$$\mathbf{F}(j\omega) = \mathbf{F}_d(j\omega) - \mathbf{U}(j\omega) \quad (3)$$

The control force vector is generated by p control force variables where $1 \leq p \leq 2k$. Thus we can define a receptance matrix $\mathbf{R}(j\omega)$ of order $2k \times p$ which contains the columns of $\Delta(j\omega)$ corresponding to the control force locations.

The steady-state measured response vector $\mathbf{Q}_m(j\omega)$ can be written as

$$\mathbf{Q}_m(j\omega) = \mathbf{Q}_d(j\omega) - \mathbf{R}(j\omega) \mathbf{U}(j\omega) \quad (4)$$

where $\mathbf{Q}_d(j\omega)$ is the response due to forces other than the control force.

If the control force vector is changed by $\delta\mathbf{U}(j\omega)$, then the new steady-state displacement vector is

$$\mathbf{Q}(j\omega) = \mathbf{Q}_m(j\omega) - \mathbf{R}(j\omega) \delta\mathbf{U}(j\omega) \quad (5)$$

The objective is to determine $\delta\mathbf{U}(j\omega)$ to minimize $\mathbf{Q}(j\omega)$. Thus equation (5) is rewritten as

$$\mathbf{Q}_m(j\omega) = \mathbf{R}(j\omega) \delta\mathbf{U}(j\omega) + \mathbf{Q}(j\omega) \quad (6)$$

If the structural parameters are known and $\mathbf{Q}_m(j\omega)$ is measured, equation (6) can be regarded as a linear stochastic equation with the unknown parameters $\delta\mathbf{U}(j\omega)$ and the error term $\mathbf{Q}(j\omega)$.

The estimated change in $U(j\omega)$ to minimize $Q(j\omega)$ as given by a least-squares estimator (ref.18) is

$$\delta \hat{U}(j\omega) = (\bar{R}^T(j\omega)R(j\omega))^{-1} \bar{R}^T(j\omega)Q_m(j\omega) \quad (7)$$

where $\bar{R}(j\omega)$ represents the complex conjugate and T denotes the transpose.

The difficulty of assigning reliable values to the elements of $\bar{R}(j\omega)$, particularly when the stiffness and damping matrices include terms due to oil-film coefficients, can be overcome by estimating the receptance matrix on-line.

If the trial force is applied to the rotor in the x direction at the i th station, the response can be written from equation (5) as

$$Q_x(j\omega) = Q_m(j\omega) - R_x(j\omega) \delta U_x(j\omega) \quad (8)$$

$Q_x(j\omega)$ denotes the measured displacement vector after application of a complex force along the x axis. Vector $Q_m(j\omega)$ is known and $\delta U(j\omega)$ is known, hence $R_x(j\omega)$ can be calculated from equation (8).

A trial force is then applied in the y direction at the i th station to give

$$Q_y(j\omega) = Q_m(j\omega) - R_y(j\omega) \delta U_y(j\omega) \quad (9)$$

This allows $R_y(j\omega)$ to be calculated.

When the process is initiated $U(j\omega) = 0$ and $Q_m(j\omega) = Q_d(j\omega)$

The control algorithm can be summarised as follows.

- (i) Sample displacements and perform a FFT to construct $Q_m(j\omega)$
- (ii) Set $\delta U_x = \begin{bmatrix} u_x \\ 0 \end{bmatrix}$ sample displacements and perform a FFT to construct $Q_x(j\omega)$
- (iii) Estimate $R_x(j\omega)$ from equation (8)
- (iv) Set $\delta U_y = \begin{bmatrix} 0 \\ u_y \end{bmatrix}$ sample displacements and perform a FFT to construct $Q_y(j\omega)$
- (v) Estimate $R_y(j\omega)$ from equation (9)
- (vi) Estimate the optimum force adjustment from equation (7)
- (vii) Calculate statistical data on $\delta \hat{U}$ (goodness of fit and standard deviation) to assess its validity. If not suitable go to (i), if suitable $\delta U = \delta \hat{U}$
- (viii) Monitor speed and displacements. Whenever updating is required go to (i).

It is not feasible to measure the displacement at all of the mass stations, thus $\mathbf{g}(j\omega)$ can be interpreted in terms of the response at the measured station. The selection of measurement sites is critical in terms of the quality of control. This has been discussed by Burrows et al (ref. 8 and ref. 9).

It is important to note that a background program ensures that the synchronous control forces are continuously fed to the magnetic actuator independent of the speed of computation of the control algorithm i.e. the previous value of \mathbf{U} is retained until a change is required. The statistical data obtained from the Least Square estimator is discussed in detail in by Burrows and Sahinkaya (ref. 7).

EXPERIMENTAL RESULTS

A typical result is shown in Figure 4, this demonstrates the effectiveness of the algorithm. For example, the amplitude response at the critical speed is reduced in Figure 4b by a factor of 30. The reduction in vibration achieved by the algorithm depends upon which mass station is considered as shown by comparing Figures 4 and 5 which are for mass station 7 and 12 respectively. It also depends upon where the displacement transducers are sited.

In practice only a limited number of displacement transducers will be available and the choice of site along the rotor is critical. The results in Figures 4 and 5 show the effect of using different measurement sites; where:

$j = 1$ denotes control measurement sites 3 and 12

$j = 2$ denotes control measurement sites 3, 7 and 12

Other locations are considered by Burrows, Sahinkaya and Clements (ref. 9).

CONCLUSIONS

The open-loop adaptive control algorithm development by the author and his co-workers provides an efficient method of controlling the vibration of rotors without the need of a prior knowledge of parameter values. It overcomes the disadvantages normally associated with open-loop control whilst avoiding the problem of instability associated with closed-loop control algorithms.

The algorithm is conceptually satisfying because it utilises the capability of magnetic bearings as fully active vibration control elements rather than limiting them to act as adjustable stiffness and damping elements, as is the case when they are used with local position and velocity feedback.

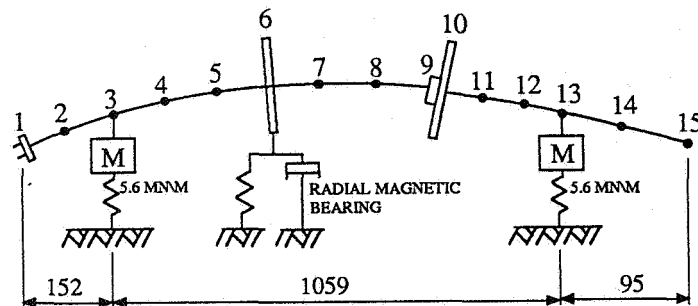
ACKNOWLEDGEMENTS

It is a pleasure to acknowledge the many research students, postdoctoral fellows, colleagues and funding bodies who have contributed to my learning curve in this fascinating field.

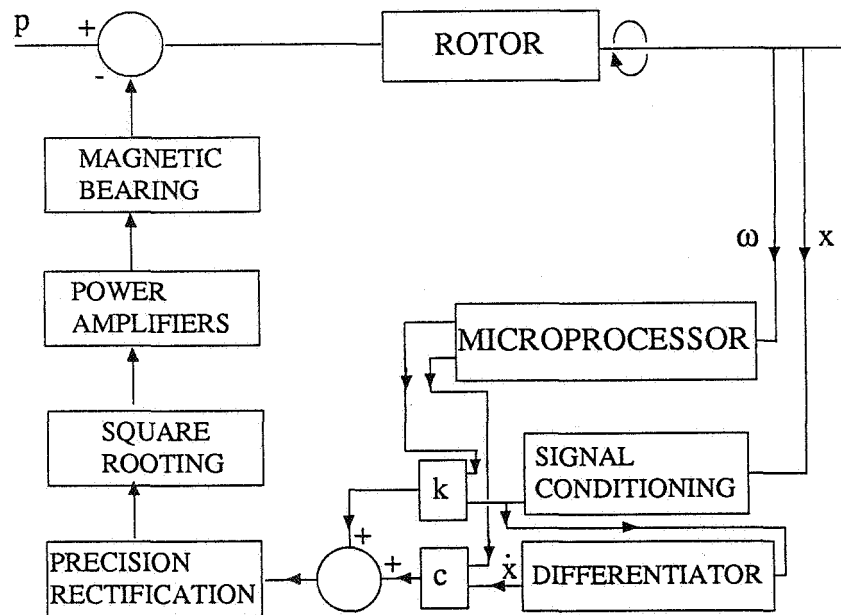
REFERENCES

1. Foster, E., Kulle, V. and Peterson R. The Application of Active Magnetic Bearings to a Natural Gas Pipeline Compressor. ASME paper 86-GT-1, Int. Gas Turbine Conf. and Exhibit., Dusseldorf, West Germany, June 8-12, 1986
2. Chan Hew Wai, C. & Morel, J. Application of an Active Magnetic Bearing for Vibration Control Near Critical Speeds in Large Rotating Machines. ASME Eleventh Biennial Conf. on Mechanical Vibration and Noise, Boston, Massachusetts, pp 151-157, 1987.
3. Heidner, M. and Kabelitz, H.-P. Reliability of Turbomolecular Vacuum Pumps: A Comparison of Rolling Element and Magnetic Bearing Systems. Jnl. Vac. Sci Technol. A8 (3), May/June 1990.
4. Schweitzer, G. Stabilization of Self Excited Rotor Vibrations by an Active Damper. Dynamics of Rotors (ed. F. I. Niordson), pp 472-493, Berlin : Springer-Verlag, 1975.
5. Salm, J. & Schweitzer, G. Modelling and Control of a Flexible Rotor with Magnetic Bearings. IMechE. Third Int. Conf. Vib. in Rotating Machinery, paper no. C277/84, pp 553-561, York, 1984
6. Bleuler, H. & Schweitzer, G. Dynamics of a Magnetically Suspended Rotor with Decentralised Control. IASTED Applied Dynamics and Control Symposium, Copenhagen, 1983.
7. Burrows, C. R. and Sahinkaya, M.N. Vibration Control of Multi-Mode Rotor-Bearing Systems. Proc. R. Soc. Lond. A386, pp 77-94, 1983.
8. Burrows, C.R., Sahinkaya, M.N. and Clements, S. Electromagnetic Control of Oil-Film Supported Rotors Using Sparse Measurements. Am. Soc. Mech. Engrs. Jnl. Vib. Acoustics, Stress and Reliability in Design, 110, pp 293-299, 1988.
9. Burrows, C.R., Sahinkaya, M.N. and Clements, S. Active Vibration Control of Flexible Rotors: An Experimental and Theoretical Study. Proc. R. Soc. Lond. A422, pp123-146, 1989.
10. Nonami, K. and Kawamata, S. Feedforward Control to Unbalance Force Cancellation for Flexible Rotor Systems. Proc. Int. Symp. on Advanced Computers for Dynamics and Design, Tsuchiura, Japan, Sept 6-8, 1989.
11. Higuchi, T., Mizuno, T. and Tsukamoto, M. Digital Control System for Magnetic Bearings with Automatic Balancing. Proc. 2nd Int. Symp. on Magnetic Bearings, Tokyo, Japan, July 12-14, 1990.
12. Darling, J. and Burrows, C.R. The Control of Propeller-Induced Vibrations in Ship Transmission Shafts. Proc. 2nd Int. Symp. on Magnetic Bearings, Tokyo, Japan, July 12-14, 1990.
13. Schweitzer, G. and Lange, R. Characteristics of a Magnetic Rotor Bearing for Active Vibration Control. IMechE Conf. on Vib. in Rotating Machinery, paper no.C239/76, Cambridge, 1976.
14. Bradfield, C.D., Roberts, J.B & Karawirdiran, R. Performance of an Electromagnetic Bearing for the Vibration Control of a Supercritical Shaft. Proc. IMechE 201, pp 201-212, 1987.
15. Haberman, H. and Brunet, M. The Active Magnetic Bearing Enables Optimum Damping of Flexible Rotors. ASME Paper 84-GT-117, 1984.
16. Passalidis, G. Active Control of Vibration of Helicopter Structures. PhD Thesis, University of Strathclyde, 1988.

17. Lim, T.M. The Development of a Simple Magnetic Bearing for Vibration Control. PhD Thesis, University of Strathclyde, 1987.
18. Burrows, C.R. and Sahinkaya, M.N. a: Frequency Domain Estimation of Linearized Oil Film Coefficients. *Jnl. Lubr. Technol.* **104**, pp 210-215, 1982 b: Parameter Estimation of Multi-Mode Rotor-Bearing Systems. *Proc. R. Soc. Lond.* **A379**, pp 367-387, 1982.
19. Sahinkaya, M.N. and Burrows, C.R. Control of Stability and the Synchronous Vibration of a Flexible Rotor Supported on Oil-Film Bearings. *Am. Soc. Mech. Engrs J. Dyn. Syst. Meas. Control* **107**, pp 139-144, 1985.



SHAFT DIAMETER = 15 MM
 DISC DIAMETER = 100 MM
 ROTOR MASS = 3.92 kg
 UNBALANCE MASS = 0.6915×10^{-4} kgm. (station 10)



x : displacement
 k : stiffness coefficient
 c : damping coefficient

FIG. 1 Lim's experimental rig

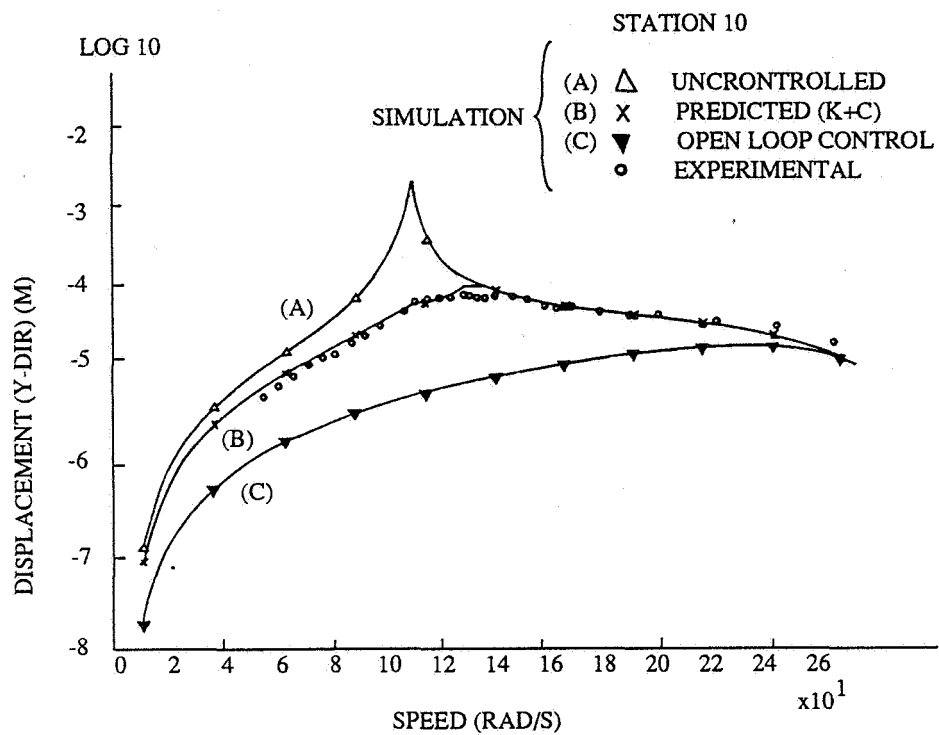


FIG. 2 Comparison of open-loop and closed-loop control (Lim's rig)

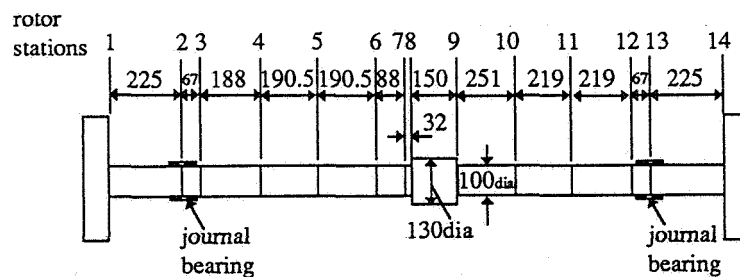


FIG. 3 Experimental rotor mass stations (Burrows, Sahinkaya, Clements)

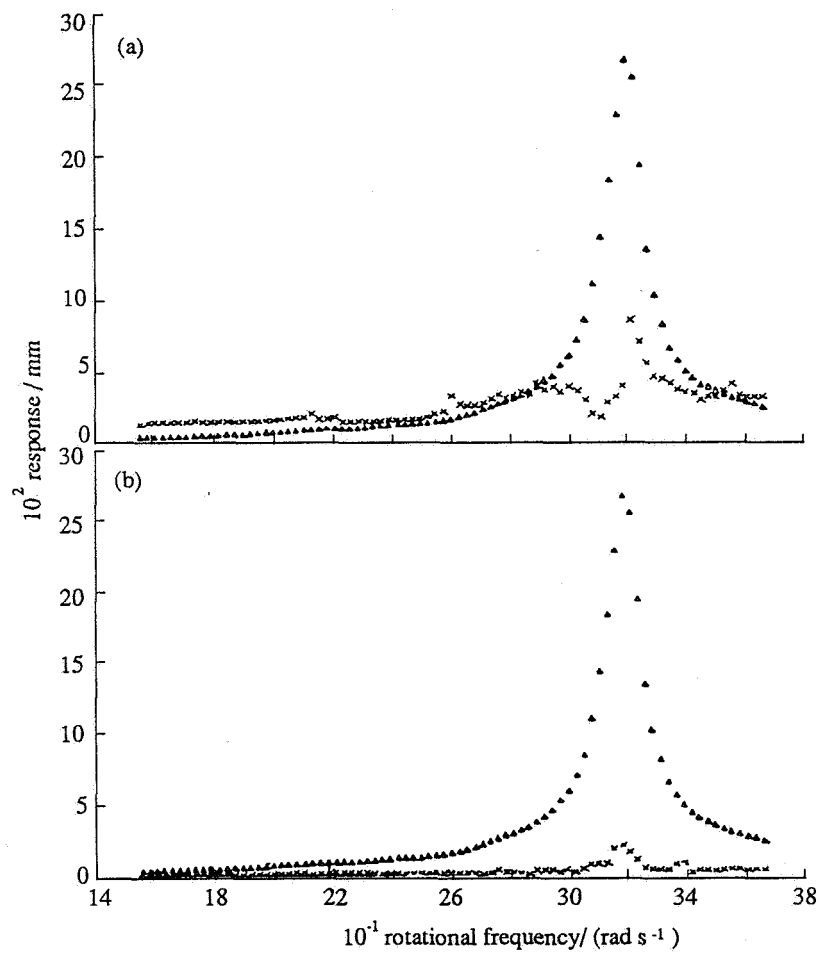


FIG. 4 Controlled and uncontrolled responses at station 7.
 (a) $j = 1$ (b) $j = 2$
 (Δ , uncontrolled; \times , controlled)

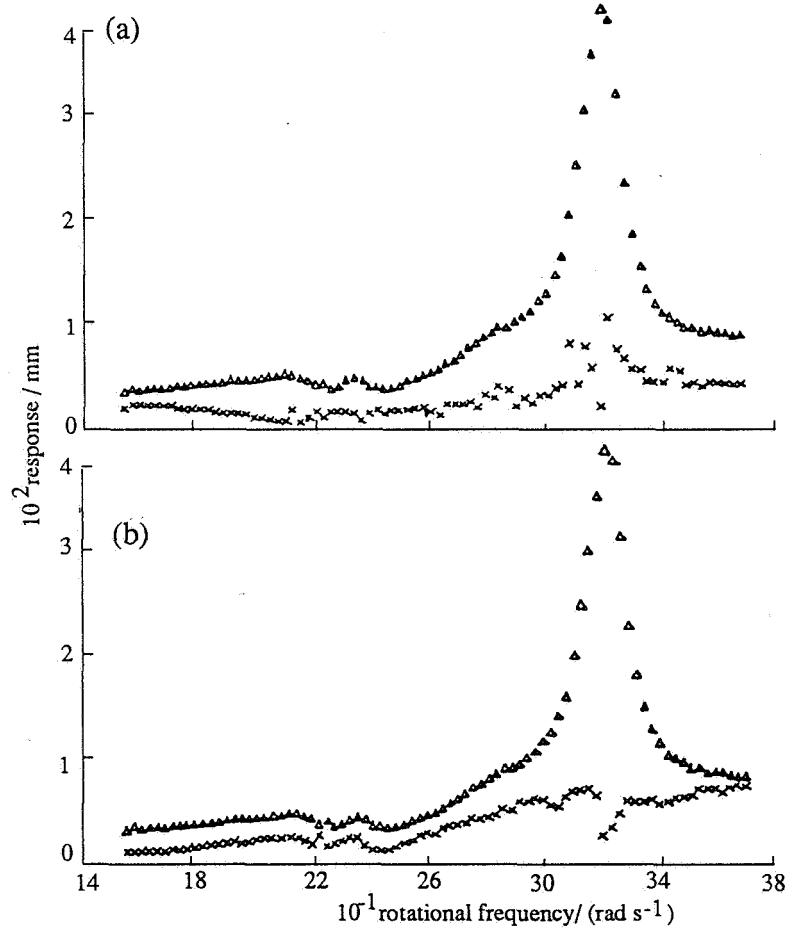


FIG. 5 Controlled and uncontrolled responses at station 12.
 (a) $j = 1$ (b) $j = 2$
 (Δ , uncontrolled; \times , controlled)

Session 13

WIND TUNNEL MAGNETIC SUSPENSION SYSTEMS

Chairman - Robert A. Kilgore
NASA Langley Research Center

N92-27801

PROPULSION SIMULATOR FOR MAGNETICALLY SUSPENDED
WIND TUNNEL MODELS

P.B. Joshi, M.R. Malonson, G.P. Sacco, and C.L. Goldey
Physical Sciences Inc.
Andover, MA

K. Garbutt and M. Goodyer
University of Southampton
England

and

P. Lawing
NASA Langley Research Center
Hampton, VA

PRECEDING PAGE BLANK NOT FILMED

INTRODUCTION

Simulation of propulsion-induced aerodynamic forces and moments, which arise as a result of interactions between propulsive jets and the free stream, is one of the most desired capabilities in magnetic suspension wind tunnels. Such a simulation has always been a difficult task, even in conventional wind tunnels. The main reasons have been the problems of introducing high pressure air into the model, questions regarding proper scaling parameters, construction of models out of metric and non-metric sections, and accurately determining the force/moment contribution to the non-metric section.

Propulsion simulation for a magnetically suspended model presents special practical problems because there can be no physical connection between a compressed air reservoir and the model. Thus, propulsive gases must be generated on-board the model and then exhausted at desired locations on the model, Figure 1. The problem involves defining proper thrust (mass flow rate and velocity) requirements for the propulsive jet(s) and accomplishing gas generation within the volume of the model. Propulsion simulation in its entirety, whether for conventional or magnetically suspended models, involves both engine intake and exhaust jet flows. Only the latter is addressed in the work presented here. Our rationale is that the first step in simulation of propulsion should be to introduce the effects of the exhaust jet and that the complexities of allowing properly matched inlet flows should be deferred to later stages of development.

Under Phase I of an investigation sponsored by NASA LaRC, the feasibility of generating exhaust jets of appropriate characteristics on-board magnetically suspended models was examined. Four concepts of remotely operated propulsion simulators were considered. Three conceptual designs involving conventional technologies such as compressed gas cylinders, liquid monopropellants, and solid propellants were developed. The fourth concept, a laser-assisted thruster, which can potentially simulate both inlet and exhaust flows, was found to require very high power levels (tens of kilowatts). This concept

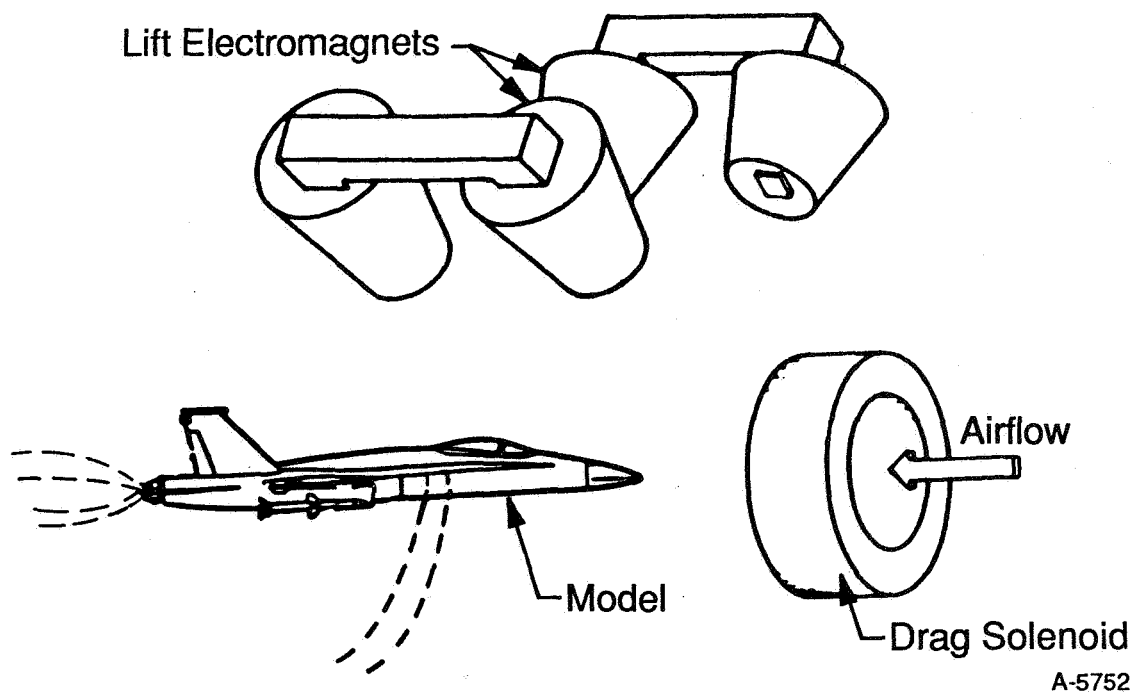


Figure 1. Schematic of Propulsion Simulation on a Magnetically Suspended Model

needs further research. The results of Phase I investigation, including a comparative evaluation of the four concepts, are discussed in Ref. 1.

The objective of current Phase II investigation sponsored by NASA LaRC was to demonstrate the measurement of aerodynamic forces/moments, including the effects of exhaust jets, in MSBS wind tunnels. Two propulsion simulator models were developed, a small-scale and a large-scale unit, both employing compressed, liquified carbon dioxide as propellant. The small-scale unit was designed, fabricated, and statically tested at Physical Sciences Inc. (PSI). It was tested in the 7-in. University of Southampton MSBS tunnel to measure forces/moments with jet on/off. The MSBS hardware and software were modified for this purpose to be compatible with the impulsive thrust forces associated with propulsive jets. The large-scale simulator was designed, fabricated, and statically tested at PSI.

This paper is in two parts. The first part presents design/development and static test data for the small-scale and large-scale simulators. The second part describes the modifications to the University of Southampton MSBS and results of the wind tunnel tests with the small-scale simulator. The paper concludes with recommendations for future developments including applications to conventional aeropropulsive testing.

PART I

PROPULSION SIMULATOR DEVELOPMENT

1. PROPULSION SIMULATOR DESIGN CONSIDERATIONS

Before describing the small-scale simulator, it is appropriate to discuss the design requirements. Since the existing MSBS wind tunnels (Ref. 2) allow the installation of relatively small models, a very limited volume is available for a propulsion device. Further, the magnetic core used for levitation also needs some space within the model, and the restrictions on the size of the propulsion simulator can indeed be significant. The largest operational MSBS wind tunnel in the U.S. at NASA LaRC has a 13-in. diameter test section. Another MSBS facility at University of Southampton, England, which is more versatile in that it has angle-of-attack variation capability, has only a 7-in. wide test section. In this wind tunnel, the model envelope would typically be 6 to 8-in. in length with 1 to 1.5-in. diameter centerbody. In the NASA tunnel, models 18-in. long by 3-in. diameter can be installed.

The design considerations are summarized in Table 1. The implementation of these requirements into the simulator design is discussed in Ref. 1.

The primary objective of the present work was to demonstrate the operation of a thrusting, propulsive model in an MSBS, and to measure the resulting forces/moments. The University of Southampton wind tunnel to be used for testing has a 7-in. octagonal test section. The small test section size and the desire to achieve high angles of attack (~ 45 deg), limits the model size. This limitation, in turn, restricts the number and the size of flow control components (a pressure regulator, an on/off solenoid valve, for example) that can be incorporated into the model. It was decided,

Table 1. General Design Considerations for Propulsion Simulators

• Compactness	Smallest size possible for demonstration in current available MSBS tunnels
• High Density Propellant	Ability to carry the largest propellant mass in a given volume inside the model to maximize run time for a specified mass flow rate
• Relatively Lightweight	To minimize the size of magnetic core within the model and currents in external electromagnets
• Remote or Minimum Interference Activation	If remote activation is not feasible, the disturbance to flow field and magnetic field must be negligibly small
• Thrust Level	Compatible with particular MSBS capability
• Thrust versus Time Characteristics	Compatible with MSBS control system capability. Stable thrust duration must be sufficiently long so that data can be obtained after model becomes steady
• Safe Operation	Propellant material should be non-toxic, non-corrosive, with minimum of particulates

therefore, to design and build two models: a small-scale simulator for demonstration in an MSBS and a large-scale simulator for static testing only. The small-scale model was developed principally to 1) demonstrate generation of an exhaust jet using CO₂ propellant, 2) guide in the design of the large-scale unit, and 3) verify the control and force/moment measurement of a thrust model in the Southampton MSBS. The larger model was developed to 1) generate exhaust jets of desired characteristics; and 2) demonstrate the feasibility of propulsion simulation on larger wind tunnel models representative of practical applications.

The large-scale simulator was designed to generate a jet with pressure ratio, mass flow, and thrust requirements outlined in Ref. 1. This design permits intermittent, on/off operation of the jet. By contrast, the small-scale simulator was designed to be such that the propellant and some components must be replaced after every jet "run". No attempt was made to tailor the jet characteristics to the requirements of Appendix A for the small-scale device.

2. SMALL-SCALE PROPULSION SIMULATOR DESIGN

Figure 2 shows the small-scale simulator design which is a 1-1/8-in. diameter cylinder, 8-in. long, with hemispherical ends. The principal components are a 16g, liquified CO₂ cylinder (manufactured by Sparklet Devices), a cap-piercing hardened pin and squib mechanism (adapted from a design by Special Devices, Inc. (SDI)), battery and electronics assembly housed in the nose, three removable sets of copper spheres, and a nozzle. These components are housed inside a tube, 1/8-in. thick, made from an electromagnetic alloy formulated by Connecticut Metals, Inc. (CMI). The total weight of the simulator is about 600g with approximately 500g of magnetizable materials. The latter includes the material of the CO₂ cylinder and other miscellaneous components such as retainer rings, fasteners, spacers, etc. Figure 3 shows the distribution of the magnetizable mass in the simulator.

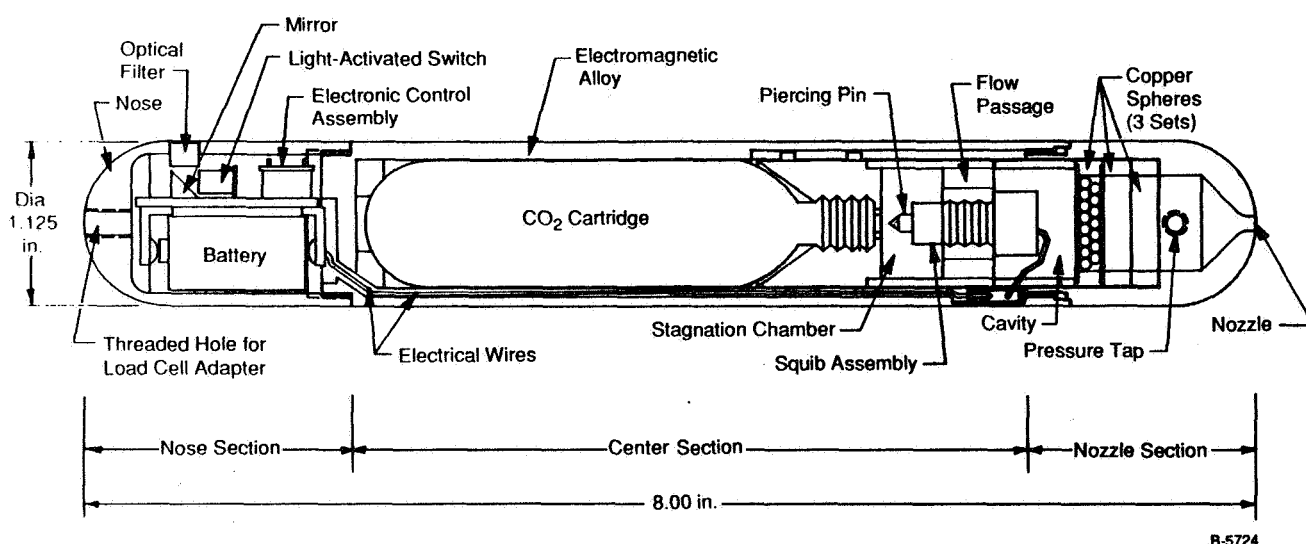


Figure 2. Small-Scale Propulsion Simulator Design

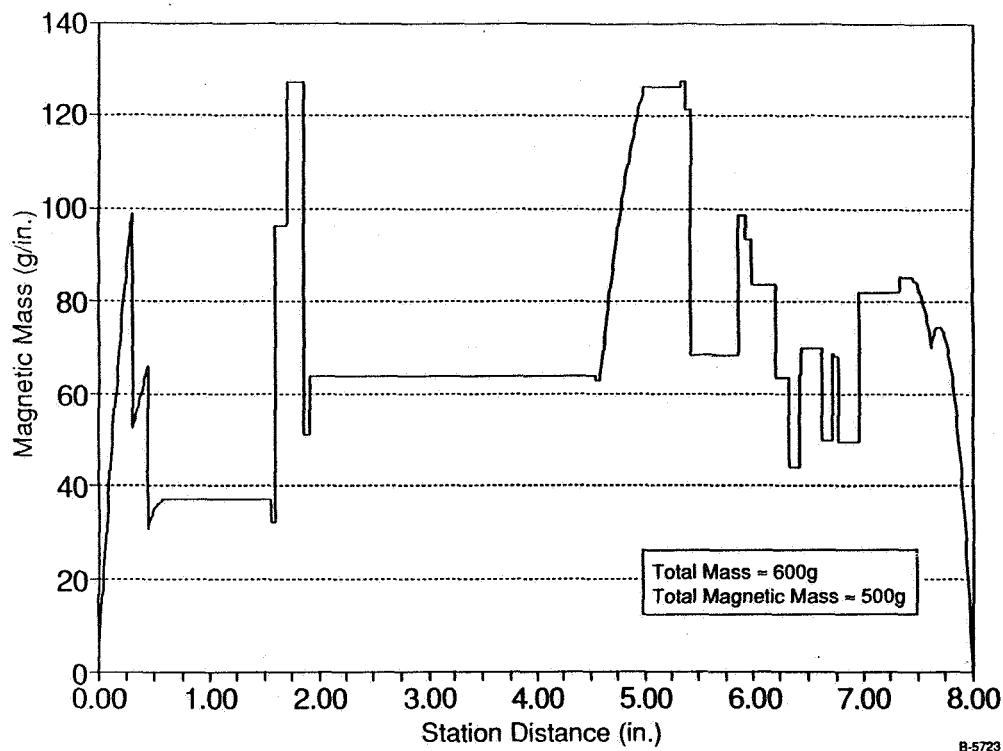


Figure 3. Magnetic Mass Distribution in the Small-Scale Simulator

The simulator consists of three major subassemblies: nose section, center section, and nozzle section. The nose section, which screws onto the center section, contains the battery (Kodak K28A) used as a power source for firing the squib (made by Cartridge Actuated Devices, Inc.) and the electronics assembly. The latter consists of a light-activated switch (EG&G, VTIC1110), a small mirror, and a silicon controlled rectifier, all mounted on a 0.06-in. thick circuit board. The battery is held inside a retaining clamp onto which the circuit board is mounted. An optical filter is embedded in the wall of the nose section. The filter allows HeNe laser wavelength (632.8 nm) to pass to the light activated switch. A pair of 22 AWG wires runs from the circuit board to the squib in the center section.

The center section of the simulator contains the CO₂ cartridge with its threaded neck screwed into a cylinder retainer which is held in place by a squib retainer. The pin-squib mechanism (made by SDI) is screwed into the threaded hole at the center of the squib retainer. The SDI design was modified such that inexpensive squibs made by Cartridge Actuated Devices could be incorporated into it. Had this modification not been done, the complete SDI pin/squib mechanism would have required replacement after each firing, costing about \$150. Our design modification makes it possible to replace the squib only, for approximately \$5 to \$10. Earlier in the program, the "standard" piercing pin (also called "large" pin) in the SDI component was used. It had an internal hollow passage 0.050-in. diameter to draw CO₂ from the cylinder. Two holes, 0.050-in. diameter, in the 0.045-in. thick walls of the standard pin, expel the CO₂ into a stagnation chamber. The gas then flows from the chamber into a cavity surrounding the squib assembly through four oval passages drilled into the squib retainer. Another pin, with smaller outside and inside diameters, and with smaller ports for expelling CO₂, was also used during development. Both pins were case-hardened to ensure reliable penetration of the diaphragm of the CO₂ cylinder. Moreover, hardening also improved the usable life of the firing pin. Two holes (not shown in Figure 2) are drilled into the wall of the center section for measuring pressure in the stagnation chamber and in the cavity upstream of the nozzle section. The two 22 AWG wires

connecting the squib to the electronics in the nose section pass through a lengthwise groove machined in the wall of the center section.

The nozzle section screws onto the back end of the center section of the simulator. It contains three baffle assemblies which can be loaded with copper spheres of 1 or 2 mm diameter. Each assembly consists of a copper housing (a ring as shown in Figure 2) with a copper wire mesh at each end for retaining the spheres. Each assembly can be individually removed and replaced by a ring made of the CMI electromagnetic alloy. The purpose of the three copper plugs was to introduce a drop in total pressure as the CO_2 negotiated a tortuous path, and secondly, to vaporize any fine solid particles of CO_2 which may be present in the flow. As will be discussed later, the copper plugs were not always effective. A convergent passage was drilled into the nozzle with a baseline diameter of 0.098 in. A separate nozzle section with exit diameters of 0.298 in. was also used. Both nozzle sections were tested. The larger nozzle, used on a 1/40-scale model, corresponds to 12-in. full-scale throat diameter. A pressure tap was drilled into the nozzle wall downstream of the copper plugs and upstream of the exit orifice.

The operation of the small-scale simulator consists of shining a HeNe laser beam onto the optical filter in the nose section. The light switch is activated and the SCR then draws approximately 1 amp current from the battery to fire the squib. Explosion of the squib drives the pin (which moves against O-ring friction) into the diaphragm which caps the CO_2 cylinder. Only about 45 psi pressure is needed to rupture the diaphragm and the squib supplies 70 to 150 psi from the gaseous products of explosion. After penetration the pin stays in place due to the friction of the O-ring inside the housing of the SDI squib assembly. CO_2 liquid-gas mixture flows through the center passage in the pin and escapes through the two holes drilled in the walls (Figure 4). Upon passage through the squib retainer (Figure 5), the CO_2 flows through the copper plug(s) into the nozzle chamber and out through the orifice producing a jet.

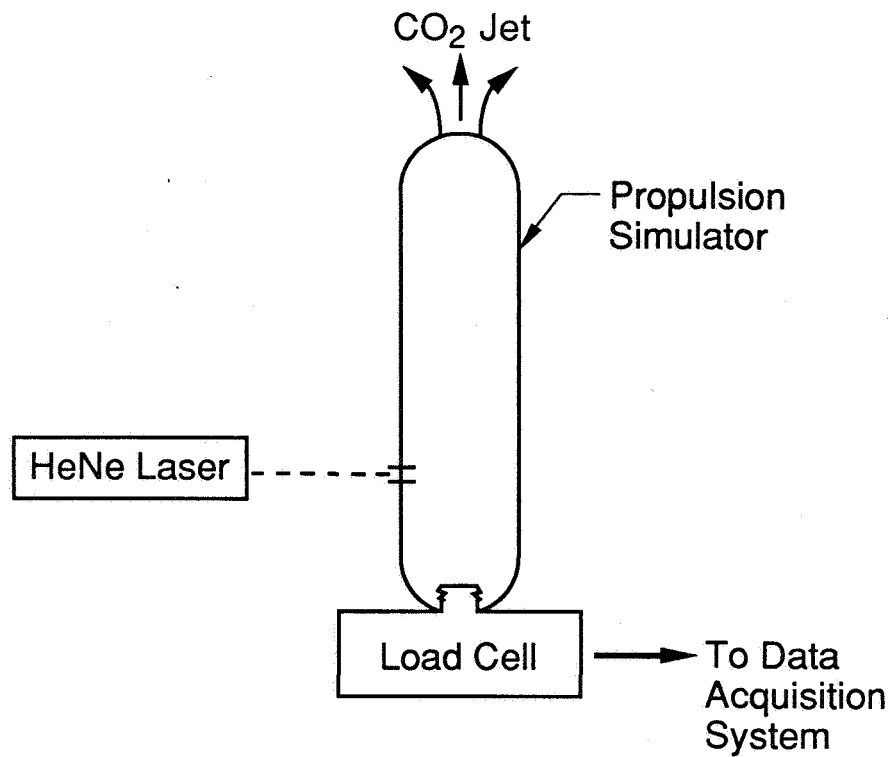
3. RESULTS OF STATIC TESTING OF SMALL-SCALE SIMULATOR

The static tests were designed to yield thrust versus time history and pressure versus time history, the latter at three locations within the simulator. The thrust versus time data are necessary for design of the MSBS control system so that the model stays in place as it reacts to the propulsive jet turning on/off. The pressure data, which are diagnostic in nature, provide important insight into the effectiveness of the copper plug(s) in creating a pressure drop and into the gas dynamic processes within the simulator.

The schematic of the static-test set-up is shown in Figure 4. A load cell manufactured by Sensotec was used to obtain force (i.e., thrust) data. The pressure transducers were supplied by D.J. Industries and located as shown in Figure 4(b). The pressure P_2 and P_1 give a measure of the effectiveness of the copper spheres in creating a pressure drop. The pressures P_2 and P_3 give a measure of the gas dynamic processes and losses due to jet impingement on the cylindrical walls of the simulator. The load cell and transducer signals were sampled at 1 kHz. Visual observations of the jet just outside the nozzle exit plane indicated whether or not mist was present. The presence of mist shows that the copper spheres were not very effective in vaporizing the tiny solid particles formed during the expansion of CO_2 from compressed liquid to vapor.

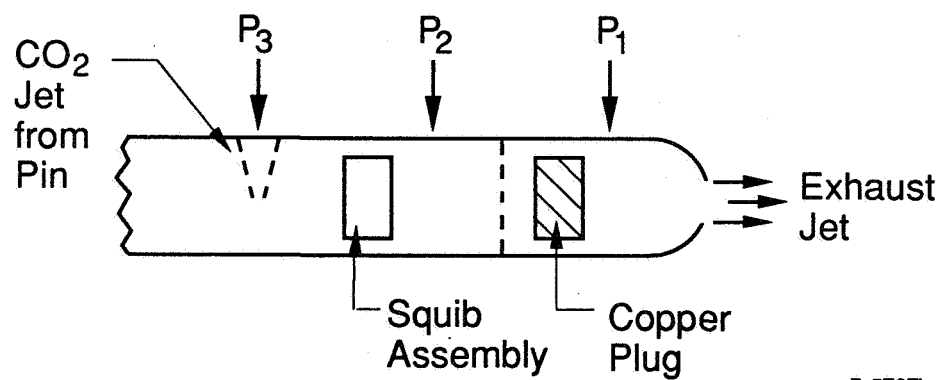
Selected data from the simulator tests are presented in Figures 5 through 8. Each figure contains thrust and pressure versus time history. The three pressures, P_1 , P_2 , and P_3 are given on the same plot. Appendix B contains the small-scale simulator test matrix.

Figure 5 shows thrust and pressure curves for the baseline simulator configuration without any copper plugs. After an initial spike which reaches 4 lbf, the thrust rises to a maximum of about 1.9 lbf in about 0.1s and decreases gradually over the next 1.2s. An average thrust of about 1 lbf over a duration of 0.5s is achieved. The rise in thrust is due to the increase of pressure as the CO_2 fills up the simulator volume. The fall in thrust thereafter is directly due to the dropping stagnation pressure inside the simulator as the CO_2



B-5727a

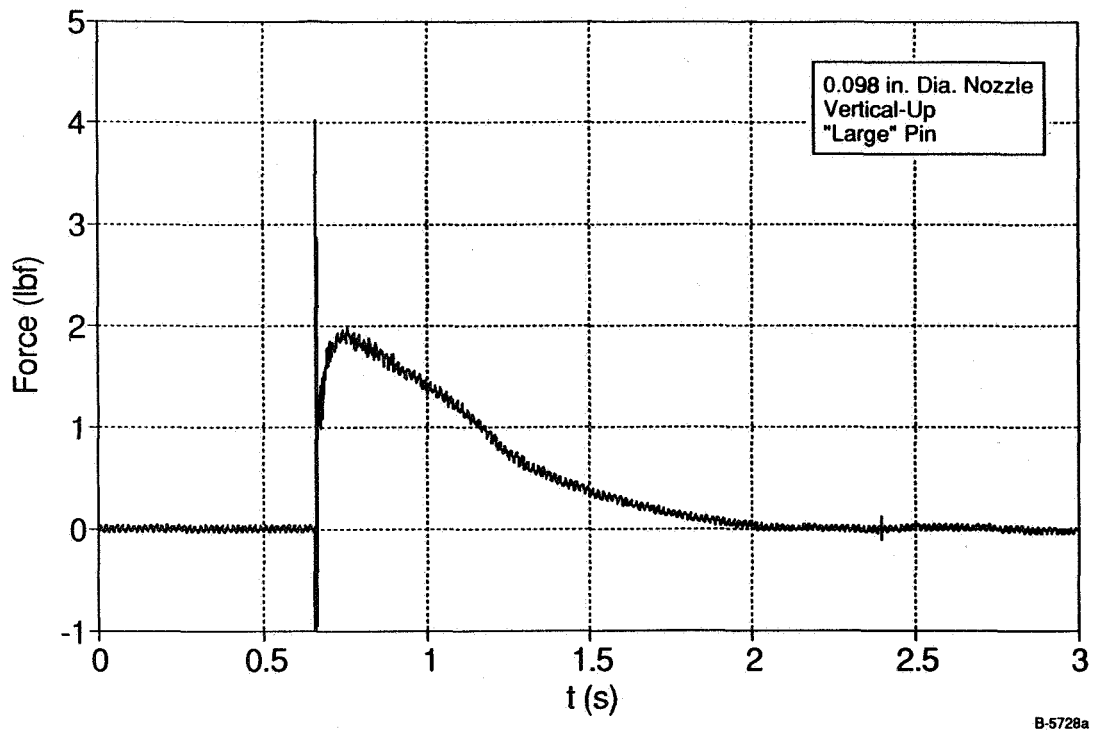
(a) Thrust Measurements



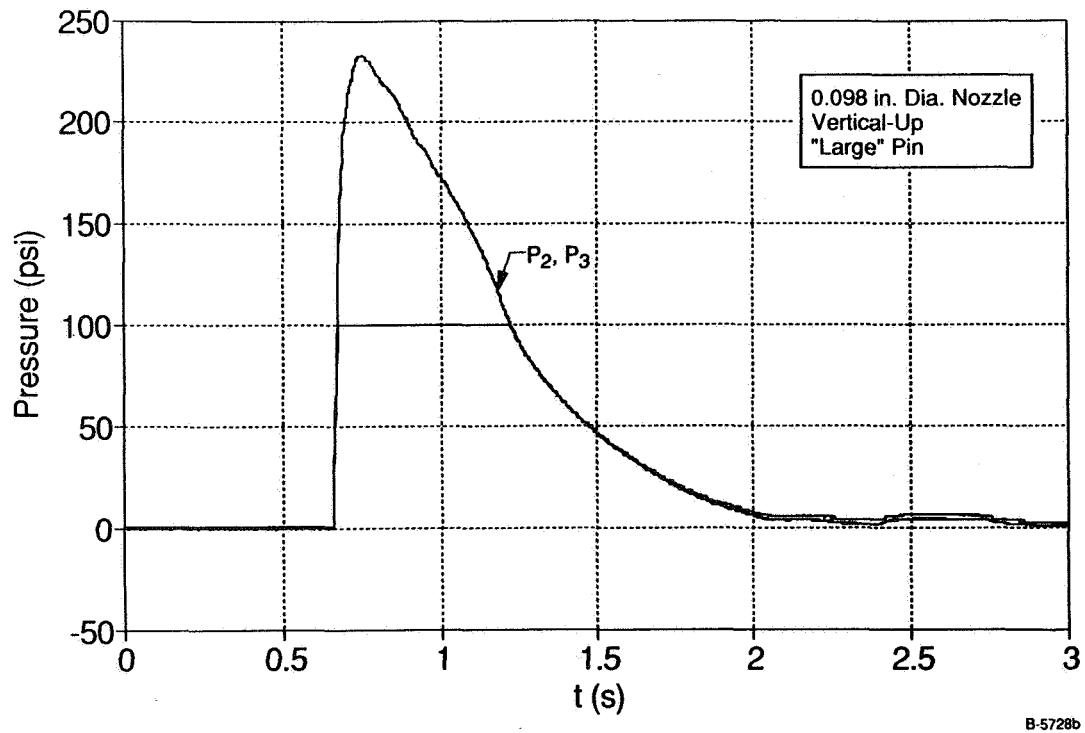
B-5727b

(b) Pressure Measurement

Figure 4. Schematic of Small-Scale Simulator Static Testing



(a) Thrust versus Time



(b) Pressure versus Time

Figure 5. Thrust and Pressure Time History for Baseline Configuration Without Copper Plug (large pin, 0.098-in. diameter nozzle, vertical up orientation)

escapes through the nozzle. The thrust behavior correlates well with the pressure history in Figure 5(b). The pressures P_2 and P_3 are coincident in this figure. Unfortunately, the P_1 transducer was overpressurized and saturated during this run. The initial spike in Figure 4(a) is an ubiquitous feature of most thrust data. It represents the impact of the piercing pin on the diaphragm of the CO_2 cylinder. The duration of this spike is a few milliseconds. It should also be pointed out the time elapsed from the instant that the laser triggers the light-activated switch to the instant the pin impacts the cylinder is of the order of 20 to 50 ms. This interval includes the electronics reaction time and the firing of the squib.

Figure 6 shows thrust and pressure histories when three sets of copper plugs, each packed with 2 mm diameter copper spheres, are placed upstream of the nozzle. A comparison of Figures 5 and 6 shows that the thrust curves are nearly the same and the pressures are also substantially similar. Thus, for the simulator with a large (or standard) piercing pin, the copper plug has little effect on the flow and pressures inside the simulator.

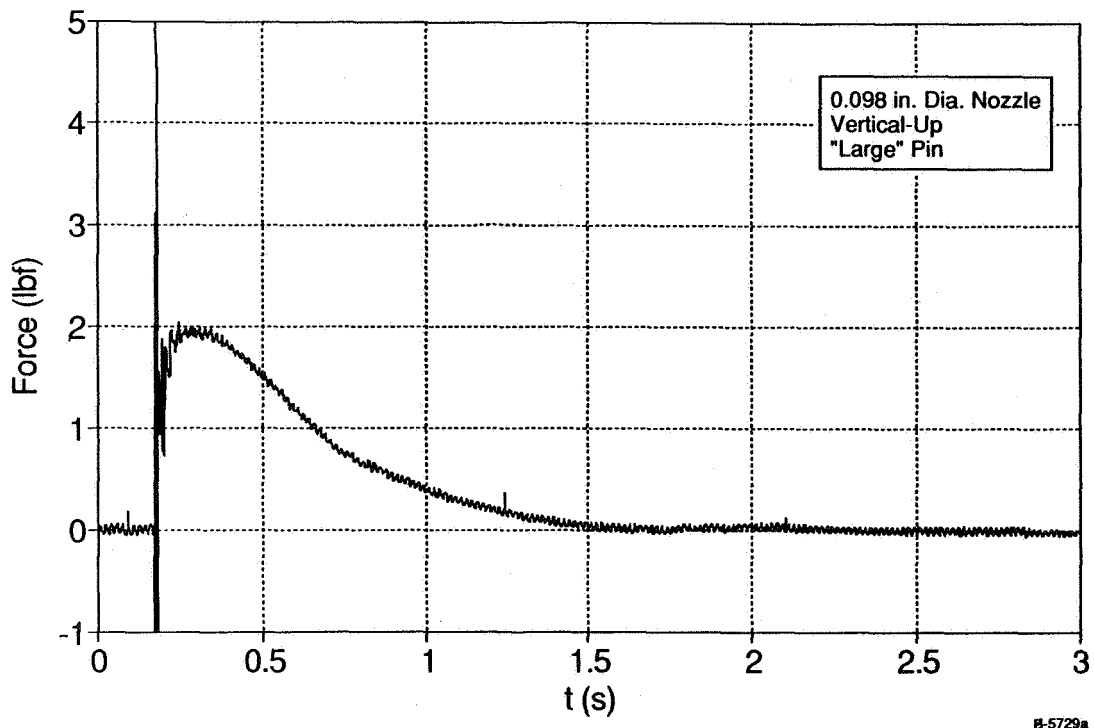
Figures 7 and 8 show the effect of simulator orientation on thrust and pressure characteristics. In Figure 7, the simulator was horizontal and incorporated the same copper plugs as the configuration in Figure 6. The peak thrust in the horizontal orientation is slightly higher and falls off somewhat faster than the vertically up orientation of Figure 6. The data in Figure 7 is also more noisy and is believed to be an artifact of the simulator cantilevered from the load cell. The pressures in Figure 7(b) are seen to be greater than those in Figure 8(b), which explains the thrust behavior. Figure 8 shows data for the simulator firing the jet vertically down. The copper plugs are the same as for Figures 6 and 7. A comparison between Figure 6 and Figure 8 reveals that the thrust is substantially higher when liquid CO_2 is drawn because greater mass of CO_2 enters the stagnation chamber in a given time. Further, the thrust maintains its higher level for about 0.5s before beginning to drop-off rapidly. This behavior suggests that the liquid CO_2 escaping into the stagnation chamber of the simulator (Figure 2) vaporizes. During this process, liquid-vapor equilibrium is maintained, and the pressure tends to remain constant. However, the pressure drops as the CO_2 vapor leaves through the nozzle. The net effect of these two opposing processes is to reduce the rate at which pressure and thrust drop. A comparison of Figures 8(b) and 6(b) shows higher pressure for the vertically down orientation. Also, the behavior of pressure with respect to time in Figure 8(b) explains the thrust history in Figure 8(a).

During the series of static tests, visual observations of the CO_2 jet from the nozzle indicated presence of white mist frequently, even with the copper plugs and bronze wool in place. Thus the effectiveness of the copper spheres in vaporizing solid particles upon contact is questionable. It is possible that the particles are so fine that they follow the gas streamlines without actually making contact with the spheres.

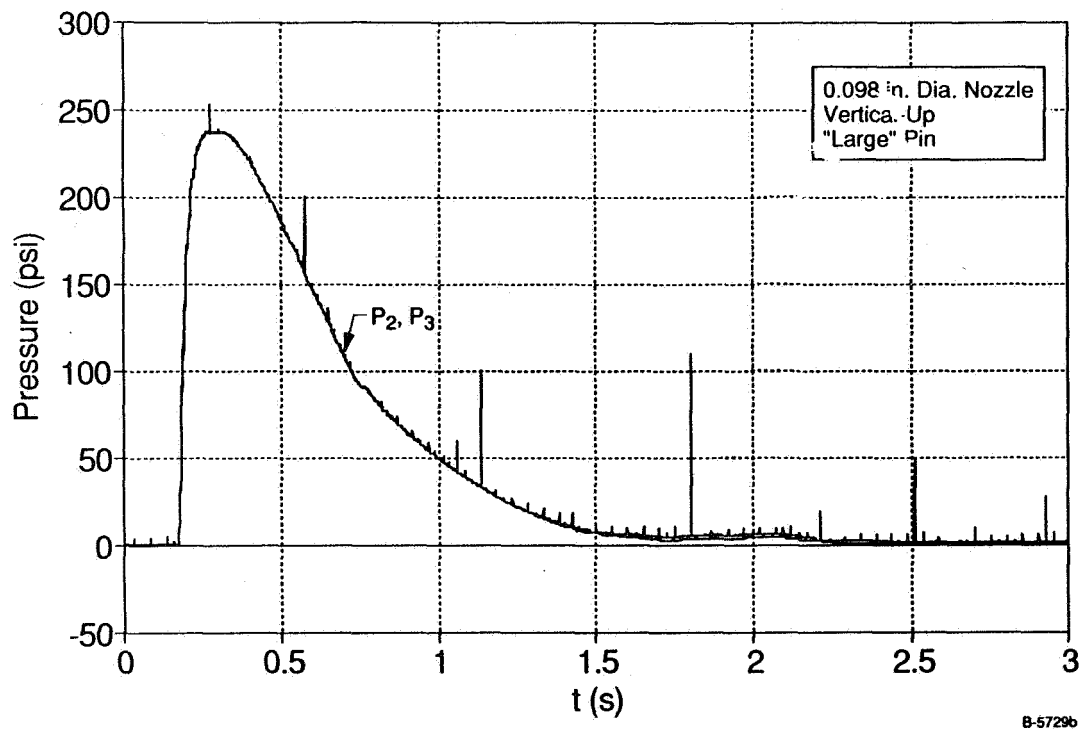
It can be summarized from results of the small-scale simulator that a working device was developed for wind tunnel test in the University of Southampton MSBS. It was difficult to insure high degree of repeatability of thrust for several reasons. First, the tolerance on the thickness of the caps of the commercially available CO_2 cylinders was unknown. Secondly, the explosive capacity of the squibs was not uniform. These uncertainties made the mechanics of cap piercing not too repeatable. Furthermore, upon piercing the cap, the metallic piece of the material sometimes remained attached to the pin, restricting the mass flow through it. Also, as the pin wore out after repeated fixings, the piercing characteristics changed, contributing further to non-repeatability.

4. LARGE-SCALE PROPULSION SIMULATOR PRELIMINARY DESIGN

As mentioned earlier, the large-scale simulator design was based upon the lessons learned from the small-scale simulator experience. The large-scale device was intended only for static testing on a thrust stand. It is apparent from the review of the small-scale test data that a pressure control component and a means of vaporizing small solid CO_2 particles must be incorporated into the large-scale design. Furthermore,

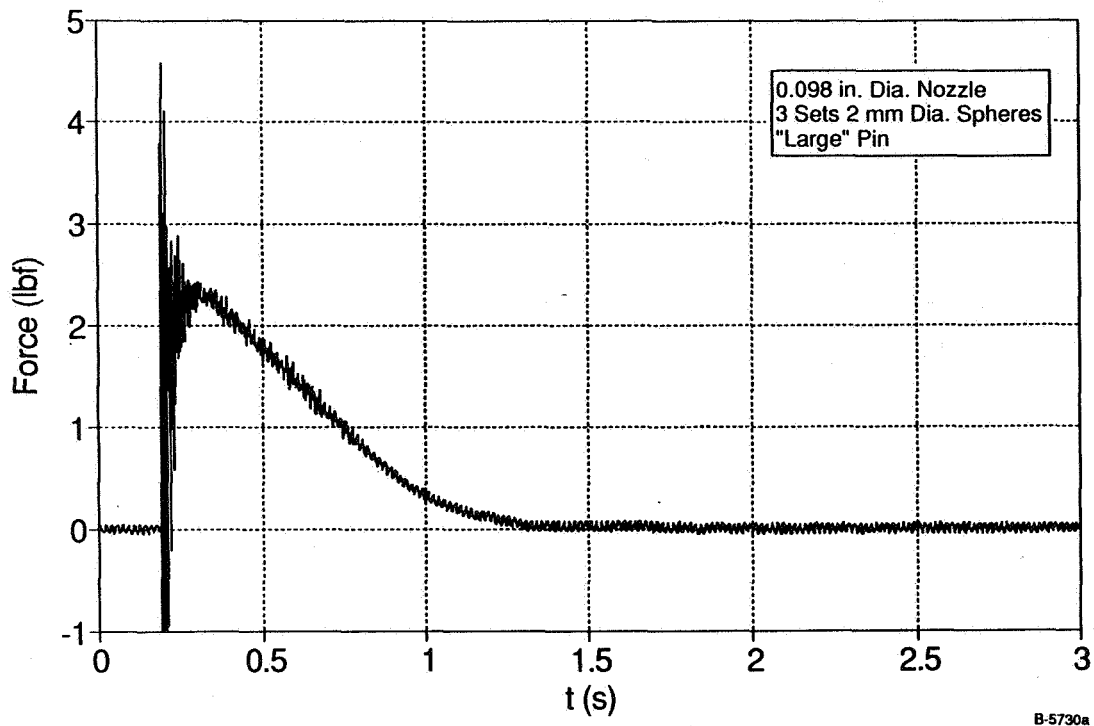


(a) Thrust versus Time

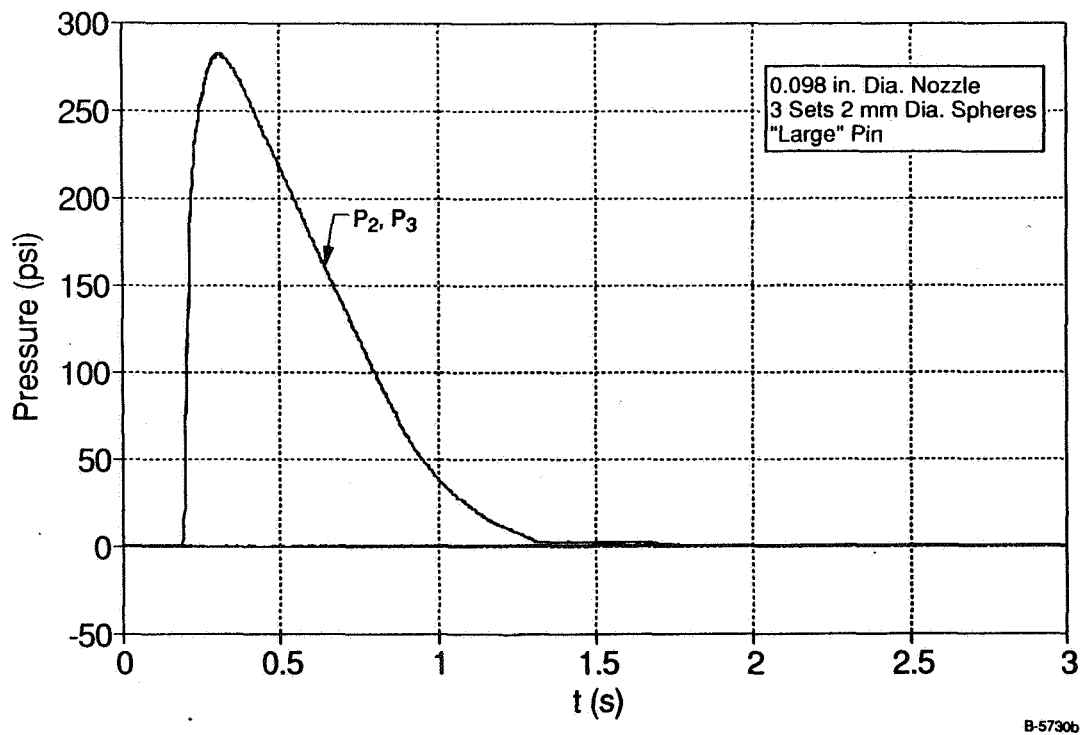


(b) Pressure versus Time

Figure 6. Effect of Three Sets of 2 mm Diameter Copper Spheres on Thrust and Pressure Time History (large pin, 0.098-in.diameter nozzle, vertical up simulator orientation)

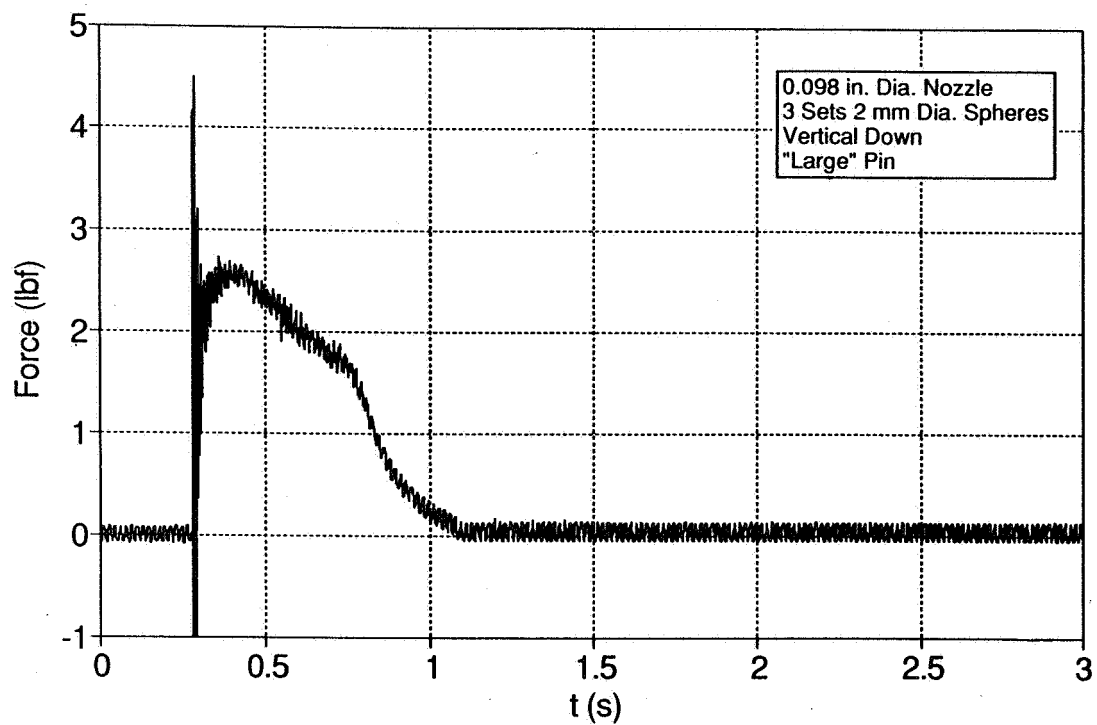


(a) Thrust versus Time

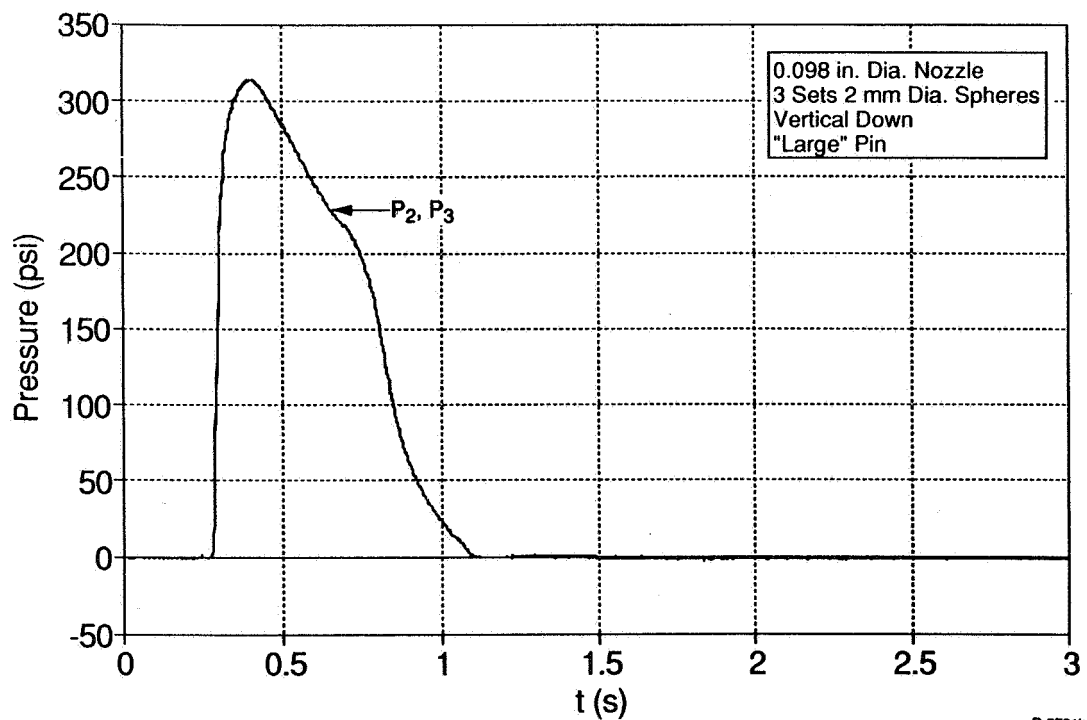


(b) Pressure versus Time

Figure 7. Effect of Horizontal Simulator Orientation on Thrust and Pressure Time History (large pin, 0.098-in.diameter nozzle, three sets of 2 mm copper spheres)



(a) Thrust versus Time



(b) Pressure versus Time

Figure 8. Effect of Vertical Down Simulator Orientation on Thrust and Pressure Time History (large pin, 0.098-in.diameter nozzle, three sets of 2 mm copper spheres)

one must be able to turn the simulator on/off during wind tunnel testing. The thrust and mass flow requirements are as defined in Ref. 1.

Taking the above requirements into account, the simulator design shown in Figure 9 was developed. The overall envelope is 2.5 in. dia. x 15 in. long. A copper reservoir holds about 200g of CO₂ when full, resulting in a total simulator weight of 5.5 Kg. Liquid, rather than vapor, carbon dioxide is drawn from the reservoir via an eductor tube to attain high mass flows (~40 g/s was achieved). The flow of liquid CO₂ is turned on/off by a miniature solenoid valve made by General Valve Corporation. It is operated by an on-board battery via a light-activated switch. CO₂ liquid flows through five coiled copper tubes which form a compact pre-heater block. It vaporizes and expands in the process, dropping its pressure. The pre-heater employs a cartridge heater which is run on external AC power prior to a propulsion test run. The power connector can be on the model on at the wall. It will be removed before a test run. The flow from the pre-heater enters a short settling/stagnation chamber and exits through a contoured nozzle. The nozzle was designed to be removable and replaceable. The pressure ratio was varied by varying the throat area.

As will be shown in Section 6, the simulator developed a thrust of 1.25 Kgf for approximately 4s. A maximum nozzle pressure ratio of 4.5 was attained.

The following paragraphs describe the main components of the large-scale simulator.

a) CO₂ Reservoir

The CO₂ reservoir, shown schematically in Figure 10(a), consists of a nickel-plated copper cylinder, 7 in. long, 2.5 in. O.D., 0.25 in. wall thickness; with a stainless steel plug threaded into its open end and sealed to the cylinder by a buna-N o-ring. The reservoir has a capacity of 200g of liquid CO₂. It was designed to withstand a pressure of 2000 psi, with a factor of safety of 4 to ultimate, and was proof-tested to 2500 psi. The copper cylinder has sufficient thermal mass to maintain the temperature, and therefore pressure, of the liquid CO₂ during the run. Furthermore, $\sqrt{\alpha t}$, i.e., the square root of the product of the thermal diffusivity of copper and the run time, equals

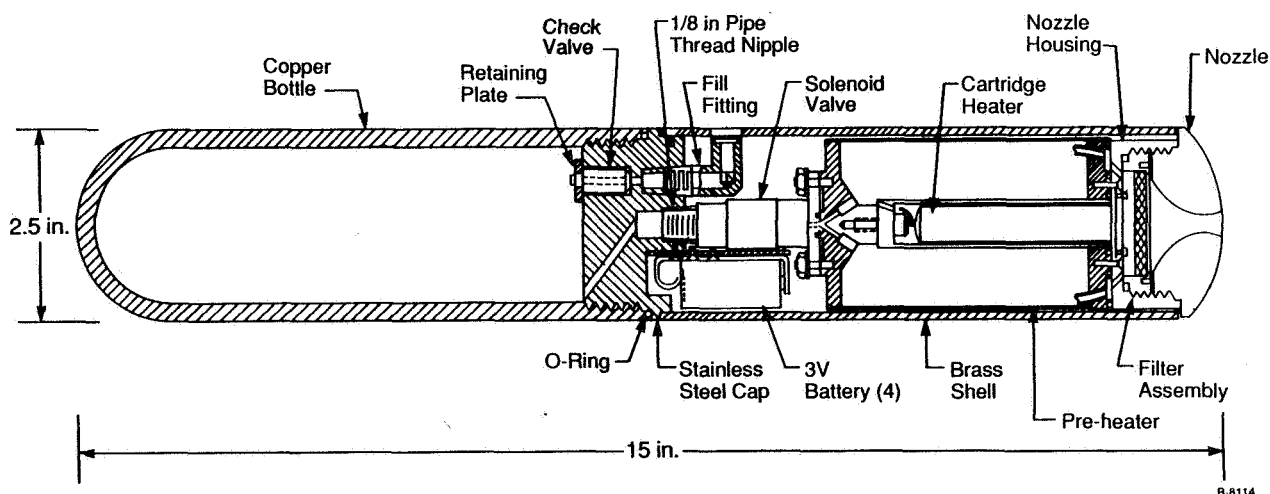
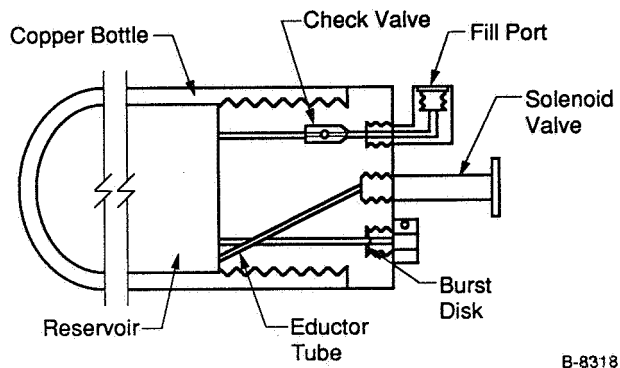
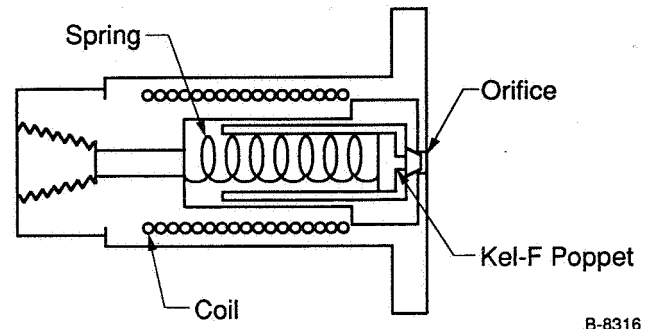


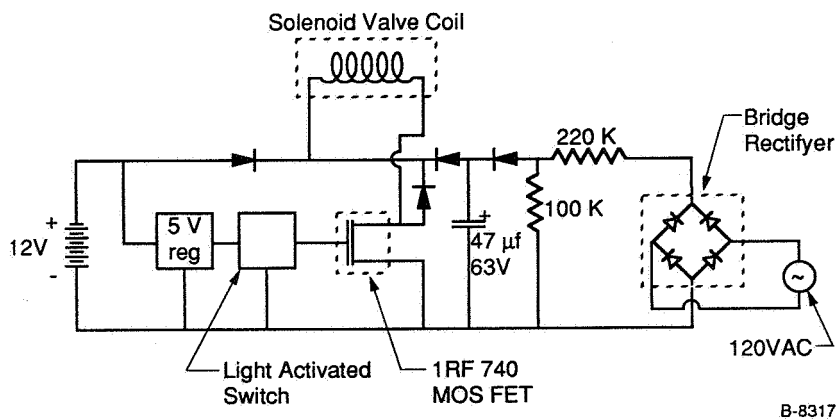
Figure 9. Design of Large-Scale Propulsion Simulator



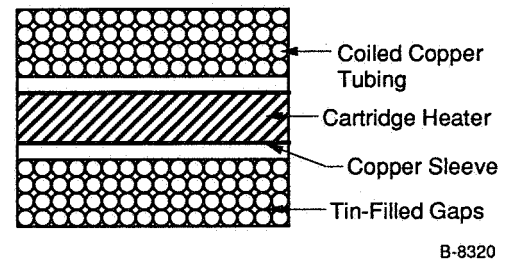
(a) CO₂ Reservoir



(b) Solenoid Valve



(c) Triggering Circuit



(d) Pre-heater/Pressure Reducer

Figure 10. Large-Scale Propulsion Simulator Components

2.1 cm, a factor of three greater than the wall thickness. Therefore, the CO₂ is able to draw heat from the entire thickness of the cylinder. The stainless steel cap contains a filling duct with a check valve (Kepner, 6000 psi max, 2 psi cracking); a burst disk (Frangible Disks, 1875 psi burst) to prevent over-pressurization; and a 0.093 in. dia. duct (eductor tube) to carry liquid CO₂ from the bottom of the cylinder to the solenoid valve.

b) Solenoid Valve

The solenoid valve, shown schematically in Figure 10(b), was manufactured by General Valve Corporation. Its dimensions are 1.6 in. long x 0.7 in. dia., and it weighs approximately 80g. It has a maximum operating pressure of 900 psi and is sealed by buna-N o-rings. The coil is rated for 6V and draws 2 amps during steady state operation. The valve operates by pulling a Kel-F poppet off of a 0.060 in. dia. orifice when the coil is activated. The valve is able to pass 40 g/s of liquid CO₂ through the orifice with an upstream pressure of 840 psig.

c) Triggering Circuit

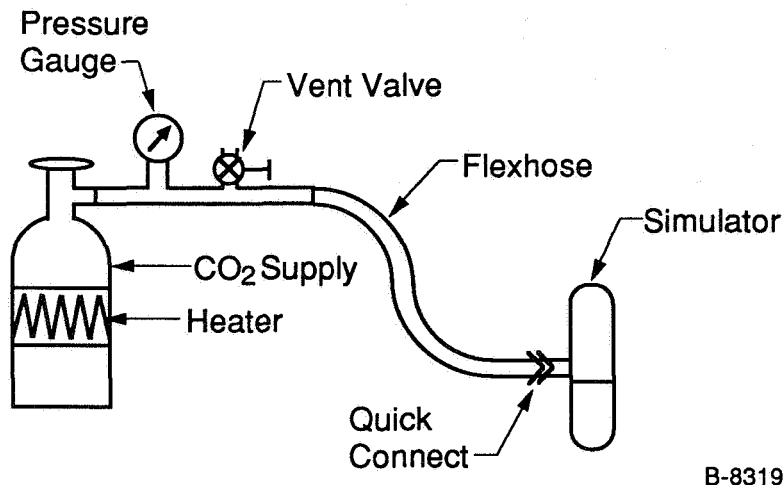
The triggering circuit is shown in Figure 10(c). Basically, it consists of four 3V batteries in series with the valve coil, with power switched by an IRF740 MOSFET, which in turn is activated by an EG&G light activated switch. Twelve volts are used because during operation the coil draws enough current to drop the battery voltage to the rated voltage of 6V. Also in series with the coil is a 47 μ f 63V electrolytic capacitor. Before each run, this capacitor is charged to 50V via external AC power and a bridge rectifier. (The capacitor charges in approximately 30s.) This capacitor sends an extra boost of current through the coil when the switch is first closed which helps to pull the valve open. Blocking diodes prevent communication between the capacitor and the batteries and prevent the capacitor from discharging to ground when AC power is removed. The light activated switch and a 5V regulator drain about 6 mA of current when the circuit is "off".

d) Pre-heater

After exiting the solenoid valve, the liquid CO₂ passes through a pre-heater to vaporize it and increase its enthalpy before entering the nozzle. The pre-heater transfers enough heat to the flow to increase its enthalpy by 180 kJ/kg, which is sufficient to prevent condensation when the CO₂ expands to 1 atm. It also drops the pressure of the flow to 70 psig in the nozzle chamber, although this pressure drop is a function of the mass flow (controlled by the solenoid valve) and the nozzle area, rather than the pre-heater characteristics. The pre-heater is shown schematically in Figure 10(d). It consists of five copper tubes (through which the CO₂ passes), each 90 in. long and 0.065 in. I.D., coiled around a copper sleeve into a 3 in. long x 2.25 in. dia. cylinder. The gaps between tubes were filled with tin to increase the thermal mass of the assembly and to increase the thermal conductivity between tubes. At the center of the copper sleeve is a 400W cartridge heater. The entire assembly weighs 1400g. Before each run, 120 VAC is applied to the cartridge heater which heats the pre-heater assembly to 75°C in 90s. During a 4s run of the simulator, the pre-heater cools to ~0°C. A one-dimensional flow and heat transfer model has been developed which predicts that at a mass flow rate of 40 g/s, the pre-heater will transfer 180 J/g to the flow. This prediction is entirely consistent with the observed temperature drop of the pre-heater.

e) CO₂ Filling

The CO₂ reservoir was filled with liquid CO₂ using the apparatus shown in Figure 11. A flex hose attached at one end to a CO₂ supply bottle was connected to the simulator via a fill fitting mated to the fill port of the simulator and a quick connect. The check valve in the reservoir cap



B-8319

Figure 11. - CO₂ Filling Scheme

prevented backfilling. In order to fill the reservoir to a higher density of CO₂ than was in the supply bottle (without pumping), the reservoir had to be cooler than the supply. This necessitated either heating the supply bottle or cooling the simulator. We chose to heat the supply bottle (with heating tape) as this was quicker and easier than cooling the simulator and kept the simulator at room temperature. A thermistor was placed on the outside of the reservoir, and the density (and therefore mass) of the CO₂ in the reservoir was determined by measuring the temperature and pressure. This determination was verified by weighing the simulator before and after filling.

5. RESULTS OF STATIC TESTING OF LARGE-SCALE SIMULATOR

Figure 12 shows the schematic of the large-scale simulator static test stand. The objective of these tests was to demonstrate the repeatability of the thrust, multiple jet operation, and a reasonably flat thrust versus time profile. The measurements were thrust, pressure in the CO₂ reservoir, and pressure at the center of the nozzle exit plane, as a function of time.

Figure 13(a) shows typical static test data for the large-scale simulator. The thrust profile is essentially flat at 2.75 lbf (1.25 Kgf) for about 4s. The time required to attain 90 percent of full thrust is approximately 0.4s. The gradual drop-off is due to CO₂ vapor after all the liquid CO₂ has changed phase. Plotted in Figure 13(c) is the exit plane pressure on the nozzle centerline. These data have been corrected for the normal shock in front of the pitot tube in Figure 12. The shock occurs because the nozzle used in the test was supersonic with an area ratio of 1.19.

Both Figures 13(a) and 13(c) show an initial "bump" which lasts for about 1s. Corresponding to this, there is an increase in pressure of the CO₂ vapor in the reservoir, following a sharp initial drop as the

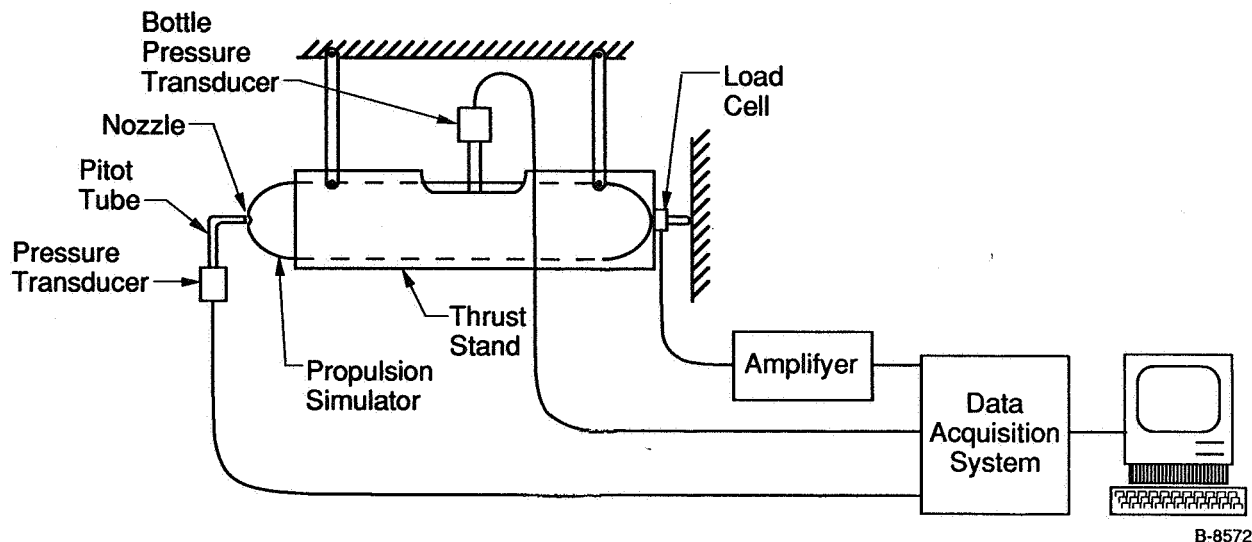
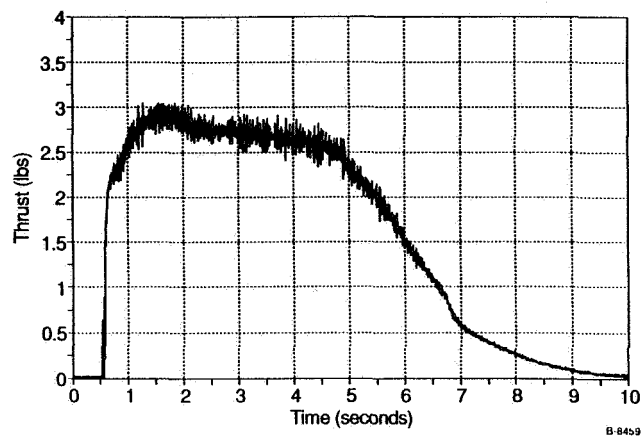


Figure 12. Schematic of Static Test Apparatus for Large-Scale Propulsion Simulator

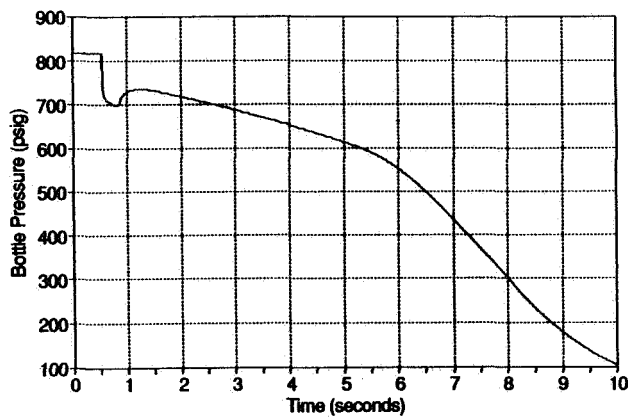
solenoid valve is opened, Figure 13(b). The increase in pressure occurs as a result of the heat transfer from the copper wall of the reservoir to the CO_2 vapor. The sharp drop in pressure is believed to be due to "over-compression" of the CO_2 liquid during the filling process. It will be shown later in this section that slight under-filling of the reservoir avoids the initial sharp pressure drop and the subsequent bump in the thrust profile.

It is noted in Figure 13(b), that there is a distinct change in the slope of the CO_2 reservoir pressure curve after 5.5s. This is the point by which sufficient liquid has been drawn from the reservoir so that only vapor remains therein. As this vapor leaves the reservoir, the pressure drops rapidly, the mass flow rate through the system is significantly reduced, leading to a rapid drop in thrust as seen in Figure 13(a). Prior to $t=5.5\text{s}$, there is always some liquid inside the reservoir which continually vaporizes. As liquid CO_2 is drawn, the pressure and temperature of the vapor above it reduces. As heat is received from the copper walls, the temperature of the CO_2 liquid/vapor system rises, resulting in vaporization of the liquid. Ideally, this process should keep a constant pressure in the reservoir, provided the temperature of CO_2 system remains roughly constant. In reality, this does not happen, and the pressure does keep dropping between 1 and 5.5s, as seen from Figure 13(b). However, the rate of pressure drop is sufficiently slow that the thrust variations are small, as seen in Figure 13(a).

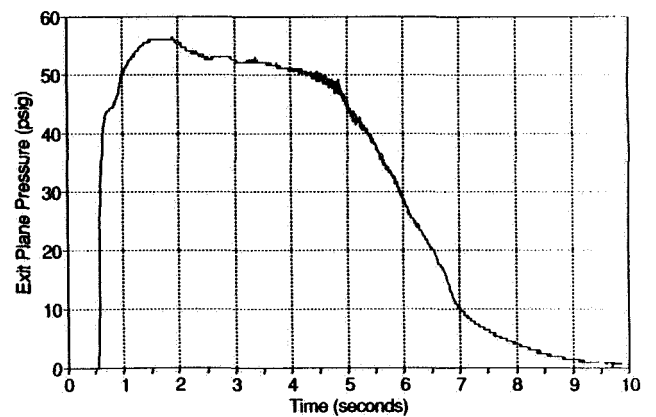
In Figure 14, the effect of under-filling the CO_2 reservoir on the thrust versus time curve is shown. It is seen from Figure 14(b) that the drop in CO_2 pressure upon activating the solenoid is much more gradual compared to over-filled case (Figure 13(b)). Also, there is no increase in the CO_2 pressure, unlike in Figure 13(b), following the initial drop in pressure. The result is that there is no bump in the thrust profile as was seen in Figure 13(a). This demonstrates that slight under-filling of the reservoir can produce a smoother thrust profile.



(a) Thrust versus Time

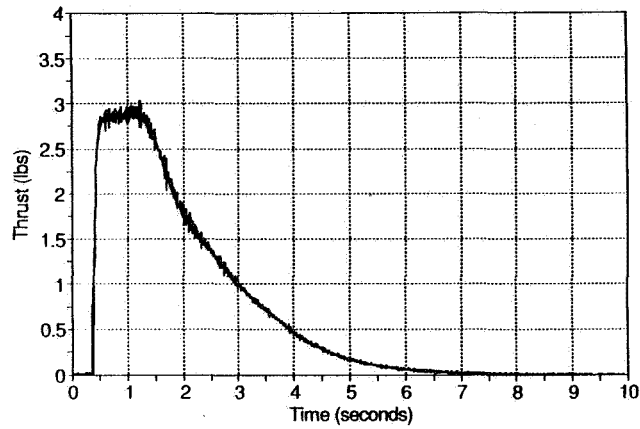


(b) Bottle Pressure versus Time

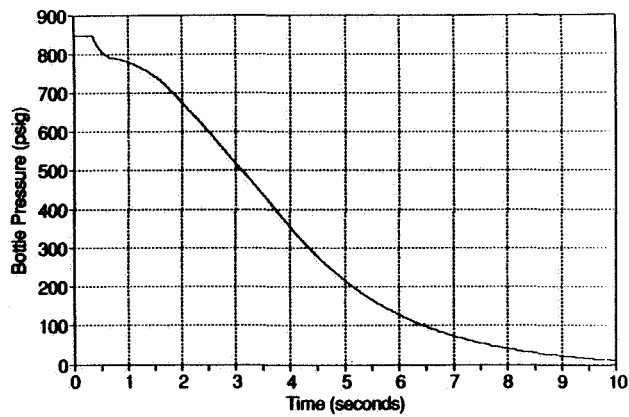


(c) Exit Phase Pressure versus Time

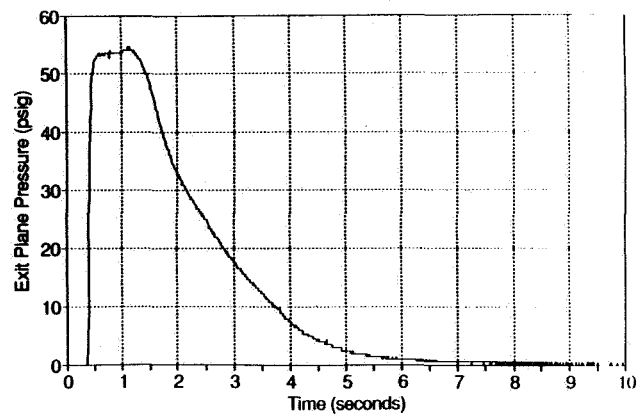
Figure 13. Large-Scale Simulator Static Test (Run 48)



(a) Thrust versus Time



(b) Bottle Pressure versus Time

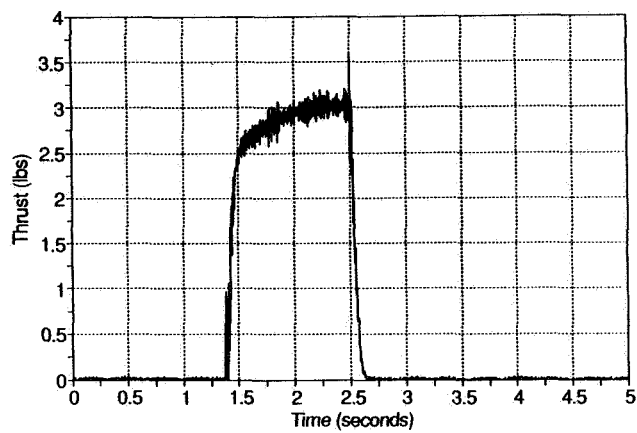


(c) Exit Phase Pressure versus Time

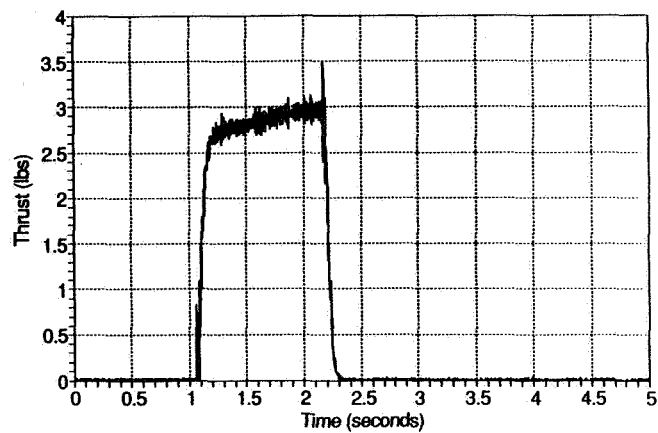
Figure 14. Effect of Under-Filling CO₂ Reservoir on Thrust Characteristics (Run 50)

Figure 15 shows the on/off capability of the large-scale simulator. This feature is necessary for producing jet pulses so that multiple runs can be made after filling the CO₂ reservoir. Note the absence of the bump in the thrust profile seen earlier for the over-filled reservoir.

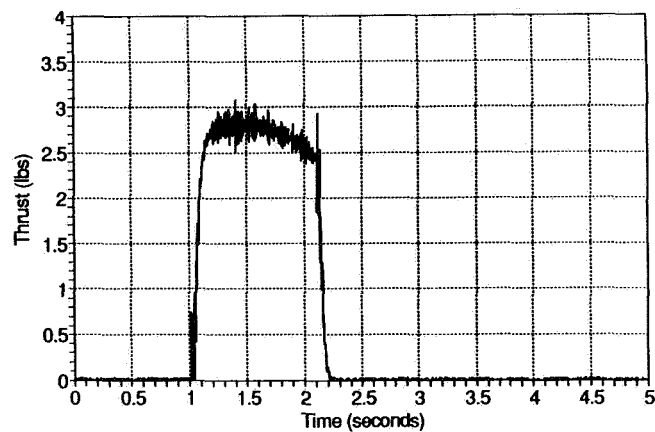
An analysis of the thrust produced by the large-scale simulator is provided in Ref. 3. It is shown that the pressure ratio and thrust are directly proportional to the area of the flow orifice (A_s) of the solenoid. In the static tests, nozzle pressure ratio of the order of 4 to 5 were obtained (Figures 13(a) and 14(a), after accounting for the normal shock at the pitot tube). The pressure ratio can be lowered by increasing the nozzle throat area. The measured thrust of 1.25 Kgf is lower than the ideal thrust calculation (1.6 Kgf) given in Appendix D. The lower thrust (1.25 Kgf) and mass flow (40 g/s) when compared to the requirements of Appendix A (3 Kgf a 80 to 100 g/s), resulted from the flow restriction in the solenoid valve ($d_s = 0.060$ in.). This particular valve, made by General Valve Co., was selected as an inexpensive, miniaturized device. In principle, a specially designed valve with a larger orifice can be incorporated in the current simulator design to yield the required 80 g/s mass flow. The current pre-heater can also handle mass flows of this magnitude.



(a) Pulse 1



(b) Pulse 2



(c) Pulse 3

Figure 15. Multiple Run Operation of Large-Scale Simulator

PART II

UNIVERSITY OF SOUTHAMPTON MSBS MODIFICATIONS FOR PROPULSIVE TESTING

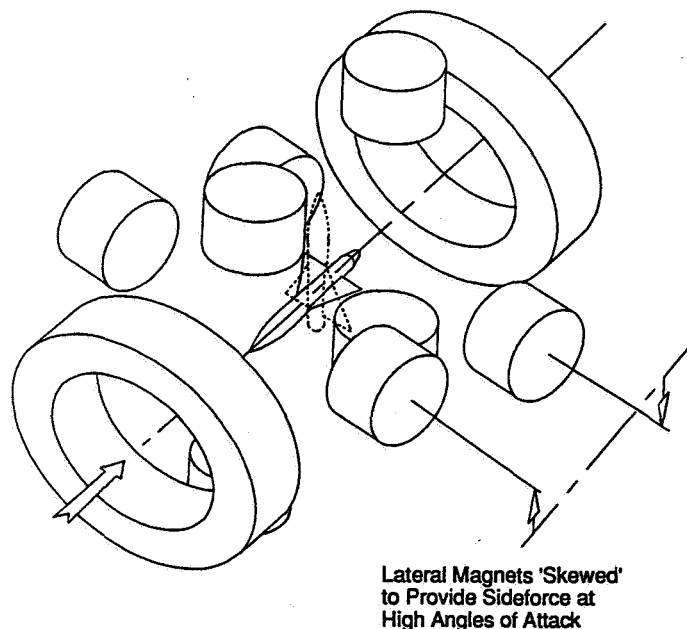
1. THE UNIVERSITY OF SOUTHAMPTON MSBS

In order to increase the versatility of the Magnetic Suspension and Balance System (MSBS) applied to the testing of wind tunnel models, development of techniques for simulation of propulsion systems is under way. The purpose of the work described in this paper was to begin to address the issue of developing exhaust flow simulators. The outcome was a set of simulators, two of which were brought to the stage of operating on board models levitated in a wind tunnel. The levitated model featured a supply of gas, discharged on command for a brief period to produce a jet exhausting at the rear.

The simulator development was carried out under NASA SBIR 87-1 whereby two styles of gas generator were developed. These were a carbon dioxide thruster with the gas stored under pressure as liquid CO₂, and a rocket thruster using a solid propellant as the gas generator.

To enable suspension and testing of the propulsion simulators at the University of Southampton, a number of modifications were required to the suspension system, the wind tunnel hardware and to the control system.

The present electromagnet configuration is shown in Figure 16(a) '++' layout is used, symmetrical apart from the skew in the lateral electromagnets. This was introduced to provide a side force at high angles of attack. Position sensing is achieved via five linear photodiode arrays and a system of laser light sheets (ref. 4). A PDP11/84 computer is currently used for control of the MSBS. Dual-phase advance control algorithms with proportional and integral feedback are employed (ref. 5).



Southampton University MSBS
Electromagnet Configuration

B-8563

Figure 16. Electromagnetic Configuration for University of Southampton MSBS

The initial aim of the wind tunnel experiments was to test at speeds up to Mach 0.2, and at angles of attack up to twenty degrees.

2. SYSTEM MODIFICATIONS

It was necessary to alter the path of the axial position sensing laser light sheet, to avoid its corruption by the model's exhaust efflux. A change was made from tail to nose scanning, after consultation with PSI over a suitable nose geometry.

A PC was integrated into the control loop to act as a data logger, and eventual replacement for the PDP11 control computer. This allowed development of more sophisticated data analysis and presentation software than had previously been feasible at Southampton.

The high angle of attack control system was modified to allow suspension of iron models. It had originally been developed for use with models with permanent magnet cores. The change was necessary because machining the relatively complex components of propulsion simulators would have been very difficult with permanent magnet alloys. To magnetize the model a steady field component is added to the suspension field. The magnetizing field is generated by contributions from all ten electromagnets, and rotates to match the instantaneous angle of attack. The unique capability of the Southampton MSBS to suspend models over a 110 degree angle of attack range is thus retained.

It was found that a field strength of around 0.02 T was required to adequately magnetize the propulsion simulator, this rather high value being a result of its self-demagnetizing geometry. A number of additional minor system modifications were made.

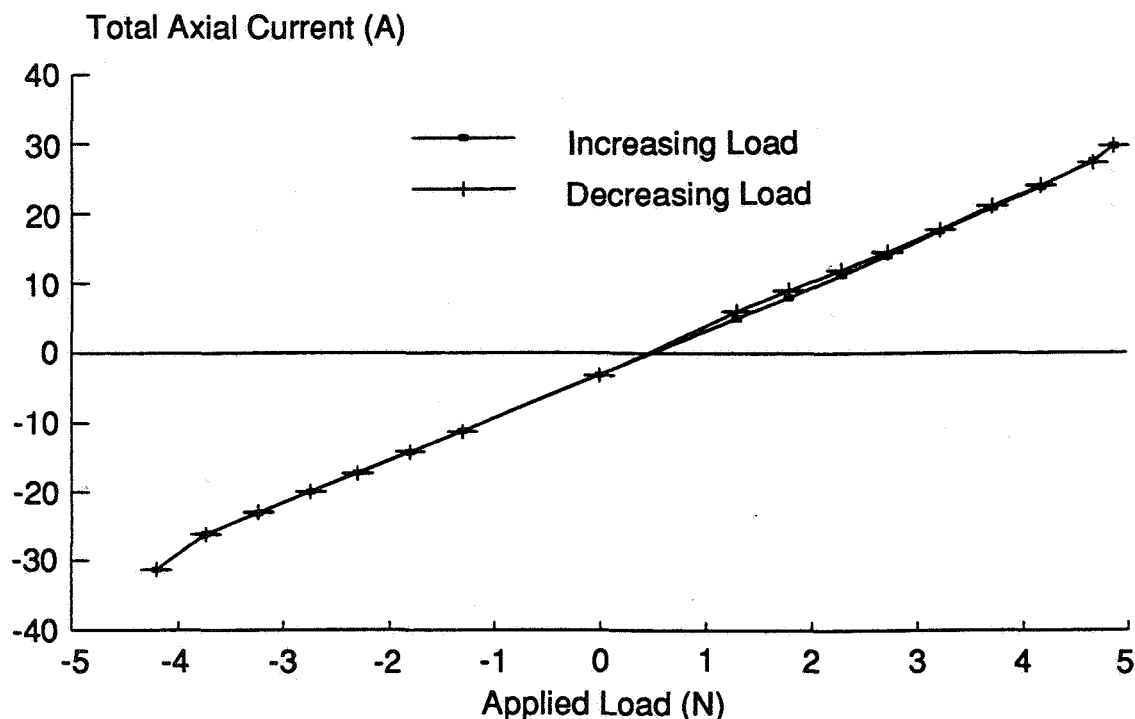
3. INITIAL SUSPENSION AND DEVELOPMENT

Following initial suspension of the propulsion simulators, attempts were made to optimize the controller in each degree of freedom. Particular attention was paid to quality of suspension. Difficulties were expected in control of the simulators under the influence of force transients associated with the thruster firing. It was demonstrated that the optimum input constants to the dual-phase advancer were angle of attack dependent, rather than being constant for all angles of attack as had been previously assumed.

Further optimization was necessary to maximize the ability of the system to resist externally applied forces in the axial direction. This was achieved primarily by ensuring that the electromagnets used for axial force generation made the minimum practicable contribution to magnetization of the model. The level of magnetization was also adjusted to give the best compromise between strong magnetization and peak force generation.

Force and moment calibrations were performed to allow extraction of axial force data at zero angle of attack, and additionally for heave force and pitching moment data at angles up to twenty degrees. Conventional calibration techniques were employed, using small weights and low friction pulleys to apply forces to the suspended model, whilst recording the changes in electromagnet currents. Figure 17 shows the results of an axial force calibration, plotting magnet currents against externally applied load. The result is linear except at the extremes, where electromagnet current limits cause a non-linear region.

At zero degrees only the two axial magnets are used to oppose the drag force, so just their two currents are recorded during the calibration process. For other attitudes a technique was developed whereby several currents were recorded during heave, pitch and axial calibrations. Run-data was processed to find the changes in these currents during a suspended thruster firing, and matrix inversion used to deduce heave force, axial force and pitching moment simultaneously.



B-8564

Figure 17. Axial Force Calibration at Zero Angle of Attack

Peak axial force capability was found to be around 4.5 N at zero angle of attack, falling to 4.0 N at twenty degrees.

Bench tests of the carbon dioxide thruster showed the peak thrust to be significantly above these values, and initial wind tunnel testing was delayed while a series of nozzle modifications gradually reduced the thrust peak to below 4 N. The rocket thruster used initially also displayed a thrust profile with an initial peak. In a later version the profile is more constant, as shown in Figure 18.

4. WIND TUNNEL TESTS

A series of firings of the carbon dioxide propulsion simulator was performed in the Southampton MSBS, at zero wind speed and up to Mach 0.1, and attitudes of zero, ten and twenty degrees angle of attack. Initially the success rate was only about 50%, with the model regularly falling out of suspension because of the high and erratic thrusts produced. Operating experience and further thrust reductions led to a much higher success rate. The rocket thruster has also been fired in suspension, and wind tunnel tests with this propulsion simulator will be performed in the near future.

5. DATA ANALYSIS AND RESULTS

The unsteady thrust profile and short run time of the carbon dioxide propulsion simulator provided particular problems for data analysis. As there was no period following a firing where the model was stationary during the thrust cycle, analysis of run-data had to address the motion transients. Software was developed to attempt to find the external forces and moments experienced by the suspended model, by considering its motion in addition to the electromagnet currents. Factors accounted for included the model's

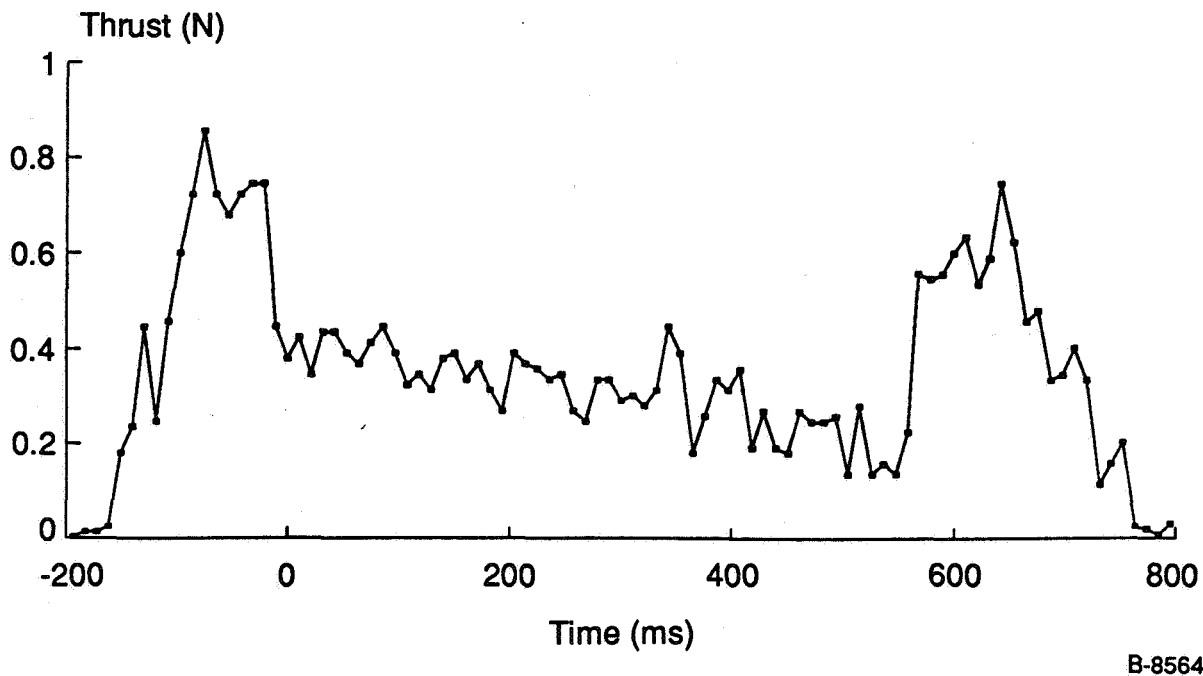


Figure 18. Rocket Motor Thrust Profile (low thrust test)

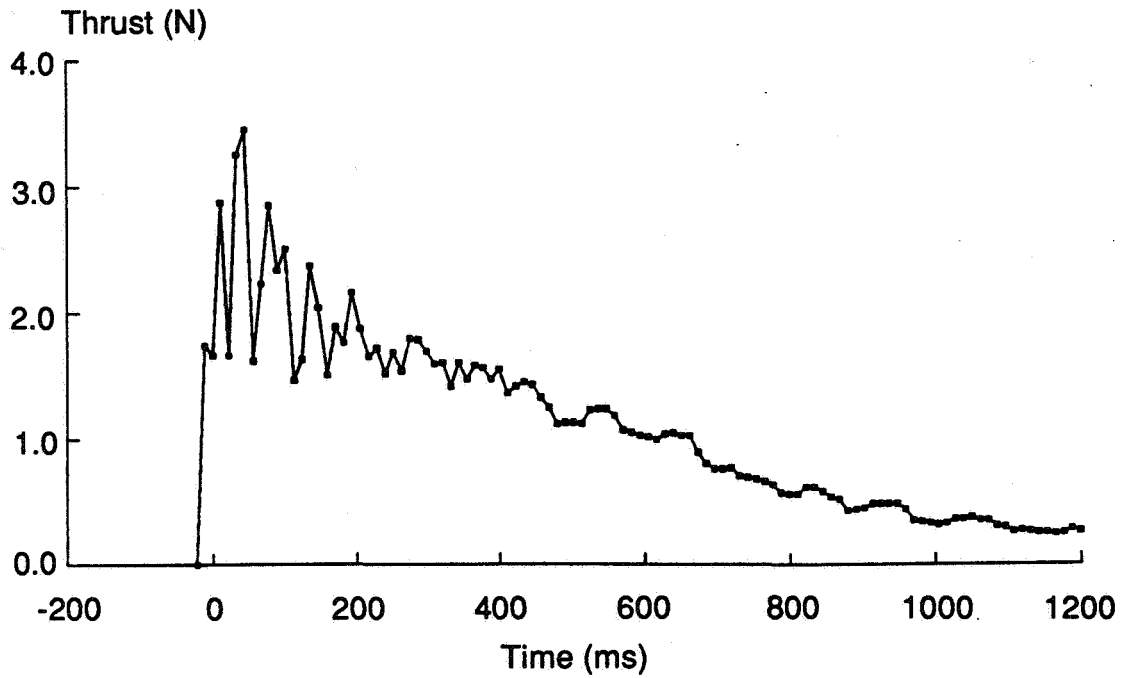
inertia, cross coupling in the position sensors, changes in level of magnetization and the relationship between calibration constant and axial position.

The aim was to extract a thrust profile similar to that demonstrated in bench tests, possibly going on to examine changes in drag coefficient caused by the presence of the exhaust plume. Unfortunately the variability of thrust produced by the carbon dioxide jet was such that no accurate measurements of this type were possible. In addition, the transient analysis did not prove satisfactory, giving external force data which did not agree closely enough with bench test results. In Figure 19, the bench test data shows an exponential thrust decay after the initial peak, while the data extracted from a test in suspension includes an oscillatory component, associated with model motion.

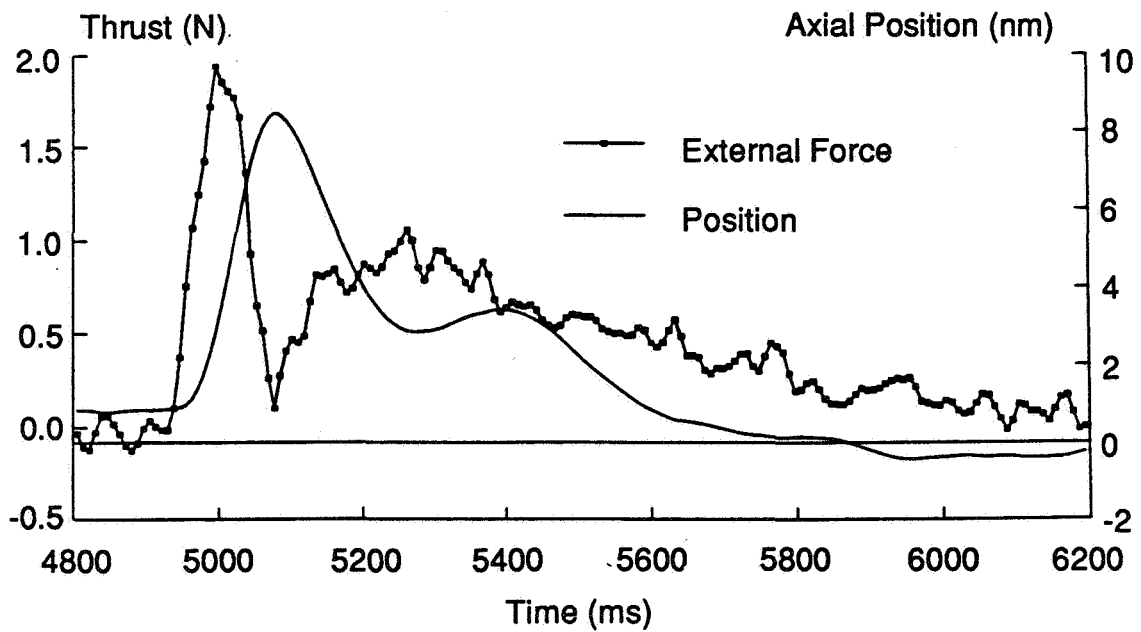
The force and moment results obtained with the model levitated were inconclusive. However the emphasis of the tests was placed on proof of concept and on overcoming some of the practical difficulties inherent in these experiments, rather than aiming to demonstrate an aerodynamic effect of the exhaust plume.

6. THRUST PROFILE AND MAGNETIC SUSPENSION

Control problems experienced using the PSI propulsion simulator were attributed to the very rapid increase in thrust to peak level when fired - the ramp lasting around 1 ms. Tests showed that the response to a demand for a step change in electromagnet current takes around 45 ms with the hardware presently in use at Southampton. The time measured to achieve peak restraining force during a suspended firing of the carbon dioxide thruster was also 45 ms, demonstrating a hardware, rather than a control software, limitation in responding to a sharply increasing thrust.



(a) Static Test Thrust Profile



B-8565

(b) Thrust Profile as Extracted from Current and Position Data

Figure 19. Measured and Extracted Thrust Profiles

Loss of control during firing was always preceded by excessive axial motion of the model, causing it to obscure the axial position sensor. A simple analysis showed that the lag between thruster firing and application of maximum restraining force made the amount of axial travel highly sensitive to variations in peak thrust. Results of this analysis are shown in Figure 20. For a low peak thrust the axial travel of the model is minimal. As the peak approaches the maximum restraining force the travel increases rapidly.

It is concluded that for reliable suspension during propulsion simulation in an MSBS, a thrust profile with a ramp to peak thrust of a similar time span to the minimum system response is necessary. Alternatively an unconventional model control system might be invoked.

The emphasis of this project was on proving that a model which carried a substantial thruster (peak thrust close to model weight) could be flown, fired and retained in controlled suspension. This aim was satisfied. It remains to develop the equipment and analysis further to the point where accurate force measurement is possible.

7. RESULTS AND CONCLUSIONS

The applicability of a wind tunnel employing Magnetic Suspension and Balance System (MSBS) to propulsive testing was demonstrated.

A small-scale propulsive device (1 in. dia. x 8 in. long), which generated a carbon dioxide jet, was designed, built, and statically tested to measure its thrust characteristics. It was successfully tested in the University of Southampton MSBS at angles-of-attack up to 20 deg.

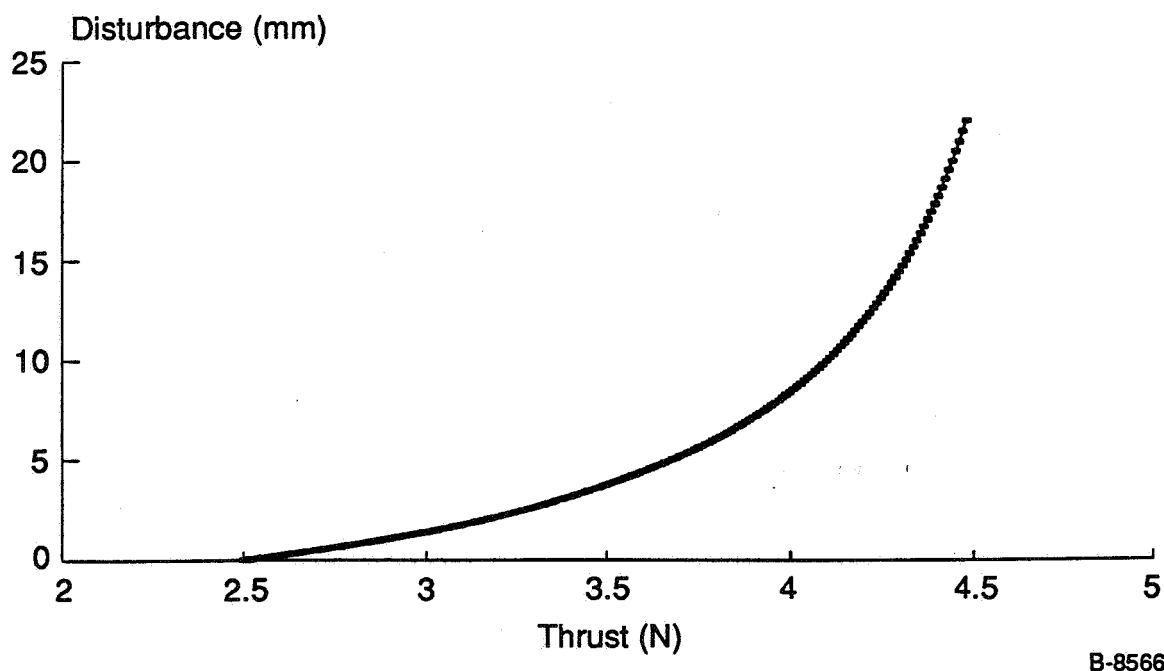


Figure 20. Results of Simplified Prediction of Model Response to Different Step Thrust Impulses

- The MSBS at Southampton was modified to keep the model stable under the action of the impulsive force generated by a thrusting model.

A large-scale propulsive device (2.5 in. dia. x 8 in. long), which generated a carbon dioxide jet, was designed, built, and statically tested to measure its thrust characteristic.

- A stable flat thrust profile was obtained over a period of 4s.
- Nozzle pressure ratios (NPR) of up to 5 were obtained. The device allows variation of NPR by varying the nozzle throat area.
- The propulsion simulator was demonstrated to operate in a pulse mode via a miniaturized solenoid valve.
- The thrust and mass flow of the current design are limited by the largest orifice (0.060 in. dia.) in the commercially available miniature solenoid valve. This limitation can be removed by using a specially designed miniature solenoid valve.

8. RECOMMENDATIONS FOR FUTURE PROPULSION SIMULATOR WORK

The present work has developed a propulsive device which can generate an exhaust jet with appropriate characteristics, such as thrust, mass flow, and pressure ratio. Although the initial motivation for this work was application to magnetic suspension, the propulsion simulators can be employed in conventional wind tunnel test applications as well. In fact, conventional testing has less stringent requirements. For example, the electronics can be located external to the simulator, pre-heater can stay on continuously, etc. In particular, with the following modifications, the large-scale device can be made highly useful for conventional applications.

- Modify solenoid for larger mass flows
 - Increase orifice diameter to ≥ 2 mm
 - Modify coil to overcome greater force
 - Recharge capacitor to higher voltage
- Operational changes
 - Automatic shut off for pre-heater
 - Power on during run
- Develop model of thermo-fluid dynamics of the simulator to understand transients and to improve short pulse operation.

The small-scale simulator developed in the current program is especially suitable for high-speed (supersonic), blow down testing. The device is compact so that it can be easily incorporated into a high-speed model; and its short thrust time (< 1 s) is compatible with blow down run times (typically few seconds). With the following modifications, the small-scale simulator can be adapted to high-speed testing.

- Replace off-the-shelf CO₂ cartridges by specially made copper bottle to store > 16 g of CO₂ and for effective heat transfer to the vapor inside the bottle.
- Replace current filling pin/squib mechanism by General Valve Solenoid.

- Locate battery-plus-electronics external to the simulator, outside the test section or as a small module attached to the support.
- Use stack of pre-heated copper balls to avoid condensation with the above modifications, it appears possible to package the simulator in an envelope 1.25 in. dia. x 10 in. long.

9. REFERENCES

1. Joshi, P.B., et al., "Propulsion Simulation for Magnetically-Suspended Wind Tunnel Models," Physical Sciences Inc., PSI-2055/TR-859, NASA Contract No. NAS1-18616, September 1988.
2. Tuttle, M.H., Kilgore, R.A., and Boyden, R.P., "Magnetic Suspension and Balance Systems, A Selected, Annotated, Bibliography," NASA TM 84661, July 1983.
3. Joshi, P.B., et al., "Propulsion Simulator for Magnetically-Suspended Wind Tunnel Models," PSI-2090/TR-1140, NASA Contract NAS1-18845, September 1991.
4. Parker, D.H., "Techniques For Extreme Attitude Suspension of a Wind Tunnel Model in a Magnetic Suspension and Balance System. University of Southampton Ph.D. Thesis, April 1989.
5. Britcher, C.P., "The Southampton University Magnetic Suspension and Balance System - a Partial User Guide. AASU Memo 83/8, April 1984.

ACKNOWLEDGEMENTS

This work was supported by NASA Langley Research Center under Contract No. NAS1-18845. The authors wish to acknowledge the comments and contributions of Dr. Evan Pugh at Physical Sciences Inc. during this investigation.

N 9 2 - 2 7 8 0 2

PRESENT STATUS OF THE MIT/NASA LANGLEY 6-INCH MSBS

Timothy Schott, Thomas Jordan, and Taumi Daniels
Langley Research Center

Charles Alcorn
Old Dominion University

PRECEDING PAGE BLANK NOT FILMED

ABSTRACT

The paper describes the latest improvements made to the MIT/NASA Langley 6 Inch Magnetic Suspension and Balance System and its present operational capabilities. Since its relocation from MIT in 1984, the system has suffered from reliability problems with original equipment. System performance is ultimately limited by noise and antiquated power supplies. Although a limited amount of funding and man hours has been expended, some significant improvements have been made to the system. The design and implementation of a new electro-magnetic position sensor has significantly reduced system noise and drift.

In January 1991, the system was demonstrated fully operational for the first time since its arrival at NASA Langley Research Center. An ogive cylinder test model was suspended while running the wind tunnel at its maximum of approximately Mach 0.5. Since that time, other aerodynamic models have been suspended with wind on.

In addition, the simulation of low-speed cavity store separation using an ogive cylinder test model is described. Methods used for flow visualization for this test are also discussed. The system is ideally suited for this type of low speed testing.

INTRODUCTION

The 6 Inch Magnetic Suspension and Balance System (MSBS) was originally designed and constructed from 1966 to 1969 under contract for NASA Langley Research Center (LaRC) by Massachusetts Institute of Technology (MIT), and was used there for research until 1982. The 6 Inch MSBS was then relocated to NASA LaRC and installed in 1984. For a period of five years, work on the system was limited to minor system improvements and maintenance. The system has suffered from reliability problems with the original equipment. As a result, significant down time has been experienced. In addition, electrical noise in the feedback control loops and antiquated power systems limit system performance.

In September 1989, an initiative to make the 6 Inch MSBS fully operational began.

Although a limited amount of funding and man hours has been expended, some significant improvements have been made to the system. Among the improvements made to the system are new electro-magnetic position sensor (EPS) electronics, control system rewiring, and new water-cooled resistors. The 6 Inch MSBS is unique among wind tunnels of this type due to its model position measurement system. All other magnetic suspension wind tunnels use optical methods.

In January 1991, an ogive cylinder test model was suspended at a Mach number of 0.5, demonstrating the system's fully operational status. The system reliability and performance before this time prevented any wind-on testing. Since then, other aerodynamic models have been suspended at lower mach numbers.

In addition, the simulation of low-speed cavity store separation using an ogive cylinder model was performed. Due to the absence of mechanical supports for the model, which are necessary for conventional wind tunnel models, an interference-free simulation resulted. As a result, the system is uniquely suited for this type of low speed testing. Flow visualization using vaporized propylene glycol further enhanced the store separation.

SYSTEM DESCRIPTION

The basic components comprising the 6 Inch MSBS are the subsonic wind tunnel, magnetic assembly, control electronics, and the power supply system. Each of these components is briefly described below.

A more detailed description of the system may be found in reference 1.

Subsonic Wind Tunnel

A subsonic, open circuit wind tunnel was fabricated by MIT for use with the magnetic balance. Figures 1 and 2 are views of the wind tunnel looking downstream and upstream, respectively. The contraction, which slides away from the test section for access, was constructed of molded plywood. Two settling chambers and a honeycomb, fabricated using ordinary drink straws, are located upstream of the contraction to reduce flow nonuniformities. The octagonal test section, which is located within the magnetic assembly, is transparent acrylic with an inside dimension of 6.25 inches and a length of 36 inches. A slight taper is employed to account for boundary layer growth. A two-piece mahogany diffuser with access doors is located between the magnetic assembly and the squirrel cage fan. The soft wood inflicts minimal damage to a test model if control is lost with wind on. The wind tunnel is capable of operating at a Mach number of 0.6.

Magnetic Assembly

A symmetrical group of subassemblies with a variety of separate control coils produce the required magnetic fields for model positioning within the test section. Figure

3 shows end and sectional views of the magnet configuration.

Two circular solenoid coils located fore and aft of the center provide both a uniform magnetizing, or bias field, as well as an axial gradient field. Each coil assembly is multiwound with separate electrical connections allowing a Helmholtz pair to be driven separately from axial control coils.

The ends of the magnetic assembly are made of two octagonal silicon steel cores with four poles, each angled toward the center of the assembly. The control windings for lift and side positioning are located between the poles and each set of four are wired in series. Current flowing through a coil excites the two adjacent poles. Therefore, the lift coils are located on each side of the core inducing a vertical flux path as seen in the figure.

The fields controlling pitch and yaw are produced by two pairs of "saddle coils" located internally between the axial solenoids and the test section. MIT chose a complicated arrangement over a simpler design to improve the field homogeneity. An inner pair of coils are rolled at 45 degrees from the vertical and an outer pair are oriented 90 degrees to the inner pair. The primary disadvantage of this arrangement is the limited visual access to the test section. An alternate configuration would have been four identical coils fitting together to form a single cylinder. The chosen configuration relies on vector addition of the field components produced at 45 degrees to the Y and Z axes. An electronic crossover circuit is necessary to mix the pitch and yaw position signals to compensate for the inherent 45 degree fields. MIT also experimented with mixing the current feedback signals for alignment purposes and improved stability. The pitch and yaw system works well for static demonstrations, but has been avoided for high speed flow testing due to difficulties with damping high frequency oscillations.

Control Electronics

The feedback control loop of the MSBS primarily consists of an electromagnetic position sensor (EPS), and compensation electronics.

Electromagnetic Position Sensor

The 6 Inch MSBS is the only magnetic suspension system that does not measure model position optically. Instead, it utilizes the linear variable differential transformer concept, resulting in superior range of model position measurement. The EPS consists of a multi-coil sensor, power amplifier, and demodulation electronics, and can measure aerodynamic model position in five degrees of freedom. The original design is presented in reference 1, and a brief explanation of EPS operation follows.

The EPS coils are configured as a multicoil differential transformer whose primary windings, a Helmholtz pair, are excited by a 20 kHz carrier sinewave. Seven pairs of symmetric, electrically opposed secondary coils are positioned to sense one axial, three vertical, and three horizontal position components. In the absence of an aerodynamic

model, voltages induced in each secondary coil pair mostly cancel due to their geometric symmetry. The presence of a ferromagnetic or electrically conductive model distorts magnetic coupling between primary and secondary windings so that amplitudes of differential voltages appearing between coil pairs are dependent upon model position. Analog circuitry adds or subtracts appropriate components to provide measurements of axial, vertical, and horizontal positions, as well as pitch and yaw angles. In particular, the three vertical components are combined to sense pitch angle and vertical position. Similarly, the three horizontal components are combined to sense yaw angle and side position.

The EPS electronics were redesigned and a complete description of the original and upgraded circuitry can be found in reference 2. The major difference in the new signal processing scheme is in the order of operations. The new design demodulates each bandpass filtered differential coil voltage with its own reference before mixing with other demodulated signals. The old design incorporates extra filtering stages and mixes the differential coil voltages prior to demodulation. Only one reference signal was used for demodulation, resulting in reduced signal amplitude due to phase differences between signals. Thus, this source of position measurement error is corrected in the new design.

After initially reporting on the redesigned EPS, the actual hardware was tested and installed within the system. Only a few minor modifications to the hardware were required. The implemented circuit has a modular design such that the following subcircuits reside on separate printed circuit boards: primary and nulling reference voltage generator board, axial coil and axial position board, vertical coil 1 and lift board, vertical coil 2 and pitch board, vertical coil 3 board, horizontal coil 1 and side board, horizontal coil 2 and yaw board, and horizontal coil 3 board. The printed circuit boards were designed to be interchangeable with only slight modification, and each fits into a particular slot in the EPS electronics chassis backplane. For example, a blank printed circuit board could be populated, and appropriate jumpers would modify the board for a particular slot in the backplane. The backplane is wired to provide power and inter-board signal paths.

As a result of the new design changes, performance has improved. One aspect of performance has been characterized by reduced drift. Figure 4 is a plot of the drift of all five channels of DC position voltage versus time. For each channel of data, the initial data value is subtracted from subsequent values. The drag position measurement has a full scale value of ± 12.5 V dc. The worst case drift is less than 0.1 % of FS/ hr. This performance is a considerable improvement over the older design, and is mainly due to the integrated circuit technology and the new signal processing scheme.

Compensation System

With the exception of replacement operational amplifiers and minor modifications, the original compensation electronics are still in use. The basic blocks are an input summing stage in which a DC offset may be added for model position changes, an integrator stage, and three lead-lag stages in series.

A mixer is used for combining proportional, integral, and compensated signals. A current feedback signal is mixed with the compensated control signal in the final stage for improved model stability. Except for pitch and yaw crossover circuits, the circuitry for each of the five degrees of freedom is basically identical. Sliding modular circuit cards are used for access to various gain potentiometers and lead-lag component switching.

This design reduces noise by eliminating long wires from panel switches to filter components. Originally, all interconnections within the compensation system were made through a patch panel for experimental purposes. The system was unreliable due to corroded contacts and is presently hard-wired.

Power Supply System

Many of the reliability problems and performance limitations of the 6 Inch MSBS are directly related to the power supply system. While at Langley, more man-hours were consumed repairing and modifying power equipment than were expended to improve system performance. MIT modified the power supply system configuration several times to increase drive current capability. The present scheme is an effective system using custom designed and salvaged components. Figure 5 is a basic schematic of the existing power supply subsystems.

The primary supplies for controlling the translational degrees of freedom are uniquely designed full wave rectifiers utilizing thyatron tubes for switching three-phase 440 Vac. Since the thyatron supplies are unipolar, they are oppositely biased through water cooled resistors by a regulated d-c power supply.

The load current may be varied in magnitude and polarity by controlling the current output of the thyatron units. A 250 V, 100 A unit is used for lift, while 120 V, 50 A units are used for side and drag. The thyatron supplies are driven directly by the ± 15 V control signals.

The regulated d-c supply consists of two B-47 aircraft starters. The two stacked units each contain two power supplies which rectify three phase 440 Vac into regulated 28 Vdc up to 1000 amperes. The four power supplies are wired in series and tapped at different points to provide appropriate voltage levels to each subsystem. The drag control coils are provided with 112 V, while lift and side are each supplied with 28 V. In addition, the Helmholtz pair for the uniform magnetizing field is driven by the 56 V tap. Before the procurement of the aircraft starters, one MIT configuration included d-c welders.

Though the saddle coils for pitch and yaw were originally driven by thyatron supplies, a motor-generator set has been in use in recent years. A large a-c motor drives three 1943 vintage aircraft generators to their maximum rpm range. The generators produce a maximum of 30 Vdc at several hundred amperes. The generators were modified by MIT to allow their fields to be driven by bi-polar, solid-state servo amplifiers

producing ± 40 Vdc at 15 A. This design allows high current of either polarity, avoiding the need for a separate bias supply. The inner saddle coils are driven by a single generator while the outer saddle coils are driven by two generators in series. MIT intended to use a similar system for all degrees of freedom as an alternative to expensive bi-polar switching power supplies.

Water-Cooled Resistors

The present configuration of the power supplies and positioning electromagnets requires power resistors to properly bias the coil loads. These low valued resistors have the potential to generate large amounts of heat, and need to be cooled. The original system used individually crafted water-cooled power resistors as shown in figure 6. Their unique construction involved a fixed length of Nichrome wire coiled within a glass tube and silver soldered at each end to a lug. A clear rubber hose was clamped over two tube holders forming a water tight jacket around the glass tube. Water flows through the tube to cool the wire inside. All metal parts were made from stainless steel.

These individually hand-crafted power resistors had a useful life of about 175 hours before failure. Failures were characterized by a gradual increase in resistance value as electrolytic corrosion of the nichrome wire at the water intake tee occurred. The sudden open circuit that resulted usually caused the system to lose control of model position. Clearly, a new design was needed to alleviate this problem.

A simple solution to this problem incorporates off-the-shelf water heater elements. As seen in figure 7, the new design includes a large aluminum tank with enough volume for all 36 of the necessary heater elements. The tank measures 30 in. O.D. and 28 in. high and has a volume of 39.5 cu ft. The resistor elements have an Incoloy sheath and range in overall length from 9 in. to 23 in. and in rated wattage from 2000 W to 6000 W. The elements are connected electrically in parallel and series combinations to achieve the desired resistances. A failure of one element can be detected by a discrete jump in total resistance. If necessary, an individual element can be easily replaced. The tank receives a continuous supply of low pressure water and includes safety interlocks. The success of this design is evident in the fact that no failures have occurred since the initial installation.

WIND TUNNEL TESTING

The first aerodynamic test conducted at Langley in the 6 inch MSBS was a store separation test. The objective of this test was to lower a suspended ogive cylinder model from a test section cavity into the freestream, allowing for cavity-model interactions to be studied.

A store separation demonstration was previously accomplished at the NASA Langley 13 inch MSBS. This facility uses optical position sensors to monitor the model position and does not allow for a wide range of vertical model positions as described in reference 3. Therefore, the suspended model remained stationary during the

demonstration while a plexiglas cavity structure, originally enclosing the model, was mechanically moved away to demonstrate store separation. Due to the unique capabilities of the 6 inch MSBS, the model can be lowered from a stationary cavity built into the test section. Optical model position detection would be very difficult with this configuration.

In preparation for the test, the test section was modified with an insert simulating the undercarriage of a fuselage. The insert, which consists of a leading edge, cavity, and trailing edge, is integrated into the existing test section. The leading edge of the insert was designed to smoothly deliver the incoming flow to the cavity. The cavity was designed specifically for an ogive cylinder test model.

The model, shown in figure 8, is one inch in diameter and five inches long. The cavity-model clearance is $1/2$ a model diameter front and rear, and $1/4$ diameter on each side. The trailing edge of the insert is a flat surface expanding the test section back to its original area. Figure 9 is a photograph of the test section with the insert.

System Calibrations

Prior to testing, several calibrations had to be completed on the system. These included a wind speed calibration; horizontal and vertical velocity profiles; drag, lift and lift position calibrations. These tests were necessary because of the physical changes in the tunnel and the fact that previous force calibrations had used a different model. Because of the reduced cross-sectional area of the tunnel, a new wind speed calibration was needed. A pitot-static tube was inserted into the center of the test section to measure the dynamic pressure. The dynamic pressure was then related to the pressure difference measured across the contraction.

During testing, the pitot-static tube is removed. However, the pressure difference across the contraction can still be monitored and the velocity obtained from the calibration. The velocity was also related to the fan speed, which can be used for a rough estimate of the wind speed. With the insert in the test section, the maximum velocity in the test section increased from Mach 0.5 to Mach 0.6. Figure 10 is a graph relating the dynamic pressure measured by the pitot-static tube and the pressure difference across the contraction.

After the wind speed calibration was completed, horizontal and vertical velocity profiles of the flow were recorded. These profiles were taken to verify that the flow was uniform across the test section. Figures 11 and 12 are horizontal and vertical profiles across the test section taken at Mach 0.5. Profiles at Mach 0.1 were also taken. Horizontally, the velocity is skewed so that there is about a three percent difference from one side to the other. There is approximately a two percent difference from the top to the bottom. Since most of the testing was done in a small area, these differences in the velocity across the test section were acceptable.

A drag calibration on the model was preformed next. The model was positioned just below the cavity, and a drag force was applied to it using weights and a pulley. A

feedback signal proportional to the drag current feedback signal was recorded as the weights were increased from 0 to 200 grams. This current feedback signal was monitored during testing to determine the drag forces on the model. The relationship between the current feedback signal and the drag was linear and a straight line fit of the data was sufficient. This data is presented in figure 13.

Two more drag calibrations were performed to investigate the relationship between drag and lift. The calibrations were carried out as before, except that a negative lift force was applied to the model during calibration. The lift force proved to have a negligible effect on the drag calibration, therefore simplifying the data reduction process.

The model was also calibrated in lift. Weights were applied to the model and the lift current feedback signal was recorded. A straight line was again fitted to the data which is presented in figure 14.

Finally, a lift position calibration was performed. The model was lowered out of the cavity and its position was monitored using a cathetometer. The cathetometer reading was correlated to the lift position signal which could be monitored during testing. The calibrations allow drag and lift forces on the model to be monitored during testing and related to the position of the model relative to the cavity.

Flow Visualization

The flow visualization system used for the store separation test consisted of two basic components. A fog generator was placed in front of the contraction to inject vaporized propylene glycol into the flow. At the test section, two 5 mW lasers and beam spreading optics were used to illuminate the flow above and below the model. The optics spread the beams into light sheets which could be positioned either perpendicular or parallel to the model. A video system including a CCD camera was used for live viewing and recording of the flow around the model.

The first series of flow visualization tests involved lowering the model from the cavity into a set of smoke streams. Figure 15 is a photo of the model suspended just below the cavity. Before experimenting with the light sheets, the test section was brightly illuminated to observe the position of the smoke streams. Figure 16 shows smoke contouring to the bottom of the model at $M=0.15$. For test runs with the light sheet, smoke streams were positioned approximately 1/2 inch from the cavity at approximately 1/4 inch spacing. The smoke streams were then observed using two longitudinal light sheets to illuminate above and below the model along its axis of symmetry.

As the model enters the oncoming flow, the smoke streams are shown to contour to the model followed by the entrainment of smoke into the boundary layer. Further lowering of the model reveals the uppermost smoke stream contouring to the top of the model. This stream is very compact along the model nose, however, as the stream reaches the forebody, it begins to expand greatly. This pattern does not occur below the model. Figure 17 illustrates this phenomena. This is believed due to separation occurring

over the upper surface (leeward side). Separation may result from the upward bending of streamlines in the vicinity of the model nose and the cavity leading edge as the flow adjusts itself to the cavity. Therefore, the model may experience an effective angle of attack with an associated cross-flow resulting in separation on the leeward side.

It was decided that further flow visualization tests were necessary to study the model-cavity interaction. A second series of flow visualization tests was attempted using a cross sheet to view the flow between the cavity and the model. The viewing area allowed access of the model nose and most of the forebody. Upon lowering the model approximately 1/4 of a diameter out of the cavity, the cross sheet revealed an undistinguishable smoke pattern between the cavity on the model that reached into the cavity. It is believed that no distinguishable patterns are revealed in this region due to the extremely high turbulence levels present in cavity flow.

However, upon further lowering the model, a distinct lightning-shaped pattern emerges from the undistinguishable pattern extending to the model. This pattern wraps around the model revealing the entrainment of smoke in the boundary layer. These patterns occur along the model nose, but the lightning-shaped pattern tends to break up along the forebody. It is not presently known what the lightning-shaped pattern represents. Figure 18 illustrates cross sheets at two locations on the model nose. Further flow measurements using, for example, Laser Doppler Velocimetry are necessary to detail this phenomena.

Store Separation Tests

The initial store separation tests occurred at fixed Mach numbers between 0.1 and 0.3. Drag forces acting on the model were extracted through a calibration of the drag current feedback signal previously discussed. Results for a Mach number of 0.25 are presented in figure 19. The turbulent nature of cavity flow is quite evident from the scatter present while the model is in the cavity. The scatter is shown to decrease as the model begins its move out of the cavity. Furthermore, the drag coefficient increases as the model begins to lower. This increase is evident until the model is completely clear of the cavity. Further lowering of the model has no effect on the drag coefficient, signaling the model is free of any cavity interactions and is completely emerged in the freestream.

Upon completion of the store separation tests at fixed Mach numbers, a series of tests was conducted with the model suspended just inside the cavity so that simultaneous lift and drag measurements could be made with increasing Mach numbers. The Mach number range for this series of tests was 0.1 - 0.5. Lift and drag coefficient data are presented in figure 20. As discussed previously, measurements do fluctuate significantly about a mean, especially at the higher Mach numbers due to the turbulent nature of cavity flow. Therefore, lift and drag values presented in figure 20 represent mean values of data taken over 30 second intervals at 1 Hz.

Results indicate a significant decrease in the drag coefficient from 0.37 to 0.15 with a Mach number increase from 0.1 to 0.3, respectively. For Mach numbers greater than

0.3, the drag coefficient remains nearly constant ($0.15 > C_d > 0.13$), therefore showing little dependence with Mach number in this range. It is interesting to note that for Mach numbers greater than 0.3 the drag coefficient of the model in the cavity is significantly lower than that measured in the freestream. Figure 19 shows that the drag coefficient of the model in the freestream is approximately 0.35.

Lift coefficient results show that for the entire Mach number test range, a small negative lift acts on the model. This was observed during testing as the model position would tend to lower with increasing Mach number as if the model was being "pushed" out of the cavity. Due to this effect, it was necessary to monitor the EPS signal so that adjustments could be made to bring the model back to its original position. A general overview of the lift coefficient data shows that trends are not as nearly pronounced as for its drag counterpart; however, some trends are established. For instance, an initial increase occurs in the lift coefficient from -0.11 to -0.06 with increasing Mach numbers between 0.1 and 0.15. After this initial trend, increasing the Mach number has little effect except for a slight decrease in the lift coefficient.

These tests were repeated using a 1/2 scaled version of the original store model. Trends in lift and drag data with varying Mach number are similar between the scaled models; however, a significant spin developed on the smaller model not observed in the original tests. The spin was counter-clockwise (front view) and signified a rolling moment produced by the cavity-model interaction. A spinning motion was not observed with the model in the freestream. The spin occurred at Mach 0.2 and was preceded by a pronounced rocking motion at lower Mach numbers. Present with this spinning motion were pronounced oscillations in pitch starting at $M=0.1$. As described earlier, these oscillations were only observed on the larger model at $M=0.3$ as the model separated from the cavity.

CONCLUSION

The initiative to make the 6 Inch MSBS fully operational was successful. The photographs of figure 21 show three views of a space shuttle model in suspension. The system's angle of attack capabilities are evident. Although roll control is not presently operational, roll stiffness using cambered model cores has been demonstrated.

Implementation of the new EPS electronics has significantly improved system performance through reduced noise and drift. System reliability was greatly improved with the addition of a new water cooled resistor system as well as rewiring the compensation system interconnections.

Simulation of cavity store separation was successfully demonstrated. Moreover, it is unlikely that the tests performed in the 6 Inch MSBS could be duplicated in other facilities. The system performed flawlessly during the tests.

The power supply system of the 6 Inch MSBS remains the primary weakness. A 1970 MIT proposal to Langley for continued studies of the system requests funding for a

complete power supply upgrade. Only a small portion of the proposal was ever implemented. Optimum performance will not be achieved without a ten-fold increase in power capability. Bi-polar, solid state power supplies would increase model stiffness and system frequency response.

Future enhancements to the system would include the replacement of existing power supplies and compensation system electronics. A minicomputer has been purchased for implementation of digital control of model position in five degrees of freedom. The system has not been fully calibrated while at Langley; therefore, a full five degree of freedom force calibration is planned. A special balance fixture designed specifically for suspension in the 6 inch MSBS has been fabricated.

ACKNOWLEDGEMENTS

The authors would like to express their gratitude to Dr. Colin Britcher of Old Dominion University for his technical guidance and support. Further appreciation goes to the Pressure and Flow Measurement Section and Photo-Optical Instrumentation Section for their assistance.

REFERENCES

1. Stephens, Timothy: Design, Construction, and Evaluation of a Magnetic Suspension and Balance System for Wind Tunnels. NASA CR-66903, 1969.
2. Daniels, Taumi S. and Tripp, John S.: Improvements to an Electromagnetic Position Sensor for a Magnetic Suspension Wind Tunnel. International Instrumentation Symposium (Albuquerque, New Mexico), May 1988, pp. 65-70.
3. Tchong, P. and Schott, T. D.: A Five Component Electro-Optical Positioning System. 12th International Conference on Instrumentation in Aerospace Simulation Facilities (Williamsburg, Virginia.), June 1987, pp.322-333.

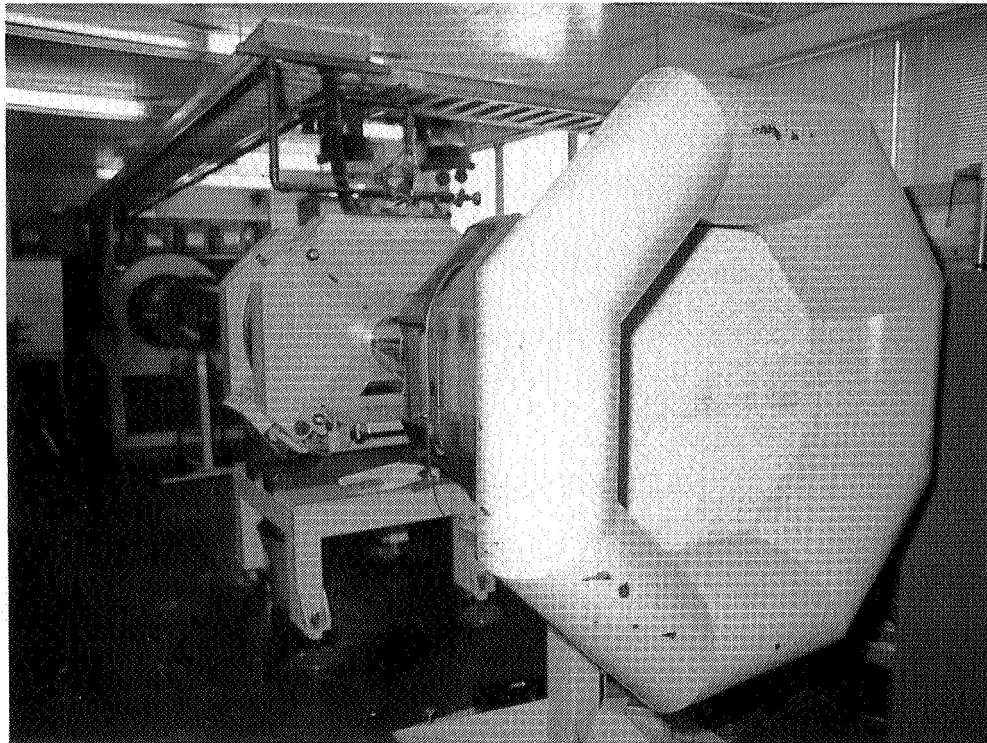


Figure 1. Downstream view of 6 inch MSBS.

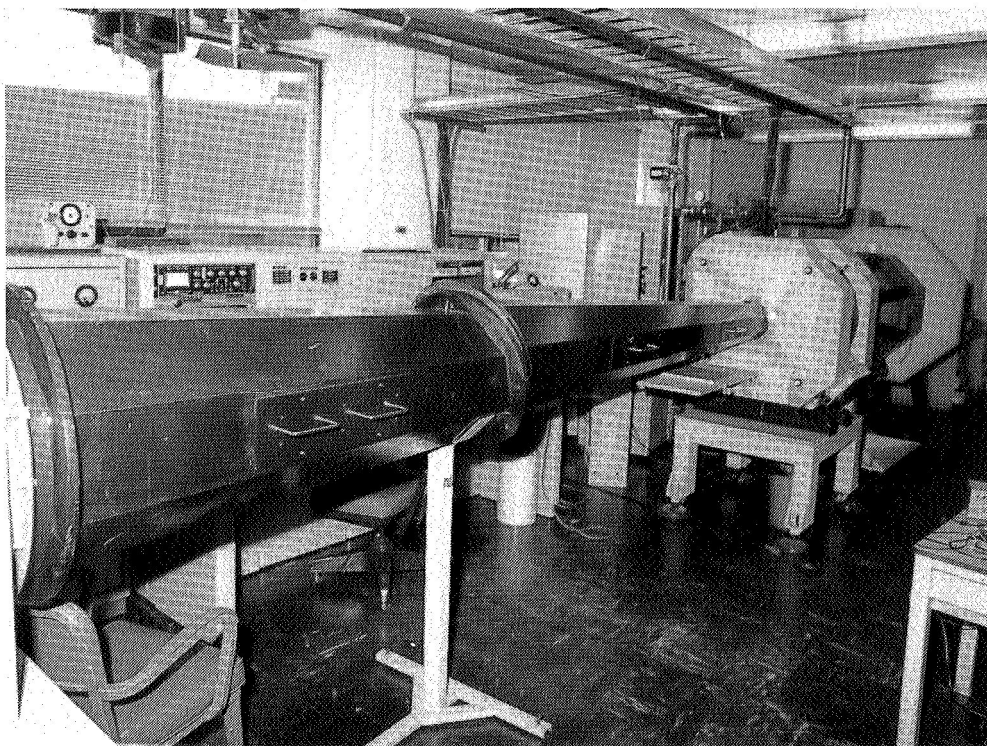


Figure 2. Upstream view of 6 inch MSBS.

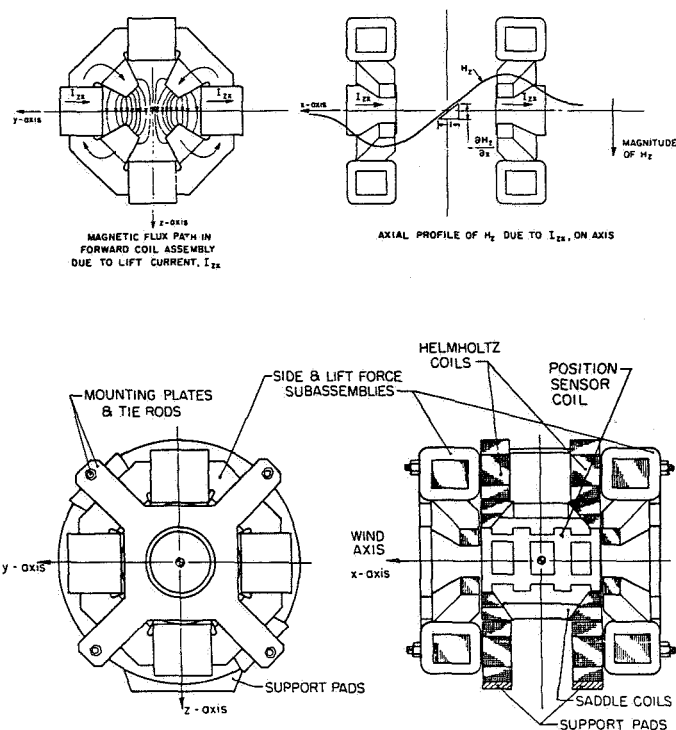


Figure 3. End and sectional views of magnet configuration.

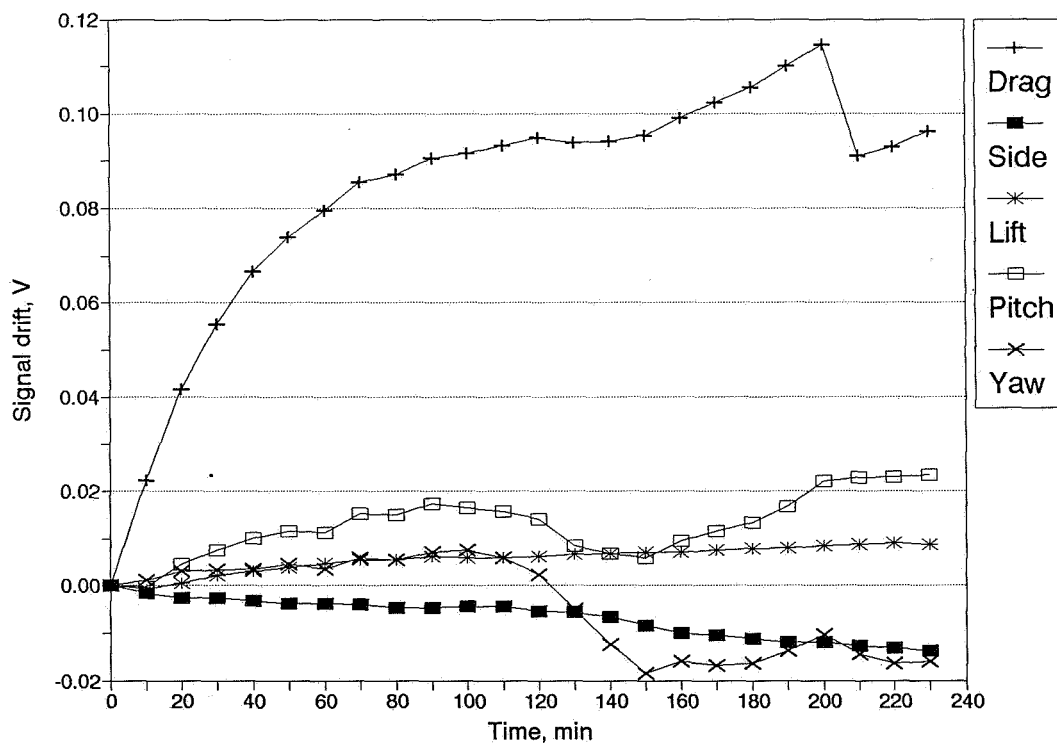


Figure 4. EPS position signal drift.

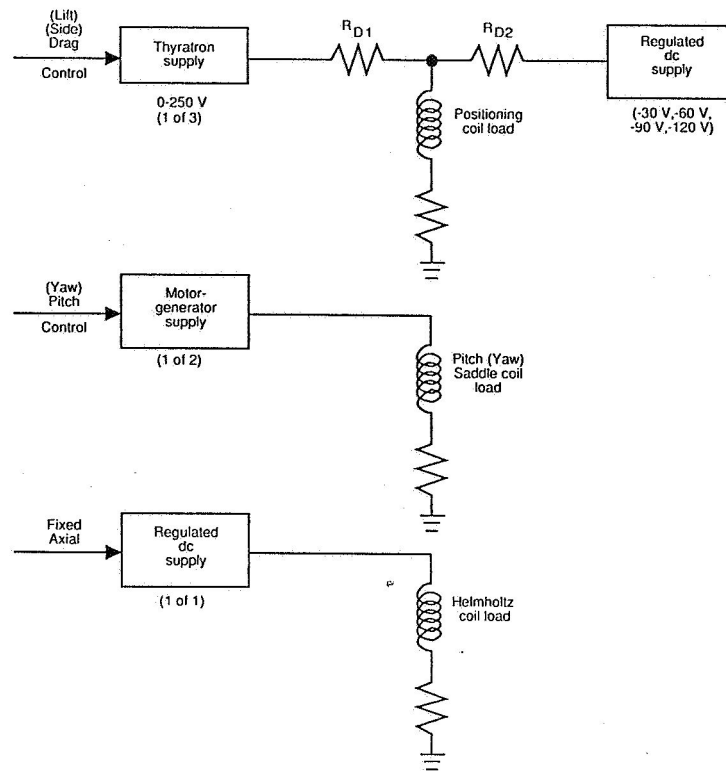


Figure 5. Power supply system schematic.

ORIGINAL PAGE

BLACK AND WHITE PHOTOGRAPH

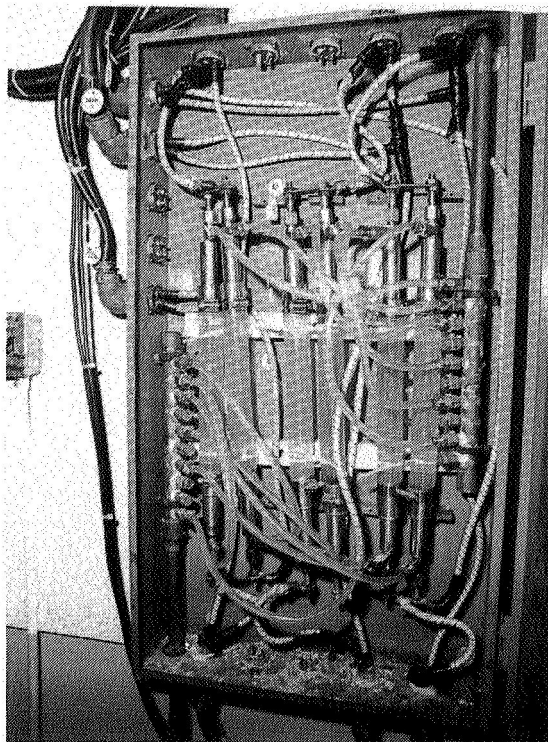


Figure 6. Original water cooled resistors.

ORIGINAL PAGE
BLACK AND WHITE PHOTOGRAPH

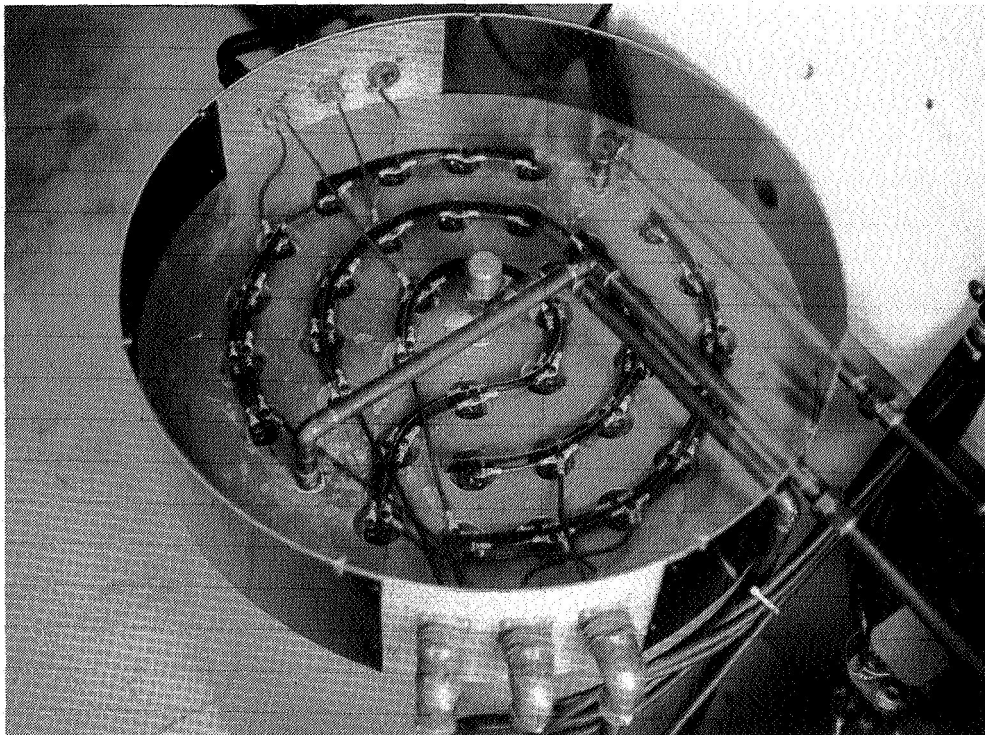


Figure 7. New power resistor system.

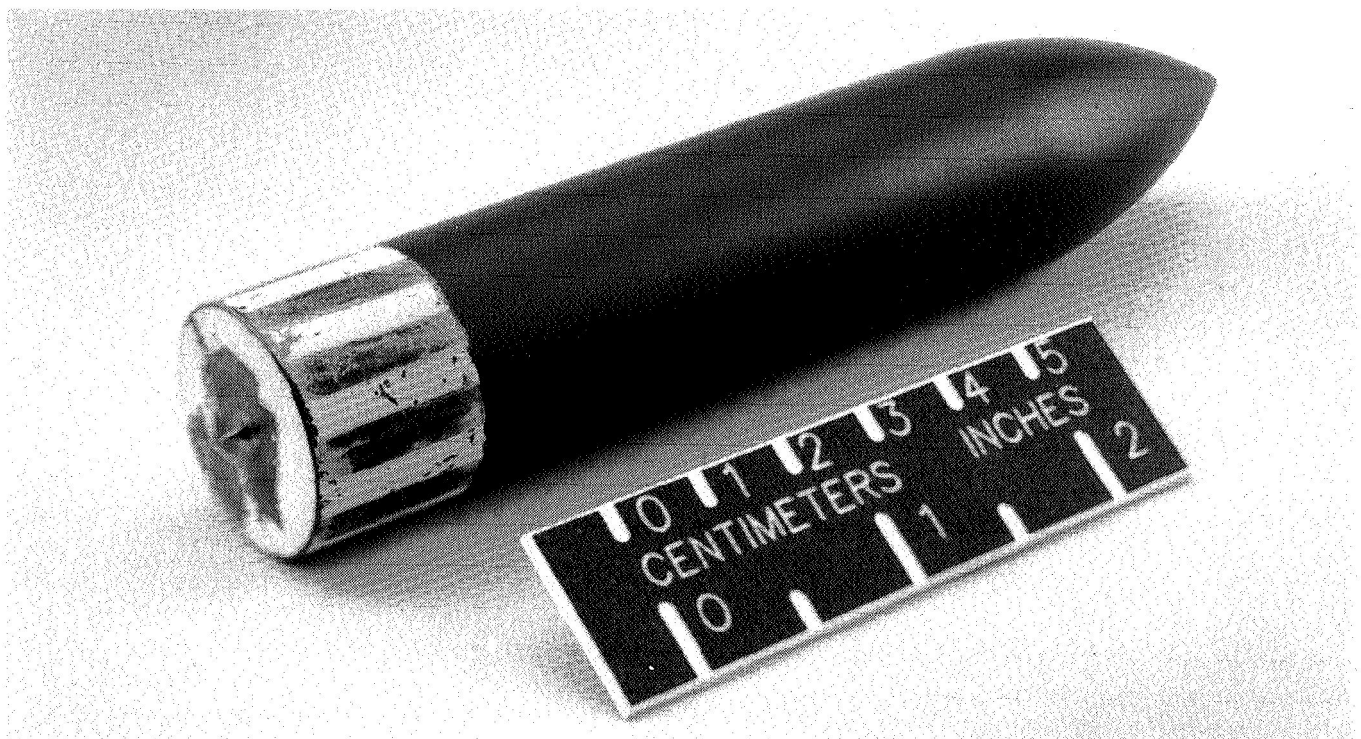


Figure 8. Store separation model.

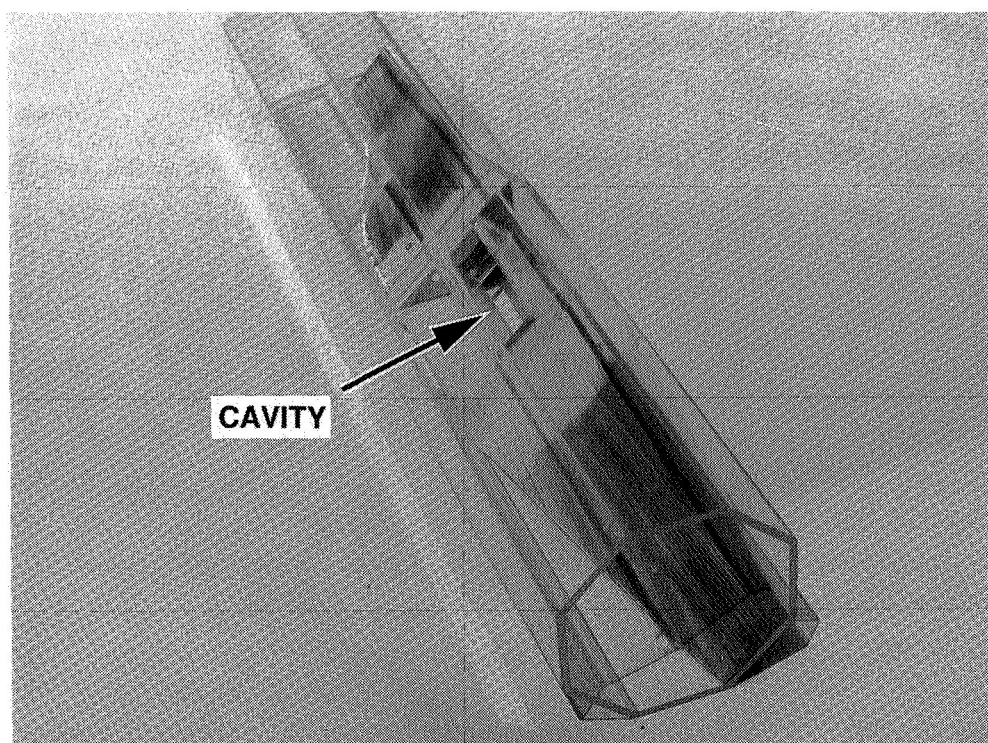


Figure 9. Test section with cavity insert.

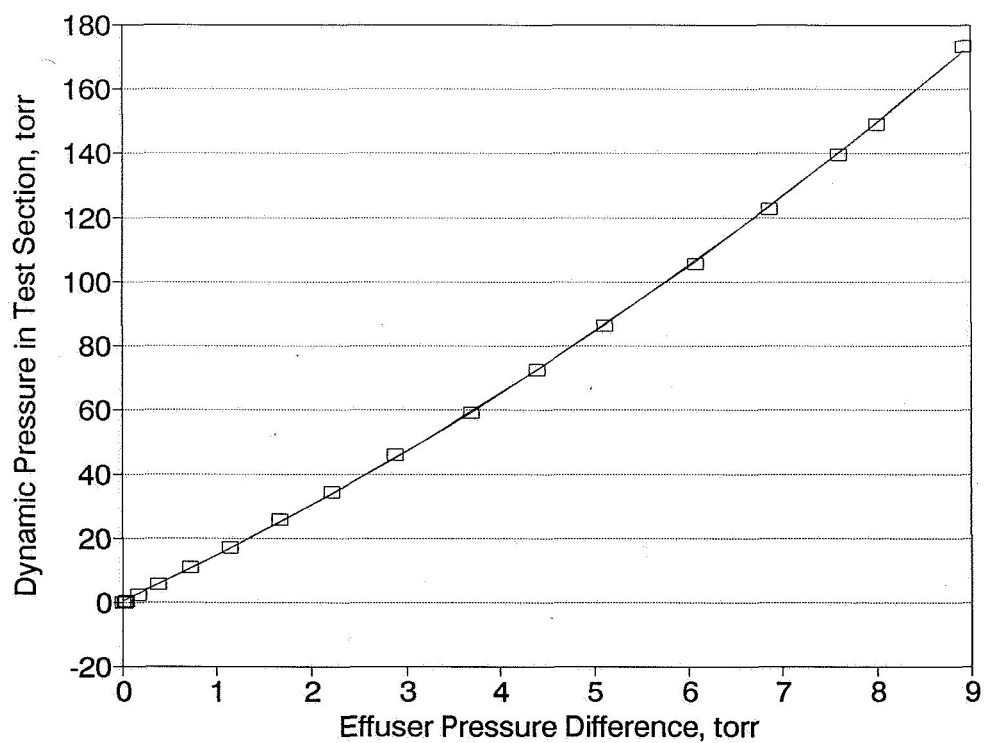


Figure 10. Test section calibration.

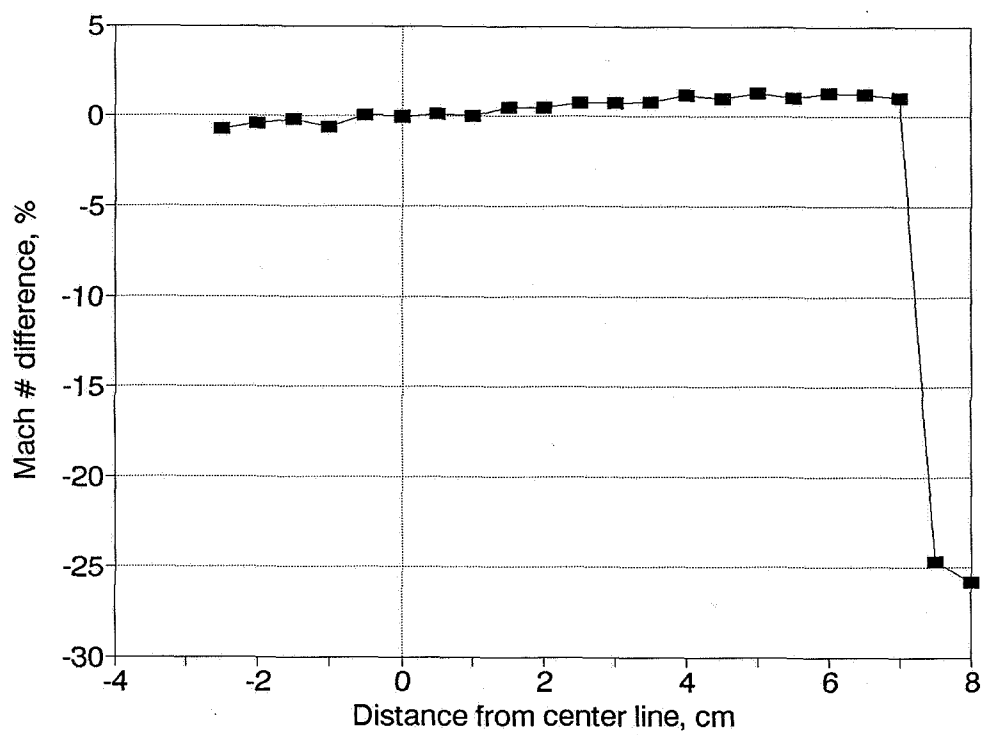


Figure 11. Horizontal velocity profile ($M=0.5$).

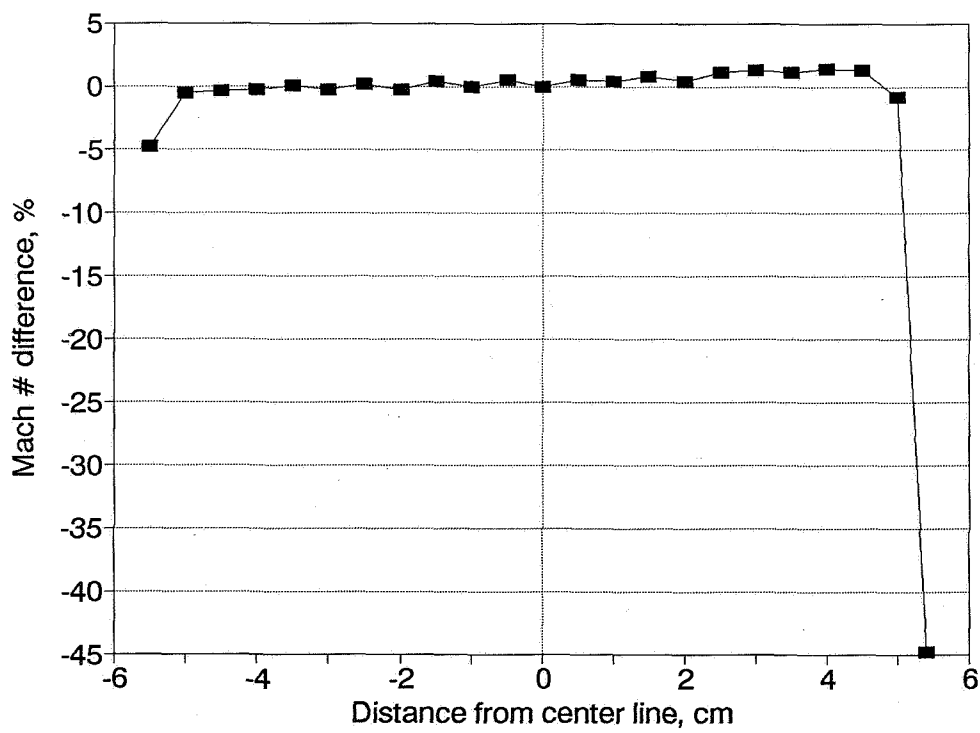


Figure 12. Vertical velocity profile ($M=0.5$).

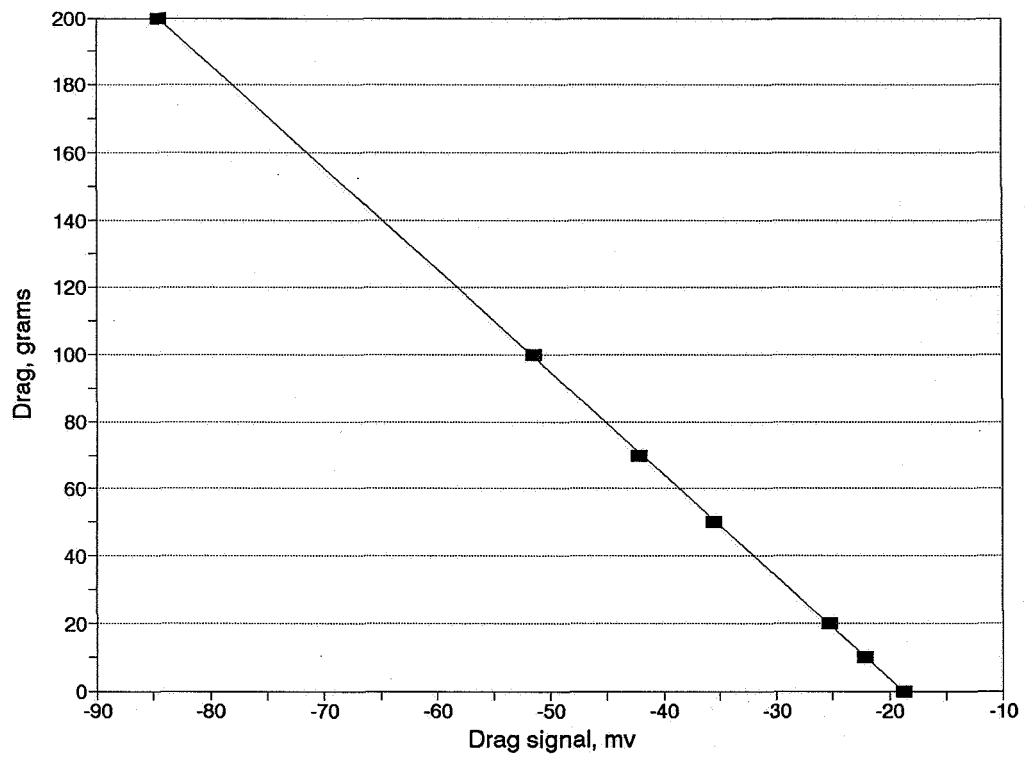


Figure 13. Drag calibration of store separation model.

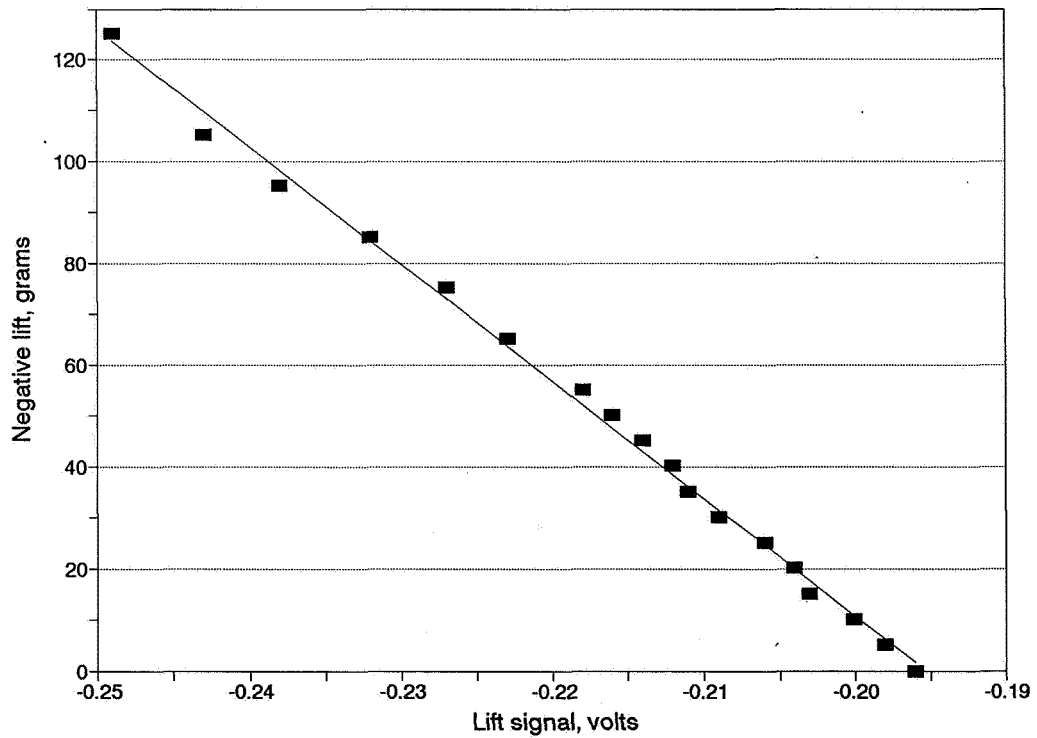


Figure 14. Lift calibration of store separation model.

ORIGINAL PAGE
BLACK AND WHITE PHOTOGRAPH

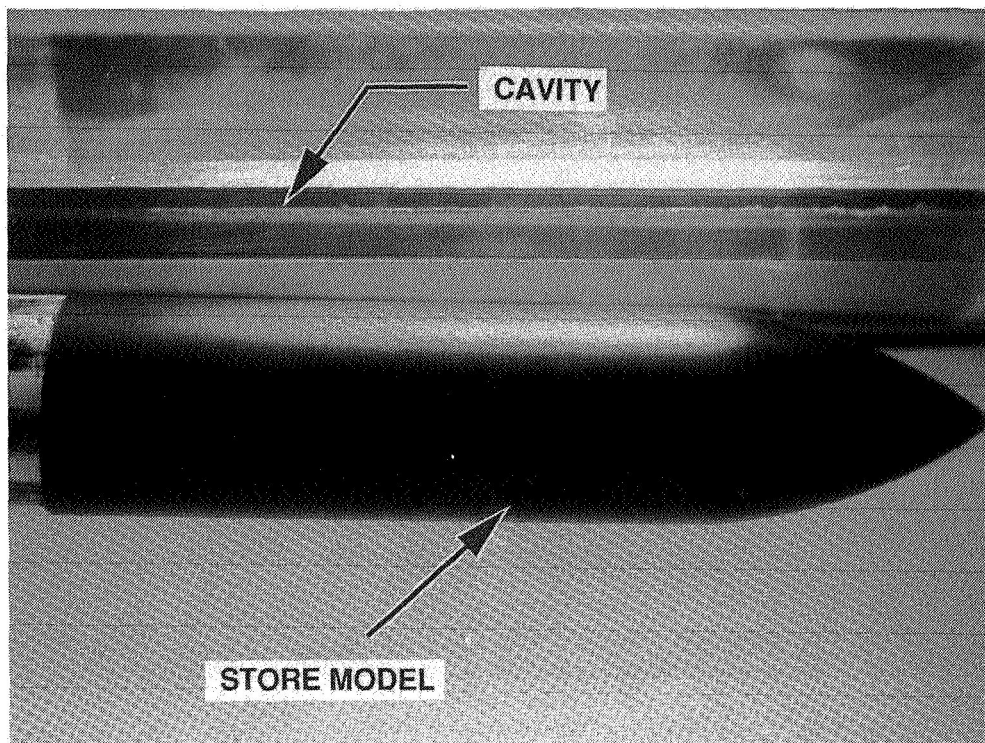


Figure 15. Suspended model below cavity.

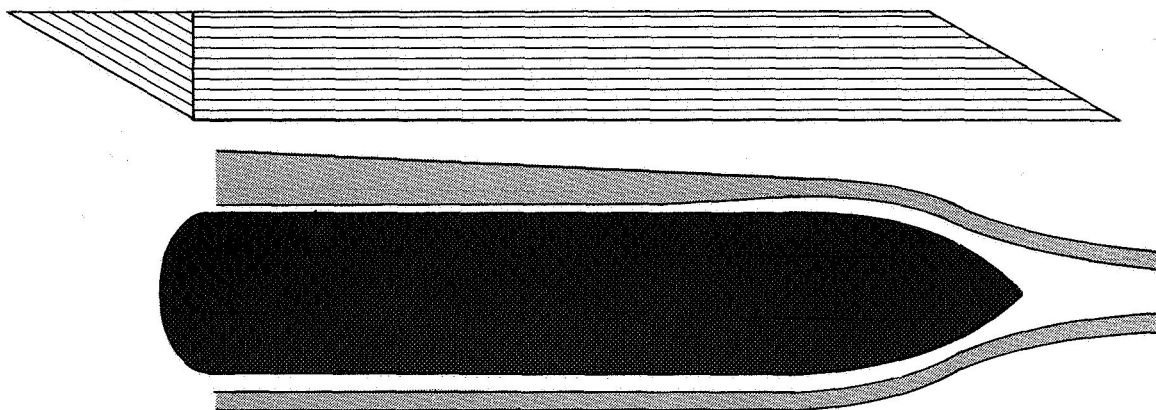


Figure 16. Smoke contouring to model.

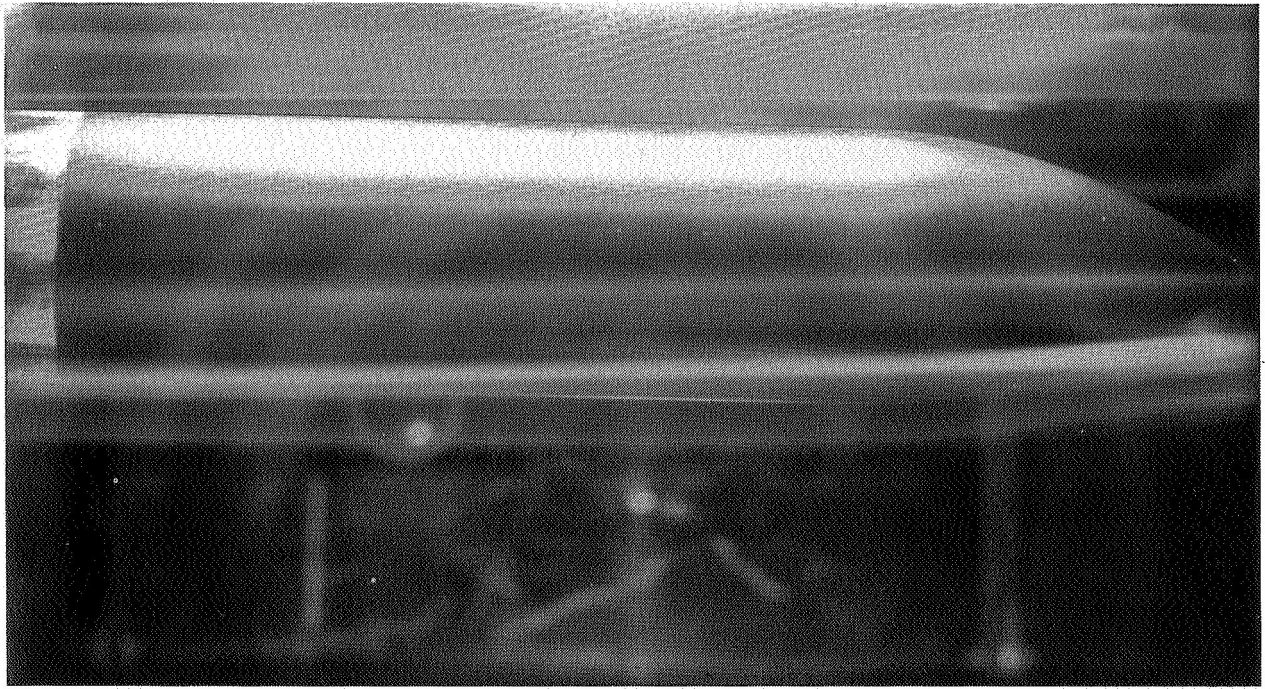


Figure 17. Longitudinal light sheet showing cavity interaction ($M=0.15$).

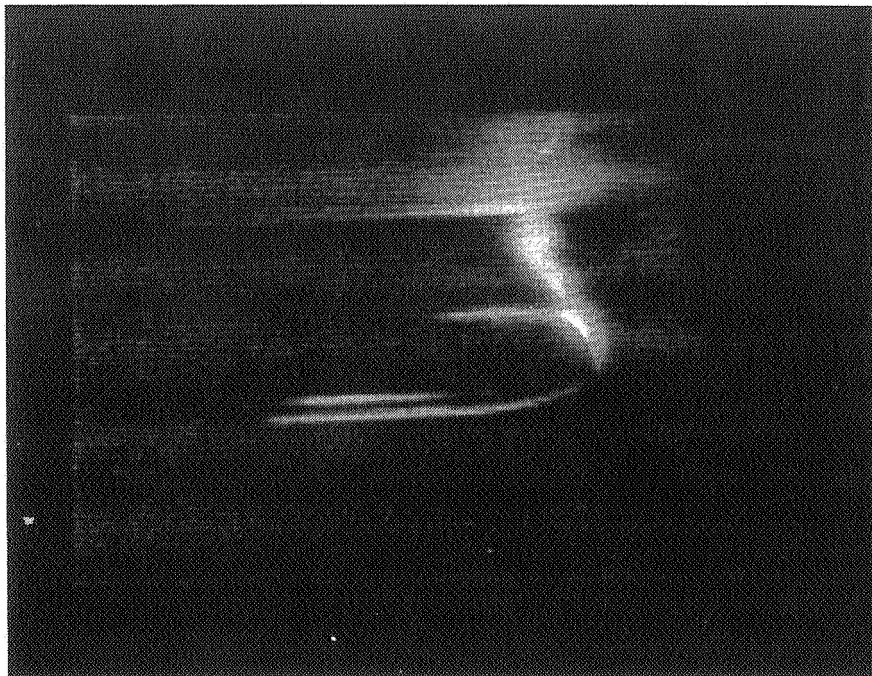


Figure 18. Cross light sheet showing cavity interaction ($M=0.15$).

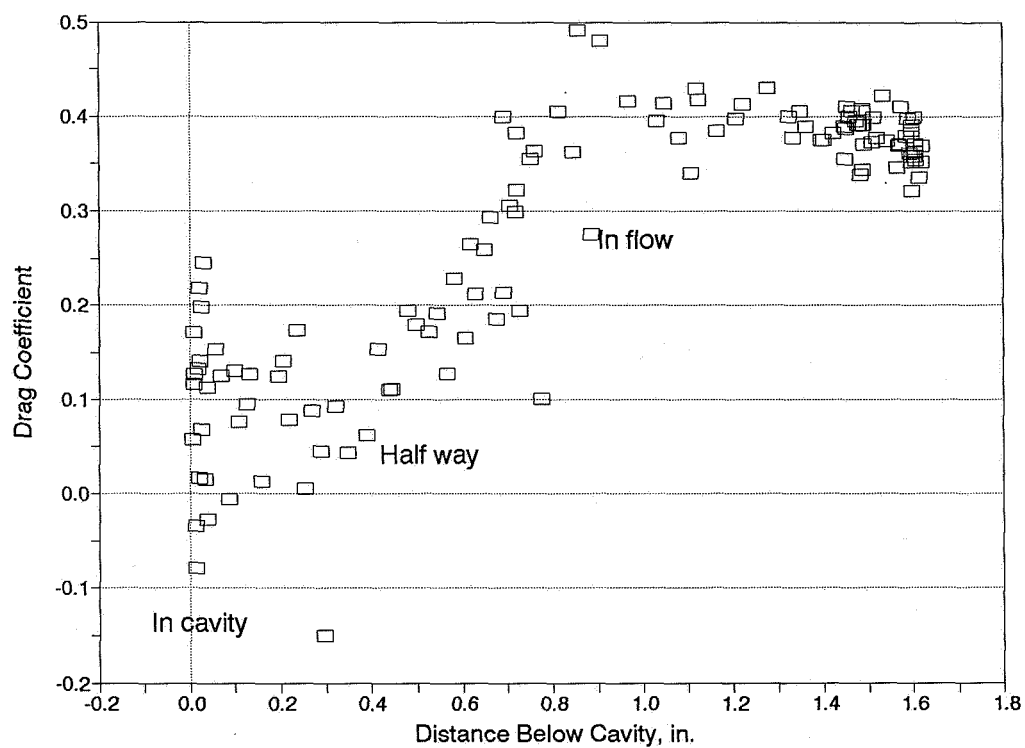


Figure 19. Effect of model position on drag coefficient.

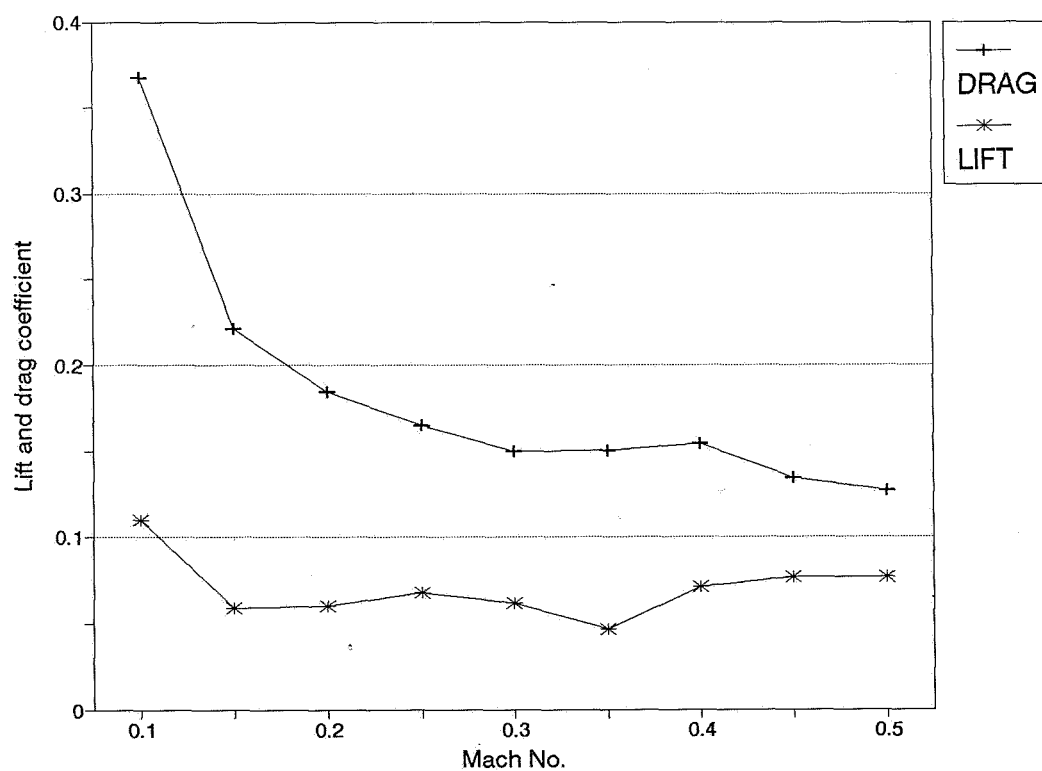


Figure 20. Effect of Mach number on lift and drag coefficient.

ORIGINAL PAGE
BLACK AND WHITE PHOTOGRAPH

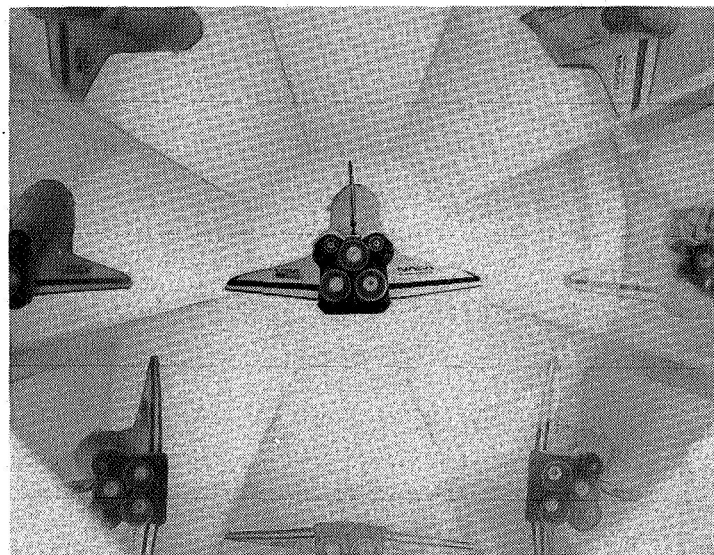
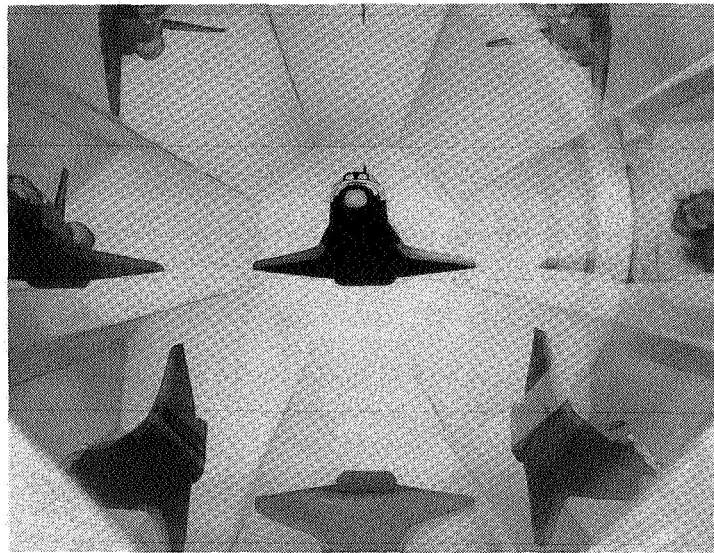
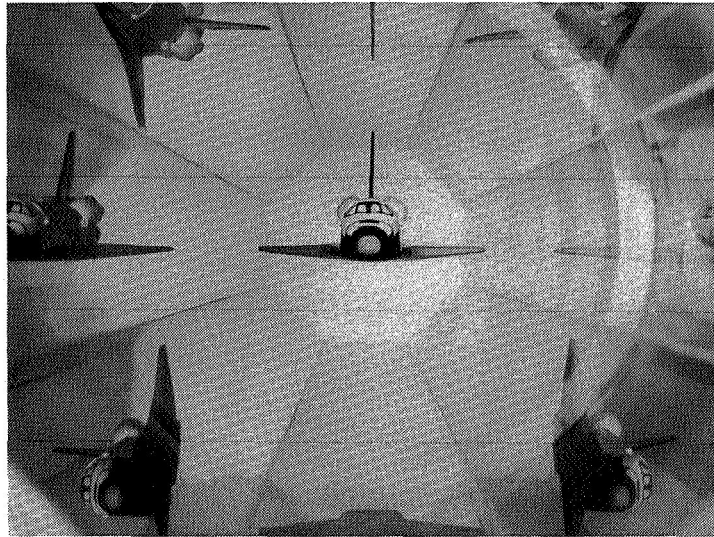


Figure 21. Three photographs of space shuttle model.

**PROGRESS OF MAGNETIC SUSPENSION AND BALANCE SYSTEMS
FOR WIND TUNNELS IN THE USSR**

Kuzin A.V.
Moscow Aviation Technological Institute (MATI)

Vyshkov Y.D.
Moscow Aviation Institute (MAI)

Shapovalov G.K.
Central Aero-Hydrodynamic Institute (CAHI)

SUMMARY

Magnetic Suspension and Balance Systems (MSBS) for wind tunnels are being developed in order to solve the principal problems of aerodynamics which cannot be solved by conventional means: measurement of aerodynamic loads acting on the aircraft models without the effects of mechanical supporting devices, and study of base pressure, etc. This paper traces the progress of MSBS for wind tunnels in the USSR. The paper describes electromagnetic configuration, position sensing, and control and calibration systems of two wind tunnel MSBS existing in the USSR. The features of high-angle-of-attack control and roll control are discussed. The results of preliminary experiments on high-angle-of-attack and roll controls, digital control, and aerodynamic testing are also presented.

INTRODUCTION

Doctor Grodzovsky G.L. was the first Russian scientist who tried to realize magnetic suspension of the model for the wind tunnel in CAHI in 1947 (ref. 1).

At present there are two systems of electromagnetic suspension for wind tunnels in the USSR. One was constructed in 1983 as a result of collaboration of the MAI and CAHI and was intended for studies of models with six degrees of freedom in a subsonic wind tunnel, the working part of which measured 400 mm \times 600 mm (ref. 2).

The second system was created in the MAI in 1989; it is designed for laboratory investigations and for development of the technology of magnetic suspension. The suspension has six degrees of freedom and its working part measures 300 mm \times 400 mm. Fig. 1 displays a model suspended in the suspension system of the Moscow Aviation Institute (ref. 3).

ELECTROMAGNETIC CONFIGURATION

Both systems were comprised of seven electromagnets which were arranged as shown in Fig. 2. All electromagnets have copper windings with natural cooling. The bias electromagnets (10, 11) are equipped with motor-driven variacs. The control electromagnets (2, 3, 4, 5) are provided with impulsive bipolar transistorized power sources. The axial electromagnet (1) is equipped with a thyristor power supply.

POSITION SENSING SYSTEM

The optical system for the determination of model position is based on usage of photodiode regions. Rays of lights of special form cross the model as shown in Fig. 3. Position of the model can be calculated with the aid of the measured position of the model shadow on the surfaces of detectors. The original design of the sensitive system (ref. 4) ensures determination of vertical and horizontal displacements of the model in one optical channel as it follows from simple expressions (Fig. 4):

$$\begin{aligned} V1 &= K1 \times Y1 + K2 \times Z1; \\ V2 - V1 &= 2K1 \times Y1; \end{aligned}$$

$$\begin{aligned} V2 &= K1 \times Y1 + K2 \times Z1; \\ V2 + V1 &= 2K2 \times Z1, \end{aligned}$$

where $Y1$, $Z1$ are displacements of the model.

CONTROL SYSTEM

Both systems of electromagnetic suspension have analog control systems. The peculiarity of MSBS for aerodynamic studies is the presence of large air gaps between the model and electromagnets. This presence of large gaps is determined by the demand of the similarity of the experimental conditions to the real ones of aircraft. The natural instability of the suspended object and the existence of limitations for value of control voltages on windings of electromagnets leads to limited area of stability of the model in space and to limited range of permissible aerodynamic leads. Figure 5 presents a structural scheme of the EMS control system in the vertical plane. An analogous scheme is used for stabilization of the model in the lateral plane. Their design-adopted control algorithms provide a maximum area of stability of the suspended object in the presence of limitations of control actions (refs. 5, 6, 7).

EXTREME ATTITUDE TESTING

There is considerable interest in the use of MSBS for suspension of winded models. Not long ago the MSBS of MAI-CAHI was modified. The MSBS was equipped with more powerful electromagnets. The light sources (lamps) and photodiode elements of the optical position sensing system were installed with the possibility of rotation (Fig. 6). This system is very good for setting the model at a high angle of attack. It is only necessary to rotate the lamps and photodiode elements during the operation of the MSBS when the model must be set at a desirable angle of attack. An axisymmetric model was thus successfully suspended over the range of angle of attack from zero to thirty degrees (Fig. 6). An angle of attack range of zero to sixty degrees is expected for axisymmetrical models without relocating lateral electromagnets. Work is presently underway to extend the useful range of angle of attack to sixty degrees. This involves using the digital control system and adaptive control algorithms.

The modified MAI-CAHI MSBS was equipped with eight electromagnets for generation magnetic roll torques (Figs. 2, 7). Several possible constructions of the optical roll attitude sensor were studied. The first successful experiments concerning roll control, including passive and active means, were made (Fig. 6).

CALIBRATING AND AERODYNAMIC TESTING

It is necessary to calibrate a given model before carrying out the aerodynamic testing. In the process of calibration, known values of static forces and moments are applied to the model and position of the model and currents of the electromagnets are measured. The range of applied forces and moments covers the range of expected aerodynamic leads. Several possible equations for magnetic forces and torques were studied. Aerodynamic leads are computed by means of a digital minicomputer PDP 11-34 on the basis of established empirical dependencies between currents of electromagnets, position of the model, and external leads. Magnetic forces and torques can be expressed as the squared forms (ref. 8):

$$Pq = \frac{1}{2} \sum_{k=1}^n Ik \sum_{l=1}^n Il \times \frac{\partial Lkl}{\partial q},$$

where Pq - force or torque; q - coordinate of position; Lkl - inductances of electromagnets.

The first aerodynamic tests were carried out and showed good results.

CONCLUSION

Present plans are to concentrate on aerodynamic tests, on comparison of conventional means results and MSBS results. Work is presently underway to develop a digital control system. Hardware PDP 11-34, ADC, DAC, and software for a digital control system are in hand now.

The authors express their gratitude to Dr. R. A. Kilgore, NASA Langley, and to the Organization Committee of the International Symposium for their support and for giving us the opportunity to present this work to the International Symposium on Magnetic Suspension Technology.

REFERENCES

1. Beliaev, L. B.; and Shermanov, P. M.: Magnetic Suspension of Models in Wind Tunnels. Surveys, Translations, Abstracts. Technical Information Department of the N. E. Zhukovsky Central Aero-Hydrodynamic Institute, Report No. 557, 1979, p. 58.
2. Vyshkov, Y. D.; Kovalnogov, S. A.; Usachev, V. N.; and Shapovalov, G. K.: Magnetic Suspension and Balance System for Low-Speed Wind Tunnel. Scientific Report of Central Aero-Hydrodynamic Institute, Vol. XVII, No. 4, 1986, pp. 94-97.
3. Kuzin, A. V.: Magnetic Suspension System for Aerodynamic Research. Instruments and Technique of Experiment, 1990, No. 4, pp. 227-230.
4. Kuzin, A. V.: Photoelectrical Sensors of the Magnetic Suspension Systems. Transactions of Colleges, Instrument Engineering, No. 4, 1990, pp. 63-67.
5. Kuzin, A. V.; and Vushkov, Y. D.: Optimisation of Control in Multicomponential System of Electromagnetic Suspension. Transactions of Colleges, Instrument Engineering, No. 11, 1987, pp. 44-49.
6. Kuzin, A. V.: Synthesis of the Magnetic Suspension Stabilization System for the Models in Wind Tunnel. Transactions of Colleges, Electromechanics, No. 5, 1990, pp. 48-57.
7. Kuzin, A. V.: Optimization of Control for Magnetic Suspension Systems. Presented at the ROMAG' 91 Conference, Alexandria, Virginia, March 13-15, 1991.
8. Vyshkov, Y. D.; Kuzin, A. V.; and Usachev, V. N.: Force Measurement Using Electromagnetic Suspension of Boated Object. Paper presented at the 2nd Conference, Force Measurements. Modern Methods and Means, Novosibirsk, 1986, pp. 43-44.

ORIGINAL PAGE
BLACK AND WHITE PHOTOGRAPH

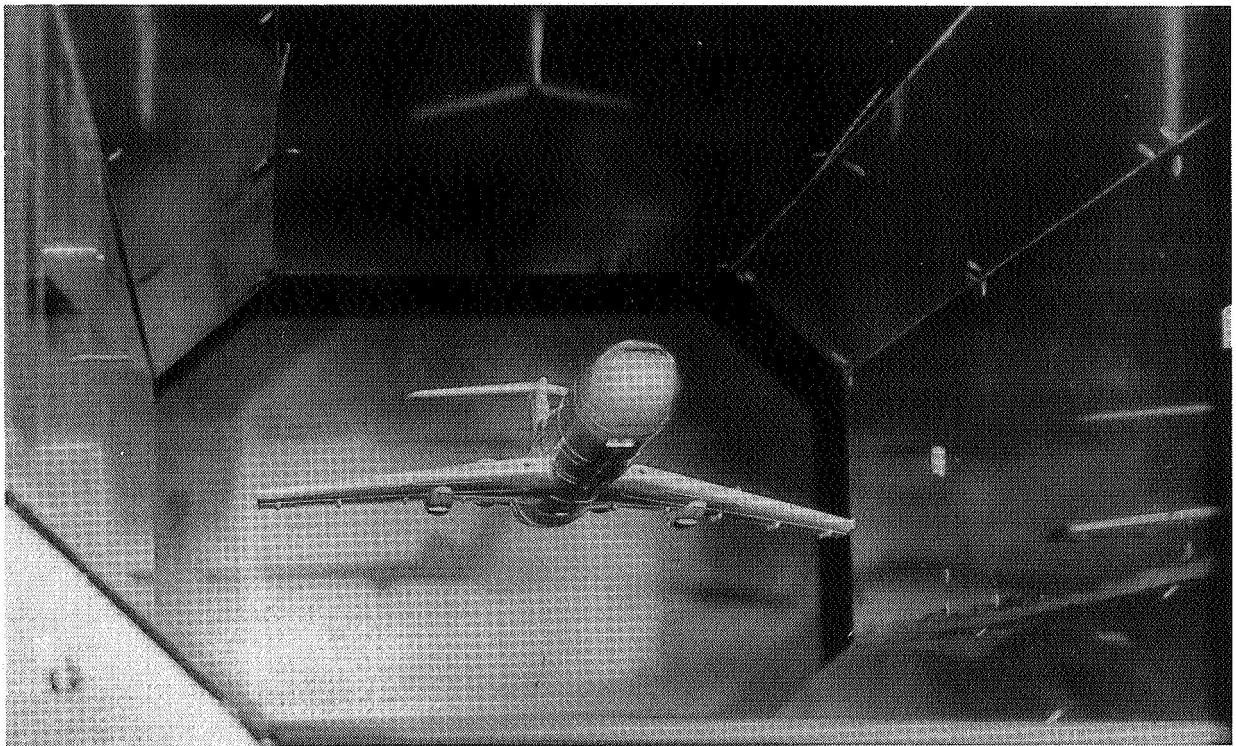


Figure 1. Model in the suspension system of the MAI.

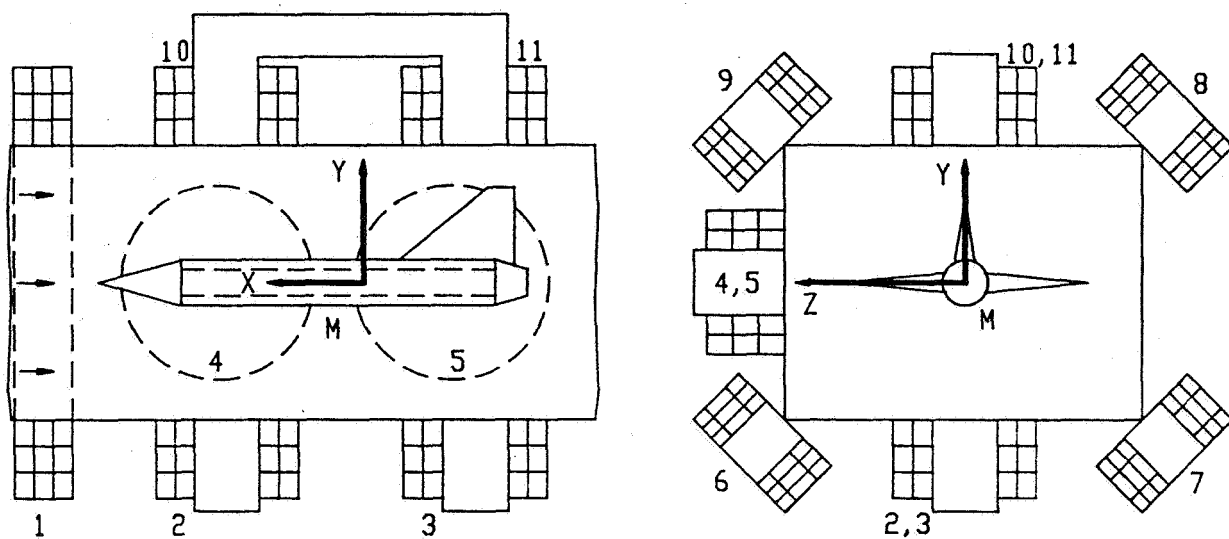


Figure 2. Electromagnet configuration.

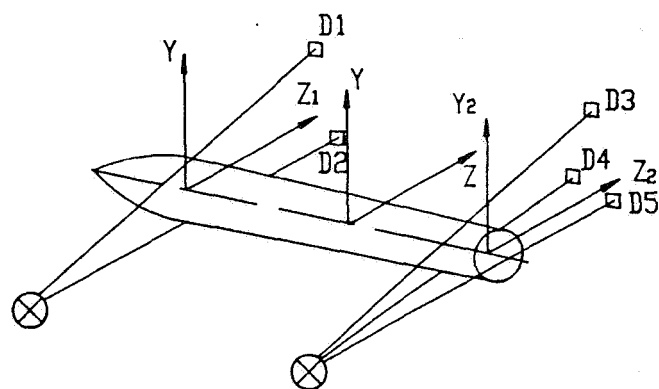


Figure 3. Position sensing system.

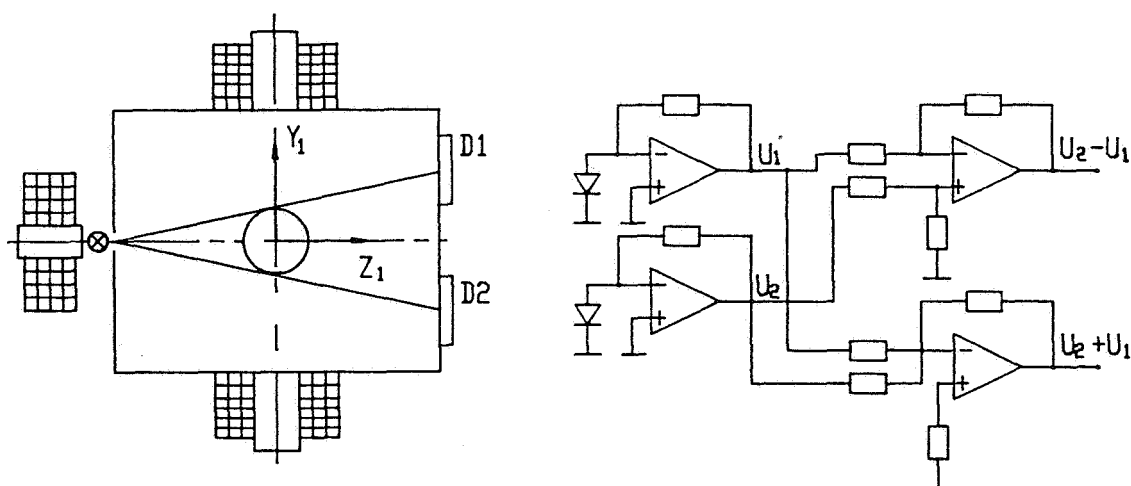


Figure 4. Signal processing.

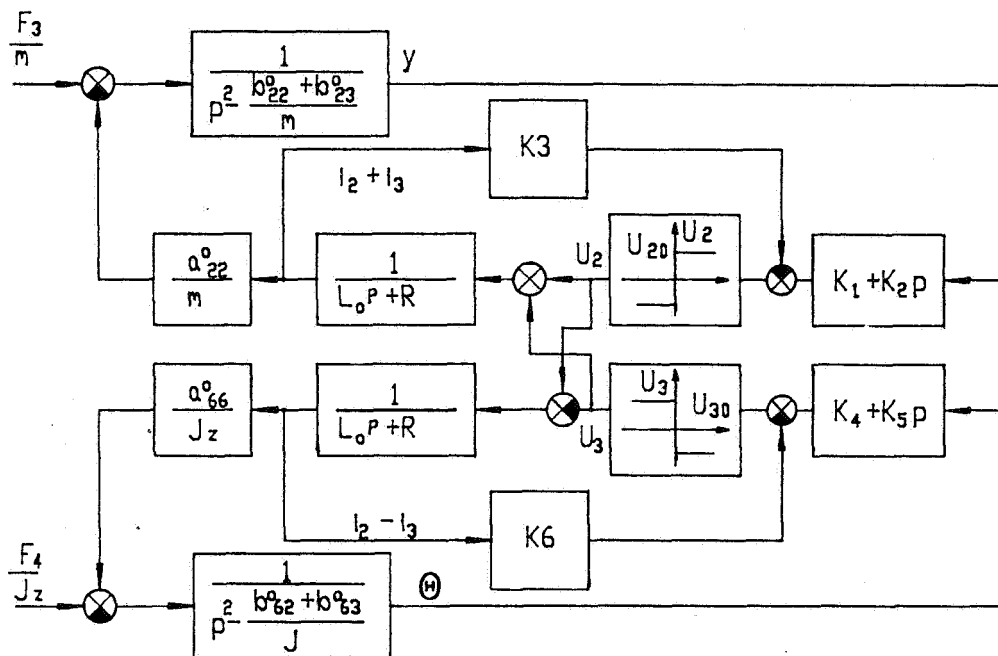


Figure 5. Structural scheme of the EMS control system.

ORIGINAL PAGE
BLACK AND WHITE PHOTOGRAPH

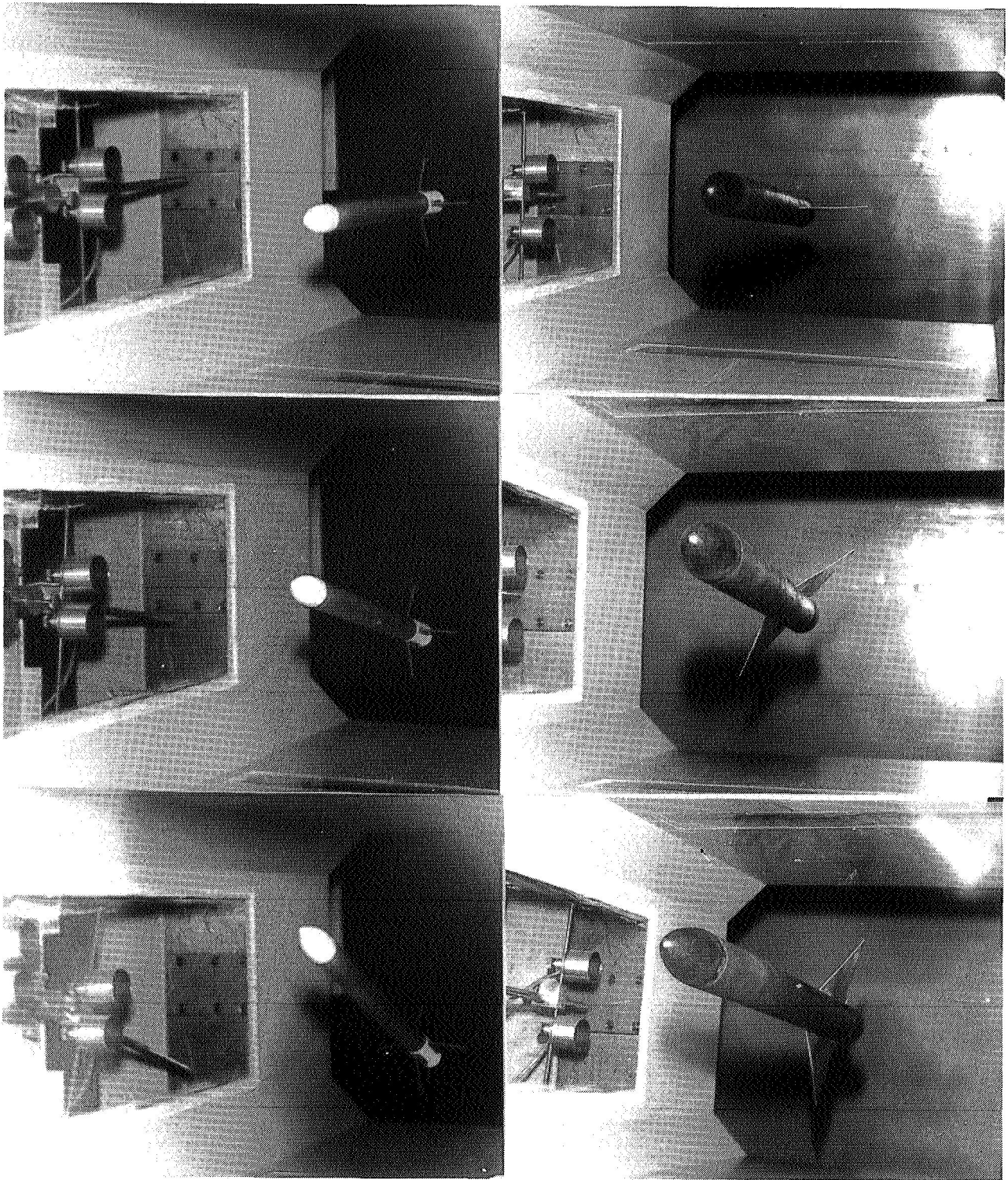


Figure 6. Extreme attitude testing.

ORIGINAL PAGE
BLACK AND WHITE PHOTOGRAPH

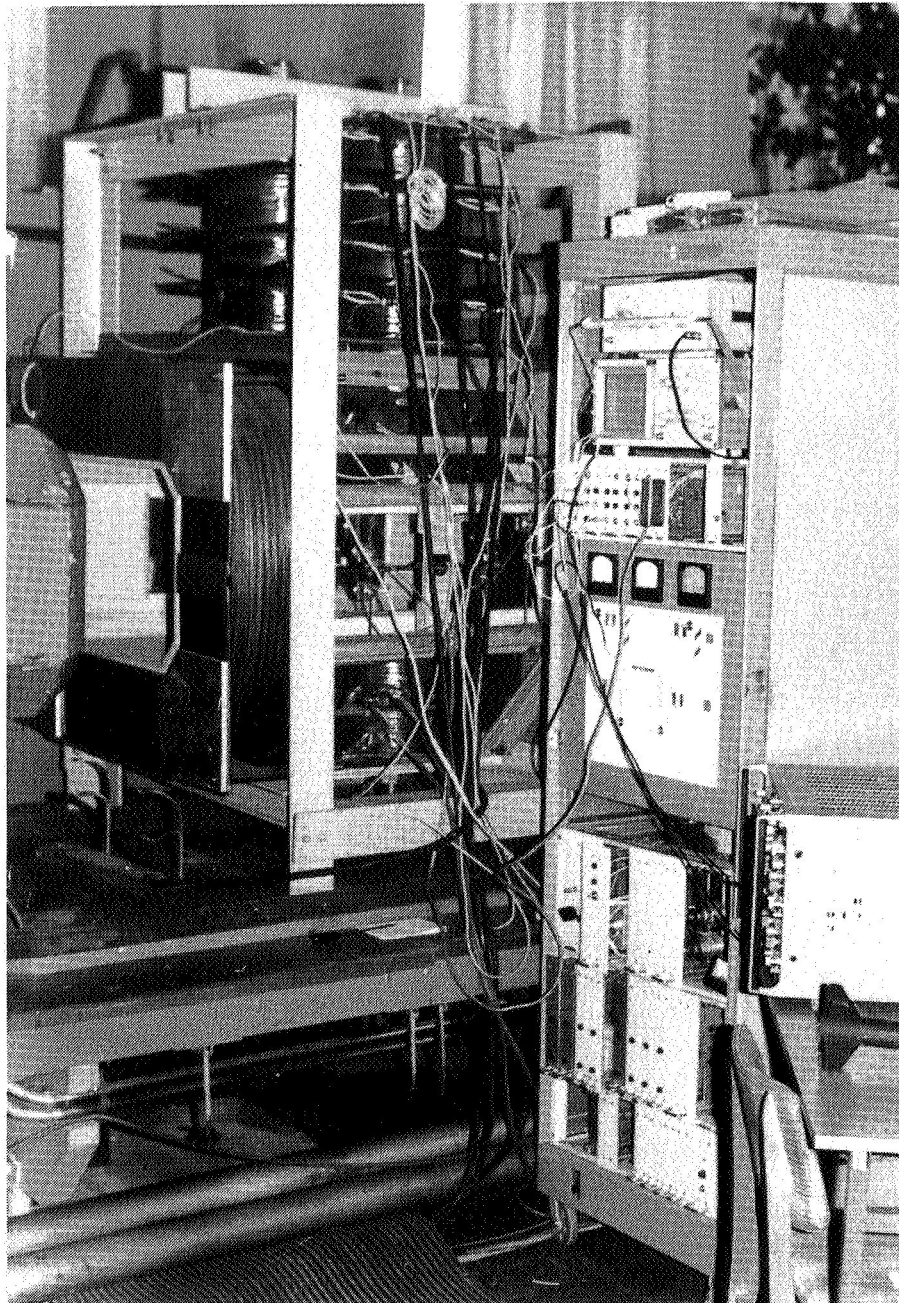


Figure 7. MSBS of the MAI-CAHL.

N92-27804

**Wind Tunnel Magnetic Suspension Systems at
the University of Southampton, England.**

Michael J. Goodyer

Department of Aeronautics and Astronautics

INTRODUCTION

The magnetic suspension system at Southampton University has been used in two rôles: as a device producing useful aerodynamic data, and a vehicle to develop and demonstrate new technology for application to a projected larger facility. Examples of both follow, beginning with an outline of the quest to develop methods for reaching high angles of attack because of current interest in researching the associated aerodynamics.

Magnetic suspension systems applied to wind tunnels were designed to levitate models in the normal attitude for flight, that is nose more-or-less into wind as seen on figure 1. This shows a typical transport model of about the normal proportions for this test section, flying at the required attitude. The model contains suitable permanent magnets and is levitated by a set of copper wire electromagnets distributed around the test section. To complete the control loop there is an optical system monitoring its position. The equipment is capable of controlling the model in all degrees of freedom.

Light beams, wider than the diameter of the fuselage but not visible in this picture, pass through windows, cross the test section converging on the central region where the model flies. We launch by hand, then close up the test section for the test.

It was found that such designs did not allow large angular excursions of the model from this attitude. Rather typically we could reach perhaps 25 degrees of pitch, limited first by a restricted field of view of the optical system. Investigations of the stalling behaviour of conventional configurations of aircraft such as that shown, also of missile and fighter aerodynamics, require higher pitch angles which leads to the first topic.

HIGH ANGLES OF ATTACK

One non-fundamental restriction, just mentioned, was caused by the nature of the optical position sensor which was incapable of monitoring large ranges of angle. More fundamental difficulties were associated with control. The electromagnet array had in the meantime evolved from a somewhat unsymmetrical set of 7 to a more symmetric group of 10. Further, the controller had been changed from analogue to digital, and the model position sensors to the use of relatively long arrays of photo-diodes coupled with broad laser light sheets which lent themselves to modification for high alpha. We set out to exploit these circumstances to reach 90 degrees angle of attack.

Two further changes were required. Investigations of the force and moment capabilities of the electromagnet had shown that it was difficult to derive a controlling side force at that angle. The geometry of the lateral control electromagnets was changed in detail as shown in figure 2 to introduce this force component. The outlines of a delta winged model are shown in solid for zero angle of attack, dotted for 90 degrees.

The functions of the electromagnets change with angle of attack. For example coils 1 and 2 are effective in resisting the drag force on a model at zero alpha but ineffective in exerting a pitching moment. In contrast at 90 degrees angle of attack they will not resist drag but are very effective in producing a pitching moment. Such rôle changes, and there are more, cannot easily be accommodated by an analog control system but can (ref. 1) with digital control. Our equipment will now suspend over the range -5 to + 95 degrees pitch. Figure 3 shows an axi-symmetric model which has been launched at zero alpha then photographed after rotating to 90 degrees in response to commands entered through the computer's keyboard. The angle sweep, from zero to 90 degrees, takes about 2 seconds.

Smoke has been introduced for this photograph to show the paths of the light beams which monitor position. The digital nature of the optical system renders it somewhat immune to smoke. Four broad beams shining diagonally upwards and across the test section are very apparent: these monitor the sides of the model. They are partly interrupted by the model as evidenced by a change of width. A fifth, much narrower beam in this view, shines across the tail to monitor axial movement.

DYNAMIC MEASUREMENTS

Usually the measurement of the aerodynamic effects of a model motion such as pitching requires the model to be oscillated, sinusoidally for convenience. This type of measurement is fairly common using a mechanical support for the model, the support also acting as an oscillator and force/moment balance. The magnetic suspension system at Southampton University was built in the first instance to explore the possibilities of carrying out these and similar measurements, with no mechanical support to restrict motion or to affect the airflow over the model. Over several years a range of techniques was developed.

Steady rotation

The first technique was simple and did not use an oscillatory motion but, instead, steady rotation. This exploited the low friction of rotation in roll (2). Wings were mounted on an axi-symmetric fuselage, figure 4, and the aerodynamic damping of the rolling motion measured. The model is viewed from the tail. It was flown at zero incidence to the flow and, with the wind on, was spun up in roll using mechanical means, then released to roll freely.

The relatively rapidly decaying roll rate was monitored with the wind on and the roll torque determined using the moment of inertia. The rear of the model carried a simple roll angle optical encoder.

Measurements of Magnus effects

Another form of dynamic measurement using steady rotation is that of Magnus force and moment. These are aerodynamic loads which can appear on spinning objects flying through a fluid, due to their spin. The effects arise quite generally, for example in sport where they can be exploited, but also in military hardware where the effect must be quantified. The magnetic suspension system can measure Magnus force quite easily and at Southampton we have carried out an extensive range of such tests exploring the effects of spin rate, model geometry, air speed and angle of attack (3,4). The model, shown on figure 5 with a variety of alternative base shapes (9 in all) alongside, was spun to high rotational speeds while levitated at the desired incidence, using air jets impinging on the model's outer skin.

Rotational speeds up to 25,000 rpm were reached with these models which had a body diameter of 22mm. The spinup device was retracted through trap doors into the floor of the tunnel, the wind turned on and the Magnus effects monitored during the subsequent slow decay in rpm. An investigation such as this, of the influence of base shape with the flow uncorrupted by a mechanical support, is a good example of the exploitation of a useful property of magnetic suspension.

Oscillatory measurements

The stability and ease of control of an aircraft in flight depends, among other things, on its tendency to align itself with the airflow in the manner of a weathercock, but also on the natural damping of disturbances, in particular angular disturbances. Each property is measured in wind tunnel tests, the latter by oscillating the model. The aerodynamic damping is measured usually by monitoring the moment required to induce steady amplitude oscillations in the desired degree of freedom. In order to obtain data from a model test which is relevant to full scale flight, among other things it is necessary to reproduce in the model test a frequency parameter $\omega l/V$ corresponding to full scale, where ω = angular frequency, l is a length scale and V is the flight speed. It can be seen that a test on a small model at the correct airspeed requires a high frequency of oscillation. This requirement is difficult to satisfy with a magnetic suspension system because the oscillatory forces are generated by an alternating component of the currents in electromagnets having high inductance. This places heavy demands on electrical power, in particular on voltage. A second source of difficulty arises because the component of the oscillating current which is overcoming the aerodynamic damping of the model's oscillation is small in comparison with the component of current which is inducing the motion. It is difficult to extract the damping component from the total current signal.

Our power supplies, which adequately suspend a model and resist steady aerodynamic loads, prove to give too restricted a frequency/amplitude envelope for dynamic testing. Mechanical equivalent equipment often exploits a resonant system: the stiffness of the support is chosen in conjunction with the mass or inertia of the model to produce an appropriately high resonant frequency. Excitation of the oscillatory motion at useful amplitudes is then easy at frequencies close to resonance, in the mode(s) of motion for which the equipment was designed. Further, the force or moment which is applied to the model at resonance is just that required to overcome the damping of the system, leading to simple measurements.

In order to overcome the difficulties identified in connection with the application of the magnetic suspension system to such testing we designed (5,6) a tuned model which had the characteristics of the mechanical system just described. The essence of the model's construction was the use of two spring-connected masses forming a resonant system. The notional construction is shown in the simplified sketch on figure 6 where it is seen that the construction introduces a pitching resonance the frequency of which is determined largely by the mechanics of the model.

The model comprises two masses coupled by a torsional spring. For convenience one mass was made the magnetic core of the model, the other its aerodynamic outer shell. The electromagnets can easily excite the resonance, now having to supply only the damping moment.

Figure 7 shows the construction of the model in more detail. A variety of wing planforms was tested on the same fuselage. Repositioning the wings allowed the axis of rotation to be varied relative to the wings. The fin was used mainly as a device providing a roll attitude signal to allow active roll control. The model was controlled in all degrees of freedom. The control of pitch introduced an unusual stability problem in that the optical position sensors monitored the fuselage which at some control frequencies moved in phase with the magnetic core but at others in anti-phase. Conventional control algorithms are very unstable.

A typical influence of airspeed on the frequency response of one version of the model is shown on figure 8. θ represents the amplitude of angular motion in pitch and M the amplitude of the applied pitching moment. There is a change in the height of the maxima with airspeed due largely to aerodynamic damping. The shift in the frequency of the peak is due to a variation of aerodynamic stiffness in pitch, in this case a negative stiffness is present leading to a reducing frequency with increasing airspeed. The signals representing aerodynamic damping and stiffness may be extracted with relative ease.

CRYOGENICS WITH THE MSBS

We have used cryogenic technology with the suspension equipment in two ways, first with a cryogenic wind tunnel, then, as a quite separate exercise, using superconductivity in the model.

The cryogenic wind tunnel

This type of wind tunnel is used to raise the Reynolds number of an aerodynamic test to match more closely the values of flight. As a demonstration of this technology for improving the quality of aerodynamic testing it was decided to modify an existing cryogenic wind tunnel to suit the MSBS. In this way the advantages of no mechanical support would be linked with high Reynolds number flow.

This is a low speed cryogenic wind tunnel having a closed circuit and is driven by an electric motor and fan. Liquid nitrogen is introduced to the circuit cooling the tunnel by evaporation. There is a vent to hold the internal pressure essentially at atmospheric. Any air or moisture in the tunnel is quickly displaced and test gas becomes pure nitrogen. Our maximum fan speed is not dependent on temperature with the result that, on cooling from room temperature to the minimum temperature of just over 80K, the maximum Reynolds number rises by a factor of about 12.

An outline of the tunnel and MSBS is shown on figure 9. The gas flow is clockwise. The modifications to the tunnel from its normal configuration involved a completely new test section leg from the screen region to the end of the first diffuser (6). One of the principal changes was to provide light paths for the optical position monitoring system. The light sources and pickups were outside the tunnel and at room temperature. The light beams shone through thick double-glazed windows, one formed by the test section itself which was manufactured from Lexan. The windows, purged in their inter-layers by dry nitrogen, were designed to keep their outsides free from condensation in the presence of a temperature difference, outside to inside, of about 200K.

Figure 10 is a photograph of the equipment taken during a cryogenic run. Two legs of the closed circuit can be seen running from the low center of the picture, to the left and then away through a right-angled bend. Most of this region is covered with a black insulating foam rubber. A circular area part way along this section contains the fan, light in this picture because it was uninsulated and covered with frost. The MSBS is supported under the framework in the center of the picture while the LN₂ supply pipe runs to the tunnel from the bottom right. The test procedure was to launch the model by hand with the tunnel at room temperature. This was the purpose of the door indicated on figure 9 positioned in the diffuser wall just downstream of the test section. The door was then sealed and the fan started in order to help circulate the cooling nitrogen. The tunnel and model cooled together to the test temperature. Measurements were made of the influence of Reynolds number on drag coefficient. The exercise also served to demonstrate the practicality of this combination of technologies.

The superconducting model.

The capital cost of a magnetic suspension system for application to wind tunnels lies largely in the electromagnet set and their power supplies. Further, if the electromagnets are superconducting at helium temperature then the running and capital costs are also affected by the helium equipment (8). The cost of this equipment depends on size and the aerodynamic loads to be carried by the model. The electromagnets must produce fields which, in conjunction with the size and strength of magnetisation of the model's core, satisfy the force specification. It is clear that the strongest possible model magnet must be used. According to calculations it had become apparent that replacing a ferromagnetic core with a superconducting coil could usefully increase the magnetic strength of the model and proportionally reduce the strengths of the

electromagnets, with cost implications. This even with the space penalty of insulation and helium in the model.

It was decided to proceed with the construction of such a model to face the design and control problems, and for demonstration purposes. The specification was written by the Department of Aeronautics and Astronautics, the model flown in their MSBS and was designed and constructed (9) in the Institute of Cryogenics.

The model comprised a lightweight superinsulated cryostat containing a superconducting coil with space for helium. There were pipes for filling with liquid helium and venting helium gas. There were electrical connections for charging the coil with current when in the superconducting state, for operating an internal superconducting switch to allow internal current circulation and hence the supply to be disconnected, and instrumentation. The model was flown with the coil in the persistent mode with all umbilicals disconnected. The superconducting lifetime was on-specification at 30 minutes.

The model, somewhat oversized for our small MSBS, in figure 11 is shown flying during a force and moment calibration session for which purpose there are weights hanging underneath. The model, circular in section, is viewed end-on looking along our octagonal test section. The calibrations were linear to the limits of resolution of our fairly good data logging equipment. The model proved easy to levitate with no control problems and as a result of these and several other good experiences with it has served to open the way (10) to using this technology on a larger scale.

FORCE AND MOMENT CALIBRATION

The loads acting on a model are derived from a relationship between them and the currents in the electro-magnets. The relationship is determined by calibration. In our case each of six force and moment components depends on the currents in ten electro-magnets. The dependence varies with the design of the magnetic core of the model, on its position and attitude. The determination of a comprehensive calibration matrix even for one core is a daunting proposition. We are deterred by the perceived complexity and labour and in practice simplify matters by calibrating selectively using a narrow range of geometric variables chosen to just cover those anticipated in the wind tunnel test.

One popular calibration method is to load the suspended model with sets of known forces and moments and to record the electromagnet currents. Extra to the list above is a factor associated with this method which further inhibits full calibration, the factor being mechanical complexity associated with providing accurately known calibration loads.

Various solutions to the calibration problem have been sought in the past. One (11) features a force balance within the model. The balance, mostly of conventional design and mounted between the model's aerodynamic shell and its magnetic core, is calibrated separately and is intended to provide the aerodynamic force/moment data during a tunnel test by telemetry. The balance and its telemetry occupy model volume which could often be used to good purpose some other way as has been discussed above in connection with the superconducting core.

For this reason we sought an alternative calibration scheme, and are updating an idea explored some time ago (12). The essential difference between their method and that described in the paragraph above is that known currents are applied to the electromagnets rather than known loads to the model. A balance, which is attached to the model just for the calibration, yields the resultant loads. Their balance proved unsatisfactory on several counts but the underlying principle was sound and is now being reinvestigated using modern technology.

A similar philosophy was adopted at MIT (13) where the balance was based on the use of air bearings.

The force balance is positioned outside the model and, if desired for brevity, may be used only to record the loads which were present during a wind tunnel test, a very attractive option. As the balance is now external to, and not part of the model, the calibration measurements are made after the test, for which the model is clamped to the balance. In the current embodiment of the scheme the recorded electromagnet currents and variations of model position/attitude from the preceding tunnel test are played back. The balance has provision to move the model to make it follow the recorded motions in the tunnel test, making use of the same optical position sensing system as was used in the wind-on tunnel test. The actual loads of the tunnel test are then measured. In principle the process can be fully automatic and quick.

We have constructed a prototype which has provision to pitch the model through a large range of angle of attack, with micro- adjustment in three translations to allow the model to be centred properly. The recorded outputs of the three force transducers will allow the derivation of three components of aerodynamic load: lift, drag and pitching moment.

CLOSING COMMENTS

This brief account of some highlights of the development of this magnetic suspension system has served to show, I hope, that even or perhaps especially with small scale equipment the University environment has contributed effectively to the exploitation and evolution of a new technology: exploitation in the creation of useful aerodynamic data which has proved possible despite small scale, evolution because the developments might not have taken place because of cost restrictions had the effort necessarily been done at large scale.

ACKNOWLEDGEMENT

Financial, material and moral support for the work reported above has been received from the British SERC and its forerunners, from NASA Langley Research Center and from the British Ministry of Defence for which we, current and past under- and post-graduate students and myself are grateful.

REFERENCES

1. Parker, D.H. Techniques for Extreme Attitude Suspension of a Wind Tunnel Model in a Magnetic Suspension and Balance System. NASA CR-181895, October 1989.
2. Goodyer, M.J. Some Force and Moment Measurements Using Magnetically Suspended Models in a Low Speed Wind Tunnel. ARL Symposium on Magnetic Wind Tunnel Model Suspension and Balance Systems, July 1966, pp.159-197 (N67-13587#).
3. Goodyer, M.J., Henderson, R.I. and Judd, M. The Measurement of Magnus Force and Moment Using a Magnetically Suspended Wind Tunnel Model. 13th International Magnetic Conference, London England, Apr. 14-17, 1975. IEEE Transactions on Magnetics, vol. MAG-11, Sept. 1975, pp. 1514-1516.
4. Henderson, R.I., Goodyer, M.J. and Judd, M. Measurements of Magnus Force on a Spinning Projectile, Including the Influence of Base Shape. Dept. of Aeronautics and Astronautics memo. AASU 75/4, December 1975, 56 pp., 59 figs.

5. Goodyer, M.J. The Magnetic Suspension of Wind Tunnel Models for Dynamic Testing. Univ. of Southampton, Dept. of Aeronautics and Astronautics - Ph.D Thesis, April 1968, Chapters 1-8 (Available from NTIS as N78-78589). Chapters 9-14 (Available from NTIS as N78-78218).
6. Judd, M. The Magnetic Suspension System as a Wind Tunnel Dynamic Balance. Presented at the 3rd International Congress on Instrumentation in Aerospace Simulation Facilities, Poly. Inst. of Brooklyn, Farmingdale, N.Y., May 1969 (ICIASF '69). IEEE publication 69C 19-AES, pp.198-206.
7. Britcher, C.P. The Magnetic Suspension and Balance System in the Cryogenic Wind Tunnel. Southampton Univ. B.Sc., Honours Project Report April 1978, 95pp.
8. Bloom, H.L. Design Concepts and Cost Studies for Magnetic Suspension and Balance Systems, Final Rept. Nov. 1980 - Mar. 1981. NASA-CR-165917, Jul. 1982, 346 pp.
9. Britcher, C.P., Goodyer, M.J., Scurlock, R.G. and Wu, Y.Y. A Flying Superconducting Magnet and Cryostat for Magnetic Suspension of Wind-Tunnel Models. In: Cryogenics, vol. 24, Apr. 1984, pp. 185-189.
10. Boom, R.W., Eyssa, Y.M., McIntosh, G.E., Abdelsalam, M.K., Scurlock, R.G., Wu, Y.Y., Goodyer, M.J., Balcerek, K., Eskins, J. and Britcher, C.P. Superconducting Electromagnets for Large Wind Tunnel Magnetic Suspension and Balance Systems. Presented at the Applied Superconductivity Conference, San Diego, CA, Sept. 9-13, 1984.
11. Roberts, P.W. and Tchong, P. Strain-Guage Balance Calibration of a Magnetic Suspension and Balance System. In: ICIAF '87 - 12th, Williamsburg, Va., June 22-25, 1987, Record (A88-36483), New York, IEEE, Inc., 1987, pp. 308-321.
12. Howford, J., Wheeler, D.I. B.Sc. Final year Honours Project Reports, Dept. of Aeronautics and Astronautics, Univ. of Southampton, 1969/70.
13. Vlajinac, Milan. A Pneumatic Calibration Rig for Use with a Magnetic Suspension and Balance System. Tech. Rep., Nov. 1967 - Aug. 1969. Wright-Patterson AFB Rep. ARL-70-0016, MIT-TR-159, Jan. 1970, 41 pp.

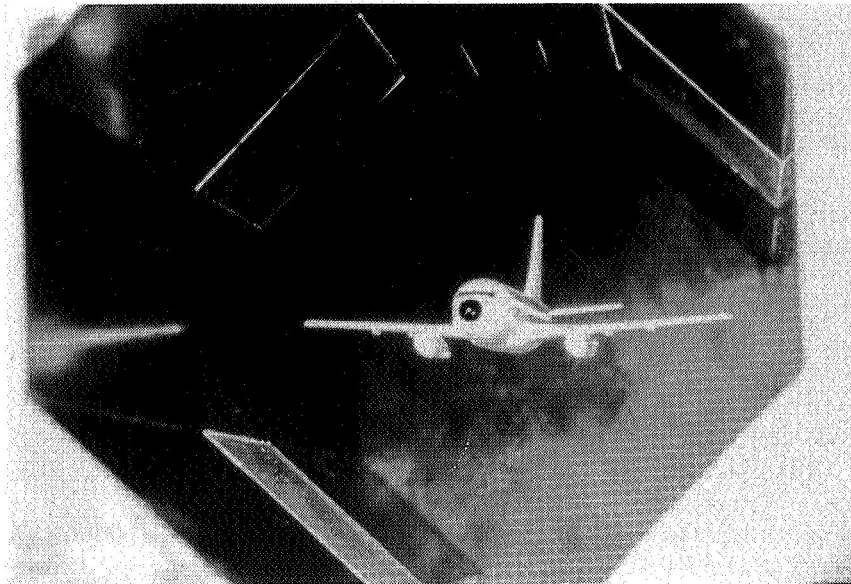
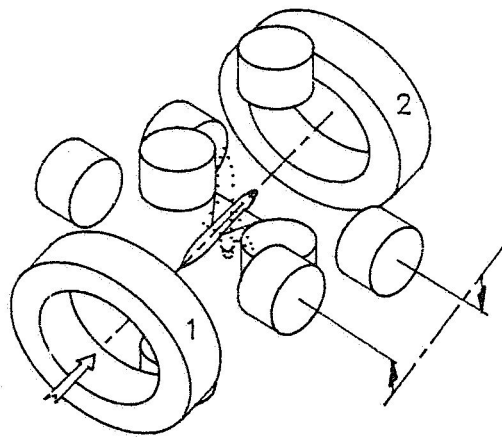


Figure 1. A transport aircraft model suspended in the test section of the 6-component magnetic suspension system at Southampton University.



Lateral electro-magnets
on both sides
are skewed to permit
suspension through an
angle of attack range
of over 90 degrees

Figure 2. The electromagnet array. Displacement of the lateral set of four for high alpha.

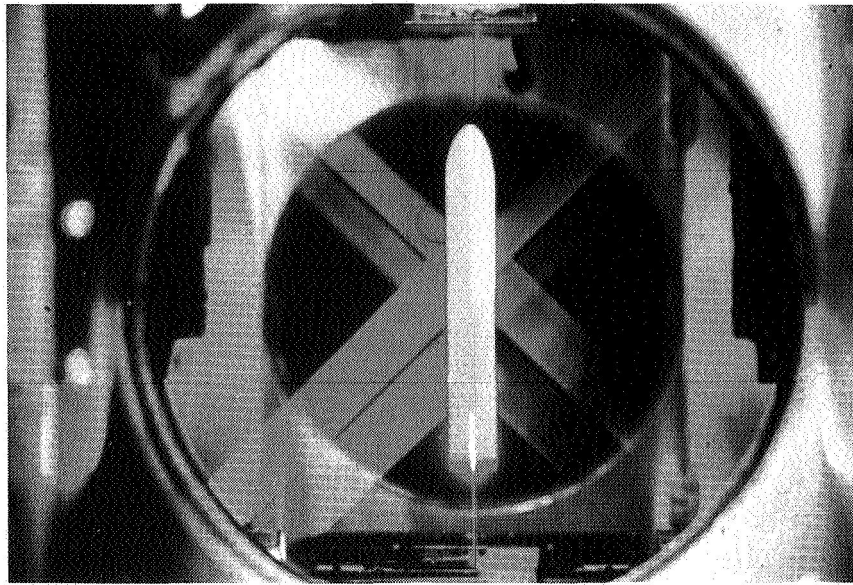


Figure 3. An axisymmetric wind tunnel model flown at 90° angle of attack.

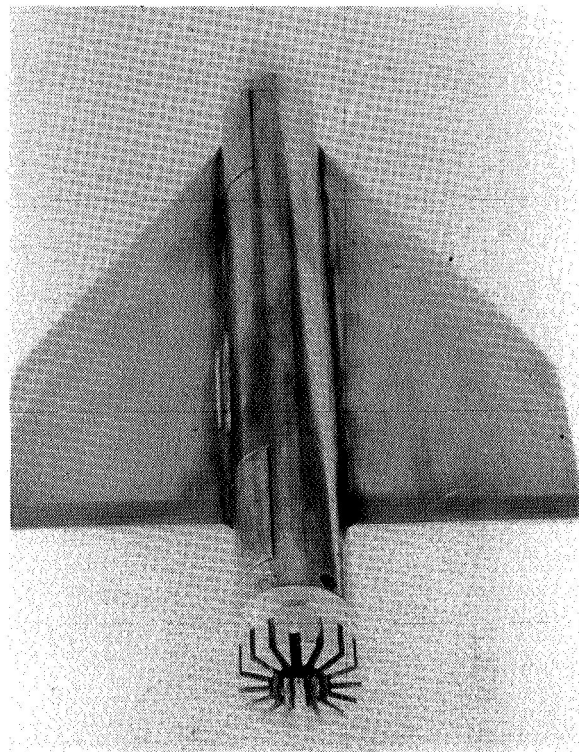


Figure 4. A wing-body model used in measurements of roll damping.

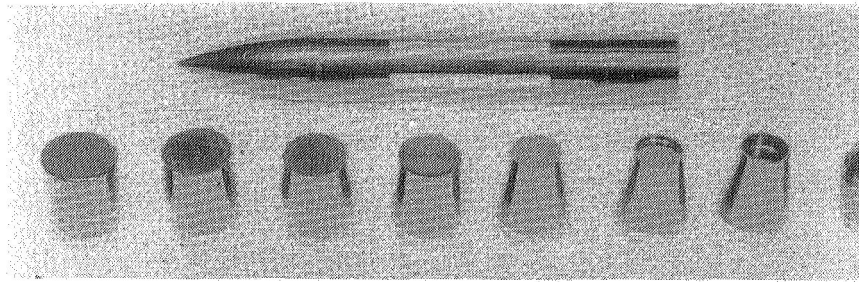


Figure 5. Ogive/cylinder model used in investigations of base shape on Magnus effects.

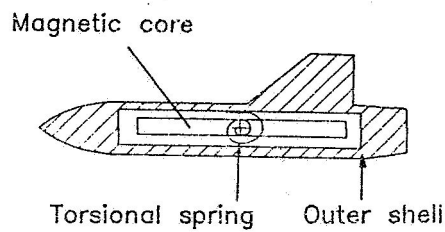


Figure 6. The essential mechanics of a two-mass tuned model.

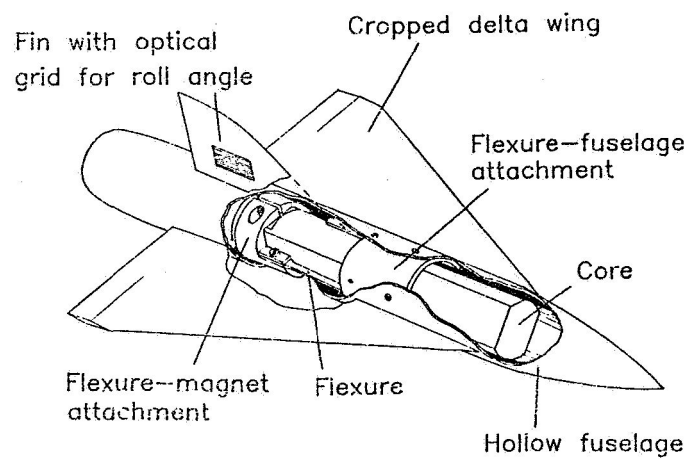


Figure 7. The pitch-tuned model.

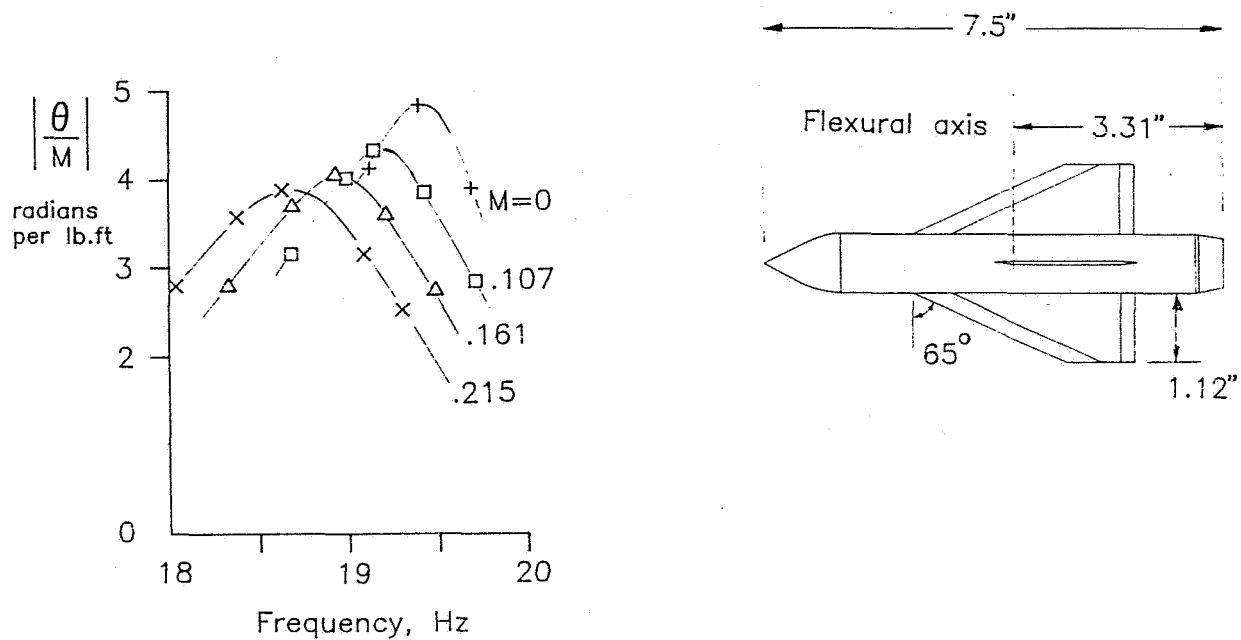


Figure 8. Effect of airspeed on frequency response in pitch for one wing planform and axis of rotation.

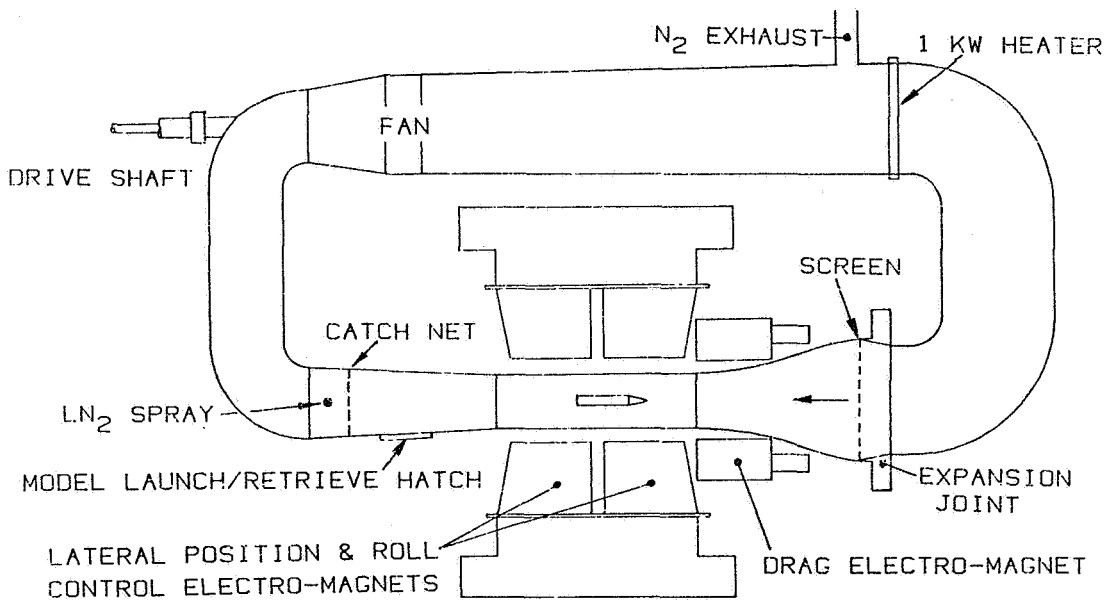


Figure 9. The 0.11m cryogenic wind tunnel and magnetic suspension system.

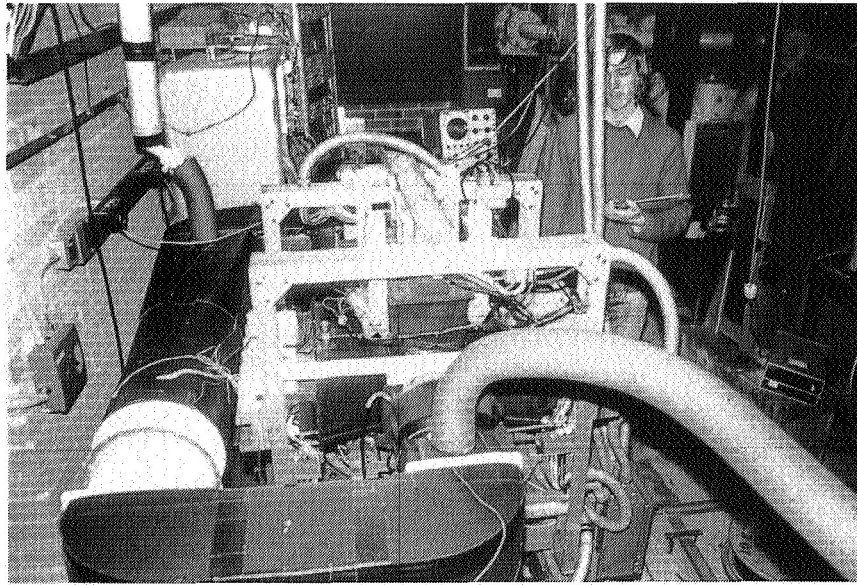


Figure 10. The MSBS operating with the cryogenic wind tunnel.

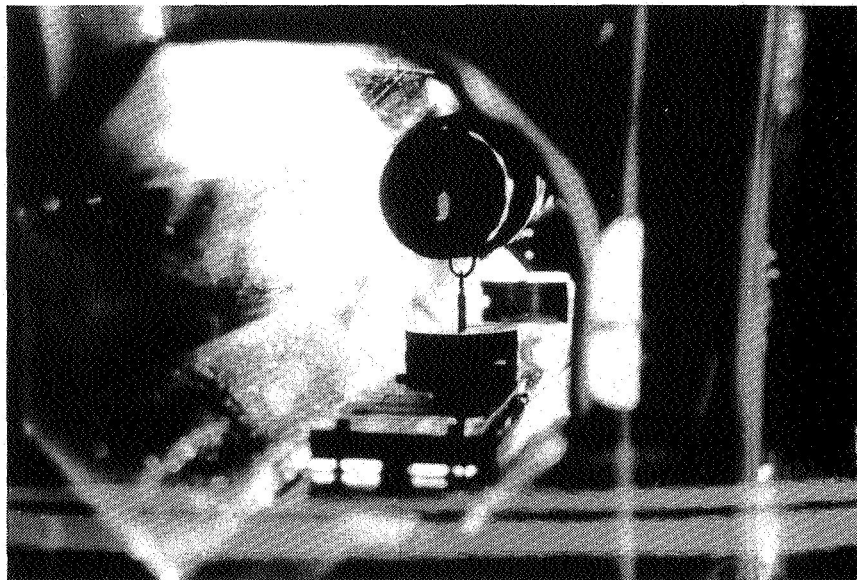


Figure 11. The superconducting solenoid model under calibration while flying in the MSBS.

Session 14

MAGNETICALLY LEVITATED TRAINS (MAGLEV) 1

**Chairman - Colin P. Britcher
Old Dominion University**

N 9 2 - 2 7 8 0 5

ATTRACTIVE AND REPULSIVE MAGNETIC

SUSPENSION SYSTEMS OVERVIEW

David B. Cope, Richard R. Fontana
Foster-Miller, Inc.
350 Second Avenue
Waltham, MA 02154

ABSTRACT

Magnetic suspension systems can be used in a wide variety of applications. The decision of whether to use an attractive or repulsive suspension system for a particular application is a fundamental one which must be made during the design process. As an aid to the designer, we compare and contrast attractive and repulsive magnetic suspension systems and indicate whether and under what conditions one or the other system is preferred.

The suspension design chosen depends upon the details of the application. There is no fundamental advantage of either attractive or repulsive systems. Rather, the specific characteristics of each system determine their applicability in any given situation. The parameters which are to be considered when designing the suspension system include size; suspension force; air gap; required suspension stiffness; volume available for magnets, coils, cooling, and controls; stability; required damping characteristics; required input power; and the operating environment, i.e., operating temperature, ruggedness, and DC or AC external magnetic field constraints.

Results of magnetic suspension studies employing permanent magnets, ferromagnets and superconducting magnets are presented. Specific examples of requirements for magnetic bearings for gas turbines and Maglev investigations are also presented.

MAGNETIC SUSPENSION REQUIRES A SYSTEM DESIGN

Introduction

Magnetic suspension design requires a systems approach. Design of a magnetic suspension system frequently involves many complicated interactions between disparate subsystems. To optimally design such a system, the designer must have an understanding of the various subsystems as well as a detailed understanding of the interface between them. Magnetic suspension systems may involve effects due to heat transfer, structural mechanics, electromagnetics, gravity, inertia, aerodynamics, material properties, thermal expansion, and cost. The system designer must be able to make intelligent technical trade-offs and compromises among these areas.

Magnetic suspension systems rely upon the concept of action at a distance, and they are primarily of interest due to the non-contact nature of the interface.

It is common to classify magnetic suspension systems according to whether the fields are attractive or repulsive. The fact that there are "fields," plural, means that at least two objects must interact and each object must have associated with it a magnetic field. In some cases, the magnetic field of one object induces a field in the other object where there would otherwise be no field. In practice, there are usually many interactions simultaneously occurring among several objects.

This paper will examine attractive and repulsive magnetic suspension systems. Detailed discussion of attractive and repulsive magnetically levitated trains will follow. The purpose is to highlight the need for a system's approach to select a system which best satisfies the goals of the program.

Attractive and Repulsive Systems

In general, attractive and repulsive systems can be described by the interaction of the equivalent currents of the interacting bodies. For non-ferromagnetic bodies the currents are simply the actual applied or induced currents. For ferromagnetic bodies, the total current is the sum of the actual currents and the equivalent currents. The equivalent currents are determined from an integration of the magnetization current density which is equal to the curl of the magnetization.^{1,2} The external magnetic field of the body and all its interactions can be described alternatively as the result of a magnetization (with no current) or current (with no magnetization).

Figure 1 shows a schematic of attractive and repulsive coils. Magnetic flux lines and resultant force are indicated. Repulsive levitation occurs due to bucking magnetic fields while attractive levitation occurs due to parallel magnetic fields.

The force generated (either attractive or repulsive) as a function of air gap separation is shown in Figure 2. This figure shows that the same magnitude of the force is generated for attractive and repulsive systems (for the same geometry and current) and it is only the direction of the force which changes as the direction of the current is changed. The direction of the force is opposite for the two schemes: the force of the attractive scheme tends to increase in the direction of the force (coil separation is decreased) while the force of the repulsive scheme decreases in the direction of the force (coil separation is increased). (Both conclusions assume constant excitation currents.)

Since the goal is usually levitation at a constant height, the attractive scheme is said to be inherently unstable while the repulsive scheme is stable. By varying the excitation currents appropriately the attractive system can be made to be stable.

The methods to generate magnetic fields are permanent magnets, electromagnets, ferromagnets, and superconducting magnets. These magnets may be combined to produce attractive or repulsive forces. Table 1 shows the combinations of the magnets

and the types of suspension systems possible with them.

Figure 3 shows a corporate structure of magnetic levitation systems as they are presently used.

There are limitations to existing technology which affect the choices for a given system. For example, although no energy is required to maintain a steady state magnetic field, superconductors will dissipate energy if subjected to varying magnetic fields. Therefore, great care is taken to isolate them from field variations. The repulsive pairing of superconductors with other superconductors and permanent magnets is not meant to imply any practical advantage of repulsive over attractive systems. The point is repulsive levitation is stable which makes plausible only small superconductor heating effects. Attractive levitation is unstable and would require significant supercurrent modulation which produces undesirable heating of the superconductor itself. Recent progress in high temperature superconductors suggests the possibility of varying supercurrents.

Material response at the operating temperature is one of the major issues for selecting magnetic suspension systems. The required operating temperature may be quite hot, ~1000 K in gas turbine engines. At high temperatures it is difficult to produce a high magnetic field. At moderate temperatures, such as room temperature, significant thicknesses of insulation are required to permit superconductors. Figure 4 shows a plot of magnet material temperature vs. magnetic field. Note the figure has a second x-axis which shows the equivalent pressure of the magnetic field. The limiting temperatures and fields for permanent magnets, ferromagnets, and high and low temperature superconductors are shown. This figure is meant to be suggestive rather than exhaustive. It is not the precise position of individual points which is important, rather the general trends. For relatively small magnetic fields at high temperatures, permanent magnets and ferromagnets generally have an advantage over superconductors. Alternatively, if higher magnetic fields are required, superconductors have a significantly greater capability than ferromagnetic materials.

Electromagnets utilizing ferromagnetic material are an important technique for magnetic suspension. The dissipated electrical power in the (normally) resistive wire, however, is the penalty of this method. Calculations of the power consumed by the attractive system are relatively sensitive to the input parameter values. In principle, the resistive power can be made arbitrarily small by using an arbitrarily large conductor cross section. It can readily be shown that for unsaturated ferromagnetic materials the power required for levitation increases linearly as the levitation pressure is increased. As the ferromagnetic material approaches saturation, the power consumed increases faster than linearly with increases in levitation pressure. Therefore, for ferromagnetic materials, there is a maximum magnetic levitation pressure.

Superconducting magnets consume no power during operation except for the refrigeration system. The power required for refrigeration is dependent upon the ambient temperature and the exposed magnet surface area and is relatively independent

of supplied magnetic pressure. For liquid helium temperature superconductors the refrigerator power consumed is sensitive to the quality of insulation between the ambient environment and the superconductor. The superconductor characteristics determine the maximum levitation pressure. Magnet design must account for the critical magnetic field and the decrease in the critical current density at elevated magnetic fields. Therefore, for superconducting magnets, there is a maximum magnetic levitation pressure.

Repulsive Maglev systems usually use superconductors to induce eddy currents in coils along the guideway or ground to provide levitation. Most commonly these coils are normally resistive conductors but, in principle, the coils could be superconducting. The levitation force supplied depends only on the induced eddy currents and is independent of lateral speed. The power dissipated in levitation, therefore, can be made arbitrarily small by increasing the normal conductor cross section or zero by use of superconductor coils. It is interesting to note that levitation at standstill is possible with superconducting eddy current coils.

Figure 5 shows a plot of magnetic levitation pressure vs. input power for specific attractive and low temperature superconducting repulsive magnetic suspension systems which have been analyzed. For both systems, an attempt was made to present favorable but reasonable results. Both systems levitate a train with a capacity of approximately 100 passengers. The attractive system attracts upward to a ferromagnetic rail while the repulsive system uses ground coil levitation. This figure neglects magnetic drag. The gap for the attractive system is 10 mm and the gap for the superconducting system is 100 mm.

The figure shows a cross-over point between attractive and repulsive systems from a power consumption standpoint. For the systems analyzed, this cross-over point occurs between approximately 10 psi and 15 psi (70 kPa and 105 kPa). In essence, attractive ferromagnetic systems provide low magnetic levitation pressure at minimum power while repulsive superconducting systems provide high pressure with minimum power.

Improvements in properties of materials can sway the relative balance between attractive and repulsive system advantages. For example, high temperature superconductors (HTSC) have greatly reduced cryogenic requirements compared to low temperature superconductors (LTSC). HTSCs may be practical in some applications with a limited gap where LTSC materials are not practical due simply to a reduction in the required thickness of insulation. New ferromagnetic materials are under development which are extending the temperature vs. magnetic field envelope of attractive systems.

In essence, ferromagnetic materials make attractive suspension schemes practical and superconducting coils make repulsive systems practical.

Above we have touched upon some of the important general issues in the system design of a magnetic suspension system. Table 2 shows a listing of these and other issues.

A discussion of each of these topics is beyond the scope of this paper. However, the effect of air gap is critical to any magnetic bearing system. The importance of the size of the air gap leads to the following discussion on scaling laws.

Scaling Laws

Scaling laws relate design parameters so the designer can easily see the effect of changing one parameter has on other parameters of interest. In the initial design stage, it is not so important to know the precise value of a parameter, as it is to understand how the situation changes by varying the parameter in a given manner.

Scaling laws can be developed to focus on any particular set of parameters. One would expect scaling laws to arise from limitations in three areas: thermal, electromagnetic and structural. The reader should note the issues involved here and use any particular scaling law only after careful consideration is given to the applicability of the law.

We consider the following systems: permanent magnet (PM) and current-based systems. The results presented here are for constant-gap scaling and scaled gap (full) scaling. Constant gap scaling is useful since in many circumstances the air gap is fixed by mechanical clearances and is relatively independent of size. Full scaling is used when the gap is increased in proportion to the size of the bearing. The magnetic energy in the gap is proportional to the load capacity of the bearing.

Generally the parameter of interest is the magnetic energy stored in the air gap. Table 3 gives the scaling laws for the magnetic energy for pressure within the gap for PM and current-based suspensions systems. The current-based systems are assumed to be limited by one of three phenomena: thermal, electromagnetic or structural. The results are given for constant gap and scaled gap. The scaling parameter, L , is the dimensionless scale factor by which a given system is scaled up ($L > 1$) or scaled down ($L < 1$).

Time-dependent effects are also important for system scaling. The ratio of the conductor thickness to the skin depth is referred to as the eddy current ratio (ECR). For $ECR > 1$, eddy current effects are important. Two common scaling relations for frequencies are constant frequency and reciprocal frequency scaling. Although the details differ, for both common frequency scaling laws ECR increases with increasing scale size. Hence, for small scale sizes, smaller eddy current effects are produced. This has important implications for small scale eddy current-generated repulsive suspension systems.

As shown in the table, the scaling law to be applied depends upon the situation under analysis and whether the gap is scaled. Current based magnetic suspension systems generally increase in gap magnetic energy at least as fast as PM-based systems, and possibly faster, depending upon the limiting factors. For current-based systems the slowest rate of increase in gap energy is for constant-stress systems, and the greatest increase in gap energy is for constant current density and constant boiling latent heat

systems. Heat transfer-limited systems are intermediate between constant stress and constant current density systems.

The advantage for current-based systems over PM systems as scale size increases becomes a disadvantage as scale size is decreased. For decreasing scale size, the gap energy of PM systems decreases no faster than the most favorable current-based system.

The generation of eddy currents is also sensitive to scale size. For the cases analyzed the effects of eddy currents increase with increases in scale size and decrease with decreases in scale size. Hence, eddy current repulsive magnetic suspension systems will readily scale up but will require careful system design for small scale applications.

In summary of the scaling laws, a system to be increased in scale size is preferably a constant current density, constant gap system and may be based upon eddy current repulsion. A system to be decreased in scale size is preferably a scaled-gap system with either PM or a stress-limited current and is not based upon eddy currents.

Thermal Management

In many applications, the management of thermal issues is an important, if not dominant, concern. In some applications, the ambient temperature may be very high. For attractive ferroelectromagnetic suspensions the power dissipated in resistive heating must be removed or the system will continuously increase in temperature. Repulsive superconductive levitation systems must provide cryogenic cooling to the superconductors.

Table 4 below shows some of the important properties of typical coolants. The purpose of this table is two-fold: to suggest why HTSCs offer such a significant improvement over LTSCs from a thermal standpoint, and to promote the consideration of LH_2 as a useful cryogen with excellent properties. The improvements of LN_2 over LHe can be seen to be in the heat of vaporization H_{fg} and in the refrigerator efficiency. Boiling LN_2 carries away 10 times the heat per kg as boiling LHe . The refrigerator efficiency is the electrical power consumed (W) per unit input thermal power (W), or Watts/Watt. As an example, if a LHe refrigerator has an input heat power of 4 Watts, the electrical power required to remove it is 7 kW.

Liquid hydrogen cryogen is becoming more commonplace as a result of two different circumstances: safety concerns are alleviated with the positive experience which has been gained handling liquid hydrogen from the space program, and the exceptional properties of materials at LH_2 temperatures are becoming well-known. In particular, the electrical resistance of high purity cryogenic aluminum will decrease by a factor of over 1000 when operated at 20 K. This makes several high current pulsed power applications feasible.^{3,4}

The remainder of this paper discusses two specific applications of magnetic

suspensions: magnetic bearing for turbine engines and magnetically levitated (Maglev) trains. Due to the limited volume available within the turbine housing, attractive magnetic bearings historically have been favored. As will be shown later, this observation agrees with the derived scaling laws. Attractive and repulsive Maglev systems have been developed in parallel by qualified and dedicated engineers. It appears that in this application the systems each have relative advantages and disadvantages with respect to one another. Non-technical factors increasingly become the basis for a system preference. Nevertheless, we shall discuss these relative advantages and disadvantages so the reader can understand the issues involved.

Magnetic Bearings for Turbines

Magnetic bearings for high speed rotor and turbine applications have been receiving an increasing amount of attention.^{5,6,7,8,9} This is primarily due to the increasingly severe requirements of the applications, the limits on conventional bearings and the non-contact nature of magnetic bearings. Other advantages of magnetic bearings are: no temperature limit of the suspended body, although, of course, the bearing material itself has limits; better bearing reliability; reduced maintenance requirements; improved perturbation damping capabilities; and magnetic follower control. This last concept is interesting since it allows an eccentric rotor to spin within the limits of the bearing housing.

In the most demanding applications, bearings for aircraft gas turbine engines, magnetic bearings may allow a 50% increase in the DN rating over conventional bearings. The DN rating is the product of the shaft diameter (in mm) and the rotational frequency (in rpm) and is presently in excess of 2.2 million with efforts under way to exceed 3.3 million.

Table 5 gives an example of the magnetic bearing requirements for a high performance gas turbine engine.

Magnetic Levitation for Transportation

Magnetically levitated (Maglev) trains are a good example of magnetic suspension systems not only because of the obvious reason, but also because from a different perspective Maglev is a System of systems. Maglev is 80% about moving people and freight, gaining right-of-way and in-flight meals and only 20% about technical issues. Levitation is but one of four or five important technical issues. Therefore, the issue of how levitation is actually achieved, although important, cannot be decided upon without due consideration of other important issues, some technical and some non-technical. We shall point out some of both types of issues below.

The attractive magnetic suspension is implemented with normally resistive electrical conductor and highly permeable cores. Attractive systems lend themselves to either the linear induction motor (LIM) or the linear synchronous motor (LSM) for propulsion.

The repulsive levitation scheme is implemented with low-temperature superconducting (SC) magnets on-board the vehicle and normal (resistive) conductor coils either on the ground or on the guideway vertical side-wall.

Superconductors dissipate energy due to alternating currents. As shown above, this energy is expensive to remove (1750 W/W for LTSC systems) and increases the possibility of SC quench. Hence, the apparent frequency of the LIM is deleterious to SC operation and operation in the LSM mode is preferred. However, there are studies being pursued presently which will examine the possibility of a superconducting LIM.¹⁰

Figure 5 conceptually shows the attractive and repulsive Maglev systems. Table 6 shows the operating characteristics of Maglev trains.

In the following subsections, we discuss each Maglev suspension scheme in additional detail.

Maglev Attractive Scheme

The overall weight of the vehicle determines the upward force required from the magnet. The available magnetic pole area then determines the required magnetic pressure, which determines the air gap magnetic field. The material hysteresis curve then determines the drive current required to achieve the specified field. The drive current determines the dissipated power. Due to non-linear magnetic saturation, this design procedure generally is repeated until the designer is satisfied that either all parameters are reasonable or an entirely new design is required.

As shown in the table above the overall mass of the attractive system is greater than for a repulsive system. Because the attractive system is weight sensitive, the levitation system has been highly optimized¹¹ and the greatest achievable levitation force per unit current is attained by design.

The support magnets are distributed uniformly down the length of the train. Each of the support magnets independently determines its air gap. Uniform distribution has the advantage of reducing the peak force loading on the guideway. Independent suspension has the advantage of minimizing the nominal air gap due to guideway perturbations. For example, if all magnets down the length of the train had to be set for the largest required air gap then the magnet currents and dissipated power would increase.

An advantage of the ferromagnetic attractive system is the inherent magnetic field shielding provided by the fact that the magnetic flux is confined to ferromagnetic materials and has only a small air gap to traverse. This advantage is often overlooked and should not be minimized. Although the effects of either low level direct current (dc) or alternating current (ac) magnetic fields on people are not well-known, there are many people concerned about potential effects thereof and this issue will have an impact on the acceptance and cost of Maglev systems.

The iron-cored long stator linear motor operates in combination with the magnetic levitation subsystem. Essentially, the excitation magnets of the motor also perform the chores of suspension magnets.¹² The guidance magnets are a dedicated subsystem operating on the attractive principle (attract-left, attract-right). With this system, the lateral acceleration is positively controlled in both directions.

It is an interesting fact that the attractive suspension system only attracts upward. Vertical perturbations in the guideway can only be positively responded to if they require an upward force. The downward force requirement is supplied only by gravity. A vertical acceleration of ± 1 g is generally sufficient for transportation applications but in force-transducer applications a greater range is frequently desired. A greater range of acceleration, of course, can readily be supplied by a levitation system which attracts downward to a ferromagnetic rail. Modulation between the upward and downward systems can provide the desired forces and accelerations.

The necessity of accurately following the guideway perturbations increases the requirements on the secondary suspension system. The secondary suspension system is the interface between the support magnets and the passengers. The function of the secondary suspension system is to smooth the ride for the passengers.

Large gap attractive magnetic suspension schemes are possible but require large ferromagnet masses, large dissipated power and large reactive power capacity.

Maglev Repulsive Scheme

The dominant technical feature of an air core superconducting maglev system is the magnetic field of the superconducting (SC) magnets. The functions of propulsion, guidance, levitation and inductive power transfer to the vehicle are accomplished by utilizing this stray flux.

Figure 6 shows a superconducting repulsive maglev system. In the figure, the vehicle is imagined to come out of the page and the view is of the right hand side of the vehicle. The left hand side is symmetrically designed. Note that there are two air gaps: one vertically and one horizontally oriented.

Lateral guidance is achieved by cross-connected propulsion coils as shown in Figure 7a and b. Drive current is supplied at one location as shown. The crossing of conductors under the guideway provides the proper field orientation for propulsion. This connection also serves to provide for balanced repulsion from the guideway walls. When the vehicle is laterally centered, Figure 7a, the flux passing through each coil is the same, the voltages are equal and opposite and no net current is induced. If the vehicle is displaced laterally, as in Figure 7b, more flux passes through the closer coil and less through the coil further from the vehicle. The flux difference drives a current which repels the vehicle from the closer coil and attracts it to the further coil--a lateral restoring force.

Figure 8 shows the coils in simplified rectangular wire form. The figure lists the

dominate force interactions which provide the vehicle propulsion, guidance and levitation.

A quench of a superconducting magnet is possible during Maglev operation. If this occurs while the Maglev train is traveling at high speed, sufficient safety mechanisms must be provided to prevent train contact with the guideway. One design approach is simply to have excess levitation capability in reserve so that, when degraded by a quench, sufficient lift remains. An implementation of this concept is shown in Figure 9.

An electrical schematic of the null flux coils is shown in Figure 10. The functional operation of these coils is very similar to that of the guidance coils. The center of the SC magnet tends to pass with equal flux passing through the upper and lower loops. If the SC magnet dips below the equal-flux point, currents are generated which tend to raise the SC magnet. If the SC magnet is above the equal-flux point, currents are generated to pull down the SC magnet. Thus the loaded vehicle rides displaced slightly downward to induce levitation forces equal to the vehicle weight.

CONCLUSIONS

We have reviewed the physics of attractive and repulsive magnetic suspension systems, discussed methods to engineer such systems, shown figures and tables of materials properties which indicate operating envelopes and regions, briefly identified some of the systems issues, discussed scaling laws, and discussed thermal issues. In addition, we presented two examples of magnetic suspensions, magnetic bearings for turbines and magnetically levitated trains.

There does not appear to be any inherent physics advantage of either suspension system. The difference between systems is in the details of the requirements for the particular application. In some applications, attractive systems have unique advantages while in other systems repulsive systems have especially desirable qualities.

Magnetic suspension design requires a systems approach. After a comprehensive system-level analysis the decision of an attractive or repulsive suspension system properly can be made.

REFERENCES

1. Jackson, J.D., Classical Electrodynamics, John Wiley, New York, 1975, p. 188.
2. Landau, L.D., and Lifshitz, E.M., Electrodynamics of Continuous Media, Pergamon Press, New York, 1975, p. 119 ff.
3. Cope, D.B., Snyder, M.D., Weisman, R.M., "The Magnetic and Structural Design of a Liquid Hydrogen-Cooled Magnet Utilizing High Purity Aluminum Conductors and a Boron/epoxy Composite as Structural Reinforcement," *Advances in Cryogenic Engineering*, Vol. 35, Ronald Fast, ed., Plenum Press, New York, 1990.
4. Eckels, P.W., et al, "Cryogenic Generator Cooling," *Advances in Cryogenic Engineering*, Vol. 35, Ronald Fast, ed., Plenum Press, New York, 1990.
5. Ulbrich, H. "Elements of active Vibration Control for Rotating Machinery," NASA Technical Memorandum 102368, May, 1990.
6. Itoh, M., Ishigaki, H., and Hida, A., "Fabrication of Y-Ba-Cu-O Superconductor for Magnetic Bearing," *IEEE Trans. on Mag.* Vol. 25, No. 2 March, 1989, p. 2518.
7. Knoth, E., Barber, J., "Magnetic Repulsion Bearings for Turbine Engines," *IEEE Trans. on Mag.*, Vol. 24, No. 6, November, 1988, p. 3141.
8. Tichy, J.A., Connor, K.A., "Geometric Effects on Eddy Current Bearing Performance," *Transactions of the ASME*, 88-Trib-15,
9. Nonami, K., "Vibration and Control of Flexible Rotor Supported by Magnetic Bearings," NASA Technical Memorandum 10088, June 1988.
10. Contract from USDOT to Intermagnetics General Corp., William R. Mischler, technical contact, (start date July 1991).
11. Meins, J., and Ruoss, W., "The Support and Guidance System," *Transrapid Maglev System*, Transrapid International, 1989, p. 79.
12. Ibid.
13. Cope, D., "Cryogenic Inductor Program," Final Report WL-TR-91-2037, Wright Laboratory, Air Force Systems Command, Wright-Patterson AFB, OH, June 1991, p. 2-20.
14. Clessow, G., et al, "The Long-Stator Propulsion System and its Power Supply," *Transrapid Maglev System*, Transrapid International, 1989, p. 50.

Table 1. Combinations of Magnetic Poles

Pole 1 --> Pole 2	Ferro- magnet	Electro- magnet	Permanent Magnet	Super- conductor
Ferromagnet	X	A - 1,3	A	A
Electromagnet	A - 1,3	A - 5, R - 5	A - 4, R	A, R - 2
Permanent Magnet	A	A - 4, R	R	R
Superconductor	A	A, R - 2	R	R

KEY:

X No interaction

A Attractive System

R Repulsive System

1. (Maglev) German Transrapid system, British Rail Birmingham Line, Japanese Air Lines High Speed Surface Transportation
2. (Maglev) Japan Rail Group (formerly Japan National Railway), MLx-nnn series
3. Turbine magnetic bearings
4. Turbine bearing (hybrid system: permanent magnets with ferroelectromagnets)
5. Metal forming due to pulsed magnetic fields and induced eddy currents.

The normal magnetic force ("levitation") can either be attractive or repulsive.

Table 2. Magnetic Suspension Issues

- Air gap dimension
- Levitation force
- Air gap pressure
- Levitation stability
- Operating temperature
- Mass of suspension system
- Power (active and reactive)
- Speed
- Suspension stiffness
- Effect of stray magnetic fields
- Aerodynamic forces of high speed trains and turbine bearings
- Inertial forces
- Thermal expansion due to guideway differential movement

Table 3. Magnetic Suspension Scaling Laws

System	Conditions	Constant Gap		Scaled Gap	
		Energy	Pressure	Energy	Pressure
1. Permanent Magnet Systems		$\sim L^4$	$\sim L^2$	$\sim L^3$	$\sim L^0=1$
2. Current-based Systems					
2.1 Heat Transfer-limited	$h=\text{constant}$	$\sim L^5$	$\sim L^3$	$\sim L^4$	$\sim L^1$
	$h \text{ scaled } \sim L^{0.6}$	$\sim L^{5.6}$	$\sim L^{3.6}$	$\sim L^{4.6}$	$\sim L^{1.6}$
	latent heat = constant	$\sim L^6$	$\sim L^4$	$\sim L^5$	$\sim L^2$
2.2 Current Density-limited	$J = \text{constant}$	$\sim L^6$	$\sim L^4$	$\sim L^5$	$\sim L^2$
2.3 Stress-limited	$\sigma = \text{constant}$	$\sim L^4$	$\sim L^2$	$\sim L^3$	$\sim L^0=1$

Note: h is the surface heat transfer coefficient of units ($\text{W/m}^2\text{-K}$) and is scaled according to the ref.¹³, J is the conductor current density of units (A/m^2), and σ is the mechanical stress of units (Pa).

Table 4. Properties of Coolants

Coolant	T_{boil} (K)	H_{fg} (J/kg)	C_p (J/kgK)	dT (K)	$C_p dT$ (J/kg)	Refrig. Eff. (W/W)
LHe	4.2	21,000	4500	1	4500	1750
LH ₂	20	443,000	10,000	5	50,000	400
LN ₂	77	200,000	2000	10	20,000	95
H ₂ O	373	2,500,000	4200	75	315,000	-

It is noteworthy that many the magnetic properties of ferromagnetic materials improve as the temperature is decreased. This may be a fruitful area for future research.

Table 5. Example Magnetic Bearing Requirements
for Aircraft Turbine Engines

<u>Parameter</u>	<u>Value</u>
DN Rating	> 3 million
Equivalent Speed	> 170 m/s = 400 mph
Diameter	5"
Rotor Speed	26,000 rpm
Axial Thrust	~4000 lbs.
Radial Load	~1000 lbs.
Bearing Compartment Temp.	1000 K
Stiffness	100,000 lb./in = 17 MN/m
Air Gap	0.010"

Table 6. Characteristic of Maglev Trains

<u>Parameter</u>	<u>Attractive Lev.</u>	<u>Repulsive Lev.</u>
Designer	Transrapid 06 ¹⁴	Foster-Miller, Inc.
Levitation Height	10 mm	100 mm
Number of Passengers	200	152
Number of Vehicles	2	2
Maximum Speed	400 kmph	500 kmph
Minimum Lev.	Standstill	25 m/s
Train Mass	122 T	66 T
Support Magnets	Distributed	Concentrated
On-board Power Consumption	240 kW	120 kW
Reactive Power	15 MW	Negligible
Aerodynamic Drag	50 kN	27 kN
Motor Type	LSM	LSM
Magnet Lift/Weight	10	7-9

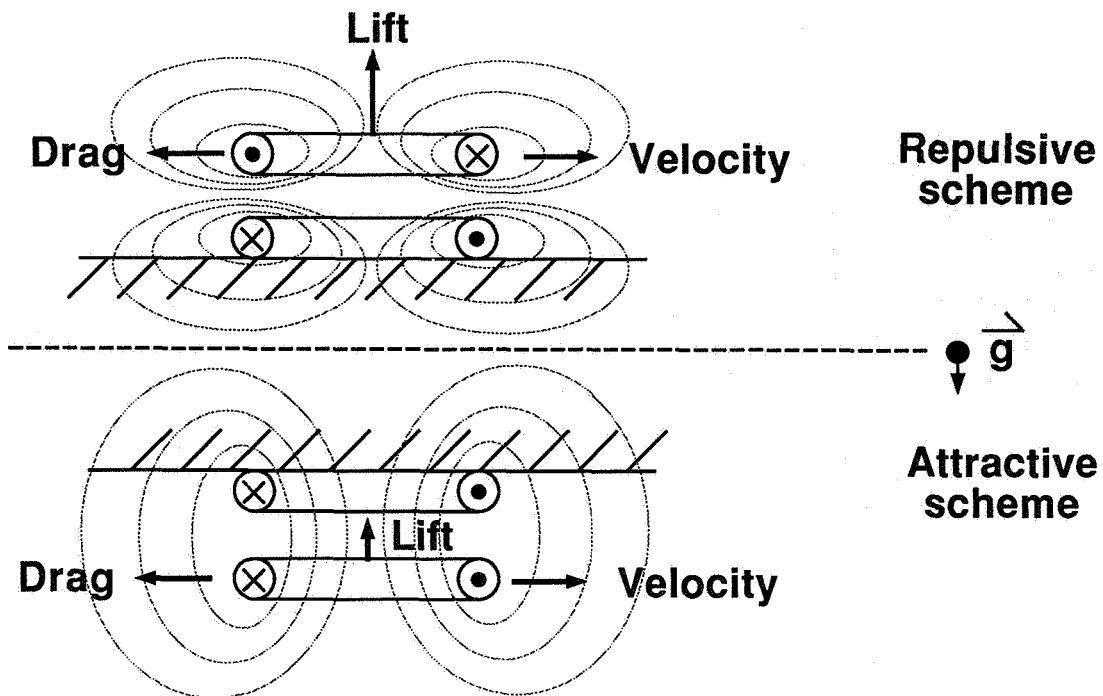


Figure 1. Attractive and Repulsive Coils

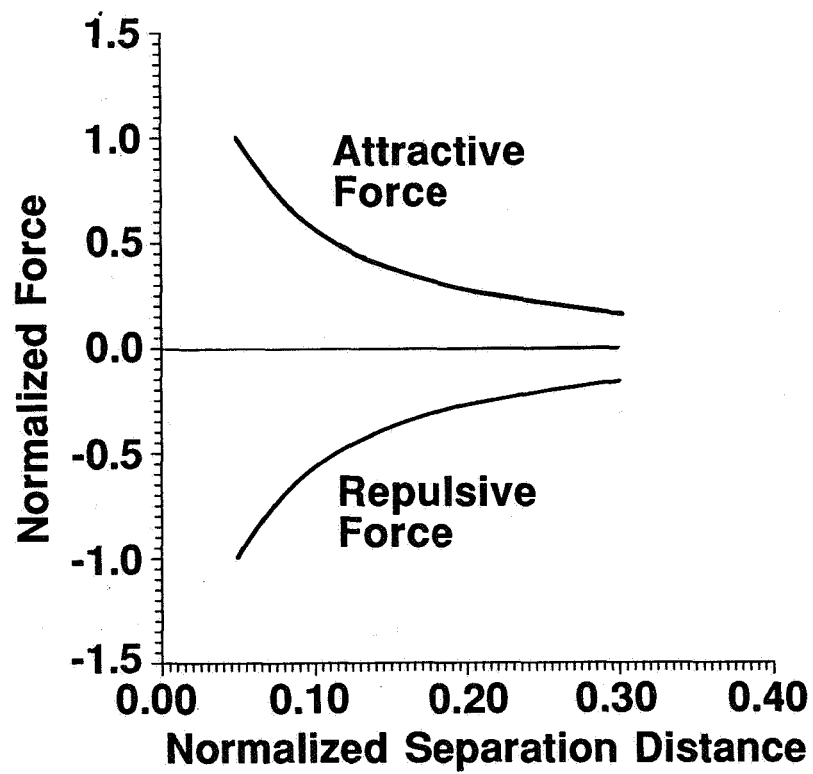


Figure 2. Axial Force vs. Coil Separation

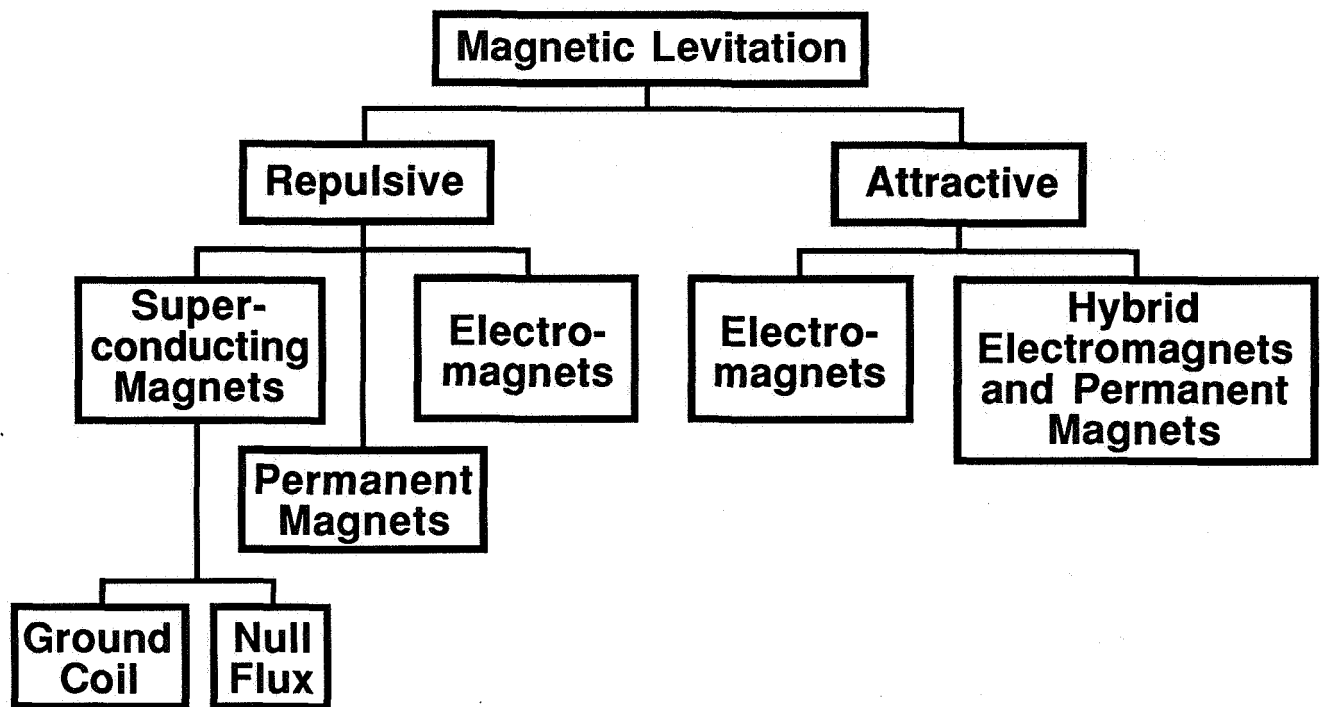


Figure 3. Magnetic Levitation Systems
Corporate Structure

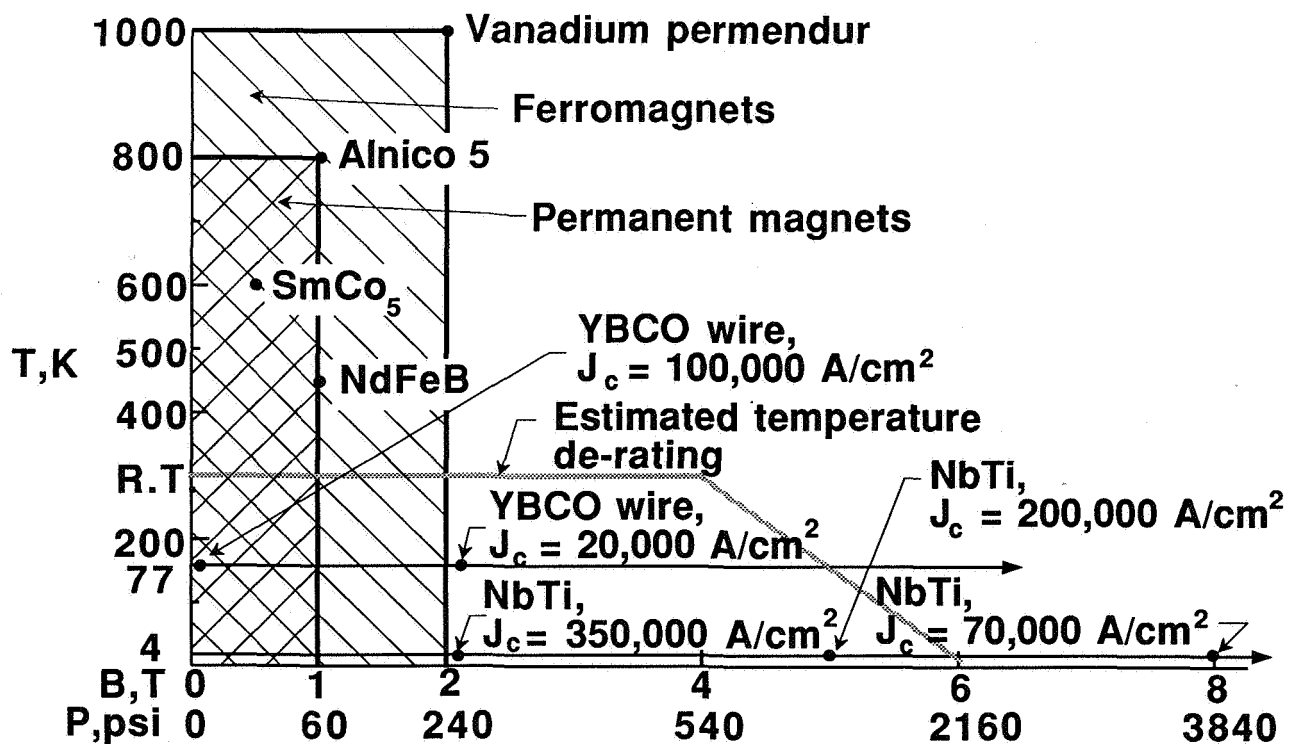


Figure 4. Temperature vs. Magnetic Field

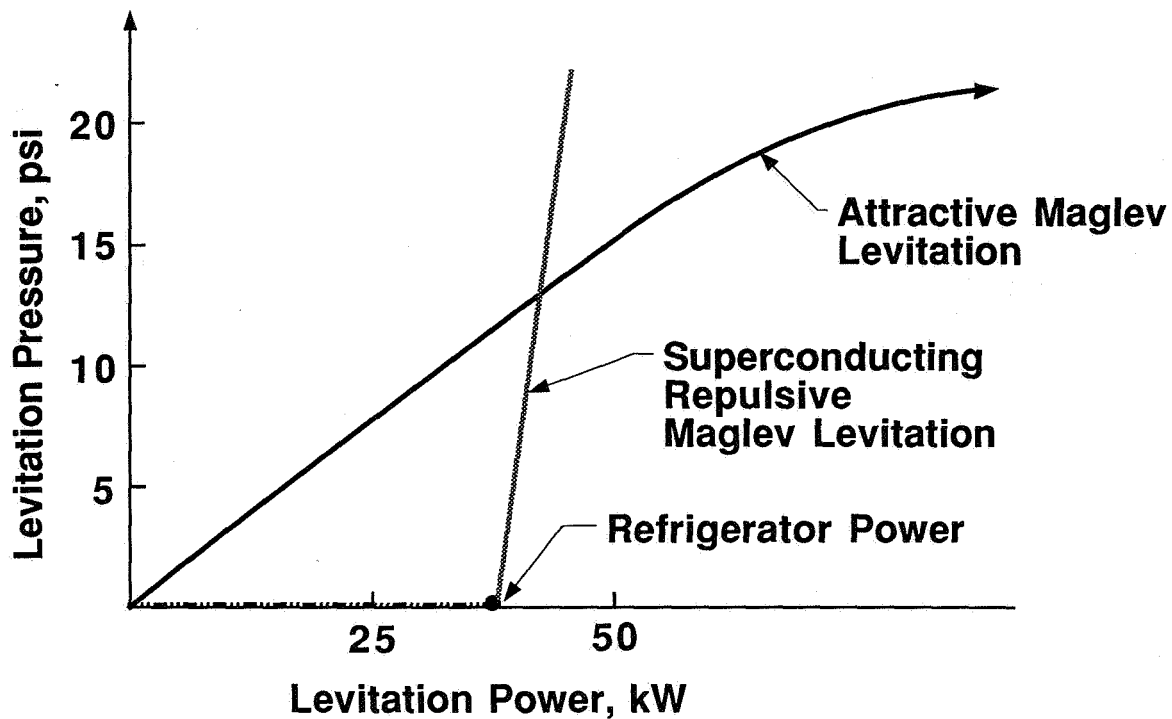


Figure 5. Levitation Pressure vs. Required Power

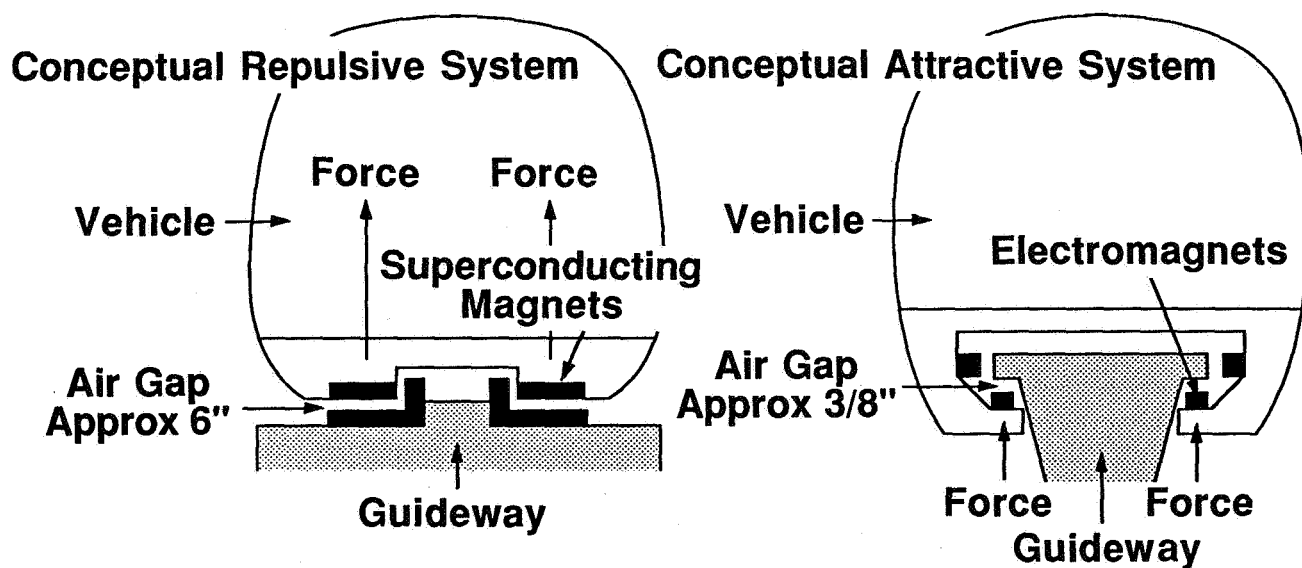


Figure 6. Conceptual Attractive and Repulsive Maglev System

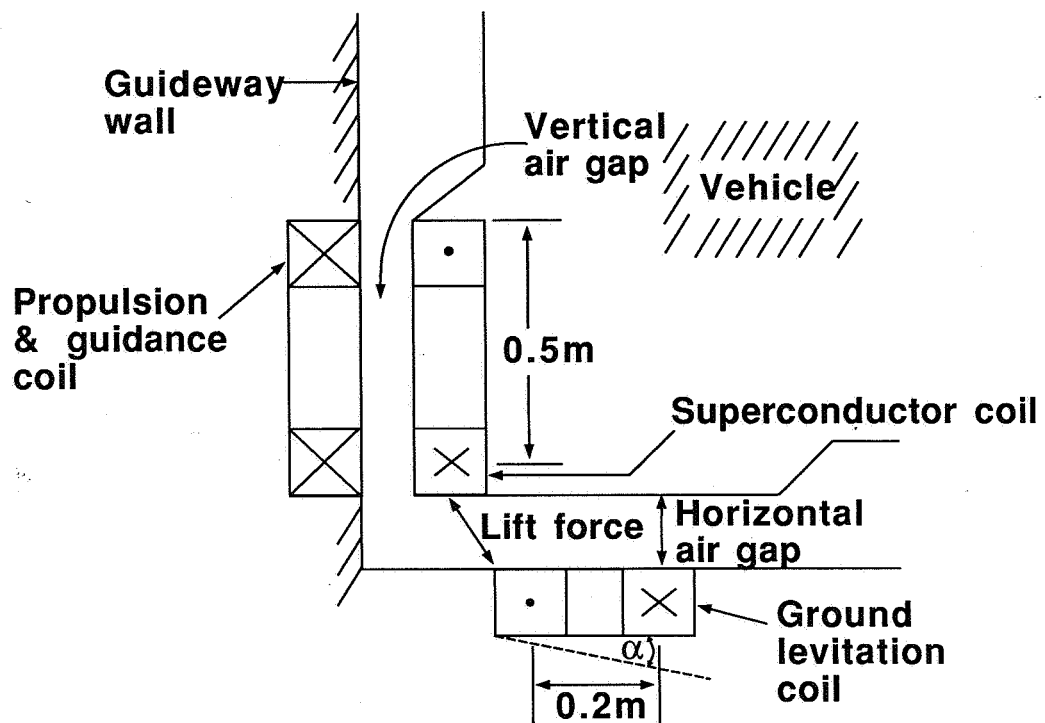


Figure 7. Ground Coil Levitation Design

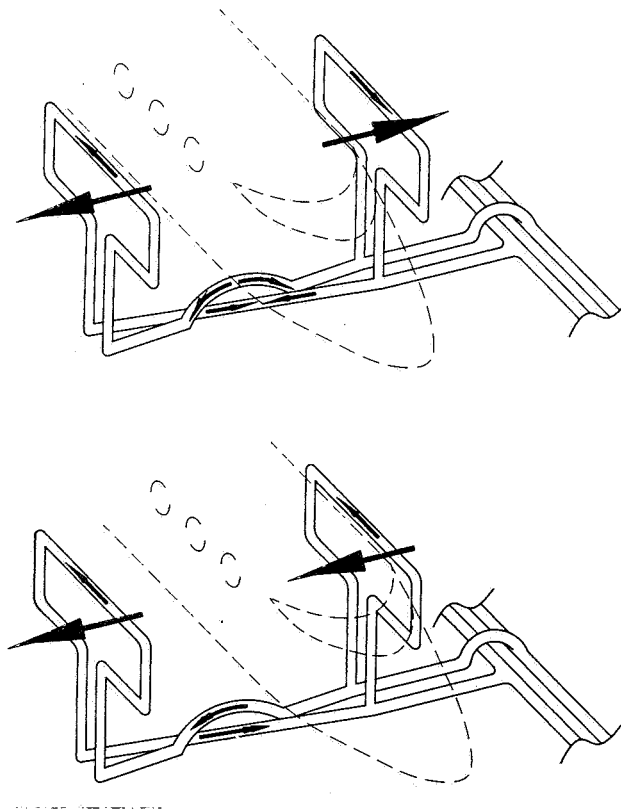
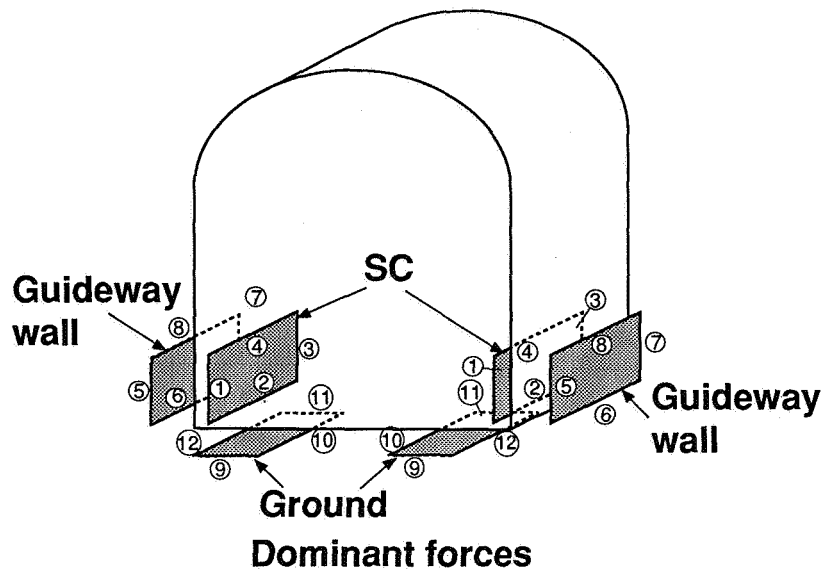


Figure 8. Guidance Coil Schematic



Propulsion: ① & ③ Interacting with ⑤ & ⑦
Levitation: ② & ④ Interacting with ⑩ & ⑫
Guidance: ① ② ③ & ④ Interacting with ⑤ ⑥ ⑦ & ⑧

Figure 9. Ground Coil Dominant Forces

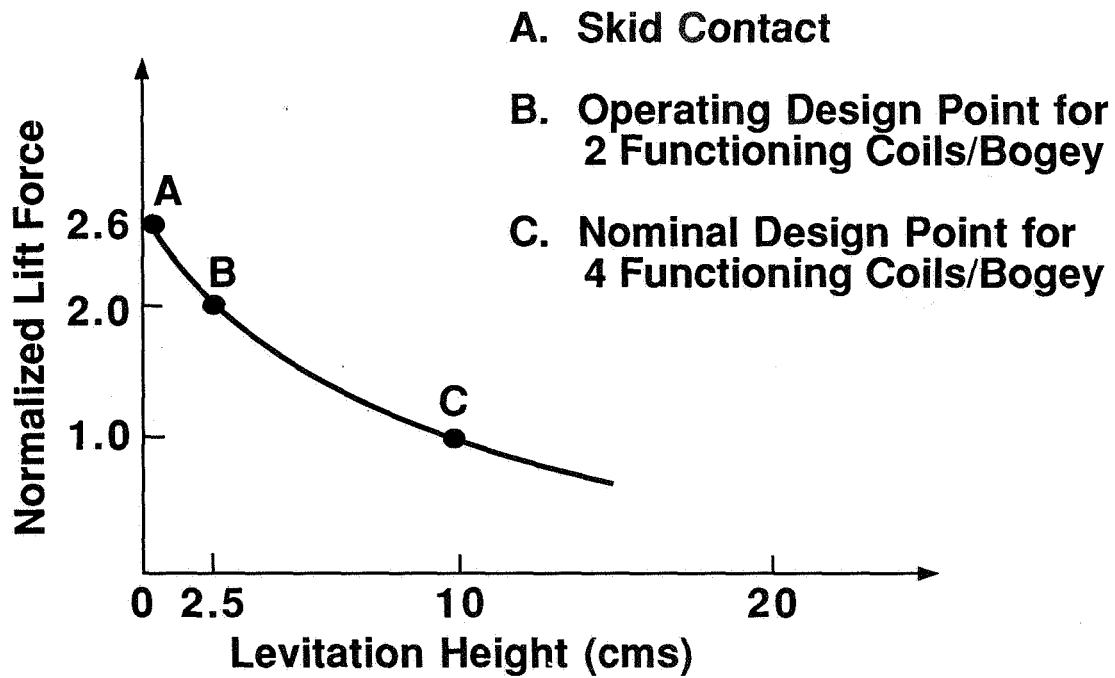


Figure 10. Magnetic Levitation as a Function of Height

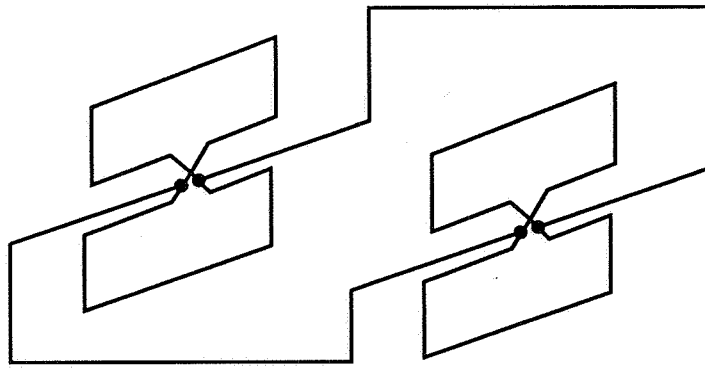


Figure 11. Null Flux Coil Electrical Schematic

N92-27806

CHANGE IN THE COIL DISTRIBUTION OF ELECTRODYNAMIC SUSPENSION SYSTEM

Hisashi Tanaka
Japan Railways, Railway Technical Research Institute

SUMMARY

At the Miyazaki Maglev Test Center, where test runs started with superconducting coils paralleled with ground levitation coils, that is, the facing levitation system, (after the development of the superconducting coil with a high magnetomotive force which makes it possible to levitate, propel and guide a maglev train only by this superconducting coil), the coil distribution has been changed to the facing levitation system where both types of coils are located perpendicular to each other, and then further changed to the side wall levitation system with practical tests near at hand on the new Yamanashi Maglev Test Line. Here, our approach to the project is introduced.

INTRODUCTION

In the days of the now defunct Japanese National Railways (JNR), a maglev transportation system featuring superconducting magnets, electrodynamic suspension, active track linear synchronous motor propulsion and null-flux magnetic guidance has been selected as a system desirable for future high-speed ground transportation. The reasons are as follows:

- (1) It is possible to run at a high-speed of 500 km/h or more.
- (2) This system is advantageous in the aspect of noise because the vehicle runs completely non-contacted with track surface, and saves the track and vehicle maintenance troubles.
- (3) The comparatively large air gap of about 100 mm between a vehicle and the track surface ensures the safety even with earthquakes.
- (4) The levitation system adopting a self-stabilizing system needs no special control.

The electrodynamic suspension is divided roughly into a system with sheet on the ground and one with coils on the ground. The coil system is adopted because

- (1) Magnetic drag is less.
- (2) The degree of freedom in design is higher.

The related work started in 1970. Since 1977 test runs have been carried out on the Miyazaki Maglev Test Track. Recently the basic technology development stage has been virtually completed, and a decision was made to proceed to practical tests on the Yamanashi Maglev Test Line which is now under construction. In step with the development of superconducting coil and with progress on related tests, the coil distribution has been modified twice. The background concept is to be described.

FACING LEVITATION SYSTEM WITH PARALLEL COILS

At the time when the Miyazaki Maglev Test Track was planned, the magnetomotive force of a superconducting coil able to be manufactured was about 450 kA, so the superconducting coils were located separately for levitation and for propulsion (Fig. 1a, Fig. 2a). The coil surface of a levitation superconducting coil (250 kA) was

faced horizontally a levitation ground coil which was also horizontally, thus constituting a facing levitation system. The coil surface of a propulsion superconducting coil (450 kA) was faced vertically. A propulsion ground coil was also vertical, thus constituting a linear synchronous motor. For guidance, instead of setting coils for this, the propulsion coils located on both sides of the track facing each other were connected to form a loop resulting in a null-flux circuit.

At the beginning, assuming that cycloconverters serve as the power converters, the technology, then had output frequency limited to about one third of the input frequency. Supposing that the input is a commercial frequency (50 Hz or 60 Hz in Japan), the pole pitch will be more than 3.5 m. The Miyazaki Maglev Test Track was intended for first stage test runs. In order to minimize the necessary track length, acceleration was set larger (0.3-0.4 g), which shortened the track length to 7 km. The length of a test vehicle was set at 10 m, which makes the length of the superconducting coil portion of the vehicle equal to 8 m. For a larger thrust, 4 poles are needed with a pole pitch of about 2 m, so the commercial frequency (60 Hz in Miyazaki Prefecture) was stepped up to 120 Hz through a motor generator. The pole pitch of 2.1 m, a multiple of 3, was taken finally because a three-phase alternating current was to be used. Consequently, the pitch for the propulsion ground coil is 1.4 m. As for the levitation ground coils, the pitch is 0.7 m, which is calculated from the pitch ratio 1:3 for levitation coil vs. superconducting coil in order to suppress the fluctuation of levitation force.

In order to concentrate thrust and brake force around to the gravity center of a vehicle because of a larger acceleration as mentioned above, an inverted-T shaped cross section was adopted for the guideway. The ground coil for both levitation and propulsion is made of rectangular aluminium wire coil and sheet mold compound. The superconducting coil is of the race track type so as to avoid the magnetic field concentration. Because the maximum empirical magnetic field about 5 T for the magnetic levitation is not so high, the wire made of niobium titanium alloy series has so far been consistently used. However, at that time the stability depended upon copper with a higher copper ratio of 5 to 6. The coil of both types for levitation and propulsion are housed in a cryostat of L-shaped cross section.

In December 1979, an ML-500 test vehicle on the inverted-T shaped guideway registered a maximum speed record of 517 km/h, surpassing the target speed, which demonstrates the high-speed running ability of this system.

For the inverted-T shape guideway, the framework mounting the superconducting magnets is designed in an arch type. In addition the opening and shutting vibrations due to repulsive forces occurred, causing the framework to be broken, which plagued us. ML-500 is an unmanned test vehicle. Taking into account the commercial version, the vehicle body is mounted on the arch shaped framework, so the vehicle becomes inevitably taller.

FACING LEVITATION SYSTEM WITH PERPENDICULAR COILS

Later, the guideway was re-modelled to a more practical U-shaped cross section. In the meantime, as it has become possible to manufacture a superconducting coil with a magnetomotive force of 700 kA class, one superconducting coil can perform all the functions of suspension, guidance and propulsion (Fig. 1b, Fig. 2b). Thus the vehicle construction has been substantially simplified. Out of necessity for propulsion and guidance, the coil surface of superconducting coil is made vertically. Thus a facing levitation system has been adopted as a levitation mechanism in which a superconducting magnet is located at right angles to a levitation ground coil. As for the ground coils, the levitation coil remains unchanged, while the propulsion one has been transferred to the side walls.

When an intrinsically stable wire using ultra-fine core has been manufactured as a superconducting wire, light weight by decreasing the copper ratio is realized and the direct contact with liquid helium is needless, making it possible to strengthen the wire through epoxy impregnation. An inner vessel has been transformed into a tube, resulting in an increased strength. In addition, a much decreased cross section of the vessel reduces the charge of liquid helium.

The superconducting coils are arranged continuously in the running direction and the passenger room comes just above the superconducting coils; accordingly, a 2.3 mm thick steel plate is laid on the floor as a magnetic shielding. As a result, the strength of the magnetic field in the room is about 20 mT on the floor surface, 10 mT on the seat, 5 mT on the passenger's back, and 3 mT at the head rest portion of a seat.

Three U-shaped MLU001 test vehicles have been manufactured. In February 1987, a 2-car unit manned by three persons registered a maximum speed of 400 km/h.

In order to investigate vehicle dynamics related to guideway irregularity, test runs have been carried out with various artificial irregularities created on the viaduct beams and in the coil distribution (Fig. 3, Fig. 4). The test vehicles have passed safely over the irregular sections with an enough air gap sustained in all test runs, which confirms the advantage of the electrodynamic suspension system with a large air gap. Further, the vehicle vibration due to the irregularity has been damped within one wave, verifying the sufficient damping ability of the system.

SIDE WALL LEVITATION SYSTEM

In parallel with test runs of the Miyazaki Maglev Test Track, the structure of a commercial maglev vehicle also has been elaborately examined (Fig. 5). At first, the maximum magnetomotive force of a superconducting coil available at that time was about 500 kA, so it has been planned to arrange the coils continuously in the direction the train is running. Thereafter, as the magnetomotive force is raised, a system in which a decreased number of coils are concentrated over the coupling position of an articulated train has been mainly examined. The decrease in superconducting magnets contributes to lighter vehicles, decreased costs, improved ride comfort derived from a larger mass ratio of vehicle body vs. bogie, and easier magnetic shielding of the passenger space. Moreover, the research on a circulating current type cycloconverter through which the output frequency is upped to about two thirds of the input frequency has been advanced, which makes it possible to decrease the pole pitch.

The MLU002 test vehicle has been built with the main target of testing the system with concentratedly distributed superconducting coils (Fig. 1c). The rated magnetomotive force has been raised from 650 kA for MLU001 to 700 kA. However, since the decrease in the number of superconducting coils lowers the electromagnetically levitated height, the copper ratio of superconducting wire has been reduced to 1 instead of 2 for MLU001 and the current density has been increased from 173 A/mm² to 219 A/mm², resulting in a reduced cross section of superconducting coil. At the same time, the cryostat's cross section has been reduced. All these efforts have contributed to maintaining the air gap of 100 mm. Consequently, however, the superconducting coils have been weakened, inducing sometimes a quenching during test runs. As a counter-measure against this, the current density has been lowered to about 180 A/mm² or less to yield a margin. In addition, the cross section of a coil and an inner vessel have been widened to increase the rigidity.

The articulated vehicle has fewer superconducting coils than the MLU002 test vehicle does, which increased the load (Fig. 1d). Moreover, to protect pacemakers implanted in a passenger's body the magnetic field of the passenger space must be minimized to about 1 T. The decrease of pole pitch is being examined to strengthen the superconducting coil and to lower the magnetic field. When these things materialize,

the straight portion of a superconducting coil will be decreased, which means a shortage of levitation force for the facing levitation system, so it has been decided to change the levitation system from facing levitation to side wall levitation. In the meantime, with a recent advance in the GTO thyristor, the power converter will be switched to an inverter, so there will be no problem when the frequency is increased due to the shortened pole pitch.

For the side wall levitation system, the levitation ground coils ("8"-figure coils) formed by invertedly connecting two loop coils are set on the side walls. The repulsive and attractive forces acting between the horizontal coil edges of both superconducting coils and "8"-figure coils yield a levitation force larger than the facing levitation system does in spite of the same current rate for both systems. With the generated levitation force being the same for both systems, the smaller induced current is sufficient for the side wall levitation system, resulting in a smaller magnetic drag. Furthermore, when the wheels run with the superconducting magnet center falling upon the "8"-figure coil center, the induced current is not generated in the "8"-figure coil and the magnetic drag due to the coil loop is null. The side wall levitation system is one in which the balance point is clear. For this system the magnetic spring coefficient in vertical direction is more rigid, so the superconducting magnets must be installed on the bogie with the elasticity being maintained.

For the side wall levitation system, using the levitation ground coil as a null-flux circuit for guidance can be constituted. Thus, it is possible to eliminate the high voltage for propulsion from the null-flux cable.

Moreover, because it is found that a greater fluctuation of the magnetic field under the conventional single layer distribution of propulsion coils generates more heat within the superconducting magnet, the coil distribution will be converted to a double layer one as a countermeasure. The commercial system will be located with a high voltage of about 22 kV to haul a larger train. Epoxy resin etc. will be used for the formation of propulsion coils.

These coil distributions have already been tested on the part of the Miyazaki Maglev Test Track (Fig. 2c, Table 1, Fig. 6, Fig. 7). While the construction of the Yamanashi Maglev Test Line is in progress, more elaborate recognition tests will be undertaken on a prolonged modified section of the Miyazaki Maglev Test Track.

The side wall to be installed with all ground coils must be erected with high accuracy to secure a good ride quality of the vehicle. The other requirements of the side wall are as follows: easy elimination of the irregularities due to aging; smaller deformation under condition of vehicle running and meteorological conditions such as insolation; less steel consumption such as reinforcing steel rods in order to lower the magnetic drag. To meet these requirements, a guideway of beam structure is under development.

As for the non-contact current collection on account of the on-board items such as lighting, air-conditioning, and refrigerator drive, the efficiency will be down in comparison with the facing levitation system which is more efficient in this respect. Special care should be taken such as providing a superconducting coil specialized for power collection.

Because the gangway runs over the upper part of superconducting magnet, the part must be shielded magnetically. The application of high-temperature superconductors to this part is being studied.

CONCLUDING REMARKS

In Japan, at first the electrodynamic suspension system was developed exclusively for passenger transportation because passenger traffic is predomi-

nant in this country. The land being mountainous, it is impossible to do without tunnels, so it is imperative to decrease the cross section of a vehicle as much as possible. In addition, taking into account conditions such as lighter vehicle, lower costs, improved mass ratio of vehicle body vs. bogie, and easy magnetic shielding, the superconducting coils in a commercial system will have to be located just over the junction between vehicles. In addition, the levitation system has been changed to a side wall levitation system, in which an ample suspension force will be secured even when the pole pitch is decreased to strengthen the superconducting coils and to lower the magnetic field on board. The two layer coils complicate the ground structure a little, raising a future problem of lowering the construction costs. A different alternative will be taken when there is no tunnel, for vacuum tube transportation, or for freight transportation, etc.

Lastly, it should be added that this development project has been subsidized by the Japanese Government.

REFERENCES

1. Fujiwara, S.: Characteristics of EDS Maglev Having Levitation Coils on the Side Wall of the Guideway, Quarterly Report of RTRI, vol. 29, no. 4, Nov. 1988, pp. 157-163.
2. Fujiwara, S.; Fujimoto, T.: Characteristics of the Combined Levitation and Guidans System Using Ground Coils on the Side Wall of the Guideway, Quarterly Report of RTRI, vol. 30, no. 3, Aug. 1989, pp. 123-126.
3. Fujimoto, T.; Fujiwara, S.: Electrodynamic Characteristics of MLU002, Quarterly Report of RTRI, vol. 32, no. 2, June 1991, pp. 50-58.

Table1 Coil Parameters of Miyazaki Side Wall Levitation

Superconducting coil	Length×Width	m	1.7×0.5
	Pole pitch	m	2.1
	Magnetomotive force	kA	700
Ground coil (per one loop)	Length×Width	m	0.55×0.31
	Number of turns		36
	Resistance	mΩ	24
	Inductance	mH	0.89
	Height of loop center	m	0.195
Between coil centers(Gap)		m	0.2

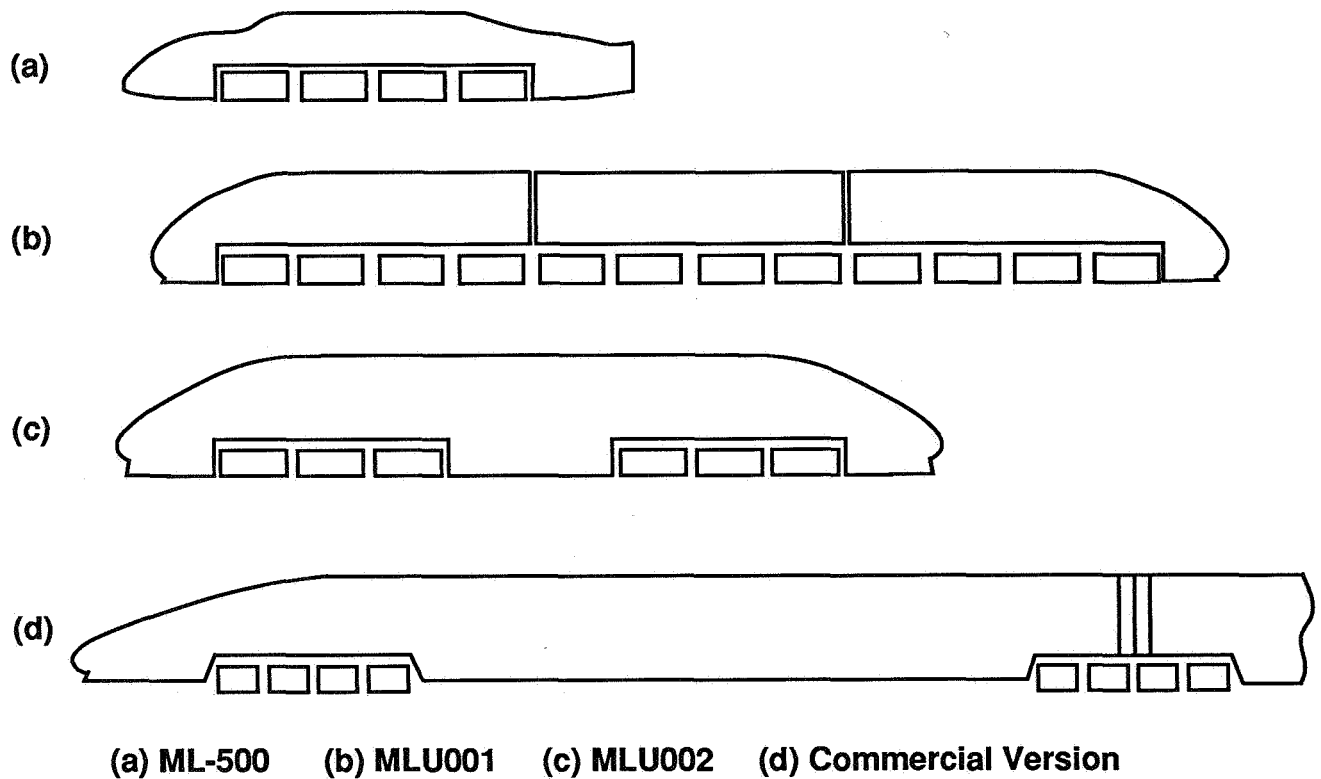
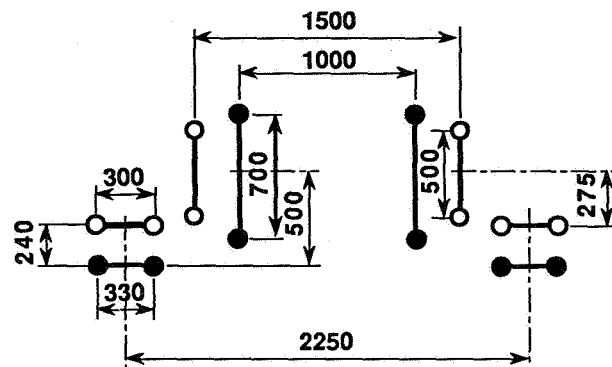
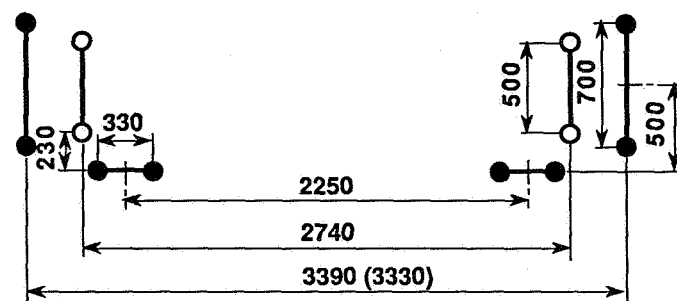


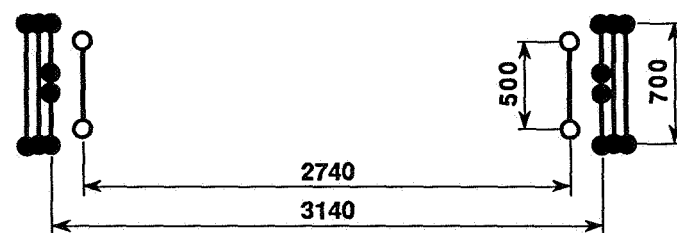
Fig.1 Coil Distribution of Test Vehicles



(a) Facing Levitation System, ML500



(b) Facing Levitation System, MLU001, ():MLU002



(c) Side Wall Levitation System, MLU002

○—○ On-board superconducting coil ●—● Ground coil

Fig.2 Coil Distribution of Miyazaki Test Track

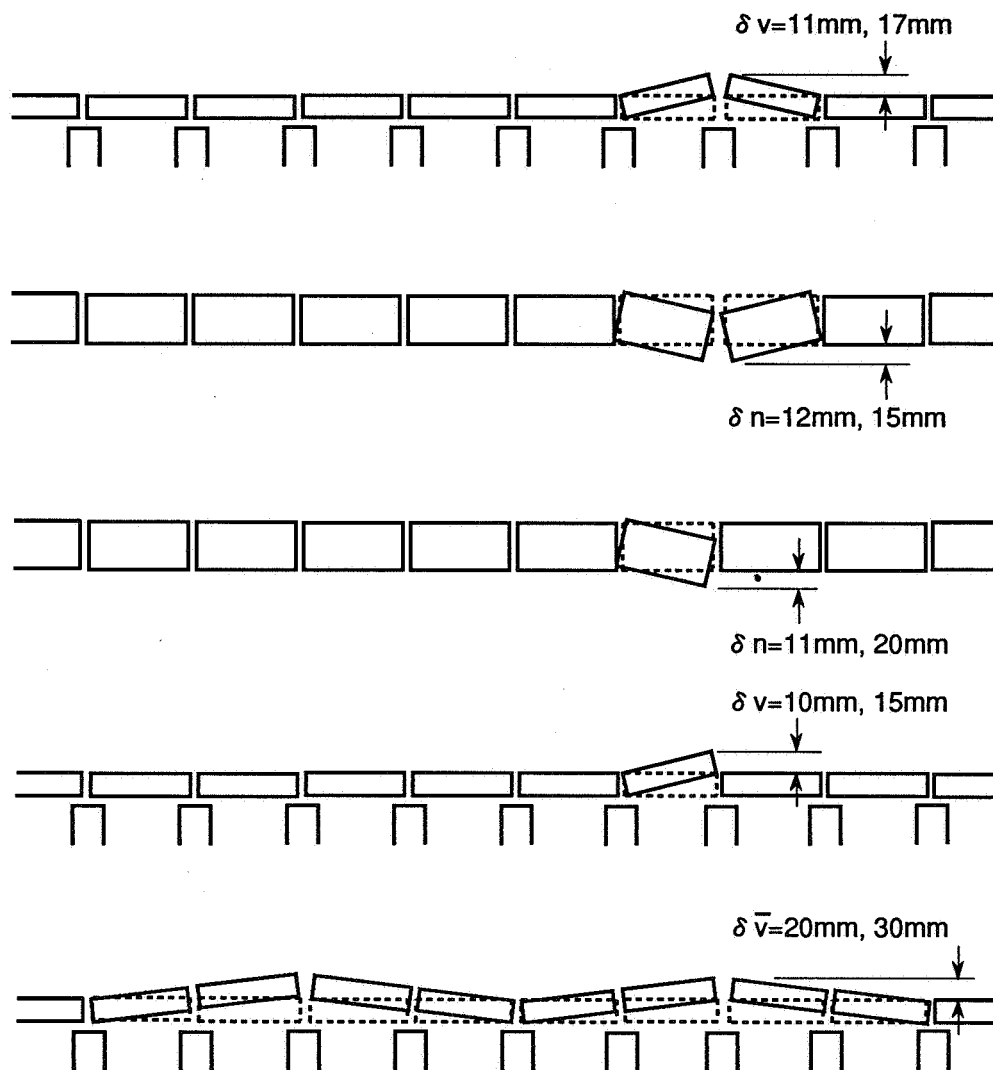
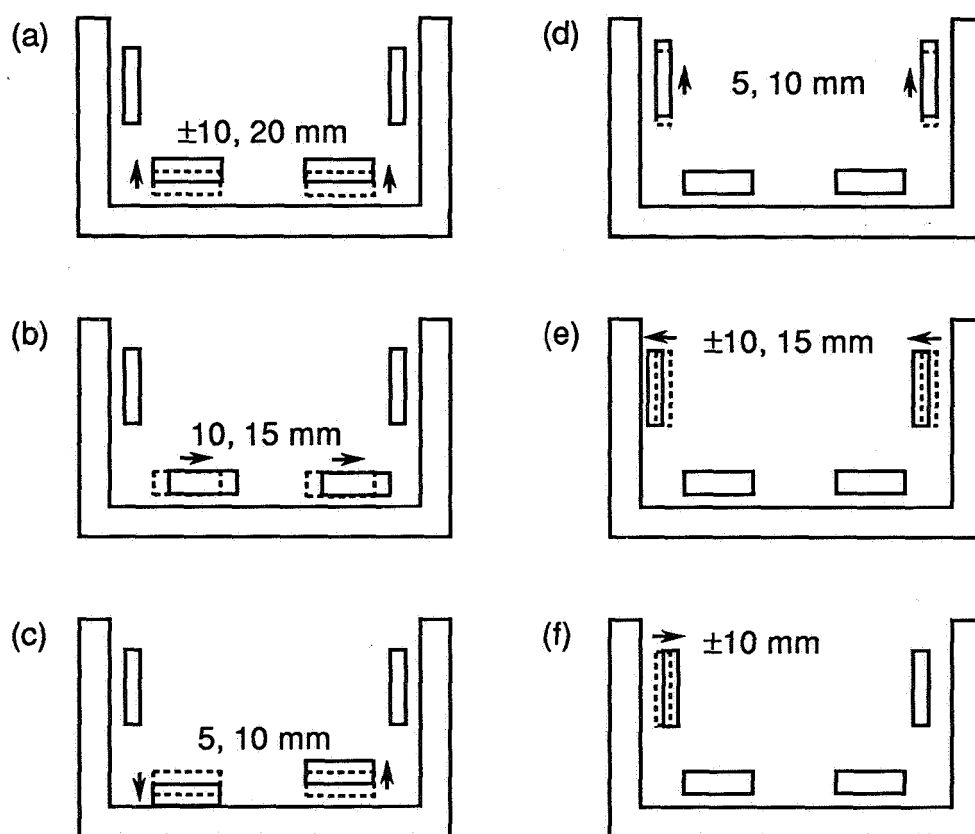


Fig. 3 Guideway Irregularity Test



$L = 46.2 \text{ m}$ ---- (b), (c)
 50.4 m ---- (a), (d), (e)
 168.0 m ---- (f)

Fig. 4 Coil Irregularity Test

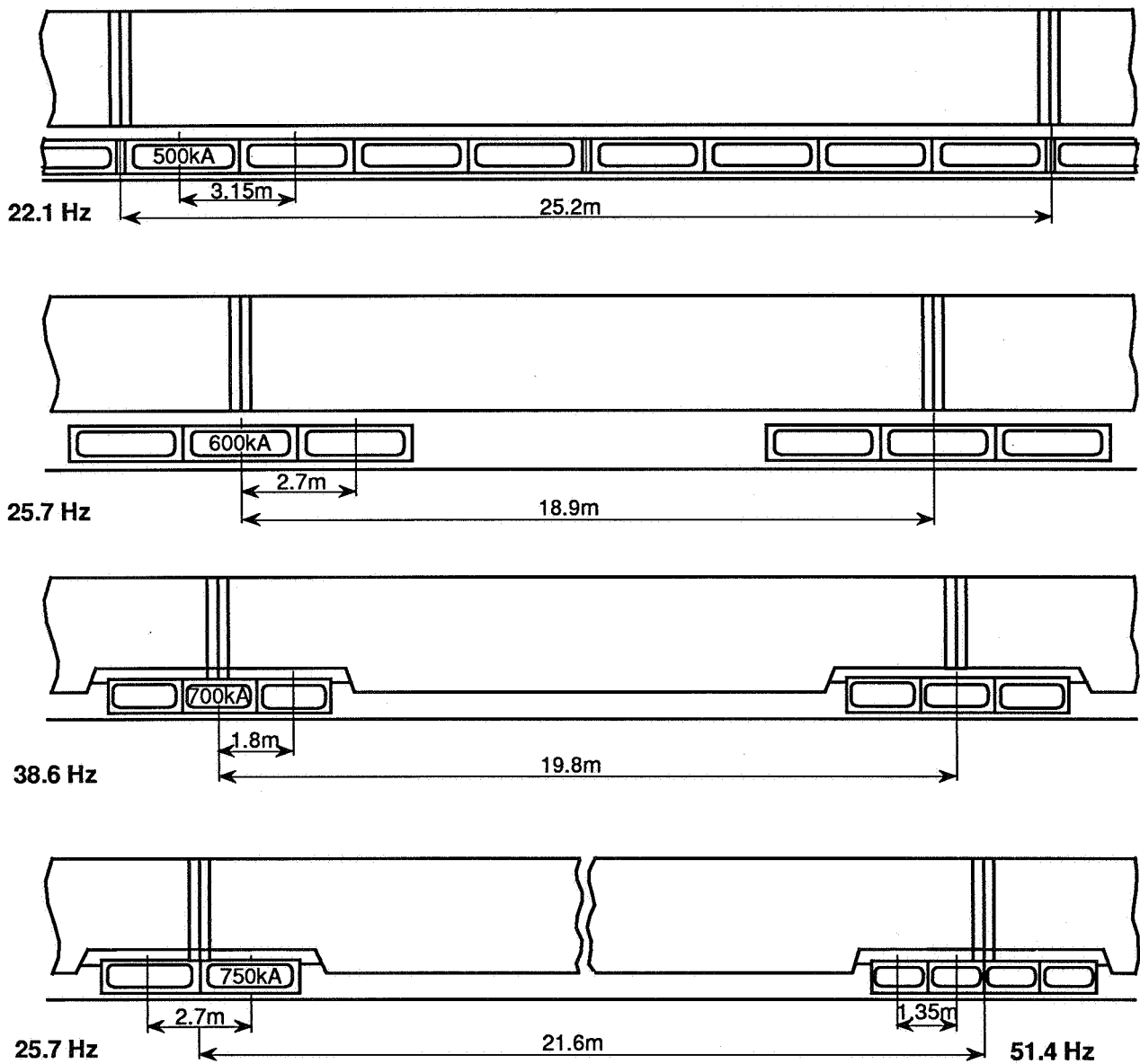


Fig.5 Progress of Investigation on Commercial System

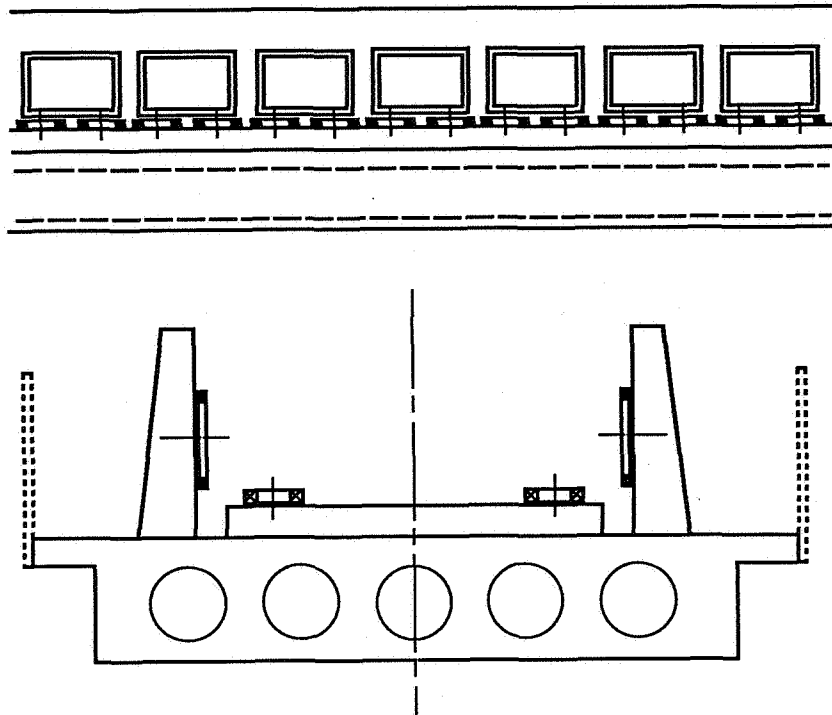


Fig.6 Miyazaki Guideway in Facing Levitation System

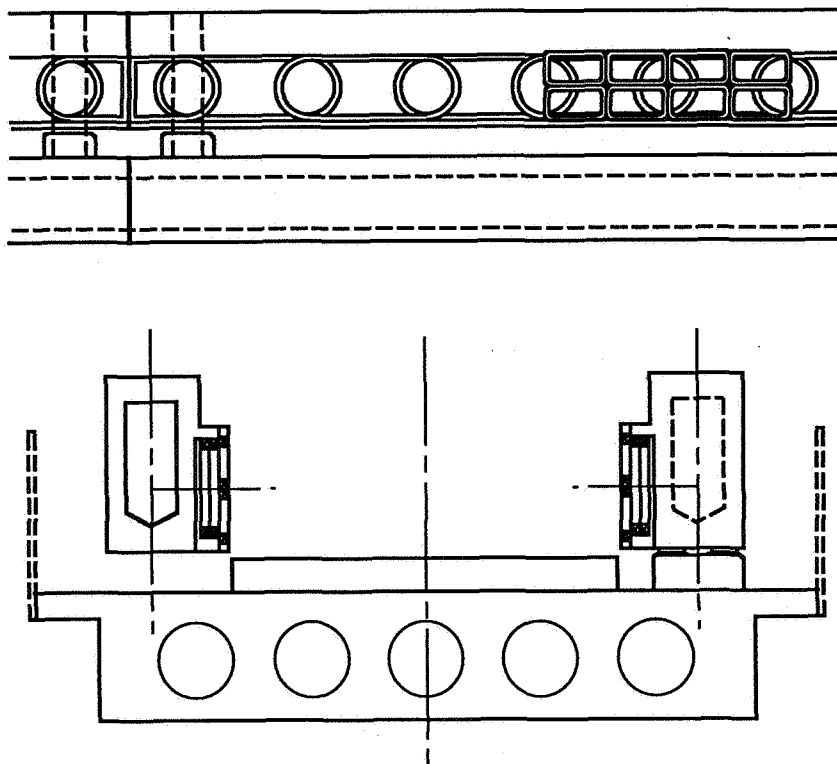


Fig.7 Miyazaki Guideway Converted to Side Wall Levitation System

N92-27807

THE CONCEPT OF THE MECHANICALLY ACTIVE GUIDEWAY
AS A NOVEL APPROACH TO MAGLEV

T. G. Horwath

TG&C Associates, Inc.
One Cessna Lane
Falmouth, Virginia 22405

22 August 1991

PRECEDING PAGE BLANK NOT FILMED

Abstract:

A maglev system suitable for operation in the United States has to meet unique requirements which determine the major system characteristics. Maglev configurations presently developed in Germany and Japan are based on conventional maglev concepts and as such do not meet all of the requirements. A novel maglev guideway concept is introduced as a solution. This concept, the mechanically active guideway, is articulated in three degrees of freedom and assumes system functions which normally reside in the maglev vehicle. The mechanically active guideway contains spatially distributed actuators which are energized under computer control at the time of vehicle passage to achieve bank angle adjustment and ride quality control. A typical realization of the concept is outlined.

1. Introduction:

The United States represents a unique environment for a maglev system. The size of the country, the location and the nature of the population centers are different from other areas of the world, and travel in terms of passenger miles per capita, for both business and pleasure, is substantially higher than in any other nation. By far the largest amount of travel is done by automobile over short to medium distances, a fact which is becoming less desirable from both economic and environmental viewpoints. Longer distance travel is done primarily by air, which is energy intensive and also detrimental to the environment. Efforts are underway to curtail the dependence of transportation on oil imports by promoting mass transit, and by doing so to simultaneously reduce pollutants. Conventional rail based mass transit is limited by insufficient connectivity with other transportation modes and by relatively low speed, for short as well as long distance travel. Maglev promises to circumvent these limitations by offering an alternative mass transit mode.

A maglev system to be suitable to the United States has to meet a set of requirements which result from the uniqueness of the environment within which it has to operate. These requirements are the following:

- (1) It must use existing right of ways, such as the median of interstate highways. The acquisition of new right of ways in highly populated areas would incur unacceptable initial capital cost.
- (2) It has to be able to carry high passenger loads, on the order of 50000 per hour per track, to justify and amortize the high initial capital investment.
- (3) It must be capable of high speeds, comparable to average block speed of air carriers, which is in excess of 300 miles per hour.
- (4) It must be able to serve stations at less than 20 mile intervals.
- (5) It has to be energy efficient, consuming less than 20 MW per mile, in bidirectional traffic.
- (6) It must be connectable to other transportation systems, like rail, subways, and highways.
- (7) It must have low construction costs, preferably 20 million dollars or less, per mile.
- (8) It must offer superior ride comfort compared to other means of transportation
- (9) It must be reliable and require low maintenance.
- (10) It has to have low environmental impact and must be aesthetic in appearance.

Some of these requirements have a great degree of influence on system characteristics of maglevs suitable for operation in the United States.

The requirement of using existing right of ways (1), for instance, dictates that the maglev be capable of negotiating tight turns, with radii of about 1.5 miles, which are typical for the interstate highway system, and railroads. Adding the requirement of high speed (3) dictates that the turns must be made at substantial bank angles, to avoid excessive side forces detrimental to stability and passenger ride comfort.

High passenger loads (2) and short distances between stations (4) can only be met by provisions for off-track loading, so that the

guideway is not occupied by parked maglevs, keeping other maglevs from transiting.

Energy efficiency (5), low construction cost (7), together with environmental and aesthetic considerations (10) require light weight cars, which in turn allow lighter guideway construction, but may compromise ride comfort (8).

Some of these requirements may be difficult if not outright impossible to meet with current maglev concepts upon which the maglev configurations presently developed in Germany and Japan are based. Meeting the requirements above becomes tractable, however, if conventional concepts, such as a fixed guideway, are abandoned.

The concept of the mechanically active guideway is introduced here. This guideway has limited articulation in three degrees of freedom and thus assumes functions which conventionally reside in the maglev vehicle. The concept of the mechanically active guideway was evolved from functions which the maglev system has to perform to meet the requirements listed above. Some of these functions will be analyzed below and the mechanically active guideway concept will be described.

2. Control of Bank:

To execute tight turns at high speed, the turning of the maglev vehicle has to be "coordinated". This is a term common in aviation with the meaning that the direction of the vector sum of gravity acceleration and centrifugal acceleration is perpendicular to the grand plane of the vehicle, resulting in new ride forces.

The centrifugal accelerations of a vehicle moving at a velocity v on a track with a radius of curvature R is

$$a_c = v^2 / R \quad (1)$$

To achieve the new ride force condition the vehicle has to bank at an angle

$$\beta = \arctan(a_c / g) = \arctan(v^2 / gR) \quad (2)$$

The total acceleration, the vector sum of centrifugal acceleration and gravity acceleration is then

$$a_t = (g^2 + a_c^2)^{1/2} \quad (3)$$

or

$$a_t = [g^2 + v^4/R^2]^{1/2} \quad (4)$$

This total acceleration is higher than the acceleration due to gravity, and the passengers of the vehicle will experience higher "g-forces" resulting in higher weight. While a small increase in weight may be hardly noticable, larger increases could result in physiological effects well known in military aviation.

From (2) and (4) we get the total acceleration as a function of bank angle

$$a_t = (1 + \tan^2 \beta) \quad (5)$$

This function is tabulated below

β	a_t
15°	1.035
30°	1.155
45°	1.414
60°	2.000
75°	3.864

Table 1

The radius of curvature of a coordinated turn negotiated at a given vehicle speed is obtained as

$$R = v^2 / b \tan \beta \quad (6)$$

which is tabulated below for two speeds, 300 km/hr and 500 km/hr

β	R(m)	
	300 km/hr	500 km/hr
15°	2442	7350
30°	1226	3411
45°	708	1970
60°	409	1137
75°	190	527

Table 2

Again, there is a strong dependence on bank angle.

The radius of a turn determined by a given rate of total acceleration, normalized to the acceleration due to gravity is determined from (2) and (5) as

$$R = v^2 / g(\alpha^2 - 1)^{1/2} \quad (7)$$

where α is the ratio of total acceleration to acceleration due to gravity. This radius is tabulated below as a function of percent acceleration increase over gravity.

B	R(m)	
	300 km/hr	500 km/hr
10%	1545	4298
20%	1067	2969
50%	633	1762
100%	408	1137

Table 3

The minimum turn radius of a maglev vehicle is thus determined by the maximum acceleration tolerated by the passengers. Assuming that a 50% increase in perceived body weight is tolerable the corresponding minimum turn radius would be 1762 meters, or a little more than one mile, at the speed of 500 kilometers per hour, or 312 miles per hour.

Entering turns can be accomplished at a minimum discomfort for the passengers by gradually increasing the bank angle until the value corresponding to vehicle speed and the turn radius is reached. Exiting turns is accomplished in reverse order. If the bank angle is increased linearly (constant rate of increase) with time for turn entering and exiting, then according to (2) the instantaneous turn radius of the transition section is defined by the differential equation

$$d/dt \{ \arctan[v^2 / gR(t)] \} = \text{const} \quad (8)$$

which, since $1/R(t) = K(t)$, the instantaneous curvature of the path, equation (8) then becomes:

$$d/dt \{ \arctan[v^2 K(t) / g] \} = \text{const} \quad (9)$$

In Cartesian coordinates, with the direction of travel before turning aligned with the x-axis, and the incidence of turn centered at the origin, the path is defined by the differential equation

$$d/dt \{ \arctan[v^2 y''(x)/g(1+y'(x)^2)^{3/2}] \} = \text{const} \quad (10)$$

where the constant is equal to the rate of change of the bank angle. One has to assure that sufficient time is allocated to complete the turn.

The immediate conclusion which can be drawn from the above results is that the bank angles of maglev guideways has to be substantial if existing right of ways with their tight turn radii are to be used. Furthermore, for a given turn radius the bank angles of the guideway required for coordinated turns (zero side forces) is strongly dependent on the speed. Significant side forces would result causing unacceptable discomfort to the passengers if the maglev vehicle were to deviate from the optimum speed required for a given bank angle. Forced speed deviations have to be expected, however, as a result of a number of conditions like system congestion and meteorological effects. In addition, one would also have to account for system power failures which would result in loss of propulsion with the vehicles coming to rest in turns at a very high bank angle, a condition equally if not more unacceptable to passengers. Constructing maglev guideways on existing right of ways, with fixed, high bank angles is therefore an unrealistic proposition.

3. Suspensions:

One of the most important characteristics of maglev systems is the stiffness of the primary suspension, which is primarily related to the weight of the maglev vehicle (including the bogies, if present) and the maximum permissible levitation gap variation, which should not exceed a small fraction (about 10-15%) of the levitation gap.

The electromagnetic maglev system has the highest primary suspension stiffness. At the typical maglev vehicle loaded weight (such as the German TR-07) of 53 metric tons distributed over sixteen levitation magnet sections, and a maximum levitation gap variation of about one millimeter (12.5% of the levitation gap), the stiffness of the individual levitation magnet section is about 32.5 Mega Newtons per meter.

Electrodynamic maglev system primary suspensions with their larger gaps have proportionally smaller stiffness. In this case, however, one has to further distinguish between repulsive bottom suspension and null-flux sidewall suspension. Contrary to the former, the stiffness of the latter is dependent on vehicle speed. Vertical stiffness component values for bottom suspension of 2.7 Mega Newtons per meter have been reported for the Japanese maglev system. The reported null-flux sidewall suspension stiffness values range between 3.82 and 7.05 Mega Newtons per meter over the speed range of levitation.

Even smaller stiffness values are expected for the Magneplane system, primarily as a result of the very large levitation gap of 25 centimeters and the commensurately larger allowable relative gap variations, which could be as large as 50% of the levitation gap width. The stiffness in this case is also nonlinear, which reflects the behavior of the electrodynamic forces over these large relative levitation gap excursions.

The stiffness of the suspension together with the mass of the portion of the car supported by it determines the natural frequency of the system. This natural frequency is given by

$$w_n = (\sigma/M)^{1/2} \quad (11)$$

where σ is the stiffness of the suspension element and M the mass supported by it. For the electromagnetic maglev system the natural frequency of the primary suspension is thus about 16 Hertz, while for the electrodynamic maglev system and the Magne Plane system, the natural frequencies are in the ranges of 4.5-7.3 Hertz and 1.2-1.7 Hertz respectively. The natural frequency of a suspension system has direct bearing on ride comfort as a result of the vibrational components transmitted to the passengers due to the guideway irregularities. Generally speaking, the higher the frequency components (the sharper the bumps) the more unpleasant the ride.

The primary suspension characteristics of the various maglev systems are summarized in Table 4 below.

System	Levitation Gap (m)	Stiffness (Nm ⁻¹)	Frequency (Hz)
EMS			
TR-7	8.5×10^{-3}	3.25×10^7	16.0
EDS			
Sheet	1.0×10^{-1}	2.70×10^6	4.5
Null Flux		3.82×10^6 -	5.3 - 7.3
		7.05×10^6	
Magne Plane	2.5×10^{-1}	1.90×10^5	1.2

Table 4

With the possible exception of the Magne Plane described by KOLM¹, the primary suspensions of the listed maglev systems are too stiff. Either massive, highly accurate and thus expensive guideway structures will be required, which will also be aesthetically unattractive, or the maglev vehicles will have to be equipped with secondary suspensions. The latter would increase the complexity of the maglev vehicles substantially, and thus be counter to the maglev vehicle design philosophy of simplicity.

4. Realizations:

The mechanically active guideway is, in principle, compatible with both electromagnetic (EMS) and electrodynamic maglev concepts. Only an electrodynamic realization will be discussed in the following.

Such a possible realization of the active guideway makes use of a box beam track (guideway) of triangular cross section, shown in Figure 1. The beam is hollow, open to the bottom for access, and could thus contain the various power and signal cables needed for the operation of the system. A similar concept employing a beam of rectangular cross section has been proposed by THORNTON². The propulsion magnets are flush mounted in the box beam. The box beam is extruded from aluminum alloy in sections which are welded together on site to form a continuous track. Curvatures for turn sections could be built in during the manufacturing process. Such curvatures would only amount to about 0.07 degrees

per meter deviation from straightness, at the minimum turn radius.

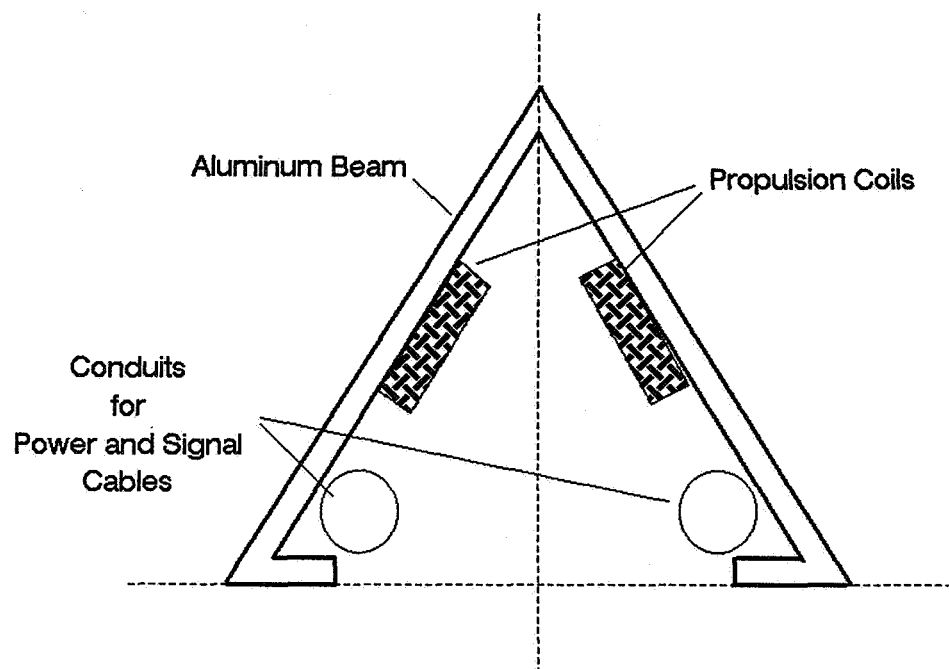


Figure 1
Guideway Box Beam

The metal beam track is secured to the concrete structure by means of actuators which would effect elastic deformations of the track for horizontal and vertical alignment and also for bank angle control. A typical cross section of such an arrangement is shown in Figure 2.

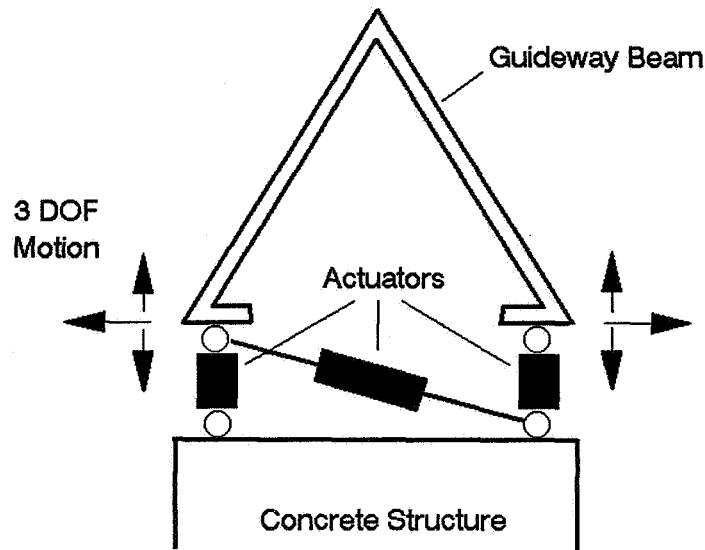


Figure 2
Guideway Beam Mounting

There are several advantages to a triangular cross section. The most important one is the greatly reduced stiffness of the suspension by the particular vector summation of the forces. Another advantage is that this cross section is easily deformable by twisting, requiring minimal actuator forces, while maintaining good mechanical stability in the vertical and horizontal directions. Furthermore, this profile makes efficient use of material. Additional advantages are incurred in the design of the vehicles riding such beams in terms of stability, efficient utilization of space, and better containment of stray magnetic fields. Better access and maintainability of guideway and vehicles are yet further benefits. Finally, there is one more very important consideration. A guideway of a triangular cross section of this kind would not permit debris to accumulate on its surface. A typical maglev car cross section on a triangular guideway is shown in Figure 3.

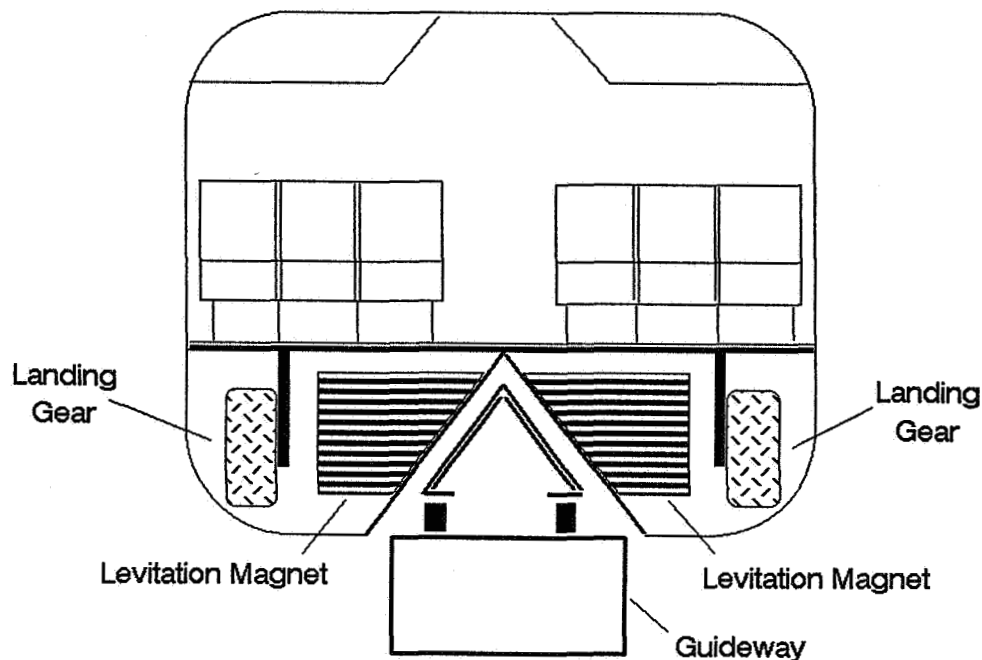


Figure 3
Typical Maglev Car

While two axis alignment would only require slight deformations, bank angle control appears to be significant at first. After all, the high speed turns at the minimum turn radii require bank angles of about 50 degrees. These bank angles, however, are achieved gradually. For a 30 degree course change, the length for the curved guideway at the minimum turn radius of 2000 meters would be about 1050 meters. Since the turn will commence with gradual change of bank angle, 500 meter long lead sections will be added for roll in and roll out. The distance over which the full bank angle will have to be established (and disestablished) is 1000 meters. The maximum torsional distortion (twisting) of the box beam required is 0.05 degrees per meter. The torque required to affect such a small deformation would be about 2×10^4 Newton meters. This would be well within the elastic range of the material. Figure 4. shows such a maglev turn.

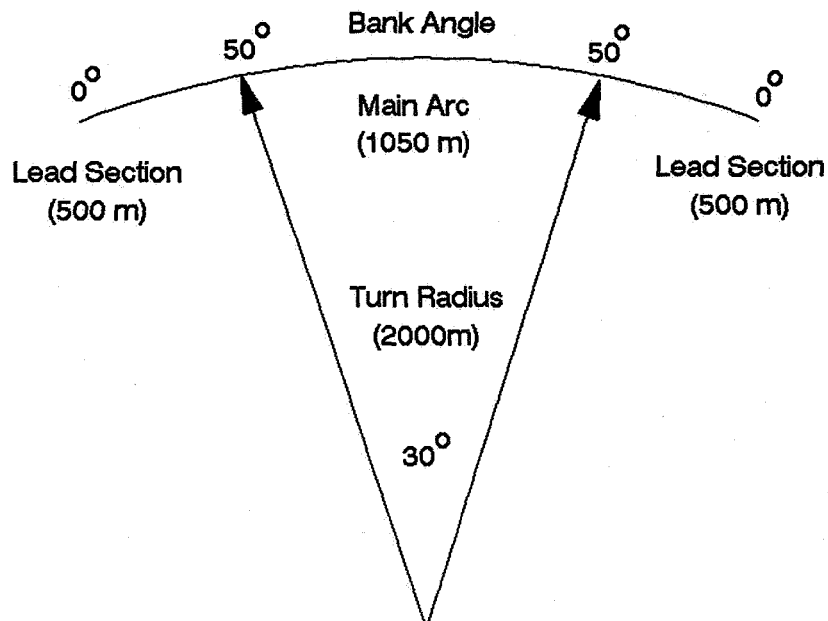


Figure 4
Typical Maglev Turn

The above example of transitioning from a level, straight section guideway to a maximum turning rate of about 50 degree bank angle is, of course, an extreme. The actuators will not have to exercise the full excursion of 50 degrees but only a fraction of this angle, since the guideway will be prebanked for some nominal speed, typically above minimum speed for levitation. The actuators would only have to fine-adjust this already existing bank angle to assure maximum coordination of the turn. The torsional stresses in the guideway sections as a result of actuator movements would therefore be less than in the example given above.

Electromechanical, as well as hydraulic actuators, could be employed to affect the required deformations of the track. Both types are very reliable. Electromechanical ones have the slight advantage that they could be powered directly from the electrical power feed and do not require the added complexity of hydraulic lines.

The actuators would be controlled globally as well as locally. Globally, from a central computer, in response to system wide parameters such as vehicle speed, traffic density, and environmental variables such as temperature, which can cause distortions of the guideway, and also tectonic activity which may

occur in rare circumstances. Local control variables would be derived from sensors on the vehicles measuring vertical and lateral acceleration levels, turn coordination, and load.

The large number of actuators distributed along the guideway would assure high tolerance to individual actuator failures. Graceful degradation of the active guideway control process would be a direct result of this high degree of system redundancy. Single actuator failure would hardly be noticeable in system performance but could readily be detected by self diagnostics provisions built into the actuator control process.

Power distribution to the guideway will be similar to other maglev systems. Typically meandering windings will form the propulsion coils which will be fed by power supply and conditioning units from wayside stations. The separation of these stations will be nominally about one mile. These wayside units will be fed by the power grid. The output voltage and frequency of these units will be set locally by computer control, in response to sensors located in the passing vehicles, and also in accordance with overall system commands given by a central control computer.

5. Conclusions

The mechanically active guideway deviates from the conventional maglev concept because it is not fixed and rigid in its installation. It is articulated in three degrees of freedom and accommodates vibration damping, bank angle control, and responds to load variations as well. This latter point may result in substantial cost savings in guideway construction in spite of greater system complexity since the capability of dynamic adjustments will allow less massive and thus less expensive concrete structures.

The mechanically active guideway concept may be paramount to making maglev a viable transportation system in the United States because of its adaptability to existing right of ways. It will further offer superior ride comfort, low environmental impact, and aesthetically pleasing appearance.

Finally, the mechanically active guideway concept represents a new design philosophy for maglev. This design philosophy recognizes the importance of coordinated turns, which are essential to tight turning radii at high speeds. It transfers many functions such as suspension, propulsion, control, and system monitoring from the vehicle to the guideway. This novel thinking, together with abandonment of a fixed, rigid guideway, severs maglevs traditional ties to its railroad heritage and establishes it as a new mode of transportation in its own right. It recognizes that maglev is not just another railroad.

6. References:

- (1) H. H. Kolm, Scientific American Vol 229, No4 (Oct 1973)
- (2) R. D. Thornton, Technology Review, April 1991

Session 15

SPACE APPLICATIONS

Chairman - Nelson J. Groom
NASA Langley Research Center

PRECEDING PAGE BLANK NOT FILMED

N92-27808

SPACE APPLICATIONS OF DIAMAGNETIC SUSPENSIONS

Ronald E. Pelrine

SRI International

Information, Telecommunications, and Automation Division

333 Ravenswood Avenue

Menlo Park, California 94025

(415) 859-3360

ITAD-733-PA-91-35

ABSTRACT

Conventional noncontact magnetic suspensions require power and sensor feedback to maintain stability of the levitated object. Magnetic suspensions using superconductors require neither power nor feedback for stability but must be maintained at low temperatures. This paper discusses a little known type of magnetic bearing that does not require power, sensor feedback, or cooling: diamagnetic suspension. While the bearing pressure for diamagnetic suspensions is typically limited to 1 gram force per square centimeter, their simplicity, environmental tolerances, and wide range of material choices suggest that they may be useful for a number of space applications. This paper discusses the fundamentals of diamagnetic suspensions as well as their potential space applications.

INTRODUCTION

Diamagnetic suspensions or bearings can best be understood by comparing them to superconductor bearings. Superconductor bearings using the Meissner effect are well known in the literature. These bearings are noncontact, consume no power, do not require feedback for stability, and are essentially dragless. However, superconductor bearings do require cooling, and the need for cooling increases cost and complexity, and lowers reliability for the system as a whole.

By contrast, diamagnetic bearings using ordinary, room-temperature materials are much less well known. Like superconductor bearings, diamagnetic bearings rely on the diamagnetic properties of materials subject to magnetic fields. Diamagnetic bearings are also noncontact, consume no power, do not require feedback, and are essentially dragless.

Compared to superconductor bearings, diamagnetic bearings have one significant disadvantage and two significant advantages. The disadvantage is that the bearing pressures for diamagnetic bearings are significantly less than those for superconductor bearings. The advantages are that diamagnetic bearings do not require cooling, and that the range of usable diamagnetic materials is huge compared to the limited number of superconducting materials available.

This paper discusses potential space applications that can make use of the advantages of diamagnetic suspensions. The basic equations of diamagnetic suspensions are discussed first, followed by discussions of specific potential applications.

BASIC EQUATIONS OF DIAMAGNETIC SUSPENSIONS

Equation 1 below gives the basic equation for diamagnetic suspensions [ref. 1]. In Equation 1, H is the magnetic field, χ is the volume magnetic susceptibility of the diamagnetic material, F is the force, and the integral is taken over the volume of the material. The gradient, **grad**, is taken with respect to the position of the diamagnetic body. All quantities are in centimeter-gram-second (cgs) units. We also assume that the diamagnetic material is isotropic and that χ is uniform in the diamagnetic body. The force F can be used to levitate a diamagnetic body. Alternatively, the diamagnetic material may be fixed, and the force can be used to levitate a magnet.

$$\mathbf{F} = (1/2) \text{ grad } \int \chi H^2 dV \quad (1)$$

In general, the magnetic field H is produced by the diamagnetic material itself, just as it is produced by nearby free currents, ferromagnetic materials, permanent magnets, and so forth. However, the magnitude of the volume magnetic susceptibility is normally much less than $1/4\pi$. For example, using bismuth, $\chi = -1.2 \times 10^{-5}$ cgs units. In this case, the magnetic fields are only slightly different from what they would be if the diamagnetic material were not present. Thus, a good first-order approximation is to calculate the magnetic field H without the diamagnetic material, and use this calculated field in Equation 1 to approximate the force.

Equation 1 can be used to estimate the magnitude of diamagnetic pressures. Consider the force in the z -direction, F_z . It is straightforward to show, using Equation 1, that

$$F_z = (1/2)\chi \int \left[d(H^2)/dz \right] dz dx dy = (1/2)\chi \int H^2 dx dy \quad (2)$$

$$F_z = (1/2)\chi \int H^2 \mathbf{k} \cdot d\mathbf{S} \quad (3)$$

where dV from Equation 1 has been replaced by $dz dx dy$ in Equation 2, and the second integral in Equation 2 is over the surface of the diamagnetic body. Equation 3 follows from Equation 2, in that $dx dy = \mathbf{k} \cdot d\mathbf{S}$, where \mathbf{k} is the unit vector in the z direction and $d\mathbf{S}$ is a vector surface element oriented outward from the diamagnetic body.

Figure 1 shows the simple case of a thin rod of cross-sectional area A oriented parallel to z and subject to a field H on one end. For this case, Equation 3 reduces to

$$F_z = (1/2) \chi A H^2 \quad (4)$$

The *bearing pressure* exerted on the rod, P , is just F_z divided by A , or

$$P = (1/2) \chi H^2 \quad (5)$$

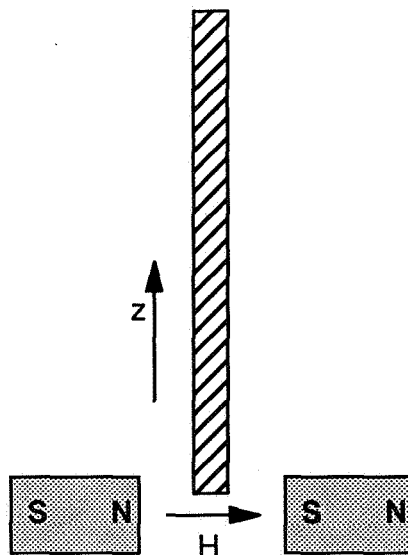


Figure 1. Rod Exposed to a Magnetic Field on One End

Although Equation 4 was derived for the special situation of a thin rod with one end in a magnetic field, this equation is generally useful for estimating the magnitude of diamagnetic bearing pressures. Very good neodymium-iron rare earth magnets generate fields up to about $H = 12,500$ oersted. Using this value of H and the susceptibility of bismuth in Equation 5 gives a bearing pressure of roughly 1000 dynes/cm^2 , or about 1 gram force per square centimeter.

Various magnetic field geometries and better diamagnetic materials, such as pyrolytic graphite, can be used to increase the bearing pressure. On the other hand, practical constraints often reduce the achievable bearing pressure. Nonetheless, 1 gram/cm^2 is a convenient bearing-pressure estimate for evaluating the basic feasibility of diamagnetic suspensions.

It should be emphasized that magnetic field limits restrict the maximum bearing pressure, but not the total force or the force-to-mass ratio of the bearing. The total force supported by diamagnetic suspension can be increased by increasing the area. The force-to-mass ratio can be increased by simultaneously reducing the thickness of the levitated object and the scale length of the magnetic field.

The methodology for evaluating diamagnetic suspensions with respect to a potential application is summarized as follows. A bearing pressure of 1 gram/cm^2 is used as a general estimate for determining the basic feasibility of diamagnetic suspensions for the application. If the application places significant restrictions on the magnetic fields or the diamagnetic materials, e.g., an application to levitate weakly diamagnetic silicon wafers, then Equation 5 should be used directly to estimate bearing pressure. If the potential application appears feasible using the general estimate, the next step is to design the diamagnetic suspension itself. Details of the diamagnetic suspension design will depend on the given application and its constraints. Once a design is established, the next step is to calculate or estimate the magnetic field H without the diamagnetic material present. Next, this approximate H is used in equations such as

Equation 3 to calculate the components of force on the diamagnetic body. Lastly, bearing stability and rigidity can be determined by considering small displacements from the assumed equilibrium position.

SPACE APPLICATIONS

It was mentioned in the introduction to this paper that diamagnetic suspensions have relatively low bearing pressures, but do not require cooling and work with a wide range of materials. These general characteristics of diamagnetic bearings will be discussed briefly with reference to space applications. Specific applications will be discussed following the general comments.

The use of bearings in space includes a number of applications with low bearing pressures. In some cases, such as containerless material processing, a low bearing pressure is related to the microgravity environment. In other cases, such as for sensors, low bearing pressure applications in space stem from the need for miniaturization and/or enhanced performance.

The lack of a need for cooling or power means that diamagnetic bearings are intrinsically very reliable, compared to other noncontact bearings. High reliability is a major asset for space applications. In fact, one potential application is to use diamagnetic bearings to provide highly reliable passive bearings to back up primary, active magnetic bearings.

The ability of diamagnetic suspensions to work with a wide variety of materials is attractive for suspensions where the material is fixed by nonbearing constraints. An example of a nonbearing constraint would be a materials-processing application that must process a given material or class of materials.

The following sections describe specific space applications where the use of diamagnetic suspensions may be advantageous.

Material Processing

Diamagnetic suspensions may be used for containerless material processing in space. This is a good application for diamagnetic suspensions, since space-based processing is done in a microgravity environment and low bearing pressure is not an issue. Additionally, diamagnetic suspensions function in vacuum, unlike acoustic levitations.

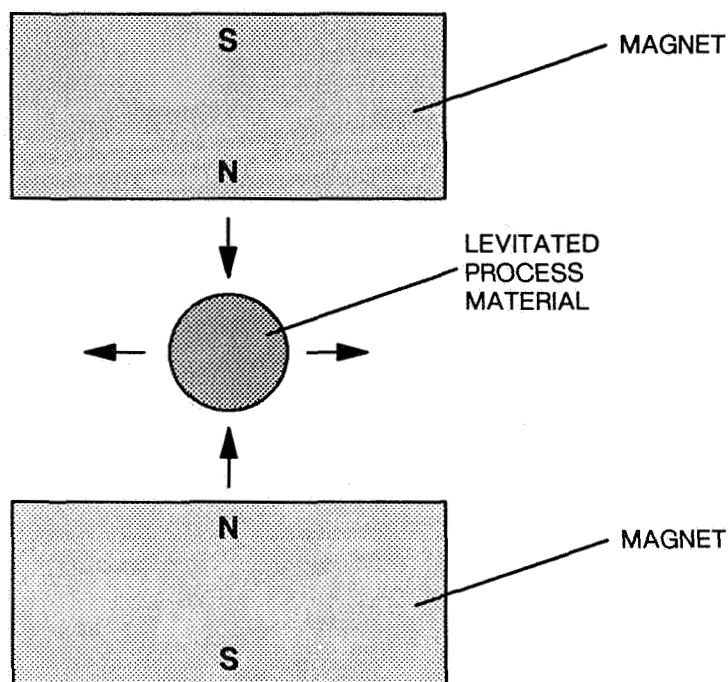
Figure 2 illustrates a simple magnet geometry for confining a diamagnetic material. Note that the magnetic field at the point midway between the magnets is zero by symmetry. Since diamagnetic materials are repelled by magnetic fields, the midway point is a stable equilibrium. This geometry is similar to that used for ferrofluid suspensions of inert objects.

The concept of using diamagnetic suspensions for materials processing is useful only if the range of materials that can be suspended is large. Fortunately, this is the case. Diamagnetic materials form one of the broadest classes of material and include metals, ceramics, the three major semiconductors (silicon, germanium, gallium arsenide), glasses, plastics, almost all organic matter, and water.

As a concrete example, consider suspending silicon. We will assume that the spacecraft may be subject to DC acceleration, a , as large as $10^{-4} g = 0.1 \text{ cm/s}^2$ during material processing [ref. 2]. To determine the basic feasibility of the concept, we need

to estimate the maximum size of a silicon object that can be supported. Suppose the typical thickness of the silicon in the direction of acceleration is L and its density (d) is 2.33 g/cm^3 . Acceleration of the spacecraft causes a pressure, P_{Si} , exerted on the surface perpendicular to the thickness L given by

$$P_{\text{Si}} = L d a = 0.233 \text{ (g/s}^2\text{cm}^2) L \quad (6)$$



Note: The arrows indicate the direction of magnetic fields.

Figure 2. Simple Configuration for Levitating a Diamagnetic Material

The susceptibility of silicon is roughly $\chi = -0.3 \times 10^{-6}$ cgs units. For comparison, this is about 1/40th the susceptibility of bismuth and about half that of water. We will also assume that our magnetic fields are restricted by practical design constraints to half the maximum value for rare earth magnets, or about 6250 oersted. Equation 5 then gives the estimated bearing pressure as about 6 dynes/cm². Using Equation 6 we then get an estimate for L as

$$\begin{aligned} 6 \text{ dynes/cm}^2 &= 0.233 \text{ (g/s}^2\text{cm}^2) L \\ L &= 26 \text{ cm} \end{aligned} \quad (7)$$

This is a large thickness of silicon, and it indicates the basic feasibility of diamagnetic suspensions for this material in space.

A valid question is whether high temperatures or phase transitions will destroy the diamagnetism. This issue needs to be addressed with respect to specific materials. However, many materials for which data is available are diamagnetic through their melting temperature. Examples include bismuth, germanium, gold, sodium chloride, and water [ref. 3].

Finally, it should be mentioned that diamagnetic suspensions using a wide variety of materials have already been demonstrated on earth. Levitation of graphite and bismuth were originally used in diamagnetic suspensions. Ponizovskii [ref. 4] gives a good survey of this earlier work. More recently, Beaunon and Tournier [ref. 5] report levitating water, wood, ethanol, and acetone, using superconducting magnets.

Sensor Applications

The earliest applications of diamagnetic suspensions were for sensors [ref. 4]. These sensors were constructed for earth-based operations, but the technology involved is well-suited for space applications.

The early work in diamagnetic sensors demonstrated high sensitivities. Two examples will indicate the sensitivities available. A tiltmeter for measuring tilting of the earth's crust caused by tidal forces was constructed by Simon et al. [ref. 6]. Sensitivity was on the order of 24 nanoradians. Ponizovskii [ref. 4] discusses a rotating mass for measuring low pressures using drag forces. The smallest measurable pressure for the device was 10^{-10} torr.

The basic idea behind diamagnetic sensors is to levitate an inertial, or proof, mass and measure its response to accelerations, rotations, magnetic fields, and so forth. A variety of signal pickup methods, such as optical, capacitive, or magnetic methods, may be used to measure the response of the proof mass. The undisturbed state of the proof mass may be stationary relative to sensor fixture. Alternatively, the undisturbed state may be rotating, as in a gyro application, or it may be oscillating.

The low gravity of space opens up additional possibilities for diamagnetic sensors. For example, one possibility is to levitate a magnet using the diamagnetic properties of a silicon chip. Such sensors would integrate the proof mass directly with the signal processing electronics. As a result, this type of sensor has the potential advantages of compactness, low cost, and high reliability. Such sensors could be used as accelerometers, gyroscopes, pressure gauges, magnetic field sensors, and the like. Levitation of magnets on earth using silicon and external, supporting magnetic fields was demonstrated by Pelrine [ref. 7].

To estimate the feasibility of silicon diamagnetic sensors, recall from Equation 7 that diamagnetic bearing pressures for silicon were estimated at roughly 6 dynes/cm². We will assume the thickness of the levitated magnet is 100 microns at a density of 7.4 g/cm³, a number that can be achieved by grinding neodymium-iron magnet material. The diamagnetic pressure will support a magnet of this thickness up to a maximum acceleration, a , given by

$$a = (6 \text{ dynes/cm}^2) / (0.01 \text{ cm} \times 7.4 \text{ g/cm}^3) = 81 \text{ cm/s}^2 = 0.08 \text{ g} \quad (8)$$

This magnitude of acceleration may be useful for monitoring and/or controlling oscillations in large space structures or microgravity experiments. Of course, the maximum allowable acceleration can be increased using highly diamagnetic films deposited on silicon, or by reducing the magnet thickness. Amorphous silicon, obtained by ion bombardment of crystalline silicon, also has a significantly larger diamagnetic susceptibility.

Lastly, an attractive area for diamagnetic suspensions is in compact, sensitive inertial navigation devices. Diamagnetic accelerometers have been investigated in the past [ref. 8], but more work appears to be needed to determine the limits of the technology.

Rotating Rings

Rotating rings or flywheels have been suggested for use as energy storage devices or for stabilizing large space structures [ref. 9]. Diamagnetic bearings may offer advantages for these types of devices.

Research is only at the basic idea stage in this area. However, since diamagnetic bearings will function without power or cooling, they are a reliable means of supporting high speed rotations. A rotating ring might be supported totally by diamagnetic bearings. Another option is to incorporate diamagnetic bearings as backups for the primary ring bearings. Still another possibility suggested by Pelrine [ref. 7] is to use diamagnetic bearings to support low-speed, start-up rotations. Induced-current magnetic bearings would then be used at higher speeds where they become effective.

Diamagnetic bearings are simple components and can be made very small. This suggests the possibility of replacing single large rotating rings with many small rings in a distributed approach. Multiple rings would have an advantage in terms of redundancy.

Another issue is the need for safety. Multiple rings may increase the possibility of a single ring failing. On the other hand, confinement of a breaking ring is easier when the rings are smaller. Normally, rotating rings require confinement structures, in case a ring breaks apart at high velocities. The confinement structure, however, adds unwanted mass to the system. For small rings, it may be possible to utilize the existing space structure as the confinement structure. A small ring breakup would then cause some local damage, but would not actually penetrate the structure. The trade-offs between the savings in mass and the risk of local damage are unknown at present.

The feasibility of diamagnetically supported rotating rings depends on the specific mission. In general, if only low accelerations are expected, diamagnetic bearings are attractive, since the bearing pressures will be low. The reverse is true for space missions involving high accelerations of rotating rings.

SUMMARY

Diamagnetic suspensions offer unique capabilities for space applications. They are frictionless, need no power or cooling, can be made very small, and function using a wide range of materials. Their only significant limitation is their relatively low bearing pressure. Typically, diamagnetic bearings are useful when bearing pressures are on the order of 1 gram force per centimeter squared or less.

A number of space applications have been identified as candidates for diamagnetic suspensions. These include containerless material processing, sensors, and bearings for high-speed rotating rings.

REFERENCES

1. Charles Kittel, *Introduction to Solid State Physics*, 2nd edition, John Wiley & Sons, Inc., New York, 1963, pp. 211-212.
2. Bonnie J. Dunbar, ed., *Materials Processing in Space*, The American Ceramic Society, Inc., Columbus, OH, 1983, Vol. 5, p. 222.
3. E.W. Washburn, ed., *International Critical Tables*, 1st edition, McGraw-Hill Book Company, Inc., 1929, Vol. VI, p. 354.
4. V. M. Ponizovskii, Diamagnetic Suspension and Its Applications (Survey), *Instruments and Experimental Techniques*, Vol. 24, No. 4, 1982, pp. 833-841.
5. E. Beaugnon, R. Tournier, Levitation of Organic Materials, *Nature*, Vol. 349, 7 February 1991, p. 470.
6. I. Simon, et al., Sensitive Tiltmeter Utilizing a Diamagnetic Suspension, *The Review of Scientific Instruments*, Vol. 39, No. 11, November 1968, pp. 1666-1671.
7. R. E. Pelrine, "Room Temperature Open-Loop Levitation of Microdevices Using Diamagnetic Materials," *Proceedings of the IEEE Micro Electro Mechanical Systems*, Napa Valley, CA, 11-14 February 1990.
8. I. Simon, *Diamagnetic Accelerometer*, U.S. Patent 3,465,598, September 1969.
9. S. M. Joshi and N. J. Groom, "Modal Damping Enhancement in Large Space Structures Using AMCD's," *Journal of Guidance and Control*, Vol. 3, No. 5, September-October 1980, pp. 477-479.

N92-27809

MAGNETIC BEARING WHEELS

FOR VERY HIGH POINTING ACCURACY SATELLITE MISSIONS

J.P. Roland
AEROSPATIALE, 78133 Les Mureaux, France

Abstract

Inertia wheels used as actuators in Attitude Control Systems remain the most frequently encountered solution for all types of scientific or military space missions : telecommunications, earth observation ... The magnetic levitation of the flywheel leads to new performances, which will be highly appreciated for very high pointing accuracy missions in the next decade.

For military and commercial earth observation missions, for optical link telecommunication missions, as well as metallurgical process missions under microgravity conditions, the need in platform stability will become stronger and stronger.

Work in progress on the Magnetic Bearing Reaction Wheel, dedicated to the HELIOS military earth observation satellite is presented. The HELIOS program is very demanding in terms of pointing accuracy. The main features of this wheel and its overall characteristics and performances are given.

Introduction

The prime advantages of Magnetic Bearings are : no wear, no lubrication, and low rotational losses. These properties are particularly appreciated in satellite Momentum Wheels, which have to operate at high rotational speeds in vacuum for long periods of time.

Less obvious but equally important properties, only reached by using Magnetic Bearing, are at first the complete cancellation of any "stiction" effect which creates limit cycle in attitude control when rotor speed is crossing zero, and then no variation with temperature of the very low "frictional" drag torque. The other induced performance is the very low level of microvibrations induced onto the platform.

These attributes, in addition to those hereabove mentioned, make them ideal for use in Reaction Wheels for Very High Pointing Accuracy missions.

The Magnetic Bearing technology has been flight-proven for the first time in the world, as part of the French earth observation SPOT programme. The satellite attitude is actuated by 3 Magnetic Bearing Reaction Wheels (MBRW), contributing to the SPOT pictures sharpness. It should be noticed there is only

one fully redundant wheel on each axis. The SPOT 1 satellite was launched on February the 21st, 1986. Designed for 2 years, it is still in operation. SPOT 2 was launched on January the 20th, 1990.

The ERS 1 (Earth Remote Sensing) satellite, a European Space Agency programme, is also actuated by 3 MBRW. It was launched on July the 17th, 1991. The quality of the first view, transmitted as soon as the 27th of July, is sharper than expected.

Those previous MBRW are based upon 1 Degree Of Freedom (DOF) actively controlled configuration. In this paper, we describe an advanced MBRW concept, based upon a 2 DOF actively controlled configuration, which has been developed in order to improve the initial concept and to lead to an extremely simplified and robust mechanical part.

The development of the 2 axis active wheel was performed under a Research & Development contract awarded by the European Space Agency (ESA). The work was started in 1982 and was completed in 1986.

This configuration is being used for the military earth observation HELIOS programme and for the new generation of SPOT (called SPOT 4) programme. The strong requirements of these programmes involve new MBRW improvements to obtain very low microvibrations.

Principles and Technologies

It is known that we can't realise, in normal conditions, a completely passive contactless magnetostatic bearing that would be stable in the 6 Degrees of Freedom.

There is at least one Degree Of Freedom in which the suspended part is in unstable equilibrium.

Stability is achieved, along passive axis ('axis' means Degree Of Freedom), as many as five, by the use of permanent magnets which create restoring forces. Along active axis, at least one, stability is achieved by actively controlled electro-magnets (called actuators). Those can be associated or not with permanent magnets.

The Magnetic Bearings developed by AEROSPATIALE are of the semi-active type: they utilize permanent magnets. Most Degrees Of Freedom are passively controlled, consistent with the application at hand. This strategy makes for high inherent reliability and low power consumption because it minimizes the amount of electronics and other active required elements. The actuators also utilize permanent magnets which produce the main part of fluxes in the magnetic circuits. The fluxes created by the coils only modulate the static flux, and by the way increase or decrease the force applied to the bearing part and make it stable. Another advantage is to provide a quasi-linear characteristic of force vs current.

Permanent magnets are operating in the attractive mode, which gives a better passive/active stiffness ratio associated to lower magnetic disturbances than in the repulsive one. The pole pieces, with one or more teeth, concentrate the flux and produce higher forces and passive stiffnesses.

Fig. 1 illustrates the basic geometries of Magnetic Bearings (MB) of 1 and 2 axis active types.

Fig. 1a shows a 1 axis active MB of the type used in the SPOT Reaction Wheel. It consists of four annular elements, arranged in two axially separated pairs. Each element consists of a radially magnetized permanent magnet ring fitted with cylindrical iron poles on its inner and outer curved surfaces.

This type of MB exerts passive (i.e. permanent magnet induced) restoring forces on the rotor when it is radially displaced (self-centering). In the axial direction, however, it is magnetically unstable.

Fig. 1b shows a 2 axis active MB of the type used in the wheel, described hereafter.

It consists of three annular elements arranged as concentric rings in a common plane. The middle element consists of a ring of axially magnetized permanent magnets sandwiched between flat ferrous pole plates. The inner and outermost elements simply consist of shaped iron rings.

In this type of MB, the rotor experiences a passive stable restoring force when it is axially displaced, but it is unstable radially. The active control has to include two independent electromagnetic coils, i.e. one for each principal radial axis.

Whichever configuration is chosen, the actuator can be separated or integrated with the static Magnetic Bearing. In both configurations, tilting stiffnesses are passive.

The coils receive their excitation signals from electronic servo-loops. The error signals of the latter are derived from the radial displacements of the suspended rotor from its nominal (centered) position.

Fig. 2 shows how the coils are incorporated in the bearing and how they exert the necessary stabilising forces. Only one coil of four is shown.

Using only speed sensors can provide stability of the rotor. In this case the lift-off of the rotor needs a particular sequence, because when the rotor is against the stop, the servo-loop is open.

In a 1 axis active MB, the unbalance rotating forces of the rotor have no effect on the servo-loop (because these forces act principally in the radial direction).

In a 2 axis active MB, a cancellation of the unbalance can be provided by a special law of the servo-loop. This becomes an advantage in applications that call for a very low transmissibility of vibrations to the surrounding spacecraft.

Compared with 1 axis active wheels, the most obvious difference is the more favourable shape : the present wheel is much flatter. It therefore takes up less volume and is much better suited to panel mounting.

The locking system could be much simpler. At the same time, it could be lighter, more robust and considerably easier to adjust.

With regard to manufacturability and serviceability, the 2 axis active concept represents a considerable improvement. Interlocking parts are entirely eliminated. Therefore, the assembly and dismantling of the wheel can be performed more quickly, leading to low costs. For example, the rotor can be simply lifted off the stator, giving access to all parts and making adjustments and eventual repairs very easy.

At last, but not least important, the 2 axis active type of bearing results in a wheel with high momentum/mass ratio. This is due to the fact that the operating speed may cross over the "critical" speed without incurring any vibrations. For this reason, this unit has been considered as a Reaction Wheel, but it can be used as a Momentum Wheel as well.

Design Description

A cross sectional drawing of the developed wheel is given in Fig. 3.

The unit incorporates the following features :

1.-Rotor.

The rotor consists of a heavy rim and a light, web stiffened, central disc portion. The high density magnets of the motor are integrated into the rim. They contribute to the required inertia.

The flat web is only needed to transmit Magnetic Bearing and auxiliary stops forces, not the locking mechanism ones.

2.-Electromechanical suspension.

A 2 axis active Magnetic Bearing-Actuator and displacement sensors levitate the rotor part so as to be completely free of contact with the fixed parts of the wheel.

2.1-Magnetic Bearing-Actuator.

Fig. 4 shows the bearing in somewhat more detail, including a top view. In this concept, the actuators are associated with the static Magnetic Bearing. This feature leads to a very compact design. The permanent magnet ring weighs only 150 grams. Four coils are distributed at intervals of 90 degrees around the inner bearing ring. Slots in the flange avoid leakage in adjacent coils.

Along each radial axis, a linear actuator consists of two diametrically opposite coils "halves", electrically connected to form an independent electric circuits. It allows us to add or subtract flux into the gap according to the sign of the current.

All the control coils are redundant.

2.2-Displacement sensors.

A system of inductive type position sensors measures the radial position of the suspended rotor and provides the necessary error correction signals. This detection is fully redundant.

3.- Electromechanical drive system.

3.1-Drive motor.

The reaction torque is set up by a brushless ironless D.C. multipole motor, integrated into the rim. In spite of this location, a special feature reduces the drag torque (induced by eddy currents).

The permanent magnets of the motor are attached to the rotor rim and thus make a useful contribution to the inertia.

The ironless armature consists of an array of copper windings embedded in an epoxy material for mechanical rigidity and support. By means of a special winding design, the ripple torque developed by the motor has been kept to less than 3% peak-to-peak of the demanded reaction torque.

3.2-Opto-electronic angular detection.

This part is basically a coarse angular encoder and generates information on the angular position of the rotor for motor commutation purposes. It is based on the interrupted light beam principle and uses solid state opto-electronic components as the light source and detection elements. To detect the rotation sign, two detectors are needed.

This design ensures high stability of the transient (instant and duration), at any speed.

All this detection is redundant.

4.- Touchdown bearings.

These provide for a safe landing of the rotor in the event of a failure occurring in the suspension electronic, or loss of power supply while rotating at speed. These ball bearings are dry lubricated. They only provide for radial support because the Magnetic Bearing gives axial support, even in the failed or switched-off condition.

Another function is to avoid peripheral contacts when slew rate is overshooting.

This central auxiliary bearing is much more simple than a peripheral one and allows higher touchdown speeds.

5.- Peripheral locking mechanism.

A locking mechanism prevents "rattling" of the rotor in the severe vibration environment experienced during launch. It consists of a number of specially shaped carbon fibre spring plates arranged around the periphery of the rotor, and which can be drawn in by a steel cable so as to force the rotor downwards onto a conical seat.

Once in orbit, the steel cable is cut by a redundant pyrotechnic device, the rotor automatically goes up due to the axial restoring force and the magnetic suspension is then engaged. On ground, locking and unlocking are manually performed.

The load path between the rotor mass and the wheel attachment points to the spacecraft is very short. This allows for high stress during the launch of the satellite without any effects on further performances.

This method of locking is light, strong and reliable. It is also very simple mechanically and very accessible. The touchdown bearings are completely off-loaded when the rotor is locked.

6.- Built-in electronics package.

This performs the control functions associated with the 2 active axes of the Magnetic Bearing. It also performs motor commutation, power conditioning and suspension monitoring functions.

All electrical elements of the wheel are 100% redundant. This includes the electronic package, the Magnetic Bearing coils, the radial position sensors, the optical commutation devices and the pyrotechnics. Only the motor windings are not redundant, but a specific technology has been applied to ensure a very high reliability to those windings.

6.1-Suspension.

For the 2 radial axes, the suspension electronic :

- processes sensor signals,
- provides the requisite transfer function (corrector) giving rotor stability. For small radial displacement, the corrector is sensitive to the speed. This makes it possible to operate the wheel on the ground without dissipating any more power than is required in zero gravity conditions. But for large displacements, such as during lift-off, it acts with the position. Thereby, the lift-off is automatically performed as soon as the electronic is switched on.
- delivers current to the actuator, by a linear amplifier with a current servo-loop (current independent of the impedance and b.e.m.f. of the actuator).

6.2-Rotation.

Data from the angular detectors are processed, then commutators of each phase are controlled in accordance to the required sign of the reaction torque. Commutators are fitted with limiters in order to avoid the transient overvoltages.

Improvements for Very High Pointing Accuracy

All the potentialities of the Magnetic Bearing had not been exploited with the first technological model, developed for ESA.

For Very High Pointing Accuracy missions, improvements of some components of the Magnetic Bearing Wheel have been developed, in order to decrease the overall mechanical noise transmitted to the satellite platform.

The Fig. 5 shows the microvibration noise generation inside a Magnetic Bearing Wheel.

This noise could be expressed either in torque unit or in force unit related to the orthogonal distance between the application point and the satellite center of mass.

The microvibration contributors, in order of magnitude, are

- the static unbalance error. This is the most important contributor. It creates a rotating force at the rotor speed.
- the dynamic unbalance error. Due to the flat shape of the rotor, it is of minor importance. It creates a rotating torque at the rotor speed.

- the ripple torque of the motor is also of minor importance if the motor is designed for. It creates high frequency spectrum noise, depending on the number of commutations per round.
- the noise, generated inside the magnetic bearing control-loop, is quite negligible.

There is obviously no tribologic noise, as encountered in Ball Bearing (races and balls noise), producing non-integer harmonics of the rotor speed.

For the first generation, due to the tight schedule, only mechanical type improvements have been implemented:

- high quality grade of rotor balancing (static and dynamic), using signal processing methods
- rotor assembly design ensuring a long-term stability of the mass distribution
- reduction of the ripple torque of the motor

The Fig. 6 shows the microvibrations, generated by the mechanically improved MBRW. The noise is expressed in N as a force, taking into account a lever arm of 1 meter.

For the next generation, improvements are foreseen, concerning the electronic part as

- optimization of the control laws of the magnetic bearing, including tracking notch filters
- electronic offset counteracting the mechanical disturbances due to the static unbalance. The unbalance is continuously estimated by observing parameters inside the servo-loops and computed with constant laws.

Taking into account these improvements, the equivalent rotor unbalance will reach values as low as $0.1 \mu\text{m}$ for a rotor of 7 kg. The improved model is under R&D development.

Characteristics/Performances of the HELIOS-SPOT4 Model

The main characteristics of the unit are

Momentum Capacity	: $\pm 40 \text{ Nms}$
at maximum speed of	: $\pm 2500 \text{ rpm}$
Reaction Torque	: $\pm 0.45 \text{ Nm}$
Slew rate	: 0.08 rd/s
Mass	
Stator	: 7.4 kg
including electronics	: 2.0 kg
Rotor	: 7.1 kg
Total	: 14.5 kg

Dimensions

Diameter	: 355 mm
Height	: 135 mm

Power consumption

Magnetic suspension (whatever speed or torque)	
from -25°C to +65°C	: 10 W
(-13°F to +149°F)	

Motor drive (at full speed and torque)	
	: 140 W

Environmental Capability

Temperature range	: -25°C to 65°C
	(-13°F to +149°F)

Vibrations (when locked)	
Sine • from 5 to 20 Hz	: 11 mm peak
from 20 to 100 Hz	: 20 g peak
Random (20-2000 Hz)	: 20 g rms

Drive Motor

Phases	: 4
Poles	: 48
Ripple torque (peak-peak)	: 3%

Magnetic Bearing

Diameter	: 165 mm
Magnetic Gap	: 0.8 mm
Mechanical Gap	: 0.2 mm
Axial stiffness	: 140 N/mm
Radial stiffness	: 480 N/mm
Tilting stiffness	: 470 N•m/rd
Active Force Constant	: 106 N/A
Friction torque	: $2 \cdot 10^{-3}$ N•m
@ 2500 rpm (proportional to the speed)	

Development Programmes

The development of the new 40 Nms 2 axis active MBRW, which is designed for both HELIOS and SPOT4 programmes, started in 1989 and is still in progress. The HELIOS satellite will be launched in 1992. Three Reaction Wheels with high torque (0.45 N.m) allow fast maneuvers of the platform.

Other space applications of the magnetic suspension are foreseen, for areas in which classical technologies with ball bearings are not well fitted. Some are already under development :

- Large Momentum or Reaction Wheel for space stations (200 to 1000 Nms), especially suitable if microgravity experiments are performed on the spacecraft.

- Kinetic Energy Storage Wheel (associated with self-balancing device)
- optical devices such as scanning mirror or telescope pointing

By another way, the development of ERS 2 satellite, including 3 "one-axis" MBRW of 15 Nms and 0.2 Nm, began in 1990. Launching is scheduled for 1994.

Conclusions

The Magnetic Bearing Wheels that we have described are believed to be among the most advanced of their kind in existence today. It marks a significant step forward in the state-of-the-art of magnetic suspension devices, as well as a substantial advancement in the technology of actuators for space applications.

This Magnetic Bearing concept is very well suited for using in Reaction Wheels, in which application they enable significant improvements in attitude control system accuracy to be achieved. Magnetic Bearing Wheels won't take the place of Ball Bearing Wheels for standard applications. They will be used for High Pointing Accuracy missions. They are also competitive to control very large platforms.

The magnetic bearing part of the wheel, being a compact and self-contained sub-assembly, could easily be incorporated into other devices, like optical devices such as scanning mirror or telescope pointing.

References

- [1] PENTLICKI C.J., POUBEAU P. : Magnetic Bearings Momentum Wheel. AIAA/CASI 6th Communication Satellite System Conference, Montreal April 1976.
- [2] POUBEAU P. :Development of a satellite flywheel family operating on "one active axis" Magnetic Bearings. 11th Aerospace Mechanism Symposium, Goddard Space Flight Center April 1977.
- [3] ANSTETT P., SOULIAC M., ROUYER C., GAUTHIER M. : SPOT the very first satellite to use Magnetic Bearing Wheels. 33rd IAF Congres September 1982 (paper 82.331).
- [4] GAUTHIER M. & ROUYER C. : Semi-active Magnetic Bearings for space application. 2nd European Space Mechanisms & Tribology Symposium, October 1985.

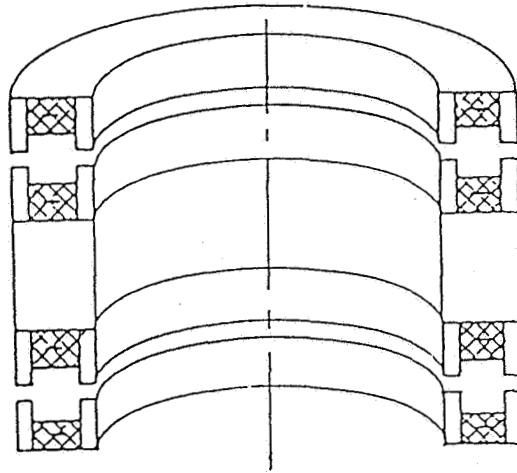


Fig. 1 a - 1 Axis Active
Magnetic Bearing

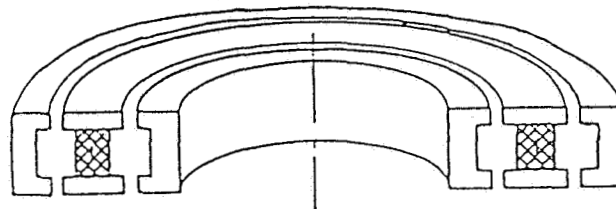


Fig. 1 b - 2 Axis Active
Magnetic Bearing

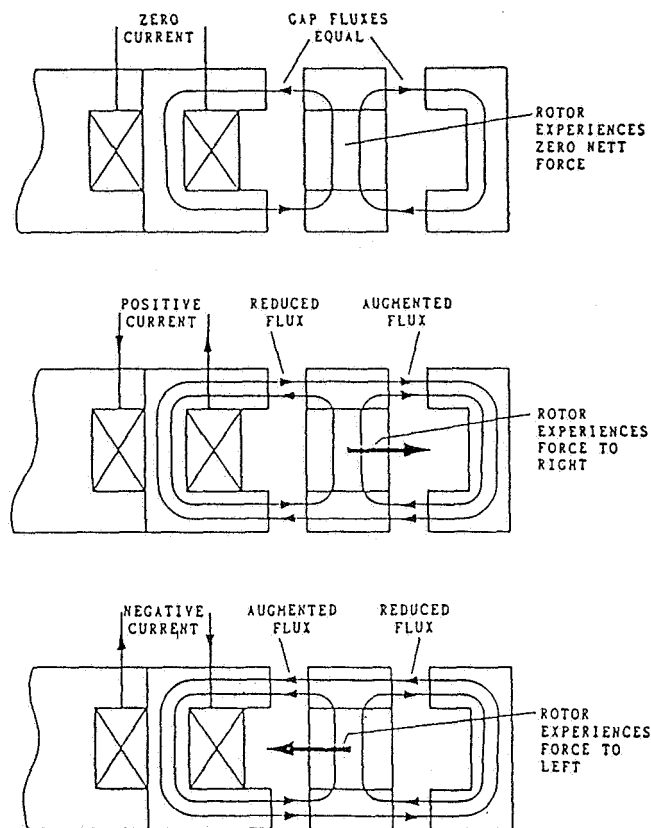


Fig 2 - 2 Axis Active Bearing principle

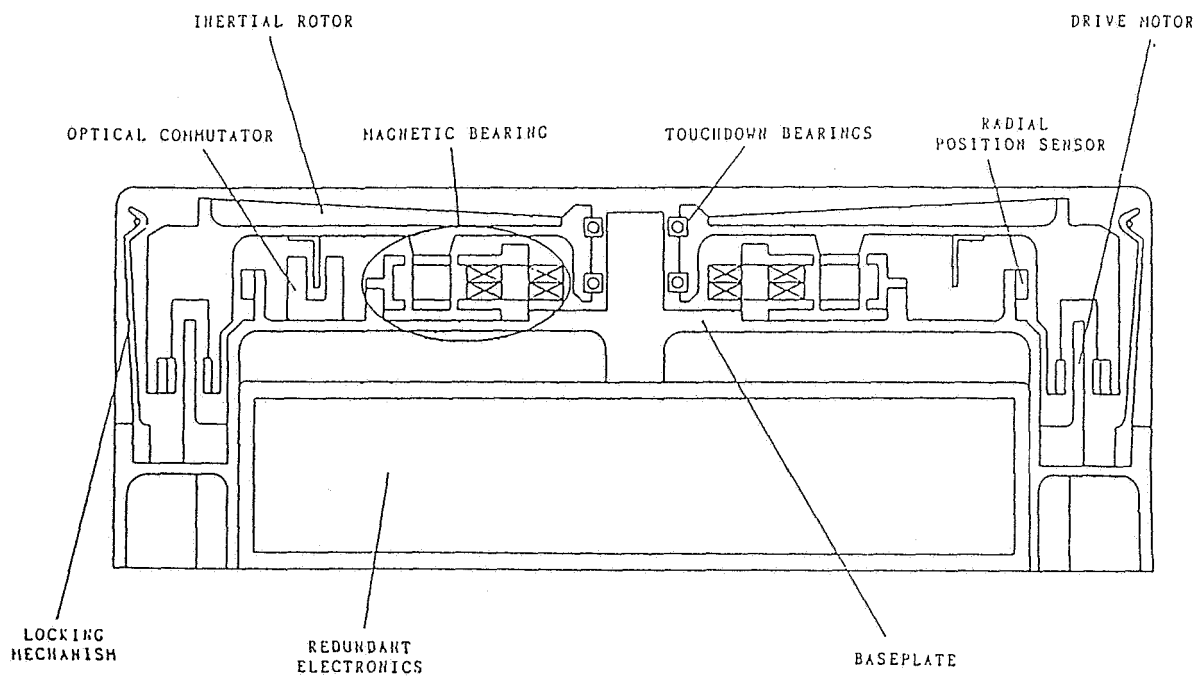


Fig 3 - Cross sectionnall view of the 2 axis active wheel

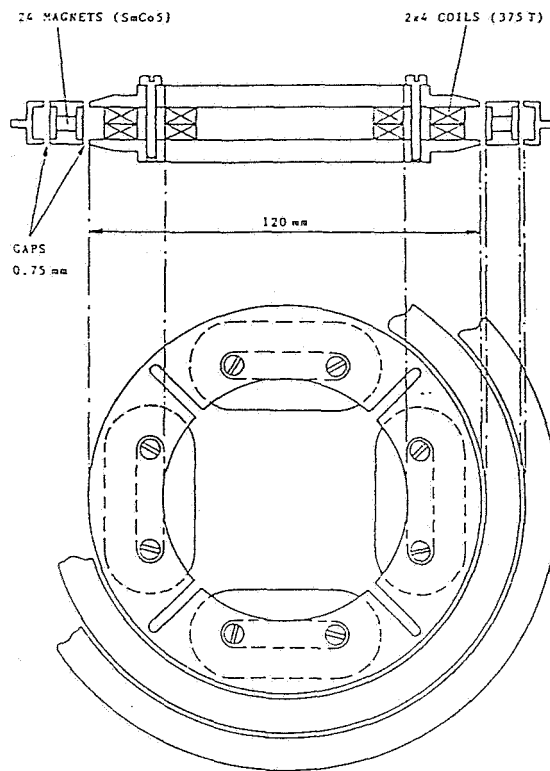


Fig 4 Top view of the bearing

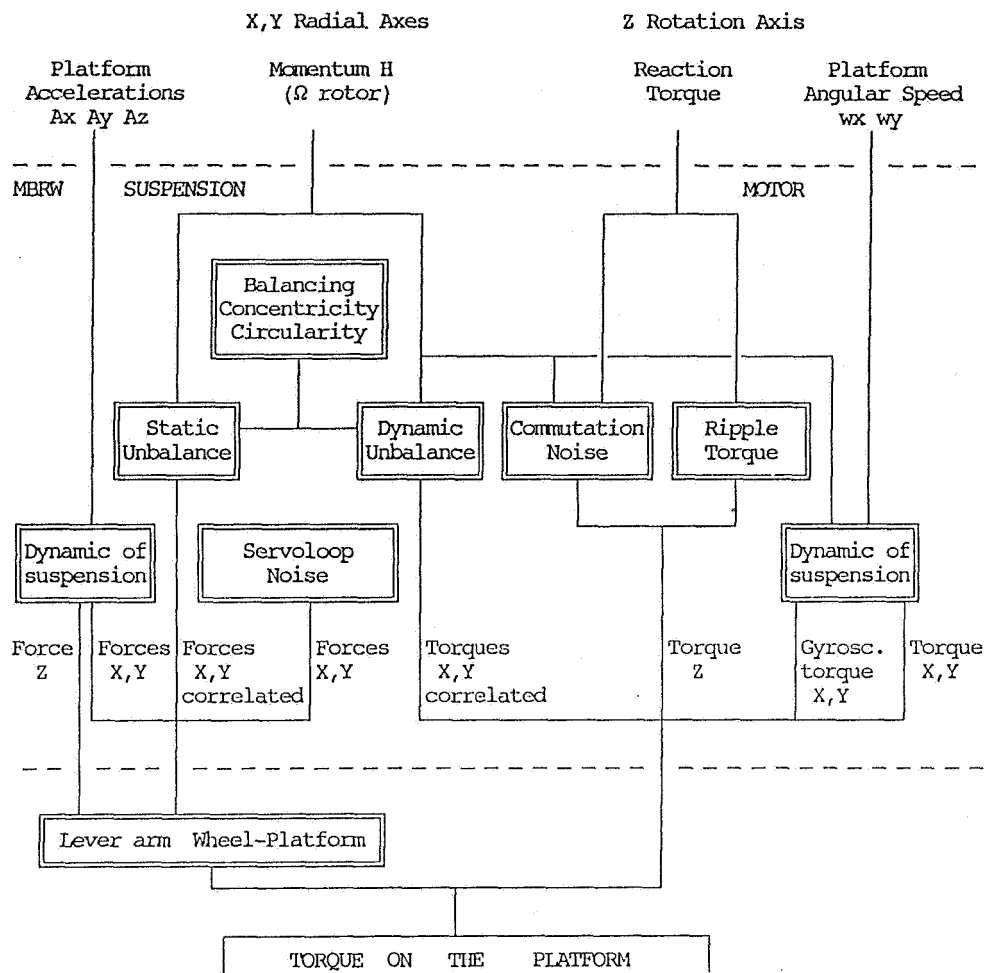
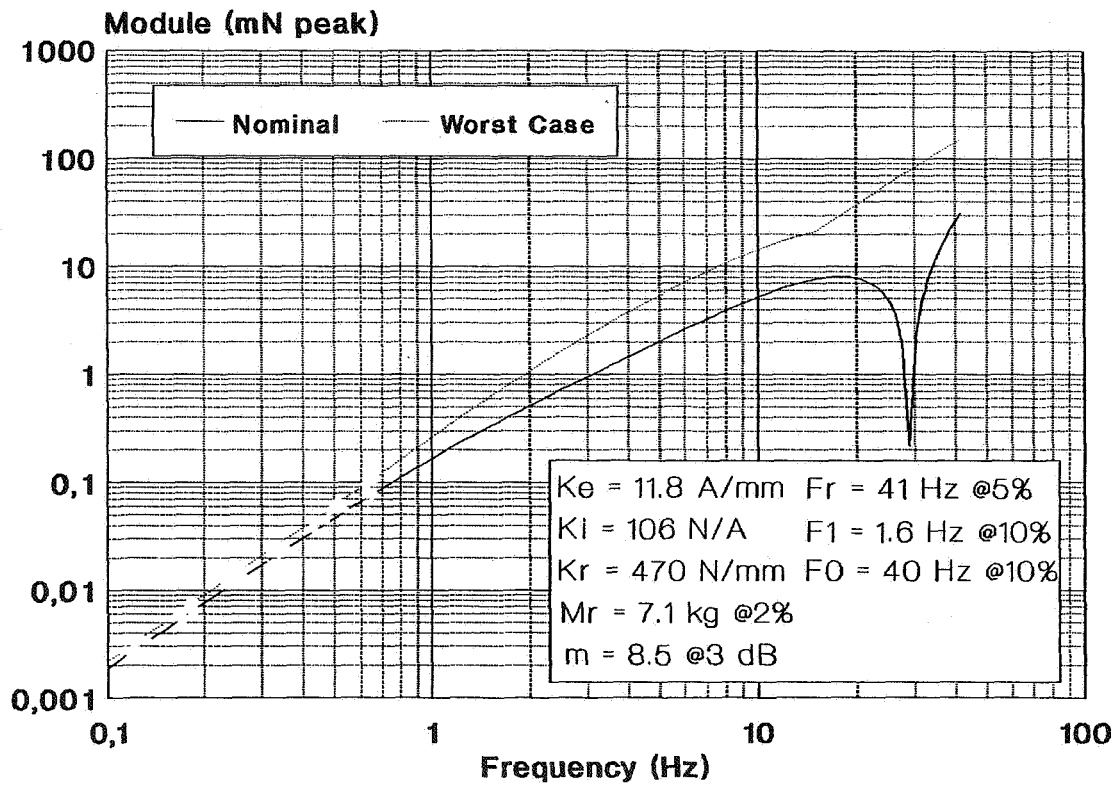


Fig 5 - Noise sources in a Magnetic Bearing Wheel

MICROVIBRATION LEVEL



August 91

Fig 6 -

N92-27810

AN ELECTROSTATICALLY SUSPENDED, MICRO-MECHANICAL RATE GYROSCOPE
NASA Contract # NAS1-19282

Timothy Hawkey
Richard Torti
SatCon Technology Corporation
12 Emily Street
Cambridge, MA 02139

1. Introduction

SatCon Technology has performed a study of micromechanical gyroscopes. The goals of this Phase I SBIR program were to define a baseline system configuration and establish technical feasibility for Phase II proof of principle, prototype fabrication. This report documents the research and presents the baseline mechanical design, sensors, control system, and electronics. This section presents a project overview and specific technical objectives. Section 2 contains a background on micromechanical technology, Section 3 the microgyroscope specifications and configuration, and Section 4 the electromechanical design. Section 5 outlines the control and electronics. Section 6 presents a preliminary sequence for microfabrication of the baseline design, and Section 7 conclusions and recommendations for further work.

2. Background

Micro-electronic fabrication technologies have recently been applied to produce novel micro-mechanical devices such as motors, pressure sensors, and linear actuators. Their small size, possible integration with electronic circuits, and potential low cost invite research. Thus far, however, few useful devices have been developed. A micro-mechanical gyroscope, proposed for this research effort, is a device that would have application to aerospace, commercial, and military systems. They could eventually be available for low cost and see widespread use in integrated navigation and control systems for micro-satellites, airplanes, and terrestrial or planetary autonomous vehicles. Other potential applications include automobiles and in control units for robotic end effectors.

The last twenty years have seen a revolution in the micro-electronics industry. Since the development of the first integrated circuit of a few transistors in the early 1970s, micro-processors over a million transistors are now routinely fabricated. In the last several years, techniques have been borrowed from the chip industry and used to fabricate micro-mechanical devices. Generally, these techniques fall into two categories, bulk micromachining and surface micromachining. A good overview of micromechanical fabrication can be found in Reference 11.

2.1 Bulk Micromachining

Bulk micromachining involves direct modification of silicon wafers with chemical etchants. Silicon crystal, it was discovered in the 1950s, can have its different crystal planes selectively etched by alkaline solutions at precise angles. Portions of the wafer can be protected by layers of silicon dioxide or silicon nitride (standard microelectronic materials) or ion implantations of boron. Bulk micro-machining is commonly used to fabricate trenches, cantilevers, cavities, nozzles, and membranes. An important associated technology to bulk micromachining is wafer bonding. Wafer bonding processes, first developed in the 1960s allow the fusion of silicon wafers together at the atomic level without adhesives. Infrared alignment devices allow wafer alignments accurate to about 1 micron.

2.2 Surface Micro-machining

Surface micromachining differs from bulk micro-machining in that most of the work is done on top of the wafer. Structural and sacrificial films are deposited on top of the wafer. After deposition, the sacrificial layers are selectively etched, leaving the micromechanical structure behind. Westinghouse Research Laboratories first applied the technique with metal films in the 1960s. In the early 1980s, researchers began using silicon dioxide as a sacrificial layer, and polycrystalline silicon as a structural material. Chemical vapor deposition (CVD) and

photolithography are used to grow the layers on the wafer and chemical or reactive ion etching (RIE) is used to remove sacrificial layers. Complex structures such as motors and linear actuators have been developed, but the lithographic processes limit the thickness and number of layers that can be patterned in this way. Each layer can be at most 3 or 4 μ thick, and structures of more than 5 layers are difficult to fabricate. Currently, standard micro-electronic materials, silicon dioxide, silicon nitride, and poly silicon are almost exclusively used in surface micromachining. Other materials such as aluminum and polyimide are being investigated and hold promise for opening new possibilities in surface micromachining.

2.3 Other Microfabrication Techniques

Surface and bulk micromachining can be used to produce a fascinating array of microdevices, but they are limited to thin film configurations for surface machined structures and the crystal planes of silicon for bulk micromachined devices. Other techniques currently under development may allow a wider range of configurations and devices to be fabricated in the future. One possibility is deep X-Ray or short ultraviolet lithography. The shorter wavelengths of X-Ray and UV radiation allow taller patterns to be produced without sacrifice in edge clarity. Other possibilities include micro electric-discharge machining (EDM) and a German developed process called LIGA which uses X-Ray fabricated, plated molds that are used to form microstructures that may be more than 100 μ tall with lateral features in the 3 μ range.

2.4 Micro-dynamics

A fundamental issue in micromechanics is the scaling of physical forces and properties in the micron domain. Some forces scale directly with object size, others with the square or cube. Mass, and hence weight scale with the object volume and decrease cubically with size. Magnetic field forces scale with area as do electric field forces. Force and torque production for electromechanical actuators are controlled by air gap energy storage. The limits on energy storage are set by metal saturation flux density in magnetic devices for magnetic field devices and electric field breakdown strength for electric devices. Typical saturation fields of 2 tesla and typical electric field breakdown of 3×10^6 volts/meter show energy storage densities of 1.6×10^6 J/m³ and 40 J/m³ respectively, explaining the preponderance of magnetic motors. For very small air gaps, however, the electric field breakdown strength increases substantially. At micron level, the electric field breakdown strength is greater than 10^8 volts/meter, allowing similar energy storage densities in electric and magnetic fields. Given the difficulties of microfabricating magnets and three dimensional coils, electric field actuation is generally preferable in microdevices.

3. Specifications and Configuration.

As with all sensors, resolution, accuracy, large dynamic range, low power consumption, small size and high bandwidth are desired. For this technology effort, the obvious primary objective was small size with the goal of eventually developing a complete two-axis rate gyro on a microchip. Maximum/minimum angular rates of 10 radians/sec and 0.1 radians/sec and 200 Hz bandwidth were chosen as specification goals to approximate what might be required for use on robotic arms. Other performance specifications were determined by process controlled geometries and parameters as discussed in Section 4.

3.1 Suspended Gyro Configuration

The initial micro-gyro configuration identified is shown in Figure 1. Configured as a

rebalance gyro, this microfabricated machine consists of three types of electroquasistatic components - the motor drive, position sensors, and the non-rotary actuators for rebalance and suspension. Like suspended macroscopic gyros, the rotor is spun by a motor to produce angular momentum, suspended and controlled by force and torque actuators, and sensed by various position sensors. As discussed in Section 2, all the sub-components are electric field devices. The term "rebalance" identifies the gyro mode of operation. When acted on by external forces, the control system is designed to hold the gyro in a constant position, rebalancing it. Knowledge of the actuator control signals and dynamics allows the inputs to be determined. Since the controlled mass (the gyro rotor in this case) is held to a nearly constant position, the linearity of the sensors and actuators is improved, and the overall dynamics are simplified. The block diagram is shown in Figure 2.

The electrostatic force can be written in linearized form for a fixed potential as

$$F = \frac{1}{2} V^2 \frac{\partial^2 C}{\partial^2 X} \Delta X$$

where ΔX represents the excursion about the equilibrium position, and the coefficient is positive. Since the force increases with decreasing distance, the motion is unstable and without other compensation requires closed loop control. In the case of a fully suspended rotor, this control must be effected in both axial and radial directions (five unstable degrees of freedom). There are therefore four sets of actuator/sensors - two for the upper and lower axial suspension and two for upper and lower radial rebalance actuator/sensors - and the motor driver actuator. Hence the multilayered configuration of the figure.

The fabrication of such a multi-actuated, multi-sensed device requires at least five sets of alternating insulating/conducting layers on the rotor. For reasonable capacitive bias currents and actuator forces, the facing areas must be at least 1-2 μm high with radial gaps of the same order. The height of this rotor will accumulate to over 5 μm . Present technology, however, only makes feasible aspect ratios (rotor thickness to gap) of up to 2/1, with 1/1 being typical. This gap in fabrication technology will have to be bridged to allow successful fabrication of a fully suspended micro-gyro.

3.2 Top Configuration

An alternate arrangement which has the advantage of using largely successful fabrication techniques is the supported top shown in Figure 3. In this case only two layered sets are used, the radial gap motor drive and the bottom actuator/sensor. The "top" has only two unstable degrees of freedom--the two tilt angles about the pivot point. The axially facing sensor/actuator provides an enhancement in capacitance over the radial gap approximating the ratio of rotor radius to height. Both sensing and actuation are accomplished with four electrodes imbedded the plane of the substrate as shown in Figure 3. If ohmic continuity is assured from the rotor bottom plate through the support spindle and into the substrate, the values of the four variable capacitors can be used to sense the direction of the inclination of the rotor axis for the normal to the substrate plane. Since this configuration will likely be first constructed as a preliminary to a fully suspended prototype, the remainder of the Phase I work focused on this configuration.

3.3 Motor Configuration

The electrostatic production of torque has long been considered for motor drives. Four classes of electroquasistatic motor actuators have emerged which have analogues with magnetically operated devices - variable capacitance, electrostatic induction, permanent electret, and electric hysteresis. In the work by Bart² induction and variable capacitance motors were studied in detail with attempts made to fabricate both axial gap and radial gap variable capacitance motors. Axial gap motors have not yet successfully been fabricated, but radial gap variable capacitance motors have been built and tested at both MIT and Berkeley. Our system therefore baselined a radial gap motor as fabricated at MIT (see Bart).

3.2 Sensor Configuration

The baseline sensor configuration chosen was capacitive position sensing using a superposition of high frequency signals between the axial control electrodes and the rotor. Decomposition of the four sensor signals (one for each axial stator electrode) provides the signals needed to control the rotor. Capacitive position sensing is commonly used in macroscopic devices, and has also been successfully applied to other micromechanical devices. The basic concept is to drive a constant current across an air gap (whose capacitance varies inversely with gap distance) and read the resulting voltage which is linearly proportional to the gap. High frequency modulation and demodulation allow good noise immunity. Though the capacitance of the microgyro axial gap will be very small (about 3×10^{-14} farads), the placement of FETs (field effect transistors) on the silicon substrate as preamplifiers as done by Schmidt³ should allow reasonable measurements to be made.

4. Electromechanical Design

The design of the motor drive and rebalance actuator is based upon the specifications discussed in Section 3 many of which were derived from known fabrication constraints and experience. Dimensions were generally conservatively chosen given the uncertainty in fabricating devices with this technology.

4.1 Sizing

The overall rotor diameter, 200μ , was chosen as the largest size that could be fabricated without significant warpage due to residual stress buildup during fabrication. The rotation rate is constrained by stress limits in the rotor and electronics limits in the motor driver circuitry. A rate of 500,000 rpm (8.3 kHz) was chosen as a reasonable extension of current motor rates (about 20,000 rpm). This is well below the ultimate spin rate (about 10,000,000 rpm) determined by material strength limits. The required electronics frequency, 25 kHz, is attainable without excessive noise problems. The motor height was set to 2.2μ , the same height as currently fabricated micromotors. The maximum value of total rotor thickness is limited by fabrication technology to about 2 times the radial gap of 1.5μ . The axial gap between substrate and rotor was set at 2μ . This represents a tradeoff between gap capacitance and rotor unstable frequency. A smaller gap would make sensor measurements more accurate at the cost of raising the unstable frequency and complicating the control problem. The 2μ gap gives a 300 Hz unstable frequency.

4.3 Sensor

The four segment rebalance sensor/actuator electrode design is similarly derived from the specifications. While it was not attempted to optimize the pattern for torque, depositing the

conducting region from 0.7 R to 1 R gives adequate rebalance torques and adequate capacitance for sensing inclinations as small as 0.008° . A possible difficulty is the actually attainable depth and uniformity of the implanted electrodes since the thermal noise limit is sensitive to circuit resistance. The sensor capacitance between each of the four electrodes and the rotor is approximately 3×10^{-14} F. With a typical commercial oscillator frequency of 100 kHz, the sensor current is about 15 nA for operation at 0.8v. Since commercial devices sense capacitance in the same range (although with larger electrode and gaps) it should be possible to use standard techniques for angle information.

4.4 Summary

The tables below give a summary of the dimensions and parameters predicted for the two degree of freedom microgyro.

Spin Angular Speed	500 kRPM
Spin Moment of Inertia	1.5×10^{-18} kgm-m ²
Precession Moment of Inertia	8×10^{-19} kgm-m ²
Minimum Angular Rate	0.01°/s
Thermal Sensor Noise	$< 0.4 \times 10^{-3}$ v
Angular Sensitivity	$< 0.008^\circ$
Sensor Electrode Capacitance	3×10^{-14} F
Sensor Operating Current (0.8 V)	15×10^{-9} A
Nominal Drive Actuator Potential	0.5 v
Drive Torque Per Pole	10-11 N-m
Rotor Radius	50μm
Radial Gap	1.5 μm
Vertical Gap	2 μm
Rotor Thickness	2.2 μm
# Stator Poles	12
# Rotor Poles	8

5. Control and Electronics Design

This section presents the controller design and closed-loop simulations of expected dynamic performance. As shown in Figure 2, and described previously, the system block diagram consists of the actuator and plant (gyroscopic) dynamics, the sensors, the controller, and the decomposition electronics. One of the goals of the controller is to keep the orientation of the rotor fixed, in the null position, relative to the orientation of the "stator" frame of the gyroscope. In addition, the controller must provide accurate measurement of the torque that is required to maintain the rotor in the null relative orientation. As usual, the simplest controller that can meet the performance objectives is desired, in order to minimize hardware complexity. In particular, a fixed-gain, linear controller is desired that can be easily implemented in analog electronics. This will force some performance and stability robustness tradeoffs, in particular because the plant dynamics are a strong function of the operating speed and are open-loop unstable. Because of the open-loop unstable nature of the plant -- an inverted pendulum at low speeds -- closed-loop control is required from zero speed to the full operational speed. The challenge, then, is to find a fixed gain controller that will provide adequate performance at all speeds.

5.1 Open-Loop Plant Dynamics

The variation of the plant dynamics from zero speed to operational speed of 500,000 rpm (8,333 KHz) is dramatic. At zero speed, the plant is a two-degree-of-freedom unstable pendulum. The two by two plant transfer function matrix relating control voltage inputs to rotor orientation output becomes diagonal in this case, with no cross-coupling between the x-direction tilt dynamics and the y-direction tilt dynamics. At zero speed, therefore, the plant can be treated as two identical single-input, single-output (SISO) systems. The important dynamics of the zero-speed plant can be seen in the Bode plots of the plant transfer functions (control voltages to rotor orientations) shown in Figure 4 below. Since the off-diagonal or cross-coupling transfer functions (x voltage to y orientation, y voltage to x orientation) are zero at zero speed, and the diagonal transfer functions are identical, only one transfer function is seen in Figure 4. At frequencies below 300 Hz, the dynamics of this parallel or diagonal transfer function are seen to be dominated by the unstable torsional spring produced by the combination actuator and motor torsional effects. The unstable spring produces the flat low frequency magnitude response between input voltage (torque) and output orientation (angle) with the 180 degrees of phase indicating an unstable spring. At frequencies above the 300 Hz unstable frequency, the transfer function falls off with a slope of minus two, caused by the double integration of torque to angle, and scaled by the voltage to torque constant (b_a) and the radial moment of inertia of the rotor (I_{rr}).

At full speed (500,000 rpm or 8,333 Hz) the plant dynamics are dominated by gyroscopic effects. The Bode plots of the plant transfer functions are shown in Figure 5 for this full speed case. Because of the x-y symmetry, the two diagonal or parallel transfer functions (x voltage to x orientation and y voltage to y orientation) are the same. Similarly, the two off-diagonal or cross-coupling transfer functions (x voltage to y orientation and y voltage to x orientation) are also the same. The plant is completely characterized by two transfer functions the parallel (diagonal) and cross (off-diagonal) transfer functions.

These two transfer functions are shown in Figure 5. Two sets of undamped eigenvalues can be seen, one at approximately 16 kHz and the other at approximately 6 Hz. These are both forward whirl modes. The higher frequency whirl mode, or "fast precession mode", is located at the frequency given by the ratio of axial to radial moments of inertia times the rotational speed. At full speed, this open-loop fast precession frequency is 15.8 kHz. The lower frequency whirl

mode, or "slow precession mode", is located at the frequency given by the unstable frequency squared divided by the fast precession frequency. At full speed, this open-loop slow precession frequency is 5.7 Hz. These fast and slow precession modes correspond to similar modes of a "classic" top spinning in a vertical position.

As the rotational speed is increased, these unstable pole pairs gradually take on a whirling nature, as indicated by the growth of the imaginary part of the eigenvalues. At a rotational speed of 320 Hz, the poles reach a stability boundary where formerly unstable modes become purely whirl modes lying on the imaginary axis. As the speed is further increased, the whirl modes split into the "fast precession" and "slow precession" modes as discussed earlier.

5.2 Controller Design

The design approach to develop a fixed-gain controller for this speed varying plant was to first examine how optimal, full-state feedback controllers change with changing plant speed. These full-state feedback controllers assume knowledge of the position and velocity of the rotor in both radial directions. Based on the behavior of these parameter-varying, full-state feedback controllers and the addition of some physical insight, a fixed-gain, full-state feedback controller can be chosen that provides reasonable performance over the full speed range. This full-state feedback controller is then implemented as an output feedback controller using lead-lag compensators to provide estimates of the velocity states. This section outlines this procedure and presents the baseline control algorithm. The following section then presents system simulations.

The first step in this design approach was to develop full-state feedback controllers for various operational speeds. These full-state feedback controllers were designed using the linear-quadratic-regulator (LQR) approach. This controller is the "optimal" initial condition regulator, which closely matches the regulator type performance goals of the controller for the micro-gyroscope.

For the zero-speed LQR design, the desired 1000 Hz bandwidth was achieved with cost-on-control-weighting of $\mu = 0.02$. This resulted in "optimally" damped ($\zeta = 0.707$) closed-loop poles at 1 kHz. Note that at zero speed, the plant is decoupled into separate x and y direction dynamics, as discussed previously. Because of this decoupling, the LQR feedback gains are also uncoupled, and only the "parallel" gains are used. This means that the x-direction torque, for example is a function of only measured x-direction orientation, and x-direction angular velocity. Because of the system symmetry, the same gains are used in the x and y-directions.

The root-locus of the closed-loop eigenvalues, $p_i(\Omega)$, as a function of the rotational speed Ω using this zero-speed state-feedback compensator, $K(0)$, is shown in Figure 6. Shown is a polar plot of the logarithm of the closed-loop frequencies, $\log_{10} |p_i|$, and the angle of the poles. Taking the logarithm of the closed loop frequencies makes this plot significantly different than conventional root-loci. The use of the logarithmic magnitude scaling allows the widely divergent closed-loop frequencies of the fast and slow precession poles to both be seen. Because of the logarithm magnitude scaling, vertical lines are not contours of constant real part of p_i , and horizontal lines are not contours of constant imaginary part of p_i , as would be the case in conventional root-loci. Radial lines, however, remain lines of constant damping as for conventional root-loci. Circles about the origin are contours of constant frequency, as is usual, however they are logarithmically scaled.

At zero-speed, as can be seen in Figure 6, the four closed-loop poles for the zero-speed

state-feedback compensator $K(0)$ are paired into two sets of well damped pole pairs with frequency of 6,000 rad/sec (1 kHz). As the rotational speed increases, the poles split into two pairs. One pair increases in frequency, the fast precession mode, and one pair decreases in frequency, the slow precession mode. These modes become decreasingly well damped as the speed increases. At full speed they both have damping of approximately 0.1. For this controller, the minimum negative real part of the closed-loop poles occurs at maximum speed in the slow precession mode. For this mode at full speed, the minimum real part of the closed-loop poles is 41 rad/sec.

For the full-speed LQR design, the desired bandwidth of 1000 Hz was achieved with cost-on-control-weighting of $\rho = 0.001$. This is significantly lower than the zero speed case ($\rho = 0.02$) and is a result of the lower plant gain at full-speed, caused by the gyroscopic effects, as discussed earlier. Because of the lower plant gain at full speed, more control effort is needed to achieve a fixed bandwidth, and therefore, less cost must be placed on control effort in the LQR design procedure. At full speed ($\Omega = 8.3$ kHz), the closed-loop poles pairs both have the same real part of -3300 rad/sec. This implies that both modes have the same decay time, a characteristic of this type of LQR approach. One of the pole pairs occurs at the desired bandwidth of 1000 Hz. The other pair occurs at the full-speed fast-precession-frequency of approximately 1×10^5 rad/sec (15 kHz). Because of their different frequencies, these closed loop poles have dramatically different damping ratios as shown in Figure 7.

This full-speed designed controller becomes unstable at low speeds because of the use of cross-proportional feedback. The cross-proportional feedback has the same phase (acts as) damping, however, its effects are not proportional to frequency (velocity) as is conventional damping. Because of this, it acts to dampen (stabilize) forward whirl modes but destabilize backward whirl modes. At full-speed, this is ideal, since the dynamics are dominated by the fast-precession, forward-whirl mode. Because of its use, the minimum real part of the closed-loop eigenvalues at full-speed, is -6000 rad/sec for the full-speed designed compensator as compared to only -41 for the zero-speed designed compensator. At low speeds, however, the use of this level of cross-proportional feedback destabilizes the closed-loop system. At zero speed, for example, the open-loop poles, which describe an inverted, decoupled, two-degree-of-freedom pendulum, can be alternatively described as forward and backward whirl modes. The use of cross-proportional feedback adds stability to the forward whirl mode, but destabilizes the backward mode. Because of this, there is a limit to the amount of cross-proportional feedback that can be used if the system is to operate at zero-speed.

Both the zero-speed, and full-speed state feedback compensators suffer from performance problems when used over the full speed range, as discussed above. The zero-speed state-feedback compensator exhibits slow decay time and low-bandwidth at full-speed. The full-speed state-feedback compensator becomes unstable at low speeds. By using a combination of these compensators, however, a tradeoff can be effected between high-speed performance and low-speed stability. This procedure involved iteratively trying linear combinations of the zero-speed compensator. The design parameters are the ratio of zero-speed to full-speed feedback gains, α , and the compensator bandwidths controlled by the cost-on-control-weighting parameters. These parameters were iterated to yield a state-feedback compensator with a minimum of 1000 Hz bandwidth and the largest minimum decay time over the whole speed range. In addition, the ratio between zero-speed and full-speed bandwidth was kept under a factor of 10.

The resulting "best" compensator uses less parallel-proportional gain than the zero-speed design and less cross-proportional gain than the full-speed design. The resulting closed-loop root-locus versus rotational speed is shown in Figure 8 along with the zero-speed case. The "best" compensator has improved damping, as can be seen in Figure 8, and decay time compared to the

zero-speed case.

5.3 Output Feedback Compensator Design and Performance

The full-state-feedback compensator discussed above was then implemented using an output feedback compensator. The full-state-feedback compensator assumes access to the radial angular velocities of the rotor, which are not directly measured. A simple lead-lag compensator is used to combine the parallel proportional and velocity state feedback terms into a equivalent output (measured rotor radial angle) compensator. In addition, critically damped high frequency pole pairs, at a frequency of 600,000 rad/sec (100 kHz) were added to all the compensator transfer functions to roll the system off. As discussed previously, the loop cross-over frequency decreases by almost a factor of ten as the speed increases from zero to full speed. A closed loop frequency response curve for one axis is shown in Figure 9.

5.4 Electronics

5.4.1 Sensor Electronics

The capacitance of the position sensor varies inversely with the distance from the sensor to the target. Over the specified measurement range, the sensor varies in capacitance from approximately 0.027 picofarads (pF) to 0.033 pF. Any stray capacitance on the sensor leads will effect the linearity of the measurement unless the leads are appropriately guarded. The ability to detect position accurately is also hampered by any load placed on the sensor capacitance by the measurement electronics.

The block diagram of the capacitive sensor interface circuit is shown in Figure 10. The sensor is driven by a 100 kHz current source so that the resultant voltage is proportional to the sensor impedance. The AC voltage produced across the sensor is buffered by a "guard" loop, full-wave rectified, and low-pass filtered to produce a DC output voltage directly proportional to distance. The effects of stray capacitance on the sensor leads are greatly reduced by driving the shield of the sensor cable with a "guard" loop. The guard loop drives the shield with a voltage identical to that across the sensor, and thus no current flow is possible. The impedance of the shield is a capacitance greater than 200 pF to ground. In order to drive this load, the voltage across the sensor is buffered by the FET input stage, a high-bandwidth differential op-amp, and a high-current buffer. The bandwidth of this follow-up loop must be high to reduce any effects of the guard capacitance upon the sensor capacitance. To reduce the input capacitance of the sensor electronics, a Field Effect Transistor (FET) input stage is used. This input stage presents a very high resistance and low capacitance load to the sensor. The FET input stage is configured as a source-follower where the source signal will exactly follow the gate (input) signal. The source terminals of the FETs are each loaded with a transistor current source. The high impedance of the current sources reduces the effect of any gate-to-source capacitance. The drain of the FETs are capacitively coupled to the buffered sensor voltage to reduce the effects of any gate-to-drain capacitance. Stray capacitance on the circuit board would be reduced by placing the buffer-loop circuitry on a copper-clad board with the copper clad driven by the guard voltage. The output of the sensor guard-loop is bandpass filtered to eliminate both DC drift and high-frequency noise effects. The signal is then full-wave rectified and low-pass filtered to produce a DC output voltage. The filter is a four-pole Butterworth, and contributes less than 10 degrees of phase error at the loop cross-over frequency.

5.4.2 Control and Read-Out Electronics

Control and read-out of the micro-gyro is accomplished simply with six op-amps: three for tilt control around the x-axis and three for y as shown in Figure 11. The first op-amp finds the difference in the signals from the capacitive sensor electronics which results in a measure of the tilt angles. The parallel-axis angle measurement is fed to the compensation stage through a lead-lag network which provides proper gain and phase margin at the loop-crossover frequency of the tilt loop. The cross-axis angle measurement is also summed into the compensation stage in order to compensate for the gyroscopic coupling between the axes. The feedback network of the compensation stage includes integral gain which ensures virtually-zero error at dc, and a high frequency pole to reduce both noise and sensitivity to unmodelled dynamics. The output of the compensation stage is fed to the two actuator drive stages where it is respectively added to and subtracted from a dc bias voltage. This differential operation about a bias voltage linearizes the electrostatic actuator. This makes the output of the compensation stage proportional to the restraint torque, and thus proportional to the input rate. Due to the electrostatic actuator requirements, the actuator driver stages are high-voltage op-amps capable of 120 volt output.

5.4.3 Motor Drive Electronics

The gyro wheel-motor is a three-phase bipolar variable-capacitance motor. Since this motor type is synchronous, i.e., produces torque only when the rotation frequency and excitation frequency are the same, it requires a variable-frequency drive source. In addition, the push-pull excitation required for each of the three bipolar phases will require six high-voltage output stages. The motor is driven with balanced bipolar voltages so that the rotor will remain near ground potential. Any voltage induced on the rotor will cause it to be strongly attracted to the grounded substrate because of its large surface area.

Motor start-up will require that the excitation frequency start at the sub-Hertz level and ramp up to the full-speed value of 25 kHz. This is accomplished with a ramp generator and voltage-to-frequency (V/F) converter. The bipolar three-phase generator takes the single-phase output of the V/F converter and produces three square-waves with 120 degrees phase difference and their complementary signal for driving the output stages. In addition, the circuit generates the signal pair which develops the bipolar waveforms. The output circuit contains six high-voltage drivers, one for each bipolar phase, and can deliver up to 120V.

6. Fabrication

This Section outlines a sequence for fabrication of the micro-gyro described above. The steps described here follow established surface micro-machining procedures as practiced at MIT. Though all of the processes described here have been performed before, their combination into the micro-gyro will be a significant advancement in the state of the art. The numbered steps and Figure 12 below show the fabrication sequence.

- 1) The rotary micro-gyro fabrication process begins with <100>, p-type silicon wafers. P-type wafers are chosen to allow the selective ion implantation of phosphorus for control electrodes in step 3.
- 2) The next steps involve etching the center pin in which the rotor will rest. A 500 Å silicon nitride etch mask must be deposited in order to define the height of the pin (Figure 12). An HF isotropic etch with no agitation will yield a shallow bottomed etch area. The etchant will undercut the edges of the Silicon Nitride mask and form a conical point beneath it. The etch is done when the nitride pattern disappears. Some experimentation will be required to determine the correct pattern diameter to produce the desired pin height after etching.⁴

- 3) This step is the selective ion implantation of phosphorous on the silicon wafer. This yields n-type regions which form the lower control electrodes. Note that when the electrodes are energized with a positive voltage on the p-type material, a reversed-bias diode is formed between the electrode material and the rest of the substrate yielding electrical isolation.⁵
- 4) A thin layer (0.5 μ) of LTO (low temperature silicon dioxide) is deposited next to form the first sacrificial spacer layer. On top of this layer is deposited 0.5 μ of poly-crystalline silicon (polysilicon). The polysilicon is heavily doped with phosphorus and patterned to form the rotor's control electrode.
- 5) The next material that is deposited is silicon nitride which will yield electrical isolation between the substrate and the stator drive electrodes and also between the rotor's control and drive electrodes. Before this can be done, windows in the first sacrificial layer (LTO #1) must be opened so that the silicon nitride layer will bond to the substrate. A 1000 Å thick layer of LPCVD stoichiometric silicon nitride can now be deposited and patterned. Note that if a thicker layer of nitride is determined to be required for improved electrical insulation, the large tensile residual stress of the stoichiometric material could cause warping of the released structure. To reduce the stress in such a case, the nitride should be deposited in a silicon rich form⁶.
- 6) The main rotor and stator structure is now deposited in the form of a 2.5 μ layer of LPCVD polysilicon. Once again the polysilicon is heavily doped with phosphorus to make it a good conductor. The patterning of this layer defines not only the rotor and stator pole configuration, but also the rotor--stator gap spacing. The current state of the art allows for aspect ratios of rotor thickness to rotor-stator gap spacing of about 2 to 1. Considerable process development would be required if this aspect ratio must be increased significantly.
- 7) The last steps in the process are used to fabricate tabs which keep the rotor in place after the final release. A second layer of sacrificial oxide (LTO #2) is deposited to a thickness of approximately 1 μ . The layer is patterned (mask #7) to open holes through which the polysilicon hold--down tabs will bond to the stator poles (poly #2). Next, 1 μ of LPCVD polysilicon is deposited and patterned to form the hold--down tabs (mask #8).
- 8) The final step in the fabrication process is the removal of the sacrificial oxide to release the rotor. This is accomplished with a simple HF timed etch. In order to keep the etch time from becoming excessive, the rotor may need to have holes strategically placed to reduce the distance that the etchant must undercut.

6. Conclusions

The results of this program are very positive. Though extensions of fabrication technology will be required for fabrication of a fully suspended microgyroscope, the potential for successful development is very good. The fabrication of a simplified top arrangement can be achieved with current technology and was studied in depth as an initial control and electronics testbed. An operational micromechanical gyroscope would have many applications in commercial, aerospace, and military sectors.

REFERENCES

1. Howe et al, "Silicon micromechanics: sensors and actuators on a chip", IEEE Spectrum, July

1990.

2. S. Bart, Modeling and Design of Electroquasistatic Microactuators, PhD Thesis, Massachusetts Institute of Technology, Cambridge MA , September 1990.
3. M. Schmidt, et all, "Surface micromachining of polyimide/metal composites for a shear-stress sensor", in IEEE Micro Robots and Teleoperators Workshop, Hyannis MA, 1987.
4. K. Petersen. "Silicon As A Mechanical Material". Proc. IEEE, 70(5):420-457, May 1982.
5. L. Tavrow, "A LOCOS-Based Microfabricated Radial-Gap Electric Motor" PhD Thesis, Massachusetts Institute of Technology, Cambridge MA, 1991.
6. H. Guckel, D.K. Showers et all, "Deposition Techniques and Properties of Strain Compensated LPCVD Silicon Nitride Films", In Technical Digest of the IEEE Solid-State Sensor and Actuator Workshop, Hilton Head Island SC, 1986.

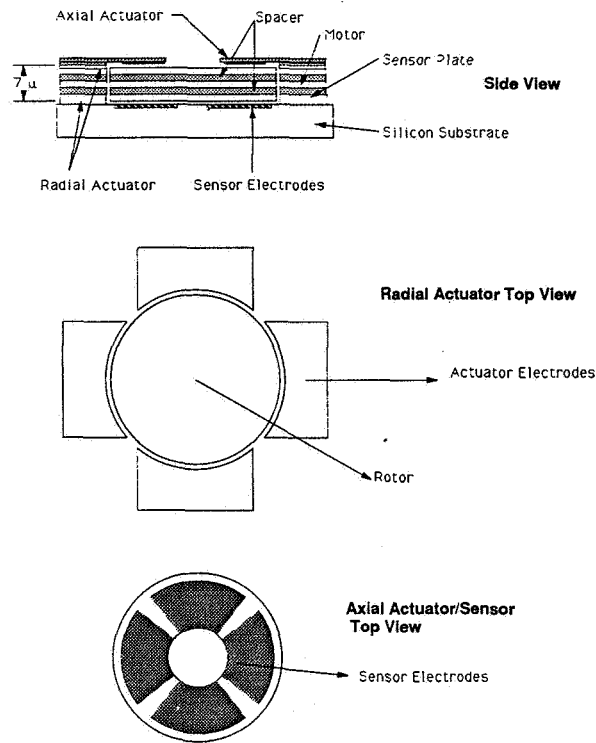


Figure 1. Fully suspended configuration

μ Gyro Block Diagram
3/15/91

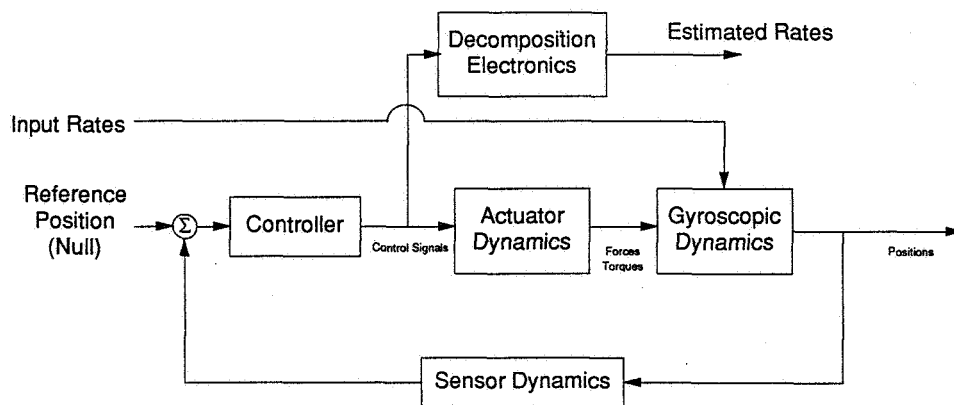


Figure 2. System block diagram

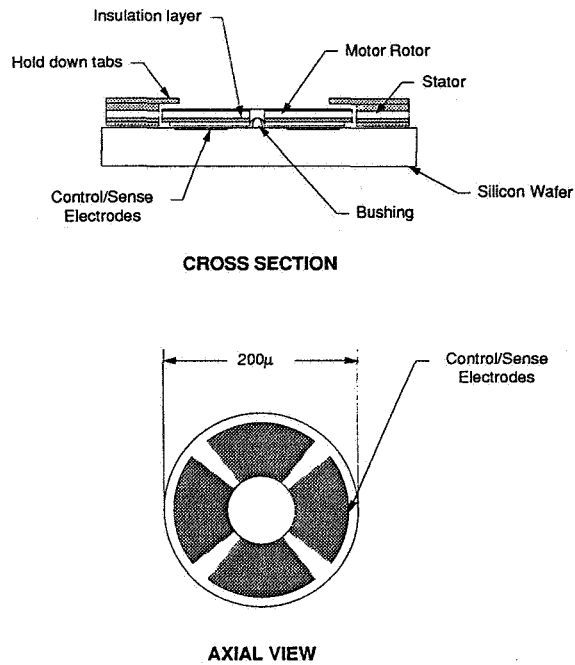


Figure 3. Top configuration

Bode Plot of Zero Speed Plant

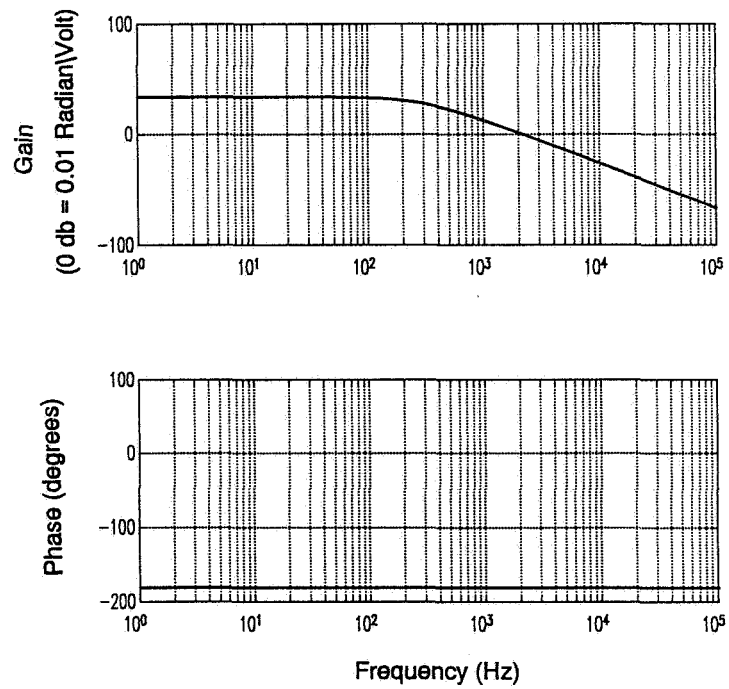


Figure 4

Comparison of Zero and Full Speed Plants

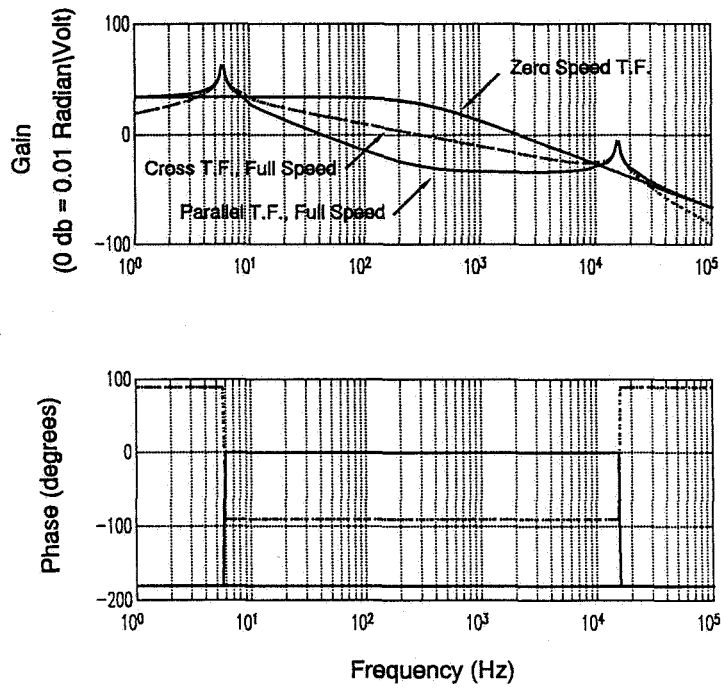


Figure 5

Root Locus of "Zero Speed" Controller

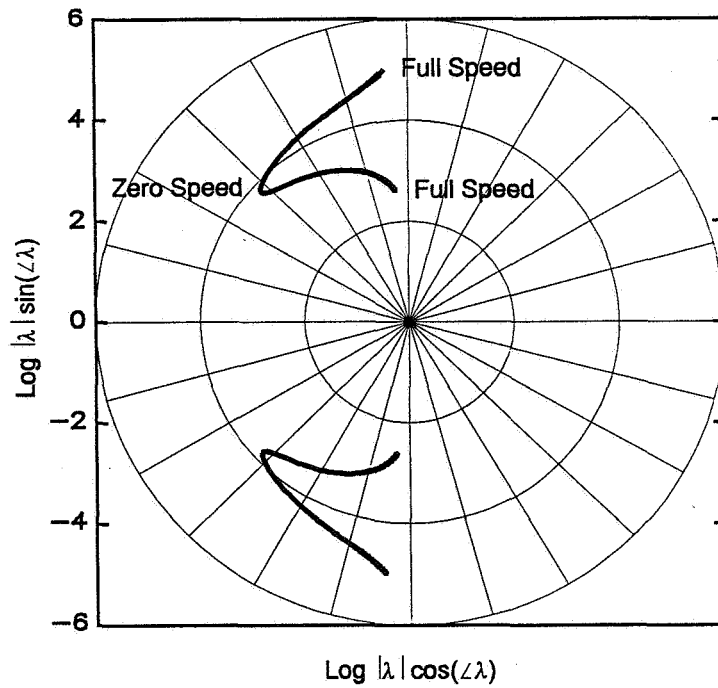


Figure 6

Root Locus of "Full Speed" Controller

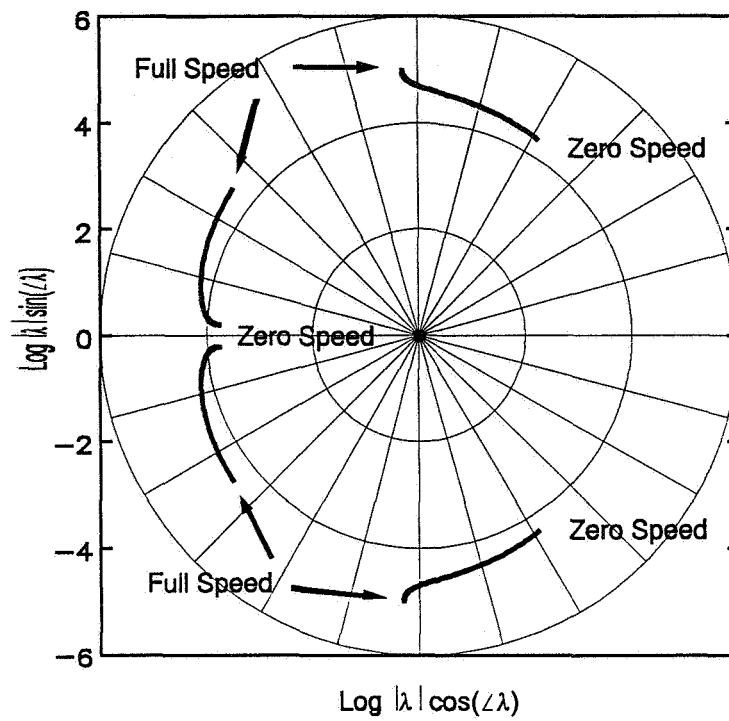


Figure 7

Comparison of "Best" and "Zero Speed" Controller

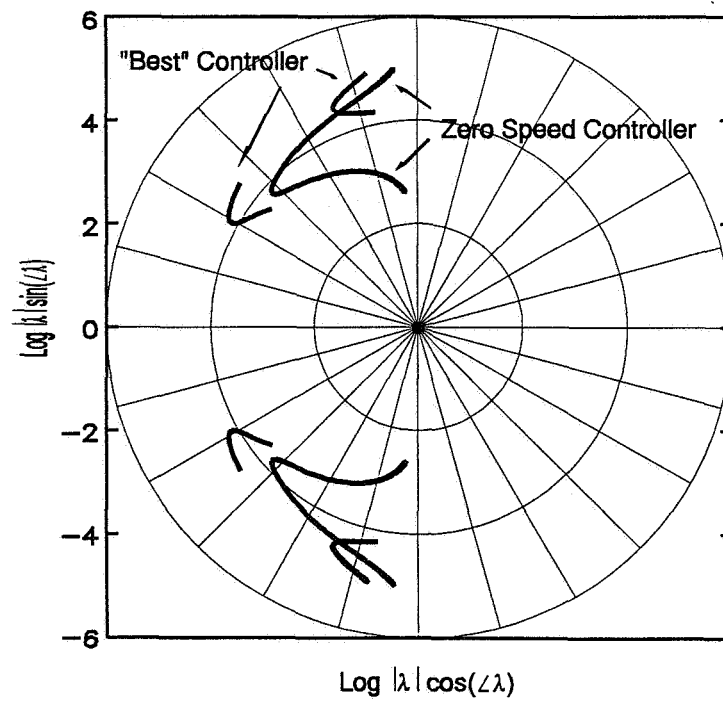


Figure 8

Input Yaw Rate to Commanded Voltage T.F.
Full Speed Operation

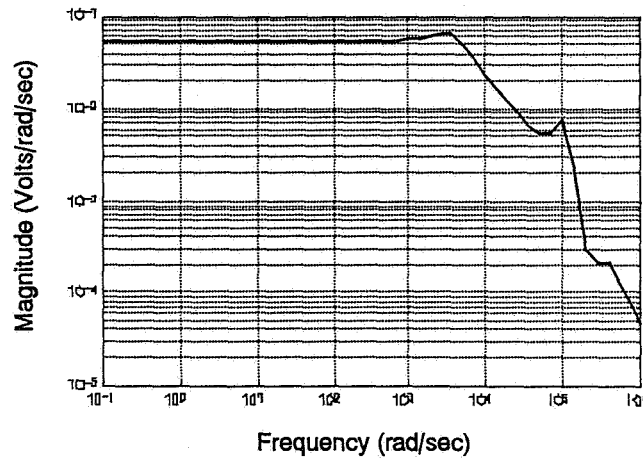


Figure 9

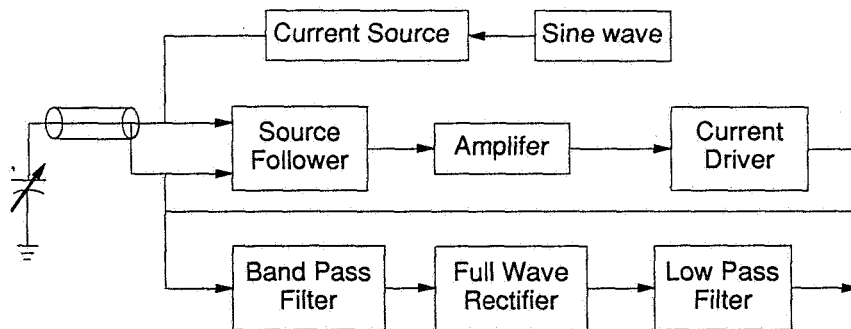


Figure 10. Capacitive sensor block diagram

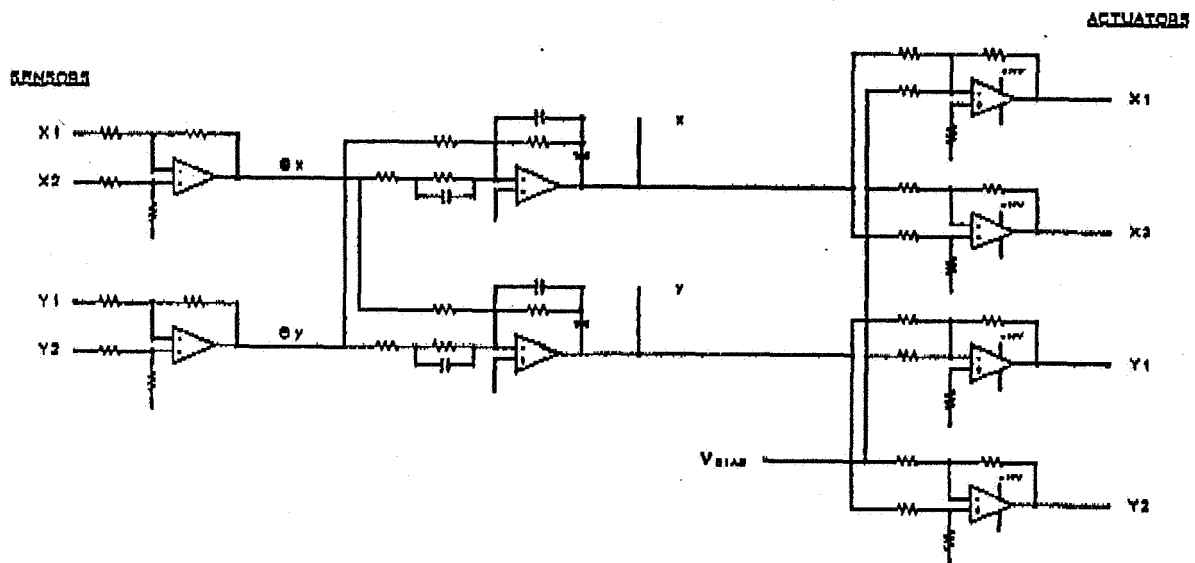


Figure 11. Readout electronics diagram

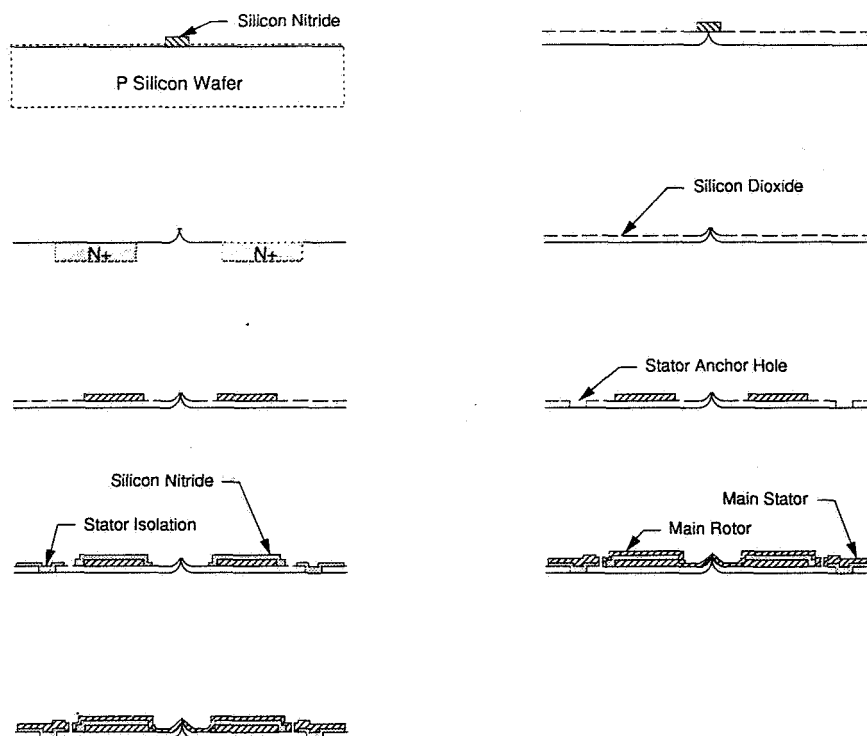


Figure 12. Fabrication sequence

Session 16

MAGNETICALLY LEVITATED TRAINS (MAGLEV) 2

**Chairman - Colin P. Britcher
Old Dominion University**

N92-27811

BATTERY CARS ON SUPERCONDUCTING MAGNETICALLY LEVITATED CARRIERS--ONE
COMMUTING SOLUTION

B. Mike Briggs and Henry Oman
M/S 8M-85, Boeing Aerospace and Electronics
P.O. Box 3999, Seattle, WA 98124

ABSTRACT

Commuting to work in an urban-suburban metropolitan environment is becoming an unpleasant time-wasting process. If paid \$15 an hour, a million people by moonlighting instead of commuting two hours to and from work each day, could earn \$6 billion per year. That income in 10 years, invested at 10 percent compounded interest, would pay off a \$100 billion bond debt by the municipality. However, saving the commuters' time rarely enters into municipal planning.

Today's embedded metropolitan commuting routes can be traced to radiating street-car tracks that brought workers from trackside villages to downtown factories. Now the urban workplaces are dispersed, and commuters drive to work on freeways which are too often choked with traffic jams. Subways and light rail have the same flaws--inconvenience, lost time, and low passenger productivity--that bankrupted the interurban trains in the 1930's.

To this commuting problem we applied the technology of communication management, a system-engineering tool that produced today's efficient telephone network. The resulting best commuting option is magnetically levitated carriers of two-passenger, battery-powered, personally-owned local-travel cars. A commuter drives his car to a nearby station, selects a destination, drives on a waiting carrier, and enters an accelerating ramp. A central computer selects his optimum 100 miles-per-hour trunk route, considering existing and forecast traffic; assigns him a travel slot, and subsequently orders switching-station actions. The commuter uses the expensive facilities for only a few minutes during each trip. His cost of travel could be less than 6 cents per mile.

BACKGROUND--HISTORY OF LIGHT RAIL

Light rail, the proposed solution to today's clogged freeways, has a basic flaw. We illustrate this flaw with Southern Pacific's "Red Electric" trains which by the early 1900's connected Portland, Oregon with Salem, Oregon. In the morning these trains collected workers along its 40-mile route and delivered them to Portland where they rode streetcars to their job sites.

Consider the four-car train operated by Conductor Kimmel and his crew, consisting of an engineman and three brakemen. No fireman was needed because the train was electrically propelled and heated. When carrying 150 people at 30 miles per hour, this crew delivered 600

C-5

passenger miles per employee hour. In comparison, one crew member on a 747 airplane creates 37,500 passenger miles per crew-member hour. Dietrich Koelle illustrated the contribution of high speed to the productivity of labor in flying a hypersonic airplane. Koelle's hypersonic airplane would cost twice as much as a Boeing 747. The liquid-hydrogen fuel cost 10 times as much as the kerosene for Luftansa's 747. Yet, because of the tremendous passenger-mile-per hour productivity from flying at Mach 4.2, the cost per seat km of the two airplanes would be the same (1).

Crew cost, which was included in the passenger's ticket, was not what drove the "Red Electric" and other electric interurban trains into bankruptcy in the 1930's. The real cause was lack of passenger convenience. The typical commuter walked from his home to the depot in the morning, arriving 10 minutes early to be sure he wouldn't miss the scheduled train. On the train he sat patiently as the train stopped at depots along the way to pick up more passengers. In Portland he got off the train and waited for a streetcar which slowly carried him to near his workplace, stopping at every intersection along the way. He then walked several blocks to his workplace. The return ride could be even worse if it rained while he waited for the streetcar and then the train.

The result was that our commuter bought a car as soon as he could afford its cost. Then he drove straight to work from his garage. He could also make side trips on his way home, and haul bulky packages. This feature of commuting transportation we call "passenger convenience."

We can ask, "With today's jammed freeways, will a commuter give up his car and ride the new and beautiful light-rail train?" Portland's new "MAX" tells one answer. The trains, tracks, and right-of-way cost \$214 million. Passenger volume was forecast to be 42,500 happy commuters per day by 1990 (2). However, the initial ridership of 24,000 dropped to 19,000 by 1988. The 19,000 trips per day (8500 commuters) contrasts with four million automobile trips per day in the Portland area. It would seem that each voter who supports the light-rail projects hopes that he will be able to enjoy a clear freeway after the other commuters ride the train.

IMPORTANT FEATURES OF COMMUTER TRANSPORTATION

In considering alternatives to freeways and light rail, we evaluate in Figure 1 the quality of past and present commuting options. Here the filled dots represent desired features. For example, the walking commuter enjoys unsurpassed route flexibility. Joseph Jenks started, in 1643 at Lynn, MA, the first manufacturing plant in America. He commuted by walking across his back yard. A later development was the New England mill town, where workers living in houses around the mill also walked to work.

The larger steel mills and electrical factories needed more workers. In 1880 Edison and Villard introduced the electric streetcar. Streetcar lines soon radiated from the factories in city

Trasportation option	ERA	Factors determining commuter desirability for use						
		Time	Route flexibility	Multi functional	Security	Cost/ml	Convenience	Safety
Walk	< 1900	○	●	○	○	●	○	●
Horse	< 1900	◐	●	○	◐	●	○	○
Street car	1900-30	◐	◐	◐	◐	◐	○	◐
Bus	> 1925	◐	◐	◐	◐	◐	◐	◐
Bicycle	< 1910	◐	◐	○	◐	◐	◐	◐
Automobile	> 1918	●	●	●	●	○	●	◐
Freeway	> 1945	●	●	◐	◐	○	●	◐
Subway		◐	◐	◐	◐	◐	◐	●
Light rail		◐	◐	◐	◐	◐	◐	●

Legend: ● Very desirable ◐ Undesirable
 ◐ Desirable ○ Very undesirable
 ◐ Marginal

Figure 1. The automobile's commuter-convenience advantage over alternative commuter transportation is being eroded by freeway traffic congestion.

centers to the suburbs where the workers lived. Riding the streetcar was more comfortable than walking. However the streetcar could travel only where the tracks were laid. Buses replaced street cars in the 1930's, and bus routes could be easily changed.

In the modern metropolitan area people live in one suburb and work in another. For example a person living in Pasadena may work in Long Beach. A hub-and-spoke rail network extending from downtown Los Angeles would require the commuter to travel to the downtown center and out again on each trip. Driving a car is much quicker. Having a bus going from every home to every workplace is not practical.

PRODUCTIVITY OF COMMUTING RESOURCES.

The bicyclist, whose personal capital cost is trivial, illustrates an important limit in the productivity of a community's capital investment. Bicycling commuters help solve our trade unbalance and the carbon-dioxide problems, besides contributing to longevity and physical well-being of their own population. The United States trade unbalance could be eliminated by not importing oil, most of which goes into propelling our automobile fleet.

The bicyclist generates 1200 passenger miles per food-equivalent of a gallon of diesel fuel. The food that he eats has its ultimate source of energy in sunlight falling on plants, and the plants consume the carbon dioxide that the bicyclist releases. However, bicycling commuters occupy space. The streets of Beijing, which are packed with bicycling commuters in the morning and evening, illustrate the first principle in moving commuters:

- o The productivity of capital investment in the transportation of people is directly proportional to the throughput, measured in passenger-miles generated per hour.

For example, a bicyclist with a reasonable headway of 15 feet and a 4-foot clearance on each side, occupies 176 square feet of pavement. Delivering in one hour a million bicyclists traveling at 7.5 miles per hour would require a street 4500 feet wide!

On the other hand, assume that the bicyclists could be parked on a 100-miles-per-hour moving belt. Now they can be packed closely together so that each cyclist occupies only 13 square feet of belt space. To deliver a million cycling commuters with this impractical method would require a belt only 25 feet wide. A more feasible arrangement might have the cyclists enter a magnetically levitated carrier which delivers them over a dedicated guideway to destinations from which each one can cycle to his workplace.

We generally increase freeway capacity by adding lanes, which occupy more land. Ultimate increases in capacity will have to come from multi-level freeways. Higher speed limits do not help because the faster-driving motorists want more headway, which is then unoccupied. The Highway Capacity Manual, TRB SR 209 1985, shows that a freeway's traffic-flow peaks at 2000 cars per hour per lane at a

speed of 34 miles per hour. At 60 miles per hour the flow is down to 1000 cars per hour per lane (Figure 2).

At a rate of 2000 cars per hour per lane, delivering a million commuters in 4-person cars requires a freeway that is 125 lanes wide.

APPLICATION OF COMMUNICATION MANAGEMENT TO MOVING PEOPLE

Communication management is a well-developed tool for moving messages. For example, when you dial a number on your telephone, a computer determines the best unused route for the call and commands switches to make this connection. Federal Express delivers parcels the next day because, within minutes after the driver picks up the parcel, the computer knows where it must go, and has planned its entire overnight movement. The U.S. Post Office once performed equivalent functions with clerks working in its railway mail cars.

Applying communication-management technology into commuting practice requires these elements:

- o Each commuter must be an entity to be transported, as on a bicycle or in an electric car.
- o He must be picked up quickly when he arrives at a station near his origin, and transported at high speed, like 100 miles per hour, to a point near his destination.
- o His movement over branch lines and main loops must be computer-controlled to place him in the best routing when considering existing traffic.

CONCEPT FOR HIGH-SPEED, HIGH PRODUCTIVITY COMMUTING

The commuter transportation system in Figure 3 could meet these requirements. The commuter drives his own standardized electric car through an entry where the computer's optical sensor identifies him for future billing, and ascertains his destination. He drives to a magnetically levitated carrier which accelerates him at a rate which achieves 100 miles per hour at the next available slot on the main line. Subsequent computer-controlled switching and off-ramping operations deliver the commuter within a few km of his destination in a few minutes (Figure 4).

We have calculated that the travel cost, including amortization of capital, need be only 6 cents a passenger mile, which is a fraction of the cost of driving a car (Figure 5).

STATUS OF AVAILABLE TECHNOLOGY

Available today are the components for building and operating the magnetically levitated and propelled commuter transportation system. For example, for aircraft flight control we are developing quad-redundant components so that an airplane can be dispatched with

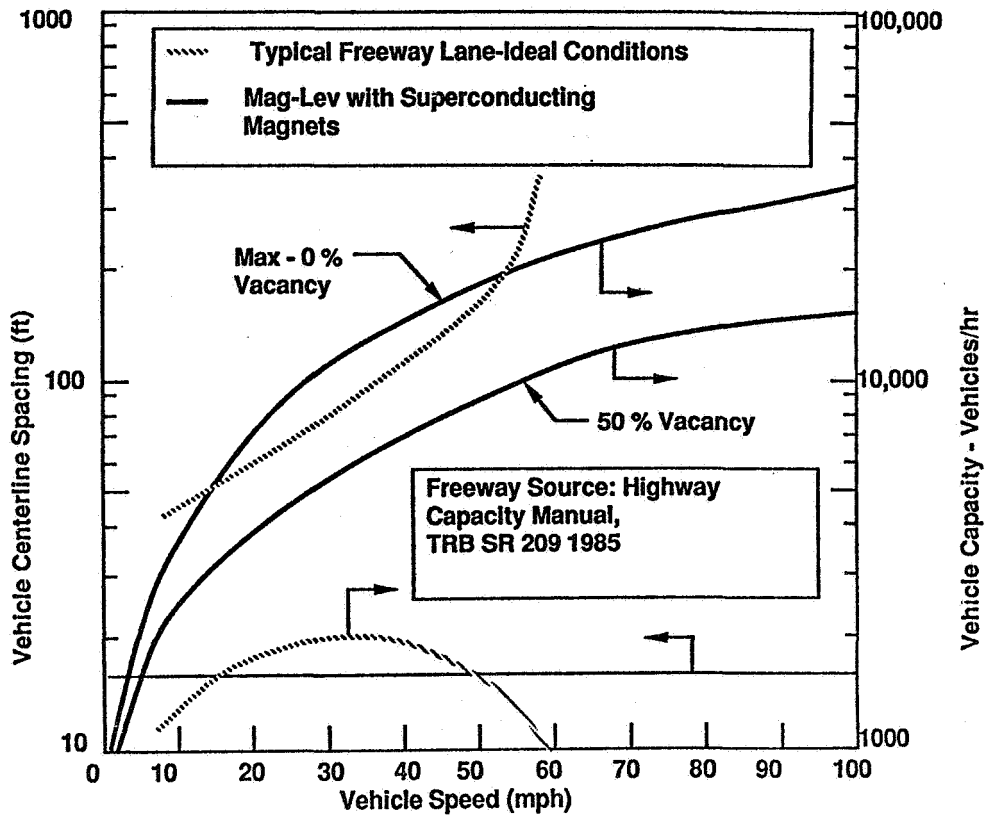


Figure 2. Freeway-lane capacity drops at speeds above 35 miles per hour because drivers need more forward clearance.

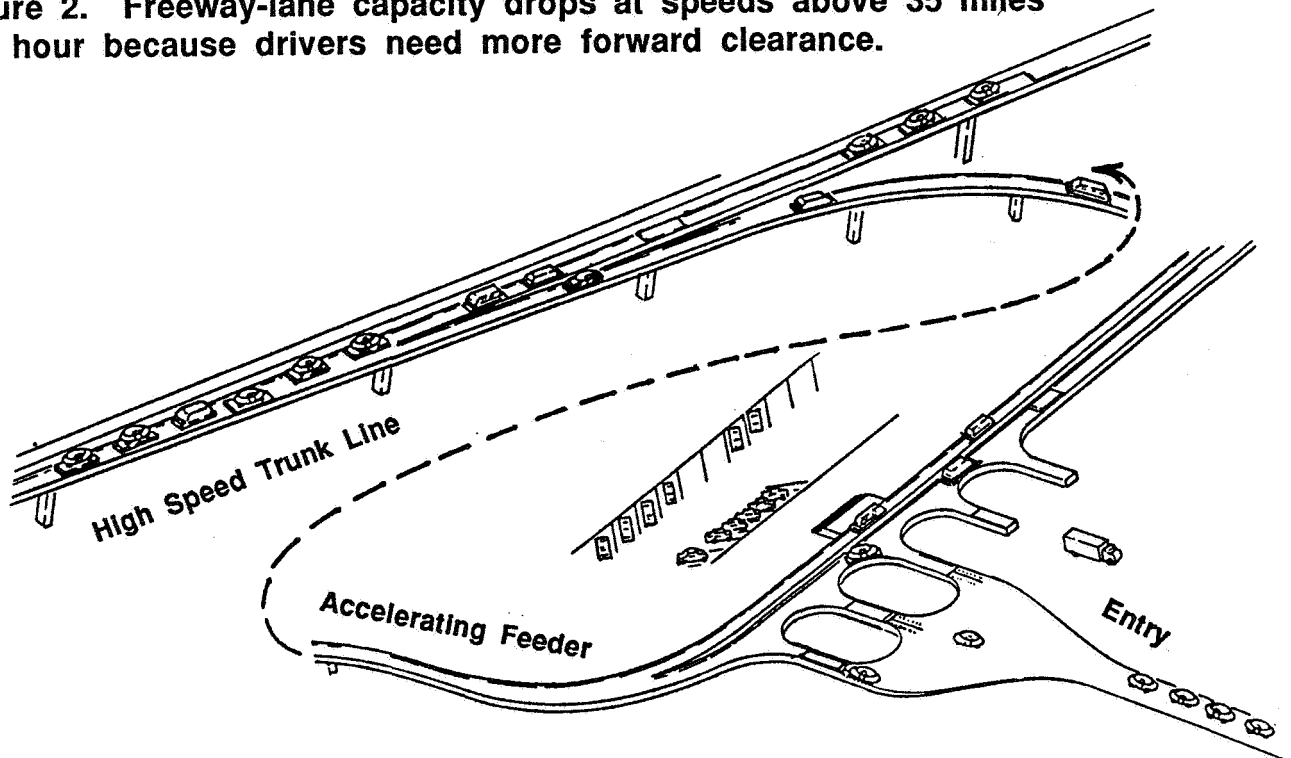
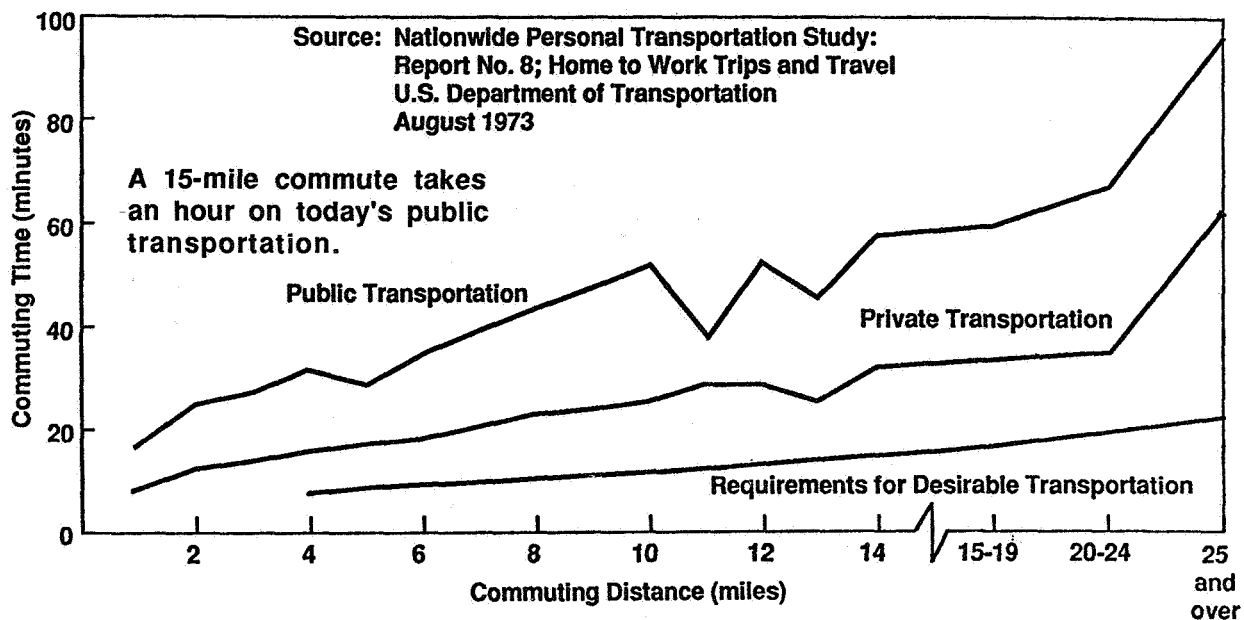


Figure 3. A commuter drives his battery-powered car onto a carrier at the entry. His car is accelerated to trunkline speed on the feeder line.



Commuting Elements	Time (minutes)			Distance (miles)			Average Speed Allocation		
	7 mi trip	15 mi trip	25 mi trip	7 mi trip	15 mi trip	25 mi trip	7 mi trip	15 mi trip	25 mi trip
Board Electric Car	0.5	0.5	0.5	0	0	0	0	0	0
Drive to system on-ramp	1.5	2.0	2.0	0.5	1.0	1.0	20	30	30
Board Mag-lev Carrier	0.5	0.5	0.5	0	0	0	0	0	0
Lower Speed Feeder Line	0.5	1.0	2.0	0.5	1.0	2.0	60	60	60
High Speed Trunk Line	3.0	7.2	12.6	5.0	12.0	21.0	100	100	100
Lower Speed Feeder Line	0.5	0.5	0.5	0.5	0.5	0.5	60	60	60
Deboard Mag-lev Carrier	0.5	0.5	0.5	0	0	0	0	0	0
Drive to Parking Lot	1.0	1.0	1.0	0.5	0.5	0.5	30	30	30
Deboard Electric Car	0.5	0.5	0.5	0	0	0	0	0	0
Total Time & Distance and Average Trip Speed	8.5	13.7	20.1	7	15	25	49	65	75

Figure 4. A 25-mile commute takes only 20.1 minutes with optimized transportation if there are no choke points.

Assumptions: Guideway is installed on existing freeways, with no real-estate purchase.
 Vehicles occupy 15-foot slots and travel 100 miles per hour on trunk lines.
 Armature power consumed by each vehicle is 50 kW.
 Commuting network has 400 miles of guideways.
 Each day guideway is loaded to 50% capacity 4 hours, 20% capacity 12 hours, and is empty 8 hours.

Capital Cost:	Guideways: 400 miles X \$ 2.0 million/mile	\$ 800 M
	Armature windings: 400 miles X \$0.5 million/mile	200 M
	On-off ramps, carriages	350 M
	Communications, computers, and programming	100 M
	TOTAL	\$ 1450 M
Annual cost at 15% capitalization		\$ 217 M
Hourly ownership cost, 0.67 X 8760 hours/ year		\$37,000
Hourly ownership cost, per mile		\$ 100
Cost per Mile per Vehicle:	Vehicle miles/hour generated on one mile of trunk	17,600
	Ownership cost per hour per mile per vehicle	\$ 0.016
	Power cost per vehicle per mile, 50 kW , \$0.07/kW	0.035
	Personnel cost, 1000 employees, \$30/hour 8 hours/day	0.006
	TOTAL COST, PER MILE PER VEHICLE	\$ 0.057

Figure 5. To the user the per-mile cost of propulsion power is twice the cost of using the high-productivity guideway.

triple redundancy even if one computer fails while passengers are being loaded. Other developed components include:

- o Magnetic-levitation and propulsion. The Japanese are building a \$2.5 billion 40-km track, 70 percent underground, for testing 500-km-per-hour magnetically levitated trains. The track will ultimately be part of a line connecting Tokyo with Osaka.
- o Small compact one-tesla helium-cooled superconducting magnets are being mass-produced for magnetic-resonance-imaging machines.
- o A variety of battery-powered electric cars with ranges up to 100 miles are being built in the United States and Japan.
- o Solid-state control is used to regulate the speed of ship-propulsion synchronous motors and large rolling-mill motors in steel-making plants.

Problems requiring further analysis are these:

- o Response to power failure. All vehicles must decelerate smoothly and come to a safe emergency-stop, followed by an orderly start-up.
- o Fail-safe design. Any accident or sabotage event must result in an orderly shutdown, followed by speedy rescue and restoration of service.
- o Carrier-to-guideway interface. The reaction of the levitation forces with the propulsion force is not inherently stable. Dynamic control will probably be required.
- o Carrier power. The carrier requires power for control and refrigeration of its superconducting magnets. Collecting electric power from a trolley would complicate guideway design.

CONCLUSION

Our present population, not having experienced the old interurban trains, enthusiastically supports light-rail as the solution to freeway congestion. Each commuter expects the light-rail trains to attract the other commuters so that he can drive quickly to and from work in his car.

The problem with personalized magnetically levitated commuting is that capital cost for a metropolitan area the size of Seattle could be 1.5 billion dollars. We are unlikely to see this much capital raised for a 10-years-ahead solution to problems. We are more likely to see more park-and-ride lots served by express buses, widening of freeways, and stop-and-go light-rail installations. Such band-aid facilities do not address the need for passenger-convenience.

On the other hand, the cost of real estate is rising, and in metropolitan areas more people commute to work each year. The freeway network will need more lanes, hence more of the expensive real estate. Neither freeway lanes nor light rail offer significantly improved productivity that reduces real-state requirements. The key to productivity is high speed, combined with uninterrupted decentralized routing. For example, in the early 1900's the New York Central railroad built four parallel tracks to carry the passenger traffic between Chicago and New York on its 20th Century Limited and other name trains. The Limited sometimes ran as four sections. That same passenger traffic between these cities could be carried today by one highly-productive 747 airplane, diverted from other routes for part of each day!

REFERENCES

1. Dietrich E. Koelle, "On the Optimum Cruise Speed of a Hypersonic Aircraft," Proceedings of the First International Conference on Hypersonic Flight in the 21st Century, University of North Dakota, Grand Forks, N.D., September, 1988.
2. G. Scott Rutherford, "Light Rail, Heavy Politics," Pacific Northwest Executive, October, 1989, pp 18-22.

N92-27812

KNOLLE MAGNETRANS,
A MAGNETICALLY LEVITATED
TRAIN SYSTEM

Ernst G. Knolle, Maglev Scientist
2691 Sean Court
South San Francisco, CA 94080

Certain statements in this document reflect the opinions of the author and are not official endorsements, either expressed or implied, by the National Aeronautics and Space Administration or the U.S. government.

1. INTRODUCTION

The Knolle Magnetrans (K-Mag) is a continuous transportation system featuring small cars in rapid succession, levitated by permanent magnets in repulsion and propelled by stationary linear induction motors (Figure 1). The vehicles' headway, speed, acceleration and deceleration are designed into the system and mechanically enforced. Passengers board dynamically and controls consist of a simple on-off relay. This paper summarizes the system design goals, describes the system components and discusses related environmental issues.

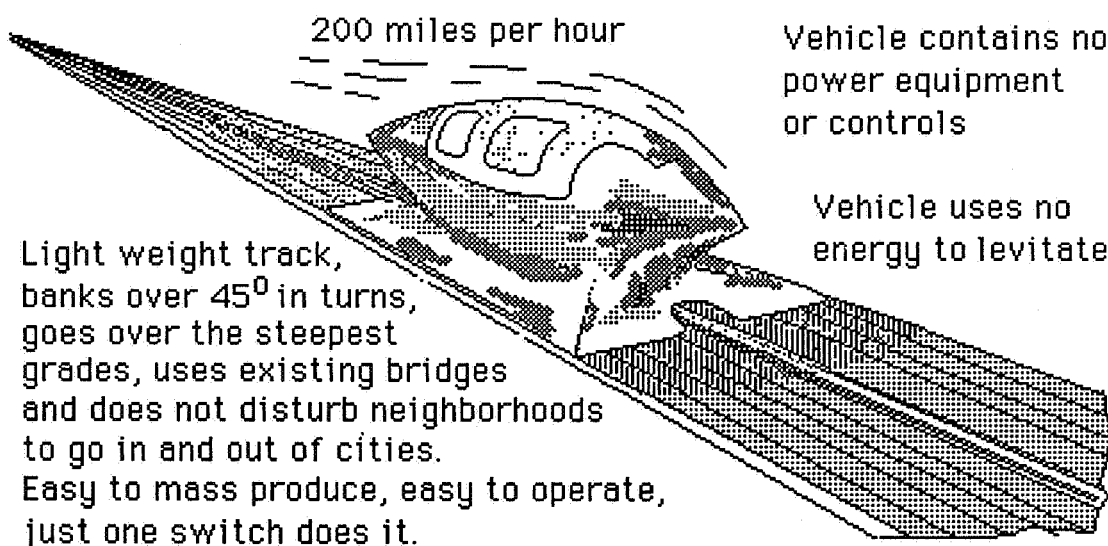


Figure 1: Knolle Magnetrans Perspective View

2. K-MAG DESIGN GOALS

As traffic congestion and urbanization increase, it becomes more and more difficult to find conventional solutions. Great progress is occurring in other fields, and it must be assumed that we can also advance in the field of transportation. Maglev technology can be the next evolutionary step.

An ideal new ground transportation system should be pleasant, convenient, and passengers should have seats, comfort, privacy, and no long waits. Passengers should be moved between points of travel (door-to-door) at least as fast as automobiles for short distances, and, ideally, as fast as aircraft for long distances. In addition, a new ground transportation system should be profitable enough to attract private enterprise. The developer of the K-Mag has set himself the following goals:

- | | | |
|-----------------------|---------------------|------------------|
| a.Safety. | e.No waiting. | i.Quiet. |
| b.Business success. | f.Direct routing. | j.Non-polluting. |
| c.Rider satisfaction. | g.Minimize walking. | k.Flexible. |
| d.High speed. | h.Energy efficient. | l.Expandable. |

3. PERMANENT MAGNETS IN REPULSION

Over 100 years ago, a maglev scientist by the name of Earnshaw experimented with permanent magnets in repulsion to suspend a vehicle over a track. The concept seemed feasible until all the iron horseshoe magnets died. Earnshaw's ideas came just a few decades too early; during his lifetime magnetic materials were not advanced enough to realize his invention. Today we have magnets that not only retain their full power indefinitely when repelled, but these new materials are 20 to 30 times more powerful than those Earnshaw used. As Table 1 shows, enormous progress was made in recent years in the discoveries of more powerful magnetic materials. Today, eleven times more powerful magnetic materials are available than just ten years ago. We successfully experimented with these new magnets by building a full-size prototype K-Mag; there is virtually no degradation in the magnets' strength after levitating a vehicle for over seven years to date.

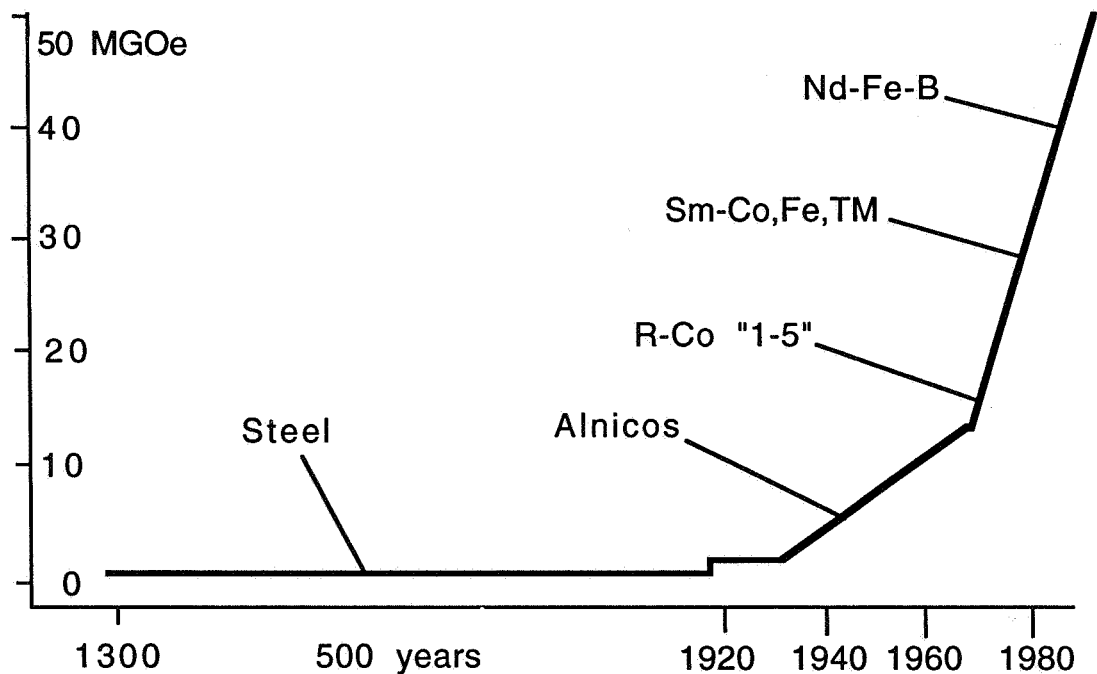


Table 1: History of Magnet Energy (BH)max

Figure 2 shows the basic components incorporated in the existing full size prototype. The rows of magnets cover the full length of the track and the full length of the car. Pairs of vertical dampers are located at the front and in the back. They are designed to minimize vertical oscillations due to track unevenness, wind and passenger movements. The lateral guides are located about one quarter of the distance from each end of the car. Their purpose is to hold the car magnets vertically above the track magnets or, when this is not possible as in curves, minimize lateral thrusts. The cars receive their propulsion and forward control from the chain by means of the car to chain attaching claw. The tubular chain in turn is driven by stationary constant speed linear motors, which may be as much as ten miles apart depending on terrain.

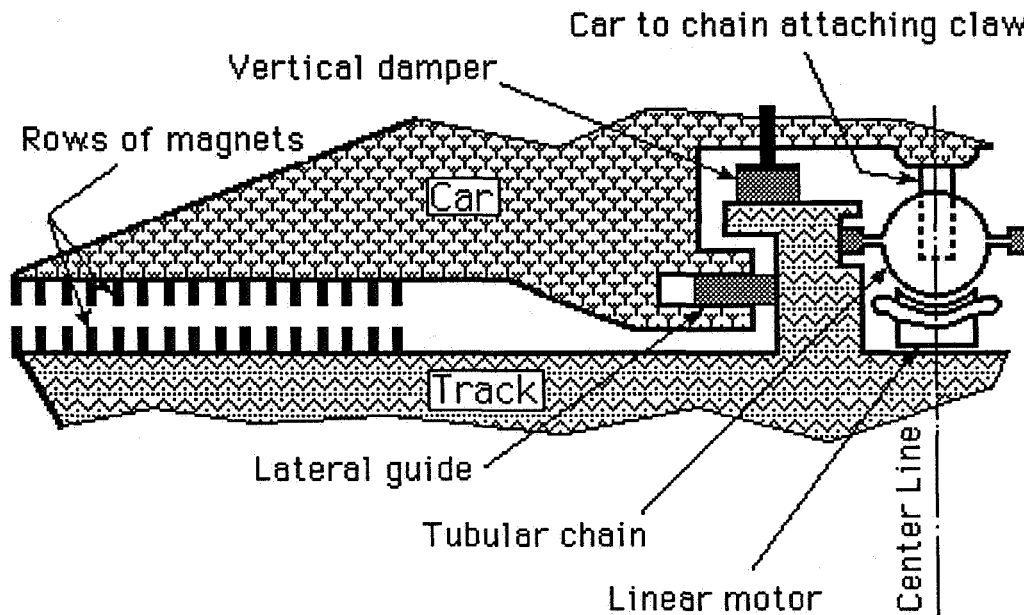


Figure 2: Car and Track Cross Section

The advantages of using permanent magnets in repulsion to levitate maglev vehicles are

- No energy is required to achieve the lift forces,
- The magnets are abundantly available at low cost,
- The magnets are easily installed,
- The magnets hold their lifting power virtually forever,
- Virtually no maintenance is required,
- The magnets are safe to operate, and
- Because the magnets are made of insulating material, there are no drag forces resulting from eddy currents.

4. LINEAR INDUCTION MOTOR (LIM) PROPULSION

The LIM idea dates back even further than the permanent magnet levitation concept, but hasn't made much progress in 150 years. A LIM is similar to a rotary electric motor but it is laid out flat. While a rotary motor has limits as to how many poles can fit into a circle, a LIM has no limit to length. However, it has the same major rotary motor shortcoming, and that is a lack of propulsion or thrust at partial or reduced speed. In rotary drives this problem is generally solved with reduction gears, but how do you attach a gear box to a LIM?

Figure 3 depicts how an adequate flux at full speed (thin line) changes its shape in the air gap to the dogleg line to generate a smaller thrust at reduced speed, just when the opposite is needed. The purpose of this drawing is to give the reader a basic simplistic understanding of the all-important electromagnetic flux flow in the air gap between stator and rotor. (Flux within the body of the stator or rotor has no effect on propulsion. Only the flux in the air gap does it.) The lack-of-thrust problem is actually much more complex. However, the K-Mag has solved this problem by mechanically assisting acceleration and hill climbing and by mechanically reusing kinetic and potential energy. The LIMs in the K-Mag run only at constant full speed and carry only a steady load.

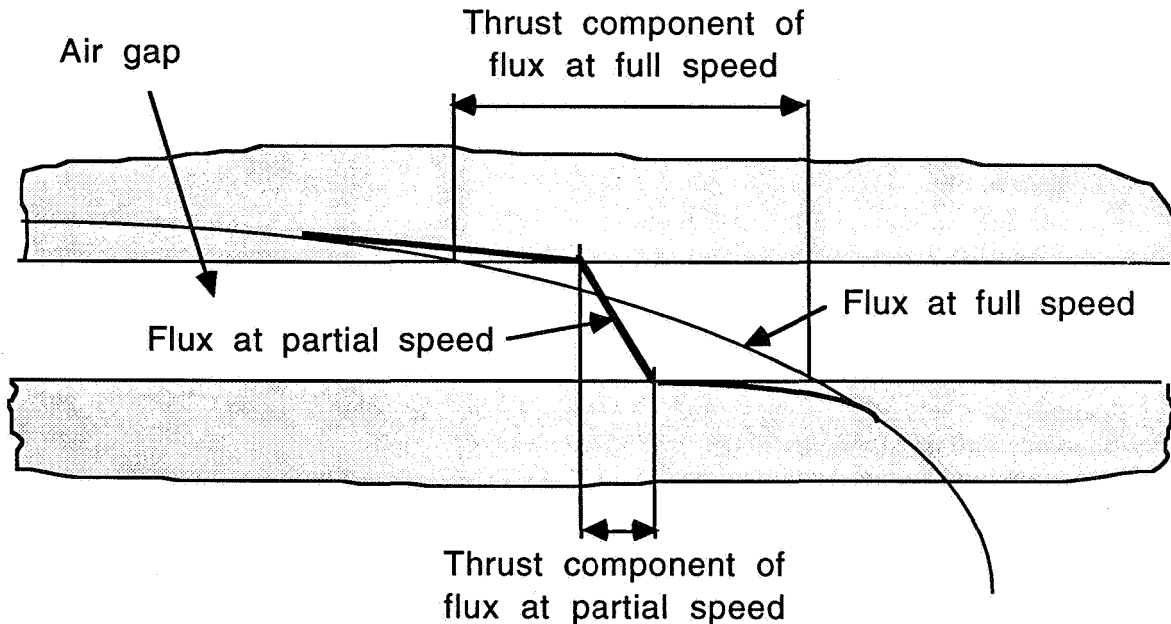
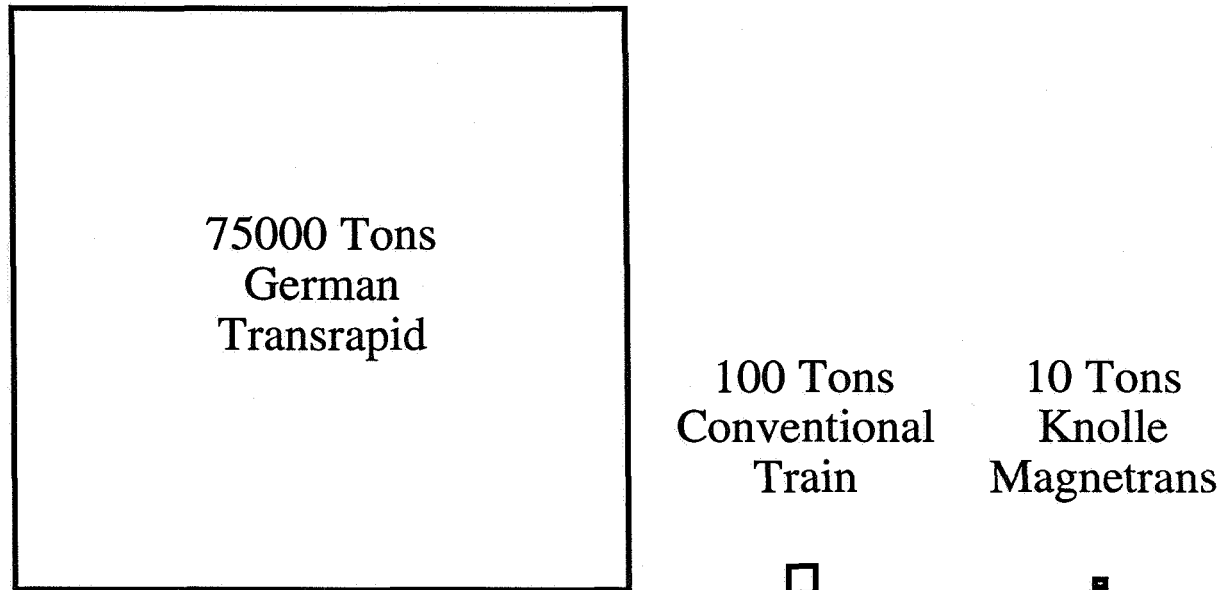


Figure 3: LIM's Loss of Thrust at Partial Speed

Other maglev developers, in Germany and Japan, build their LIMs enormously large to compensate for the lack of propulsion when accelerating and going uphill. The whole undersides and sides for the full length of their vehicles are covered with (LIM) motor windings and the tracks for their full length are also covered with (LIM) motor windings. The weight of the LIM hardware (wound primary and secondary) used on these systems is simply staggering. Figure 4 shows a chart which compares the weight of wound motor components of the German 'Transrapid' maglev with that of a conventional high speed train. It is based on a three million passengers per year

proposal to link Las Vegas with Los Angeles. Also shown is how small the wound motor weight of the K-Mag would be for the same route.^{1, 2}



**Figure 4: Motor Weight Comparison, Las Vegas to Los Angeles
Proposed 230 Mile Route**

The size of motor weight will naturally affect construction, operation and maintenance costs. The comparison also shows that maglev technology in the form of the K-Mag can also be a substantial improvement over conventional rail technology. Also interesting is that the Transrapid proposal calls for trains to follow each other at one hour intervals in each direction. Thus, their single track would be used less than one percent of the time. In contrast, the K-Mag track would be used every four seconds.

5. K-MAG - A CONTINUOUS TRANSPORTATION SYSTEM

Continuous transportation systems generally use evenly spaced cars physically connected to form closed loops driven by stationary motors at constant speed. This technology is not new. In 1908, I. Kiralfy obtained a U.S. Patent for a continuous system where passengers would step onto a moving belt and then transfer into small cars which were propelled in a continuous loop. Escalators, moving walkways, ski lifts, the Soulé system and the Disneyland people mover are all examples of successful continuous transportation systems. If a continuous system is moving at a high speed unsafe for passengers to board or exit, then a form of mechanical speed changer is used to assist at stations.

¹ "Propulsion and Power Supply System of the Transrapid 06 Vehicle, Design and Test Results, Part I: Propulsion", International Conference on Maglev Transport '85, pages 75 - 82 (R. Friedrich, et al).

² Executive Summary, Las Vegas to Los Angeles High Speed/Super Speed Ground Transportation System Feasibility Study, January 27, 1983, The Budd Company, Technical Center.

The major advantages of most existing continuous systems are automation, simplicity, steep climbing ability and high capacity; for example, in escalators and ski lifts. The major disadvantages are the inability to vary capacity or to do switching, except that capacity could be reduced by turning the system off intermittently or by reducing speed during low use periods, as in the early morning hours, for instance.

The K-MAG is a continuous transportation system which uses permanent magnets in repulsion for suspension and constant speed stationary LIMs for propulsion. Figure 5 shows small cars that are permanently attached to a continuously moving endless long-linked chain. Chain guide rails along the track are used to guide the chain stretched out between stations, but force it to fold up in stations. This folding causes the chain and cars to slow down and come together in stations. Passengers board from moving platforms which run beside the cars. The chain is driven by stationary LIMs located at intervals along the way. The cars have flat bottoms covered with longitudinal rows of permanent magnets that repel themselves above identical magnets on the track. The speed differential between line speed and station speed is determined by the length of the chain links. If the links are 18 feet long, the system could run at 200 mph between stations and at escalator speed in stations.

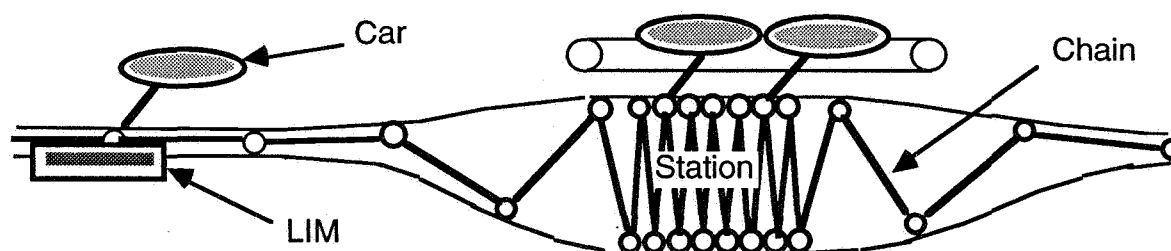


Figure 5: Chain Folding at Stations

6. ENERGY USE

	Average mph	Average pmpg
Japanese super-conducting maglev MLU-001.....	120 ³	2
German maglev Transrapid 006.....	120 ⁴	17
1960 Cadillac with 4 occupants	60	50
Boeing 737 200/300 coast-to-coast	600	100
Economy car with 4 occupants	60	120
Knolle Magnettrans at 25% occupancy.....	190	200

Table 2: Energy Use Comparison

Table 2 shows a comparison of energy use, expressed in passenger miles per gallon (pmpg), of several modes of transportation. Conversion calculations of electrical energy into gallons of fuel reflects power generation, distribution and converter efficiency. Even with assumed

³ Same as Footnote 6.

⁴ Pennsylvania High Speed Rail Feasibility Study, Executive Summary, Parsons Brinckerhoff/Gannett Fleming, February 1985, page 10, "Typical Trip Times".

occupancy of only 25% (75% empty seats), K-Mag greatly exceeds German and Japanese maglevs, both in energy efficiency and average speed. The latter is mainly due to K-Mag's ability to produce very high traction for acceleration and hill climbing as shown in Chart 1.^{5, 6}

7. TRACTION

Traction is an important component of vehicle performance. It shows ability to accelerate and climb grades. It should be viewed together with the energy use shown in Table 2. A high energy use might be excused if it is accompanied by high performance. However, the reverse is the case with the German and Japanese maglevs. Not only do they use excessive amounts of energy, their traction is also the lowest. The mechanically enforced K-Mag, on the other hand, can accelerate at several Gs and climb very steep grades without reduction in speed. Chart 1 shows a traction comparison of several modes of transportation.

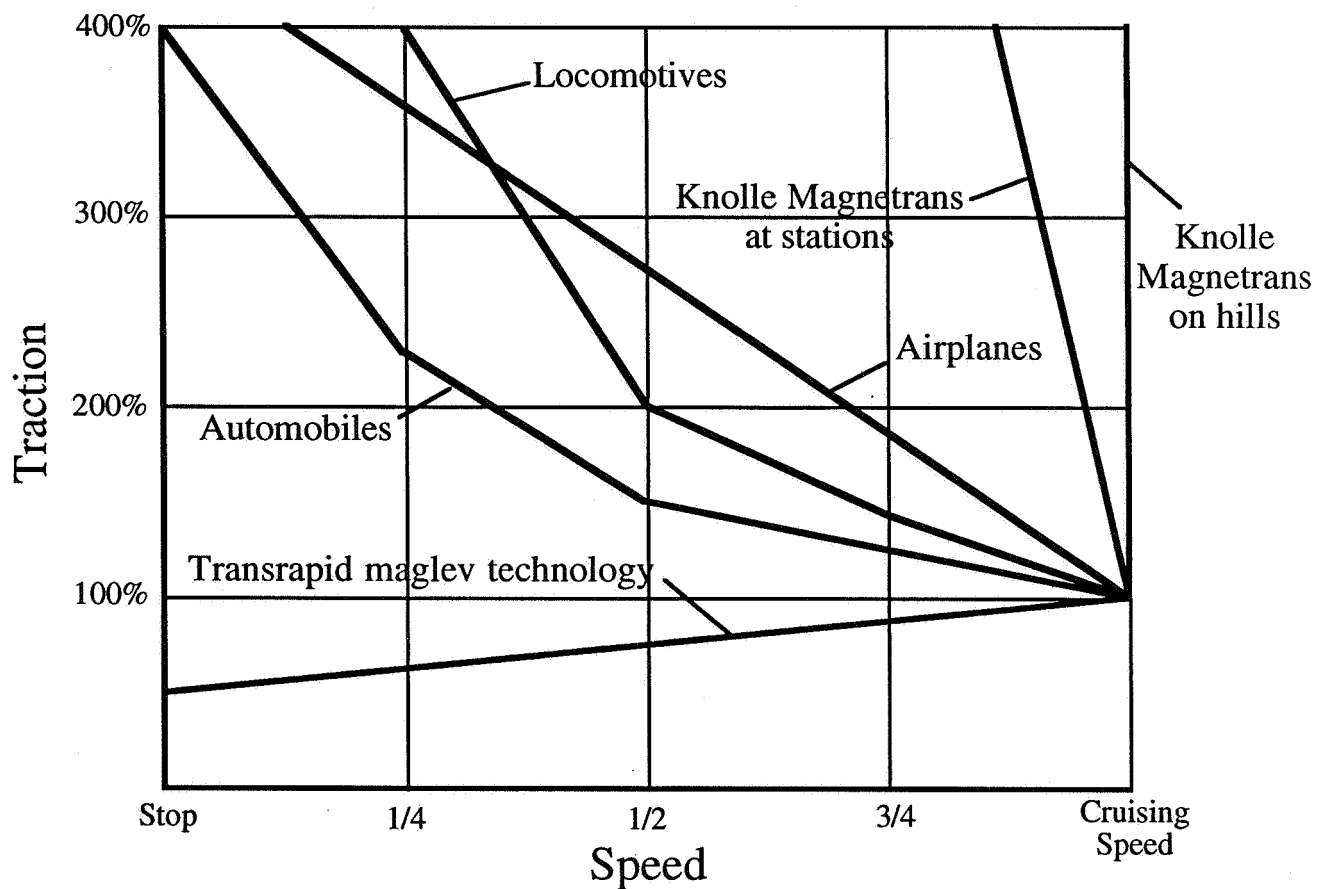


Chart 1: Comparison of Traction

⁵ "The Vehicle Transrapid 06, Specification and Experience under Practical Conditions", International Conference on Maglev Transport '85, pages 115 -121 (J. Gaede).

⁶ "LSM Propulsion System of the Miyazaki Maglev Test Track", International Conference on Maglev Transport '85, pages 91 -98 (K. Nakamura, et al).

The traction of each mode was arbitrarily taken as 100% at cruising speed, and the additional capabilities calculated from recorded history. As an example, (based on general assumptions) the traction generated by an automobile at cruising speed of 60 mph could be increased by 50% at 30 mph and by over 100% at 15 mph through changing to lower gears.

8. ELECTROMAGNETIC RADIATION

Electromagnetic radiation is an unavoidable byproduct of maglev technology. However, the K-Mag has a safe level of electromagnetic radiation. Figure 6 shows a drawing of the measured (permanent magnet) radiation in the K-Mag, and Figure 7 is a drawing of the measured (dangerous low frequency) radiation around Japan's superconducting maglev MLU-001. (Low frequency radiation is about ten times as dangerous as permanent magnet generated radiation). The MLU-001 radiates over one hundred times the level which is presently considered safe by the Environmental Protection Agency.^{7, 8}

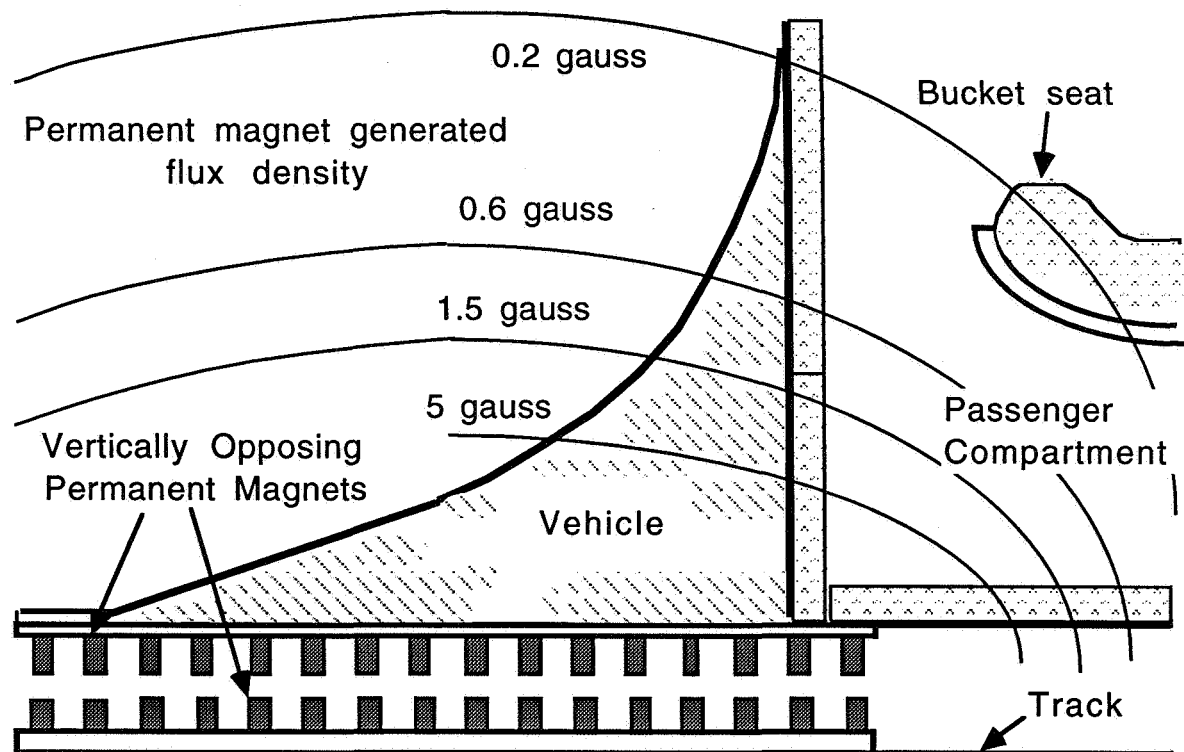


Figure 6: K-Mag's Safe Level of Electromagnetic Radiation

⁷ "Magnetic Field Shielding for Electromagnetic Maglev Vehicles", International Conference on Maglev and Linear Drives, 1987, pages 53 - 66 (W. F. Hayes).

⁸ Competitive Request for Proposal Number, DTFR53-91-R-00021, "Maglev System Concept Definition", U. S. Department of Transportation, Federal Railroad Administration, February 22, 1991, page 13.

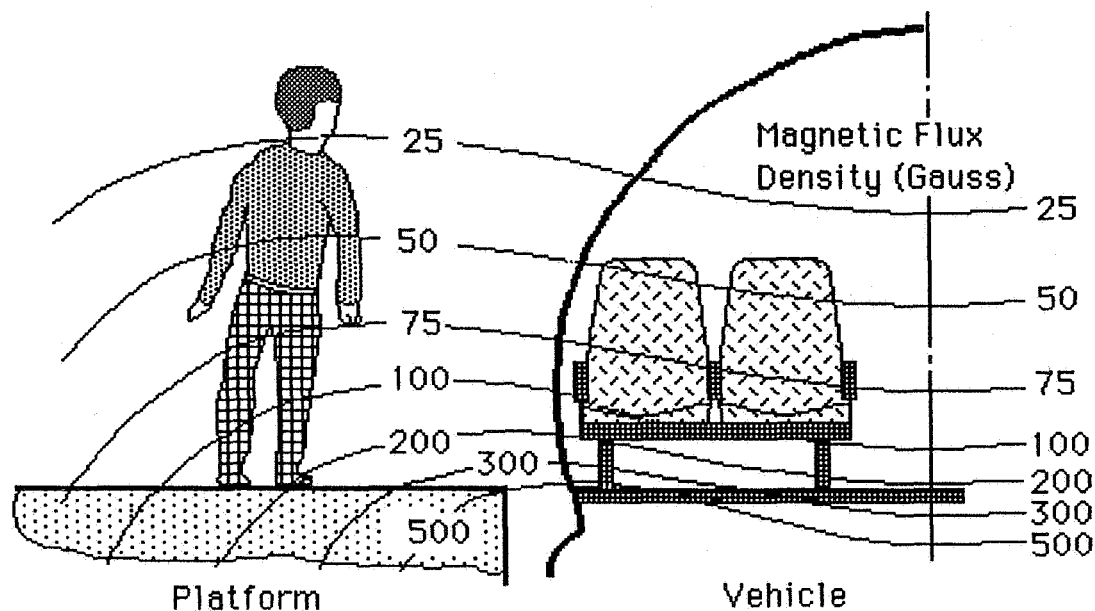


Figure 7: Dangerous Magnetic Radiation at Japan's MLU-001

9. OTHER INFORMATION AND EXHIBITS

A copyrighted technical description of the K-Mag is contained in the ASCE publication "Automated People Movers II" (References 1). Further information is also contained in "White Paper on High Performance High Efficiency Maglev, E. G. Knolle" submitted to the U.S. Department of Energy, 15 June 1990 (Reference 2). Available from the author are several short articles on specific aspects of maglev technology. Presently before the Federal Railroad Administration is a proposed study contract "Knolle Magnettrans, Maglev System Concept Definition Technical Proposal" dated April 22, 1991 (Footnote 8). Additionally, a full size K-Mag prototype vehicle on a short section of track is available for inspection in California, as well as full size test components. The concept of the chain folding mechanism is patented (Footnote 3).

10. CONCLUSION

The K-Mag concept shows that magnetic levitation can be accomplished at low cost without use of energy with permanent magnets in repulsion. The absence of on board energy requirement also means absence of heavy on board electrical equipment, which makes vehicles very light. The lack of traction by standard LIMs during acceleration and hill climbing is solved by the K-Mag with mechanical headway controls. The LIMs in the K-Mag are used efficiently at constant speed under constant load. Kinetic and potential energy is mechanically recovered. The result is extremely high energy efficiency while providing superior and safe service (low electromagnetic radiation).

Suitable for both short and long distances, the K-Mag technology is now ready for full size testing. Plans, cost estimates and a feasibility study have been made for a five mile long high

speed oval test track. Government assistance would be appreciated. However, new venture risks might be better assumed by private enterprise.

10. REFERENCES

1. 1989 Ernst G. Knolle, "Knolle Magnettrans High Speed Maglev People Mover", *Automated People Movers II*, Library of Congress Catalog Card No: 89-17833, ISBN 0-87262-73.1-4, pp 871-880.
2. 1990 Ernst G. Knolle, "White Paper on High Performance High Efficiency Maglev", submitted to U.S. Department of Energy, 15 June 1990.
3. 1969 U.S. Patent No.3,320,903, Re. 26673, 1969, Articulated Train System, Ernst G. Knolle, inventor.

COMPUTATION OF MAGNETIC SUSPENSION OF MAGLEV
SYSTEMS USING DYNAMIC CIRCUIT THEORY

J. L. He, D. M. Rote and H. T. Coffey

Center for Transportation Research, Energy Systems Division
Argonne National Laboratory, Argonne, IL 60439, USA

ABSTRACT

Dynamic circuit theory is applied to several magnetic suspensions associated with maglev systems. These suspension systems are the loop-shaped coil guideway, the figure-eight-shaped null-flux coil guideway, and the continuous sheet guideway. Mathematical models, which can be used for the development of computer codes, are provided for each of these suspension systems. The differences and similarities of the models in using dynamic circuit theory are discussed in the paper. The paper emphasizes the transient and dynamic analysis and computer simulation of maglev systems. In general, the method discussed here can be applied to many electrodynamic suspension system design concepts. It is also suited for the computation of the performance of maglev propulsion systems. Numerical examples are presented in the paper.

INTRODUCTION

A maglev system uses three electromagnetic forces: the levitation, propulsion, and guidance forces. These forces determine the dynamic performance of the maglev vehicle. The computations of these magnetic forces may differ slightly from those in conventional electrical machines for the following reasons. First, knowledge of three-dimensional time- and space-dependent magnetic forces are required in a maglev system because the six directions of motion of a maglev vehicle are determined by these magnetic forces. Second, space harmonics, which result from the end-effect and the discontinuous distribution of the magnets aboard the vehicle, play much more important roles in the performance of a maglev vehicle. Thus, the performance analysis based on a fundamental traveling wave used in most conventional machines is inadequate. Third, transient and dynamic performance associated with vehicle motions, not steady-state performance, is emphasized in the maglev system.

Several approaches are widely used for the computation of magnetic forces in maglev systems. The finite-element method is one of the more powerful numerical techniques for solving Maxwell's field equations. For given boundary conditions and specified system geometry, one is able to obtain sufficient information for a system by using two- and three-dimensional finite-element computer codes. However, when a system involves relative motions with space and time dependences, the finite-element method becomes difficult because a great amount of computing time is required to obtain the force-speed or force-time characteristics. In addition, most commercial finite-element computer codes that are available do not include the problems associated with moving conductors. Fourier transformation and harmonics analysis, in combination with numerical techniques, is another powerful method in maglev analysis that can be

*Work supported by the Federal Railroad Administration through interagency agreement DTFR53-91-X-00018 with the U.S. Dept. of Energy, Illinois State Challenge Grant No. 90-82122 from the Illinois Department of Commerce and Community Affairs, Office of Technology Advancement and Development, and by the U.S. Dept. of Energy, Office of Conservation and Renewable Energy.

used to determine the lift and drag forces in a continuous sheet guideway. The method, however, is usually limited to a two-dimensional steady-state analysis with an assumption of infinite guideway width.

The dynamic circuit theory, also called general machinery theory or mesh-matrix method, is a suitable approach for maglev applications. It can overcome some of the limitations mentioned above and can be used to perform three-dimensional electrodynamic analysis of maglev systems. The dynamic circuit theory treats an electrodynamic system in terms of space- and time-dependent circuit parameters governed by a set of differential equations in matrix form. When plate or sheet conductors are considered, the method divides the conductors into many zones, each of which carries a different current. The lumped-circuit parameters for every conducting zone are then determined, and a system of equations are formed. Once the system of equations is solved for the current distribution, the forces acting between the electrodynamic system components can be readily calculated in a straight forward manner. Therefore, the performance of the system can be investigated. Since the equations are usually solved for the currents in the time domain, the method is well suited for transient and dynamic analysis and for the computer simulation of electrodynamic systems, such as maglev trains, electromagnetic launchers, and other electrical machines. In particular, the method is currently being used at Argonne for the computer simulation of laboratory experiments, the design and analysis of maglev test facilities, and studies of conceptual maglev system designs.

Analyses of rotating electrical machines based on the general theory of electrical machines are discussed by Morgan (ref. 1). Analyses of linear machines using the mesh-matrix method have been reported (refs. 2 and 3). The dynamic circuit theory used for electromagnetic launcher analysis and simulation was discussed in several publications (refs. 4,5 and 6). As in the maglev system, the transient and dynamic performance is emphasized in electromagnetic launcher analyses. In the launcher analyses, however, a relatively short time period --a fraction of a second-- is considered because of the hypervelocity of the projectile. In addition, capacitor banks or a pulsed generator is used as the power source for electromagnetic launchers. The dynamic circuit theory used for the computation of a continuous sheet suspension was discussed by a Canadian maglev group (refs. 7 and 8). In this group's model, the dynamic circuit theory was combined with a harmonic analysis. The superconducting magnets aboard the vehicle were replaced by a current sheet that was expressed in terms of a Fourier Series. A d-q transformation, which is usually used to transform a rotating machine into a stationary primitive machine, was applied to the direction of motion for all harmonics. The performance of the continuous sheet guideway was determined on the basis of the circuit solutions in combination with the superposition theorem.

Although the dynamic circuit theory was discussed with respect to other applications in several papers, the applications of the theory to various maglev suspension and propulsion systems have not been discussed. In particular, using dynamic circuit theory to simulate the performance of a complete maglev system has not been discussed in previous papers. In this paper, we apply the dynamic circuit theory to several electrodynamic suspension systems, including a loop-shaped coil suspension, a figure-eight-shaped null-flux suspension, and a continuous sheet suspension. We also emphasize a direct computation of magnetic forces without using Fourier and d-q transformations or past computation processing. The paper provides mathematical models for various suspension systems and discusses their similarities and differences in using dynamic circuit theory. These models can be used for the development of computer codes that are necessary for the design, analysis, and

simulation of large-scale maglev systems. Indeed, work on the development of computer simulation codes that account for both the electrodynamics and mechanical dynamics of maglev vehicles interacting with guideways is currently in progress at Argonne.

The paper consists of seven parts. The second part introduces the dynamic circuit theory. The third part discusses the computation of magnetic forces for loop-shaped coil suspensions. The fourth part deals with the computation of figure-eight-shaped null-flux coil suspension systems. The magnetic forces in the continuous sheet-type suspension system are considered in the fifth part. Numerical examples are given in the sixth section, and conclusions are presented at the end of the paper.

GENERAL MODEL

Power Conservation and Forces in a Maglev System

A maglev system can be represented by the dynamic circuit model in which the system energy, power, and forces, as well as other quantities, are expressed in terms of their circuit parameters. Those circuit parameters, in general, are functions of time and space. Thus, the dynamic and transient performance of a maglev system can be determined on the basis of the solution of the dynamic circuit model.

In general, we may consider a maglev system in which m vehicle coils or conductors interact with n guideway coils or conductors to produce either levitation and guidance forces, or propulsion forces. All of these coils are assumed to be connected to individual power sources. Thus, the superconducting coils aboard the vehicle can be represented by letting the terminal voltages and resistances of the vehicle coils vanish, the passive guideway conductors can be represented by letting their terminal voltage vanish, and the propulsion system can be represented by connecting a polyphase power source to the guideway stator coils. If we let $[i]$ and $[e]$ be column $(m+n)$ matrices made up of the individual currents and voltages associated with the vehicle and guideway coils or conductors, respectively, $[L]$ be a square $(m+n) \times (m+n)$ matrix, each element of which represents either the self-inductances of the vehicle and guideway coils (or mutual inductance between the vehicle coils and guideway coils) and $[R]$ be a diagonal $(m+n)$ elements) matrix composed of the individual vehicle coil and guideway coil resistances, then we can write the system voltage equations in matrix form, based on Kirchhoff's voltage law, as follows:

$$[e] = [R][i] + \frac{d}{dt}([L][i]) \quad (1)$$

We may assume that a maglev vehicle involves three-dimensional motions caused by the change of the mutual inductances between the vehicle and guideway coils in three dimensions. Letting v_x , v_y , and v_z be the velocities of the vehicle in the x , y , and z directions respectively, we can rewrite Eq. (1) in terms of a speed voltage, a voltage induced due to a relative motion, as

$$[e] = [R][i] + v_x[G_x][i] + v_y[G_y][i] + v_z[G_z][i] + [L]\frac{d}{dt}[i] \quad (2)$$

where $[G_x] = d[L]/dx$, $[G_y] = d[L]/dy$, and $[G_z] = d[L]/dz$. The total time-dependent power input to a maglev system is

$$P = [i]^T [e] = [i]^T [R] [i] + [i]^T [L] \frac{d[i]}{dt} + v_x [i]^T [G_x] [i] + v_y [i]^T [G_y] [i] + v_z [i]^T [G_z] [i] \quad (3)$$

where the superscript T stands for the matrix transpose. Since

$$\frac{1}{2} \frac{d}{dt} \{ [i]^T [L] [i] \} = \frac{1}{2} v_x [i]^T [G_x] [i] + \frac{1}{2} v_y [i]^T [G_y] [i] + \frac{1}{2} v_z [i]^T [G_z] [i] + [i]^T [L] \frac{d[i]}{dt} \quad (4)$$

Eq. (3) can be rewritten as follows

$$P = [i]^T [e] = [i]^T [R] [i] + \frac{d}{dt} \left\{ \frac{1}{2} [i]^T [L] [i] \right\} + \frac{1}{2} v_x [i]^T [G_x] [i] + \frac{1}{2} v_y [i]^T [G_y] [i] + \frac{1}{2} v_z [i]^T [G_z] [i] \quad (5)$$

Equation (5) shows the power conservation of a maglev system. We note in Eq. (5) that the term on the left represents the total electrical power input to the system, which may include the power from a stationary power system and the power from the batteries aboard the vehicle. The first term on the right-hand side represents the dissipated power of the system, which may include the power losses both in the guideway coils and in the vehicle coils if superconducting magnets are not used aboard the vehicle. The second term represents the time rate of change of the magnetic energy stored in the system, and the last three terms on the right-hand side represent the converted mechanical power which results in the three-dimensional motion of the vehicle. Finally, the three force components F_x , F_y , and F_z acting on the vehicle can be obtained from Eq. (5) by dividing the terms of the converted mechanical power by their corresponding velocity components v_x , v_y , and v_z , yielding the following:

$$F_x = \frac{1}{2} [i]^T [G_x] [i] \quad (6)$$

$$F_y = \frac{1}{2} [i]^T [G_y] [i] \quad (7)$$

$$F_z = \frac{1}{2} [i]^T [G_z] [i] \quad (8)$$

According to the conventional notation, we may refer to F_x as the force in the direction of motion, which could be a propulsion force or a magnetic drag force, depending on the applications of the model, F_y in the horizontal direction, which could be a guidance or a horizontal perturbation force, and F_z in the vertical direction, which represents a levitation or a vertical perturbation force.

When the model is used to determine the magnetic drag of an EDS maglev system, the input electrical power term in the right-hand side of Eq. (5) is zero. Assuming a vehicle moving in the x direction with a speed v_x and neglecting the

induced voltage due to the horizontal and vertical perturbation, we obtain a new power conservation equation from Eq. (5) as follows:

$$[i]^T[R][i] + \frac{d}{dt} \left\{ \frac{1}{2} [i]^T[L][i] \right\} + \frac{1}{2} v_x [i]^T[G_x][i] = 0 \quad (9)$$

In this case, the third term on the right-hand side represents the mechanical power required by the system to overcome the magnetic drag power of the system. Thus, the longitudinal component of the magnetic force of a maglev system can be obtained from Eq. (9) as follows:

$$F_x = \frac{1}{2} [i]^T[G_x][i] = -\frac{1}{v_x} [i]^T[R][i] - \frac{d}{dx} \left\{ \frac{1}{2} [i]^T[L][i] \right\} \quad (10)$$

Equation (10) shows that the longitudinal component of the magnetic force consists of two parts. The first part is a dissipative term that represents a drag due to the ohmic loss, and the second part is due to the change of the magnetic energy stored. The second part of the force is considered to be a nondissipative or conservative force that may be negative or positive, depending on the change of the magnetic energy stored in the system in the direction of motion.

Transformation for the Coil Connections

A maglev system usually involves many coils that may logically be connected in several different groups to perform different functions, such as levitation, guidance, and propulsion. For instance, the figure-eight-shaped null-flux coil guideway can be viewed as two loop-shaped coils connected in opposite direction, and the propulsion coils, in general, are connected into three groups to form three-phase armature windings. Other maglev systems are expected to have even more complicated coil connections in order to perform an integrated maglev function. The dynamic circuit model can be applied to many maglev systems, if the transformation of the coil connections are considered.

General transformations for solving electrical machine problems were discussed by Morgan (ref 1). The transformation for the coil connections is particularly useful for the maglev simulation and analysis on the basis of the dynamic circuit model. Since the vehicle and guideway coils are usually connected in different configurations that may need different transformations, it is necessary to partition all the matrices by rows or columns to form submatrices. Thus, the previously defined current and voltage matrices expressed in terms of submatrices are

$$[i] = \begin{bmatrix} I_v \\ I_g \end{bmatrix} \quad (11)$$

and

$$[e] = \begin{bmatrix} E_v \\ E_g \end{bmatrix} \quad (12)$$

where \mathbf{I}_v , \mathbf{I}_g and \mathbf{E}_v , \mathbf{E}_g , are the current and voltage submatrices of the vehicle coils and guideway coils, respectively. The subscripts v and g stand for the vehicle and guideway, respectively. The inductance matrix becomes

$$[\mathbf{L}] = \begin{bmatrix} \mathbf{L}_v & \mathbf{L}_{vg} \\ \mathbf{L}_{gv} & \mathbf{L}_g \end{bmatrix} \quad (13)$$

where the \mathbf{L}_v and \mathbf{L}_g are the inductance submatrices of the vehicle coils and guideway coils, respectively. $\mathbf{L}_{vg} = \mathbf{L}_{gv}$ are the submatrices that represent the coupling between the vehicle coils and guideway coils. They are the most important part of the system because all magnetic forces are generated from this coupling. Similarly, the resistance matrix in the system may be partitioned into submatrices \mathbf{R}_v and \mathbf{R}_g as follows:

$$[\mathbf{R}] = \begin{bmatrix} \mathbf{R}_v & 0 \\ 0 & \mathbf{R}_g \end{bmatrix} \quad (14)$$

The \mathbf{R}_v becomes a zero submatrix when superconducting coils are used aboard the vehicle. One can define a transformation matrix $[\mathbf{T}]$ as

$$[\mathbf{T}] = \begin{bmatrix} \mathbf{T}_v & 0 \\ 0 & \mathbf{T}_g \end{bmatrix} \quad (15)$$

where \mathbf{T}_v and \mathbf{T}_g are the transformation submatrices for the vehicle coils and the guideway coils, respectively, which depend on the connection of the coils. \mathbf{T}_v may be a unit submatrix if the transformation is only applied to the guideway coils. By introducing the prime quantities as a new system after transformation, one can obtain, on the basis of power invariance for the current

$$[\mathbf{I}] = [\mathbf{T}][\mathbf{I}]' \quad (16)$$

and for the voltage

$$[\mathbf{V}]' = [\mathbf{T}]^T [\mathbf{V}] \quad (17)$$

The inductance matrix and its derivative matrix of the new system are as follows:

$$[\mathbf{L}]' = [\mathbf{T}]^T [\mathbf{L}] [\mathbf{T}] \quad (18)$$

$$[\mathbf{G}]' = [\mathbf{T}]^T [\mathbf{G}] [\mathbf{T}] \quad (19)$$

$$[\mathbf{R}]' = [\mathbf{T}]^T [\mathbf{R}] [\mathbf{T}] \quad (20)$$

By substituting the prime quantities in Eqs. (16) to (20) into Eqs. (1) to (10), one can obtain the power conservation and force equations for the new system. Typical examples for the use of the transformation will be discussed in the following sections.

COMPUTATION OF THE LOOP-SHAPED COIL SUSPENSION

Considerable attention has been given to suspension schemes in which the superconducting coils are levitated above a loop-shaped coil guideway, as shown in Fig. 1. The coil guideway may be superior to the continuous sheet guideway because of the former's relatively low magnetic drag force (ref. 9). The loop-shaped coil guideway, however, produces force pulsations that do not arise in the continuous-sheet guideway. A steady-state analysis of the loop-shaped coil guideway was performed by Hoppe et al. (ref. 10) on the basis of the Fourier transform method in combination with steady-state circuit analysis. The dynamic circuit model is well suited for the determination of the dynamic performance of the loop-shaped coil guideway.

When the dynamic circuit theory is applied to the loop-shaped coil guideway, the model becomes relatively simple, because the currents in the superconducting coils aboard the vehicle are usually fixed; the voltages across the individual loop coils are zero, and a connection transformation for the guideway coils is not needed. Neglecting vertical and horizontal perturbations and assuming m superconducting coils moving above n loop-shaped guideway coils, we obtain a system of voltage equations for the loop-shaped coil guideway from Eq. (2) as

$$\begin{bmatrix} R_1 & & & \\ & R_2 & & \\ & & \dots & \\ & & & R_n \end{bmatrix} \begin{bmatrix} i_1 \\ i_2 \\ \dots \\ i_n \end{bmatrix} + \begin{bmatrix} L_{11} & L_{12} & \dots & L_{1n} \\ L_{21} & L_{22} & & L_{2n} \\ \dots & \dots & \dots & \dots \\ L_{n1} & \dots & \dots & L_{nn} \end{bmatrix} \frac{d}{dt} \begin{bmatrix} i_1 \\ i_2 \\ \dots \\ i_n \end{bmatrix} = -v_x \begin{bmatrix} G_{11} & G_{12} & \dots & G_{1m} \\ G_{21} & G_{22} & & G_{2m} \\ \dots & \dots & \dots & \dots \\ G_{n1} & \dots & \dots & G_{nm} \end{bmatrix} \begin{bmatrix} I_1 \\ I_2 \\ \dots \\ I_m \end{bmatrix} \quad (21)$$

where I_j ($j=1,m$) are the currents in superconducting coils aboard the vehicle, L_{ij} ($i=1,n$ and $j=1,n$) is the mutual inductance between the i^{th} and j^{th} loop coils on the guideway, and R_i ($i=1,n$) is the resistance of the i^{th} loop coil. Both L_{ij} and R_i are constant if the dimensions of the loop coil are selected. G_{ij} ($i=1,n$ and $j=1,m$) is the derivative with respect to x of the mutual inductance between the i^{th} loop coil on the guideway and the j^{th} superconducting coil aboard the vehicle and is a function of space and time. The unknowns in Eq. (21) are the currents of the loop coils in the guideway. The formulas used to evaluate self-inductances and the mutual inductances can be obtained (refs. 9 and 11) and the derivative of the mutual inductances can be determined numerically from the mutual inductances. Equation (21) cannot be solved directly because matrix $[G]$ in the right-hand side is a function of time and position. One simple numerical approach is to solve Eq. (21) at successive time steps with step size Δt . Thus, for given initial conditions and determined matrix $[G]$, one can solve Eq. (21) as a set of linear algebraic equations for the unknowns di_j/dt ($j=1,n$), rather than solving the linear differential equations for i_j . The currents at time t are found by adding $di_j/dt \Delta t$ to the previous currents, i.e.

$$\begin{bmatrix} i_1(t) \\ i_2(t) \\ \dots \\ i_n(t) \end{bmatrix} = \begin{bmatrix} i_1(t-\Delta t) \\ i_2(t-\Delta t) \\ \dots \\ i_n(t-\Delta t) \end{bmatrix} + \begin{bmatrix} di_1/dt \\ di_2/dt \\ \dots \\ di_n/dt \end{bmatrix} \Delta t \quad (22)$$

Iterations between Eq. (21) and (22) will determine the currents in all loop coils as a function of time. The currents as a function of position are also obtained from the above results because of the relation $\Delta x = v_x \Delta t$. After finding currents in the loop coils, we are able to determine the longitudinal, the lateral guidance, and the vertical suspension forces of the system as functions of time and displacement from Eq. (6) to (8):

$$F_x = \sum_i^n \sum_j^m i_i G_{x,ij} I_j \quad (23)$$

$$F_y = \sum_i^n \sum_j^m i_i G_{y,ij} I_j \quad (24)$$

$$F_z = \sum_i^n \sum_j^m i_i G_{z,ij} I_j \quad (25)$$

The three components of the magnetic force given by Eq. (23) to (25) include force pulsations, which depend on the geometry and the material characteristics of the loop coils. Time-average forces can be found from Eq. (23) to (25) by taking the time averages over any desired period. In practice, it is a reasonably good approximation to consider only the mutual inductances between the several coils on the left and right of a given coil. Thus, Eqs. (23) to (25), and all the mutual inductances and their derivative matrices discussed previously, are simplified. Finally, the total power dissipated in the loop coils as functions of time or position is

$$P = [i]^T [R] [i] = \sum_{i=1}^n R_i i_i^2 \quad (26)$$

Similarly, one can determine the time average power from Eq. (26) by taking its time average over any pulsation period.

COMPUTATION OF THE FIGURE-EIGHT-SHAPED NULL-FLUX COIL SUSPENSION

The figure-eight-shaped null-flux coil suspension and guidance system shown in Fig. 2 is a variation of the null-flux suspension concept invented by J. Powell and G. Danby in the late 1960s. It is currently being incorporated into the new Japanese maglev system¹² and has become a very important maglev concept. The major features are that it can provide both suspension and guidance forces with a relatively small magnetic

drag. In particular, it can provide zero magnetic drag at the null-flux equilibrium point and can be very helpful in starting a maglev vehicle. The Japanese have succeeded in designing and testing several versions of the electrical dynamic suspension (EDS) maglev system based on this null-flux suspension concept.

The computation of figure-eight-shaped null-flux suspensions discussed in the literatures (refs. 12 and 13) was based on field and harmonic analyses. In this section, we apply dynamic circuit theory to the figure-eight-shaped null-flux coil suspension system. As mentioned before, one of the advantages of the approach is that it can predict transient and dynamic performance based on a simple and direct solution. For general purposes, we assume that m superconducting coils interact with n figure-eight-shaped null-flux coils as shown in Fig. 3 and that the n null-flux coils comprise $2n$ loops. Assuming the currents in the superconducting coils are fixed and neglecting the speed voltage terms resulting from the motions in the y - z plane, we can write general voltage equations in matrix form for the $2n$ -loop system. Since the currents in the upper loops equal those in the lower loop but have the opposite spatial orientation, the system has only n -unknown currents, and we can apply a connection transformation to the system as discussed previously. Using Eq. (16) we can determine the transformation submatrix for the guideway coils T_g from the current relations, $i_j = -i_{n+j}$ ($j=1,n$) as follows:

$$T_g = \begin{bmatrix} 1 & & & -1 & & \\ & 1 & & & -1 & \\ & & \ddots & & & \ddots \\ & & & 1 & & -1 \end{bmatrix}^T \quad (27)$$

Since the transformation is only applied to the guideway null-flux coils, the transformation submatrix for the vehicle coils T_v is a unit matrix. Using Eqs. (2), (15) to (20), and Eq. (27), we obtain the voltage equations in matrix form for the null-flux coil system after transformation as

$$\begin{bmatrix} R'_1 & & & \\ & R'_2 & 0 & \\ & 0 & & R'_n \end{bmatrix} \begin{bmatrix} i_1 \\ i_2 \\ \vdots \\ i_n \end{bmatrix} + \begin{bmatrix} L'_{11} & L'_{12} & \dots & L'_{1n} \\ L'_{21} & L'_{22} & & L'_{2n} \\ \dots & \dots & \dots & \dots \\ L'_{n1} & \dots & \dots & L'_{nn} \end{bmatrix} \frac{d}{dt} \begin{bmatrix} i_1 \\ i_2 \\ \vdots \\ i_n \end{bmatrix} = -v_x \begin{bmatrix} G'_{11} & G'_{12} & \dots & G'_{1m} \\ G'_{21} & G'_{22} & & G'_{2m} \\ \dots & \dots & \dots & \dots \\ G'_{n1} & \dots & \dots & G'_{nm} \end{bmatrix} \begin{bmatrix} I_1 \\ I_2 \\ \vdots \\ I_m \end{bmatrix} \quad (28)$$

where i_j ($j=1,n$) is the current in the j^{th} null-flux coil and the prime is omitted because the currents in a $2n$ -loop system are equal to that in an n -null-flux-coil system. The I_j ($j=1,m$) are the currents in the superconducting coils. The individual elements in the coefficient matrices after transformation are given as follows:

$$R'_j = R_j + R_{n+j} \quad j = 1, n \quad (29)$$

$$L'_{ij} = (L_{ij} + L_{n+i, n+j}) - (L_{i, n+j} + L_{j, n+i}) \quad i = 1, n \text{ and } j = 1, n \quad (30)$$

$$G'_{ij} = G_{ij} - G_{n+i, j} \quad i = 1, n \text{ and } j = 1, m \quad (31)$$

where the prime quantities in the left-hand side represent the lumped-circuit parameters of the null-flux coil system. R'_j is the resistance of the j th null-flux coil, L'_{ij} is the mutual inductance between the i th and j th null-flux coils, and G'_{ij} is the derivative of the mutual inductance between the i th null-flux coil and the j th superconducting coil. The right-hand side represents the parameters before transformation. Thus, R_j and R_{n+j} are the resistances in the upper and lower loops of the j th null-flux coil respectively, L_{ij} ($i = 1, 2n$ and $j = 1, 2n$) is the self or mutual inductances between the individual loop coils, and G_{ij} and $G_{n+i, j}$ are the derivatives of the mutual inductances between the upper and the lower loop of the i th null-flux coil and the j th superconducting coil respectively. If we assume all loops of the null-flux coil to be identical, Eqs. (29) and (30) can be simplified as follows:

$$R'_j = 2R_j = 2R \quad (32)$$

$$L'_{ij} = 2(L_{ij} - L_{i, n+j}) \quad (33)$$

Using Eqs. (31) to (33), we can rewrite Eq. (28) in terms of the individual loop-coil parameters as follows:

$$\begin{bmatrix} R & & & \\ & R & & \\ & & \dots & \\ & & & R \end{bmatrix} \begin{bmatrix} i_1 \\ i_2 \\ \dots \\ i_n \end{bmatrix} + \begin{bmatrix} L_{11}-L_{1, n+1} & L_{12}-L_{1, n+2} & \dots & L_{1n}-L_{1, 2n} \\ L_{21}-L_{2, n+1} & L_{22}-L_{2, n+2} & & L_{2n}-L_{2, 2n} \\ \dots & \dots & \dots & \dots \\ L_{n1}-L_{n, n+1} & \dots & \dots & L_{nn}-L_{n, 2n} \end{bmatrix} \frac{d}{dt} \begin{bmatrix} i_1 \\ i_2 \\ \dots \\ i_n \end{bmatrix} = -\frac{v_x}{2} \begin{bmatrix} G_{11}-G_{n+1, 1} & G_{12}-G_{n+1, 2} & \dots & G_{1m}-G_{n+1, m} \\ G_{21}-G_{n+2, 1} & G_{22}-G_{n+2, 2} & & G_{2m}-G_{n+2, m} \\ \dots & \dots & \dots & \dots \\ G_{n1}-G_{2n, 1} & \dots & \dots & G_{nm}-G_{2n, m} \end{bmatrix} \begin{bmatrix} I_1 \\ I_2 \\ \dots \\ I_m \end{bmatrix} \quad (34)$$

Several important points should be noted in Eq. (34). First, the currents induced in the null-flux coils are due to the speed voltages in the right-hand side of Eq. (34). The speed voltages are given by the product of the vehicle speed v_x , superconducting coil current I_j ($j=1, m$), and the derivative of the mutual inductance between the moving vehicle coils and the stationary guideway coils. This means that the suspension force depends upon the product of the above three factors. Secondly, by comparing Eq. (34) with Eq. (21), one can show that the currents induced in the null-flux coil guideway are much smaller than that in the loop coil guideway for given superconducting coil currents and vehicle speeds. Equation Eq. (34) shows that for the best situation, (which assumes the

superconducting coils to be far away from the null-flux equilibrium point, that is, $L_{ij} \gg L_{n+i,j}$ and $G_{ij} \gg G_{n+i,j}$, the current induced in the null-flux coil guideway is only about one-half of that in the loop-shaped coil guideway because the speed voltage term in the right-hand side of Eq. (34) is about one-half of that of Eq. (21). From the view point of the lumped electric circuit parameters, the resistance and the self-inductance in each null-flux coil are two times larger than that in a single loop coil. In addition, the currents may be further reduced due to the reversed connection between the upper and lower loop coils which would result in a negative contribution from their mutual inductance. Both factors are observed in Eq. (34). Thus, we can conclude that the suspension forces in the null-flux coil guideway are much smaller than that in the loop-shaped coil guideway.

The three-dimensional magnetic forces, the longitudinal magnetic force F_x , the null-flux lift F_y , and the vertical guidance force F_z , are obtained from Eqs. (6) to (7), and (31) as follows:

$$F_x = \sum_{i=1}^n \sum_{j=1}^m i_i I_j \left[\frac{\partial M_{i,j}}{\partial x} - \frac{\partial M_{n+i,j}}{\partial x} \right] \quad (35)$$

$$F_y = \sum_{i=1}^n \sum_{j=1}^m i_i I_j \left[\frac{\partial M_{i,j}}{\partial y} - \frac{\partial M_{n+i,j}}{\partial y} \right] \quad (36)$$

$$F_z = \sum_{i=1}^n \sum_{j=1}^m i_i I_j \left[\frac{\partial M_{i,j}}{\partial z} - \frac{\partial M_{n+i,j}}{\partial z} \right] \quad (37)$$

Equations (35) to (37) illustrate that all magnetic forces in the null-flux coil guideway are determined by the difference of the forces acting on the upper loop and the lower loop coils. All magnetic forces vanish at the null-flux equilibrium point, as expected.

CONTINUOUS SHEET SUSPENSION

A continuous sheet guideway is one of the basic levitation methods for electrodynamic suspension maglev systems. The repulsive levitation force is generated by the interaction between the superconducting coils aboard the vehicle and the eddy currents induced in the conducting sheet. The computation of lift and drag forces for a continuous sheet guideway is discussed in the literature (refs. 14 and 15). In particular, combining the Fourier transformation method with a numerical approach seems to be a powerful method. Most of these methods, however, neglect edge effects due to the finite width of the guideway and are based on steady state analyses.

When the dynamic circuit method is applied to a continuous sheet guideway, it divides the plate or the sheet conductors into many zones as shown in Fig. 4, each of which carries a different current. The circuit parameters for every conducting zone are then determined, and the system of equations is formed. The number of conducting zones is determined by the need for accurate computation. When the current distribution is known by solving the system of equations, the performance of the system can be calculated. When the circuit parameters are evaluated on the basis of a finite

length of the conducting zone in the y direction, the edge effect of the guideway is taken into consideration.

If we assume m superconducting magnets moving above a conducting sheet guideway which is divided into n conducting zones, we can write the voltage equations for the sheet guideway in matrix form as

$$\begin{bmatrix} R_1 & & & \\ & R_2 & 0 & \\ & & \ddots & \\ & & & R_n \end{bmatrix} \begin{bmatrix} i_1 \\ i_2 \\ \vdots \\ i_n \end{bmatrix} + \begin{bmatrix} L_{11} & L_{12} & \dots & L_{1n} \\ L_{21} & L_{22} & & L_{2n} \\ \dots & \dots & \dots & \dots \\ L_{n1} & \dots & \dots & L_{nn} \end{bmatrix} \frac{d}{dt} \begin{bmatrix} i_1 \\ i_2 \\ \vdots \\ i_n \end{bmatrix} + \begin{bmatrix} V_{s1} \\ V_{s2} \\ \vdots \\ V_{sn} \end{bmatrix} = -v_x \begin{bmatrix} G_{11} & G_{12} & \dots & G_{1m} \\ G_{21} & G_{22} & & G_{2m} \\ \dots & \dots & \dots & \dots \\ G_{n1} & \dots & \dots & G_{nm} \end{bmatrix} \begin{bmatrix} I_1 \\ I_2 \\ \vdots \\ I_m \end{bmatrix} \quad (38)$$

where R_i and L_{ij} ($i,j=1,n$) are the resistances and inductances of the conducting zones, and G_{ij} is the derivative of the mutual inductance between the i^{th} conducting zone and the j^{th} superconducting coil. In Eq. (38) a column voltage matrix $[V_s]$ appears which represents the unknown voltages across the finite width of the conducting sheet. We may call this a side-voltage which does not exist in either the loop-shaped coil guideway or the figure-eight-shaped coil guideway. To solve the currents induced in each conducting zone, two additional conditions must be imposed. First, the total current flowing in the conducting sheet must be zero. Second, side-voltages across all conducting zones must be equal, that is

$$i_1 + i_2 + i_3 + \dots + i_{n-1} + i_n = 0 \quad (39)$$

and

$$V_{s1} = V_{s2} = \dots = V_{sn-1} = V_{sn} = V_s \quad (40)$$

Thus, Eqs. (38) to (40) involve $n+1$ equations. For given initial current conditions, we can solve the $n+1$ equations as a set of coupled linear equations for n unknown current derivatives and one side-voltage V_s . The currents in the conducting zones at time t are obtained by adding $di/dt \Delta t$ to the currents at $t-\Delta t$ as shown in Eq. (22). Continuous iterations will determine the currents in all the conducting zones as a function of time or displacement. Following the solution of these currents, we are able to find all magnetic forces acting on the superconducting coils as given by Eqs. (6) to (8). In the continuous sheet guideway, F_x is the longitudinal magnetic force, F_y is the lateral force due to the edge effect in the finite width guideway, and F_z is the repulsive suspension force.

NUMERICAL EXAMPLES

Several computer codes for different guideway options have been developed based on the model discussed in this paper. Numerical examples are given only on the figure-eight-shaped coil suspension because of the limited length of this paper. Table 1 shows the dimensions of a superconducting coil and the null-flux coils used as numerical examples. A computer simulation is performed on a single superconducting coil

moving above a null-flux coil guideway with a 20-cm equivalent air-gap, as shown in Fig. 2. The time-averaged null-flux lift, magnetic longitudinal force (which equals the magnetic drag force), and the horizontal guidance force are shown as functions of the vertical displacement in Fig. 5. This figure shows that, as expected, all time-averaged forces disappear at the null-flux equilibrium point, and that they are symmetrical about the axis $y=0$. Fig. 6 shows the time-averaged forces as a function of vehicle speed from which one can see that the lift-to-drag ratio is about 20 at a high speed, and that a drag peak appears at 20 m/s. This implies that the dimensions of the null-flux coils may be optimized; for instance, the resistance of the null-flux coil may be reduced. Two options may be considered for the reduction of the coil resistance: one is to increase the cross-section of the aluminum coils, and the other is to use a copper conductor for the null-flux coil guideway.

Force fluctuations associated with the null-flux coil guideway are shown in Fig. 7, which shows that all forces fluctuate around their average values. Typical fluctuations for the null-flux lift and the horizontal guidance forces are about 10%. The frequency of the fluctuations is determined by the vehicle speed divided by the average length of the null-flux coil. Thus, for $v=67$ m/s and a coil length of 0.55 m, the frequency is 122 Hz.

Table 1 Dimensions of Superconducting Coils and Null-flux Coils

Superconducting coil		
length	1.5	m
width	0.5	m
current	550	kA-T
Figure-eight-shaped null-flux coils		
length	0.5	m
height/loop	0.35	m
gap between upper and lower loops	0.05	m
gap between null-flux coil	0.05	m
cross-section	9	cm ²
material	aluminum	
Equivalent Air gap	20	cm

CONCLUSION

Dynamic circuit theory, as applied to the maglev problem, treats all magnetic forces acting between components of a maglev system as arising from changes in magnetic energy stored in that system. This paper shows that mathematical models based upon this theory can be readily constructed to represent moving vehicle magnets interacting with stationary conductor arrays distributed on a guideway. Models of three types of guideway conductors were considered in order to demonstrate the utility and versatility of the approach. Very general expressions were given for the forces between vehicle and guideway components for all three types of guideway conductors. This showed that, in general, single-loop conductors provide larger lift force than null-flux loop conductors. Numerical results of computer codes based on the mathematical model of a null-flux loop guideway conductor array were also given. In conclusion, the dynamic circuit theory provides a powerful approach to analyzing complex and heretofore difficult to handle problems involved in maglev system design.

REFERENCES

1. Morgan, A. T.: General Theory of Electrical Machines. Heyden & Son Ltd., London, 1979.
2. Elliott, D. G.: Matrix Analysis of Linear Induction Machines. Final Report prepared for FRA, Dept. of Transportation, Office of Research and Development, Washington, D.C. 20590, Sept., 1975.
3. Ooi, B. T.: A generalized Machine Theory to the Linear Motor. IEEE Trans. Power Apparatus and Systems, Vol. PAS-92, No. 5, July/Aug. 1973, pp. 1252-1259.
4. He, J. L.; Levi, E.; Zabar, Z. and Birenbaum, L.: Concerning the Design of Capacitively Driven Induction Coil Guns. IEEE Trans. on Plasma Science, Vol. 17, No. 3, June 1989, pp. 429-438.
5. He, J. L.; Zabar, Z.; Levi, E. and Birenbaum, L.: Transient Performance of Linear Induction Launchers Fed by Generators and by Capacitor Banks. IEEE Trans. on Magnetics, Vol. 27, No. 1, Jan. 1991. pp. 585-590.
6. Elliott, D. G.: Mesh-Matrix Analysis Method for Electromagnetic Launchers. Fourth Symposium on Electromagnetic Launch Technology, Austin, Texas, April 12-14, 1988.
7. Ooi, B. T.: A Dynamic Circuit Theory of the Repulsive Magnetic Levitation System. IEEE Trans. Power Apparatus and System, Vol. PAS-96, No. 4, July/Aug. 1977, pp. 1094-1100.
8. Jain, O. P.: Further Applications of the Dynamic Circuit Theory to the Electrodynamic Repulsive Magnetic Levitation Systems. Ph.D. Dissertation, Department of Electrical Engineering, McGill University, Montreal, Canada, July 1978
9. Nasar, S. A. and Boldea, I.: Linear Electric Motors: Theory, Design, and Practical Applications. Prentice-Hall, Inc., Englewood Cliffs, N. J., 1987.
10. Hoppie, L. O.; Chilton, F.; Coffey, H. T. and Singleton, R. S.: Electromagnetic Lift and Drag Force on a Superconducting Magnet Propelled along a Guideway Composed of Metallic Loops. Proc. of Applied Superconducting Conf., May 1-3, 1972, Annapolis, Maryland, IEEE Pub. No. 72CH0682-5-TABSC.
11. Grover, F. W.: Inductance Calculations Working Formulas and Tables. Dover Publications, Inc., New York, 1962.
12. Fujiwara, S.; and Fujimoto, T.: Characteristics of the Combined Levitation and Guidance System Using Ground Coils on the Side Wall of the Guideway. International Conf. Maglev '89, July 1989, pp. 241-244.
13. Saitoh, T.; Miyashita, K.; and Kiwaki, H.: Study for Harmonic Ripple of Electromagnetic Force in Superconducting Magnetically Levitated Vehicle with Non-Rectangular Ground Coils. International Conf. Maglev'89, July 1989, pp. 245-250.
14. Coffey, H. T.; Chilton, F.; and Hoppie, L. O.: The Feasibility of Magnetically Levitating High Speed Ground Vehicles, prepared by Stanford Research Institute for U. S. Dept. of Transportation, FRA, Report FRA-10001, Feb. 1972.
15. Reitz, J. R.; and Davis, L. C.: Force on Rectangular Coil Moving above a Conducting Slab. Journal of Applied Physics, 43(4), April 1972, pp. 1547-1553.

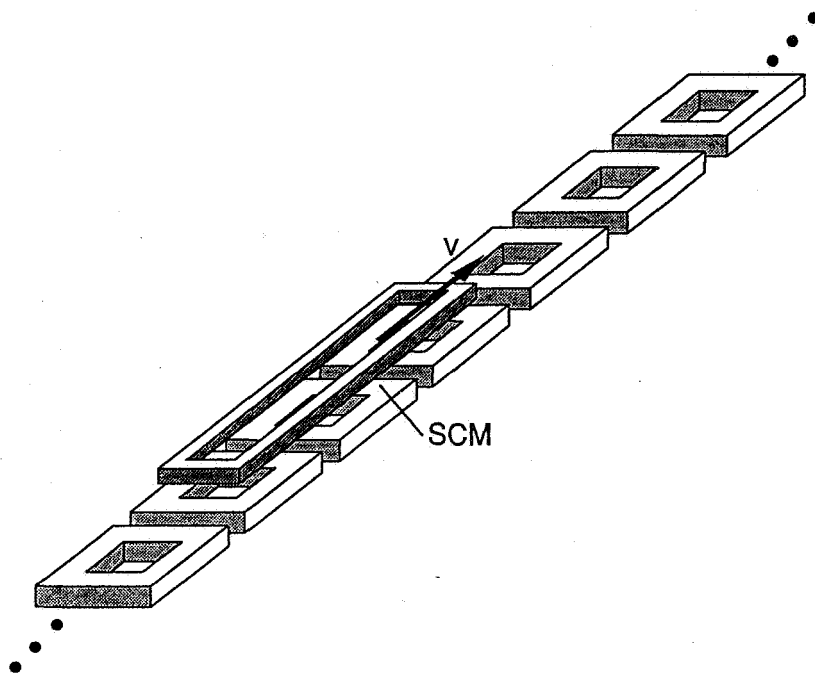


Fig. 1 A Sketch of Loop-shaped Coil Suspension

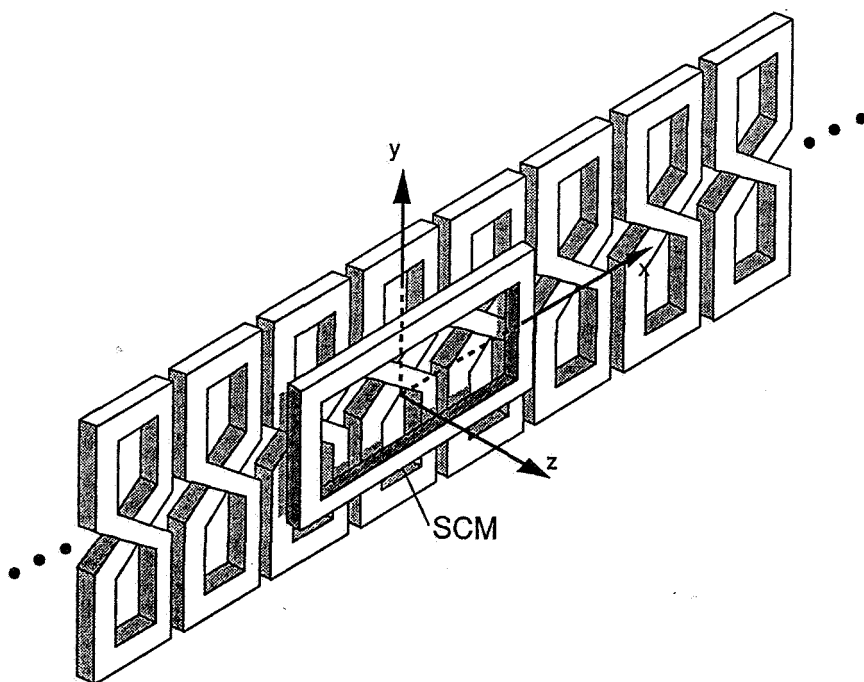


Fig. 2 A Sketch of Figure-Eight-Shaped Coil Suspension

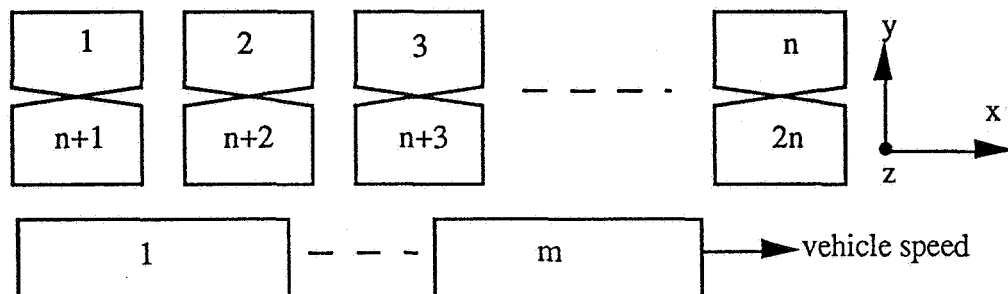


Fig. 3 Dynamic Circuit Application to the Figure-Eight-Shaped Null-Flux Coil Suspension

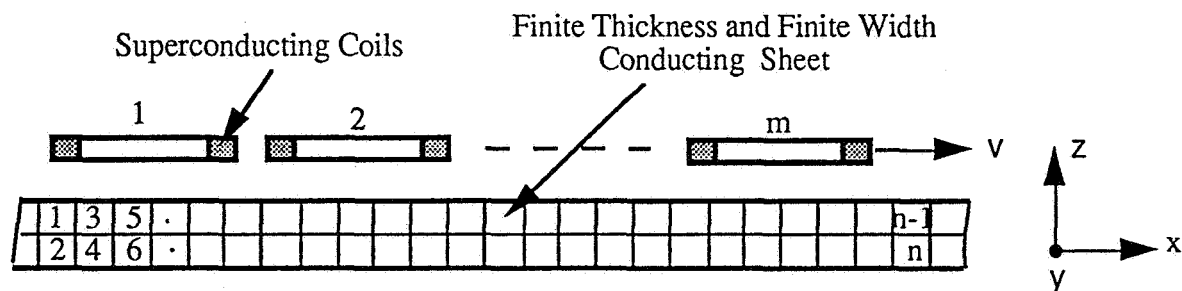


Fig. 4 Dynamic Circuit Theory Application to the Finite Thickness and Finite Width Continuous Sheet Guideway

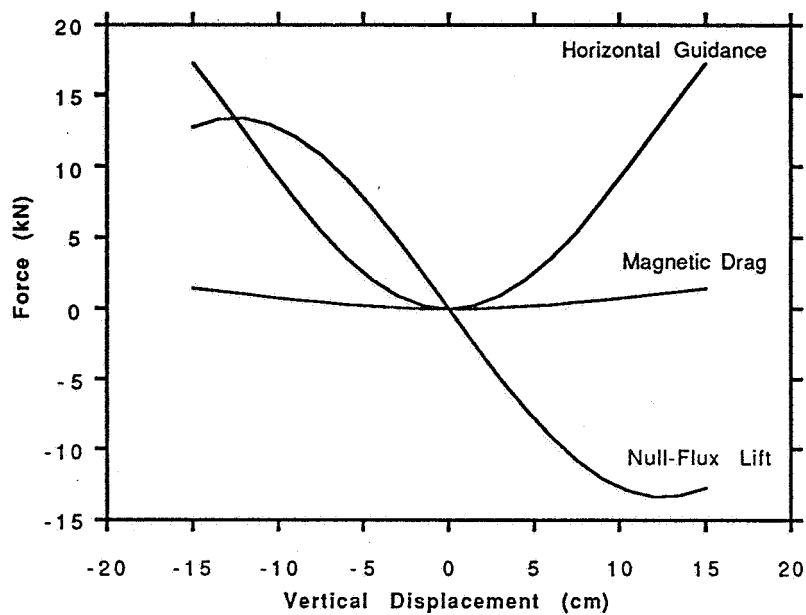


Fig. 5 Time-Averaged Null-Flux Lift, Magnetic Drag, and Horizontal Guidance Forces vs. Vertical Displacement with a Vehicle Speed of 67 m/s

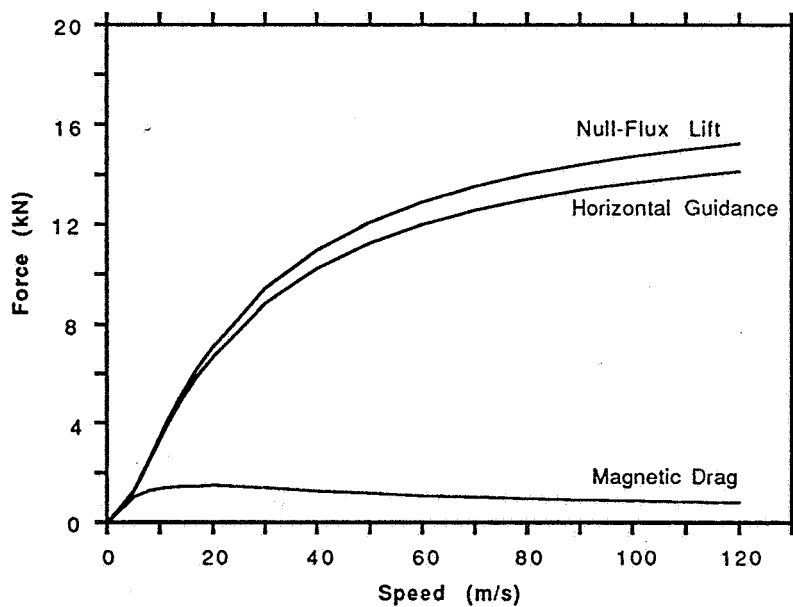


Fig. 6 Time-Averaged Null-Flux Lift, Magnetic Drag, and Horizontal Guidance Forces vs. Vehicle Speed with 11-cm Vertical Offset

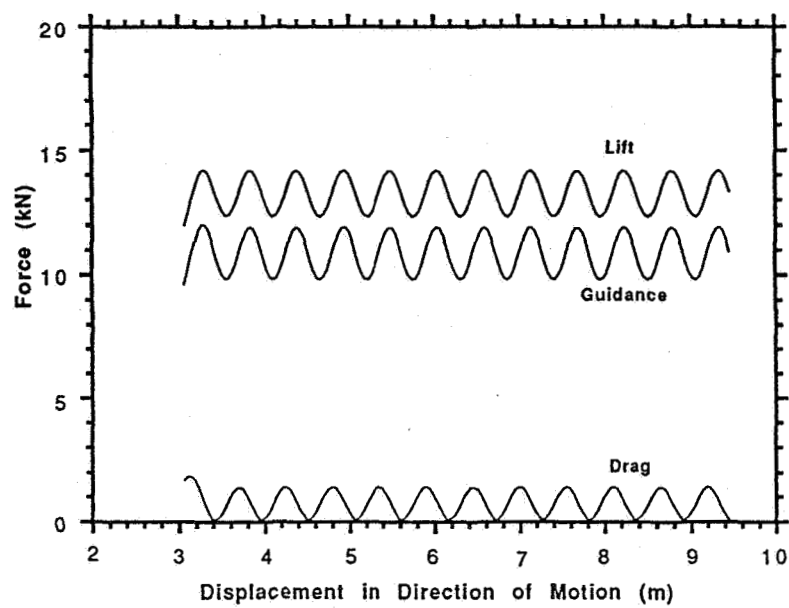


Fig. 7 Force Pulsations in Null-Flux Coil Suspension System

Session 17

LARGE-GAP MAGNETIC SUSPENSION SYSTEMS

Chairman - Nelson J. Groom
NASA Langley Research Center

**LARGE-GAP MAGNETIC POSITIONING SYSTEM
HAVING ADVANTAGEOUS CONFIGURATION**

**Paul Chong
Colin Commandeur
Harold Davis
Lorne Whitehead**

Department of Physics
University of British Columbia
6224 Agricultural Road
Vancouver, B.C., Canada, V6T 1Z1

SUMMARY

Most simple large-gap magnetic positioning systems, which operate in the absence of substantial gravitational acceleration, involve the use of magnetic components on at least two opposite sides of the positioned object. If gravity is present, such systems generally require the magnetic components to be located above the levitated object. These configurations can sometimes interfere with the use of magnetic positioning systems.

A magnetic configuration has been devised in which the positioned object is maintained in a stable orientation and position on one side of an opaque plane surface entirely by means of magnetic components on the other side of the plane. The system is effective with or without gravity, and can operate in any orientation. In this system, the positioned object need only contain a simple dipole magnet. The positioning components consists of a group of permanent magnets creating a magnetic field configuration which stabilizes the levitated dipole in all but one degree of freedom, and a magnetic position sensing and force feedback system to actively stabilize the object in the one unstable direction. The system utilizes very low power at equilibrium and can maintain gaps of 50 mm.

INTRODUCTION

Large gap magnetic suspension systems can have a wide variety of configurations and a wide range of applications¹. This paper concerns a specific class of large-gap magnetic suspension systems in which all of the components required to achieve suspension are located on one side of an opaque plane barrier and the suspended object is on the other. Of particular interest is a system for use in a gravitational field in which the system components are located below, and the suspended object above, a horizontal plane.

This class of levitation system has a number of potential applications such as the display of objects and the movement of objects within sealed atmosphere enclosures. However, to date there has been little work in this field because in practise it is very difficult to achieve stable magnetic suspension from below or, in the absence of gravity, from just one side of a suspended object.

A brief review of a more conventional suspension system will help to explain this difficulty. Figure 1 shows the well known components of a simple "suspend from above" system². The suspended object is a simple magnetic dipole, in this case with north pole up. The required upward force to counteract gravity is provided by a control magnet

positioned above the suspended dipole, with south pole down, so as to attract the suspended dipole. This magnet has an electronically controlled strength, which is varied in response to the signal from the height sensor, so as to achieve stability against displacement in the otherwise unstable vertical direction. This type of system is very common because the components are simple, and especially because the control system consists of just one channel. In other words, this system is naturally stable in five of the six degrees of freedom – it naturally returns from displacement in either of the horizontal directions, it returns to the vertical if the dipole moment is rotated about either of the two horizontal axes, and it is neutrally stable against rotation about the vertical axis.

In the absence of gravity, the system of Figure 1 will not work because the controlled magnet is designed to produce only a controlled attractive force. In the presence of gravity, we may attempt to place the control magnet beneath the suspended magnet, and reverse its polarity, so as to cause a force of repulsion, rather than attraction, as shown in Figure 2. Such a system is fully capable of countering the force of gravity, and in fact such a system is intrinsically stable against displacements in the vertical direction, since the upward magnetic force increases in response to a drop in height. Unfortunately, this system is very unstable with regard to rotation about either horizontal axis, or with regard to displacement in either horizontal direction, meaning that a very sophisticated four channel control system would be required to stabilize the suspended object.

Attempts have been made to simplify the control requirements through the use of more complex suspended magnets³. In essence, this approach mechanically couples a number of systems of the type shown in Figure 2, to give the configurations shown in Figure 3a, 3b. Such arrangements employ the natural vertical stability of Figure 2 to achieve orientational stability as well. Even with this improvement, however, such arrangements still require stabilization against displacement in two horizontal directions, which substantially complicates any control system. Moreover, such systems require the force of gravity to achieve stability. Also, the complicated geometry of the magnets can be problematical. Clearly it would be desirable to find an alternate magnet configuration which would make it possible for a simple dipole to be stable in all but one degree of freedom, as is the case for the system of Figure 1, but with the magnets creating the applied field positioned entirely below the suspended object.

PERMANENT MAGNET CONFIGURATION

Figure 4 depicts an idealized permanent magnet configuration and a coordinate system which will be used throughout the remainder of this paper. The configuration consists of two parallel infinitely long bar magnets, each vertically magnetized with north pole up, and each having a uniform magnetic dipole moment per unit length of magnitude ρ (Cms⁻¹). The origin of the coordinate system is equidistant between the magnets and is in the plane containing the center line of both magnets. The x direction lies in this plane, perpendicular to the magnets, and the y direction is also in this plane, but parallel to the magnets. The z direction in this geometry is vertical. As shown, the distance from the origin to the center of each magnet is x_0 .

By virtue of the symmetry shown in Figure 4, the magnetic field due to these magnets, which will generally be described as $\vec{B}_0 = (B_{x0}, B_{y0}, B_{z0})$, will be purely vertical along the z

axis. In the idealized case where the bar magnets have a height and width which is very small relative to their separation, the vertical field component B_{z0} can be evaluated simply, as expressed in the following relation, in SI units:

$$B_{z0} = \frac{\mu_0}{\pi} \rho \frac{z^2 - x_0^2}{(z^2 + x_0^2)^2} \quad (1)$$

Differentiation of (1) with respect to z yields the following useful relation,

$$\frac{\partial B_{z0}}{\partial z} = \frac{2\mu_0}{\pi} \rho \frac{(3x_0^2 - z^2)z}{(z^2 + x_0^2)^3} \quad (2)$$

Figure 5 is a graph of $B_{z0}/\mu_0 \rho x_0^{-2}$ and $\frac{\partial B_{z0}}{\partial z}/\mu_0 \rho x_0^{-3}$, vs z/x_0 . As can be seen, B_{z0} is negative for $-1 < z/x_0 < 1$, and positive everywhere else. The region for which $z/x_0 > 1$ is of particular interest because this region is substantially above the bar magnets; it contains a local maximum of B_{z0} , at the point $z/x_0 = \sqrt{3}$, and it maintains a constant magnetic field direction throughout the region. The maximum field strength implies a stable location for a suspended magnetic dipole. Another way to recognize this is to recall that the force on a magnetic dipole is in general given by

$$\vec{F}_m = (F_{mx}, F_{my}, F_{mz}) = \vec{\nabla}(\vec{D} \cdot \vec{B}_0) \quad (3)$$

where $\vec{D} = (D_x, D_y, D_z)$ is the magnetic dipole moment in units of $\text{Cm}^2 \text{ s}^{-1}$. Along the z axis, a free dipole will align vertically with the vertical field and (3) simplifies to

$$F_{mz} = D \frac{\partial B_{z0}}{\partial z} \quad (4)$$

where $D = |\vec{D}|$. Thus $\frac{\partial B_{z0}}{\partial z}$ is proportional to the vertical force which the magnets of Figure 4 would exert on a freely suspended dipole on the z axis, and the graph of $\frac{\partial B_{z0}}{\partial z}$ in Figure 5 shows that this force is upward for positions below $z/x_0 = \sqrt{3}$, and negative above this point, which is required for stability against displacement in the vertical direction. By virtue of the symmetry about the YZ plane in Figure 4, it is apparent that this system is neutrally stable in the y direction, and hence it is unstable only in the x direction. As already noted, the suspended dipole is orientationally stable and hence this system achieves the goal of positioning a suspended magnetic dipole, with only one unstable degree of freedom.

However, a number of practical issues must be considered in developing a useful system. Obviously, the bar magnets cannot be infinitely long and, furthermore, it is desirable to introduce some positive stability in the y direction. Another practical question is whether the actual field strengths from ordinary magnets can produce stability in general, and stable levitation in the earth's gravitational field in particular. Lastly, there is the critical question of whether a practical controlled magnetic force application system can operate from below to stabilize the dipole magnet against displacements in the x direction.

These practical issues are addressed below. The main concept of this system, however, is the ideal geometry described above, which has the key feature of providing stable levitation from below with only one unstable degree of freedom. That the system works at all is

non-intuitive; indeed most scientists casually examining Figure 4 do not expect an upward force to be possible due to the proximity of opposite poles on the suspended dipole and the bar magnets. The authors do not have a simple intuitive explanation for the results shown in (1), (2) and (4) but it will be shown that the system does have good stability in the vertical direction.

PRACTICAL CONSIDERATIONS

In practise, the truncation of the infinite bar magnets of Figure 4 is no problem at all since the field contribution from portions of the magnets for $|y/x_0| \gtrsim 4$ is negligibly small. Furthermore, achieving a slightly positive stability rather than neutral stability in the y direction can be achieved through a variety of configurations of small magnets. Generally, properly oriented magnets which are placed on the y axis symmetric about the origin will tend to repel the dipole towards the origin and will not impede vertical stability providing their fields are much weaker than the main levitating fields.

To consider the question of field strengths in practical systems, consider the system shown in cross section in Figure 6. Although these magnets have a finite physical extent, and are truncated at $y = \pm 95 \text{ mm}$, equations (1) and (2) still provide a good approximation to the field along the z axis and equation (4) provides a good approximation to the vertical force on the suspended dipole.

The ceramic bar magnets have residual field $B_r = 0.38 \text{ T}$, corresponding to a magnetization $M = \frac{B_r}{\mu_0} = 3.024 \times 10^5 \text{ Cm}^{-1}\text{s}^{-1}$. With the dimensions shown, this yields a magnetic dipole moment per unit length of $\rho = 266 \text{ Cms}^{-1}$. The rare earth suspended magnet has a residual field $B_r = 1.08 \text{ T}$ corresponding to a magnetization $M = \frac{B_r}{\mu_0} = 8.59 \times 10^5 \text{ Cm}^{-1}\text{s}^{-1}$. With the dimensions shown, this yields a magnetic dipole moment $D = 5.53 \text{ Cm}^2\text{s}^{-1}$. The density of this material is $8.304 \times 10^3 \text{ Kg m}^{-3}$, yielding a mass of $5.34 \times 10^{-2} \text{ Kg}$ and a gravitational force at the earth's surface of about $F_g = -0.524 \text{ N}$.

This information, used in equations 1, 2, and 4 yields the results graphed in Figure 7. The curves showing B_z and $\frac{\partial B}{\partial z}$ vs z have the same shape as in Figure 5, and are shown to provide a quantitative feel for their magnitude. The force F_m passes through zero at $z \simeq 87 \text{ mm}$, corresponding to a gap between the top of the ceramic magnets and the bottom of the rare earth magnet of 71 mm . This would be the point of stable positioning in the absence of gravity. The curve F_n plots the net force on the suspended magnet in the earth's surface gravitational field. The stability point is shifted to $z \simeq 70 \text{ mm}$, which is still well within the useful operating region where the minimum possible elevation is 50 mm to get any levitation. In fact, the magnet could still support a substantial additional weight (or negative weight) without leaving the "well" of stability. At this value of z , the predicted gap between the top of the ceramic magnet and the bottom of the rare earth magnet is 54 mm , compared to the value of 50 mm observed in our lab with the actual truncated magnets. Thus the approximations of equations 1, 2, and 4 are useful under these circumstances.

A number of active magnetic system configurations have been tried to stabilize the suspended magnet in the y direction. Figure 8 shows schematically a typical system. The Hall probe is sensitive to magnetic field in the x direction. To first order, the value of this field is proportional to the displacement of the suspended magnet in the y direction. The

purpose of the air core electromagnet coils is to provide a restoring force in the x direction only. It is especially important that the coils not impart a torque on the suspended magnet, nor forces in other directions, as this can result in the energizing of oscillation modes in the other degrees of freedom.

This implies that the desired magnetic field from the control coils should be zero at the point of stable levitation, and that its vertical component should have a strong horizontal gradient. The symmetry in Figure 8 ensures that the vertical magnetic control field will be zero wherever $x = 0$, and hence so will be its gradient in the y and z directions implying that any force can only be in the x direction. The correct orientation of the coils results in the field in the x direction being zero as well, ensuring there is no torque applied to the suspended magnet. Thus the desired pure horizontal force can be applied effectively with this configuration.

One problem with the above design is that the Hall probe detects the applied field from the coils, and also is sensitive to tipping of the suspended magnet. Both of these effects can be cancelled out by a variety of methods, but in practice this is often not necessary as the associated effects are not too serious.

A last practical consideration concerns damping. As with other magnetic suspension systems, some type of damping is required to prevent a gradual build up of energy in one or more modes of oscillation. Eddy current damping by a copper plate placed between the magnetic apparatus and the suspended object has been used to improve stability but at large levitation distances the damping forces are small. We have successfully used a simple proportional-derivative controller for the active control axis to introduce damping. The derivative control comes from the time dependent value of displacement of the levitated object which is measured by a Hall effect sensor. A series capacitor is able to differentiate the displacement signal without introducing excessive noise to the control electronics. However this damping is only effective on translation in the y direction and on rotation about the x and y axes.

Another disadvantage of this system is that the coil configuration shown in Figure 8 is a rather inefficient means of providing a horizontal gradient of vertical field, due to the other requirements the coils must satisfy. We have typically had to use a voltage to current amplifier with a 600 W maximum output to provide a stability "well" in the y direction only 1 cm wide. Fortunately, however, at equilibrium, very little dissipation of power is required, so under normal conditions the coils are not required to dissipate much heat as the RMS input power is less than one watt.

CONCLUSIONS

The system demonstrates that stable levitation can be achieved in a simple, innovative way with all components located to one side of the levitated object. The levitated object must contain a powerful magnet dipole. Only one axis of active control is required and the controller can use a very simple proportional-derivative strategy with position signals coming from Hall effect sensors. The rate control provides damping to the system.

An arrangement of economical ceramic permanent magnets provides the primary levitating and stabilizing forces. The levitated object naturally stays within a magnetic

potential energy "well" in two of the translational axes. The magnetic dipole aligns with the magnetic field to give moment stability in two rotational directions. However, the levitating object can rotate freely about an axis pointed away from the levitating components and is neutrally stable on this axis.

Within the area in space where the magnetic field defines an appropriate magnetic flux density gradient, levitation is stable and relatively strong. However, if the levitated object is perturbed beyond definite limits, it catastrophically loses stability and is attracted to the primary levitating magnets. Certain types of perturbations lead to oscillations which grow in amplitude with time until the stability bounds are exceeded. Future work is required to improve the stability of levitation by increasing energy dissipation from oscillations. This can be done by adding passive eddy current dampers or by additional active control electromagnetics.

The active control system needs to be modified to allow levitation to start "softly" from a rest state rather than require the levitated object to be placed manually into the magnetic field at the correct location for levitation. Additionally, it is desirable to be able to control some of the levitation parameters such as height above the plane or orientation of the object in space. With continuing development, more applications will be found which will use the unique characteristics of this levitation system.

SYMBOLS

Values are given in SI units.

x, y, z	coordinates of levitation system (m)
x_0	half width of main magnets (m)
\vec{B}_0	magnetic flux density, free field (T)
B_r	residual magnetization (T)
\vec{D}	magnetic dipole moment (Cm^2/s)
$\vec{\rho}$	magnetic dipole moment per unit length (Cm/s)
\vec{M}	magnetization vector ($\text{Cm}^{-1}\text{s}^{-1}$) = (Am^{-1})
μ_0	magnetic constant = $4 \pi \times 10^{-7}$ (TmA^{-1})
F_{mz}	force on magnetic dipole, vertical (N)
F_g	gravity force on magnetic dipole (N)
F_n	net vertical force = ($F_{mz} - F_g$)

ACKNOWLEDGMENT

This work was partially supported by a grant from the Industry Liaison Office of the University of British Columbia.

REFERENCES

1. Britcher, C.P.: Large-Gap Magnetic Suspension Systems. Presented at the International Symposium on Magnetic Suspension Technology—1991. NASA CP-3152, 1992.
2. Goodall, R.M.: The Theory of Electromagnetic Levitation Physics in Technology, 16, (5), 1985, pp. 207–213.
3. U.S. Patent 4,585,282: Magnetic Levitation System, issued to R. W. Bosley on April 29, 1986.

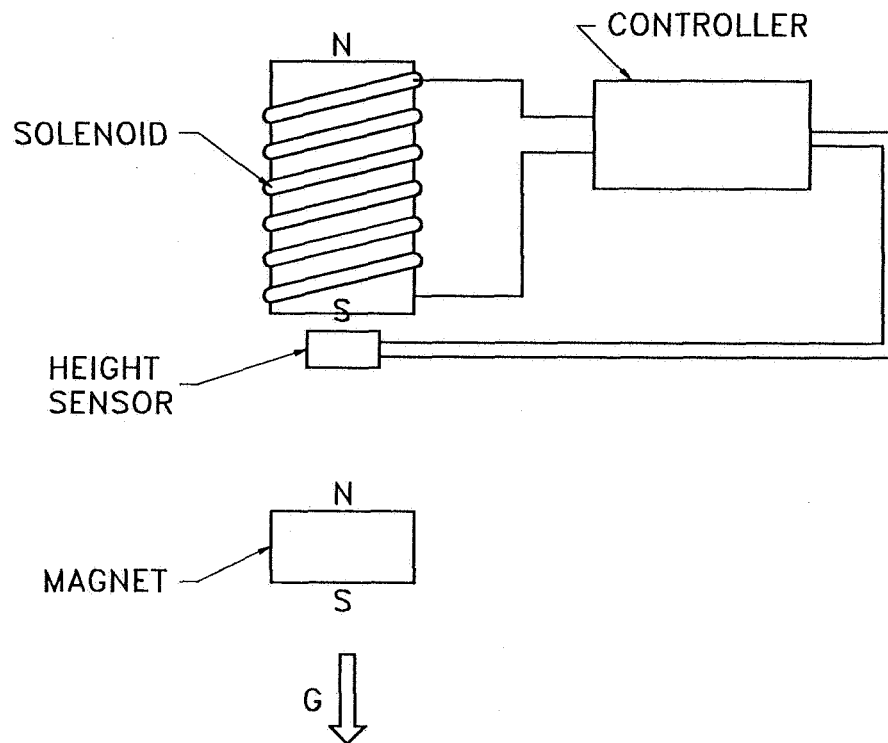


Figure 1. Magnetic levitation by attraction from above in gravity.

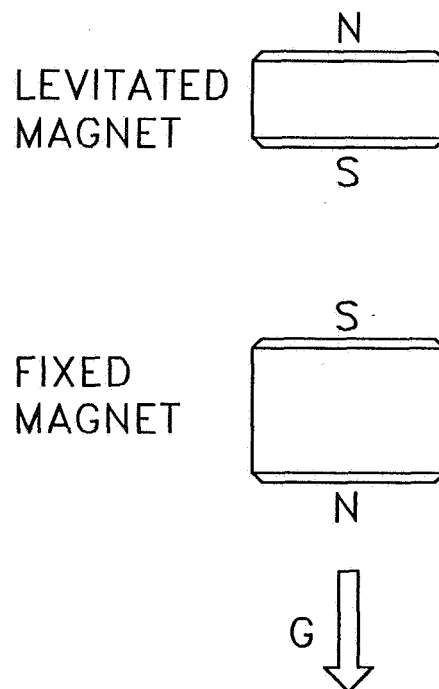


Figure 2 Magnetic levitation by repulsion from below in gravity.

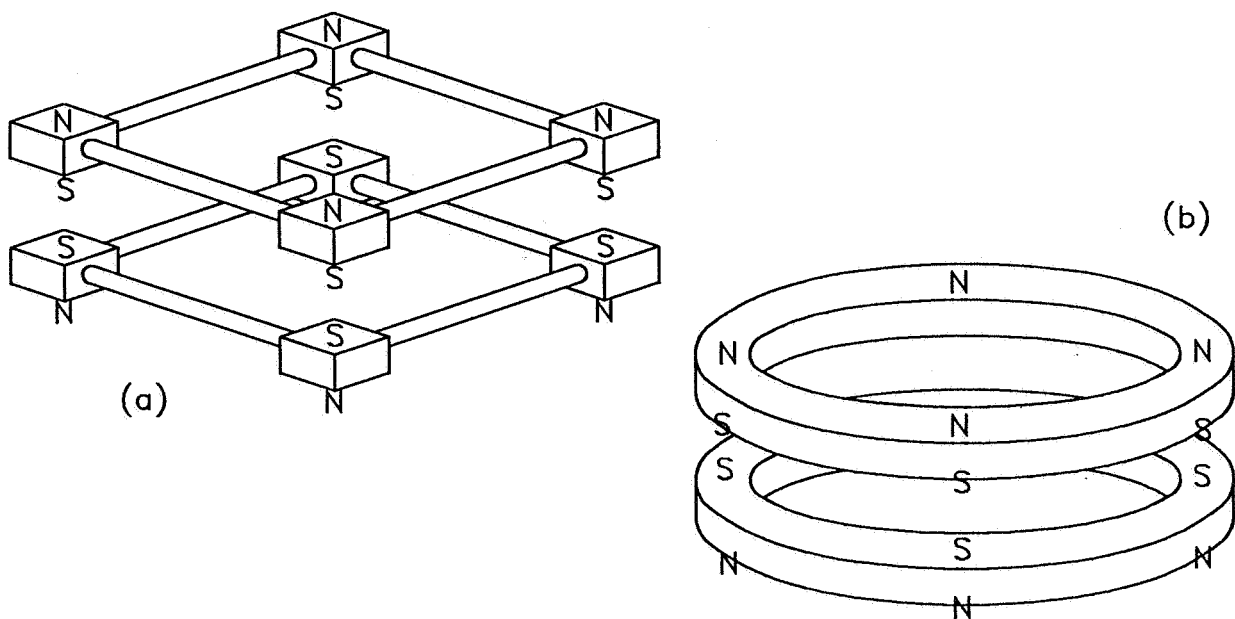


Figure 3 Levitation by repulsion using several magnets in gravity.

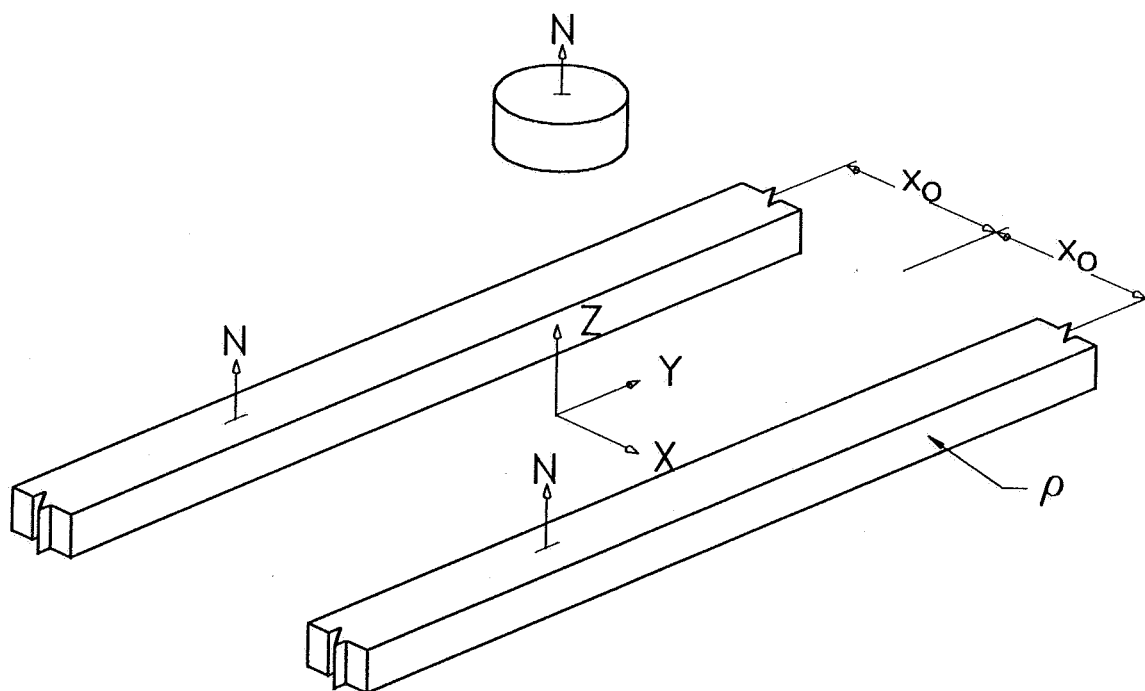


Figure 4 Idealized permanent magnet configuration for stable levitation.

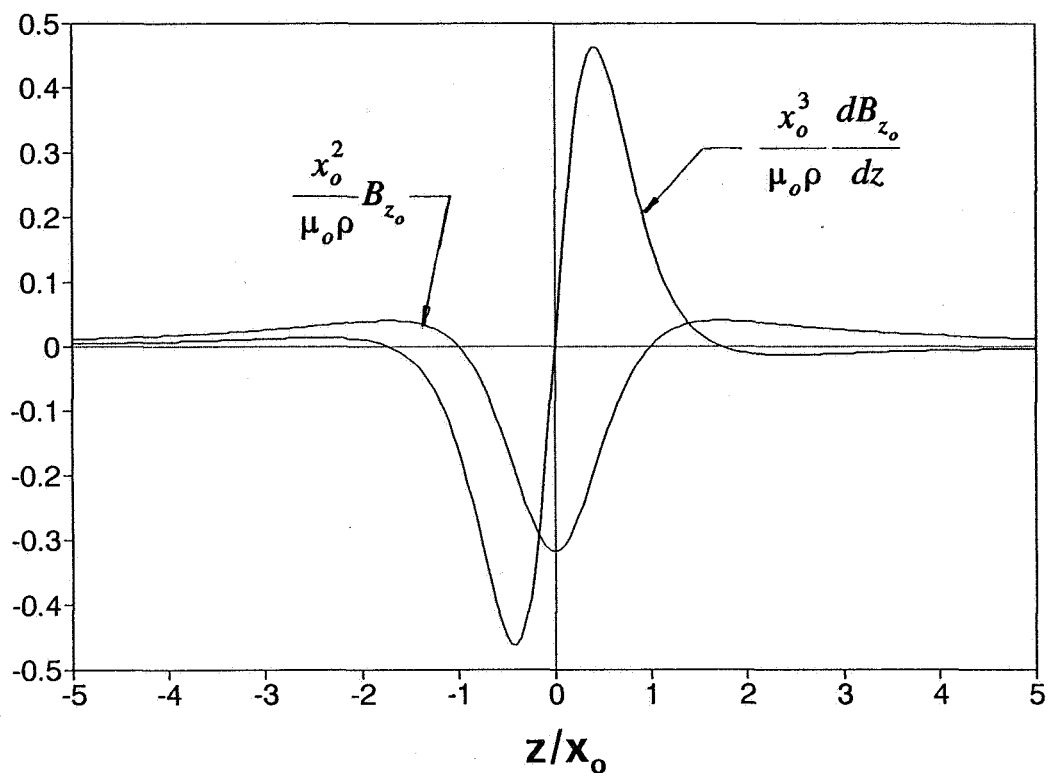


Figure 5 Dimensionless magnetic flux density and density gradient in the vertical (z) direction between two infinitely long horizontal bar magnets spaced $2x_0$ apart.

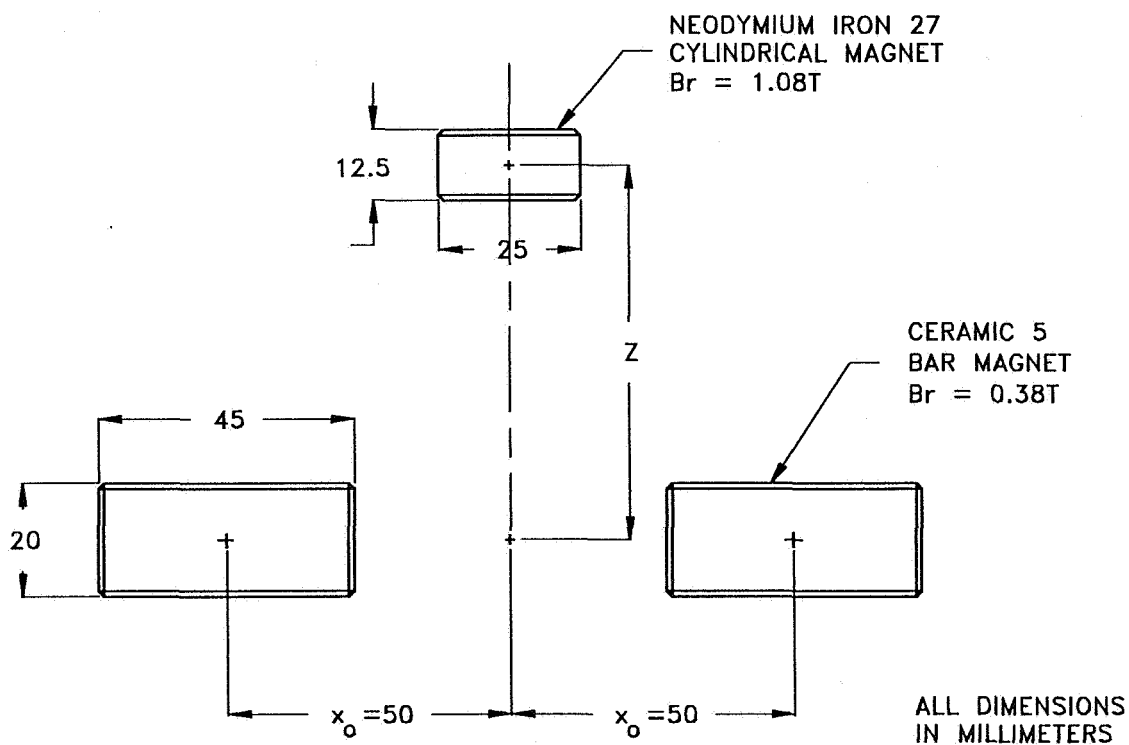


Figure 6 Geometry used for calculating magnetic field strengths.

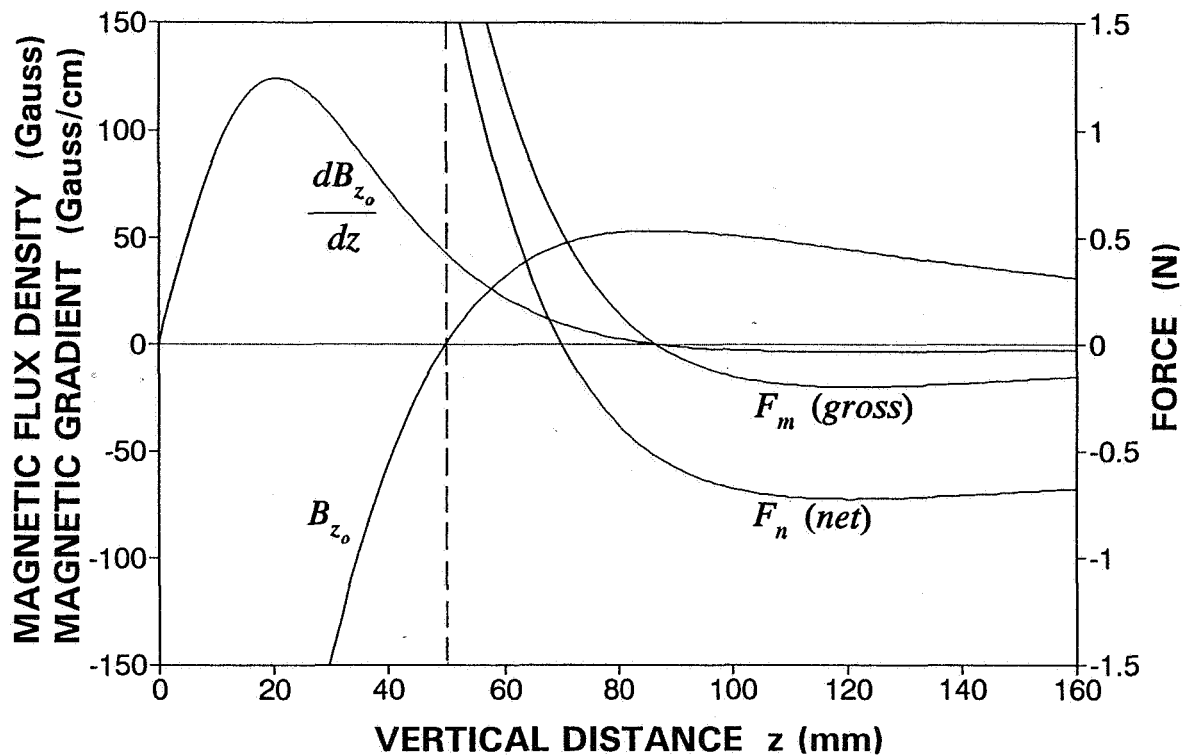


Figure 7 Calculated magnetic flux density and gradient in the vertical direction and the calculated gross and net levitating forces for system geometry shown in Fig. 6. Weight of the cylindrical magnet = 0.5 N.

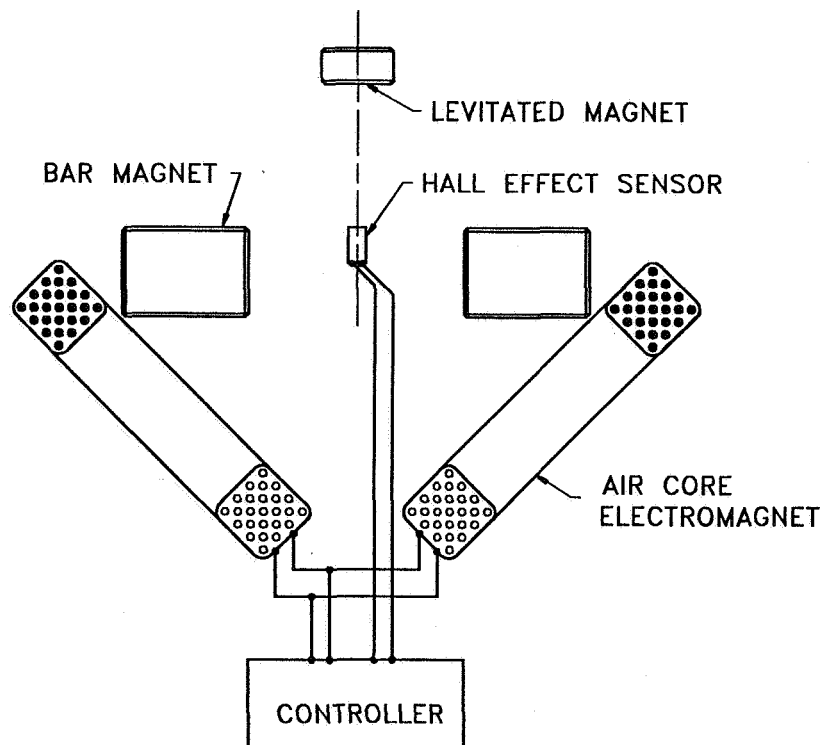


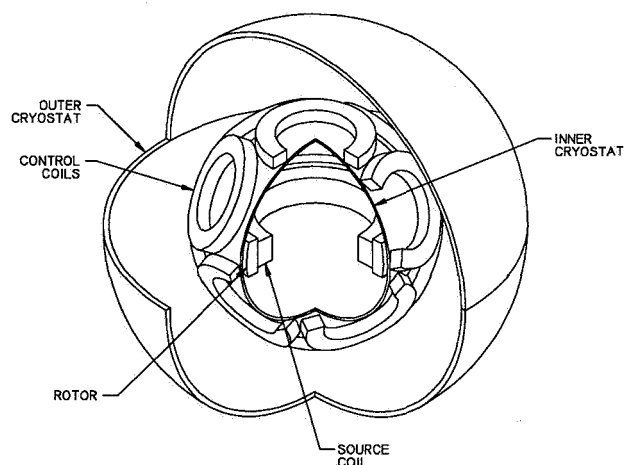
Figure 8 Active magnetic control configuration for the x axis.

PERFORMANCE OF A SUPERCONDUCTING LARGE-ANGLE MAGNETIC SUSPENSION

James R. Downer
Dariusz A. Bushko
Vijay Gondhalekar
Richard P. Torti
SatCon Technology Corporation
12 Emily Street
Cambridge, MA 02139

SatCon Technology Corporation has been working toward the development of an advanced-concept Control Moment Gyro (CMG). The advanced-concept CMG is sized for use as a slewing actuator for large space-based payloads. The design features a magnetically suspended composite rotor which contains a persistent-mode superconducting solenoid magnet. The rotor is suspended and gimballed by the interaction of the fields produced by the superconductor and an array of cryoresistive ("hyperconducting") coils. The rotor spins in a liquid helium environment, while the control coils are liquid-hydrogen cooled. This design is only capable of meeting the requirements of many high-performance slewing applications (27,000 Nm). The use of the magnetic suspension as rotor bearings, gimbal bearings, and gimbal torquers also substantially reduces the mass of the CMG system.

MAGNETICALLY SUSPENDED CONTROL MOMENT GYROS (CMGs)



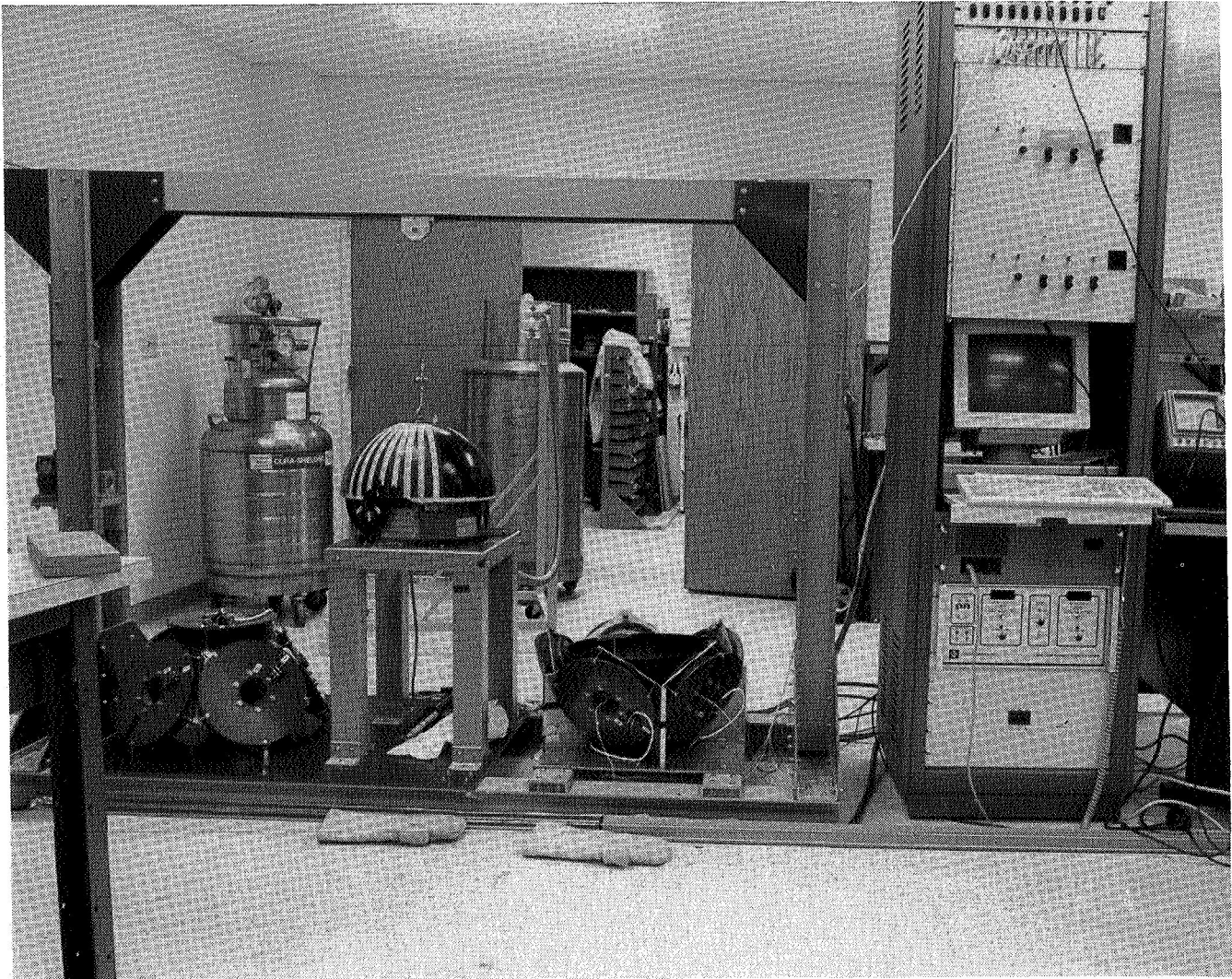
- o **Dual Use of Magnetic Suspension**
 - **Rotor bearing**
 - **Gimbal system**
- o **Advanced Magnetic Suspension**
 - **Superconducting magnet**
 - **"Hyperconducting" control coils**
- o **Eliminates Mechanical Gimbal Assemblies**

In order to demonstrate this technology, SatCon has developed a demonstration for the required control system technology required for the advanced-concept CMG. The demonstration is called a superconducting Large-Angle Magnetic Suspension (LAMS). The demonstration hardware consists of a suspended body which consists of a persistent-mode superconducting magnet and its associated dewar. The control coils used for suspension are air-core normal (non-superconducting) copper coils. An innovative combination of sensors is used to sense the position of the suspended body in five degrees-of-freedom. The controller was implemented on a digital signal processor.

SUPERCONDUCTING LARGE-ANGLE MAGNETIC SUSPENSION (LAMS)

- o Control System Demonstration**
- o Suspended Body:** **Superconducting Magnet & Dewar**
- o Suspension Hardware:** **Air-core Normal Coils**
- o Sensor system:**
 - Capacitive for translation**
 - Mutual induction (variometer) for rotation**
- o Controller:** **Digital Signal Processor**

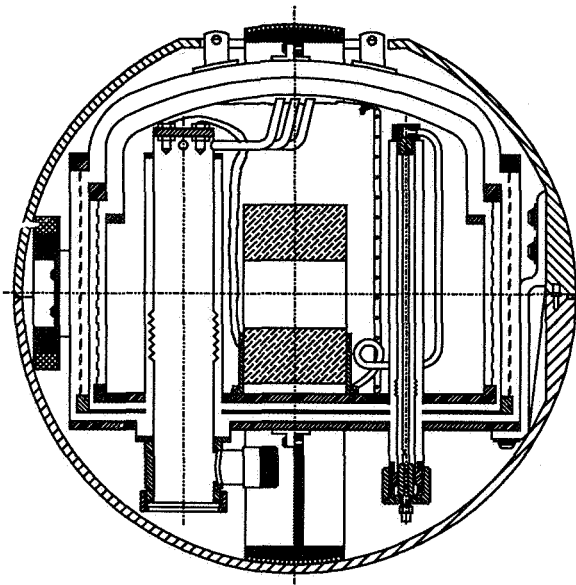
This photo shows the superconducting LAMS experiment. The hardware consists of the suspended body on its support stand, an array of twelve control coils mounted on two halves of a welded stainless steel support structure, and a crane-lift assembly which is used to move the parts of the system. A control console consists of the interface electronics for the sensors, power amplifiers for the control coils, control computer, and magnet power supply.



ORIGINAL PAGE
BLACK AND WHITE PHOTOGRAPH

The drawing at the left is a cut-away view which shows the internal arrangement of the components on the suspended body. The central feature is the superconducting solenoid magnet. This is a commercially available magnet of niobium titanium wire which produces a maximum bore field of 8.2 Tesla and is capable of operation in a persistent mode. The temperature of the magnet is maintained at 4.2 °K by a vacuum-insulated dewar which holds approximately 7 liters of liquid helium. The dewar is surrounded by a spherical shell of conductive plastic which acts as a target for the capacitive sensors which provide the translational position of the suspended body.

Superconducting Magnet and Dewar



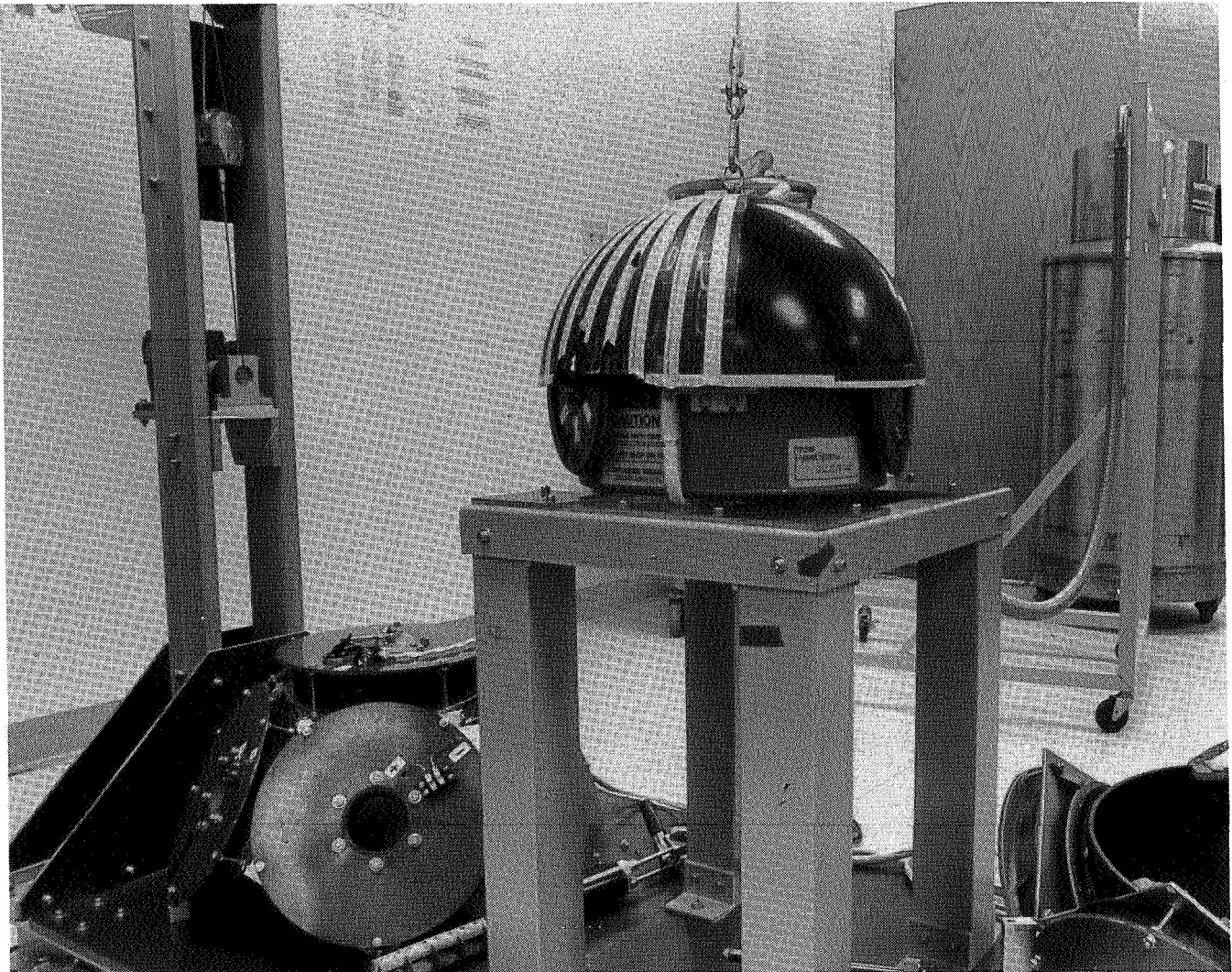
- o **Magnet:**

- **Material:** Niobium Titanium
- **Field:** 8.2 Tesla
- **Persistent mode operation**

- o **Dewar:**

- **Total weight:** Approx. 48 lbs.
- **Helium capacity:** 7 liters

This photo shows the suspended body on its support stand. The bottom half of the spherical shell has been removed for service (filling with liquid cryogen) and has been placed in the lower half of the control-coil support structure at the lower right corner of the photo. The upper half of the control-coil support structure and the current-lead assembly for the superconducting magnet are visible at the left-hand side of the photo.



ORIGINAL PAGE
BLACK AND WHITE PHOTOGRAPH

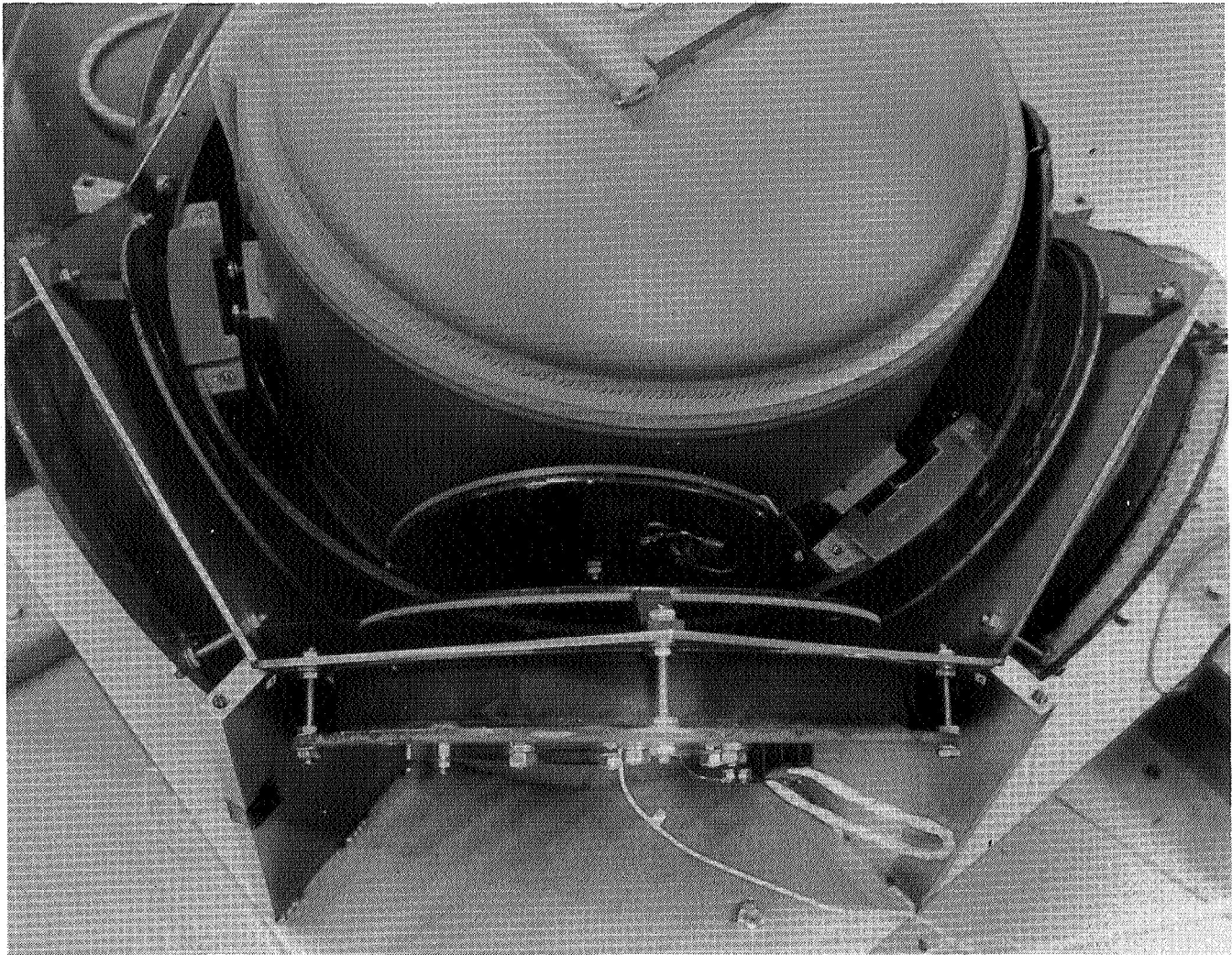
This photo shows the filling process for the dewar. A flexible transfer line is used to supply liquid into the cryostat. The photo shows liquid nitrogen being transferred. The liquid nitrogen is used to pre-cool the dewar to 77 °K. Pressurized gaseous helium is then used to purge the liquid nitrogen. The dewar is then filled, further cooled and filled with liquid helium.



ORIGINAL PAGE
BLACK AND WHITE PHOTOGRAPH

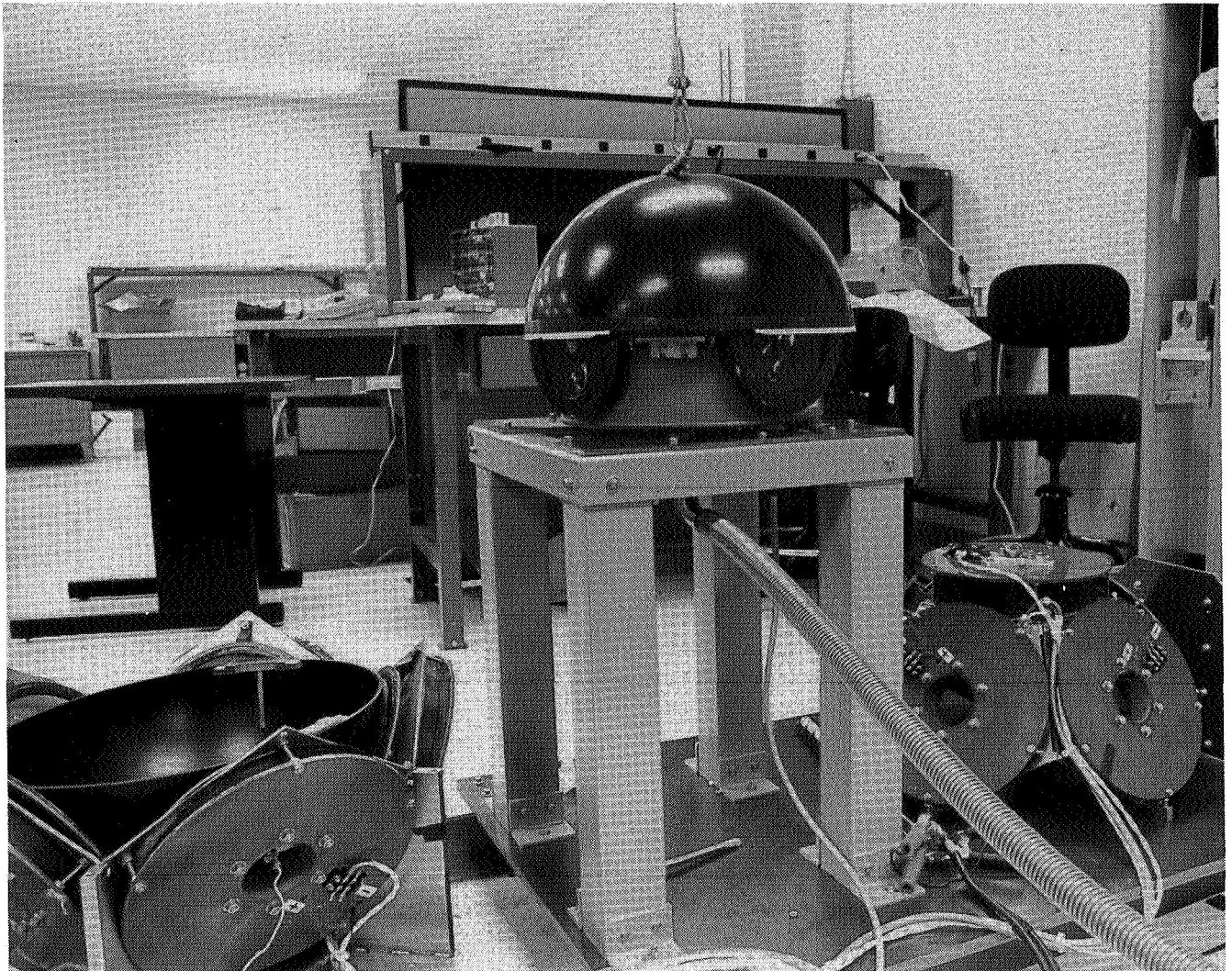
This photo shows the hardware for the position sensor systems. Leads for the capacitive translational sensor system are shown exiting from the bores of the control coils in the lower half of the control coil support structure.

The upper half of the spherical shell of the suspended body has been removed to show three coils which are attached to the dewar. An array of coils is also shown attached on the interior wall of the control-coil support structure. The ten stationary coils are driven with a high-frequency sinusoidal current and the voltage of each is monitored. The voltage is a measure of the mutual inductance of the rotating and stationary coils and therefore, also of their angular separation.



ORIGINAL PAGE
BLACK AND WHITE PHOTOGRAPH

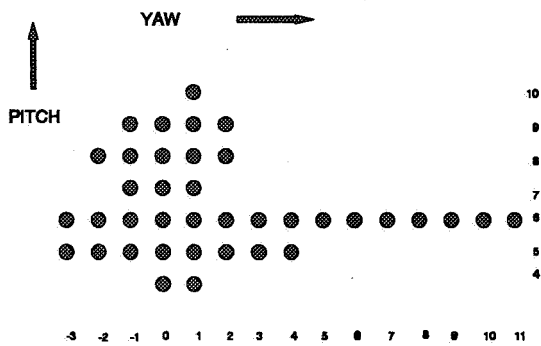
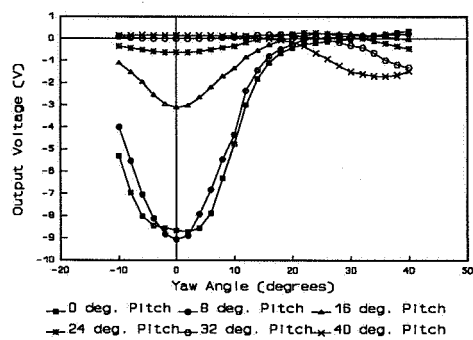
This photo shows more detail for the suspended-body portion of the rotation sensing system. There are three coils attached to the dewar on the suspended body. The terminals of these coils are shorted through capacitors to create a passive tuned inductor-capacitor system at the resonant frequency of the stationary transmitting coils. The stationary transmitting coils are similarly tuned to the excitation frequency.



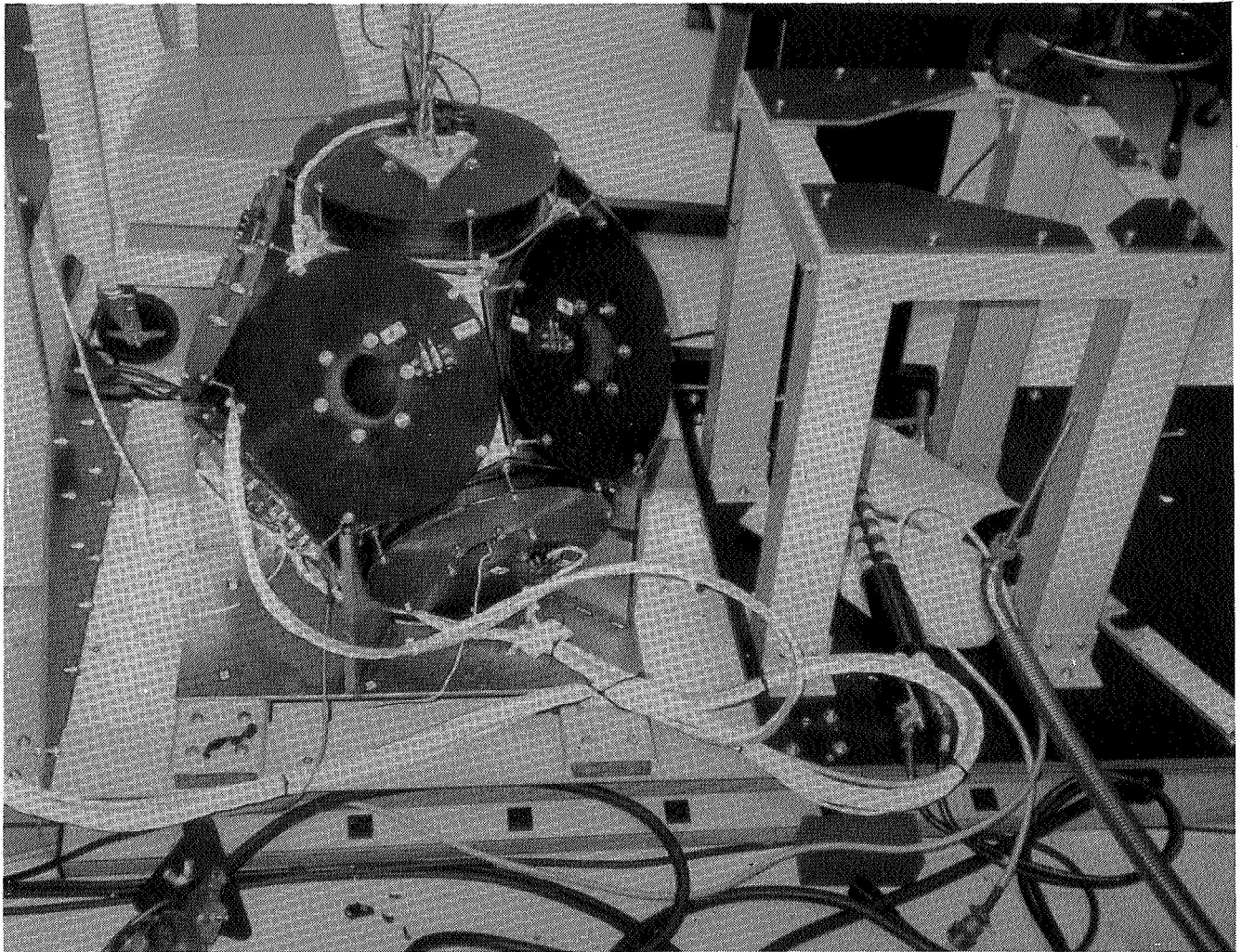
ORIGINAL PAGE
BLACK AND WHITE PHOTOGRAPH

This figure shows the output of the rotating sensor system and the resulting angular range. The figure at the left-hand-side is the voltage of one transmitting coil as a function of the relative yaw and pitch of a passive coil. The outputs of three transmitting coils were sampled and the pitch and yaw angles were inferred by an iterative algorithm implemented in the digital signal processor. The figure at the right-hand side shows the range over which the algorithm was stable. This indicates the allowable gimbaling range of the superconducting LAMS.

SENSOR SYSTEM OPERATION



This photo shows the assembled superconducting LAMS ready for test. The upper half of the control coil support structure has just been lowered via the crane and attached to the lower half. The dewar has sufficient helium storage capacity for a one hour experimental run.



ORIGINAL PAGE
BLACK AND WHITE PHOTOGRAPH

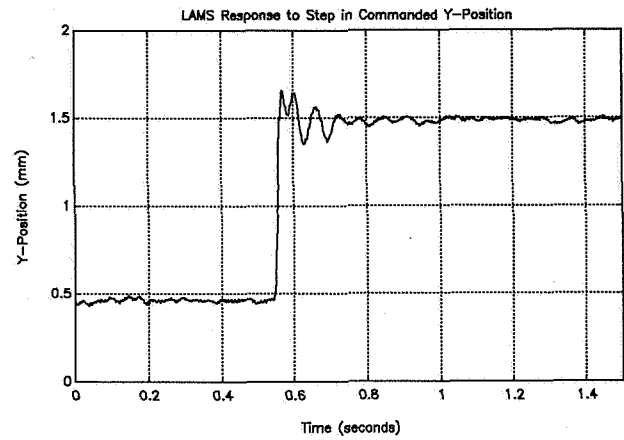
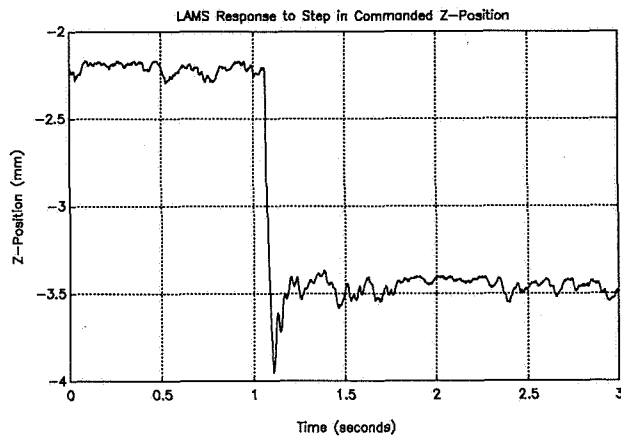
The control for the superconducting LAMS was done in a reference frame which was fixed with respect to the solenoid. This allowed the controller to be implemented as five single-input-single-output lead-lag compensators. The controller acted as a regulator for the translational position of the suspended body. Two of the three available analog inputs were used to provide command signals for the rotational control loops. There were four analog outputs available for troubleshooting of the controller during development. The vertical position of the suspended body was regulated to a reference position which was provided by the user via the keyboard.

Five Degree-Of-Freedom Suspension

- o Simple Lead Lag Controller**
- o Regulation around nominal center position**
- o 3 Auxillary Analog inputs**
- o 4 Auxillary Analog outputs**
- o Vertical reference input via keyboard**

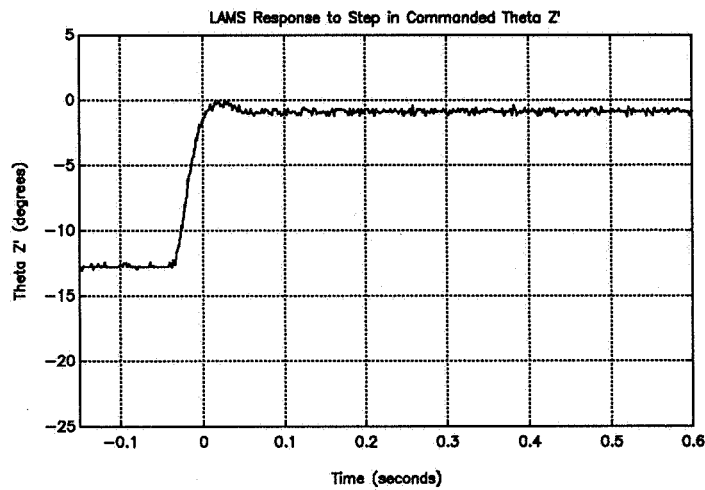
These figures show the transient responses of the translational controllers. The figure at the left shows the result of a commanded downward step in the vertical position (height) of the suspended body. The figure at the right is the response to a commanded step along one of the horizontal axes.

Performance of Superconducting LAMS Translational Controllers



This figure shows the response of the superconducting LAMS to a commanded step change in one of the rotational degrees-of-freedom. This particular angle is the yaw angle. This demonstrates the capability of using the superconducting LAMS as a replacement for a mechanical gimbal system.

Performance of Superconducting LAMS Rotational Controllers



The superconducting LAMS demonstration experiment was performed for the NASA Langley Research Center under Small Business Innovation Research (SBIR) funding. The first phase was an analytical study during which SatCon developed the analytical tools necessary to design the full-scale CMG system and finalize the design requirements. The performance of the full-scale system was also estimated. The demonstration experiment was identified during Phase I and carried out during Phase II. This experiment, which was described in this paper demonstrated the control system technology necessary to simultaneously suspend and gimbal a persistent-mode superconducting magnet and its associated dewar.

SATCON SUPERCONDUCTING LAMS SBIR PROGRAM

o Phase I:

- Developed analytical tools**
- Developed CMG design**
- Estimated performance**
- Identified technology demonstration experiment**

o Phase II:

- Demonstrated LAMS control system for suspension and gimbaling**
- Suspended and gimballed commercially-available superconducting magnet and associated dewar**

N92-27816

THE LARGE-ANGLE MAGNETIC SUSPENSION TEST FIXTURE

Colin P. Britcher, Mehran Ghofrani

Department of Mechanical Engineering and Mechanics, Old Dominion University

Thomas C. Britton

Lockheed Engineering and Sciences Company

Nelson J. Groom

Spacecraft Controls Branch, NASA Langley Research Center

INTRODUCTION

As part of a NASA effort to develop the technology and techniques required to demonstrate the magnetic suspension of objects over wide ranges of attitudes, a small-scale demonstration project has been undertaken. The objectives here are to suspend a cylindrical element containing a permanent magnet core, to demonstrate stability and control in five degrees-of-freedom, and to permit controlled rotation of the model in one degree-of-freedom over the full range of 360 degrees. Further constraints are that all suspension and control electromagnets are to be behind a flat plane, located some distance from the model. Since this is a ground-based experiment and in order to maintain generality, the plane is chosen to be horizontal with the model levitated above the plane by repulsive forces.

Potential applications for large-gap magnetic suspension systems capable of controlled excursions through large angular ranges include the manipulation and pointing of space payloads, microgravity vibration isolation and the suspension of models in wind tunnels. Indeed, controlled suspension of a model through an angular (angle-of-attack) range of around 100° has already been demonstrated in a wind tunnel system [1].

Design studies for a hypothetical large-scale system were undertaken in 1987-88 [2,3,4]. The specifications for this system required that a model be "levitated" above a clear floor surface and be capable of being oriented arbitrarily in azimuth. The air-gap (between model and electromagnets) was very large, around 1 meter. Several approaches were examined, with all studies concluding that such a device was feasible, at least insofar as electromagnets of appropriate size were within current technological limits. The most promising of these early concepts appeared to be the arrangement of several electromagnets in a flat or "planar" array, a configuration studied by several groups. Madison Magnetics Incorporated (MMI) [4] suggested a geometry refined to a circular quasi-axisymmetric arrangement of five electromagnets, since the principal model rotation

required was about the vertical axis (the axis of the circular array) and it is clear that a minimum of five electromagnets are required for control in five degrees-of-freedom.

The principal uncertainty in this design was the control of the model, particularly over the wide range of orientation. A suspension system of this particular type had not been attempted before, since various design features were quite unusual :

- i) "Levitation" entirely by repulsive forces (attractive forces usually employed).
- ii) No attempt to "decouple" electromagnets (normally the electromagnet configuration is developed so as to provide at least some natural decoupling between degrees-of-freedom).

It was therefore decided to proceed with design and construction of a small-scale proof-of-concept demonstration system, in order to verify the feasibility of this design approach and to permit control system development. It was decided to follow the MMI design in general layout, but with a levitation height (air gap between electromagnets and model) reduced to 0.1 meters. This configuration is illustrated in Figure 1.

HARDWARE DESCRIPTION

An array of five, room temperature, copper electromagnets are distributed evenly on a 13.77 cm radius. The coils are wound with 509 turns of AWG 10 enamelled copper wire on bakelite forms, with iron cores. There is no provision for active cooling, it being felt that operation of the LAMSTF would be rather intermittent in nature. The design maximum steady-state current is around 15 Amperes (Coil 1), limited by the coil temperature rise. At 15 Amps, the temperature rise is around 1.5°C/minute, giving perhaps 30 minutes useful run-time. Temperature sensors with over-temperature alarms and power cut-outs are also fitted. The electromagnets are mounted on a heavy aluminum plate 1.27 cm (0.5 inches) thick. The electromagnet assembly is illustrated in Figure 2.

The suspended element consists of 16 wafers, 0.3135 cm long (0.1235 inches) and 0.7963 cm diameter (0.3135 inches) of Neodymium-Iron-Boron (Nd-Fe-B) permanent magnet material epoxied into an aluminum tube, 5.32 cm long (2.095 inches) and 0.9525 cm (0.375 inches) outside diameter. The estimated magnet mass is 20.03 grams (by subtracting the alloy tube weight from the total). The total model mass is 22.5 grams. The moment of inertia about the transverse axis was measured with a bifilar pendulum technique and found to be $5.508 \times 10^{-6} \text{ kg.m}^2$.

The position sensing system follows traditional wind tunnel MSBS practice of multiple light beams partially interrupted by the model. The beams are arranged in two orthogonal planes (vertical and horizontal) in this case. The light sources are miniature infra-red light-emitting

diodes, intended for use with fiber-optics. The light receivers are matching infra-red phototransistors. Due to the beam dispersion of around 20 degrees (included cone angle) from the transmitter, miniature plano-convex collimating lenses (6 mm diameter and 12 mm focal length) were added to both transmitter and receiver, primarily in order to increase the signal level at the receiver. Also, some care was taken to shield and screen the light path. The complete sensor system is mounted on a framework which is initially fixed in one orientation relative to the suspension electromagnets. However, the design permits rotation of the framework about a vertical axis, either manually, or by some form of motor drive to be added later. A schematic diagram of the assembly is shown in Figure 3, and the installation of the sensors on the electromagnet array is shown in Figure 4.

To facilitate early comissioning of the LAMSTF system, an analog controller was constructed, again following traditional wind tunnel MSBS practice. Position sensor signals are summed-and-differenced, where appropriate, to derive motion signals in the five model degrees of freedom required, that is: axial, lateral, and vertical translation and pitch and yaw rotations. Each signal passes through conventional, dual, series phase-advance compensators. A marked departure from previous controllers is the incorporation of extensive decoupling at the output of the controller, discussed more fully later. A block diagram of the controller and outlines of the circuitry employed is shown in Figure 5. An important difficulty to be overcome by the controller is stabilization of the three unstable modes of motion, found in this type of suspension system [5], illustrated in Figure 6. The most important modes are the so-called "compass needle" modes, where the model is attempting to reverse its direction in the axial component of applied field. The natural frequency is quite high in this application, around 10 Hz. The controller must overcome this instability and provide the appropriate stiffness and damping.

Each electromagnet is driven by a transistor switching power amplifier, rated at $\pm 150\text{V}$ and $\pm 30\text{A}$ continuous, up to 60A peak with full four-quadrant operation. The switching frequency is 22kHz. Six amplifiers, with associated D.C. power supplies and control electronics are installed as shown in Figure 7.

HARDWARE PERFORMANCE

Each electromagnet has a resistance of around $0.74\ \Omega$, not including connecting leads, and an inductance of around 27.5 mH, with iron cores present. Mutual inductances are estimated at 1.6 mH and 0.37 mH, adjacent and non-adjacent electromagnets respectively. There is some uncertainty and ambiguity in the inductance values, due to eddy current effects discussed below.

If flux from an electromagnet penetrates a conducting medium, eddy currents will be

generated in that medium when the current in the electromagnet is varied. This is of some concern in magnetic suspension applications since control of the suspended or levitated object is generally maintained by constant adjustment of the electromagnet currents. If eddy currents are generated during these adjustments, then the rate of change of field at the model (corresponding to the rate of application of forces and moments) might be reduced, or subject to a phase lag. The mounting of the five LAMSTF electromagnets on a heavy aluminum plate was intended to permit a full assessment of the effects of eddy currents on suspension stability.

Following a simplified approach, wherein the eddy current circuit is supposed to be invariant with excitation frequency, it can be shown that the terminal characteristics of the electromagnet will be as follows :

$$V = I \left(\frac{R + (L + \frac{R}{R_e} L_e) s + (\frac{L L_e - L_m^2}{R_e}) s^2}{1 + \frac{L_e}{R_e} s} \right) \quad - (1)$$

where R_e , L_e are the resistance and inductance of the eddy current circuit and L_m is the mutual inductance between primary (electromagnet coil) and secondary. Continuing, the field components generated (at the suspended object) can be expressed as

$$B = I \left(k + \frac{k_e L_m s}{R_e + L_e s} \right) \quad - (2)$$

where k , k_e are constants representing the field generated at the suspension location by the electromagnet and the eddy current respectively. The break frequency is clearly the inverse of the time constant of the eddy current circuit. It is argued in this application that the factors k_e , L_e/R_e and L_m can be estimated by geometrical analysis and by careful measurements of electromagnet terminal characteristics. An obvious objection to this representation is the fact that the penetration depth (skin depth) of eddy currents will decrease with increasing frequency, leading to changes in eddy current circuit resistance and so forth. However, the frequencies of interest in this application are quite low, so that this effect will be small.

Measurements of the terminal characteristics of a LAMSTF coil are summarized in Figure 8, with typical results of calculations based on Equation (1). Careful comparison reveals a significant phase defect from ideal, centered around the natural frequency of the eddy current circuit. The actual electromagnets show two separate defects, one at a relatively low frequency, related to currents in the alloy plate, and another at a much higher frequency, due to the (unlaminated) iron core.

The magnetic field generated by each electromagnet has been calculated using the computer program VF/GFUN. This uses an integral equation formulation, only requiring discretization of the iron regions in a problem. Some field measurements have been made to validate the computations, with acceptable overall agreement. The set of field and field gradient components generated at the model centroid have been calculated and are presented in Table A below. It should be noted that these values are for a single isolated coil and core. There is some evidence of magnetization of adjacent cores, resulting in small distortions of these fields.

TABLE A - Computed field and field gradients from a single coil
(1 Amp, Tesla and Tesla/meter $\times 10^{-6}$)

Coil#	B _x	B _y	B _z	B _{xx}	B _{xy}	B _{xz}
1	240.9	0	-106.3	2118.2	0	-2852.7
2	74.4	229.1	-106.3	-1289.4	1107.2	-881.5
3	-194.9	141.6	-106.3	816.6	-1791.5	2307.9
4	-194.9	-141.6	-106.3	816.6	1791.5	2307.9
5	74.4	-229.1	-106.3	-1289.4	-1107.2	-881.5

Following Reference 6, and restricting the model orientation to the datum, torques and forces are related to applied fields and gradients in the following way :

$$\begin{bmatrix} T_y \\ T_z \\ F_x \\ F_y \\ F_z \end{bmatrix} = \text{Vol } M_{\bar{x}} \begin{bmatrix} -B_{z1} & -B_{z2} & -B_{z3} & -B_{z4} & -B_{z5} \\ B_{y1} & \ddots & & & \\ B_{xx1} & & \ddots & & \\ B_{xy1} & & & \ddots & \\ B_{xz1} & & & & \ddots \end{bmatrix} \begin{bmatrix} I_1 \\ \\ \\ I_5 \end{bmatrix} \quad - (3)$$

The coefficients B_{z1} etc., are as given in Table A. By setting each element of the left-hand side vector to a non-zero value in turn, with all other values zero, the required current distributions to generate each force or moment component indepedently can be deduced from the normalized current vectors resulting.

$$\begin{bmatrix} I_1 \\ I_2 \\ I_3 \\ I_4 \\ I_5 \end{bmatrix} = \begin{bmatrix} 0.625 & 0 & 1 & 0 & 1 \\ 1 & 1 & -0.809 & 0.618 & 0.309 \\ 0.768 & 0.618 & 0.309 & 1 & -0.809 \\ 0.768 & -0.618 & 0.309 & 1 & -0.809 \\ 1 & -1 & -0.809 & -0.618 & 0.309 \end{bmatrix} \begin{bmatrix} T_{y \text{ demand}} \\ T_{z \text{ demand}} \\ F_{x \text{ demand}} \\ F_{y \text{ demand}} \\ F_{z \text{ demand}} \end{bmatrix} \quad - (4)$$

By use of this demand allocation matrix, the control system is statically decoupled into model degrees of freedom. There are still dynamic couplings, due to the natural modes of motion, as discussed in [5], chiefly a coupling from axial motion into pitch. The supposition is, of course, that if these couplings are weak enough they simply appear as disturbances to the relevant degrees-of-freedom of the controller. The demand allocation matrix is implemented by the the circuitry illustrated in Figure 5, by appropriate selection or setting of input resistors to the summers.

Using best estimates of model mass, core volume and magnetization, the equilibrium levitation currents can also be found :

$$\text{Vol} = 2.498 \times 10^{-6} \text{ m}^3; \quad M_{\bar{x}} = 955,000 \text{ A/m (1.2 Tesla);} \quad F_z = 0.221 \text{ N}$$

The required B_{xz} is found to be 0.0926 T/m. Directly from Equation 4, the equilibrium suspension currents should therefore be

$$(I_1, I_2, I_3, I_4, I_5) = (-12.984, -4.012, 10.504, 10.504, -4.012)$$

Preliminary suspension tests, such as shown in Figure 9, have shown currents of

$$(I_1, I_2, I_3, I_4, I_5) = (-15.5, -5.9, 12.4, 12.1, -5.9)$$

- which is reasonable agreement, considering the large number of estimated or computed values involved.

DIGITAL CONTROLLER

The analog controller was only intended to permit demonstration of suspension, preliminary operation, and hardware checkout and characterization. Due to the variation of coupling coefficients (equations 3,4) with yaw orientation, a digital controller with adaptive decoupling is essential for demonstration of 360° yaw rotation. The calculation and adaptation will follow the procedures outlined in References 5,7.

The control approach being followed is based on Linear Quadratic Gaussian (LQG) control theory. A Kalman filter is used to provide state estimates (position, orientation and corresponding rates) for input to an Integral Feedback Regulator. Feedback gain matrices have been obtained from a discrete-time simulation of the controller, which has been developed using Matrix_x/SystemBuild. This control synthesis approach follows work contained in Reference 7. The hardware configuration, illustrated in Figure 10, consists of a data acquisition system, hosted by a PC-XT class controller, communicating with 68020/68881 computer through dual-port RAM. The A/D and D/A converters are all 12-bit types, communicating with the LAMSTF hardware through current-loop interfaces. Control hardware is presently complete and software is nearing completion. The digital controller will be installed immediately upon completion.

ACKNOWLEDGEMENTS

This work was partially supported by NASA Grant NAG-1-1056, Technical Monitor, Nelson J. Groom.

REFERENCES

1. Parker, D.H.: Techniques for Extreme Attitude Suspension of a Wind Tunnel Model in a Magnetic Suspension and Balance System. NASA CR-181895, October 1989.
2. Groom, N.J.: Description of the Large-Gap Magnetic Suspension System (LGMSS) Ground-Based Experiment. Technology 2000. NASA CP-3109, Vol.2, pp.365-377, March 1991.
3. Britcher, C.P.: Technical Background for a Magnetic Levitation System. NASA CR-178301, May 1987.
4. Boom, R.W.; Abdelsalam, M.K.; Eyssa, Y.M.; McIntosh, G.E.: Repulsive Force Support System Feasibility Study. NASA CR-178400, October 1987.
5. Groom, N.J.; Britcher, C.P.: Stability Considerations for Magnetic Suspension Systems using Electromagnets Mounted in a Planar Array. NASA CP-10066, Vol.1, pp.355-376, March 1991.
6. Groom, N.J.: Analytical Model of a Five Degree of Freedom Magnetic Suspension and Positioning System. NASA TM-100671, March 1989.
7. Groom, N.J.; Schaffner, P.R.: An LQR Controller Design Approach for Large-Gap Magnetic Suspension Systems (LGMSS). NASA TM-101606, July 1990.

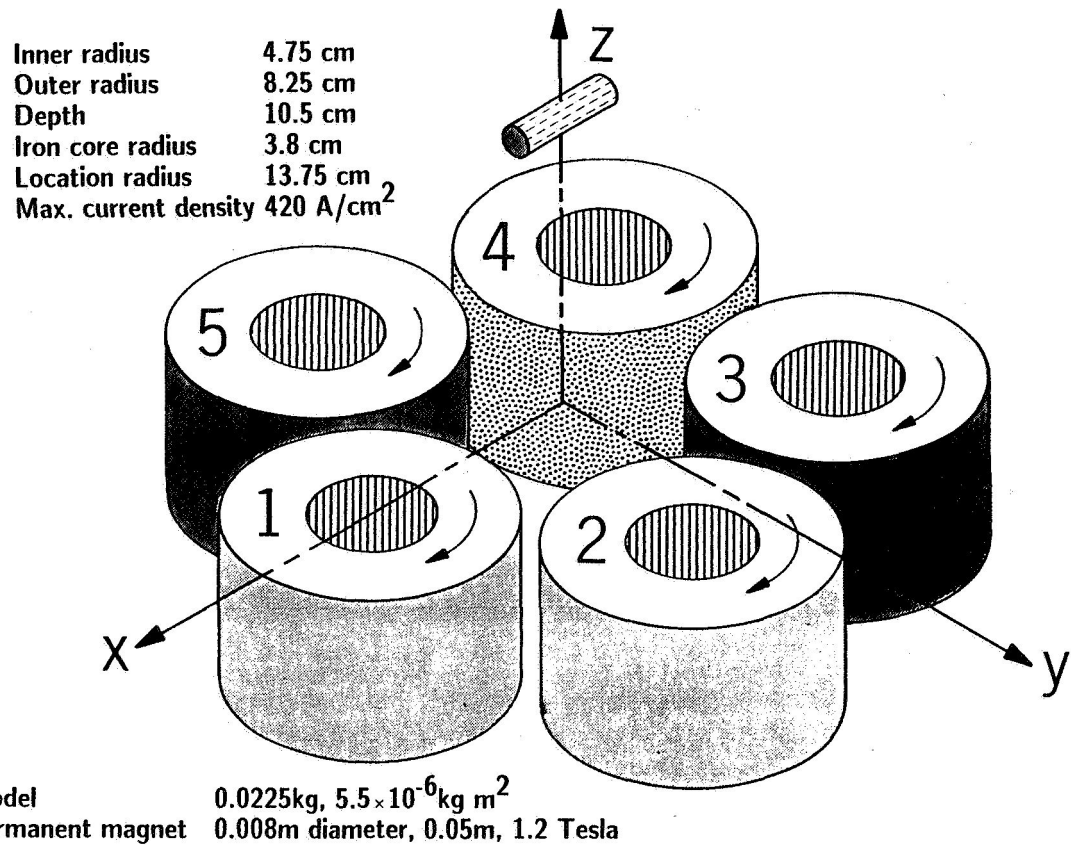


Figure 1 - Large-Angle Magnetic Suspension Test Fixture (LAMSTF) Configuration

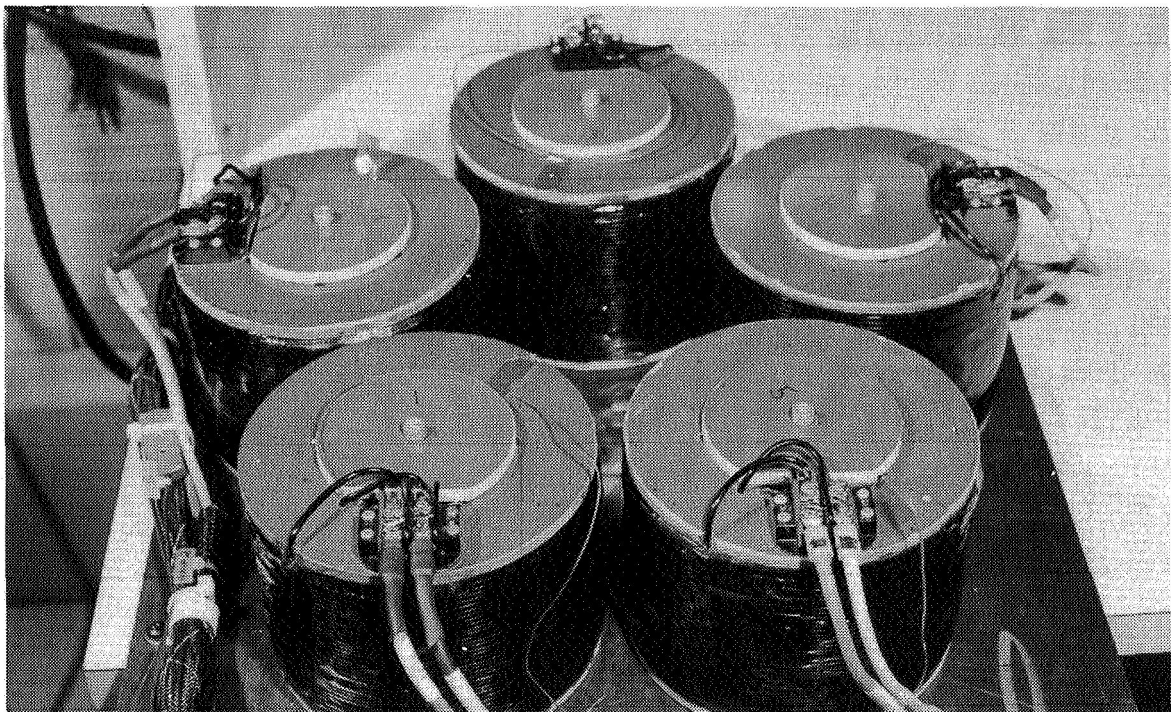


Figure 2 - LAMSTF Electromagnet Assembly

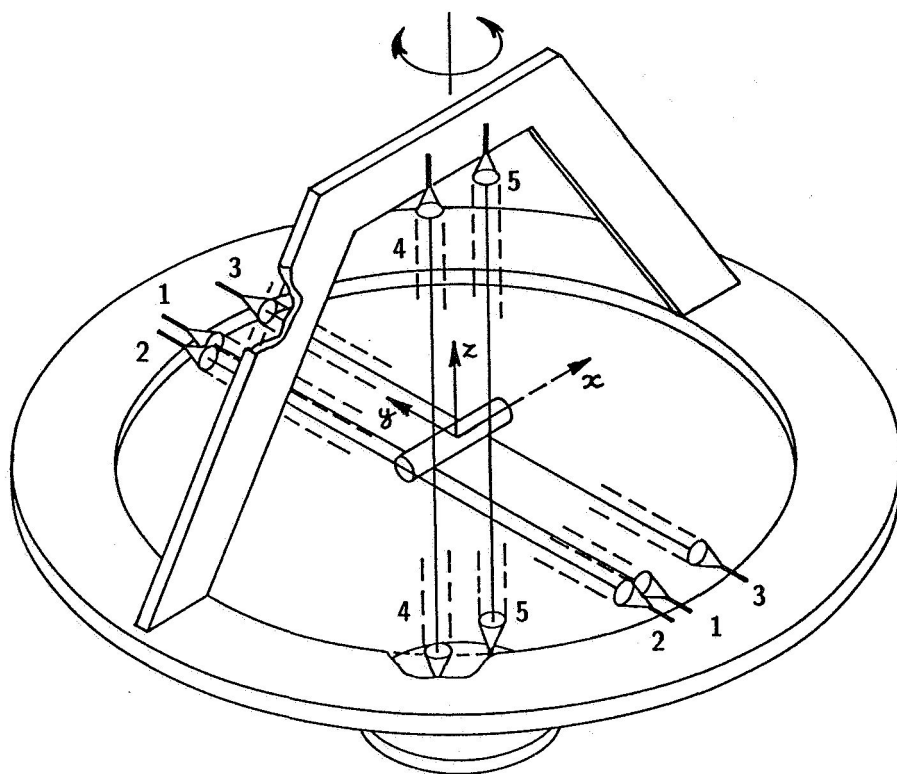


Figure 3 - Sensing System Schematic

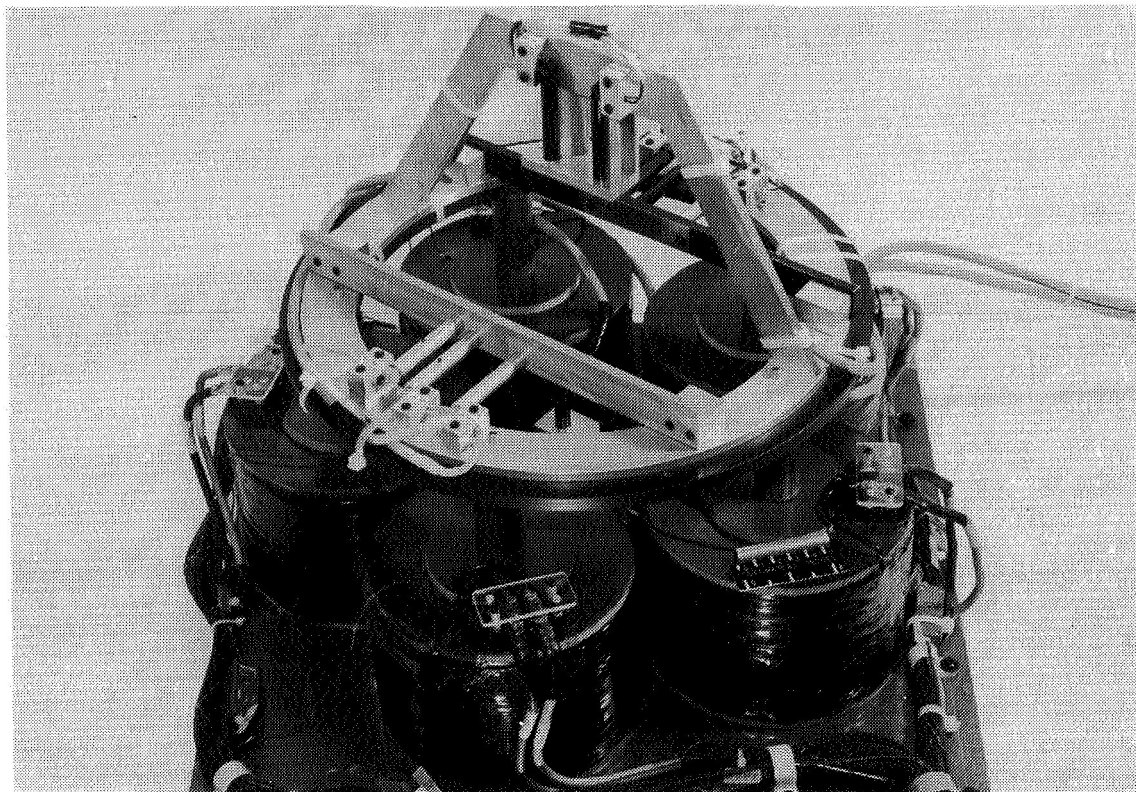


Figure 4 - Sensing System Installed on Electromagnet Assembly

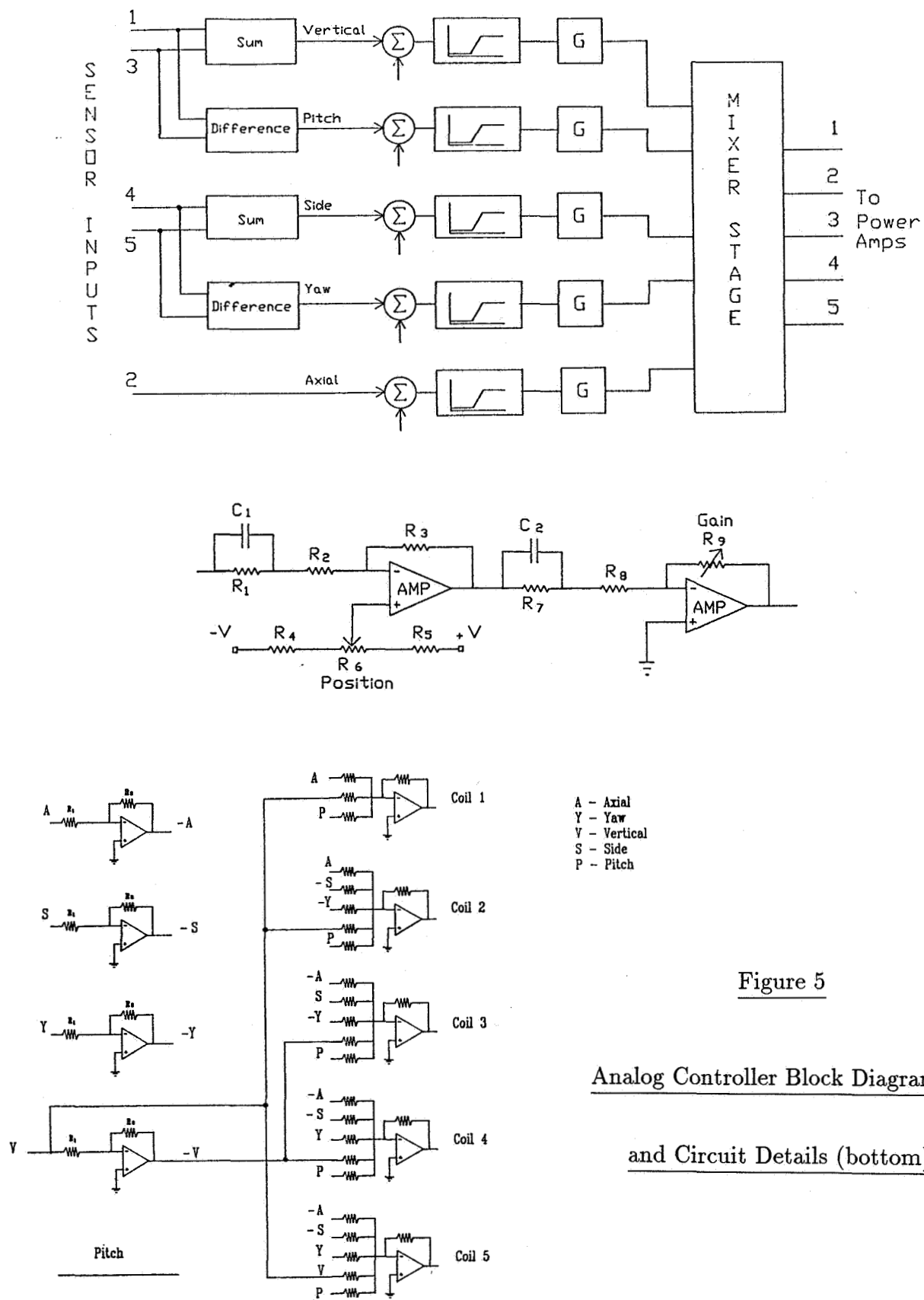


Figure 5

Analog Controller Block Diagram (top)

and Circuit Details (bottom)

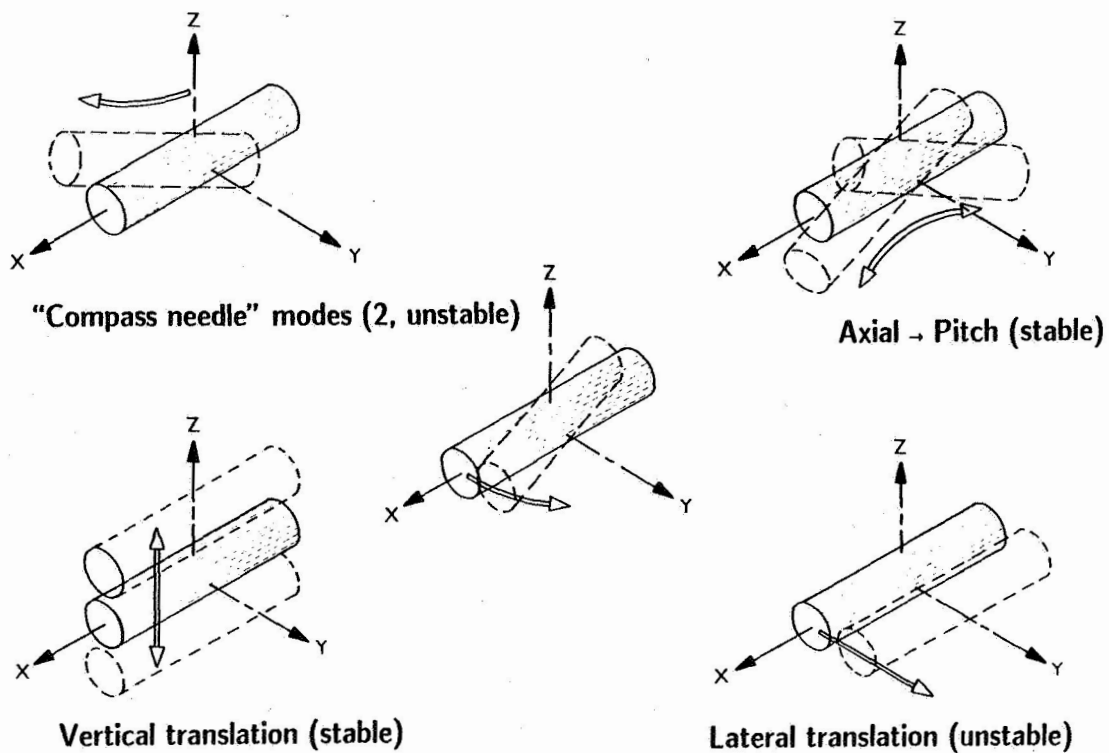


Figure 6 - Natural Modes of Suspended Element

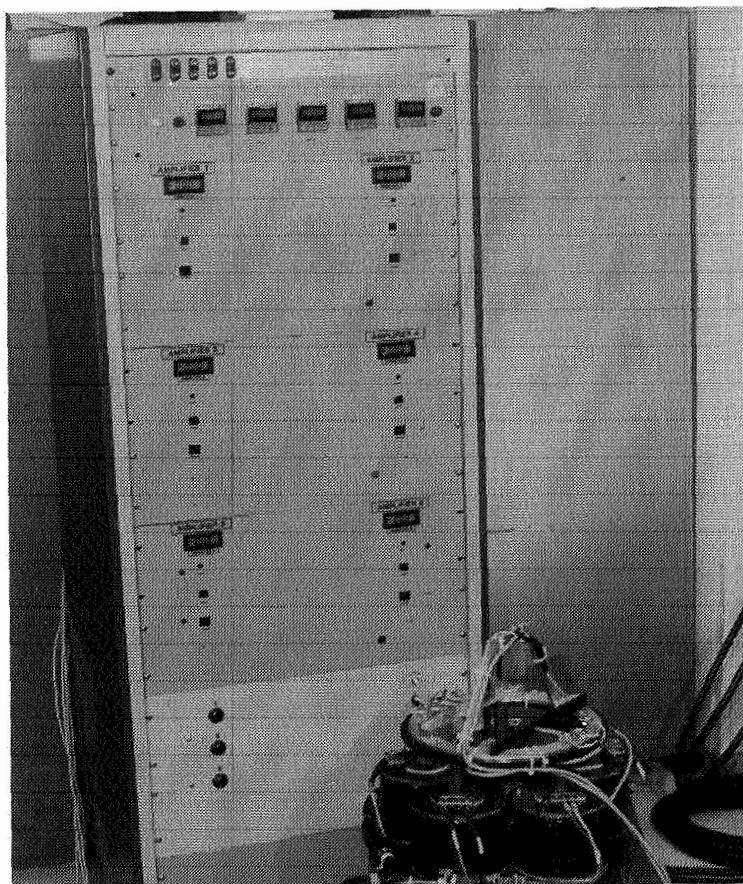


Figure 7 - LAMSTF Power

Supply Assembly

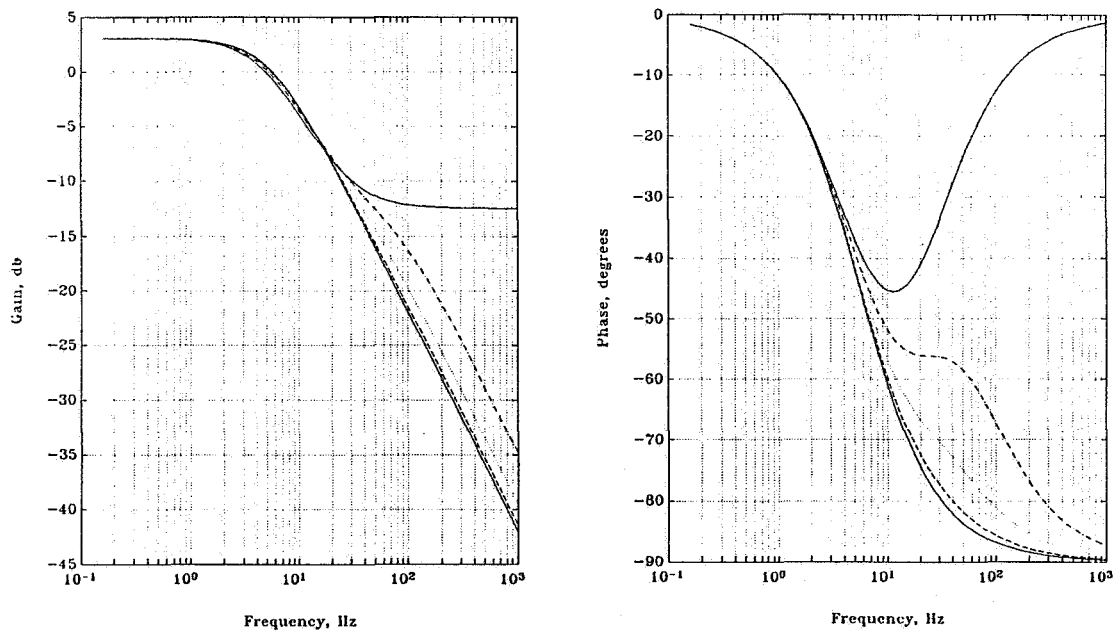
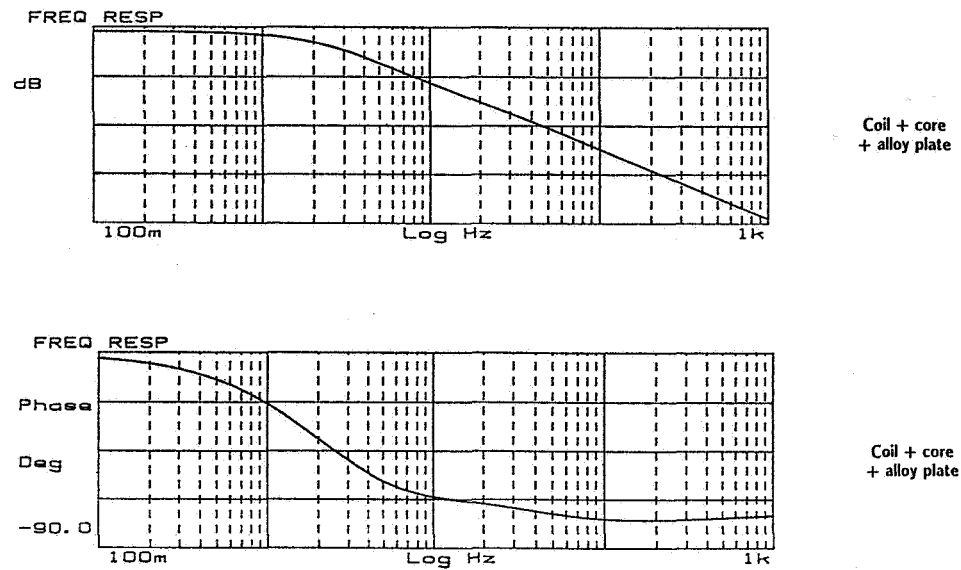


Figure 8 - Coil Terminal Characteristics
 LAMSTF coil (top) and single time-constant model (bottom, using Equation 1)

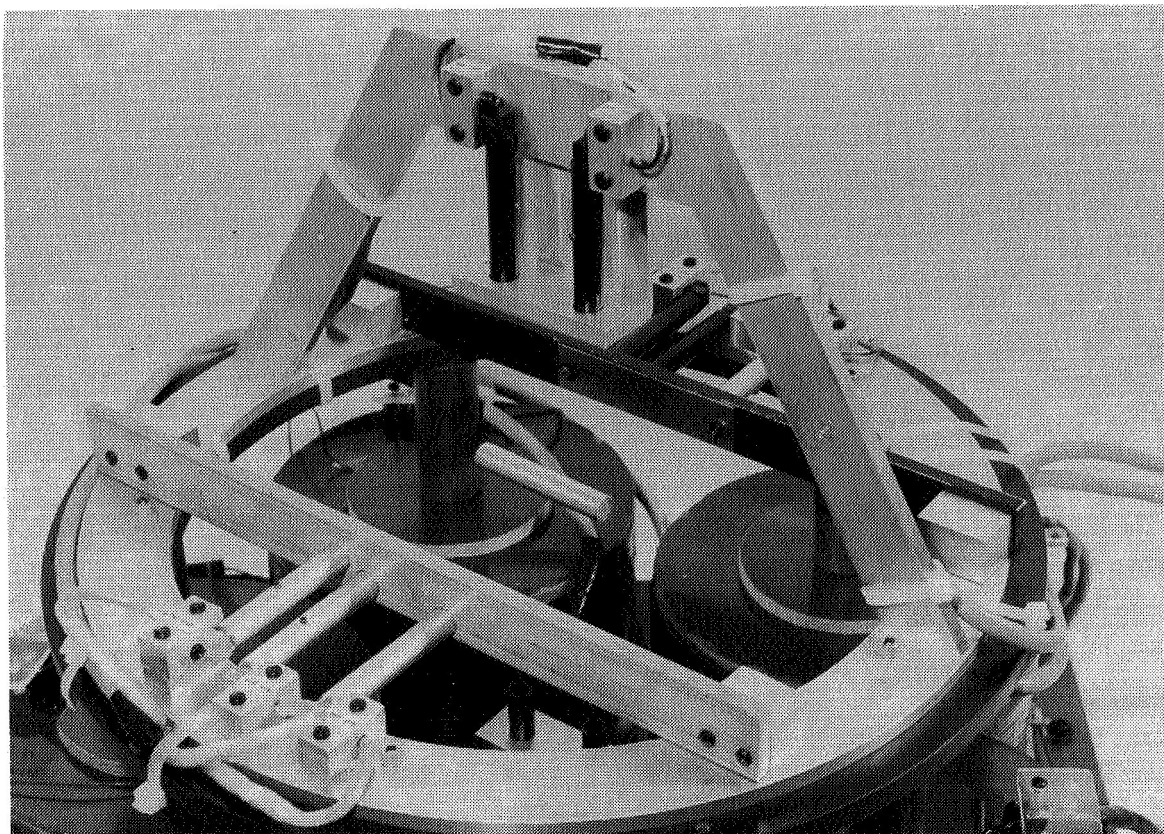


Figure 9 - LAMSTF Operating with Analog Controller

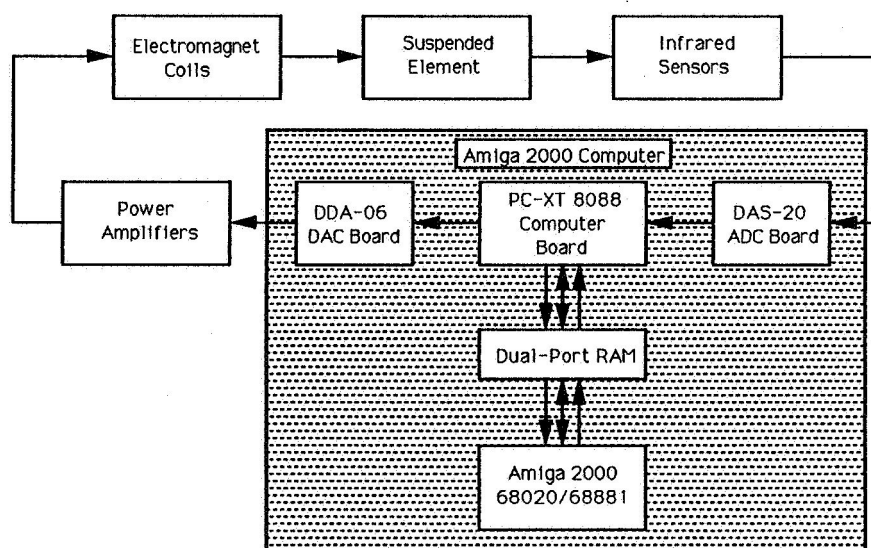


Figure 10 - Digital Controller Block Diagram

ATTENDEES

Alcorn Charles W. Alcorn
Phone: 804-683-3720
Old Dominion University
Dept. of Mechanical Engineering
Norfolk VA 23529-0247

Allan A. P. Allan
Phone: 804-924-6233
University of Virginia
Department of Mech. and Aero. Engrg.
Charlottesville VA 22903

Banerjee Bibhuti Banerjee
Phone: 804-924-6233
University of Virginia
ROMAC Labs, Mech & Aero Engrg.
Thornton Hall, McCormick Road
Charlottesville VA 22903

Batterson James G. Batterson
Phone: 804-864-4059
NASA Langley Research Center
Mail Stop 161
Hampton VA 23665-5225

Bichsel J. Bichsel
Phone: 1-256-51-19
Eidgenossische Technische Hochschule
Institut für Elektrotechnische
Entwicklungen, ETH Zentrum/ETZ F
CH-8092 Zurich
SWITZERLAND

Boehm Josef Boehm
Phone: 061-745 5000
University of Salford
Physics Department, The Crescent
Salford M5 4WT
UNITED KINGDOM

Allaire Paul E. Allaire
Phone: 804-924-3292
University of Virginia
Mechanical Engineering Department
Thornton Hall McCormick Road
Charlottesville VA 22903

Anderson Willard W. Anderson
Phone: 804-864-1718
NASA Langley Research Center
Mail Stop 479
Hampton VA 23665-5225

Barrett Lloyd Barrett
Phone: (804) 924-6210
Univ. of Virginia
Dept. of Mech. and Aero.
Engrg.
Charlottesville VA 22903

Bernhardt Helmut Bernhardt
Phone:
Nebenstrasse 2B
D-W-6330
Wetzlar 22
GERMANY

Boden K. Boden
Phone: 02461-614604
Kernforschungsanlage Julich GmbH
Abteilung IGV
Postfach 1913
D-5170 Julich
GERMANY

Bondarenko Herman A. Bondarenko
Phone: 06452-4-38-46
The Sumy Frunze Machine Building
Science and Production Amalgamation
G. Kursky Avenue
Sumy 244609
U.S.S.R.

Briggs B. M. Briggs
Phone: 206-657-3735
Boeing Aerospace and Electronics
P. O. Box 3999
M/S 3C-PC
Seattle WA 98124

Britton Thomas C. Britton
Phone: 804-864-6619
Lockheed Engr. & Sciences Co.
NASA Langley Research Center
Mail Stop 161
Hampton VA 23665-5225

Castleman Bruce W. Castleman
Phone: 813-539-5708
Honeywell Inc.
Mail Station 350-1
13350 U.S. Highway 19 South
Clearwater FL 34624-7290

Cope David B. Cope
Phone: 617-890-3200
Foster-Miller Inc.
350 Second Avenue
Building 1
Waltham MA 02154-1196

Davis Harold Davis
Phone: 604-822-2961
The University of British Columbia
Department of Physics
6224 Agricultural Road
Vancouver, B.C. V6T 1Z1
CANADA

Derrickson G. Stephan Derrickson
Phone: 719-633-8333
The Spectranetics Corp.
96 Talamine Court
Colorado Springs CO 80907

Britcher Colin P. Britcher
Phone: 804-683-3720
Old Dominion University
Dept. of Mech. Engg.
Norfolk VA 23529-0247

Burrows Clifford R. Burrows
Phone: 0225 826935
University of Bath
School of Mechanical Engineering
Claverton Down
Bath BA2 7AY
ENGLAND

Chu Wei-Kan Chu
Phone: 713-743-8250
Texas Center for Superconductivity
University of Houston
4800 Calhoun
Houston TX 77004-5506

Daniels Taumi S. Daniels
Phone: 804-864-4659
NASA Langley Research Center
Mail Stop 238
Hampton VA 23665-5225

de Rochemont L. P. de Rochemont
Phone: 617-926-1167
Radiation Monitoring Devices, Inc.
44 Hunt Street
Watertown MA 02172

Dhar Debasish Dhar
Phone: 804-924-3291
University of Virginia
ROMAC Labs, Mech & Aero Egnrg
Thornton Hall, McCormick Road
Charlottesville VA 22903

Doederlein Ted A. Doederlein
Phone: 805-275-5483
Phillips Laboratory
OLAC PL/STSS
Edwards CA 93523-5000

Downer James R. Downer
Phone: 617-661-0540, X203
SatCon Technology Corporation
12 Emily Street
Cambridge MA 02142

Dress David Dress
Phone: 804-864-5126
NASA Langley Research Center
Mail Stop 287
Hampton VA 23665-5225

Dutton Jeffrey L. Dutton
Phone: 804-688-3807
Newport News Shipbuilding
4101 Washington Avenue
Dept. E55
Newport News VA 23607

Eisenhaure David B. Eisenhaure
Phone: 617-661-0540
SatCon Technology Corporation
12 Emily Street
Cambridge MA 02139-4507

Fenn Ralph Fenn
Phone: 617-661-0540
SatCon Technology Corporation
12 Emily Street
Cambridge MA 02139

Forbes David A. Forbes
Phone: 804-688-7954
Newport News Shipbuilding
4101 Washington Avenue
Dept. E55
Newport News VA 23607

Foucault Jean-Pierre Foucault
Phone: 14-65-71-160
ONERA
29 Avenue De La Division Leclerc
Chatillon 92320
FRANCE

Gaffney Monique Gaffney
Phone: 617-661-0540
SatCon Technology Corporation
12 Emily Street
Cambridge MA 02139

Garbutt Keith S. Garbutt
Phone: 703 595000, X3384
University of Southampton
Department of Aeronautics
Southampton, Hants S09 5NH
UNITED KINGDOM

Gavrilov Victor P. Gavrilov
Phone: 06452-2-55-80
Severodonetsk Manuf. Assoc. "AZOT"
5, Chimikov
Severodonetsk 349940
U.S.S.R.

Ghofrani Mehran Ghofrani
Phone: 804-683-3720
Old Dominion University
Dept. of Mechanical Engineering
Norfolk VA 23529-0247

Girault J. P. Girault
Phone: 32-21-71-71
Societe Europeenne de Propulsion
Div. Propulsion a Liquides et Espace
B. P. 802
F-27207 Vernon
FRANCE

Goodyer Michael J. Goodyer
Phone: 703-592374
The University of Southampton
Dept. of Aero. and Astro.
Hampshire S05 5NH
ENGLAND

Halbach Klaus Halbach
Phone: 415-486-5868
UC Lawrence Berkeley Lab
MS 2-400
Berkeley CA 94720

Hawkey Timothy Hawkey
Phone: 617-661-0540
SatCon Technology Corp.
12 Emily Street
Cambridge MA 02139

Hibner David H. Hibner
Phone: 203-565-2238
Pratt & Whitney
400 Main Street
MS 163-09
East Hartford CT 06108

Holmberg Neil Holmberg
Phone: 804-864-6970
NASA Langley Research Center
Mail Stop 457
Hampton VA 23665-5225

Givan Garry Givan
Phone: 513-255-1286
US Air Force
WL/POSL
Wright Patterson AFB OH 45433-6563

Groom Nelson J. Groom
Phone: 804-864-6613
NASA Langley Research Center
Mail Stop 161
Hampton VA 23665-5225

Hampton Roy D. Hampton
Phone: 804-924-3767
University of Virginia
ROMAC Labs, Mech & Aero Engrg
Thornton Hall, McCormick Road
Charlottesville VA 22903

He Jianliang He
Phone: 708-972-2558
Argonne National Laboratory
9700 S. Cass Avenue
Bldg. 362
Argonne IL 60439

Hollis R. L. Hollis
Phone: 914-945-1653
IBM
T. J. Watson Research Center
P. O. Box 218
Yorktown Heights NY 10598

Horwath T. G. Horwath
Phone: 703-371-3531
TG&C Associates
1 Cessna Lane
Falmouth VA 22405

Howard John D. Howard
Phone: 609-921-2792
VSE International
127 McCosh Circle
Princeton NJ 08540

Ishikawa Hideyuki Ishikawa
Phone: 313-454-1500
American Koyo Corp.
47771 Halyard
Plymouth MI 48170

Jensen Carol Jensen
Phone: 818-302-9705
Southern California Edison
P. O. Box 800/Room 455G01
2244 Walnut Grove Avenue
Rosemead CA 91770

Joffe Benjamin Joffe
Phone: 818-354-6444
Jet Propulsion Laboratory
4800 Oak Grove Drive
MS 251
Pasadena CA 91109-8099

Johnson Dexter Johnson
Phone: 216-433-6046
NASA Lewis Research Center
21000 Brookpark Road
Mail Stop 23-3
Cleveland OH 44135

Jones Brian R. Jones
Phone: 415-423-3058
Lawrence Livermore Nat. Laboratory
P. O. Box 808
Livermore CA 94550

Jordan Thomas L. Jordan
Phone: 804-864-4713
NASA Langley Research Center
MS 238
Hampton VA 23665-5225

Joshi Prakash B. Joshi
Phone: 508-689-0003
Physical Sciences, Inc.
20 New England Business Center
Andover MA 01810

Joshi Suresh M. Joshi
Phone: 804-864-6608
NASA Langley Research Center
Mail Stop 230
Hampton VA 23665-5225

Judd Michael Judd
Phone: 617-981-7734
MIT Lincoln Laboratory
P.O. Box 73
77 Massachusetts Avenue
Lexington MA 02173

Juengst Carl D. Juengst
Phone: 206-773-8602
Boeing Aerospace
P. O. Box 34113
Mail Stop 82-24
Seattle WA 98124-1113

Kaplan Nicholas Kaplan
Phone: 301-628-3481
AAI Corporation
5401 Linton Road
Sykesville MD 21784

Keckler Claude R. Keckler
Phone: 804-864-1716
NASA Langley Research Center
Mail Stop 479
Hampton VA 23665-5225

Keesee John Keesee
Phone:
Magnetic Bearings, Inc.
609 Rock Road
Radford VA 24141

Kelliher Warren C. Kelliher
Phone: 804-864-4172
NASA Langley Research Center
Mail Stop 416A
Hampton VA 23665-5225

Kilgore Allen Kilgore
Phone: 804-864-5033
Vigyan, Inc.
30 Research Dr.
Hampton VA 23666

Kilgore Robert A. Kilgore
Phone: 804-864-5020
NASA Langley Research Center
Mail Stop 274
Hampton VA 23665-5225

Kipp Ronald W. Kipp
Phone: 215-824-4887
Kingsbury, Inc.
10385 Drummond Road
Philadelphia PA 19154

Kneschke Tristan Kneschke
Phone: 215-542-0700
LTK Engineering Services
Two Valley Square, Suite 300
512 Township Lane Road
Blue Bell PA 19422

Knight Josiah D. Knight
Phone: 919-660-5337
Duke University
Dept. of Mech. Engrg & Matrl Science
Durham NC 27706

Knolle Ernst G. Knolle
Phone: 415-871-9816
Knolle Magnettrans
2691 Sean Court
San Francisco CA 94080

Knospe Carl Knospe
Phone: 804-982-2603
University of Virginia
Dept. of Mech. & Aero. Engrg
Thornton Hall, McCormick Road
Charlottesville VA 22903

Kroeger John C. Kroeger
Phone: 602-561-3175
Honeywell Satellite Systems
P. O. Box 52199
Phoenix AZ 85072-2199

Kuzin Alexander V. Kuzin
Phone: 095-297-6511 (fax)
Moscow Aviation-Tech. Institute
Subfaculty "Microprocessor Systems,
Electronics, and Electrical Engg."
Petrovka, 27, Moscow, K31 103737
U.S.S.R.

Larsonneur Rene Larsonneur
Phone: 01-2562539
Mechatronics Group
Robotics Institute
ETH Zurich
Zurich CH-8092
SWITZERLAND

Lewis Pete Lewis
Phone: 804-864-7238
NASA Langley Res. Cen.
MS 440
Hampton VA 23665-5225

Meeks Crawford R. Meeks
Phone: 818-886-0250
AVCON
19151 Parthenia Street
Suite G
Northridge CA 91324

Melzer Eckhard B. Melzer
Phone: 551-709-2142
German Aerospace Research Establishment
Central Division Windtunnels
W-3400
Gottingen
GERMANY

Motter Mark Motter
Phone: 804-864-6978
NASA Langley Research Center
Mail Stop 442
Hampton VA 23665-5225

Nelik Lev Nelik
Phone: 908-859-7019
Ingersoll-Rand Company
Advanced Tech. Research and Dev.
942 Memorial Parkway
Phillipsburg NJ 08865

Lashley Christopher M. Lashley
Phone: 301-982-2093
Fare, Inc.
4716 Pontiac St. Suite 304
College Park MD 20740

McMichael Chase K. McMichael
Phone: 713-743-8262
Texas Center for Superconductivity
University of Houston
4800 Calhoun
Houston TX 77204-5506

Meier R. H. Meier
Phone: 614-392-8382
Cooper Industries
105 North Sandusky Street
Mount Vernon OH 43050

Morris Michelle L. Morris
Phone: 804-864-4179
NASA Langley Research Center
MS 416A
Hampton VA 23665-5225

Muto Masai Muto
Phone: 3-5276-6785
Railway Technical Research Inst.
Hiei-Kudan-Kita Bldg. 5F,
4-1-3, Kudan-Kita
Tokyo 102
JAPAN

Neumeyer Charles L. Neumeyer
Phone: 212-839-1643
Ebasco Services, Inc.
2 World Trade Center
New York NY 10048

Nguyen Tiep Nguyen
Phone: 704-547-4371
Univ. of North Carolina - Charlotte
Precision Engineering - ARC
Charlotte NC 28223

Oman Henry Oman
Phone: 206-878-4458
Boeing Aerospace and Electronics
19221 Normandy Park Dr., S. W.
Seattle WA 98166

Owen Andrew K. Owen
Phone: 415-321-5630
Complere Inc.
P. O. Box 1697
Palo Alto CA 94302

Paden Prof. Brad Paden
Phone: (805) 893-8165
Univ of CA
Dept. of Mech. Engg
Santa Barbara CA 93106-5070

Pang Da-Chen Pang
Phone: 301-405-5327
University of Maryland
Department of Mech. Engg.
College Park MD 20742

Pelrine Dr. Ronald E. Pelrine
Phone: 415-859-3360
SRI International
333 Ravenswood Avenue
EL137
Menlo Park CA 94025

Petukhova Irina A. Petukhova
Phone: 06452-9-6193
Severodonetsk Manuf. Assoc. "AZOT"
5, Chimikov,
Severodonetsk 349940
U.S.S.R.

Poovey Tony Poovey
Phone: 704-547-4371
Univ. of North Carolina-Charlotte
Precision Engineering - ARC
Charlotte NC 28223

Price Douglas B. Price
Phone: 804-864-6605
NASA Langley Research Center
Mail Stop 161
Hampton VA 23665-5225

Putman Thomas H. Putman
Phone: 412-256-1169
Westinghouse Electric Corp.
1310 Beulah Road
Science and Technology Center
Pittsburgh PA 15235

Queen M. A. Queen
Phone: 704-547-4371
University of North Carolina
Precision Engineering - ARC
Charlotte NC 28223

Raffi Rhonda C. Raffi
Phone: 617-661-0541
SatCon Technology Corporation
12 Emily Street
Cambridge MA 02139-4507

Rao Dantam K. Rao
Phone: 518-785-2489
Mechanical Technology, Inc.
968 Albany Shaker Road
Latham NY 12110

Reid John B. Reid
Phone: (415) 568-1500
United Magnet Tech.
1824 Woodsdale Dr.
Concord CA 94521

Richey Albert E. Richey
Phone: 518-456-5456
Intermagetics General Corp.
P.O. Box 566
Guilderland NY 12084

Ritter Jim Ritter
Phone:
NASA Langley Res. Ctr.
MS 904
Hampton VA 23665-5225

Rock Col. J. C. Rock
Phone:
Dept. of the Air Force
6410 McKeon
San Antonio TX 78218

Roland J. P. Roland
Phone: 1-34-92-27-48
Aerospatiale
Route de Verneuil 78
Etablissement des Mureaux, BP96
78133 Les-Mureaux
FRANCE

Rosado Lewis Rosado
Phone: 513-255-6519
US Air Force
WL/POSL
Wright Patterson AFB OH 45433-6563

Rothwarf Frederick Rothwarf
Phone: 703-758-0247
ATE, Ltd.
11722 Indian Ridge Road
Reston VA 22091

Salcudean S. E. Salcudean
Phone: 604-822-3243
University of British Columbia
Department of Electrical Engineering
2356 Main Mall
Vancouver, B. C. V6T-1W5
CANADA

Sanders Clark Sanders
Phone: 704-547-4371
Univ. of North Carolina at Charlotte
Precision Engineering - ARC
Charlotte NC 28223

Schott Timothy D. Schott
Phone: 804-864-4715
NASA Langley Research Center
Mail Stop 238
Hampton VA 23665-5225

Scott Michael A. Scott
Phone: 804-864-4347
NASA Langley Research Center
MS 230
Hampton VA 23665-5225

Scurlock Ralph G. Scurlock
Phone: 703-592-046
The University of Southampton
Institute of Cryogenics
Hampshire SO9 5NH
ENGLAND

Shmilovich Alex M. Shmilovich
Phone: 301-309-0230
Maglev Technology, Inc.
14160 Saddle River Dr.
Gaithersburg MD 20878

Stephens Stuart Stephens
Phone: 612-544-2721
Fluidyne Engg.
5900 Olson Mem. Hwy
Minneapolis MN 55422

Takahata Ryoichi Takahata
Phone: 0729-77-4094
Koyo Seiko Co., Ltd.
Research & Development Center
24-1 Kokubuhiganjyo-cho
Kashiwara, Osaka 582
JAPAN

Tcheng Ping Tcheng
Phone:
NASA Langley Res. Cent.
MS 238
Hampton VA 23665-5225

Thevenot Wayne Thevenot
Phone: 202-737-9300
Maglev USA
1455 Pennsylvania Ave.
Washington DC 20024

Shewfelt Kurt Shewfelt
Phone:
Allied Signal Aerosp.
2525 W. 190th St.
Dept. 35, MS T53
Torrance, CA 90509

Siegwart Roland Y. Siegwart
Phone: 01 256 35 64
Institute of Robotics
Mechatronics Group
ETH Zurich
Zurich CH-8092
SWITZERLAND

Studer Phillip A. Studer
Phone: 301-593-7241
Magnetic Concepts
10313 Ridgemoor Drive
Silver Spring MD 20901

Tanaka Hisashi Tanaka
Phone: 81-425-73-7205
Railway Technical Research Institute
2-8-38 Hikari-cho
Kokubunji-shi
Tokyo
JAPAN

Terentiev Alexander N. Terentiev
Phone:
Institute of Chemical Physics
U.S.S.R. Academy of Sciences
117977 Moscow
U.S.S.R.

Tozoni Oleg Tozoni
Phone: 301-309-0230
Maglev Technology, Inc.
14160 Saddle River Dr.
Gaithersburg MD 20878

Trumper David L. Trumper
Phone: 704-547-4324
Univ. of North Carolina at Charlotte
Precision Engineering - ARC
Room 222
Charlotte NC 28223

Unman Prof. Daniel J. Inman
Phone: (716) 636-2593
Univ. of Buffalo
Dept. of Mech and
Aerosp. Engg.
Buffalo NY 14260

Vij Kewal K. Vij
Phone: 403-250-4792
NOVA Husky Research Corp.
2928 - 16th Street N.E.
Calgary, Alberta T2E 7K7
CANADA

Whitestone Robert C. Whitestone
Phone: 301-267-3458
David Taylor Research Center
Code 2712
Annapolis MD 21402

Yeh Ting-Jen Yeh
Phone:
MIT
77 Massachusetts Avenue
Room 35-332
Cambridge MA 02139
617-253-2108

Zhao Hong-Bin Zhao
Phone: 861-2561144-2594
Tsinghua University
Dept. of Engg Phys.
Beijing 100084
CHINA

Tryggvason Bjarni Tryggvason
Phone: 613-993-4106
Canadian Space Agency
P. O. Box 7014
Station V
Vanier Ontario K1L 8E2
CANADA

Vaidya Subhash R. Vaidya
Phone: 215-758-7355
Gardner Cryogenics
2136 City Line Road
Bethlehem PA 18017

Wassermann Johann Wassermann
Phone: VIENNA-58801-5478
Technical University of Vienna
Wiedner-Hauptstrasse 8-10
Vienna A-1040
AUSTRIA

Won Dr. Dong-Yeon Won
Phone: 042-820-2000
Korea Atomic Energy
Research Institute
P. O. Box 7
Daejun, 305-353
KOREA

Youcef-Toumi Kamal Youcef-Toumi
Phone: 617-253-2216
Massachusetts Institute of Tech.
77 Massachusetts Avenue
Room 35-233
Cambridge MA 02139

Zydron Millard Zydron
Phone: 804-688-8693
Newport News Shipb
E52 B600
4101 Washington Ave.
Newport News VA 23607

REPORT DOCUMENTATION PAGE			Form Approved OMB No. 0704-0188	
Public reporting burden for this collection of information is estimated to average 1 hour per response, including the time for reviewing instructions, searching existing data sources, gathering and maintaining the data needed, and completing and reviewing the collection of information. Send comments regarding this burden estimate or any other aspect of this collection of information, including suggestions for reducing this burden, to Washington Headquarters Services, Directorate for Information Operations and Reports, 1215 Jefferson Davis Highway, Suite 1204, Arlington, VA 22202-4302, and to the Office of Management and Budget, Paperwork Reduction Project (0704-0188), Washington, DC 20503.				
1. AGENCY USE ONLY (Leave blank)	2. REPORT DATE May 1992	3. REPORT TYPE AND DATES COVERED Conference Publication		
4. TITLE AND SUBTITLE International Symposium on Magnetic Suspension Technology		5. FUNDING NUMBERS 590-14-11-02		
6. AUTHOR(S) Nelson J. Groom and Colin P. Britcher, Editors				
7. PERFORMING ORGANIZATION NAME(S) AND ADDRESS(ES) NASA Langley Research Center Hampton, VA 23665-5225		8. PERFORMING ORGANIZATION REPORT NUMBER L-17092		
9. SPONSORING/MONITORING AGENCY NAME(S) AND ADDRESS(ES) National Aeronautics and Space Administration Washington, DC 20546-0001		10. SPONSORING/MONITORING AGENCY REPORT NUMBER NASA CP-3152, Part 2		
11. SUPPLEMENTARY NOTES Nelson J. Groom: Langley Research Center, Hampton, VA; Colin P. Britcher: Old Dominion University Research Foundation, Norfolk, VA.				
12a. DISTRIBUTION/AVAILABILITY STATEMENT Unclassified-Unlimited Subject Category 18		12b. DISTRIBUTION CODE		
13. ABSTRACT (Maximum 200 words) In order to examine the state of technology of all areas of magnetic suspension and to review related recent developments in sensors and controls approaches, superconducting magnet technology, and design/implementation practices, a five-day International Symposium on Magnetic Suspension Technology was held at the Langley Research Center in Hampton, Virginia, on August 19-23, 1991. The symposium included 17 technical sessions in which 55 papers were presented. The technical sessions covered the areas of bearings, sensors and controls, microgravity and vibration isolation, superconductivity, manufacturing applications, wind tunnel magnetic suspension systems, magnetically levitated trains (MAGLEV), space applications, and large gap magnetic suspension systems. A list of attendees appears at the end of the document.				
14. SUBJECT TERMS Magnetic bearings; Magnetic suspension; Large gap magnetic suspension; Small gap magnetic suspension; Sensors, Superconducting magnetic suspension systems; Control systems			15. NUMBER OF PAGES 504	
			16. PRICE CODE A22	
17. SECURITY CLASSIFICATION OF REPORT Unclassified	18. SECURITY CLASSIFICATION OF THIS PAGE Unclassified	19. SECURITY CLASSIFICATION OF ABSTRACT Unclassified	20. LIMITATION OF ABSTRACT	

NSN 7540-01-280-5500

Standard Form 298 (Rev. 2-89)
Prescribed by ANSI Std. Z39-18
298-102

NASA-Langley, 1992

PRECEDING PAGE BLANK NOT FILMED